Cyprus University of Technology
Faculty of Engineering

Doctoral Dissertation

Evaluation of a Magnetic Resonance Imaging guided focused ultrasound system for prostate ablation

Theocharis Drakos

Limassol, September 2021

CYPRUS UNIVERSITY OF TECHNOLOGY

FACULTY OF ENGINEERING

DEPARTMENT OF ELECTRICAL ENGINEERING, COMPUTER ENGINEERING AND INFORMATICS

Doctoral Dissertation

Evaluation of a Magnetic Resonance Imaging guided focused ultrasound system for prostate ablation

Theocharis Drakos

Limassol, September 2021

Approval Form

Doctoral Dissertation

Evaluation of a Magnetic Resonance Imaging guided focused ultrasound system for prostate ablation

Presented by

Theocharis Drakos

Supervisor: Faculty of Engineering, Christakis Damianou, Professor

Signature _____

Member of the committee: Faculty of Engineering, Takis Kasparis, Professor

Signature _____

Member of the committee: Faculty of Pure and Applied Sciences, Costas Pattichis, Professor

Signature _____

Cyprus University of Technology

Limassol, September 2021

Copyrights

Acknowledgements

First and foremost, I am extremely grateful to my supervisor, Prof. Christakis Damianou for his invaluable supervision, support, enthusiastic encouragement and useful critiques during my PhD study. His immense knowledge and plentiful experience have encouraged me in all the time of my academic research.

Additionally, I would like to express gratitude to my lab colleagues and research team (Marinos Giannakou, Antria Filippou, Nikolas Evripidou, Anastasia Antoniou, and Giorgos Evripidou) for their collaborative efforts and great source of support during my dissertation. Special thanks to Dr. Marinos Giannakou for the tremendous assistance with the development of the robotic device.

My grateful thanks are also extended to Dr. Georgios Menikou for his valuable guidance related to the MRI experiments (MR thermometry results and MR compatibility of the robotic device) and the veterinarian Kyriakos Spanoudes for the assistance to the animal experiments that were performed during this research.

I wish to thank all the people whose assistance was a milestone in the completion of this project.

Last but not the least, I would like to thank my family and friends for all the unconditional support all these years to complete my dissertation.

Abstract in English

Prostate cancer is one of the most prevalent health threats for men worldwide. Although there are successful treatments for prostate cancer, a percentage of cases of men diagnosed with prostate cancer is led to death. Since there is an increasing trend in men being diagnosed with prostate cancer, the development of new treatments with higher successful rates and reduced side effects leading to a better quality of life of men is of utmost importance. In this dissertation, high-intensity focused ultrasound (HIFU) is recommended for the treatment of prostate cancer. The technology was combined with medical robotics and the treatment procedure was guided using Magnetic Resonance Imaging (MRI) which is known to be superior than ultrasound guidance. A 4-degrees of freedom (DOF) endorectal robotic system was 3D-designed and developed to treat prostate cancer at early stage.

Prior to the evaluation of the robotic system, agar-based tissue-mimicking materials were developed and characterized so as to mimic human tissue. The effect of agar, silicon dioxide, and evaporated milk concentration on the acoustic and thermal properties of tissue-mimicking materials was investigated. A new tissue-mimicking material containing agar and wood powder was proposed for Magnetic Resonance-guided Focused Ultrasound (MRgFUS) applications. The acoustic, thermal, and MR properties of the agar/wood powder tissue-mimicking material were estimated. Wood powder was found to enhance the absorption and attenuation coefficient of agar-based phantoms. The new developed phantom matched adequately the acoustic and thermal properties of human tissues and was evaluated for MRgFUS thermal protocols. A new method to estimate ultrasonic absorption coefficient of phantoms and tissues is described. The absorption coefficient of the developed phantoms was measured using this new, accurate, and fast technique. The change in absorption coefficient according to the variation of agar, silicon dioxide, and evaporated milk was investigated. The agar was found to best control the absorption coefficient while the increase of agar, silicon dioxide (up to 4 %) and evaporated milk concentration resulted in an increase of the absorption coefficient of agar-based tissue-mimicking materials.

The initial evaluation procedure involved the selection and evaluation of the focused transducer. A 3.2 MHz transducer was selected after being evaluated through simulations and experiments in agar-based phantoms and excised tissues. The near-field heating of the transducer was also investigated and a 40 s time delay resulted in safe temperatures in the near-field region. The MR compatibility of the 4-DOF robotic system was tested for MR sequences

that are used to obtain MR thermometry data during a treatment. There was an insignificant drop to the signal-to-noise ratio of the MR thermometry images and therefore the 4-DOF robotic device was found to be MR compatible and can be used in MRgFUS prostate cancer therapies. The accuracy of the robotic device of the two computer-controlled axes (X and Θ) was estimated. At small linear movements (1 mm) of the X-axis, the maximum error was calculated at 73 μm while at small angular movements (1^o) of the Θ-axis, the maximum error was 0.09^o. The robotic device is capable of performing multiple sonications with high accuracy. Finally, the robotic system was evaluated in phantoms and excised tissues in a laboratory setting and MRI environment. Discrete and overlapping lesions were produced with variable lesion diameter and length, demonstrating the efficacy of the system to produce reproducible and controllable lesions. The evaluation was completed with the *in vivo* efficiency of the system, utilizing a rabbit thigh model.

Keywords: prostate cancer, focused ultrasound, MRI, tissue-mimicking materials, absorption coefficient, MR robotic system

Abstract in Greek

Ο καρκίνος του προστάτη είναι μία από τις πιο διαδεδομένες απειλές για την υγεία των ανδρών παγκοσμίως. Παρόλο που υπάρχουν επιτυχημένες θεραπείες για την αντιμετώπιση του καρκίνου του προστάτη, ένα ποσοστό των περιπτώσεων ανδρών που έχουν διαγνωστεί με καρκίνο του προστάτη οδηγείται στο θάνατο. Δεδομένου ότι υπάρχει μία αυξανόμενη τάση στους άνδρες να διαγιγνώσκονται με καρκίνο του προστάτη, η ανάπτυξη νέων θεραπειών με υψηλότερο ποσοστό επιτυχίας και μειωμένες παρενέργειες που οδηγούν σε καλύτερη ποιότητα ζωής των ανδρών είναι ύψιστης σημασίας. Σε αυτή τη διατριβή, συνιστάται η τεχνολογία υπέρηχου υψηλής έντασης για τη θεραπεία του καρκίνου του προστάτη. Η τεχνολογία συνδυάστηκε με ιατρική ρομποτική και η διαδικασία θεραπείας καθοδηγήθηκε χρησιμοποιώντας μαγνητική τομογραφία η οποία είναι γνωστό ότι είναι ανώτερη από την καθοδήγηση με διαγνωστικούς υπέρηχους. Ένα ενδοπρωκτικό ρομποτικό σύστημα με 4 βαθμούς ελευθερίας σχεδιάστηκε σε τρισδιάστατο λογισμικό και αναπτύχθηκε για τη θεραπεία του καρκίνου του προστάτη σε πρώιμο στάδιο.

Πριν από την αξιολόγηση του ρομποτικού συστήματος, αναπτύχθηκαν και χαρακτηρίστηκαν πλασματικά υλικά με βάση την αγαρόζη ώστε να μιμούνται τον ανθρώπινο ιστό. Διερευνήθηκε η επίδραση της αγαρόζης, του διοξειδίου του πυριτίου, και της συγκέντρωσης του εξατμισμένου γάλακτος στις ακουστικές και θερμικές ιδιότητες των πλασματικών υλικών. Ένα νέο υλικό μίμησης ιστού που περιέχει αγαρόζη και σκόνη ξύλου προτάθηκε για εφαρμογές MRgFUS. Υπολογίστηκαν οι ακουστικές, θερμικές, και μαγνητικές ιδιότητες του υλικού μίμησης ιστού αγαρόζης/σκόνης ξύλου. Η σκόνη ξύλου βρέθηκε ότι βελτιώνει τον συντελεστή απορρόφησης και εξασθένησης των πλασματικών υλικών με βάση την αγαρόζη. Το νέο ανεπτυγμένο πλασματικό υλικό ταιριάζει επαρκώς με τις ακουστικές και θερμικές ιδιότητες των ανθρώπινων ιστών και αξιολογήθηκε για θερμικά πρωτόκολλα MRgFUS. Περιγράφεται μία νέα μέθοδος για τον υπολογισμό του συντελεστή απορρόφησης υπερήχων των πλασματικών υλικών και ιστών. Ο συντελεστής απορρόφησης των ανεπτυγμένων πλασματικών υλικών μετρήθηκε χρησιμοποιώντας μία νέα, ακριβή και γρήγορη τεχνική. Διερευνήθηκε η αλλαγή του συντελεστή απορρόφησης σύμφωνα με τη διακύμανση της αγαρόζης, του διοξειδίου του πυριτίου και του εξατμισμένου γάλακτος. Η αγαρόζη βρέθηκε να ελέγχει καλύτερα τον συντελεστή απορρόφησης ενώ η αύξηση της αγαρόζης, του διοξειδίου του πυριτίου (έως 4%) και της συγκέντρωσης του εξατμισμένου γάλακτος οδήγησε σε αύξηση του συντελεστή απορρόφησης των πλασματικών υλικών με βάση την αγαρόζη.

Η αρχική διαδικασία αξιολόγησης περιλάμβανε την επιλογή και αξιολόγηση του εστιασμένου μορφοτροπέα. Ένας μορφοτροπέας με συχνότητα 3.2 MHz επιλέχθηκε μετά από αξιολόγηση μέσω προσομοιώσεων και πειραμάτων σε πλασματικά υλικά και ιστούς. Διερευνήθηκε επίσης η θέρμανση σε κοντινό πεδίο εφαρμογής του μορφοτροπέα και η χρονική καθυστέρηση 40 δευτερολέπτων βρέθηκε αρκετή για δημιουργία θερμοκρασιών που δεν επηρεάζουν υγιείς ιστούς στην περιοχή κοντά στο πεδίο εφαρμογής των υπερήχων. Η μαγνητική συμβατότητα του ρομποτικού συστήματος δοκιμάστηκε για αλληλουχίες μαγνητικού τομογράφου που χρησιμοποιούνται για τη λήψη δεδομένων θερμομετρίας MR κατά τη διάρκεια μίας θεραπείας. Υπήρξε μια ασήμαντη πτώση στην αναλογία σήματος ως προς το θόρυβο των εικόνων θερμομετρίας και συνεπώς η ρομποτική συσκευή αποδείχθηκε ότι είναι συμβατή με μαγνητικό τομογράφο για χρήση της τεχνολογίας MRgFUS σε θεραπείες καρκίνου του προστάτη. Υπολογίστηκε η ακρίβεια της ρομποτικής συσκευής των δύο ελεγχόμενων από υπολογιστή αξόνων (Χ και Θ). Σε μικρές γραμμικές κινήσεις (1 mm) του άξονα Χ, το μέγιστο σφάλμα υπολογίστηκε στα 73 μm ενώ σε μικρές γωνιακές κινήσεις (1^o) του άξονα Θ, το μέγιστο σφάλμα ήταν 0.09^o. Η ρομποτική συσκευή μπορεί να εκτελεί πολλαπλές ριπές υπερήχων με υψηλή ακρίβεια λόγω των μηχανισμών αργής κίνησής της. Τέλος, το ρομποτικό σύστημα αξιολογήθηκε σε πλασματικό υλικό και ιστούς τόσο σε εργαστηριακό περιβάλλον όσο και σε περιβάλλον μαγνητικής τομογραφίας. Διακριτές και αλληλεπικαλυπτόμενες βλάβες παρήχθησαν με μεταβλητή διάμετρο και μήκος αλλοίωσης, αποδεικνύοντας την αποτελεσματικότητα του συστήματος για την παραγωγή αναπαραγώγιμων και ελεγχόμενων βλαβών. Η αξιολόγηση ολοκληρώθηκε με την *in vivo* απόδοση του συστήματος, χρησιμοποιώντας ένα μοντέλο μηρού κουνελιού.

Table of Contents

List of Tables

List of Figures

List of Abbreviations

Abbreviation	Definition
2D	2-Dimensional
3D	3-Dimensional
ABS	Acrylonitrile Butadiene Styrene
ADC	Apparent Diffusion Coefficient
AJCC	American Joint Committee on Cancer
BPE	Benign Prostatic Enlargement
BPH	Benign Prostatic Hyperplasia
BPO	Benign Prostatic Obstruction
BSA	Bovine Serum Albumin
BSE	Back-Scattered Electron
CCW	Counterclockwise
CW	Clockwise
DAQ	Data Acquisition
DC	Direct Current
DFOV	Displayed Field of View
DICOM	Digital Imaging and Communications in Medicine
DOF	Degrees of Freedom
Dox	Doxorubicin
DRE	Digital Rectal Exam
DWI	Diffusion-Weighted Imaging
EBRT	External Beam Radiotherapy
EPI	Echo-Planar Imaging
ESWL	Extracorporeal Shockwave Lithotripsy

ETL	Echo Train Length
FDA	Food and Drug Administration
FOV	Field of View
FRFSE	Fast Recovery Fast Spin Echo
FSE	Fast Spin Echo
FSPGR	Fast Spoiled Gradient
FUS	Focused Ultrasound
GnRH	Gonadotropin-Releasing Hormone
GRE	Gradient Echo
H & E	Hematoxylin and Eosin
HIFU	High-Intensity Focused Ultrasound
IMRT	Intensity-Modulated Radiation Therapy
IR-FSE	Inversion Recovery Fast Spin Echo
M-HIFU	Mechanical-HIFU
mpMRI	multiparametric MRI
MRgFUS	Magnetic Resonance-guided Focused Ultrasound
MRI	Magnetic Resonance Imaging
NEMA	National Electrical Manufacturers Association
NEX	Number of Excitations
NIPAM	N-isopropylacrylamide
NUI	Non-Uniformity Index
PC	Prostate Cancer
PD	Proton Density
pFUS	pulsed Focused Ultrasound
PIA	Proliferative Inflammatory Atrophy
PIN	Prostatic Intraepithelial Neoplasia

PRF	Proton Resonance Frequency
PRFS	Proton Resonance Frequency Shift
PSA	Prostate-Specific Antigen
PVA	Polyvinyl Alcohol
QOL	Quality of Life
rBW	receiver Bandwidth
RF	Radiofrequency
ROI	Region of Interest
SE	Spin Echo
SEM	Scanning Electron Microscopy
SMA	Subminiature version A
SNR	Signal-to-Noise Ratio
TE	Echo Time
TI	Inversion Time
TMM	Tissue-Mimicking Material
TPM	Template Prostate Mapping
TR	Repetition Time
TRUS	Transrectal Ultrasound
TTM	Transient Thermoelectric Method
US	Ultrasound
USB	Universal Serial Bus

1 Introduction

1.1 Introduction to the doctorate thesis

The prostate is a part of the male reproductive system and an exocrine gland which encloses the male urethra. It is located just beneath the bladder, in front of the rectum, and it is the major male reproductive gland related to male fertility. The prostate gland is essential for the necessary functions of male fertility and is a direct target of numerous prevalent benign and malignant diseases including prostatitis, benign prostatic hyperplasia (BPH), and prostate cancer (PC). Among all prostatic diseases, prostatitis might affect fertility by a higher potential. Prostate inflammation might have a causative role in the complex process of prostate degeneration leading to prostate carcinogenesis. The remodeling of prostate tissue caused by an inflammatory injury might promote the structural changes that are commonly associated with both benign and malignant disease.

Worldwide, PC has become one of the most common and dangerous cancer forms that affect males' health life and if it is not diagnosed early and no treatments are followed, it can lead to death. It is well known that the majority of PC incidence occurs mostly in elderlies. For that reason, doctors recommend men over a certain age (around 50 years-old) to undertake appropriate diagnostic tests. The sooner the patient is diagnosed with PC, the shorter and more successful the treatment will be. For example, in Cyprus, as reported from the local Ministry of Health in 2013 [1], an epidemiologic study has revealed increasing cancer trends with PC being the most common in men. In 2012, 489 men were diagnosed with PC, with this number accounting as the largest percentage (28 %) of men's cases diagnosed with cancer, while the year after this number slightly increased to 494 which constituted a 28.3 %. In Europe, 345,000 new cases of PC were estimated in 2012 with these cases accounting for 24 % of all new cancers in the same year [2]. In 2015, the estimated number of new PC cases was about 365,000. Currently, in statistical research in the United States, it is estimated that this year 191,930 men will be diagnosed with PC and 33,330 deaths will occur [3].

The study of prostate anatomy and the corresponding cancer that might grow either at the prostate gland or at the surrounding regions has been important for the development of new therapies that overcome the health issue of male cancer. Several invasive, minimally invasive, and non-invasive treatments have been tested, investigated, and developed over the last decades. Ordinary treatments could be either the delivery of special drugs to regulate specific

cells or in the worst-case, surgery. Hormone therapy (or androgen deprivation therapy) is a special therapy that controls the level of male hormones. Testosterone is the main male hormone that is related to the prostate gland [4]. PC is hormone-sensitive or hormone-dependent and therefore more production of testosterone helps the prostate cancerous cells to grow uncontrollably. The target of hormone therapy is to reduce the production rate of testosterone in order to stop feeding the cancerous cells and thus eliminate or delay the growth of PC. This reduction in hormone production rate can be achieved through the use of medicines or surgery. Prostate surgery (or prostatectomy) is the other ordinary treatment of PC [5]. During that surgical procedure, the prostate gland can be completely or partially removed. The complete removal of the prostate gland could eliminate the possibility of metastasis when cancer has not spread beyond the prostate gland to nearby sites (usually to lymph nodes). In that case, along with the entire prostate gland and seminal vesicles, the regional lymph nodes are additionally removed.

In a modern technological age where the development of technology is increasing rapidly, specialists, engineers, and doctors work together to create and develop new, more technologically advanced treatments for PC. It is important for patients to have a number of options so that in consultation with their private doctor to decide the treatment that will pursue. Even though the treatment decision will be a divergent decision of the patient, a team of doctors and other professionals discuss and recommend the best treatment options. A variety of factors are taken into account including the location of cancer, how far it has grown or spread (stage), the type of cancer, Gleason score, prostate-specific antigen (PSA) level, age, patient preference, general health, and level of fitness.

The existing therapies of PC can be classified into whole prostate gland therapy and focal therapy. Expectant management or active surveillance [6], surgery [5] (radical prostatectomy, robotic-assisted laparoscopic radical prostatectomy), radiotherapy/brachytherapy [7], and cryosurgery [8] belong to the whole gland therapy, while vascular targeted photodynamic therapy [9], transurethral microwave therapy [9], irreversible electroporation [10], transurethral and transrectal HIFU [11-13] are therapies which can ablate a focal region of the prostate gland. Focal therapy can reduce the amount of damage to the prostate gland and healthy surrounding tissues while still treating the tumor effectively. The targeted tumor is known as the index lesion which is often defined as the largest tumor with the highest grade. Other secondary smaller tumors might exist in the prostate gland and focal therapy is superior in those cases, compared to whole gland therapies.

Focal therapy is a treatment option for patients with early localized PC who previously had to choose between active surveillance and more invasive treatment with a greater risk for side effects. In general, focal therapy is an overall term referring to several minimally invasive treatments that target only those parts of the prostate gland where cancer is diagnosed. The treatment's goal is to ablate, or destroy small tumors within the prostate while minimizing damage to adjacent tissues and leaving them intact. Evaluation of this technology is essential before translating preclinical knowledge to clinical practice on humans. Conceptually, focal therapy has the potential to minimize toxicity associated with the treatment without compromising cancer-specific outcomes. Moreover, it has a lower risk for side effects such as impotence, urinary incontinence, and decreased bowel function compared to other traditional therapies. Some limitations include the inability to accurately stage or grade cancer, suboptimal imaging capabilities, uncertainty about the natural history of untreated cancer foci, post-treatment monitoring challenges, and lack of quality of life (QOL) data compared to alternative treatment strategies. Clinical use of HIFU in PC treatment has been tested and approved by many health organizations in both Europe and Asia [13] for years. Some promising results of HIFU were also achieved in managing various malignancies, including pancreas, liver, kidney, breast, bone, and essential tremor [14]. HIFU uses the energy of high-intensity sound waves to create heat and destroy cancer cells. The local tissue temperature could be elevated to higher than 60 °C by thermal effect. The thermal effect causes tumor cell destruction via coagulation necrosis in HIFU therapy. The mechanical effects include micro-streaming, radiation force, and cavitation. There are three main categories of HIFU devices for clinical use, including extracorporeal, interstitial, and trans-rectal. Extracorporeal probes are used to target tumor lesions through the skin, the trans-rectal instrument is designed to treat prostate tumors and interstitial devices are used to treat esophageal tumors and tumors of the biliary duct [15]. HIFU is a minimally invasive, non-ionizing, and outpatient procedure giving the advantage to patients to have a quick recovery. It can be repeated in the future and unlike some other PC treatments, it does not limit the option to have radiation therapy or surgical treatment at a later time. This means that HIFU can also be used as a salvage therapy in case other PC treatments fail.

The application of ultrasound (US) in clinics is no longer limited to diagnosis. HIFU is being promoted as the only completely non-invasive and extracorporeal method to treat primary solid tumors and metastatic disease. The key of HIFU treatment is delivering the energy required to raise the tissue temperature to a cytotoxic level sufficiently fast such that the tissue vasculature does not have a significant effect on the extent of cell killing. Large tumors can be treated using

multiple elementary lesions placed side by side, so that the coagulated zones overlap [16]. HIFU systems are operated by specially designed robotic positioning devices in order to follow a pattern for covering a complete tumor area.

Today, there are three commercially available transrectal ultrasound-guided HIFU systems, one transrectal MRgFUS system which has received a CE mark and it is at the clinical trial stage, and one transurethral MRgFUS system which is offered for commercial treatment. The three latest versions of ultrasound-guided systems are the Sonablate 500 (Sonacare Medical, LLC, Charlotte, North Carolina, USA), Ablatherm (EDAP TMS, Lyon, France), and Focal One (EDAP TMS) which is the upgraded version of Ablatherm. These medical systems have already received worldwide approval from many healthcare organizations such as the Food and Drug Administration (FDA), Health Canada, CE mark, Roszdravnadzor, CFDA, CDSCO, MHLW, MFDS, and Taiwan FDA. The only available transurethral MRgFUS system is the Tulsa-Pro (Profound Medical Corp., Mississauga, Canada) which has received CE mark approval for clinical treatments in Oceania and the Middle East. The only transrectal MRgFUS system that has received CE mark is the ExAblate 2100 (Insightec Ltd., Tirat Carmel, Israel). The latest versions of the ultrasound-guided devices use a single probe that houses a focused ultrasound (FUS) for treatment and a non-focused transducer for imaging. Sonablate 500 needs several probe heads to complete a single treatment while the Ablatherm probe is positioned robotically by the physician via an extremely precise software. Moreover, Ablatherm has high accuracy of 0.1 mm, is fully automated, provides three scientifically tested and optimal energy levels for de novo radiation failure or HIFU retreatment conditions and can keep the treatment time under two and a half hours [17]. On the other hand, Sonablate 500 has a significant risk of rectal injury, it requires manual probe movement, it has poor quality and its small treatment field extends treatment time from three and a half hours to five hours. Tulsa-Pro and ExAblate 2100 are devices that use MRI thermal properties as feedback.

The Sonablate 500 system consists of a console (called Sonasource), two transrectal probes of different focal lengths, a probe arm, a multi-axis stepper for probe support and positioning and a pump/chiller for circulating and cooling water [17]. The rectal wall is sensitive to temperature changes and the system provides continuous monitoring of the temperature of the rectal wall and continually measures the distance between the rectal wall and the prostate gland. The transrectal probe houses a single crystal for both imaging and treatment, which also allows for real-time imaging. This is accomplished by using a concave rectangular element cut from a spherical crystal surface that has a central 10 mm diameter segment used for imaging. An

operating frequency of 4 MHz was determined to provide both sufficient image quality and effective treatment.

The Ablatherm device includes a treatment table, a probe positioning system, a US power generator, a cooling system for preservation of the rectal wall, a computerized control module with software, and a treatment and imaging endorectal probe which incorporates both a biplane imaging and treatment transducer. It also has inbuilt controls that correct or stop the treatment procedure automatically as well as adjust the endorectal position of the probe 3-dimensionally (3D) when the probe is too close or far away from the rectal wall. An external motion sensor and internal safety circuits detect any technical malfunction or patient movement and accordingly stop the procedure instantly.

The ExAblate 2100 system includes a treatment table that docks to the MRI scanner with the patient lying supine on the table, an ergonomic cradle (FUS probe and robotic motion unit), an operator console (for treatment monitoring and MR imaging), and a cooling system. This system uses MR imaging and thermometry to ensure that sufficient heat is delivered to the tumor while leaving adjacent tissues unaffected.

Although ultrasound-guided HIFU devices have already been shown they can treat PC, they have the disadvantage of using ultrasonic systems for imaging in order to provide feedback of the prostate during the treatment procedure. This real-time ultrasonic monitoring of the treatment does not provide good tissue to necrotic area contrast and neither provides feedback on temperature change, thus performing the procedure without optimal accuracy. MRgFUS technology utilizes MRI which provides 3D anatomy for precise tumor targeting, thus continuously monitoring the tissue effect for controlled treatment and post-treatment contrast imaging for accurate conduct validation of the treatment. The MRgFUS procedure in clinical manifestation was established for the treatment of symptomatic benign uterine tumor and palliative treatment for patients with painful bone metastases [18]. In this research, MRI was used to monitor the thermal effects of the developed 4- DOF robotic system which, for that reason, should be MR compatible in order to perform PC treatments using FUS under MRI guidance. Therefore, the MR compatibility of the robotic device was tested for its capability to be used in MRgFUS treatments.

1.2 Thesis motivation

The motivation of the current research has been the commercially available HIFU systems that use transrectal probes under ultrasonic imaging and the transfer of these clinical applications to an MRI environment that shows a promising and useful tool for better and more accurate treatment of PC. The 4-DOF robotic device of this thesis is an advanced version of a 2-DOF robotic device that was previously designed and tested for MRgFUS applications [19]. The main goal of this research was to test, modify, improve, and evaluate an MR compatible robotic device for providing PC solutions using FUS.

MRI has advantages over diagnostic US in the HIFU field. Although diagnostic US has few advantages such as real-time monitoring and much lower price, it is not available for thermometry, artifacts can be obvious, while the image quality may become worse during the procedure due to manipulator variability. However, MRI provides clear and high-resolution images with a larger field of view (FOV). Moreover, based on the significant advantages that MRI offers to HIFU application over the US, there is a limitation to the components of the robotic device which must be non-ferromagnetic materials without interfering with the MRI scanner during the treatment procedure. Besides, the robotic device must operate properly without being affected by the strong electromagnetic field of the MRI scanner. The confined physical space of the MRI scanner challenges medical intervention; even the magnets with open architecture provide only a limited working space at the expense of image quality [20]. In the last decade, the use of robots inside the MRI scanner is a very attractive solution; a robot manipulates the intervention instruments while MR images provide continuous feedback on the position of the robot-controlled instruments as well as the procedure of treating a tumor. However, the design of a system operating inside or close to the bore of a high-field MRI scanner is of significant complexity and a challenge for many researchers.

Evaluation of such MR compatible robotic devices before performing preclinical trials and receiving approval for clinical trials, requires experiments on tissue-mimicking materials (TMMs). During this thesis, TMMs have been developed and evaluated to mimic human soft tissue. The developed TMMs have been extensively used to evaluate the 4-DOF robotic system in both laboratory setting and MRI environment.

HIFU is an emerging technology that is being studied for over six decades. This technology features a transducer that focuses high-intensity acoustic waves into a small area, resulting in temperature elevation. The greatest advantage of HIFU is the ability to induce lethal cell

temperatures to the target while sparing the surrounding tissue, completely non-invasive. Besides, the small area covered by the focus has a diameter of approximately 1-3 mm depending on the acoustic parameters, thus it can selectively target small volumes without requiring surgical invasion. With HIFU instead of surgically removing a tumor, US destroys the tumor by raising the local temperature to 60-70 ^{o}C. Different HIFU parameters can be selected depending on the disease. Continuous acoustic waves result in temperature elevation caused by the friction of the ultrasonic waves with the tissue. During the US sonication, the cancer cells on the focus are coagulated and destroyed due to the lethal temperatures that are generated. To monitor the changes in the tissue, MRI is the ideal imaging method because it can detect temperature changes which are very useful for the control of the thermal dosage. Along with the MRI imaging, a robotic system is required to navigate the transducer to the target accurately and reliably. The first systems positioned the transducer with manual mechanisms, but this was inefficient and hard to achieve small spatial changes. A positioning device is proposed for the navigation of the transducer so as to provide accurate targeting for the treatment of PC. Specific limitations must be considered to ensure the safety of a robotic system in the MRI scanner. Due to the strong magnetic field generated by the magnet of the MRI, these devices must be composed of non-magnetic materials in order not to interfere with the imaging coil and avoid creating missile effects. A compact design is also required to fit in the MRI scanner. The device must be adequately accurate for HIFU targeting and reliable while operating in the MRI scanner. The evaluation of the robotic system which was performed during this research remains the most necessary part from all stages of developing a robotic system. During the evaluation, the robotic system was also successfully tested for preclinical therapy.

1.3 Project aim and objectives

As previously mentioned, the main goal of this doctorate thesis was to evaluate a 4-DOF robotic device that is intended to be used at a first stage for the treatment of PC and a later stage for the treatment of BPH. The evaluation of the robotic device included various objectives which are the following, in order in which they were performed:

- Development of an agar/silica/milk phantom to be used as TMM in the experiments.
- Development of agar/wood powder phantom to be used as soft TMM in the experiments.

- Acoustic, thermal, and MR characterization of the agar/silica/milk and agar/wood powder phantom.
- Simulations of candidate spherically-focused transducers using an MRgFUS software.
- Experiments in a laboratory setting in phantoms for evaluating the two candidate spherically-focused transducers.
- *In vitro* experiments in a laboratory setting for evaluating the optimized spherically-focused transducer.
- *In vitro* experiments in a laboratory setting for testing the accuracy of the robotic positioning device.
- Experiments in an MRI scanner for testing the accuracy of the robotic positioning device in a rectum-mimicking phantom.
- Evaluation of the motion of the robotic device using digital calipers and MRI imaging.
- *In vitro* experiments for testing the ability of the robotic device to create ablations in an MRI scanner.
- Evaluation of the MR compatibility of the selected transducer and robotic system.
- *In vivo* experiment in rabbit using the robotic positioning device in an MRI scanner.

1.4 Thesis outline

The first part is a comprehensive introduction to the general subject of this doctoral research, including the main information about this work. The main problem of PC that exists is generally analyzed, existing devices with similar technology are mentioned and the importance and necessity of this research are emphasized.

The second part describes the anatomy of the prostate gland, the diseases that might affect the prostate, and its physiology by mentioning its normal and abnormal functions after cancer appearance. The lobes and zones of the prostate gland are also presented to fully understand the anatomy of the prostate before proceeding to HIFU applications. A bibliographic review of PC including the history of PC, symptoms, statistics, diagnostic techniques, and current therapies (invasive, minimally invasive, and non-invasive) is also described.

The third part includes a brief history of HIFU, basic principles of this technology, advantages and disadvantages, and the guidance methods that are possible to be used in combination with the HIFU technology. The commercially available PC robotic devices are also mentioned. The robotic devices included in this part are both for transrectal and transurethral applications.

Furthermore, some HIFU applications for other treatments are presented for indicating the enormous potential of this technology in the healthcare field. Furthermore, this part discusses preclinical and clinical trials for PC treatment using the existing HIFU robotic devices.

The fourth part presents the 4-DOF prostate robotic device that was designed, developed, and evaluated. The piezoelectric motors and optical encoders that were adapted to the robotic device are mentioned. Other devices of the robotic system such as the electronic system and medical cart as well as the developed MRgFUS software are also discussed.

The fifth part discusses the development of an agar-based TMM that was significant for execution of the experiments. Acoustic, MR, and thermal properties of the phantom with materials of various concentrations are additionally presented.

The sixth part explains an experimental setup and a method that was investigated to estimate the ultrasonic absorption coefficient of TMMs and excised tissues. The absorption coefficient of phantoms with different concentrations of agar, silicon dioxide, and evaporated milk were estimated using this fast and simple method.

The seventh part presents a soft tissue-mimicking phantom that was developed using agar and wood powder to evaluate MRgFUS systems. The acoustic, MR, and thermal characteristics of the TMM were measured.

The eighth part discusses the evaluation of the robotic system. The candidate transducers were simulated to extract ultrasonic characteristics. The two transducers were later evaluated in phantoms and excised tissues. The system was also evaluated for its motion accuracy, MR compatibility, and motion functionality. The device was evaluated *in vitro* in phantoms and excised tissues. It was also evaluated *in vivo* using a rabbit thigh model. The robotic system was used to create overlapping and discrete lesions in phantoms and excised tissues using different grid patterns and ultrasonic parameters.

The ninth part is a discussion of the dissertation and suggesstions for future expansions of the proposed 4-DOF robotic system for treating the most common male cancer.

2 Anatomy, histology, physiology, and pathology of the prostate gland

2.1 Introduction

Urologists and pathologists have been concentrated on the study of the anatomic structures of the human prostate gland and their relationship to pathologic diseases, especially prostate carcinoma development and prognosis, since the resurgence of radical prostatectomy in the late 1980s. The interconnections of the prostate gland with the surrounding organs have been studied since the frequency of the prostate disorders has been on the increase, affecting not only the reproductive system of men but generally the QOL. For that reason, recognition of the prostate gland is a crucial part of a better understanding of how the prostate gland functions and reacts under various conditions. The prostate's anatomy also plays a role in testing and diagnosing certain conditions. Herein, prostate gland anatomy was significant to be studied in detail for the design and development of the 4-DOF robotic device's probe which houses the focused transducer. The robotic device was designed to destroy cancerous cells of the prostate gland and restore the prostate to its normal function non-invasive with as minimum side effects as possible. Histology of the prostate gland is one of the strongest prognostic factors to medical checkup of the grade of prostate health.

This part of the thesis discusses a bibliographic review of the anatomy, functionality, and histologic view under a microscope of a normal healthy prostate gland. Furthermore, PC local and global statistical studies are also presented.

2.2 Anatomic location of the prostate gland and surrounding tissues

Prostate anatomy must be studied in detail so that new, more accurate, and non-invasive PC treatments can be developed without the creation of side effects. The prostate gland is an integral part of the reproductive system in the male body and despite its small size, it still forms as the most important accessory gland. It is a six-sided amalgamation of glandular and fibromuscular tissue that resides in the pelvic cavity [21]. The adult prostate gland surrounds the urethra immediately below the base of the urinary bladder, posterior to the inferior symphysis pubis, superior to the urogenital diaphragm, and anterior to the rectum as illustrated in Figure 2.2.1 [21].

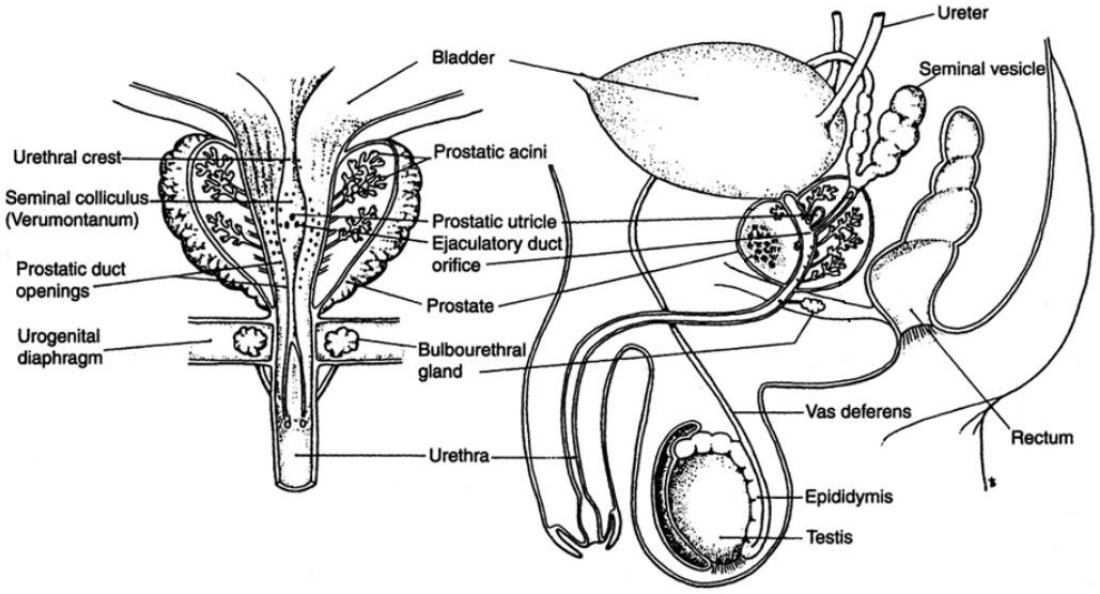

Figure 2.2.1: Frontal (left) and sagittal (right) views of a healthy prostate gland [21].

The apex of the prostate is attached to the urogenital diaphragm. The average dimensions of a healthy prostate gland are approximately 5 cm x 3 cm x 3 cm (volume of around 25 ml) and in males of ages 20 to 50 it weighs 20 grams, while it increases to 30 grams in those 60 to 80 years of age [22].

2.3 Anatomy and physciology of the prostate gland

There are two main elements in the prostate, the grandular and stromal elements which are enclosed together within a pseudocapsule. A smooth muscle is located at the inner layer of this pseudocapsule while the outer layer is covered by collagen [23]. The prostate gland has a conical shape and surrounds the urethra at the location where it exits the bladder. It is divided into several lobes as shown in Figure 2.3.1.

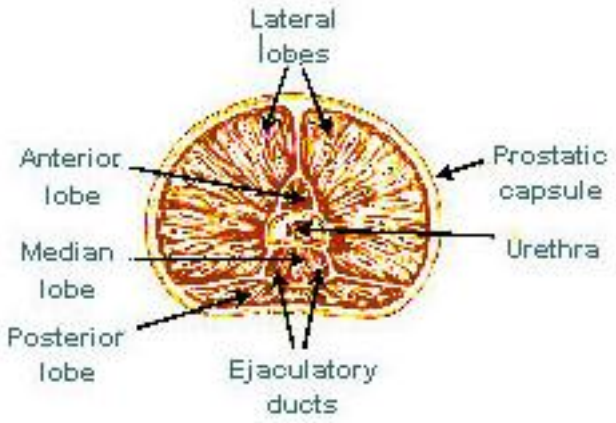

Figure 2.3.1: Prostate gland lobes [24].

The anterior lobe lies in front of the urethra and describes the anterior portion. It is void of glandular tissue, being shaped totally of fibromuscular tissue [24]. The lateral lobes are separated by the prostatic urethra and form the main mass of the gland and are continuous posteriorly. The media lobe is a wedge of gland situated between the two ejaculatory ducts and the urethra and it is a cone-shaped portion of the gland. Its upper surface is related to the trigone of the bladder. The posterior lobe depicts the posteromedial part of the lateral lobes that can be palpated through the rectum during a digital rectal exam (DRE). The prostate can be divided into four main zones which are the central zone, transition zone, peripheral zone, and anterior fibromuscular stroma as illustrated in Figure 2.3.2 [25].

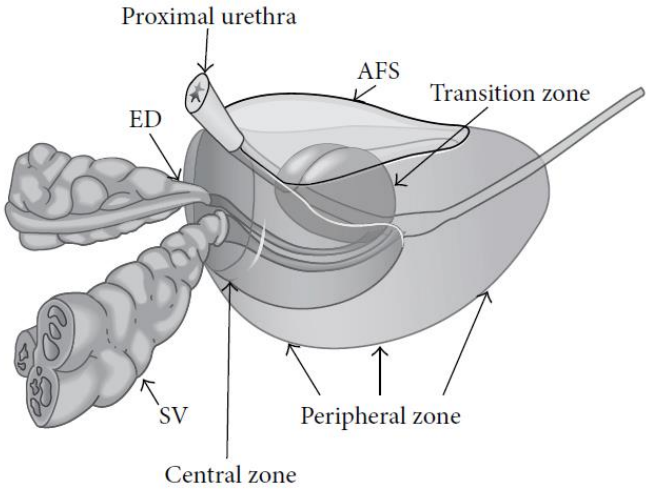

Figure 2.3.2: Zonal anatomy of the prostate gland [25]; SV: seminal vesicles; ED: ejaculatory ducts; AFS: anterior fibromuscular stroma.

Each lobe has its functionality and purposes as found from urologists and scientists through the study of the prostate gland. The largest proportion of the prostate gland is the peripheral zone that comprises around 70 % and surrounds the urethra at the distal. The most important point of this zone is that it more easily develops carcinoma, chronic prostatitis, and post-inflammatory atrophy than the other zones. It has higher signal intensity on T_2-weighted MRI sequences because it contains ductal and acinar elements with interwoven smooth muscle [25]. On the other hand, the central zone accounts for around 25 % of the prostate gland, and the transition zone only 5 %. The transition zone is the portion of the prostate that enlarges due to BPH.

The main feature of the prostate gland is to generate prostate liquid, one of the components of semen. The prostate gland additionally consists of smooth muscle cells (around 30 %) to aid propel seminal fluid into the urethra. The muscular tissues of the prostate gland properly

transport the semen, in addition to the seminal fluid, from the prostate gland and through the urethra, out of the body [26]. Though prostate fluid is partially acidic, an additional liquid in seminal fluid made by the critical vesicles, leaves semen somewhat alkaline or basic. This alkalinity aids shield semen and also prolong its life [27]. The prostate works using androgens simply described as male hormonal agents. The most vital of these hormones is testosterone, particularly dihydrotestosterone. The secretion of this hormone right into the body assists managing prostate feature as well as appropriately maintaining the prostate functioning [28]. However, while the prostate is in an excellent location for supplying this crucial liquid as well as squeezing points along when the moment is right, its placement around the urethra can be a liability if the gland swells or expands. An inflamed prostate compresses the urethra and aggravates the wall surfaces of the bladder, interfering with normal urination.

2.4 Histology of a healthy prostate gland

The histology study of the prostate gland is of great importance to investigate the proper function of the prostate and the effect of its malfunction after the appearance of various diseases. Histological changes of the gland can provide solutions in difficult cases of many patients who have developed symptoms of PC or other diseases, but cannot be diagnosed in any other way. It is also an additional disease confirmation for experts to confirm the diagnosis of prostatic disorders and differentiate between prostatic conditions that present with similar symptomatology [29]. One important advantage of histological exams is that benign lesions can be differentiated from malignant lesions as well as grade different types of malignant lesions. Moreover, the staging of prostatic tumors is achieved by histopathological studies. The establishment of histopathological diagnosis of prostatic disorders requires light microscopic examination of hematoxylin and eosin (H & E)-stained tissue sections [30]. Generally, men usually lack signs of prostatic disorders at a DRE or transrectal ultrasonography without manifest PC. Some diagnostic methods lack specificity for detection of PC and sometimes these methods give false-positive results of clinical examination. An example is the granulomatous prostatitis which leads both to the possibility of a lesion during a DRE and very high PSA concentrations [30]. To avoid misdiagnosis, it is recommended that pathologists should perform needle biopsies and read them blindly without taking into consideration the outcome of previous clinical examinations.

As can be observed by histological views in Figure 2.4.1.a, the prostate gland is a fibro musculo-glandular organ. From the microscope, the prostatic urethra, colliculus seminalis, and

the utriculus are visually recognizable [29]. The glandular element is in the form of alveoli as tubules of small, multiple irregularly branching alveolar glands. These alveoli might include corpora amylacea or prostatic concretions. Moreover, these glands are embedded in a fibromuscular stroma with smooth muscle collagenous and elastic fibres and are seemed to be distributed throughout the gland. The prostate can be divided into the outer larger zone and the inner smaller zone. The outer zone is composed of large branched glands and is a site for cancer. The inner zone is composed of sub-mucosal glands and is a site for BPH. Histological examinations are important for prostatic diseases since they can differentiate acute from chronic conditions, give more accurate diagnostic results, evaluate metastasis, and provide tissue study at a generic level for further investigation [29]. In Figure 2.4.1.b and 2.4.1.c, the structure and sectional anatomy of the prostate gland are illustrated, respectively.

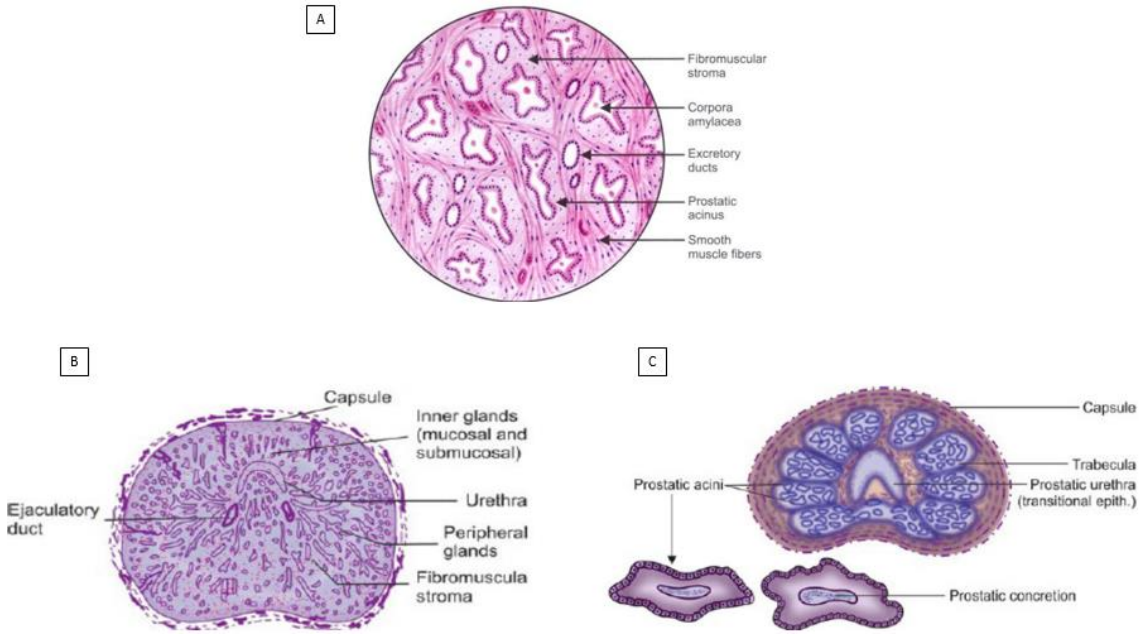

Figure 2.4.1: a) Normal histology of prostate gland, b) Structure of prostate gland, and c) Sectional anatomy of prostate gland [29].

2.5 Diagnostic images of a healthy prostate gland

The latest technological advances in US applications have resulted in numerous new aspects of prostate gland analysis. Structural analysis is performed for the estimation of prostate volume, study of echotexture, and outline of tissue stiffness or elasticity [22]. The functional analysis demonstrates macrovascularity and microvascularity, which are tissue perfusion indicators. US is usually used and well-related for prostate assessment. US and its different

techniques can be used to provide adequate information for prostate disorders such as acute and chronic prostatitis, BPH, and PC according to Mitterberger *et al.* [22]. However, detection and delineation of prostate pathology with imaging remains a challenging endeavor. US has many advantages including real-time imaging, contrast agents have been developed to provide better image quality and it is a low-cost medical machine. Acute bacterial prostatitis can appear as a hypoechoic rim around the prostate as shown in Figure 2.5.1. A prostate abscess appears sonographically as a hypoechogenic walled-off collection of fluid [22].

Figure 2.5.1: US imaging of the prostate gland in a 55 year-old man who had a PSA level of 3.25 ng/ml [22].

Computed Tomography (CT) scan is a modality with evidence-based guidelines. The CT scan can be used to evaluate extension into the bladder and lymph nodes to help stage cancer or to consider a sampling of the lymph node before treatment. During a CT scan, the prostate gland appears homogeneous as shown in Figure 2.5.2, smoothly marginated, elliptical, round, or triangular infravesical soft tissue with a density approaching that of skeletal muscle [31].

Unlike US and MRI, CT cannot illustrate internal prostatic architecture. The border of the prostate oriented in the direction of the urinary bladder hardly stands out. Partial quantity artefacts occurring from these frameworks can mask slight abnormalities on the bladder wall surface or contours of the prostate. The parenchymal density is about 40-65 Hounsfield units (HU) [31].

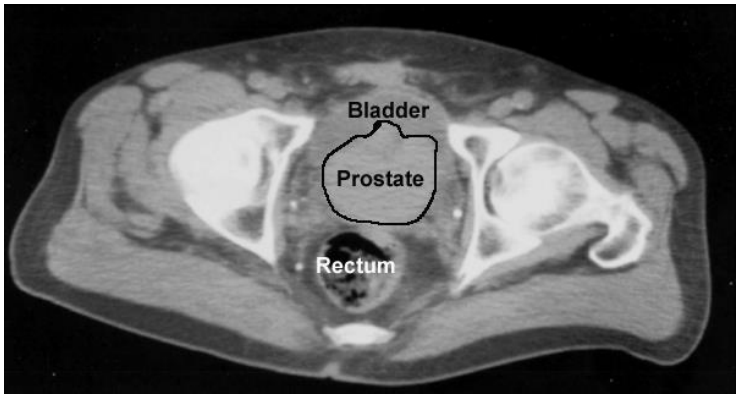

Figure 2.5.2: Non-contrast pelvic axial CT of a patient [32].

MRI has been thoroughly studied for its capability to detect PCs. MRI permits better visualization of prostate zonal anatomy and location, as well as extent of a tumor within the gland [33]. Patients are imaged with both a whole-body scanner with pelvic phased-array coil, as well as an endorectal coil which includes a magnetic coil placed directly into the rectum. T_1 and T_2-weighted images are obtained, but cancer visualization is generally performed on T_2-weighted images where cancer appears dark [33]. Ultimately, MRI has the greatest ability to improve local staging before therapy. Figure 2.5.3 shows a T_2-weighted image with fat suppression of a patient with an enlarged central zone due to BPH.

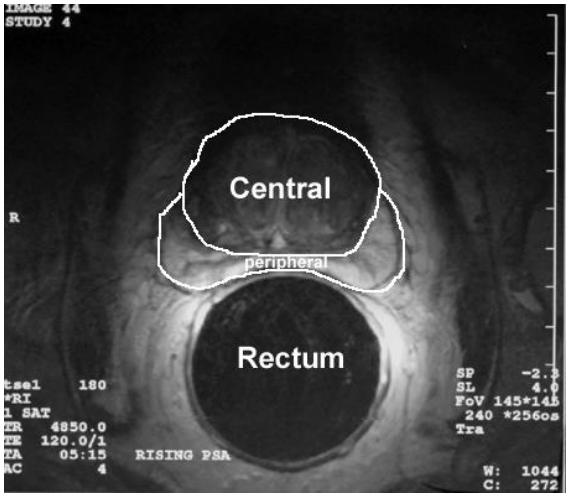

Figure 2.5.3: T_2-weighted image with fat suppression of a patient with BPH [32].

2.6 Ultrasonic characteristics of a healthy prostate gland

Prostate ultrasonic characteristics are important for understanding the conditions under which HIFU waves will travel and how they will be affected during their dissemination in the prostate gland. The most significant ultrasonic characteristics for HIFU ablation purposes are the

acoustic and thermal properties. Since the proposed robotic device is guided by MRI, some MR parameters (T_1 and T_2) are also important. Table 2.6.1 lists the acoustic, thermal, and MR characteristics of the prostate gland as found from the literature.

Table 2.6.1: Main ultrasonic characteristics of the prostate gland [34,35].

Density (kg/m^3)	1045
Propagation velocity (m/s)	1561
Attenuation (dB/MHz-cm)	0.78±0.24
B/A	7.5
Thermal conductivity (W/m/K)	0.51±0.03
Specific heat capacity (J/kg/K)	3400±300
Perfusion rate (kg/m^3/s)	1.7±1.3
T_1 (ms)	1597±42
T_2 (ms)	74±9

2.7 Prostate gland pathology

A prostate might be affected by three main diseases; prostatitis, prostatic hyperplasia, and prostatic adenocarcinoma, as found in the bibliographic review. In this section, the aforementioned prostatic diseases are explained. More emphasis is given to prostatic adenocarcinoma/PC which leads a significant number of men to death. The analysis of PC starts with a brief history and how PC was discovered for the first time as well as the first treatment techniques. The staging and Gleason score of the prostate are also explained. Furthermore, recent PC statistics are discussed including the percentage of PC in various parts of the world, the number of deaths, and the overall prognostic cases in the upcoming years. Lastly, the available diagnostic and treatment methods of PC as well as their advantages and disadvantages are reported.

2.7.1 Prostatitis

Prostatitis is a prostatic disease that inflames the gland and in some cases the surrounding area. Prostatitis is considered to be the third most common urological disease in men [36]. This disease mainly affects the urinary tract and it might affect men of all age groups compared to other prostatic disorders such as PC and BPH which usually affect men of older ages. It is usually classified according to the type of illness, presentation, and etiology as reported in the National Institute of Health [37]. The categories include acute bacterial prostatitis, chronic bacterial prostatitis, chronic pelvic pain syndrome, and asymptomatic inflammatory prostatitis. Prostatitis may cause some men with severe pain, with the symptoms of the disease influencing the QOL of men. Treatment of the different categories of prostatitis depends mainly on antibiotic therapy. Different antibiotics may be used for each category and for different treatment periods (longer treatment time for more advanced prostatitis).

2.7.2 Prostatic hyperplasia

BPH is another pathologic disease of the prostate gland. This disease causes the prostate gland and surrounding tissue to expand abnormally and leads mainly to urological problems. During a man's life, the prostate gland has two main growth periods; the first is early in puberty when the gland doubles in size and the second begins about age 25 and continue growing for the rest of a man's life [38]. As a man gets older, the prostate gland enlarges and when this enlargement is uncontrollable it can cause urological and painful problems. The prostate enlargement squeezes the urethra and the bladder wall becomes thicker. Lower urinary tract symptoms might appear when the bladder becomes very weak and loses the ability to empty due to prostate enlargement. The average weight of a prostate that is identified at biopsy examination to contain BPH is 33±6 g [39]. Just 4 % of the prostates in men greater than 70 years old reach dimensions greater than 100 g. An analysis of a logistic growth curve of BPH lesions removed at prostatectomy indicates that the development of BPH is launched most likely prior to the patient being 30 years old [38].

Some terms that are used for prostatic hyperplasia is BPH which describes the enlargement of the smooth muscles and cells of the prostate gland, a condition of BPH known as benign prostatic enlargement (BPE) where the prostate gland has enlarged, and benign prostatic obstruction (BPO) where the enlarged gland and surrounding tissue cause a blockage. Around

50 % of men with BPH develop BPE or BPO [38]. BPH is rarely a life-threatening condition today where deterioration of symptoms and urinary flow is often slow and serious outcomes such as renal insufficiency are rare. Several symptoms of BPH which have been observed include incomplete bladder emptying, frequent urination, intermittency (stop and start several times during urination), urgency (cannot wait), a weak urine flow, urine straining, and nocturia (wake up several times in the night).

Many theories have been proposed to explain the cause of BPH [40]. Male hormones and more specific a powerful testosterone androgen (dihydrotestosterone) has been found to stimulate prostatic cell growth and it is the major cause of prostate enlargement between puberty and young adulthood [40]. It is also the fundamental suspect in prostate enlargement in later adulthood. Family history can be another cause of developing the disease as well as some other factors such as socioeconomic status, smoking, diet, race, and sexual activity [40].

There are many diagnostic tests for BPH [38]. The first step to diagnose BPH is a questionnaire (BPH symptom score index) for which the patient provides urinary symptoms information. If the questionnaire is not adequate, some other diagnostic tests might follow including DRE, urine tests (urinalysis, post-void residual volume, uroflowmetry, urodynamic pressure-flow study), diagnostic scans such as US, cystoscopy, MRI, CT, and blood tests (PSA, urinary blood tests) [38].

The main treatments of BPH are the active surveillance, prescription drugs, and surgery. However, a patient following a doctor's advice has many treatment options, including less invasive, such as prostatic urethral lift (compress the enlarged prostate to move it out and of the way), water vapor thermal therapy, prostatic stent, transurethral microwave thermotherapy, and catheterization [38]. Figure 2.7.2.1 shows the size difference between a normal prostate and prostate with BPH.

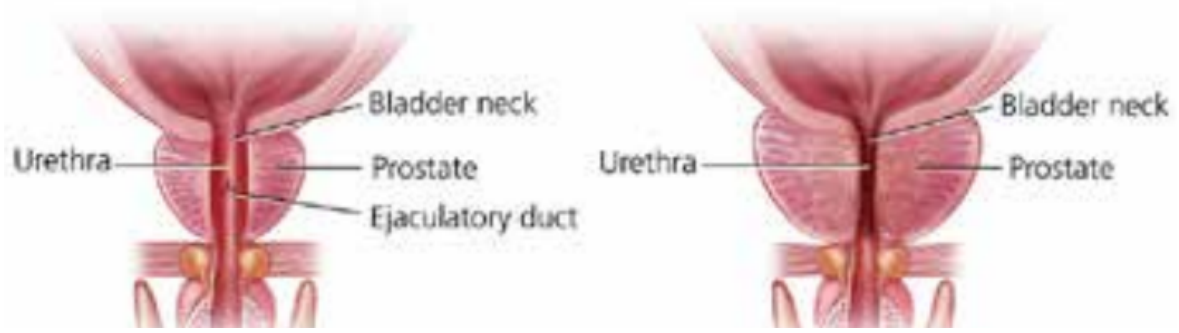

Figure 2.7.2.1: A) Normal prostate and B) Enlarged prostate [38].

2.8 Prostatic adenocarcinoma (prostate cancer)

2.8.1 Brief history of prostate cancer

In 1538, the anatomist Niccolo Massa described the prostate and the anatomist Andreas Vesalius illustrated the prostate for the first time. The first case of PC was described by J. Adams [41] who was a surgeon at The London Hospital in 1853. After a regular histological examination, Adams found for the first time PC and noted in his report that this case was "a very rare disease" without knowing that more than 160 years later this disease would become a major health issue for many people. In 1905, the academic urology was raised, and the first radical perineal prostatectomy was performed by Hugh H. Young [42]. Young *et al.* reported the results of prostatectomies of 50 patients and concluded that the treatment gave a cure for PC and showed no local spread. Charles B. Huggins [43] used estrogen to oppose testosterone production in men having metastatic PC in 1941. Besides, Schally and R. Guillemin [44,45] determined gonadotropin-releasing hormone (GnRH) in reproduction, and GnRH receptor agonists were discovered and this was the beginning of the use of hormone therapy for treating PC. Moreover, chemotherapy drugs were studied for the first time to treat PC in the 1970s [46] whereas in 1983, Patrick Walsh [47] developed radical retropubic prostatectomy. The first brachytherapy treatment was described in 1983 [48]. In the early 20th century, radiation therapy using intraprostatic radium implants was developed and in the middle of the same century, it was replaced by external beam radiotherapy (EBRT).

2.8.2 Prostate cancer staging

It is extremely important to diagnose correctly the PC staging of every patient before proceeding with any therapy. Two important classification systems are mainly used to describe a patient's staging of cancer. The first system is the TNM (revised tumor, nodes, metastasis), introduced by the American Joint Committee on Cancer (AJCC) and the Union for International Cancer Control (UICC). The second system is the Jewett system that was initially introduced in 1975 [49]. Metastatic properties of PC might be unifocal, multifocal with clear index and one or more separate secondary tumor foci with smaller volumes (most common), and multifocal with unclear index tumors. Figure 2.8.2.1 shows the metastatic properties of PC and Figure 2.8.2.2 shows the different ablation strategies.

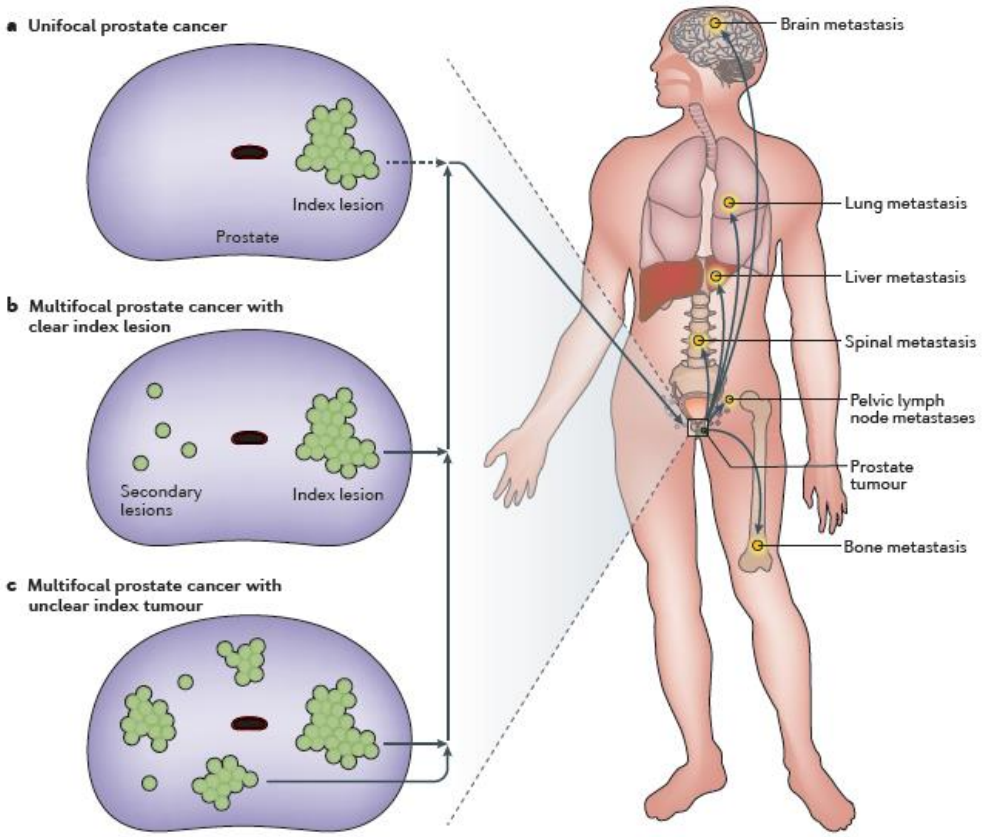

Figure 2.8.2.1: Metastatic properties of PC [50].

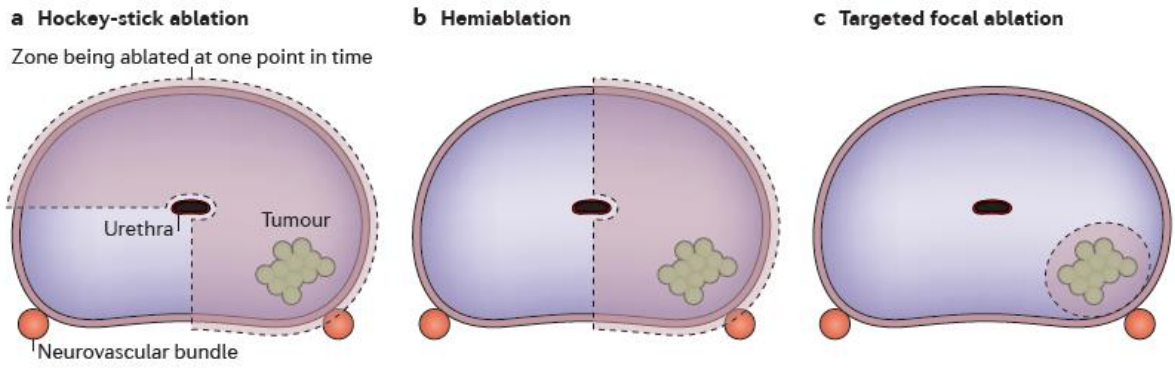

Figure 2.8.2.2: Different ablation strategies [50].

2.8.3 Prostate cancer Gleason score

The Gleason scoring system is defined by a scale of 1 to 5 (Figure 2.8.3.1). Grade 1 cells resemble normal prostate tissue. Cells closest to 5 are considered “high-grade” and have mutated so much that they barely resemble normal cells [51].

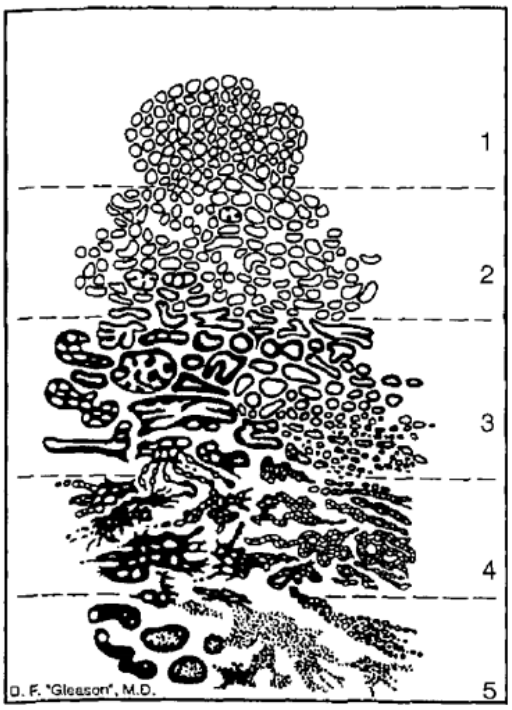

Figure 2.8.3.1: Drawing of histologic patterns of prostatic adenocarcinoma by emphasizing the degree of glandular differentiation and relation to stroma (Gleason score) [52].

Table 2.8.3.1 lists the grade group system and Gleason score as well as the level of the risk of each group.

Table 2.8.3.1: The grade group system and Gleason score [51].

Risk Group	Grade Group	Gleason Score
Low	Grade Group 1	Gleason Score ≤ 6
Intermediate favorable	Grade Group 2	Gleason Score 7 (3+4)
Intermediate unfavorable	Grade Group 3	Gleason Score 7 (4+3)
High	Grade Group 4	Gleason Score 8
High	Grade Group 5	Gleason Score 9-10

2.8.4 Prostate cancer statistics and facts

Under clinical statistics, it has been shown that PC constitutes 29 % of all cancers in men and it is the second-highest cause of death after non-melanoma skin cancer among men of all ages

[53,54]. It is also estimated that 1 in 6 men will be diagnosed with PC however, thanks to prevention and modern therapeutic methods it is predicted that only 1 in 36 men will be led to death due to PC [55]. In 2010, the American Cancer Society estimated the number of new cases expected in the USA for the same year as shown in Figure 2.8.4.1. Among men, cancers of the prostate, lung (and brochus), and colorectum account for 52 % of all diagnosed cancers [56]. Figure 2.8.4.2 indicates long-term trends (1975-2006) in cancer incidence rates for all cancers combined, and for selected cancer sites by sex.

Estimated New Cases*

Males			Females		
Prostate	217,730	28%	Breast	207,090	28%
Lung & bronchus	116,750	15%	Lung & bronchus	105,770	14%
Colon & rectum	72,090	9%	Colon & rectum	70,480	10%
Urinary bladder	52,760	7%	Uterine corpus	43,470	6%
Melanoma of the skin	38,870	5%	Thyroid	33,930	5%
Non-Hodgkin lymphoma	35,380	4%	Non-Hodgkin lymphoma	30,160	4%
Kidney & renal pelvis	35,370	4%	Melanoma of the skin	29,260	4%
Oral cavity & pharynx	25,420	3%	Kidney & renal pelvis	22,870	3%
Leukemia	24,690	3%	Ovary	21,880	3%
Pancreas	21,370	3%	Pancreas	21,770	3%
All Sites	**789,620**	**100%**	**All Sites**	**739,940**	**100%**

Figure 2.8.4.1: Ten leading cancer types for the estimated new cancer cases in 2010 [56].

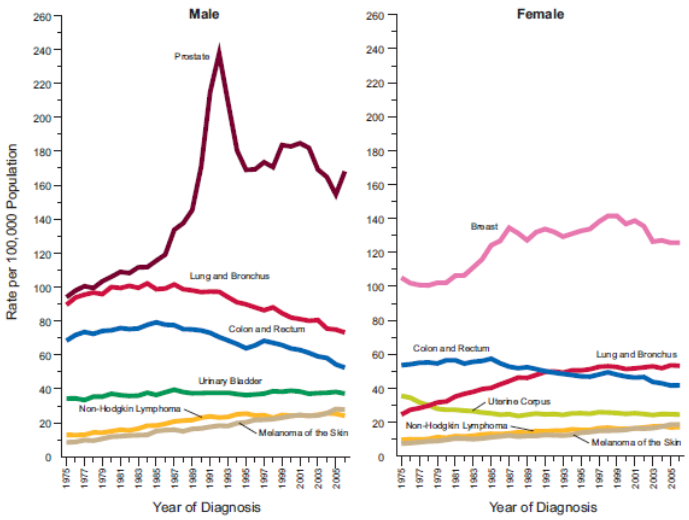

Figure 2.8.4.2: Annual age-adjusted cancer incidence rates for selected cancers by sex in the USA from 1975 to 2006 [56].

Today, the best screening tool to detect PC is the PSA test which is a blood test that counts the amount of PSA in blood and suggests continued overdiagnosis [57,58]. PSA is a protein that is produced by tissue in the prostate. In a specific research study to find the first prostate treatment

choice of most men, it was found that 44 % of men chose radical prostatectomy as their first choice to treat PC, thinking it was the best treatment type for cure [59]. Nowadays, in a modern healthcare world, the need of discovering new technologies to avoid surgery and its subsequent consequences is greater than ever before. By discovering many different types of treatment, patients are provided with the opportunity to choose their treatment type according to their wealth and always following their doctor's advice.

If radical prostatectomy and general prostate surgery are satisfying to fully cure PC, then the main question is why spending money and time in order to find new cancer treatment methods. This question was answered by revising the most usual side effects of different prostate treatment types [60]. For radical prostatectomy, it was shown that the long-term side effects were urinary incontinence (15-50 %) and sexual dysfunction (20-70 %). For electron beam radiation therapy, around 45 % could expect erectile dysfunction, 6-25 % bowel dysfunction, and 2-16 % urinary dysfunction. For brachytherapy, the majority of men encountered distressing urinary symptoms, 18 % diarrhea, 19 % persistent rectal bleeding, and 21-36 % decreased erectile function [60].

All the above therapies create painful symptoms after treatment and sometimes manipulate the normal function of organs that are related to the prostate and general urinary system of men. Moreover, some clinical trials have revealed the expediency of focal ablative methods using HIFU and cryosurgery [61]. Focal techniques will be improved as imaging techniques allow for better pathological estimations [62-64].

In the USA, the National Cancer Institute [65] presented a different statistical analysis of American citizens suffering with PC. As shown in Figure 2.8.4.3, between the years 2010 and 2014, the number of new cases of PC accounted for 119.8 per 100,000 men per year while the number of deaths was 20.1 per 100,000 men per year. Another important point is that around 11.6 % of men are expected to be diagnosed with PC over the course of their lifetime.

Also, new cases and deaths due to PC were estimated for various common types of cancer in 2017. In the first place was breast cancer with 252,710 new cases and 40,610 deaths, in the second place was lung and brochus cancer with 222,500 new cases and 155,870 deaths while PC was in the third place with 161,360 new cases and 26,730 deaths.

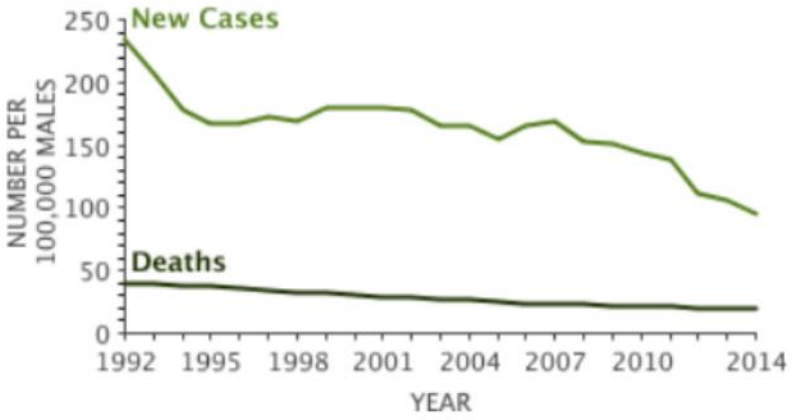

Figure 2.8.4.3: New cases and deaths (number per 100,000 males) are illustrated with respect to year (1992-2014) [65].

Moreover, new cases of PC by age group were recorded as illustrated in Figure 2.8.4.4. For the age group 45-54, the percentage of new cases was 9.3 %, for the age group 75-84 was 15.3 %, and for the age group more than 84-year-old was just 3.9 %. The highest percentage of new cases was accounted for 32.8 % and 38.2 % for the age groups 55-64 and 65-74, respectively.

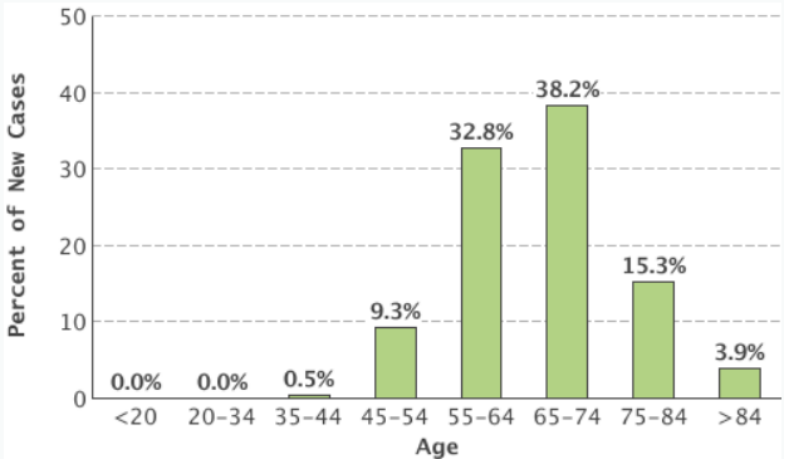

Figure 2.8.4.4: Percentage of new cases of PC with respect to age group based on 2010-2014 cases in the USA [65].

The latest statistics of cancer that have been published by the World Health Organization have highlighted PC to be the most frequent male cancer (excluding non-melanoma skin cancer) in Cyprus [66]. The number of new cases of PC among males of all ages was 821 out of a total of 2873 cases constituting the 28.6 %. From this number, the 22.4 % (184 cases) led to death. Among all new cases from both sexes, PC still remains the top cancer with the highest cases

(15.7 %) above breast cancer (14.5 %). Figure 2.8.4.5 illustrates the cancer statistics of Cyprus in 2020 as given by the World Health Organization.

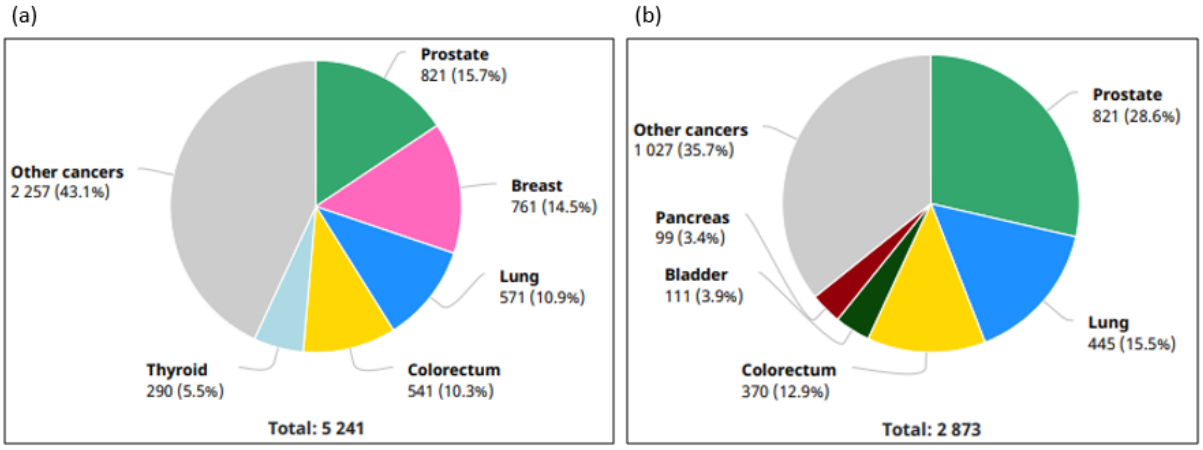

Figure 2.8.4.5: Number of new cancer cases in Cyprus in 2020 a) for both sexes of all ages, and b) for males of all ages [66].

2.8.5 Diagnostic methods of prostate cancer

There are different methods to diagnose PC. PSA is the most common diagnostic method. A PSA level below 4 ng/mL means that the prostate is healthy [57]. Another method is the transrectal ultrasound (TRUS) in which a small probe (approximately the width of a finger) is placed in the rectum. This probe produces sound waves and creates echoes that are picked up by the probe. These echoes are then processed by a computer giving an US image of the prostate. It is also used during a prostate biopsy to guide the biopsy needle. If PSA and TRUS methods show that there might be PC, then a prostate biopsy is followed to see if cancer is present. Another method to check if there is a PC is imaging. One imaging test is a bone test where a small amount of radioactive material is put into a vein to check if PC has spread to other parts of the body. Other imaging tests are the CT scan, MRI, and ProstaScint scan (uses an injection of low levels of a radioactive substance to find cancer that has spread beyond the prostate) [67].

2.8.6 Treatment methods of prostate cancer

PC can be treated with different methods depending on the condition. The treatment options may include expectant management or active surveillance, surgery, radiation treatment, cryosurgery, hormone therapy, chemotherapy, and vaccine treatments [67]. All these

treatments have been used and result in different advantages and disadvantages for the various stages of cancer. The treatments that are used to treat PC until today are explained below:

*Expectant management or active surveill*ance: This treatment is mostly used on very old men who have other major health problems and it is a watchful waiting, observation, active surveillance, or expectant management [6].

Surgery: If cancer does not spread outside the gland, then surgery is a common choice to cure PC with the major type of surgery is radical prostatectomy where the surgeon removes the whole prostate gland and some of the tissue around it according to the National Comprehensive Cancer Network [5]. Radical prostatectomy can be performed using different ways [5] such as radical retropubic prostatectomy (open approach through a single long cut in the lower belly-abdomen), radical perineal prostatectomy (open approach through a single long cut in the skin between the anus and the scrotum), laparoscopic radical prostatectomy (small cuts in the skin through which special long tools are used to remove the prostate) and robotic-assisted laparoscopic radical prostatectomy (the surgeon uses and controls robotic arms to perform the surgery through small cuts).

Radiation therapy: Radiation therapy is a treatment that uses high-energy rays to kill cancer cells [68]. The interaction of the high energy rays with cancer cells leads to the destruction of cancer cells and more specifically to the destruction of any cell that interacts with high energy rays (MV energy beams). EBRT is used to treat earlier-stage cancers or in some cases to relieve symptoms if cancer has spread and it is not possible to be completely cured. Fractionation of the radiation beams gives better treatment according to a radiobiology study [69]. For radiotherapy, the ideal treatment planning is to focus the energy beam to cancer tissue and avoid any other healthy tissues that might be exposed to this radiation. Today, there are many methods of radiotherapy to minimize the exposure of radiation beam to healthy tissues such as intensity-modulated radiation therapy (IMRT) [70], 3D-conformal radiation therapy (CRT) [34], conformal proton beam radiation therapy [71], and stereotactic body radiation therapy (SBRT) [72]. With these methods, there is more chance to increase the success rate and reduce side effects.

Brachytherapy: Radioactive materials are placed directly in the prostate. The healthy tissues around the prostate have lower side effects since the radiation affects only a short distance. Brachytherapy can be separated into two types; permanent where the radioactive elements lose

their radioactivity over time, and temporary where the radioactive elements have strong radioactivity and are left for a short time.

Cryosurgery: During cryosurgery, PC is treated by freezing the cells with cold metal probes. Most often, doctors use TRUS to guide the probes into the prostate. Then, cold gases are passed through the probes which create ice balls that destroy the PC cells.

Hormone therapy: The main target of hormone therapy which is also called androgen deprivation is to lower the levels of the male hormones (androgens) such as testosterone or to completely stop them from influencing PC cells.

Chemotherapy: Chemotherapy is the therapy that uses specific drugs to treat cancer [73]. These drugs are usually injected into a vein (given intravenously) but sometimes can be swallowed in a pill form. The drugs enter the bloodstream and destroy the cancer cells. Chemotherapy is often used if a PC has spread outside the prostate gland. It is not expected that it will destroy all cancer cells, but it might slow cancer's growth and reduce any symptoms. Some chemo drugs that are particularly used are the docetaxel (Taxotere®) and cabazitaxel (Jevtana®) [67].

Vaccine treatment: A vaccine that is used to treat advanced PC is the Sipuleucel-T (Provenge®) [74]. This vaccine can be made only from each patient's blood cells. The procedure that is followed is that at the beginning white blood cells are removed from the patient's blood and send to a lab. The white blood cells are then exposed to a specific protein from PC cells. Afterward, the cells are checked by the doctor and given back to the patient intravenously. This procedure is done twice, two weeks apart, so that the patient gets three doses of cells. Following this procedure, the cells cause other immune system cells to attack the PC in the body.

Men with low-risk localized PC who are considered suitable for radical treatment should first be offered active surveillance [75]. Table 2.8.6.1 lists the risk stratification criteria for men with localized PC.

Table 2.8.6.1: Risk stratification criteria for men with localized PC [75].

	PSA (ng/ml)		**Gleason score**		**Clinical stage**
Low risk	<10	and	≤6	and	T1-T2a
Intermediate risk	10-20	or	7	or	T2b-T2c
High risk	>20	or	8-10	or	T3-T4

2.8.7 Other prostatic diseases

Another disease of the prostate gland is the prostatic intraepithelial neoplasia (PIN). This disease is related to how the prostate gland cells change by looking at them under the microscope. Around half of all men have PIN by the time they reach age 50. If a man has a low-grade PIN where the cells look normal, then there is no reason to concern for PC, but if a man has a high-grade PIN where the cells look abnormal, then there is a 20 % possibility to have PC [67] and men with this condition must have a repeat prostate biopsy.

Proliferative inflammatory atrophy (PIA) is another disorder of the prostate. It can be found during prostate biopsy where the prostate cells look smaller than normal and there are signs of inflammation. Nevertheless, PIA is not cancer but in some cases, it may lead to high-grade PIN with a possibility to create PC.

3 High-intensity focused ultrasound technology, preclinical, and clinical studies

3.1 Introduction

US waves have been utilized in various areas in the field of healthcare for many years. Depending on different ultrasonic factors, US has been proposed to have various applications from diagnostic to therapeutic purposes. In the beginning, US became known as a powerful diagnostic tool for fetal imaging. For many years, other capabilities of US have been investigated including destruction using high intensities to eradicate cancerous tumors. Diagnostic US is a passive method aimed at characterizing the tissue structure and function in place, naturally, while therapeutic US is an active US that alters tissues and/or their functioning either permanently or temporarily. HIFU has been applied for various therapies such as brain [76], PC [13], kidney [77], breast cancer [78], uterine fibroids [79], cardiac valves [80], and recently essential tremor [81]. These therapies have been performed by taking advantage of the thermal properties of HIFU to elevate temperature in tissue. The temperature increase in the tissue can be achieved at a specific depth since US waves propagate in the tissue and their mechanical energy is converted into heat. This ability of US waves eliminates the need for invasive therapies and surgery. However, HIFU requires precise targeting and monitoring for better treatment. This can be achieved by using robotic devices guided by existing imaging systems. HIFU procedure is a very successful medical system for the ablation of PC cells at an early stage. It is also capable of removing cancer cells from small affected areas, but it might not work well when the tumors have spread beyond the prostate. HIFU procedure is far less invasive than traditional PC treatments. For that reason, the possibility for a patient to develop any side effects is less but there are still steps to be taken to find the side effects that might occur after HIFU treatment. Moreover, HIFU treatment time is much less than a prostatectomy, taking only a few hours and naturally the patient can return at home the same day because of the limited complications of the procedure. On the other hand, HIFU treatment may have a chance of creating damage to surrounding areas and nerves. Another disadvantage of HIFU is that there is not a lot of information about its effectiveness or side effects that might arise later in life. Also, when any cancer cell is not been fully ablated, then there is a large possibility for cancer recovery. To sum up, HIFU treatment is successful in dealing with the early stages of

PC. Because of this, any cancerous cells that have progressed beyond the prostate cannot be dealt with, and as a result, it is only a viable option in the early stages.

3.2 History of HIFU

The first researcher who investigated the possibility to ablate tumors non-invasively using HIFU was Lynn *et al.* in the 1940s. In the next decade, Fry brothers (William Fry and Francis Fry) carried out work to treat neurological disorders at the University of Illinois [82]. Single and multiple elements were used to create lesions in the pallidofugal and nigral complexes in the brains of patients with hyperkinetic and hypertonic disorders. Many cases of patients with Parkinson were treated successfully but the study was suspended due to difficulties in imaging and targeting of sites in the brain.

In the 1970s, hyperthermia was investigated by using HIFU at lower intensities and check the possibility to treat tumors [83]. The main idea was to increase the tissue temperature at 43 ^{o}C and maintain that temperature for an extended time. Unfortunately, this concept was unsuccessful since there was not any feedback (specific method) from the temperature of the tumor.

The next breakthrough emerged with the creation of extracorporeal shockwave lithotripsy (ESWL) in the 1980s [16]. The U.S. FDA approved the use of ESWL as a method for the treatment of kidney stones in 1984. This was the first-ever approved therapeutic use of HIFU.

In the 1990s, a rediscovery of HIFU for tumor therapy occurred with the advancement of new technologies, especially sophisticated imaging techniques such as MR thermometry. In 1994, the first commercial device (Sonablate 200) received CE approval and launched in Europe for BPH treatment. The device was developed by Focus Surgery Inc. which later had been renamed to SonaCare Inc. The device has been used to treat patients and its clinical efficacy and possible side effects have been investigated. Ablatherm in the 2000s was also approved for PC therapy in Europe, Canada, South Korea, and Australia [84].

As of 2012, clinical trials in the USA for the Sonablate 500 are underway for men with PC and others who have suffered radiation failure [85]. The use of MRI was first cited and patented in 1992 [86,87]. The technology was later transferred to Insightec in Haifa, Israel in 1998. The Insightec ExAblate 2000 became the first MRgFUS device in the USA to receive regulatory

approval from the FDA. Insightec was awarded a premarket approval from the FDA in 2016 to market its ExAblate Neuro program for treating essential tremor [88].

3.3 Physics and mechanisms of HIFU

Currently, the majority of US technologies is used for clinical imaging. The US waves are longitudinal waves and their frequency range is between 1-10 MHz. The main disadvantage of US waves is that they require a specific medium to propagate. US waves use the phenomenon of piezoelectricity.

The intensity range of diagnostic US is in the range of 0.1-2 W/cm^2. HIFU uses a thousand times higher intensity than diagnostic US (500-10000 W/cm^2). The main factor that produces heat elevation is the friction of the US waves with the tissue and the spherically-focused waves. Lesions can be produced by a temperature change of 60-100 ^{o}C. This high-temperature change can destroy cancerous cells. The focused transducer induces low intensity at the front face of the element and high intensity at the focal point. There are three different ways to focus US waves at a focal point in the tissue. The easiest way is to use a spherical element or a lens that its geometry focuses the US waves on a single point (Figure 3.3.1.a).

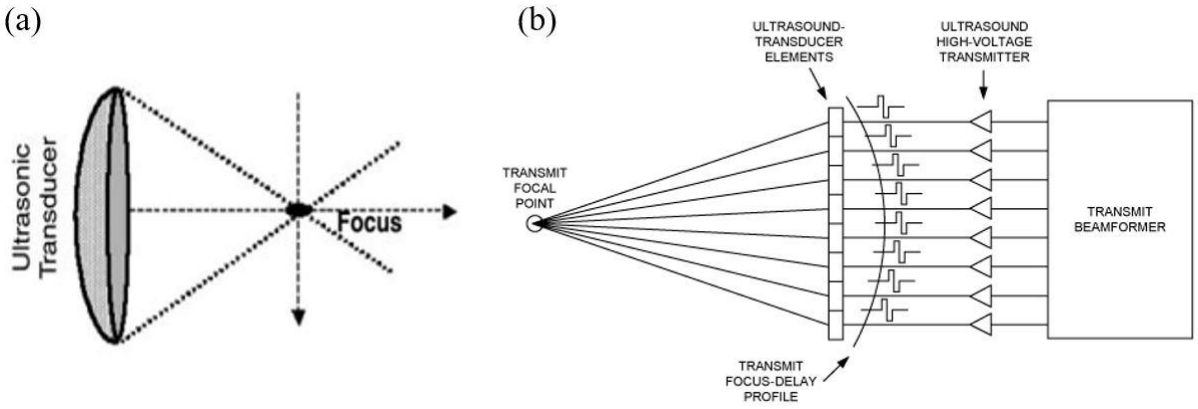

Figure 3.3.1: a) Single element focused transducer, and b) multi-element phased array transducer [89].

Three main parameters to achieve the distance of the focal point as well as the thickness of the focal beam are the diameter of the piezoelectric element, the wavelength of the element, and the geometric radius of curvature.

The other way which is much more complicated is the use of a phased array transducer (Figure 3.3.1.b). A phased array might include many elements and the focal beam can be electronically

steered by activating different elements. The main disadvantage of a phased array is that each element must receive an amplified signal, therefore many amplifiers are needed (in a matter of cost), as well as a complicated algorithm is required to organize the activation time of the elements.

During a HIFU sonication, different physical mechanisms might be developed when the US waves interact with tissue. Microbubbles that could possibly exist in the tissues or might appear (randomly or intentionally by injection) have both positive and negative impacts on US applications. A microbubble compresses, remains stable, and expands during stable cavitation, then inertial cavitation happens and ultimately the microbubble destructs leading to an uncontrollable increase in temperature.

The two main mechanisms of HIFU are the thermal effect (Figure 3.3.2.a) where the temperature is increased up to 60 to 100 ^{o}C and cavitation (Figure 3.3.2.b) where there is an interaction of US with microbubbles.

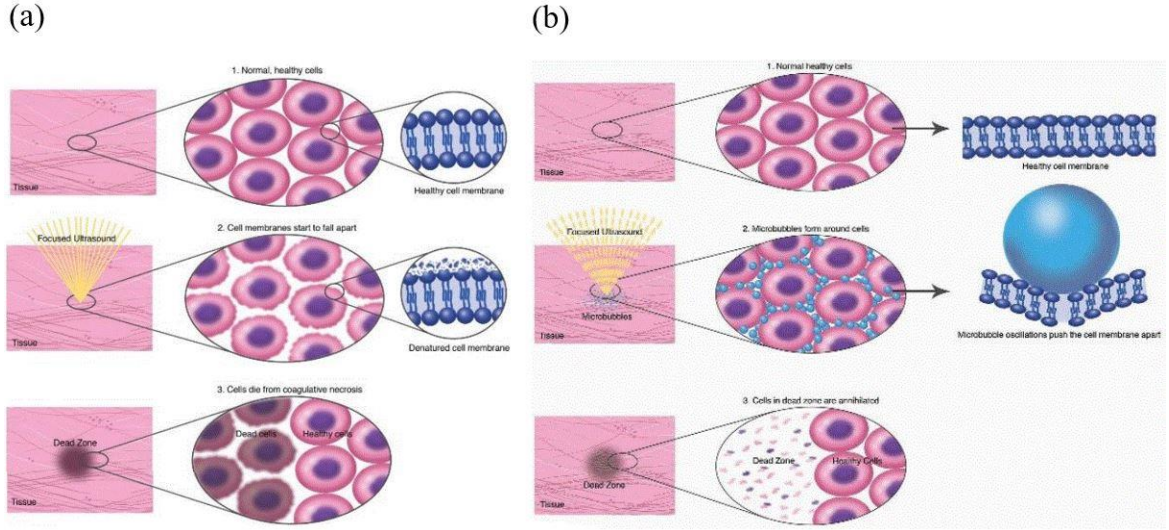

Figure 3.3.2: The main mechanisms of HIFU, a) Thermal effect, and b) Cavitation [90].

The measurement of HIFU acoustic power and power field is also of great importance for HIFU systems. Hydrophones (membranes, needle) are mainly used to investigate the power field of a transducer while the acoustic power is measured using a power meter (radiation force balance method). Thermal dose is another parameter of HIFU and is expressed as the time in minutes for which the tissue has to perform at 43 ° C to have the same biological damage as produced by the actual temperature, and which can change over time during a long exposure.

The diagram in Figure 3.3.3 shows how HIFU can be used to destroy tissue in the body where the sound waves propagate through many layers of tissue. Because of the focal gain, only tissue at the focus is destroyed.

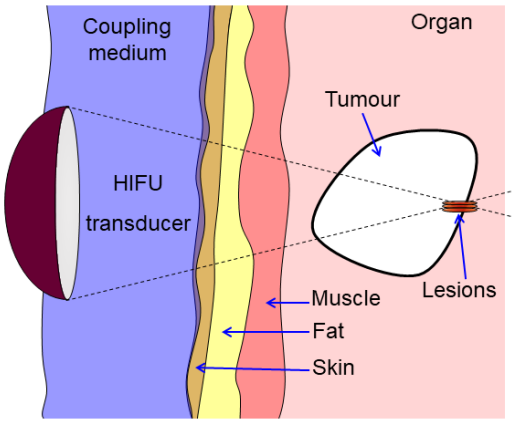

Figure 3.3.3: Schematic diagram of HIFU for the treatment of a soft tissue tumor [91].

Other applications of HIFU are the Blood-Brain Barrier opening, Alzheimer, Parkinson (essential tremor), targeted drug delivery, neuromodulation, clot lysis, sonoporation, and local hyperthermia.

3.4 Multiparametric MRI and image guidance options of HIFU

Until now, there are no blood or urine-based biomarkers that can reliably detect a tumor in the prostate but improvements in MRI techniques have enabled the radiologist to play a key role in the risk stratification and management of patients. Instead of using a PSA test or biopsy, multiparametric MRI (mpMRI) is the new imaging technique to detect prostate tumors. The functional sequences of mpMRI are dynamic contrast-enhanced (DCE) and diffusion-weighted imaging (DWI) including the calculation of apparent diffusion coefficient (ADC) maps. MRI cannot detect all prostate tumors and has poor sensitivity for low volume Gleason score 3+3 disease [92].

Recently, in a study, Ahmed *et al.* [93] used mpMRI as a triage test to check if mpMRI can allow men to avoid unnecessary biopsies and improve diagnostic accuracy. In total, 740 men underwent 1.5 T mpMRI followed by both TRUS-biopsy and template prostate mapping (TPM)-biopsy. During TPM-biopsy it was found that 408 men had cancer, with 230 of 576 men clinically significant. For clinically significant cancer, mpMRI was more sensitive than TRUS-biopsy and less specific.

Both MRI- and US-guided techniques can be used to estimate the distance between the skin and the superficial or deep surface of the tumor, regardless of whether the involved skin and chest wall areas can be directly imaged. Nevertheless, MRI is more precise and reproducible than US in establishing the exact location and extent of cancer in a given patient, as well as the amount of spread. The improvement of 3 T MRI from the previous 1.5 T MRI additionally increases the ability of MRI to define tumor boundaries. MRI enables a larger scanning range and provides more reliable images than US. MRI can be used to recognize ipsilateral axillary, supraclavicular, and parasternal lymph nodes positive for lesions with less user variability than US [94,95]. MRI recognizes isoechoic lesions that are not apparent using US imaging. Altogether, MRI is a more comprehensive technique for locating lesions. Real-time 3D US provides 3D structural images [96]. The gross target volume and borders of normal tissue can be precisely established, the surrounding vital organs can be protected, and a complete ablation of the tumor at the same time can be attained. However, MRI offers excellent 3D images at a higher spatial resolution and more quickly than the 3D US in most situations. MRI is not appropriate for patients with magnetic metal implants. The resulting artifacts influence the quality of imaging, and more importantly, implants may endanger patients during HIFU therapy. US-guided HIFU does not have this contraindication. Real-time imaging US guidance is useful, providing real-time imaging at a relatively low cost, although with a limited FOV, spatial resolution, and contrast resolution.

During HIFU treatment guided with MRI, feedback is a major characteristic of accurate treatment. Since HIFU is a thermal procedure, non-invasive temperature monitoring can be achieved with MRI-based temperature-sensitive MR parameters such as the proton resonance frequency (PRF), the diffusion coefficient, T_1, and T_2 relaxation times, the magnetization transfer, the proton density, and temperature-sensitive contrast agents [97]. MR thermometry provides high temporal and spatial resolution to precisely monitor the temperature distribution within the targeted tumor and predicts the outcome of the thermal treatment. Fast temperature mapping can be achieved with echo-planar imaging (EPI) or segmented-EPI acquisitions. The most significant problem for temperature monitoring with PRF phase mapping is motion. Motion artifacts can be divided into intra-scan motion and inter-scan motion [97]. De Poorter *et al.* [98] in a study showed that high-quality temperature images can be acquired from gradient-echo sequences with an accuracy of 0.2 ^{o}C in phantoms. Finally, Salgaonkar *et al.* [99] combined HIFU treatment with MR thermometry, and experiments were conducted in tissue-equivalent phantoms.

3.5 HIFU robotic systems

3.5.1 MR compatible materials

A robotic system that is intended to work in MRI must be MR compatible for many reasons such as MR safety, preservation of image quality, and ability to operate unaffected by the scanner's electromagnetic fields [100]. The image quality needs to be high in order to obtain accurate results. The monitoring of temperature change in real-time at the treatment location where necrosis might occur is an important point for using FUS under MRI guidance. An accurate temperature change can be recorded only if the image quality of the acquired MR images is sufficient for proper image processing using MR thermometry.

Any ferromagnetic material must be avoided entirely since this type of material causes image artifacts and distortion [101]. Non-ferromagnetic metals such as aluminum, brass, titanium, high strength plastic, and composite materials are permissible, but they might cause imaging artifacts due to their interactions with the MR-field gradients [102]. Acrylonitrile Butadiene Styrene (ABS) and other 3D printing materials are MR compatible [103].

3.5.2 MR compatible actuators/motors and digital encoders

MR image artifacts may be caused due to the use of piezoelectric based-actuators. Piezoelectric actuators have been extensively used for MRI applications and shown to be MR compatible. Various types of MR compatible piezoelectric-based actuators have been developed and used in MRI-guided therapeutic applications [104,105]. The motion of medical robots is performed via the actuators and each DOF needs an encoder (linear or rotational) that works as detector of the motion. During motion of a robotic system, the encoders and signals that are transferred via a cable, can create artifacts and distort or shift the MR images by decreasing the homogeneity of the magnetic field. Moreover, the activation of the FUS transducer might cause artifacts to the MR images.

An MRI medical robotic system can be tested for MRI-compatibility by evaluating the effect of the stage on image artifacts, Signal-to-Noise Ratio (SNR), and magnetic field (B_0) homogeneity. The use of each stage in the MRI scanner is evaluated with different pulse sequences. Proper attention to materials used in device design, electronic shielding and object placement as well as location and orientation in the MR field can help control the effects of

imaging artifacts. According to the FDA and the American Society for Testing and Materials (ASTM), three levels of MRI device classification are defined [106,107] as MR safe (safe to use in all MR environments), MR unsafe (poses a risk to the patient or the operator) and MR conditional (safe to use in a specific MR-environment).

The MR compatibility can be evaluated based upon changes in SNR. SNR is the signal in the center of a homogeneous phantom or tissue, divided by the noise intensity in the periphery as defined by the National Electrical Manufacturers Association (NEMA) standard for determining SNR in MR images [108]. The signal is defined as the mean pixel intensity in the region of interest (ROI). The noise is defined as the root mean square (RMS) signal intensity in an ROI outside of the tested material.

Medical robotic systems that are suitable in MRI-environment have been reported so far [100,109-119] and a review of the deteriorations which these robotic systems create in the SNR of an MR image are discussed. The robotic systems are mainly systems for prostate interventions using needle [109-111], surgical assisted robots [100,112], surgical robot for deep brain stimulation [113], image guided interventions [114], diagnostic and therapeutic interventions in the abdominal and thoracic cavities [115], heart diseases [116], and transnasal neurosurgery [117]. Additionally, the clinical Philips Sonalleve MRgFUS system was also tested for MR compatibility [118].

The SNR according to the distance of different types of motors from the center of the MR bore was estimated [119-121]. The SNR according to the distance from the center of the MR bore of a conventional joystick was also tested and it was observed that when the joystick was placed 15 cm away from the phantom object, it did not cause any distortion to the MR image. The piezoelectric (ultrasonic) motors, even though they are magnetism free, due to their operating high frequency currents can create image distortion if operated closer than 0.5 m from the image isocenter [121]. The Shinsei motors are widely used for MR compatible robotic systems [100,101,118,121,122] while Nanomotion motors are used only in few cases possibly due to their high price [101,110]. However, it was observed that as the Nanomotion motors move away from the edge radiofrequency (RF)-coil, the SNR remarkably increases until a distance of 0.6 m, while further removal does not show any change in the SNR [121]. Another important result is that with more severe operating conditions like higher voltage or higher speed, the SNR drops.

A device shall be considered as "MR compatible" if its use in the MR-environment does not adversely impact the image quality. A comparison of the SNR between three types of motors was performed [101]. It was observed that the pneumatic cylinder and controller cause no negative impact on the SNR, the Nanomotion motor slightly reduces the SNR under 3 T, while under 1.5 T the reduction is significant. Pneumatic actuators are an ideal choice for MR compatibility since they are electromagnetism free, but they are hardly controllable. The Shinsei motor causes large reduction in SNR compared to the Nanomotion motor and the pneumatic cylinder. In all cases where the Shinsei motors have been tested for MR compatibility, it was found that the SNR showed no reduction with the motors disabled whereas with activation of the motors they do not significantly affect the SNR nor create artifacts in the MR images. In another case, the MR compatibility of the Shinsei motors was examined using fast imaging with steady-state precession (FISP) sequence [111]. The SNR variation of ultrasonic motor under different conditions was measured. The SNR with motor unwired showed a 6.9 % reduction, with motor wired but not powered there was a slightly higher loss of SNR (7.6 %), with motor powered but not actuated a loss of 11.7 %, motor actuated at half max speed a loss of 13.8 %, and motor actuated at max speed a reduction in the SNR of 13.7 % was observed. The results using the Shinsei motors demonstrate the good compatibility of the piezo-motor with the MR-environment and consequently the piezo-motors are considered as MR compatible. Moreover, the change in the SNR by the addition of motors in MRI of 1.5 and 3 T was compared [101]. The SNR loss is greater on 1.5 T MR scanner than on 3 T scanner.

Studies were performed to evaluate the effect of SNR after shielding the robotic device, motors and wiring of the devices [110,115,119,124]. Shielding of the electronic parts of the robotic devices improves the SNR and avoids artifacts in MR images. In a study [110], by turning the controller on with motors disabled reduced the SNR by 50 % without shielding. The SNR was reduced by 80 % without RF shielding and 40-60 % with RF shielding. In another study [119], the quality of MR image was improved by adding a shield cloth around a motor (spherical ultrasonic motor). At the center of the imaging volume, the SNR without the shield was 11 while with the shield the SNR increased to 77. Shielding of the Shinsei ultrasonic motors was tested in order to achieve higher SNR in MRI-environment [115]. During the SNR measurement having a phantom inside the MRI room and when the motor was deactivated, the SNR dropped when the unshielded motor was activated. After shielding the motor, the SNR recovered to high values.

The activation of the encoders also affects the SNR of the MR images [110,112]. Encoders are activated when the motors move in order to know when the motors should stop. Thus, encoders and motors are usually activated together to create motion of the robotic device. Despite that motors and encoders are operated relatively close to the scanner's imaging isocenter, the system still causes negligible interference with the scanner. The success of the scanner tests described in a paper [112] has shown that the sources of imaging interference produce an acceptably low contribution to the SNR-variation of the imaging. Configurations were the phantom only, motor and encoder unpowered with controllers direct current (DC) power supply turned on, and motor running at a specific speed. The SNR with motor deactivated was improved while with motor activated there were no statistically significant variations between baseline (with phantom only) and motor running conditions. The MR compatibility of the encoders was also examined using fast low angle shot (FLASH) 2-dimensional (2D) gradient echo (GRE) sequence [110]. The SNR with encoder unwired showed a minor reduction of 0.4 % and with encoder wired but not powered, there was a loss of 1.7 %. Lastly, the SNR with encoder in power showed a reduction of 2.6 %.

MR compatible focused transducers are constructed by companies active in the field of HIFU (Sonic Concepts, Imasonic, Biopac Systems, FUS Instruments, Medsonic Ltd.). In a study [126], the MR compatibility of a ring transducer was examined. T_1 images of a pork and a ring transducer during HIFU sonication showed that the noise occurred between the ring transducer and the pork. The source of noise could be the eddy current generated by the closed loop circuit such as the grounding electrodes of the ring transducer. However, the MRI interference from HIFU did not occur in the ROI and the ring transducer could emit HIFU to ablate the pork as planned in the process of MR imaging. In another study [127], an MR-compatible HIFU system was successfully adapted to perform localized mild hyperthermia treatment in rodent models and focused transducers with sector-vortex lenses were tested for MR compatibility. The effect of MR compatible focused transducers housed in US probes on MRI monitoring were evaluated [128]. It was found that MR compatible US probes with backing material containing a specific amount of a material (ferrite) did not disturb MR monitoring, except within a few mm radius from the US probe's position. Lastly, a Sonic concepts transducer was tested for MR compatibility [129]. When the transducer was introduced in the MRI (activated) without DC supply activation, the SNR dropped drastically, meaning that the RF artefact of the transducer caused major artefacts despite the use of a low-pass filter.

Robotic systems, ultrasonic motors, and encoders either with shielding or not, were tested for MR compatibility using various MRI sequences [101,110,113-118,123,129]. The most common MR sequences that are used to monitor treatment and obtain high resolution images are the T_1-weighted, T_2-weighted, Spin Echo (SE), Fast Spin Echo (FSE), GRE, Fast Spoiled Gradient (FSPGR), and EPI. A comparison between these common MR sequences was performed and it was concluded that they show similar SNR behavior [110,113,116-118]. A body RF-coil was used to acquire SE and GRE images of a compact linear motion stage which is actuated with ultrasonic motor [113]. The system revealed a limitation when the motor was very close to the isocenter. The limitation was that some pulse sequences (GRE, DWI, and FSE) may introduce extensive noise on the encoder signal line, resulting in device malfunction.

3.5.3 MR compatible robots

HIFU is an emerging technology that has the potential to treat various deceases completely non-invasive. The US can induce thermal effect as well as mechanical, by setting up the parameters according to the application. When delivered in form of continuous wave it can, within seconds, raise the temperature to lethal levels which results to a complete coagulation of the tissue [130]. The contrast between necrotic and normal tissue with MRI is better than using US imaging and this has been confirmed in several studies [131-133]. For larger tumors though, it is impossible to cover the entire area with just one sonication. Since the focal area of a transducer covers approximately 1-4 mm in diameter, in order to ablate large tumors it is necessary to maneuver the transducer for generating overlapping lesions. For this reason, a positioning device is required for the accurate motion of the transducer. With such systems performing a FUS surgery is much safer and the time duration is reduced. Also, the accurate motion of the transducer is a significant factor in the efficiency of the treatment.

The development of an MRI-safe positioning device is challenging since the materials and the size are limited. The positioning device must be composed of non-magnetic materials. The size is also limited by the available space in the coil of the MRI scanner. MR-safe positioning device refers to the device that is not hazardous in any way and does not generate interference with the MRI scanner nor is affected by the strong electromagnetic field of the MRI scanner [134-136].

The first positioning device that was developed, used hydraulic principles for the actuation however it proved unreliable and the motors interfered with the MRI scanner [137,138].

Placing the motors away from the MRI to reduce interference resulted in complicated systems and thus the concept of a hydraulic positioning device was abandoned. Recently, many positioning devices have been developed and some of them have already been tested in clinical trials. Robotic systems nowadays use piezoelectric motors or pneumatic principles for the actuation since they are accurate.

A very successful system is Insightec's ExAblate 2000 [139]. This device is driven with piezoelectric motors and is embedded in the patient's table. It has been primarily designed to be used for the treatment of uterine fibroids [140,141] and leiomyomata [142,143] but was later also used for the treatment of PC [144,145], breast cancer [146-148], liver cancer [149,150], pain palliation and bone metastasis [151-154]. Some artifacts were observed, possibly caused by the piezoelectric motors [102] but the SNR was later increased significantly by placing the motors away from the imaging coil. Following the success of the ExAblate 2000, Insightec introduced the ExAblate 4000. This is a very promising system to execute a complete non-invasive transcranial FUS delivery into the brain. It is composed of hundreds of elements in order to spread the acoustic waves in a larger surface across the skull, thus reducing significantly the risk of overheating the skull bone. The potential of this device to focus in the brain though an intact skull can be applicable for the treatment of a stroke, brain tumors, and functional disorders. The main disadvantage of the phased array is the high cost and complexity of operation.

Most of the robotic devices are designed for a specific use. Positioning devices have been manufactured initially for small animal trials. Subsequent positioning devices were made for treatment of organs accessible by HIFU. A good example of these positioning devices is a computer control three-axis robot that has been developed by Chopra *et al*. [104] which intended to be used on small animal models. This particular system was designed using aluminum, beryllium copper, and ceramic balls which are non-magnetic. The motion was enabled with the use of piezoelectric motors. A precise motion was established with optical encoders.

Another robotic system that can be used for the treatment of various organs has been developed by Damianou *et al.* [155]. It has the ability to navigate the transducer in three dimensions. Also, it includes a flexible coupling design that enables targeting to various anatomies. This robot was mainly composed from ABS and brass rods. The motion is enabled with a belt and pulley system and the motion is established by three piezoelectric motors. The amount of motion is monitored by optical encoders in real-time for adequate accuracy and reliability. An advantage

of this device is that it does not require to be integrated in an MRI table and thus it can be used in any typical available MRI scanner. The 6 kg weight can be considered to be portable and it can be easily prepared for operation in minutes.

Mylonas *et al.* [156] introduced an MR conditional robotic system for the treatment of brain diseases. It was designed with a similar concept from a previous system [155] with less complexity. The motion was energized by three piezoelectric motors, and the conversion of the rotational motion to linear was achieved with a rack and pinion pair. A positioning device designed by Yiallouras *et al.* [19] was specialized for the treatment against PC. This device was very small and compact with a length of 24.5 cm, width of 19.5 cm, and a weight less than 2 kg. It was made out of ABS plastic and its motion was activated by two piezoelectric motors. The device included 2-DOF (forward and reverse) as well as angular motion with 180 degrees range. The use of optical encoders ensured the amount of motion was executed by the device with an accuracy of 20 μm. This device was designed to perform treatment endorectally so that the transducer accesses the prostate. It was also able to be placed in any available MRI scanner due to its very small size.

Different means have been used for the evaluation and treatment planning of MRgFUS applications. For example, the ONDA HIFU gel can provide visual contact with the focus to enable observation of a lesion as it is created. Currently for preclinical trials, *ex vivo* human skull has been utilized but it is required to be fresh in order to preserve the properties of a human skull. Recently Menikou *et al.* [157] has developed an MRI compatible human head model for FUS surgery. This particular head model was a combination of a skull that was made out of ABS material and agar solution that mimicked the brain tissue. The skull model was based on CT scan data of random patients and its acoustic properties were similar to those of human skull. Also, the geometry of the skull was close to human and it could be easily customized to a specific patient. Similarly the attenuation coefficient of the agarose gel was matched to that of a typical brain by varying the concentration of silica in the gel [157].

3.6 Available approved HIFU devices for prostate cancer therapy

3.6.1 Sonablate HIFU device

The Sonablate system (Sonacare Medical LLC) is a minimally invasive robotic device that delivers precise and focused ablative energy [158]. It is the first commercialized probe for

HIFU ablation of prostate. A customized plan for each patient's individual prostate needs can be created. This device transmits sound waves at a desired location within the prostate. Sonablate system is depicted in Figure 3.6.1.1, its probe is shown in Figure 3.6.1.2 and its main characteristics are indicated in Table 3.6.1.1.

Figure 3.6.1.1: Sonablate 500 system (Sonacare Medical LLC) [158].

Figure 3.6.1.2: Sonablate HIFU probe (Sonacare Medical LLC) [158].

Table 3.6.1.1: System specifications of Sonablate HIFU device [159].

System Cost (approx.)	$450000
Disposable Cost	$2400
Weight	300 lbs.
Set Up/Clean Up Time	15-20 min/20-30 min
Treatment Time	Ablates 10 cc/hr
Transportable	Yes
Multimodality	Yes
Tele-monitoring	Yes
Probes included	2
Probe Size	33 mm
Coupling Medium	Degassed water
Patient Position	Lithotomy
Rectal Wall Distance Monitoring	Yes
Rectal Wall Temp. Monitoring	Yes
Patient Movement Sensor	No
Organ Movement Feedback	Yes
Reflectivity Index Monitor	Yes
Number of Transducers	4 (2 for imaging, 2 for therapy)
Imaging Frequency	6.3 MHz
Therapy Frequency	4 MHz
Transducer Focal length	Dual focal lengths (4 cm and 3 cm)
Robotic/Motorized	Yes

The main intriguing characteristics are the probe size (33 mm width), transducer focal length (dual focal lengths of 3 and 4 cm), imaging frequency (6.3 MHz) and therapy frequency (4 MHz). Sonablate system has several available probes that are chosen by the operator according to the size of the lesion. For a lesion of 10 mm in length and 2 mm in diameter and a single beam, a 25 or 45 mm focal length probe is used, while for a lesion of 10 mm in length and 3 mm in diameter and a split-beam, a 30, 40 or 45 mm focal length probe is used. The treatment procedure is often performed in 3 coronal layers starting from the anterior part of the prostate and moving to the posterior part with at least one probe switch during the treatment. Dorsal

position is chosen during the procedure under anesthesia. Figure 3.6.1.3 shows the treatment planning (image fusion between MRI and US images) of the Sonablate system.

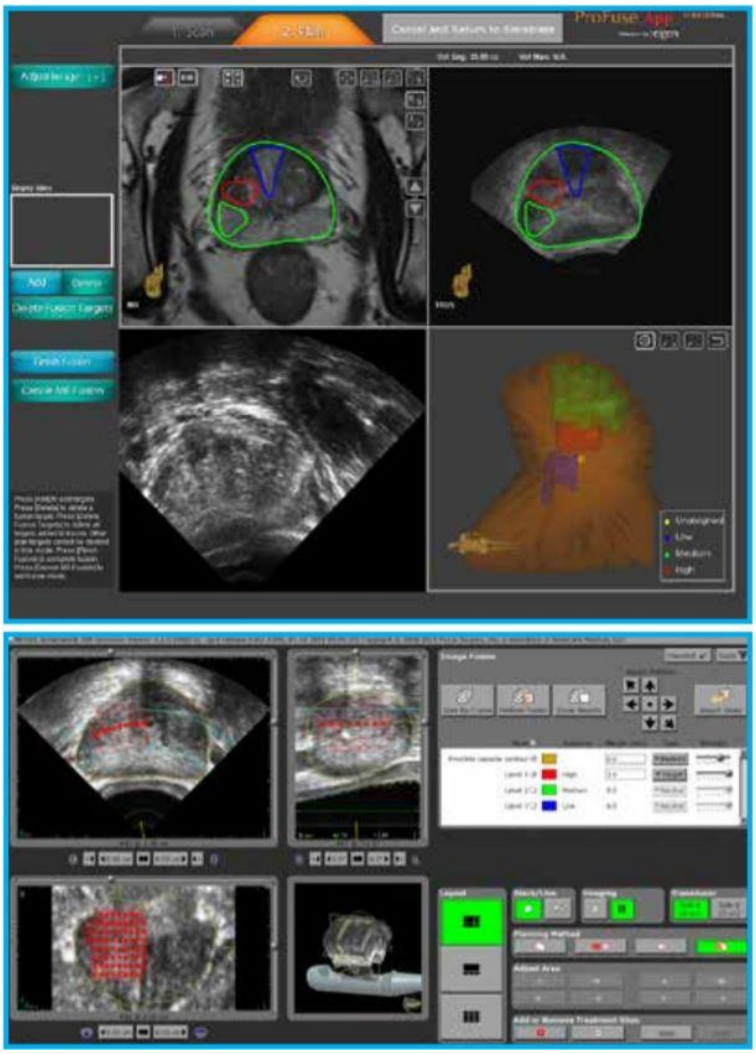

Figure 3.6.1.3: HIFU treatment planning of Sonablate. MRI and US images are fused for better targeted treatment [158].

3.6.2 Ablatherm and Focal One HIFU devices

The Ablatherm HIFU device (Edap TMS) has been developed since 1993 for the radical treatment of localized PC [160]. The whole device includes a treatment module, a control module, and a probe with both therapy and imaging transducers. This HIFU technology has a unitary lesion of 19 mm to 26 mm height, 1.7 mm width, an automatic dispatching of the HIFU lesions, precise destruction of the tissue, precise robotic movements, real-time tracking, and adjustment of energy delivered [160]. It also includes safety features such as rectal cooling, patient movement detection, and real-time rectal wall monitoring. At the focus, the US waves create a temperature increase (approximately 85 ^{o}C) and destroy the tissue. The Ablatherm

device is depicted in Figure 3.6.2.1, its probe is shown in Figure 3.6.2.2, and its main characteristics are listed in Table 3.6.2.1. In Figure 3.6.2.3, three main treatment phases of the Ablatherm device are depicted.

Figure 3.6.2.1: Ablatherm HIFU device (Edap TMS) [161].

Figure 3.6.2.2: Ablatherm HIFU probe showing the treatment and imaging probes [160].

Figure 3.6.2.3: The three main phases (image, plan, treat) of the Ablatherm HIFU device [160].

Table 3.6.2.1: System specifications of the Ablatherm HIFU device [159].

System Cost (approx.)	$750000
Disposable Cost	$1200
Weight	950 lbs.
Set Up/Clean Up Time	15-20 min/20-30 min
Treatment Time	Ablates 10 cc/hr
Transportable	Yes
Multimodality	No
Tele-monitoring	No
Probes included	1
Probe Size	36 mm
Coupling Medium	Proprietary gel
Patient Position	Lateral
Rectal Wall Distance Monitoring	Yes
Rectal Wall Temp. Monitoring	Yes
Patient Movement Sensor	Yes
Organ Movement Feedback	No
Reflectivity Index Monitor	No
Number of Transducers	2 (1 for imaging, 1 for therapy)
Imaging Frequency	7.5 MHz
Therapy Frequency	3 MHz
Transducer Focal length	4.5 cm
Robotic/Motorized	Yes

The first phase is the 3D imaging of the prostate before treatment begins (using a 7.5 MHz transducer), the second is the treatment planning and the last is the robotic treatment where the robotic device follows the treatment plan [160]. The Ablatherm system includes the patient's bed, a probe positioning device, an US power generator, a cooling system, and an US scanner. It also uses a safety ring that stabilizes the rectal wall during transducer movements, a patient motion detector that stops the treatment if the patient moves during the firing sequence, and a control of the distance between the rectal wall and the transducer. Due to the fact that the shape of a lesion depends on gland perfusion, treatment parameters are different. It uses a 5 s treatment pulse and 5 s shot interval for the first HIFU session in primary care, 4.5 s treatment

pulse and 5 s shot interval for the second session in primary care and 4 s treatment pulse and 7 s shot interval for local relapse after EBRT. Lateral position is used under anesthesia and treatment is performed from the apex to the base of the prostate. At the end of a HIFU session, a Foley-type urinary catheter or suprapubic tube is positioned.

A comparison between Sonablate HIFU system and Ablatherm was performed [159]. Clinical data showed 87 % negative biopsy for Sonablate and 68 % for Ablatherm. The stackable lesion of Sonablate is 12 mm while for Ablatherm is 24 mm. In Figure 3.6.2.4 some differences for hemi-gland and focal ablation are shown between Sonablate and Ablatherm HIFU medical devices.

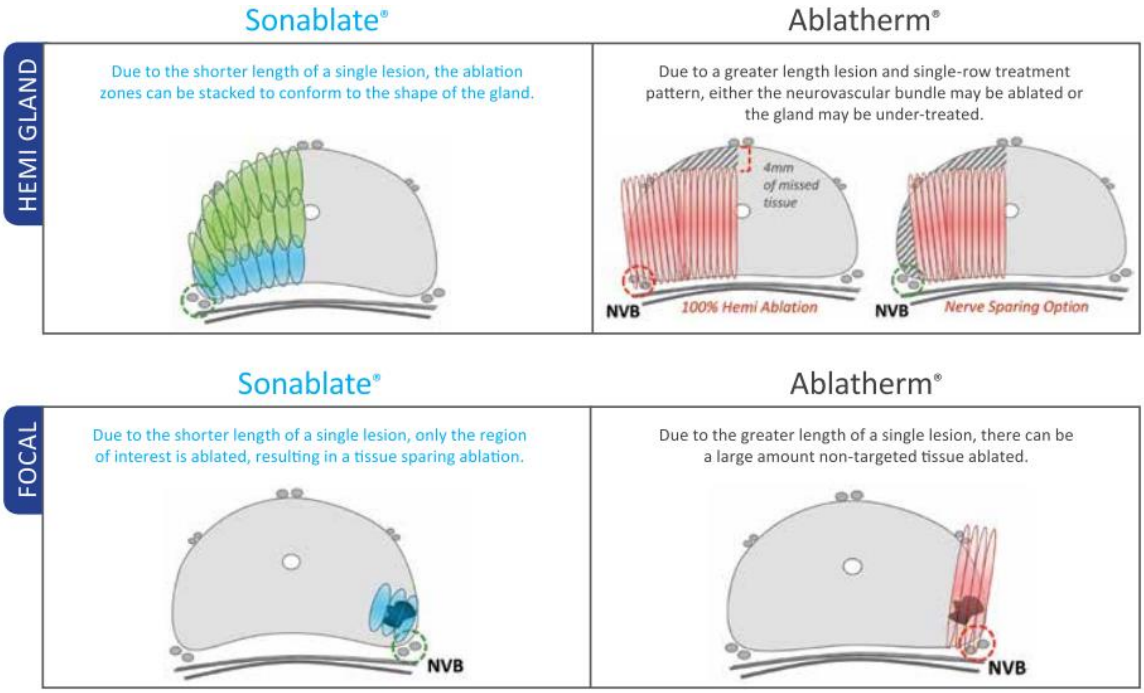

Figure 3.6.2.4: Comparison between Sonablate and Ablatherm for hemi-gland and focal ablation [159].

Focal One (Edap TMS) has some advantages over Ablatherm HIFU. Focal One is more accurate and uses MR-fused imaging. MR images can be imported from PACS (Picture Archiving Communication Systems) and there is an elastic fusion which automatically matches the 3D contours of the prostate on the US and MRI images [161]. Moreover, Focal One produces a non-invasive, precise and efficient therapeutic HIFU energy for a precisely defined area that needs to be treated. It also uses contrast-enhanced US for validation of treated areas, it has capability to review the treatment images as well as make a comparison with MRI images. Another advantage is that it can track and adjust the delivered energy in real-time. Focal One

is depicted in Figure 3.6.2.5 and some steps of the pre- and pro-treatment procedure are shown in Figure 3.6.2.6.

Figure 3.6.2.5: Focal One HIFU device (Edap TMS) [161].

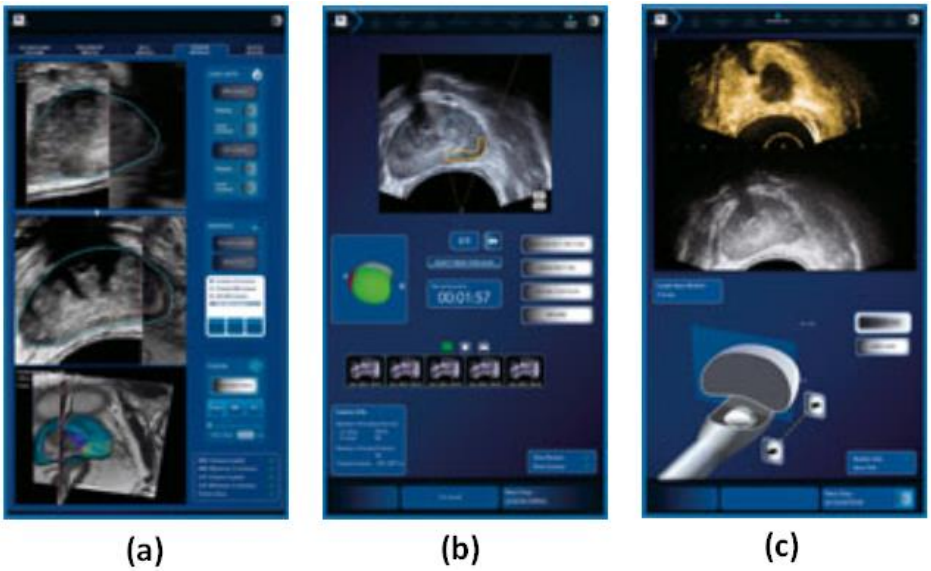

Figure 3.6.2.6: Steps of the treatment procedure of Focal One; (a) MRI import and fusion, (b) Precise contouring of zone to be treated, and (c) Validation of treated area [161].

3.6.3 ExAblate HIFU device

The ExAblate system (Insightec Ltd.) was designed for image-guided therapy and approved for MRI-guided prostate ablation. The treatment process is monitored in real-time using MRI-based temperature measurements [162]. ExAblate's trans-rectal transducer consists of a 1000-element covered by an endorectal balloon that contains degassed water (14 ^{o}C). Also, its frequency is 2.3 MHz and it can steer in x, y, and z axes in real-time [163]. The ExAblate system as attached on the MRI bed is depicted in Figure 3.6.3.1. Figure 3.6.3.2.a shows the

probe of the system, Figure 3.6.3.2.b shows the treatment plan, and Figure 3.6.3.2.c shows an MR thermometry result during an experiment in a TMM.

Figure 3.6.3.1: ExAblate 2100 HIFU device attached on the MRI bed [162].

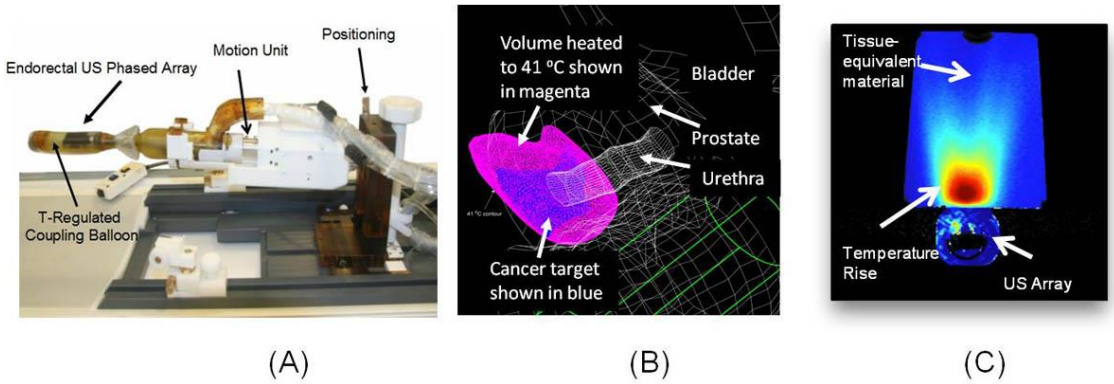

Figure 3.6.3.2: ExAblate 2100 HIFU device (Insightec Ltd.) a) probe, b) treatment plan, and c) MR thermometry [162].

3.6.4 Transurethral HIFU devices

Many researchers have developed catheter-based US devices guided with MR thermometry for PC therapy. Diederich *et al.* [164] has developed four types of transurethral applicators; (1) a sectored tubular transducer device with directional heating pattern and rotation, (2) planar and (3) curvilinear devices with narrow heating patterns and rotation, and (4) multi-sectored tubular device capable of dynamic angular control without applicator movement. Then, using these four types, *in vivo* experiments were conducted in canine prostates by acquiring MR temperature imaging in order to test the devices and find different treatment strategies. The multi-sectored transurethral applicators can dynamically control the angular heating profile and target large regions of the prostate in short treatment times. The MR recorded temperature of 52 ºC with catheter-based applicators can produce precise thermal ablation of the prostate in 5-

40 minutes. Ross *et al.* [165] has also constructed and tested two types of catheter-based US applicators using 90^{o} sectored tubular (3.5 mm outer diameter x 10 mm) and planar transducers (3.5 mm x 10 mm). These catheter-based applicators were MR compatible and capable of manual rotation of transducer array within a 10 mm cooling balloon. Tests were performed in 3 canine prostates using MRI guidance. Coagulated areas were noticed using single sonications with the 90^{o} tubular applicator covering 80^{o} wedge of the prostate and extending 1-2 mm outside the urethra to the outer boundary of the gland. Thermal lesions of around 30^{o} extending to the prostate boundary were produced using single sonications with the planar applicator whereas, multiple sequential sonications showed controllable coagulation of 270^{o} continued section of the prostate extending to the capsule boundary.

Furthermore, Chopra *et al.* [166] has reported a prototype system developed for MR-guided transurethral PC treatment and tested various components of this system such as the heating applicator design, rotational motor and RF electronics. This system consisted of a planar transducer and was MR compatible, while MR temperature measurements were obtained up to 6 mm from the device. Experiments were performed in phantoms as well as in a canine model. The experiments showed that the patterns of thermal damage agree with quantitative measurements of the spatial heating pattern acquired during treatment. In 2010, Chopra *et al.* [167] has reported the development of MRI-controlled transurethral US therapy. Temperature feedback algorithms and results from numerical and experimental modelling were obtained in animals and humans. The developed temperature feedback control algorithms using MR thermometry showed that spatial treatment accuracy of a few millimeters *in vivo* could be achieved. Surrounding tissues can remain undamaged if correct measurements are taken into account during the treatment planning.

In addition, Siddiqui *et al.* [168] has tested transurethral US therapy in both canines and humans using MRI guidance. A single element transducer was used to treat nine dogs and an urethral applicator with multiple transducers was used to treat another eight dogs. During the experiments the spatial temperature distribution was measured every 5 s with MR thermometry using the proton resonance frequency shift (PRFS) method. Also, 5 patients were treated before receiving radical prostatectomy and around 30 % of the gland volume was targeted. The average spatial precision of the treatment was 1-2 mm while the correlation between thermal, anatomical, and histologic images was equal or less than 3 mm. The treatment time was reported to be less than 30 minutes.

Lastly, Diederich *et al.* [169] designed and tested an applicator for transurethral US thermotherapy. A tubular multi-transducer applicator was designed (2.5 mm in diameter, 6 mm long, and 6.8 MHz). Computer simulations have showed that 1.4-2.0 cm radial therapeutic zones can be produced within prostate in 15-30 minutes. After *in vivo* thermal dosimetry characterizations, it was indicated that therapeutic temperatures between 50 and 90 ^{o}C are controllable and attainable in the circumferential and longitudinal directions with effective radial heating.

Profound Medical Corp. is a medical device company that has developed ground-breaking technology in the area of localized PC using transurethral devices. Many clinical trials were conducted using Profound's devices [170-171]. In a recent case study, Mueller-Wolf *et al.* [170] used Tulsa-pro device as shown in Figure 3.6.4.1 to treat patients with PC. The US applicator, endorectal cooling device, and positioning system of Tulsa-pro are placed inside the scanning room on the MRI bed. The treatment delivery console and system electronics remain outside the scanning room, in the console and equipment room, respectively. The device uses a linear array of ten planar rectangular transducers (4-4.8 MHz) and it was CE approved in Europe in 2016.

Chin *et al.* [171] also used Tulsa-pro device to determine its clinical safety and feasibility. Overall, 30 patients with mean age of 69 years were treated. From these patients, 24 were at low risk disease while the remaining 6 at intermediate risk. The median US treatment time was 36 minutes and the prostate volume 44 cc. Side effects were observed after the procedure. Main result of this study was that 12-months follow-up positive biopsies showed 61 % decrease in total cancer length, clinically significant disease in 9 of 29 patients and any disease in 16 of 29 patients [171]. Figure 3.6.4.2.a shows the US applicator as placed in the urethra and Figure 3.6.4.2.b shows the Tulsa-pro on the MRI table. Figure 3.6.4.3 presents MR thermometry results in one full rotation of the US applicator.

Figure 3.6.4.1: Tulsa-pro system components. Figure courtesy of Profound Medical Corp. [170].

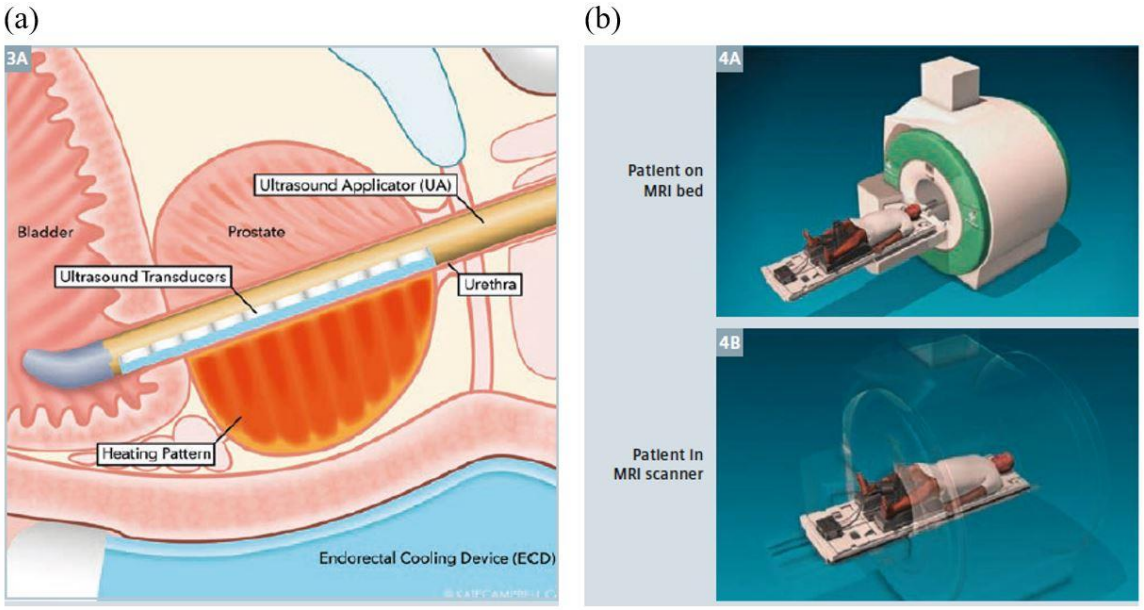

Figure 3.6.4.2: a) Tulsa-pro endorectal cooling device, and b) patient on MRI bed [170].

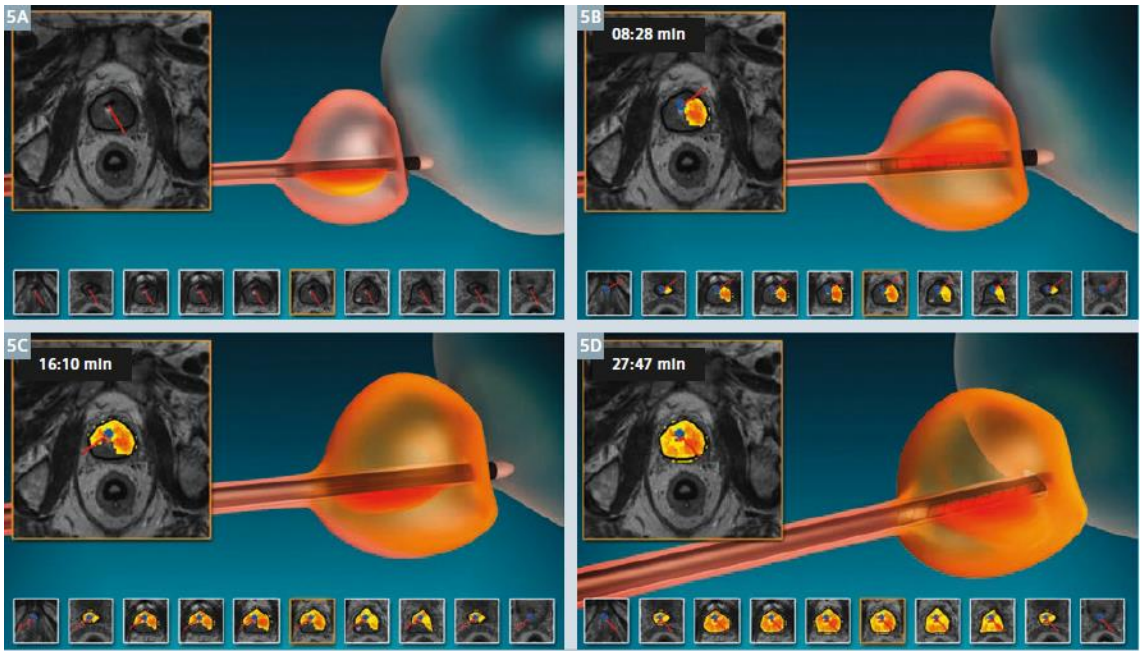

Figure 3.6.4.3: Temporal evolution of an MRI-guided Tulsa-pro treatment, completed in one full rotation of the US applicator [170].

3.7 Review of preclinical and clinical trials of existing HIFU devices

3.7.1 Preclinical studies

Animal trials are usually the step in testing a new drug or a new device before proceeding to human treatments only if the animals' tests are successful. Researchers have designed, produced, and tested diverse HIFU transducers on animals for treatment of cancer diseases

[172-184]. Every HIFU transducer must be tested both on TMMs and animals before transferring the technology to clinical tests.

In a study, a transducer system has been developed and animal experiments were conducted to test its ability in treating prostate rectally [172]. The therapy transducer was composed of 96 elements operating at 3.6 MHz and the imaging probe was operating at 6.5 MHz. Focal points were observed from 30 to 60 mm. Experiments were performed both *in vitro* (swine liver) and *in vivo* (prostate gland of dog). The particular transducer created coagulation necrosis at the targeted points at depth of 30 to 50 mm from the transducer surface within the prostate tissue of hound dogs. Moreover, Sasaki *et al.* [173] has constructed a therapeutic transducer (Figure 3.7.1.1) for transrectal treatment of PC and tested it on animals.

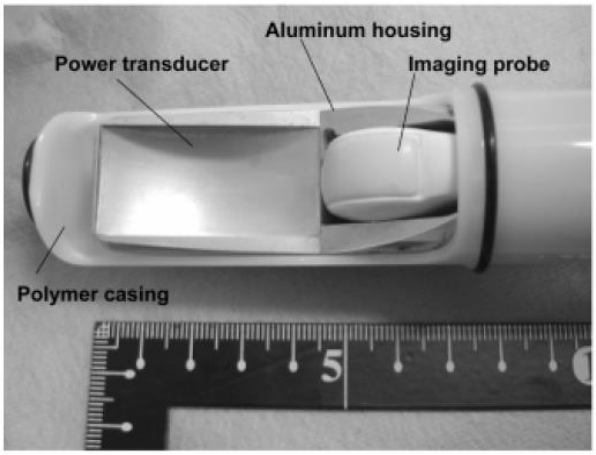

Figure 3.7.1.1: Split-focus therapeutic transducer of 3.25 MHz combined with a small imaging ultrasonic probe of 6.5 MHz for transrectal treatment of PC [172].

The transducer operated at 3.25 MHz and was combined with a small imaging ultrasonic probe that operated at 6.5 MHz. It was also a prototype split-focus power transducer because when the two elements had opposite phases, the focused beam was split into two [174]. The HIFU transducer was tested on nine female Japanese white rabbits. Special tumor implantations (VX2 tumors) were added into the liver of each rabbit. The sonication time was 4 s at peak intensity of 6 kW/cm^2. It was found that HIFU caused contiguous thermal necrosis in the rabbit liver and VX2 tumor.

Furthermore, in another research study was proved that there is a possibility to ablate around 90 % of the prostate with transrectal HIFU while surrounding healthy structures are not affected [175]. The therapeutic effect of HIFU in stem cell murine neuroblastoma (C1300) was also tested [176]. All animals (rats) died in the control arm within 35 days, while 47 % (HIFU) and 67 % (repeated HIFU) of animals survived more than 200 days without showing any cancer

recovery. The use of a mechanical HIFU (M-HIFU) was investigated for better cancer therapy prior tumor removal using surgery [177]. Additionally, the role of HIFU and activator of transcription 3 (STAT3) was explored to extract an anti-tumor immune response by using a transplant tumor model of PC. A study was conducted in a mouse PC cell line with activated STAT3. No tumor resumption and distant metastasis were appeared using either combined M-HIFU with surgery and surgery alone.

Hoogenboom *et al.* [178] has created a system to evaluate diverse HIFU ablation methods in mouse tumors using MRI guidance. The specific system was setup to increase knowledge of pathologic and immunologic changes to different HIFU ablation methods. Experiments were conducted on 21 mice inside a MR system. The HIFU treatment was applied in mice melanomas. HIFU treatment was separated into three types: thermal (continuous wave), mechanical (5 ms pulsed wave), and intermediate setting (20 ms pulsed wave). The HIFU transducer was operating at a central frequency of 3 MHz, 37 W acoustic peak power, 52 W electrical peak power, 48 mm diameter and focus depth between 30 and 80 mm. A positioning device was used to control the HIFU transducer (MR compatible piezoelectric motors, 30 x 30 mm trajectory execution range, active transducer cooling system and trajectory planner software) [178]. After HIFU ablation, histopathologic analysis was performed. The results showed accurate transducer focusing at the tumor without damaging any surrounding healthy tissue. Temperatures of greater than 60, smaller than 50 and smaller than 44 ^{o}C were reached during thermal, intermediate, and mechanical HIFU ablation, respectively. MR thermometry was performed during MRI guidance to image and measure the temperature changes [178].

Moreover, Chapelon *et al.* [179] investigated the therapeutic effect of HIFU on Dunning R3327 prostatic adenocarcinoma implanted into rats. The experiments were separated into two studies. In the first study, 49 rats were treated using HIFU. Of the 49 rats, 30 appeared with complete tumor necrosis. In the second study, 25 rats having AT2 subline were treated with HIFU at intensity of 820 W/cm^2 and 24 appeared with complete tumor necrosis. These results imply that HIFU could be a treatment of small cancerous tumors like prostate carcinoma [179].

Animal trials of the Sonablate HIFU device for treatment of BPH began in 1988 at Indiana University Medical Center [180]. HIFU coagulation necrosis followed by reabsorption of the necrotic periurethral tissue was proved using a dog model. The Ablatherm device was used to investigate the possibility of metastases increase in an animal model [181]. A metastatic rat PC was implanted into rats and was exposed to HIFU (Ablatherm) or the rats were sham treated. The number of metastases was examined 12 weeks later. As a result, metastasis was observed

in 3 out of the 13 rats exposed to HIFU and in 4 out of the 16 sham-treated rats. HIFU exposure does not enhance metastatic spread of animal tumors [181].

HIFU has been used to create intraprostatic coagulation necrosis lesion in the canine prostates of 37 dogs [182]. The lesions were homogeneous coagulation necrosis. The transducer at the focal point reached a temperature of 85 ^{o}C. As a result it was proved that localized prostatic cancer can be destructed using HIFU transrectally [182]. The Sonablate-500 HIFU device was used and canine prostates of 20 dogs were treated [183]. It was concluded that transrectal HIFU has the ability of destroying prostatic tissue without affecting the surrounding healthy tissues. HIFU has had effect in the treatment of experimental hepatoma [184]. Morris hepatoma were injected into 40 rats and 10 of them received HIFU treatment only, while another 10 received both chemotherapy and HIFU. The result was that HIFU significantly reduces tumor size [184].

3.7.2 Clinical studies and outcomes of histotripsy

In a review paper, Roberts *et al.* [185] outlined the development of histotripsy as a new technology for focal therapy and discussed results of clinical research trials. The basic background of histotripsy was explained as well as future research of this technology using preclinical models of BPH, PC, renal masses, and renal stones. In 2012, Schade *et al.* [186] used ACE-1 prostate tumor model and evaluated the possibility of treating prostate tumors with histotripsy. In total, 10 canine subjects received transrectal US guided percutaneous intraprostatic injection of ACE-1 canine PC cells. These prostates were examined with histology to check the development of tumor and histotripsy treatment effect. After the HIFU lesions, growth in the prostatic capsule was observed [186]. Glandular lobules, fibrous septa, periurethral stroma with desmoplastic reaction and areas of central necrosis in histology were found and examined. In four subjects, lymph node and pulmonary metastases were developed. Darnell *et al.* [187] characterized the inflammatory response and quantified patterns of collagen deposition 6 weeks after *in vivo* canine prostate histotripsy. Eight canine prostates received histotripsy to their left half to produce an intraparenchymal zone of tissue homogenization. Six weeks after therapy, canine prostates were sectioned and stained with H & E for histologic evaluation, CD3, CD20, and Mac387 immunohistochemistry to characterize the inflammatory components and picrosirius red staining to identify collagen. The results showed that seven out of eight treated prostates had only minimal residual inflammation [187]. Tissue loss was obvious to the treated side of all prostates whereas four showed a net decrease in collagen

content. In conclusion, *in vivo* histotripsy of canine prostate produced a decrease in prostate volume coupled with a limited inflammatory and fibrotic response [187].

3.7.3 Clinical trials for BPH treatment

Clinical trials on patients with BPH have been performed using two different existing HIFU devices, the Sonablate prototype (Focal Surgery Inc., now Sonacare Medical, LLC) and the Sonablate-200 [188]. In these clinical trials, 35 and 22 patients were treated with Sonablate and Sonablate-200 respectively, in order to check the differences of the two prototype devices and according to the results decide which one is the best so as to make improvements for better and more accurate BPH treatment. Pre- and post-operative evaluations were also performed using the International Prostate Symptom Score (IPSS) and QOL. According to the study by Uchida *et al.* [188], the Sonablate-200 has thinner transrectal probe (18 mm) than Sonablate (30 mm), a transverse section monitor, the available treatment region was expanded, the transverse sectors to be ablated increased from 7-9 (4-9 mL of tissue volume) to 17 transverse sectors (6-15 mL of tissue volume), a semi-automatic cooling process was added and finally, the new Solablate-200 automatically stops treatment when the temperature of the solution within the probe reaches 37 ^{o}C. Moreover, another important point was that the average treatment zone length and treatment time were 24.8 mm and 44.5 minutes in the group which was treated using the Sonablate prototype and 41.7 mm and 51.5 minutes in the group using the Sonablate-200 [188].

In addition, the Sonablate HIFU device was used in another study [189] for the treatment of BPH in 25 patients. Before and after treatment of each patient, the American Urological Association (AUA) symptom score, peak urinary flow rate (Qmax) and QOL score were evaluated. The results showed that five patients with large glands (greater than 80 g) did not receive a successful treatment but the remaining 20 patients showed mean AUA symptom score of 20.25 to 9.56, Qmax of 9.2 to 13.7 mL/s, and QOL score of 4.75 to 2.50. The duration of the HIFU treatment was between 45 to 110 minutes.

Other clinical trials investigated the clinical efficacy and safety of HIFU for the treatment of BPH [16]. In total, 62 patients were treated using TRUS probes for FUS surgery as well as imaging of the prostate. It was found that HIFU was safe and efficient for the treatment of BPH [16]. Furthermore, during clinical studies using HIFU to treat BPH, generation of microbubbles and cavitation [190] was observed. Data was captured and analyzed for these micro-bubbles

and cavitation. Tissue temperature was measured, and autopsies of HIFU-treated animal prostates were used. A total of 26 animals were treated with survival times ranging from 24 hours to 12 weeks post-treatment. Human clinical studies were also performed, and the first 15 patients were treated with a protocol that did not include bladder neck ablation with only 59 % of those patients treated effectively [190].

3.7.4 Clinical studies and outcomes of existing ultrasound-guided HIFU devices

Many clinical studies using the existing ultrasound-guided HIFU devices have been reported so far [191-216]. In a study [191], 12 men received hemiablation treatment using the Ablatherm HIFU device. Two patients died from other causes but there was no evidence of any cancerous disease for the 58 % of all other patients within 10 years.

The exploration of other possible side effects of salvage HIFU (Ablathem HIFU system) after prostatectomy or EBRT was examined by Topazio *et al.* [192]. This new side effect was the recto-urethral fistula and was mentioned as “rare case”. A 68-year-old patient was examined, and the specific side effect was found and treated with no evidence of the fistula found 24 months post-treatment.

Furthermore, 227 patients received PC treatment using the Ablatherm HIFU device [193]. In this study, patients with T1-T2 localized PCs, PSA less or equal than 15 ng/ml, Gleason score less or equal than 7, prostate volume less or equal than 40 cc and with no previous radical treatments for PC were included. The results showed that post-HIFU biopsies were negative in 196 patients, bladder neck and urethral stenosis were the only side effects that appeared after HIFU treatment and the actuarial 5-year disease-free survival rate was 66 %. On the contrary, Ide *et al.* [194] reported how deoxyribonucleic acid (DNA) is damaged after the treatment of PC using HIFU by treating 14 patients suffering from PC. The expression of human checkpoint kinase2 (Chk2), the phosphorylation of ataxia telangiectasia-mutated kinase, histone H2A variant (H2AX), p53, and the number of apoptotic cells in human PC were examined.

Outcomes from the treatment of 704 patients using the Ablatherm HIFU device were previously reported [195]. The HIFU device was used to treat 704 patients from which the 78.5 % was of intermediate or high-risk disease. Statistical results showed cancer specific survival rate of 99 %, metastasis-free survival of 95 % and 10-year salvage treatment-free rates of 98 % for low risk, 72 % for intermediate risk and 68 % for high risk patients. The following side effects were reported; incontinence (4 %), obstruction (4.6 %), infection (2.1 %), rectourethral

fistula formation (0.23 %), perineal pain (0.7 %), and other morbidity (4.4 %). It was demonstrated that HIFU treatment can lead to high cancer survival rate and high metastasis-free survival rate [195].

In a clinical trial, the Ablatherm HIFU device was also used by Blana *et al.* [8]. In total, 140 patients with criteria selection of T1-T2 NxM0 PC, PSA level less than 15 ng/ml and Gleason score less or equal than 7 were involved in the experiments. The fundamental result was that control prostate biopsies were negative in 86.4 % of patients [8]. The actuarial biochemical failure-free survival rates at 5 and 7 years were 77 % and 69 % respectively, while the actuarial disease-free at 5 and 7 years were found to be 66 % and 59 % respectively.

On the other hand, Uchida *et al.* [196] used the Sonablate HIFU device to treat 181 patients having specific selection criteria according to American Society for Therapeutic Radiology and Oncology Consensus Panel. The prostate was treated in one (156 patients), two (22 patients) or three (1 patient) HIFU sessions for a total of 209 procedures where the median time of treatment and hospitalization was 152 minutes and 4 days, respectively. HIFU treatment was performed in 10 men and after analyzing the HIFU results, it was found that HIFU therapy completely eradicated 3 of 10 tumors and destroyed a mean of 53 % of tumor in the other 7 remaining patients [197]. Muto *et al.* [198] compared 70 patients who received whole-gland HIFU treatment (Sonablate 500) with 29 men who received the transitional zones spared on the unaffected site. Twelve months later, a negative biopsy rate of 82 % was found with no statistically significant difference between the two groups. After HIFU treatment and data analysis of the results, it was found that the 2-year biochemical disease-free survival rates in patients with low risk, intermediate risk, and high risk were 85.9 %, 50.9 %, and 0 %, respectively [198]. Moreover, Ahmed *et al.* [199] performed HIFU hemiablation in 20 patients and 6 months later the biopsy results were negative for cancer in 89 % of patients.

Furthermore, in 2003, Thuroff *et al.* [200] published results using the Ablatherm HIFU device and found that 87 % of the patients showed a negative biopsy of 92 %, 86 %, and 82 % in the low, intermediate, and high-risk groups, respectively.

HIFU was used to treat 19 patients who were proven to have local PC with the biopsy diagnostic method [201]. These patients initially received radical prostatectomy. The patients were reluctant to have radiotherapy treatment. The treatment was almost completely successful with 17 out of 19 patients (89.5 %) classified as a success. Side effects such as acute urinary retention and stress urinary incontinence were noticed. These two side effects were solved

using prolonged urethral catheterization and pelvic floor exercises. In 3-years experiments in 184 patients with PC, the Ablatherm transrectal HIFU device was used and the patients underwent 232 sessions with mean duration of 90 minutes under anesthesia at 2.25 or 3.0 MHz, 50 W and penetration depth of 25 mm [202]. The results were promising because after follow-up biopsies, 80 % of the patients were found to be cancer free and the tumor mass declined more than 90 % in patients with residual cancer. No side effects such as fistula, grade II or III incontinence and rectal mucosal burn were observed [202].

Some results for the treatment of PC using both available approved HIFU devices (Sonablate and Ablatherm) were reported [203]. The mid- and long-term progression free survival rates were approximately 70 % while negative post-operative prostate biopsies were almost 85 %. In another study case, Challacombe *et al.* [204] during a 3-year period treated 43 patients with localized PC using the Ablatherm HIFU device with the patients separated for primary HIFU treatment (31) and salvage HIFU treatment (12). It was shown that the limited series was unable to support treatment using HIFU device for localized PC with good efficacy and no side effects [204].

In another clinical trial [205], 146 patients with biopsy-proven stage T1-T2 N0M0 PC were treated using the Ablatherm HIFU device [205]. The results showed that 93.4 % of all patients presented negative control cancer biopsies and 12 % showed transurethral resection after HIFU due to obstruction. Moreover, Rove *et al.* [206] collected different published papers and compared the two US-guided FUS medical devices (Ablatherm and Sonablate). For the Ablatherm system, the negative biopsy rates after 3 months ranged from 80 to 90 % in most studies whereas for Sonablate negative biopsy rates ranged from 64 to 87 %. Long-term disease-free rates for Ablatherm were 77 % at 5-years follow-up after treating 120 patients while for Sonablate was 78 % after treating 181 patients [206]. PSA level of 0.5 ng/ml or less was reached in 42 to 84 % of patients treated with Ablatherm.

In 2009, clinical trials were performed using the Sonablate HIFU device and outcome data of the treatment of 172 men were reported [13]. Side effects using validated patient questionnaires, biochemical and histology were also stated in the particular study. There was no evidence of cancer after one HIFU session in 92.4 % (159 out of 172) of patients [13]. The histological changes in the human prostate after radiotherapy and salvage HIFU were investigated for the first time by Chalasani *et al.* [207]. More specific, a 65-year old patient with localized PC was treated with the Sonablate HIFU device after receiving EBRT for low-risk cancer, and four weeks later prostatorectal fistula was found and was later repaired. A

comparison between a single and repeated HIFU treatment (Ablatherm-prototypes and Ablatherm device) was carried out [208] in 223 patients from which 174 received one treatment and 49 received a second treatment after HIFU. The cumulative incontinence rate (12.2 %) and cumulative impotence rate (55 %) were remarkably increased for patients who received a second HIFU treatment while there was also a rise in morbidity if transrectal HIFU was repeated [208].

Another side effect was observed after clinical trial in a patient [209]. This patient developed urinary retention, urinary tract infections, and intermittent stress but a new side effect appeared after salvage HIFU therapy (first therapy was IMRT). That new side effect was pubic bone osteomyelitis stemming from a prostatopubic fistula. This case was extremely rare but significant for salvage HIFU therapy of PC.

Prostate swelling and intraprostatic point shift was estimated during HIFU treatment (Sonablate 500) using a real-time US as image guidance [210]. HIFU treatment was performed in 44 patients and three HIFU sessions were needed to cover the whole prostate including the anterior zone (session 1), middle zone (session 2), and posterior zone (session 3). During session 1, the most prostate swelling and intraprostatic point shift [210] was found.

Ripert *et al.* [211] evaluated the tolerance, feasibility, and efficacy of PC salvage EBRT after a HIFU failure treatment. In this study, 69 HIFU procedures were implemented in 60 patients, 48 patients in first-line and 12 patients in second-line (salvage therapy after EBRT). Among the patients treated in first line, HIFU therapy failed in 35 patients during the follow-up while the overall disease-free survival rate was 83.3 % at 36.5 months. From this study, it was concluded that the feasibility and good tolerance of salvage radiotherapy after HIFU failure was possible [211]. Recently, outcomes of a single-session HIFU treatment using the Sonablate for patients suffering from PC were reported [212]. In total, 171 patients received HIFU therapy. From this number of patients, 44 were diagnosed as disease failure. The overall and cancer-specific survival rates at 5-years were 98.8 and 100 % respectively whilst the metastasis-free survival rate at 5-years was 99.4 %. Single-session HIFU therapy is a promising and possible curative approach to PC when treated with either hormonal therapy or pre-operative transurethral resection of the prostate [212].

In two other studies, Uchida *et al.* [213] performed in the first study 28 HIFU treatments in 20 patients using the Sonablate-200 HIFU device with a complete response acquired in 100 % of patients who showed negative post-operative prostate biopsy. In the second study, the

biochemical disease-free survival rates were evaluated by treating 63 patients with stage T1c-2b N0M0 PC using the Sonablate HIFU device system [214]. The overall biochemical disease-free rate was 75 %. Follow-up biopsies showed that 55 patients were found to be cancer-free. Moreover, Mearini *et al.* [215] in a study has treated 30 patients with PC using Sonablate 500 HIFU device. Before the HIFU treatment and 3-6 months after surgery, the patients underwent urodynamic study. The results showed that there was a markable improvement in bladder outlet, maximum flow at uroflowmetry, decrease in postvoid residual at 6-month follow-up and a concomitant significant reduction of detrusor pressure at opening and at maximum flow [215]. Song *et al.* [216] reviewed many medical records of all patients who underwent salvage HIFU treatment (Ablatherm HIFU device) with transrectal US guided after EBRT failure. Prostate MRI and bone scintigraphy were performed in all patients and no evidence of distant metastasis was found [216]. In this clinical trial, 13 patients with a median age of 68 years and median follow-up of 44.5 months after HIFU therapy were evaluated. The overall biochemical recurrence-free rate was 53.8 % and the complication rate evaluated at 38.5 %.

All these clinical studies have been mostly performed using the two ultrasound-guided transrectal HIFU medical devices (Ablatherm and Sonablate) which have already received CE marking. The researchers of all-important clinical studies, the device that was used, patients involved in the studies, and the main outcomes and conclusions are summarized in Table 10.1.1 in the appendix section (Summarize of the review of clinical studies of the existing HIFU devices).

3.7.5 Preclinical and clinical trials of MR-guided HIFU devices

Until now, most clinical studies for the treatment of PC were performed using FUS guided with US imaging, despite the fact that US is real-time monitoring, the acquired images might not be clear, and ablation might not be seen. Today, MRI gives clear images and some clinical studies were conducted to treat PC with HIFU using MRI guidance. In a study, Rosa *et al.* [217] used HIFU, laser, and photodynamic therapies with MRI guidance. It was concluded that emerging thermal focal therapies show promise as a treatment option in low- and intermediate-risk PC. Chang *et al.* [218] also investigated endorectal MRI and MR spectroscopic imaging for the detection of PC with high accuracy. In this clinical trial, 88 patients were positive with biopsy proven PC and endorectal MRI and MR spectroscopic imaging preceded before receiving radical prostatectomy. Two independent readers found the largest tumor and the volume of

abnormal tissue at MR spectroscopic imaging using MRI (1.5 T whole-body MR scanner with pelvic phased-array coil). These two readers found dominant tumor in 50 and 58 patients; 42 and 48 of these were dominant treatable lesions at histopathology respectively. In conclusion, patients with dominant treatable tumor seen in T_2-weighted MRI with at least 0.54 cm^3 might be candidates for MR-guided focal treatment.

Furthermore, Lindner *et al.* [219] reported the first North American clinical experience of treatment of localized PC with focal MRI-guided transrectal FUS. Clinical experiments were conducted in a 51-year-old patient with PC and the patient underwent mpMRI (3 T) with endorectal coil, followed by a confirmatory transrectal US guided extended mapping biopsy. The HIFU procedure was performed in a 1.5 T GE Excite Twinspeed MR scanner using the ExAblate 2100 prostate system. The ablation time for each macrosonication was 160 s. Each sonication was monitored by MR thermometry. The patient was within the scanner for 3.5 hours and the treatment time was around 70 minutes [219]. After a week and 1-month follow-up, the patient did not show any side effects. Repeat MRI at 1 month showed persistent ablated non-perfused tissue at the right mid-gland [219].

In a study of 26 men [220] who were diagnosed with PC using mpMRI and histology on transperineal template mapping biopsy underwent HIFU treatment. A non-rigid image registration software was developed, and was used to transfer data at the location and limits of the index lesion as given by mpMRI. This software was able to detect the location of the target lesion automatically for each individual patient and register a 3D transrectal ultrasonography volume [220]. McDannold *et al.* [221] tested a transrectal MRgFUS system (ExAblate 2000, Insightec Ltd.) in a canine prostate model. Each half of the canine prostate model was targeted with high energy for ablation while the other half with lower energy sonications to test the device for localization of the focal spot before thermal tissue damage. Then all sonications (n = 155) were observed with PRFS MR temperature imaging, contrast-enhanced MRI, and histology [221].

Another study using the ExAblate 2100 (Insightec Ltd.) was published by Napoli *et al.* in 2012 [146]. Five patients after having biopsy and mpMRI were diagnosed with PC and treated with MRgFUS before receiving radical prostatectomy. During the treatment procedure, the accumulation of thermal damage in the target zone and the tissue temperature were monitored using MR thermometry. After histopathologic analysis, the results showed extensive coagulative necrosis and no tumor at the treated area [146]. The mean maximum temperature in the target lesions was 81 ± 2 ^{o}C with a rectal wall temperature of 35 ^{o}C. The number of

sonications was between 7 and 11 with a mean duration time of 13 s for each sonication. The average procedure time was 84 minutes [146]. In addition, Zini *et al.* [144] compared current status of HIFU and MRgFUS. In this review, it was concluded that MRgFUS therapy has some advantages over regular HIFU for lesion targeting and real-time temperature monitoring [144]. Also, MRgFUS reviews and clinical trials are still limited and more studies need to be performed for validation of its positive effect in patient outcomes.

DWI sequence was used to evaluate tissue damage in 19 canine prostates with cryoablation or HIFU ablation therapy [222]. In all cases, the ADC was measured and it was observed that the ADC decreased during treatment which appeared to complicate DWI MR thermometry. As the tissue recovered and regenerated, the ADC increased. In result, it was shown that DWI MRI could be a promising method to monitor prostate thermal therapies [222]. Hazle *et al.* [223] also tested MRI-based techniques for guidance and thermal monitoring during transurethral HIFU therapy of implanted tumors in an *in vivo* canine prostate model. Transmissible venereal tumors were grown in the right lobe of the prostate in four dogs. Thermal dose calculations in multiple image planes were estimated using temperature-sensitive MRI with a fast-interleaved gradient-echo EPI sequence. The MRI results were compared to those from histologic analysis. It was found, as verified by histopathologic analysis, that the size of tissue necrosis after treatment was underestimated using gadolinium enhanced MRI [223].

The potential of MR-guided pulsed focused ultrasound (pFUS) for the enhancement of drug uptake in prostate tumor *in vivo* using doxorubicin (Dox) was investigated [224]. Experiments were conducted in animal prostate tumor models using human PC and HIFU treatment system (ExAblate 2000, Insightec Ltd) in a 1.5 T GE MR scanner. The models were separated into three groups of 8. Group 1 received pFUS and Dox, group 2 received Dox only, and group 3 was the control. The Dox concentration was measured using a fluorometer and the Dox distribution was evaluated using a fluorescence microscope. As a result, the Dox concentration increased in the pFUS treated group compared to the group with Dox only [224].

In a study, So *et al.* [225] mentioned that the efficacy analyses of HIFU are limited and that there is lack of evidence that HIFU gives an improved side effect profile compared to other regular treatments like surgery or radiation. As stated [225], HIFU treatment should be used only in clinical trials for the treatment of PC. Rouviere *et al.* [226] explained various imaging techniques (transrectal US, MRI) for the detection and treatment of PC using therapies such as radiotherapy, FUS, cryotherapy and brachytherapy. The possible use of MRI-guided therapies was reported [227] for prostate biopsy, PC therapy using brachytherapy, and focal therapies.

Muller *et al.* [228] has also tested mpMRI so as to identify patients diagnosed with PC with a treatment followed using focal therapies. The results showed that mpMRI is the best imaging technique for focal therapy since it can localize small tumors [228]. The biopsies were no longer necessary when mpMRI was available since it is accurate enough to grade tumor aggressiveness. Lastly, Resnick *et al.* [229] reported different therapeutic strategies for PC including surgery, HIFU, adjuvant, and neoadjuvant therapy.

4 Four-DOF prostate robotic system

In this part, the design procedure to develop the medical system (robotic system, transducer, electronic system, and software) is described. For the design of the robotic system, each part is explained and presented in order to entirely resemble the final product. The robotic device includes 2 computer-controlled axes and 2 manual axes. The electronic system and the MRgFUS software are also described. The two-candidate transducers that were housed in the robotic device' probe are presented and their efficiency was calculated using the radiation force balance method.

4.1 Robotic device overview

A new prototype version of the robot was derived from a previous older version having many modifications including the addition of Y and Φ axes. The developed robotic device was designed with 4 motion axes. Two computer-controlled axes: 1) a linear axis for motion along the rectum (X-axis), 2) an angular axis for rotation within the rectum (Θ-axis), and two manual axes: 1) a linear axis to lift the robot up and down since the height of the rectum varies from patient to patient (Z-axis), and 2) an angular axis to set the entry angle to the rectum (Φ-axis). There is another linear axis (manual) which is on the base of the device for the left to right adjustment of the device (Y-axis) but if the device is intended to be fixed on the MRI table, this motion will not be available.

The entire robotic system was developed using the software Microstation (V8, Bentley Systems, Inc., Exton, PA, USA). After completion of the design, drawings of the individual parts were sent to a 3D printer (FDM400, Stratasys Ltd., Eden Prairie, Minnesota, USA) for production. All 3D-printed parts of the device were made out of ABS. All stages were driven by piezoelectric ultrasonic motors (USR60-S3N, Shinsei Corporation, Kasuya Setagaya-ku, Tokyo, Japan). Angular encoders (US Digital Corporation, Vancouver, WA, USA) were placed on each stage to ensure accurate movement. The positioning device was designed so that it can be placed on the patient table of any conventional high-field MRI system with a cylindrical magnetic bore. It was assumed that the patient is lying in supine position on the table with slightly elevated legs to provide an optimal access to the rectum for the focused transducer. The motor and encoder cables pass into the magnet room through a grounded connection panel.

The motor and encoder signals are sinusoidal and below 100 kHz avoiding RF interference with the MRI (64 MHz).

The X-axis and Θ-axis were used to maneuver the ultrasonic transducer, which was located inside the probe, during treatment. The accuracy of the motion was established with the use of high-resolution optical encoders. X-axis and Θ-axis were operated through the software or the manual controls of the electronic driver's enclosure. The user has the option to operate the device by either the manual motion menu or the automated motion control menu. With the manual motion, the user can move the device in a predefined distance and direction. The automated menu was used to maneuver the transducer in a grid pattern. The automated motion control was used to deliver the ultrasound in relatively large targets, as the focus of the transducer is small (approximately 1-2 mm).

The other axes (Y-axis, Z-axis and Φ-axis) were operated manually. These axes were designed to enable the appropriate placement of the device in order to set the insertion path of the probe, with regards to each patient's rectum anatomy. It was realized after use, that manual adjustment of the Y-axis, Z-axis, and Φ-axis was preferable than the computer-controlled motion. The speed reduction resulting from the mechanisms, provided an easy to control motion with minimal effort. The motion mechanisms were designed and adjusted to create the ideal motion characteristics for easy adjustments of the device. The manual axes enabled the user to move the probe accordingly so that the patient would maintain a comfortable posture for the probe insertion; an important aspect as the patient must remain still during the entire treatment. The Y-axis, Z-axis, and Φ-axis were operated manually by levers and knobs as they were designed to enable the appropriate placement of the device. Initially, the device was designed with all the axes controlled by a computer (through the developed software), but after doctor suggestions, the Z-axis and Φ-axis were revised to be operated by hand.

The linear axis (X-axis) was designed to move the ultrasonic transducer forward and backwards. It has a range of 50 mm. Figure 4.1.1 shows the exploded view of the X-axis. The exploded view illustrates all components associated with the X-axis and how the parts were assembled. The complexity of the X-axis was better demonstrated with the exploded view drawings. The parts were separated and placed in the appropriate assembly sequence which was followed to develop this stage.

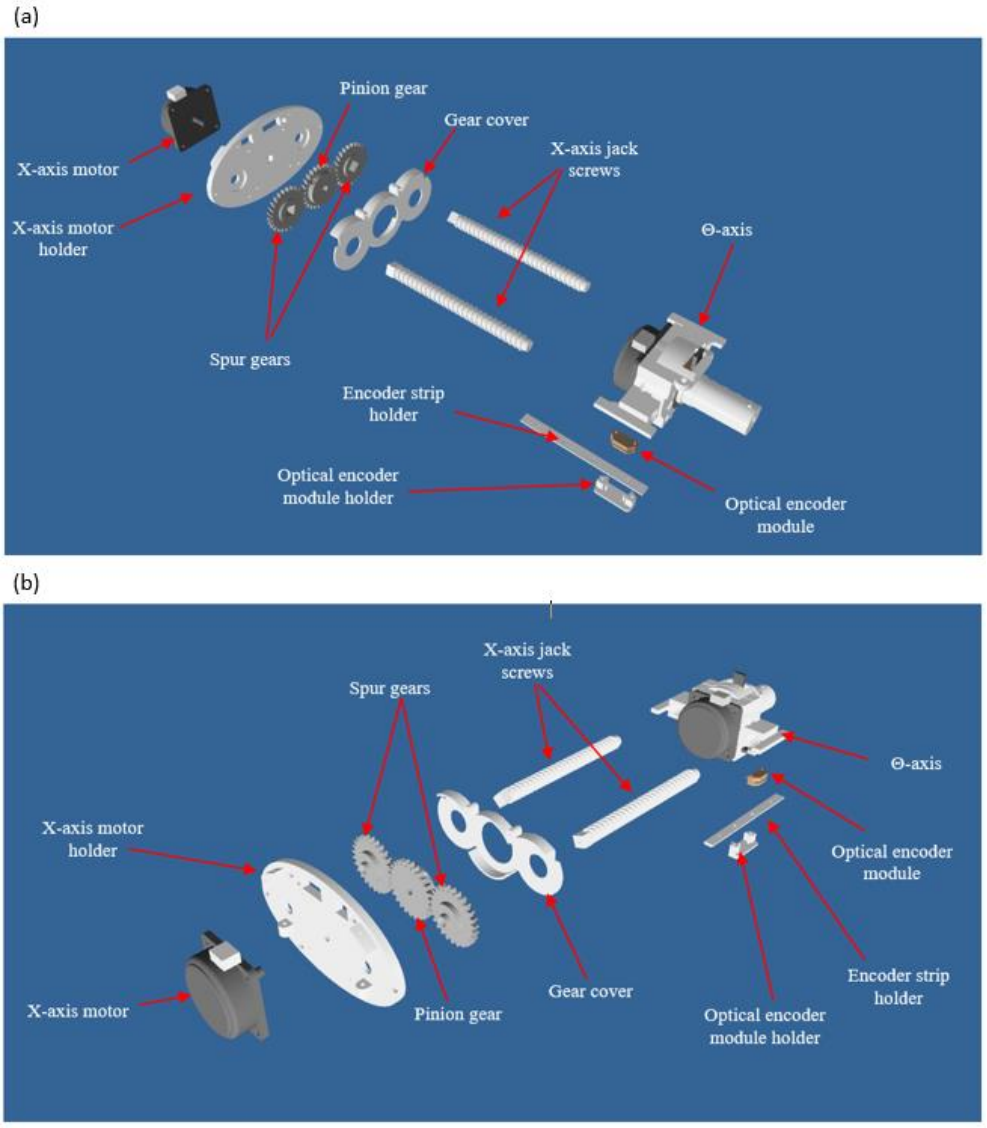

Figure 4.1.1: a) Front exploded view of the X-axis, and b) rear exploded view of the X-axis.

Figure 4.1.2 shows the CAD drawing of the linear axis (X-axis) for motion along the rectum. The ultrasonic motor was coupled to the pinion gear which rotated the spur gears thus, enabled the simultaneous rotation of the two jack screws. This design as shown in Figure 4.1.2, enabled the two jack screws to apply uniform force on both sides of the Θ-axis and therefore, the X-axis motion was smooth and precise. In addition, the twin jack screw required smaller length, so the device was kept compact. The compact design improved the device aesthetically, which is a crucial factor for the commercialization of the device. The motion accuracy of the X-axis was established by the optical encoder which in conjunction with the plastic strip provided feedback to the electronic system. The plastic strip had increments of 500 lines per inch thus, the resolution of the system was high, ensuring the precise motion of the device. The optical encoder measures the motion of the device by converting and sending the information in a

series of pulses to the software. The encoders verify that the motion is performed successfully which ensures the reliability and accuracy of the positioning device.

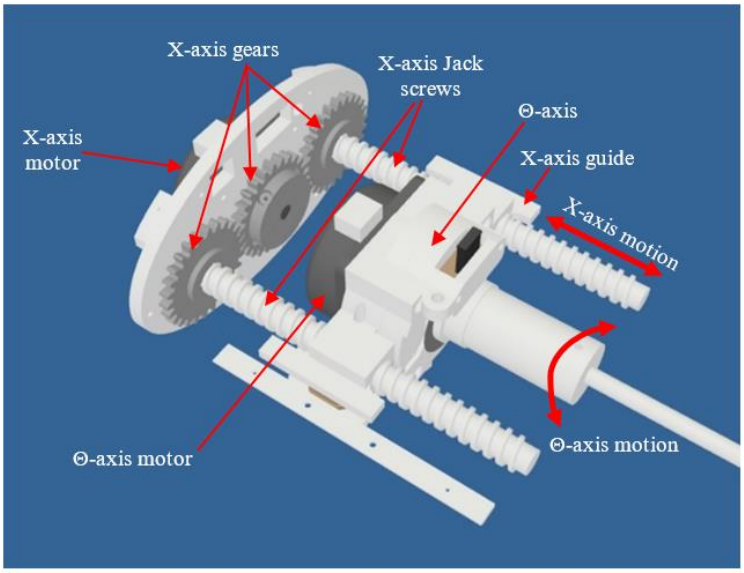

Figure 4.1.2: CAD drawing of the linear axis (X-axis).

The angular stage (Θ-axis) incorporates a planetary gearbox which reduces the angular speed of the motor. The output of the Θ stage was connected to the transducer via a shaft as shown in Figure 4.1.3.

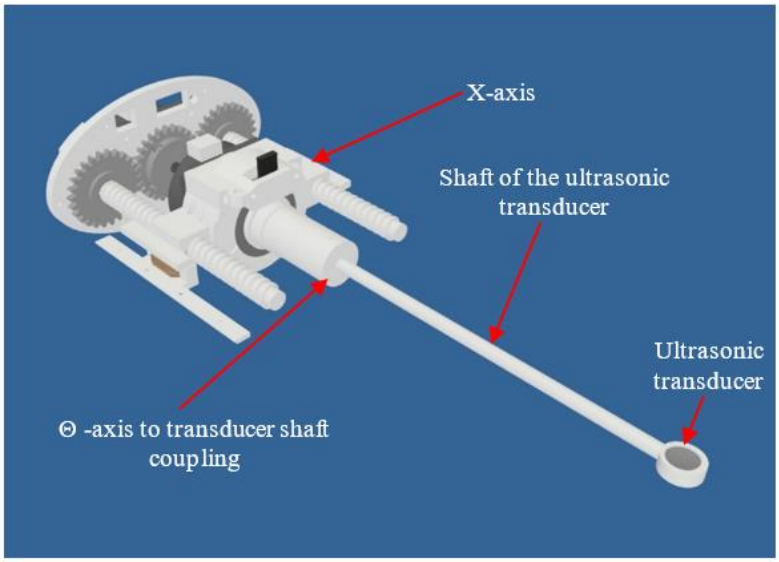

Figure 4.1.3: Ultrasonic transducer attached to the Θ-axis.

Figure 4.1.4 shows the corresponding angular axis for the rotation of the transducer within the rectum. An optical encoder was used to detect the motion of the output shaft (Θ-axis). The Θ-axis was the most complex mechanism on this device. Figure 4.1.4.b shows the cross-section of the two-stage planetary gear unit. The first stage had a ratio of 4:1 (meaning that for 4 rotations of the motor the output will perform 1 rotation). The motor rotates the “sun gear”

which was placed in the center of the mechanism. The “planetary gears” are rotated by the “sun gear” inside the first stage “ring gear”. The “planetary gears” are thicker which enable them to couple simultaneously to the second stage “ring gear”.

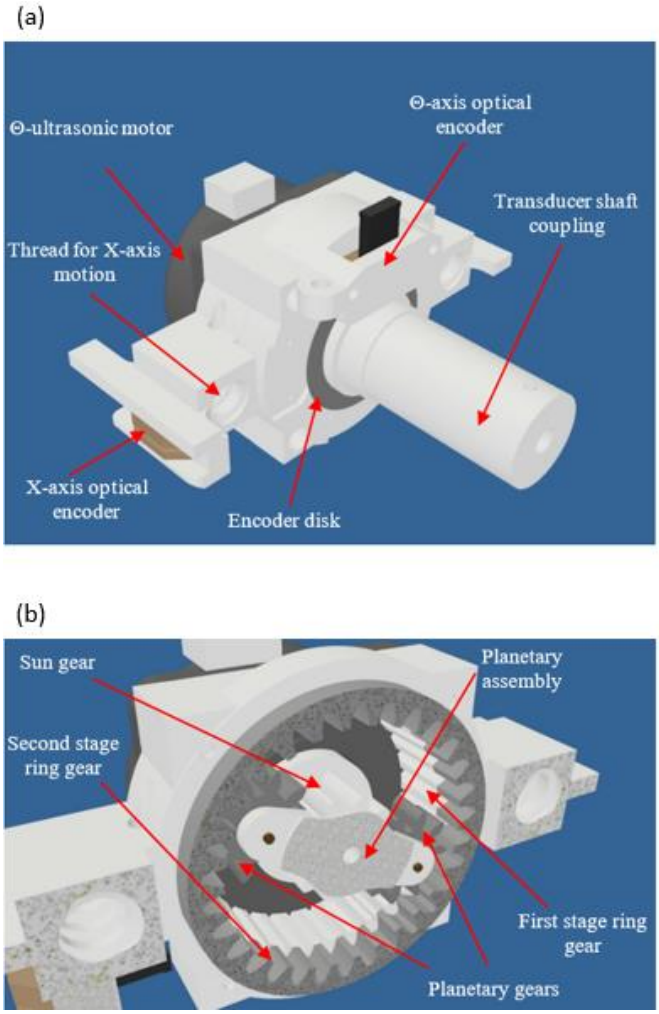

Figure 4.1.4: Angular axis (Θ-axis) a) view of the outside part, and b) view of the inside part and the mechanism.

The second stage “ring gear” was designed with one tooth less compared to the first stage “ring gear” which caused the rotation of the second stage. Figure 4.1.5 shows the exploded view which demonstrates the placement of all the Θ-axis components. Figure 4.1.6 shows the diagram of the X and Θ-axis components assembled together. The planetary mechanism was chosen since it was the most compact unit compared to equivalent mechanisms, that offered such a high reduction ratio. In addition, it was symmetrical, therefore it was the best option to overcome the space limitations. Another benefit of the planetary mechanism (due to its small size) was the improvement of the overall appearance of the device. The optical encoder of the Θ-axis was paired with a plastic disk with a resolution of 2500 lines for a full rotation (360º). This design provided the necessary motion accuracy to the angular stage to safely and reliably

steer the ultrasonic beam. The Θ-stage has a range of motion of 180°, 90° clockwise (CW) and 90° counterclockwise (CCW).

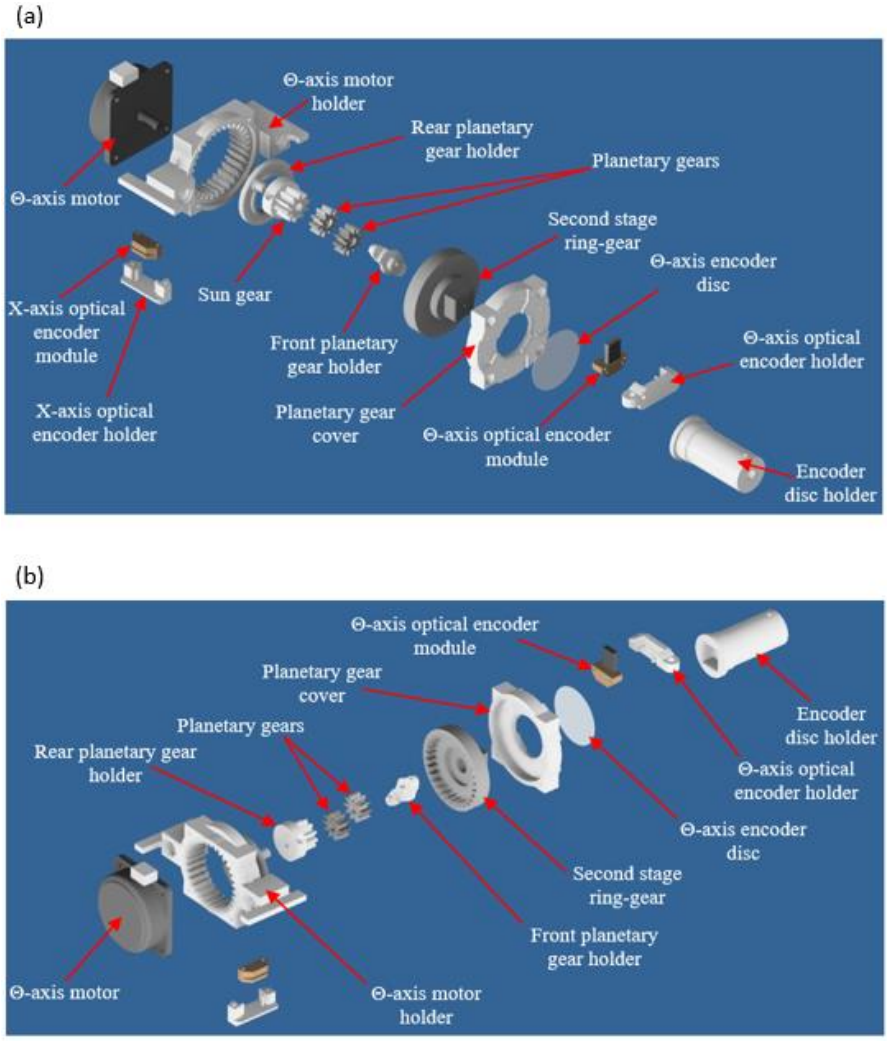

Figure 4.1.5: a) Front exploded view of the Θ-axis, and b) rear exploded view.

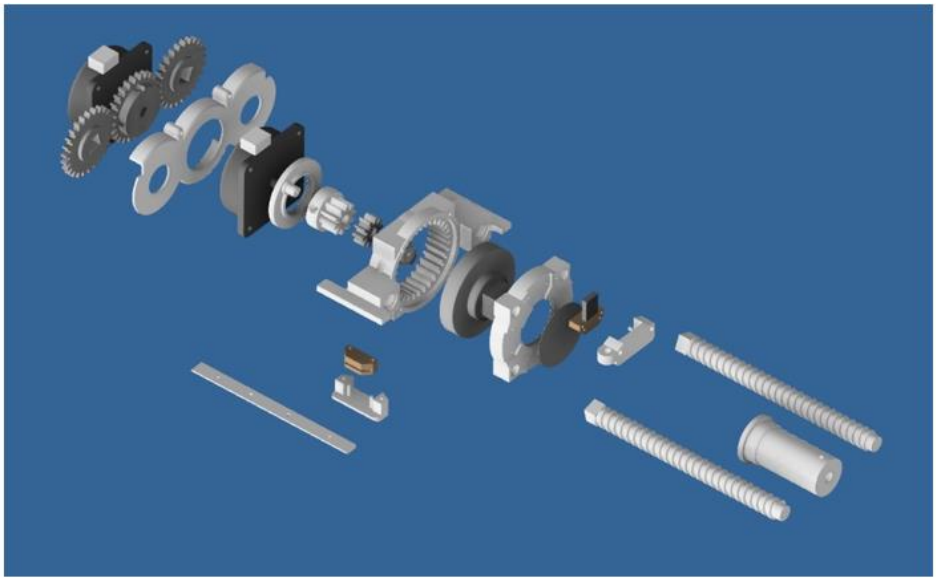

Figure 4.1.6: The exploded diagram of the X and Θ-axis components.

The Z-axis was supported by guides of the Z-axis frame, as shown in Figure 4.1.7. The Z-axis frame at the bottom section included male guides for the Y-axis. In the middle a “T” shaped slot for the placement of the Y-axis locking mechanism was included. Between the guides, a cylindrical coupling was added which supports the lower end of the Z-axis jackscrew. On the top, a slot was made to attach the Z-axis bottom shaft holder and on the Z-axis jackscrew, a structure was used to couple to the Z-axis shaft.

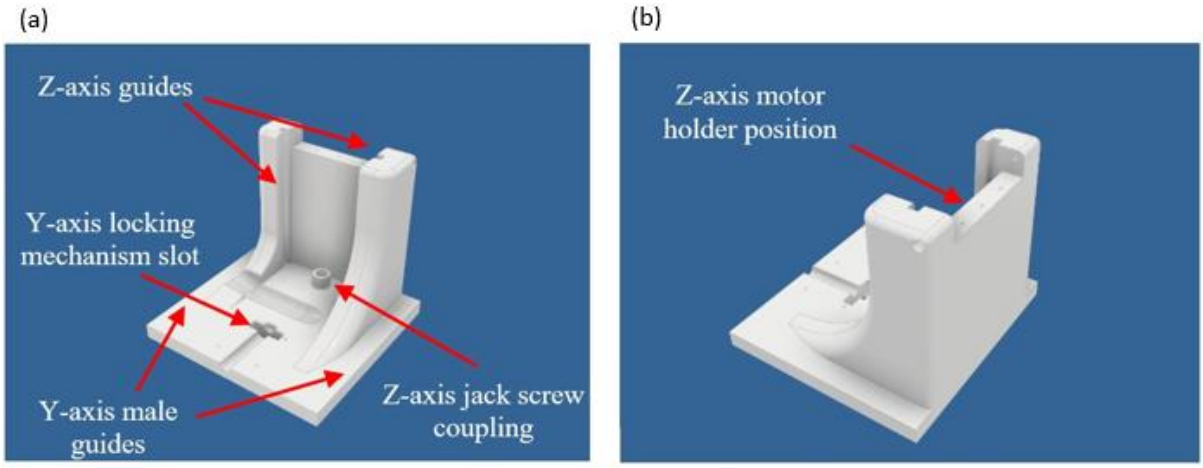

Figure 4.1.7: Z-axis frame a) front view, and b) rear view.

The Z-axis bottom shaft holder included a guide for the Z-axis shaft disk which was located around the Z-axis shaft. The Z-axis shaft was secured to the device between the Z-axis bottom shaft holder and the Z-axis top shaft holder. The two holders allowed some clearance for the Θ-axis shaft which allowed the Z-axis shaft to rotate like a bearing. The Z-axis jack screw was attached to the Z-axis shaft. Before attaching the Z-axis hand lever to the Z-axis shaft, the Z-axis hand knob shaft was inserted to the Z-axis hand knob. The Z-axis hand knob shaft included a cylindrical head to secure the Z-axis hand knob to the Z-axis hand lever. The shaft was attached to the hand lever through the coupling and fastened by a screw at the bottom of the hand lever.

The hand knob was loosely fitted to the hand knob shaft to allow rotation around the shaft. This feature of the hand lever made it easier for the user to rotate the Z-axis lever. The hand lever, shaft, and knob assembly were attached to the shaft via a coupling. The coupling was made to secure the hand lever perpendicular to the device.

The Φ-axis rear cover was coupled to the Z-axis jackscrew. After the Φ-axis rear cover was attached to the jackscrew, the endpoint collar was inserted to limit the downward range, thus preventing the Φ-axis to rub against the base, while the user adjusts the Y-axis.

Both the Φ-axis worm gear and the Φ-axis gear were placed inside the Φ-axis covers. The Φ-axis gear was attached to the X and Θ axes frame and then the Φ-axis mechanism was sealed by the covers. The entire assembly was attached to the Z-axis. The assembly of the Φ-axis was finalized with the addition of the Φ-axis knob that was attached by coupling to the rear end of the shaft.

The relation between the components of the Φ-axis is shown in Figure 4.1.8.a. For the Z-axis, a jackscrew mechanism was designed like the X-axis, but with only a single jackscrew that converts the angular motion into linear. For this reason, the Z-axis was simplified as there is no space limitation as in the X-axis mechanism. Despite the simplified design, it operated as smoothly as the X-axis. The jackscrew was operated manually through a hand lever situated on the top of the Z-stage. The jackscrew of the Z-axis was coupled to the Φ-axis as shown in Figure 4.1.8.b. The Z-axis frame structure was thick and rigid to support the Φ-axis which carried the X and Θ-axis. On the inner side of the frame, the linear guides supported the Φ-axis for the up and down motion. The Z-axis has a range of motion of 60 mm.

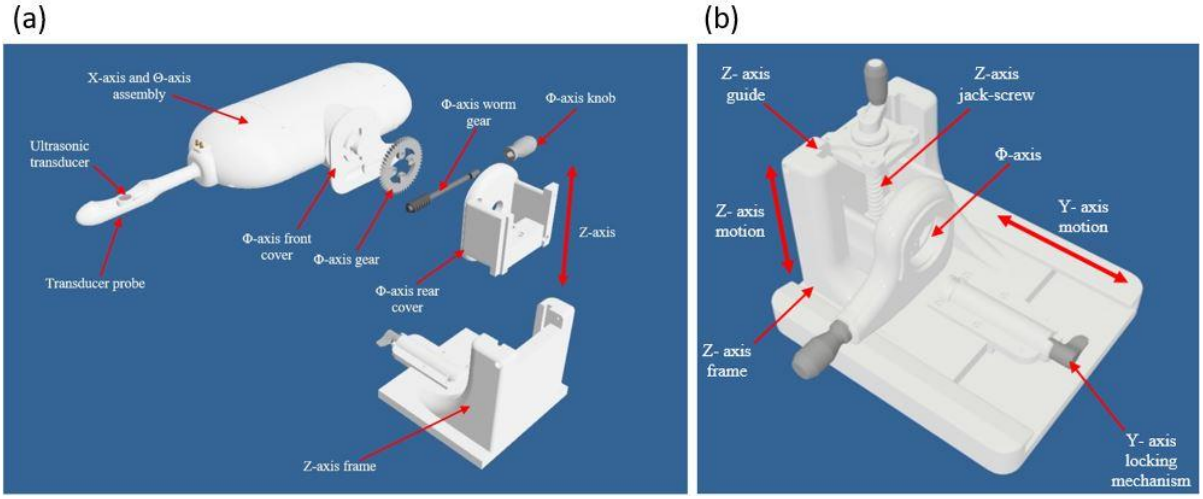

Figure 4.1.8: a) Φ-axis exploded view, and b) linear axis to lift the robot up and down (Z-axis) and manual axis to move left and right (Y-axis).

Figure 4.1.9.a shows the CAD drawing of the angular axis to set the entry angle to the rectum (Φ-axis). The Φ-axis enabled the device to be tilted so that the probe can be oriented with the patient's rectum. The Φ-axis was designed to move with a different type of mechanism to the Θ-axis known as a worm drive, as shown in Figure 4.1.9.b. This mechanism featured a large-diameter gear that was driven by a worm gear. For a full rotation of the worm gear, the large gear was rotated by a single tooth. This allowed the user to make fine adjustments as the required range of motion was small. The dimensions of this mechanism were better suited for

this application as they were relatively small, which allowed the placement of the positioning device closer to the Z-axis.

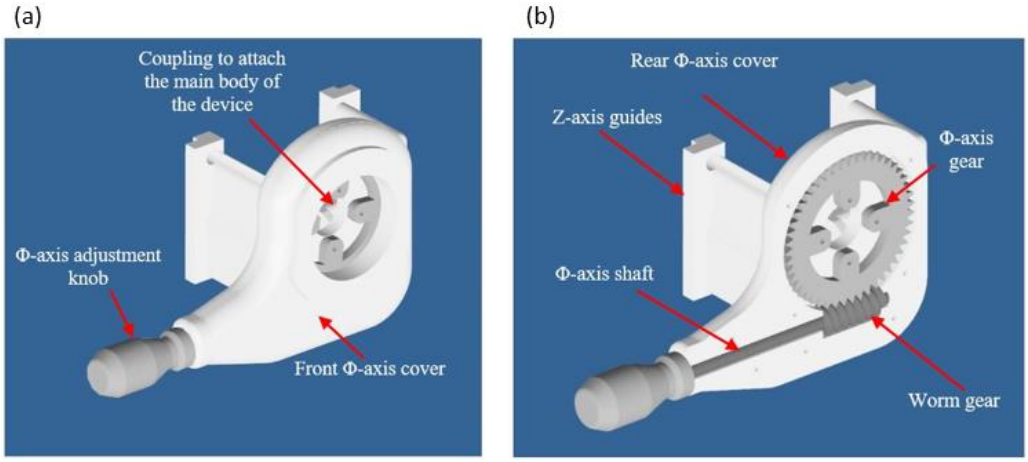

Figure 4.1.9: a) CAD drawing of the angular axis (Φ-axis), and b) mechanism of the axis (worm drive).

The Φ-axis gear was attached to the main body of the robot and the whole mechanism was sealed inside the covers. The covers also kept the gear coupled to the worm gear and supported the X and Θ-axis to the positioning system. The gear case was also sealed so that the worm drive prevented any contact between the mechanism and the personnel or the patient. The sealed mechanism also improved the appearance and kept the lubricants inside the gears which helped to eliminate noise and minimize wear of the mechanism during adjustments due to reduced friction. The worm gear included a shaft that was extended outside of the enclosure on the rear side of the robot with a knob attached to it. The knob was operated manually. An additional advantage of using mechanisms such as the jackscrew and the worm drive is that these are self-locking type mechanisms. This meant that the height and angle of the device can be changed only by the user, which was done by either the hand lever for the Z-axis or the knob for the Φ-axis. The device benefits from this design as it does not require any additional locking mechanisms in order to secure the placement of the probe. The use of a self-locking type of mechanisms for the Z and Φ-axes which supported the X and Θ stage was necessary as the weight of the device and the probe were constantly applied on them, thus it was easier to be controlled manually.

To complete the assembly of the Z-axis, the Y-locking mechanism was installed. The Y-locking mechanism was supported by the Y-axis locking mechanism extension. This part was attached to the bottom right side of the Z-frame. It was designed to extend the Z-frame to house the shaft of the Y-axis locking shaft so that it can be easily reached by the user. On the bottom right corner, a cutout was designed to create a halt for the shaft. A second cutout was designed

in the middle of the Y-axis locking mechanism cover to limit the motion at 90°. This prevented the user from moving the mechanism too far to the point that the mechanism could be released. The Y-axis lock was completed with the attachment of the Y-axis locking lever. The locking lever was attached to the shaft via a coupling that was accessible laterally. The Y-axis was completed by sliding the Z-frame inside the guides of the base (Figure 4.1.10).

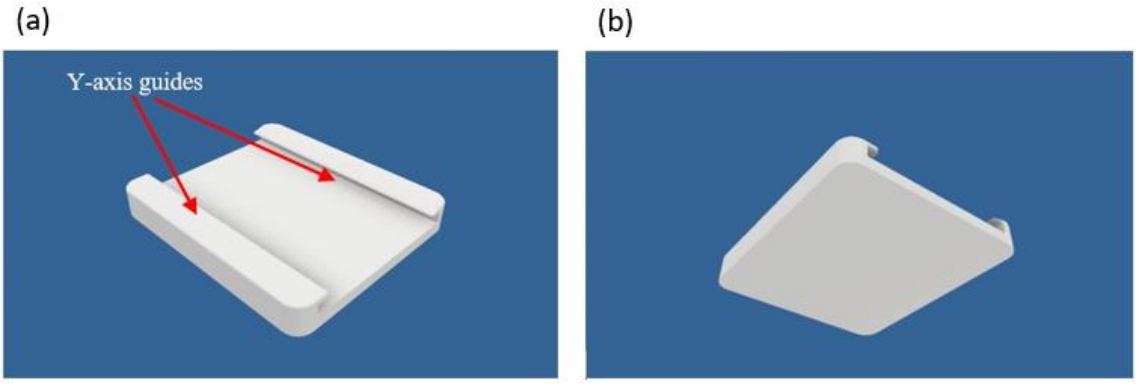

Figure 4.1.10: Base of the device (Y-axis) a) top view, and b) bottom view.

Figure 4.1.11 shows how the Z and Y-axis parts were assembled together.

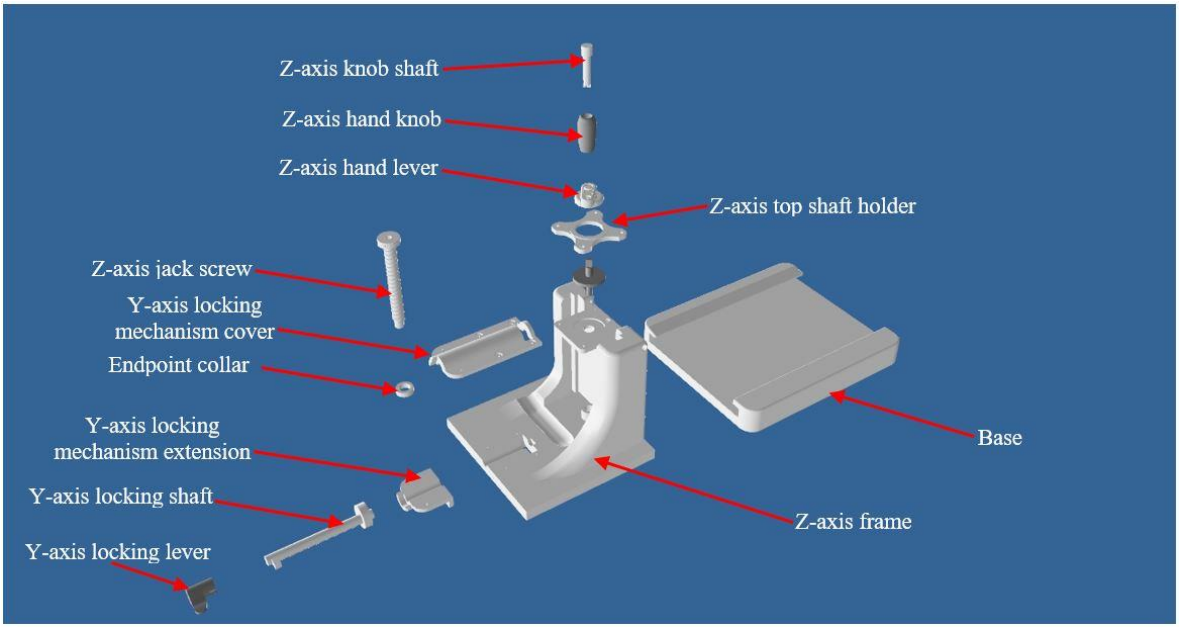

Figure 4.1.11: Z-axis and Y-axis assembly.

The final shape of the design was completed with the installation of the covers and the probe. To prepare the probe, the seal mechanism was installed. The seal mechanism was composed of the front O-ring holder and the rear O-ring holder. The O-ring holders were used to secure the inner and outer O-rings. A second grove for the inner O-ring was made on the rear O-ring holder, but was not necessary and caused unnecessary resistance to the X-axis, so it was

eventually removed. To fill the gap between the O-ring holders and the seal mechanism cover, a tension spacer was designed. The O-rings were held together with the seal mechanism rear cover. The seal mechanism rear cover was secured with four long screws. By adjusting the tension of the screws, the force that squeezed the O-rings was able to be adjusted.

By adjusting the screws, the O-rings were pressed against the interfaces to ensure that the probe (Figure 4.1.12.b) was watertight. The tension adjustment was necessary since it establishes optimal sealing which is of high importance. Additionally, the O-rings allowed the transducer shaft to move the transducer insight the probe. If the O-rings were too tight, it would result in a stiff joint that resists motion. On the other hand, a loose joint could cause water to leak from the rear shaft interface into the X and Θ-axis enclosure. The seal mechanism exploded view is shown in 4.1.12.a.

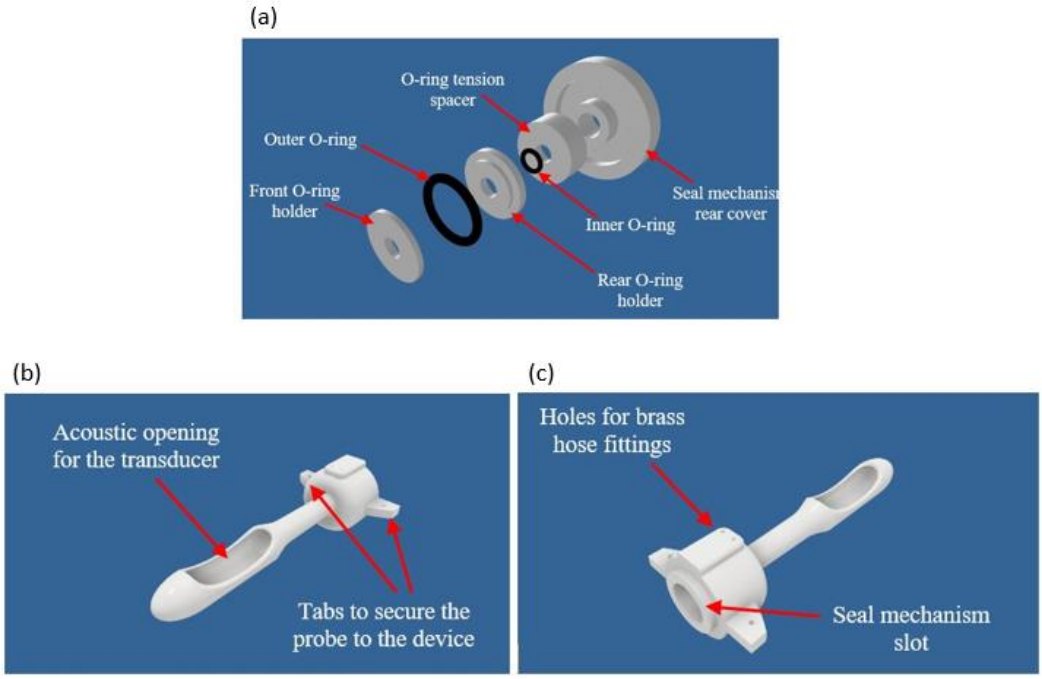

Figure 4.1.12: a) Seal mechanism exploded view, Transducer probe b) front view, and c) rear view.

After the seal mechanism was fitted to the probe, the transducer was inserted and the probe assembly was completed. The coaxial cable tube was inserted from the rear of the device to the front so as to insert the transducer cable. The coaxial cable tube was designed to protect the transducer cable from the moving parts of the device. Two front cover detachable tabs were designed to hold the front covers and the probe to the X and Θ axes frame. Figure 4.1.13 shows the transducer case.

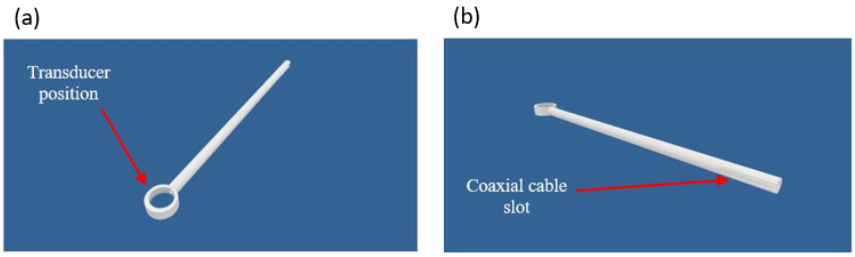

Figure 4.1.13: Transducer case a) front view, and b) rear view.

The front top cover (Figure 4.1.14.a and 4.1.14.b) and front bottom cover (Figure 4.1.14.c and 4.1.14.d) were used to attach the probe to the X and Θ axes frame. The front cover detachable tabs were preferred as this was the part that absorbed the forces which the probe was subjected to. This design was adopted for maintenance purposes of the transducer and probe. The rear top cover (Figure 4.1.14.e and 4.1.14.f) and rear bottom cover (Figure 4.1.14.g and 4.1.14.h) were installed. Connectors for the encoders, motors, and transducer were placed on the rear of the device. The placement of the connectors was easily identified by the user to access the cables.

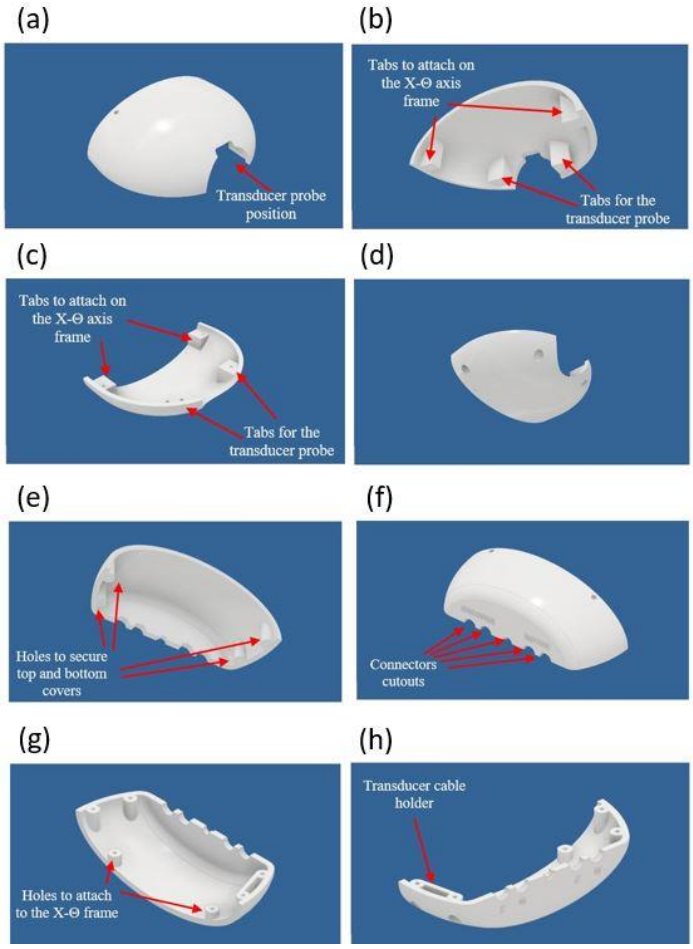

Figure 4.1.14: Front top cover a) front view, b) rear view, Front bottom cover c) top view, d) bottom view, Rear top cover e) bottom view, f) top view, Rear bottom cover g) front view, and h) rear view.

At the base of the device, the Y-axis guides were used so a motion from left to right was achieved. The Y-axis was designed so the positioning device could be aligned with the patient on the MRI bed. The Y-axis was operated manually. It has a range of 90 mm. This axis did not require any motorized mechanism, as the device was light and could be moved manually. This adjustment was set only in the initial setup and after that, it was locked during the entire procedure of the treatment. The positioning device was locked by the Y-axis locking lever which applied force between the Z-axis frame and the base of the device as shown in Figure 4.1.15 (a and b). After the X and Θ-axis were assembled, the two computer-controlled axes were put together inside the covers. Figure 4.1.15 (c and d) shows the exploded view of the X- and Θ-axis. A large number of parts highlight the complexity of the robot. The high complexity design of the computer-controlled axes was necessary to accomplish a highly accurate and reliable motion which is essential for this medical application.

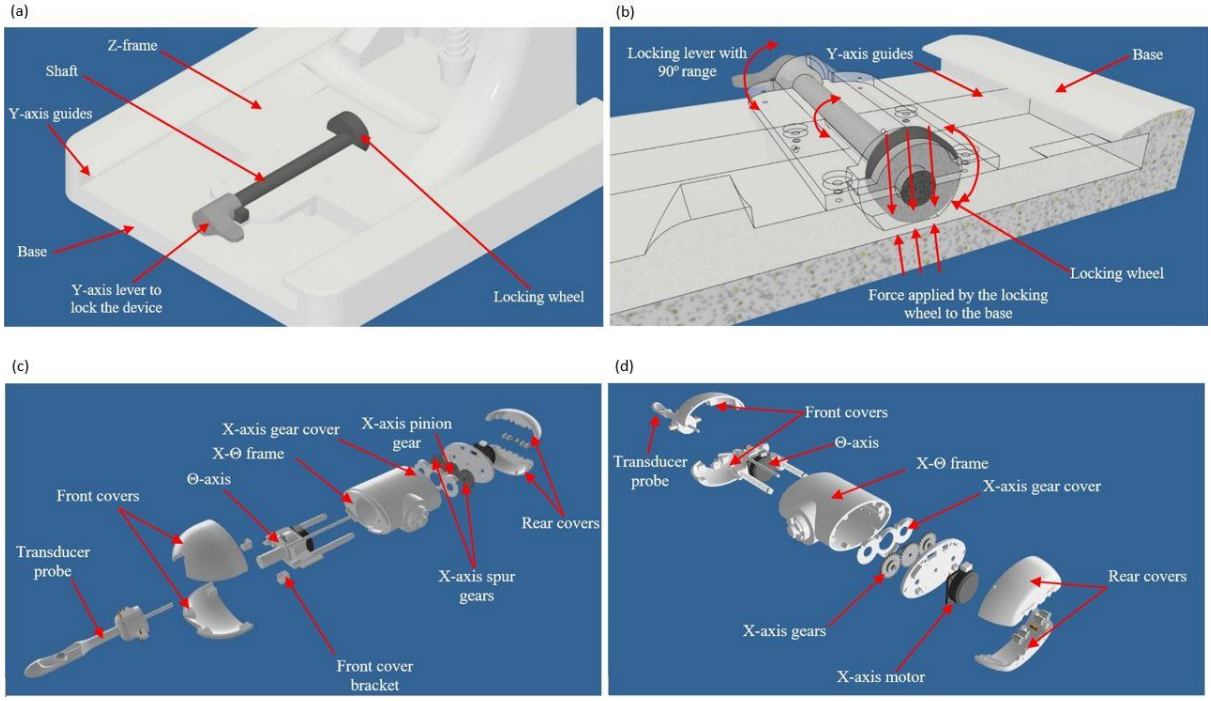

Figure 4.1.15: a) Y-axis mechanism with the locking mechanism, b) Y-axis mechanism cross-section with transparency to demonstrate the mechanism in detail, Exploded view of the PC controlled axis c) front view, and d) rear view.

The locking lever was connected to the eccentric wheel and upon rotation the higher side was forced against the base. The placement of the wheel allowed the user to lock the device in the desired location by rotating the lever 90° CCW. The Y-axis was released by rotating the Y-lever 90° CW. The device has compact dimensions to allow enough space for the patient inside any commercial MRI scanner. All the components were made from non-magnetic materials

that do not pose any danger inside the high magnetic field generated by the MRI magnet thus preventing imaging artifacts. The placement of the patient in the MRI is shown in Figure 4.1.16. Figure 4.1.17 shows photos of the developed device.

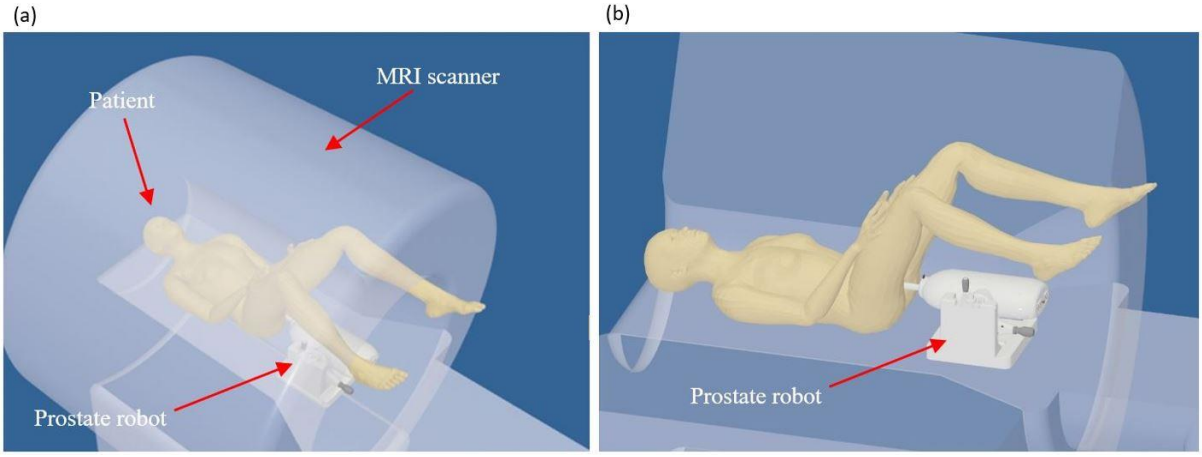

Figure 4.1.16: The configuration inside the magnet of the MRI and the placement of the device.

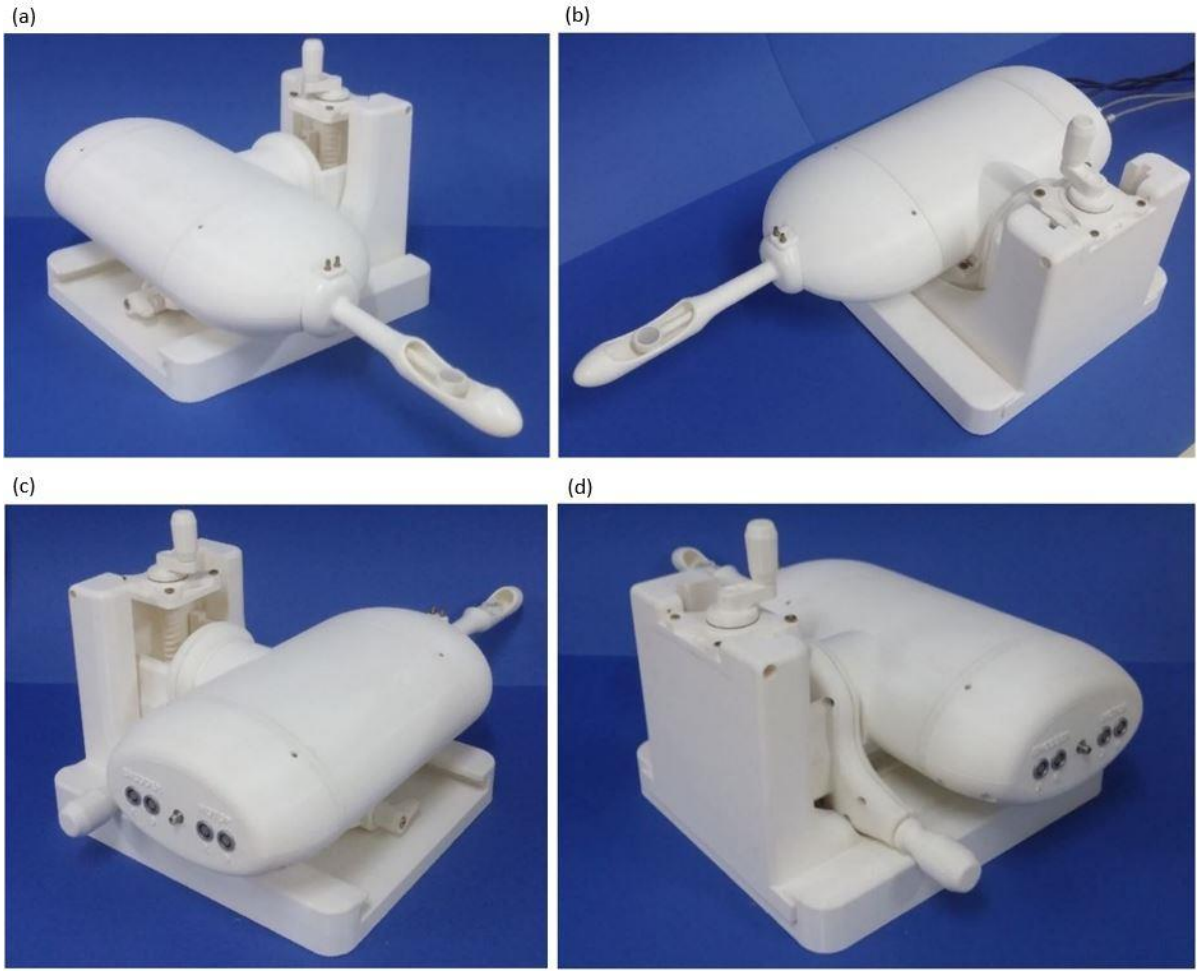

Figure 4.1.17: Photos of the positioning device.

Figure 4.1.18 shows the positioning device with the cables for encoders, motors, and transducer attached. This is how the device is connected inside the MRI scanner. The non-magnetic connectors (4-pin, Fischer, Morges, Switzerland) are specifically designed for medical applications. These connectors feature a locking mechanism that prevents them from accidentally detaching. To detach the connectors a sleeve around them must be pulled simultaneously with the connector. For the transducer cable, a subminiature version A (SMA) connector was used which transferred the high power to the transducer reliably.

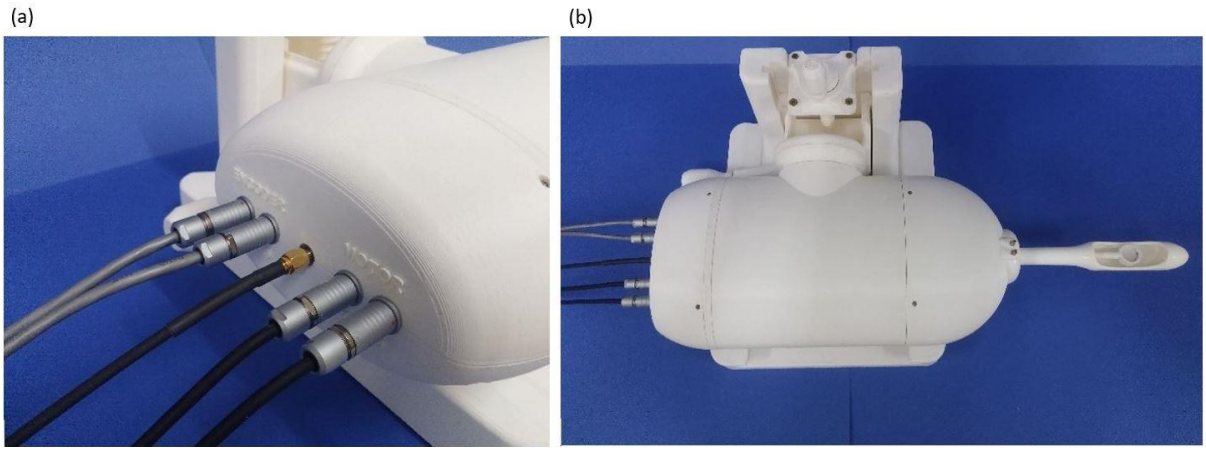

Figure 4.1.18: a) Connectors attached to the rear of the robot, and b) top view of the robot with the cables attached.

4.2 Transducer design and overview

Two transducers of a diameter of 17.3 and 25 mm, single elements, spherically-focused, and MR compatible were initially produced to be tested in order to select the possible transducer that would be used to ablate prostate tumors. Based on the location of the transducer compared to the prostate, the radius of curvature was selected close to 40-45 mm. The transducers were used only for therapy. Imaging of the prostate was performed by MRI.

The selection of the transducer was challenging as it should offer good ultrasonic penetration to deliver sufficient levels of acoustic intensity so as to ablate prostate tissue. Other characteristics of the candidate transducer were its resistance to high intensities and long lifespan. The outer diameter of the element was required to be small enough so that the probe size to be small as well and fit in the rectum thus reducing patient discomfort. At the same time, the transducer should be able to induce the necessary heat to ablate the target. The transducer material of the 4.4 MHz transducer was made out of P762-type piezoceramic (Meggitt, Kvistgaard, Denmark) as shown in Figure 4.2.1. The transducer material of the 3.2 MHz

transducer was supplied by the Piezo Hannas Tech Co., Ltd. (Wuhan City, HuBei Province, China). A backing material (epoxy) was used behind the transducer element. Since the energy produced was sufficiently high, there was no need to add a matching layer. The transducer's impedance was matched to 50 Ω.

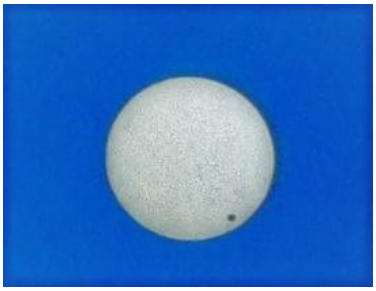

Figure 4.2.1: Photo of the piezoelectric element for the 4.4 MHz transducer.

Photos of the developed transducers (4.4 and 3.2 MHz) are illustrated in Figure 4.2.2.

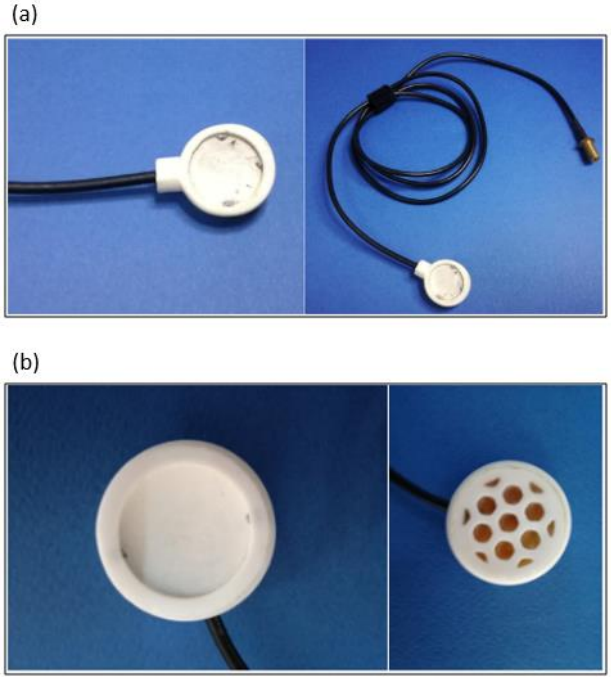

Figure 4.2.2: Transducer with tuning frequency of a) 4.4 MHz, radius of curvature of 44 mm, and diameter of 17.3 mm, and b) 3.2 MHz, radius of curvature of 45 mm, and diameter of 25 mm.

The transducer is required to be MR compatible so that MR thermometry of the thermal field can be acquired. The compatibility of the source with the MRI was tested using a TMM containing agar/silica/evaporated milk. To reduce the influence on the MRI image, a low-pass filter (L8959, Anatech Electronics, Manhattan, USA) was used with a cut-off frequency of 10 MHz. The plastic that houses the transducer was 3D built with a digital manufacturing system (Stratasys). The concept of the transducer is shown in Figure 4.2.3.

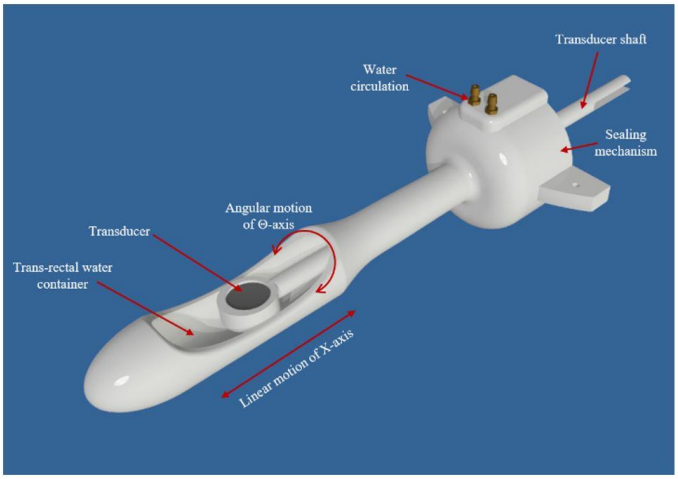

Figure 4.2.3: Concept of the transducer.

The probe hosts the transducer using a waterproof mechanism. Since the shaft was designed to move backward, forward and angularly, a mechanism was required to keep the water inside the probe. Two plastic pieces were designed to secure two O-rings inside the back of the probe. As shown in Figure 4.2.4, one O-ring (larger) was placed on the outer surface to block water between the seal mechanism and the inner surface of the probe. A smaller O-ring was placed in the inner edge of the mechanism and the transducer shaft interface.

The design of the probe was made with the smallest possible diameter and the appropriate shape in order to minimize the patient's discomfort while inserting the rectum. The structure of the probe was made in such a way that allows water bubbles to flush from the transducer chamber. To reduce the water bubbles from the transducer probe chamber, a secondary chamber that was higher than the transducer chamber was designed on the back of the probe. As the air bubbles tend to rise on the surface of the water, the higher height of the secondary water chamber helped to prevent air from being trapped inside the transducer chamber. If some air was trapped in the transducer chamber, a pump was used to reverse the operation, thus creating a vacuum and pulling the remaining air bubbles out of the probe.

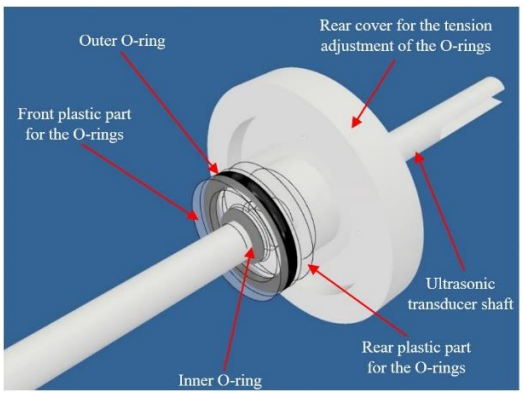

Figure 4.2.4: The CAD drawing of the seal mechanism that was used to hold the transducer inside the probe.

On the top of the secondary chamber of the probe, two brass nipples were added to attach soft silicone hoses for water circulation. One brass nipple was used to feed the probe with freshwater and the other allowed water to escape. The return line was also used to create a vacuum forcing air evacuation during preparation. Figure 4.2.5 shows the cross-section of the endorectal probe which displays its internal structure. A medical condom was used to keep water inside the probe.

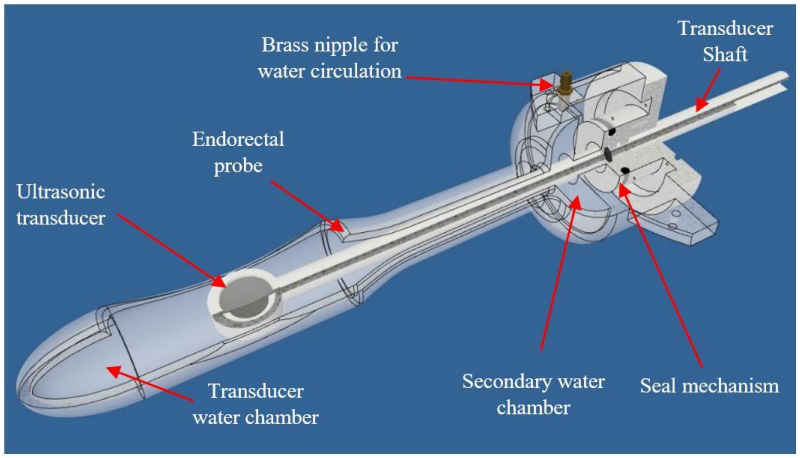

Figure 4.2.5: Cross-section of the endorectal probe and the piezoelectric transducer.

More details of the probe assembly are shown in Figure 4.2.6 which illustrates the exploded view of the probe with the seal mechanism and the transducer.

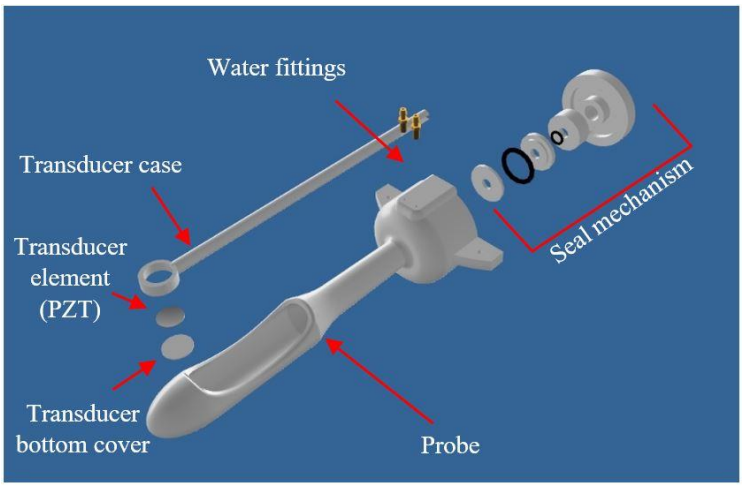

Figure 4.2.6: Transducer and probe (exploded view).

The probe was mounted on the positioning device by the two tabs on each side of the secondary chamber, as shown in Figure 4.2.7. The two tabs were pressed between the top and bottom front covers of the positioning device and were fixed via screws. The rear end of the transducer shaft was attached to the Θ-axis output coupling. The transducer cable exited through the slot on the side of the shaft and then through a tube that was placed above the axes to protect it

from the moving parts. The other side of the transducer cable was soldered to a female SMA connector on the rear of the device.

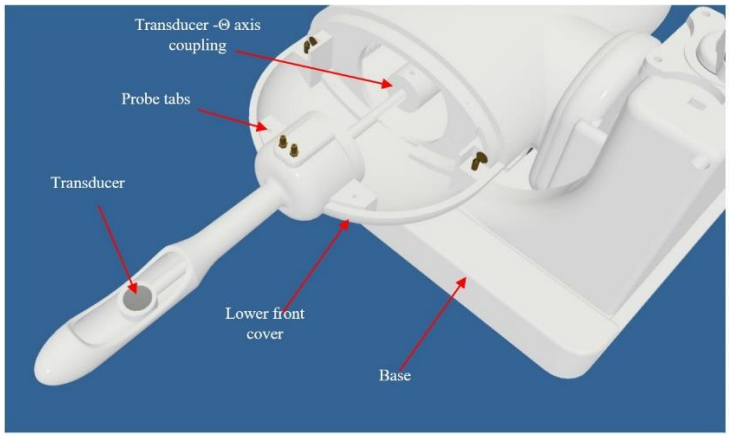

Figure 4.2.7: The endorectal probe attached to the positioning device using the two taps on the left and right of the secondary water chamber.

Figure 4.2.8 shows a photo of the probe installed on the positioning device. The transducer is visible in the middle of the acoustic window.

Figure 4.2.8: Photo of the probe with the transducer.

4.3 Transducer efficiency

The efficiency of the candidate transducers was measured using an ultrasonic power meter (UPM-DT100N, Ohmic instruments Co., St. Charles, Missouri, USA). To measure the acoustic power, the ultrasonic power meter was filled with degassed water and the transducer was placed on the top. The element of the ultrasonic transducer was immersed in the water facing down. The ultrasound beam was targeted to the cone sensor of the power meter and the transducer was adjusted until the peak acoustic power was measured. When acoustic energy was applied to the cone, the resultant force was directly proportional to the total radiated power. The peak acoustic power measurement indicated that all the acoustic power produced by the transducer was measured by the power meter. The efficiency of a transducer indicates the percentage of

the electrical power which is converted to acoustic power. The mean efficiency of the 4.4 MHz transducer was calculated at 37 % from the slope of a linear fit that was applied to the measurements as shown in Figure 4.3.1.

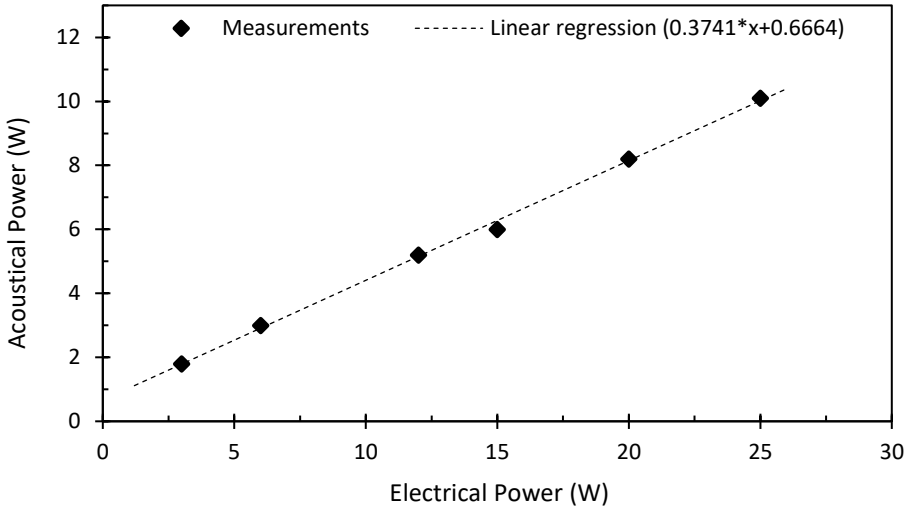

Figure 4.3.1: Acoustical versus electrical power for the 4.4 MHz transducer. The efficiency was estimated by the slope of the linear regression.

The efficiency of the 3.2 MHz was also estimated by a linear fit that was applied to the measurements as shown in Figure 4.3.2. The efficiency of this transducer was 30 %.

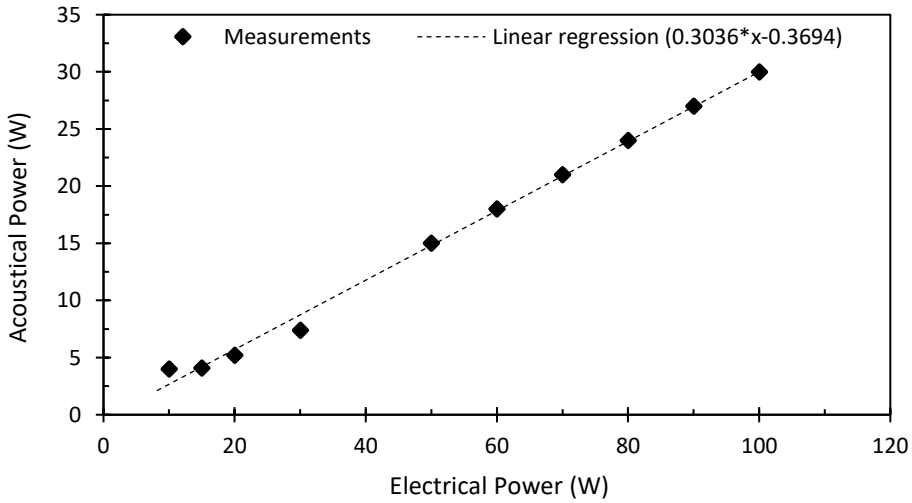

Figure 4.3.2: Acoustical versus electrical power for the 3.2 MHz transducer. The efficiency was estimated by the slope of the linear regression.

4.4 Electronic driving system

The robot's electronic system includes four motor drivers (D6060, Shinsei Corporation, Kasuya Setagaya-ku, Tokyo, Japan), a data acquisition (DAQ) card (NI USB 6251, National

Instruments, Austin, Texas, USA), a DC power supply, and a relay. It is responsible to initiate commands for the robot movements. The electronic system is controlled by a universal serial bus (USB) 6251 (National Instruments) DAQ card which interfaces with a computer via a USB port. It receives commands from a custom-made software written in C sharp. This software makes the device easy to operate since without it the user would perform the commands manually. By using the software, the user simply selects the direction and distance of the motion. This provides accuracy as the software operates the device quickly and reliably.

The electronic system was developed to control the robotic device which includes the large motors (USR60-S3N, Shinsei Corporation). The DC supply converts alternating current (AC) to DC. The voltage was converted from 230 V to 24 V. The motor drivers control the motors via switches or the DAQ card. The commands were converted into an appropriate signal that was needed by the motor to perform motion. The DAQ card was used to convert the analog signal to digital signal with a format recognized by the software. The relay was used to switch the pump ON and OFF to feed the probe with degassed water. To enclose the electronics of the control system, an enclosure was designed using the Protocase designer software (New York, USA). The driver and DAQ holders were 3D-designed and printed. The front and rear view of the electronic system is shown in Figure 4.4.1 and 4.4.2, respectively.

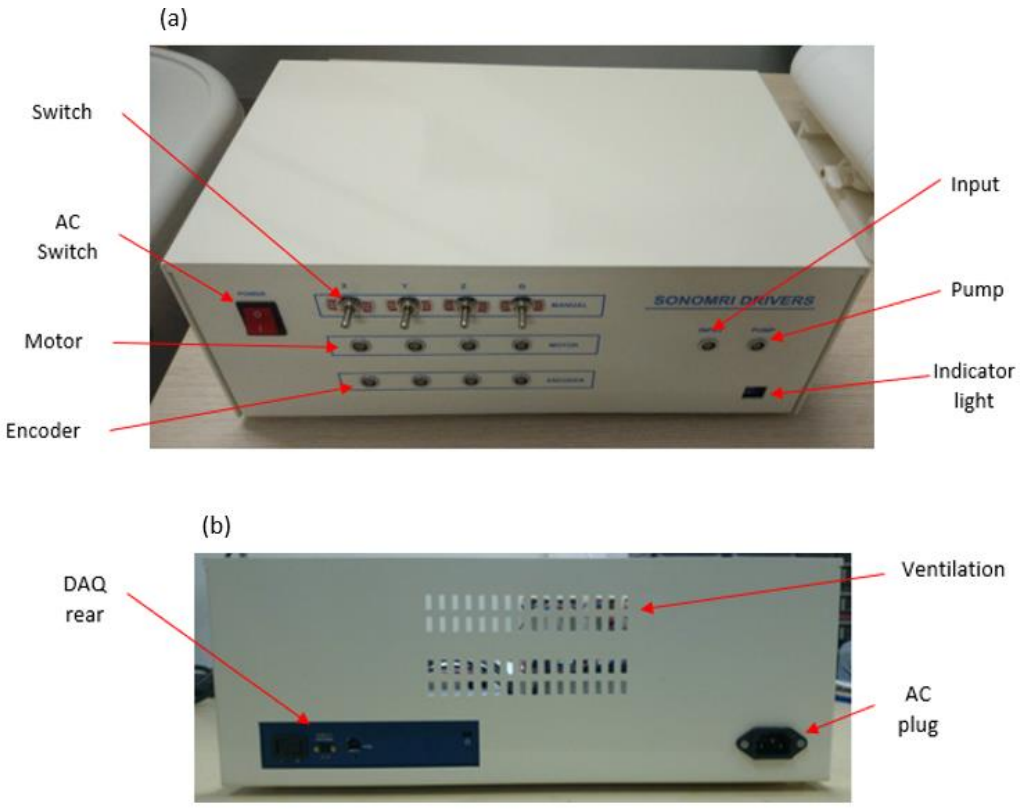

Figure 4.4.1: Electronic driving system a) front, and b) rear view.

4.5 MRgFUS software of the robotic system

A software platform that controls the 4-DOF prostate positioning device has been previously developed. However, through the evaluation procedure of the robotic system needs arose for modifications and improvement of the software.

The software was written in C sharp and controls the focused ultrasound control system guided by MRI. The main tasks of the software platform include the transducer movement (motion of the robotic device), control of ultrasonic parameters, Digital Imaging and Communications in Medicine (DICOM) viewer for MR-guided procedures, and real-time graph chart of temperature reading using thermocouples. The software communicates through a DAQ card with the piezoelectric ultrasonic motors. The user can also operate and set-up a grid pattern.

The design of the software underwent some improvements and modifications. The modifications are the following: a) there is a menu at the top of the form that consists of the settings and options, signal generator type (the application controls two types of signal generator), b) the main window of the software platform was separated into three tabs (control of the prostate robot, control of a robot operating 3D and 2D linear stages respectively, ultrasound control panel), c) at the right-hand side of the interface, there is a list box that lists all the commands that are executed during execution of the application, and d) form that controls a thermocouple to gather temperature samples on regular intervals during HIFU protocol.

Figure 4.5.1 shows the main interface of the software platform. The robotic system, signal generator, and grid pattern operations can be executed by the main window of the software platform.

Figure 4.5.2 shows a screenshot of the software while a grid pattern of 5 x 5 sonication was executed. There is an option to cancel, pause, and resume the operation after completing any single step. DAQ device settings are used to configure the robot axis to the corresponding digital input/output pins. The overhead factor for each linear or angular axis can also be chosen for the best accuracy motion results of the robotic device.

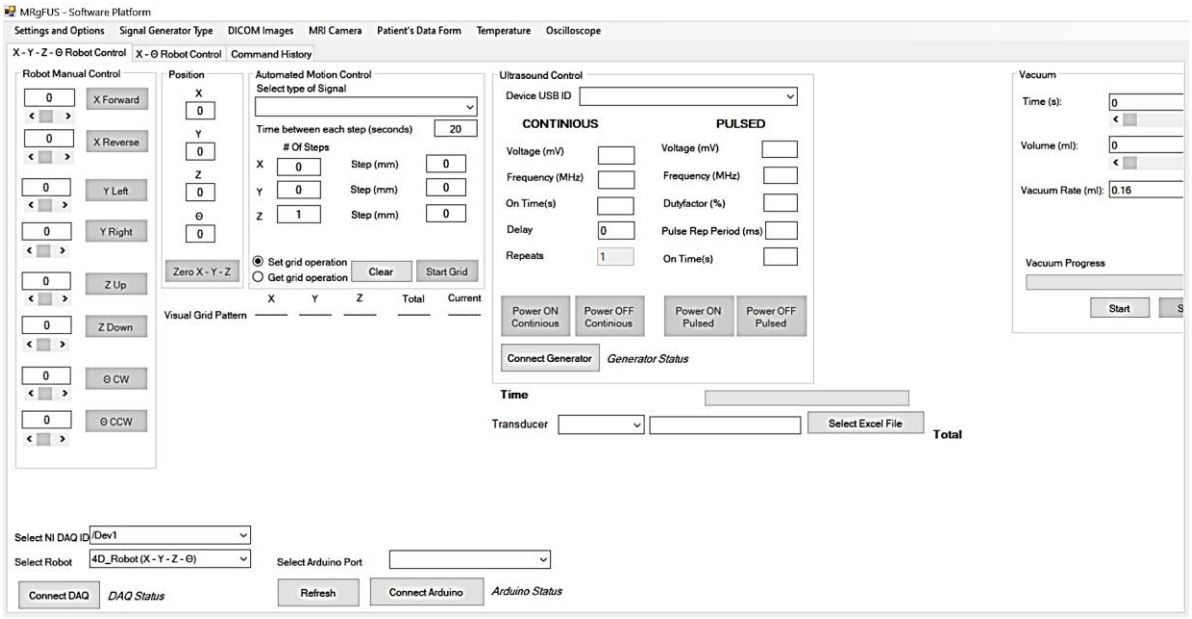

Figure 4.5.1: Main window of the software platform.

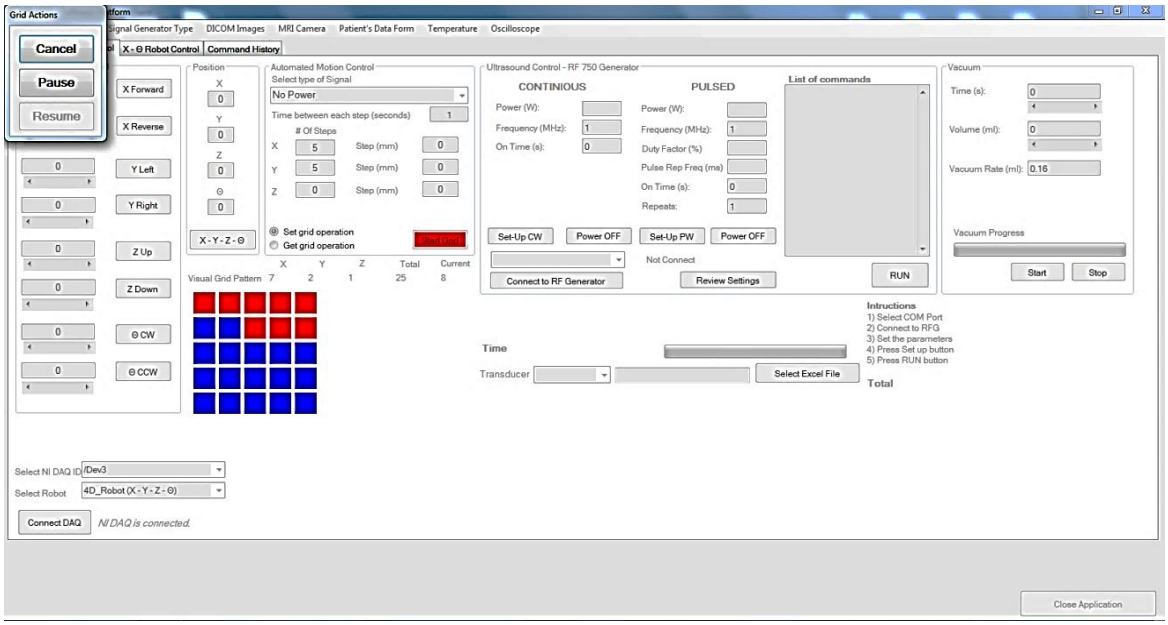

Figure 4.5.2: Grid operation in progress.

5 Development of agar-based phantoms

5.1 Introduction

Initially, phantoms were designed and constructed to mimic various parts of the human body for medical imaging applications. Phantoms are mostly used to image, analyze, evaluate, and check the performance of various medical imaging devices such as US, computed tomography, and MRI. Another application of phantoms is their usage in many research and development projects. With the use of phantoms, living tissues are avoided. HIFU develops rapidly, thus a reusable phantom that has both thermal and acoustic properties close to that of soft tissue is needed.

There are several commercial phantom options available for MRgFUS therapies, such as those by ATS (ATS Laboratories Inc., Bridgeport, CT, USA) and ONDA (Onda Corporation, Sunnyvale, CA, USA). CIRS (Computerized Imaging Reference Systems Inc., Norfolk, VA, USA) [230] develops phantoms that are only used for US imaging.

US phantoms can be separated into two types; one mimics the acoustic features of tissue (speed of sound, attenuation, absorption, etc.) while the other is to approach the sonographic appearance of tissue which is usually used for biopsy training aid [231]. Ideal phantoms should have approximately the same ranges of speed of sound, attenuation, absorption and scattering coefficients as soft tissue. These features should be controllable using appropriate phantom materials and their variation should be small within room temperature changes.

Since the discovery of diagnostic US, researchers have been concentrated on the production of phantom materials which will imitate tissue's acoustic properties. Many different types of TMMs can be found in literature for reproducing soft tissue [232-241]. These types of phantoms can be uniform single-component phantoms which are the simplest phantoms and more complex phantoms which mimic specific anatomy of a soft tissue. Some materials that are used for phantom construction and can be found in literature studies are gelatin [232], agar [233], polyvinyl alcohol (PVA) [234], polyvinyl chloride (PVC) [235], polydimethylsiloxane (PDMS) [236], silicone [237], and zerdine (CIRS Inc.). A number of low-cost, easily made, US gel-based TMMs have been introduced for diagnostic US imaging tests, biopsy needle training, elastography and use with MRgFUS treatment techniques [230-237].

Gelatin gels [232] can provide a wide range of stiffness close to that of soft tissues and they are usually constructed with particulate suspension (flour or soluble fibre medications) to increase echogenicity. However, gelatin phantoms require refrigeration and they have low melting point (45 ^{o}C) making them unsuitable for HIFU applications.

Agar-based gels are cheap and easy to be produced, durable in high temperatures, non-toxic and disposable but they lack long term stability and repeatability of acoustic properties over time [233,238,239]. Under ideal storage conditions, agar gels can remain stable up to two and a half years [233] and can serve as a perfect replacement for gelatin gels which suffer from temperature dependent structural instability [240].

Phantoms for use in MRI systems, made from water-based agar gels along with a copper salt, have been previously described [241]. The T_1 and T_2 relaxation values in these materials are strongly dependent on the concentrations of agarose and copper ions in the phantom with the T_1 value depending more on the copper and the T_2 value depending more strongly on the concentration of dry weight agarose [241]. The possibility of developing materials which mimic soft tissues simultaneously for US, MRI, and CT arose when a new TMM was developed for US in which the attenuation property is controlled through the concentration of evaporated milk [233]. Ultrasonic propagation speed and frequency-dependent attenuation coefficient are already well approximated by these materials.

The investigation of ultrasonic properties such as attenuation and absorption is essential in understanding the physics and mechanisms that control the interaction of MRgFUS with biological tissues and in developing appropriate numerical models of acoustic propagation. Assessment of attenuation and propagation velocity of the ultrasonic beam in tissue is necessary for characterizing acoustic propagation in imaging and therapy purposes, whereas the mechanism of acoustic absorption is important in therapeutic applications since it controls the amount of energy deposition in the form of heat.

5.2 Phantom materials and development procedure

The developed phantoms involved an appropriate choice of concentrations of agar, silicon dioxide, evaporated milk, and water. After a series of iterations involving variation of the concentrations of all materials, the fundamental parameters of phantom were matched as close as possible to soft tissue parameters.

Three phantom versions with the same formula but different quantities and material dimensions were produced. All phantom versions contained agar (Merck KGaA, EMD Millipore Corporation, Darmstadt, Germany and M144, Columbia Blood Agar Base, HiMedia Laboratories, Mumbai, India), silicon dioxide (S5631, Sigma Aldrich, St. Louis, Missouri, USA), evaporated milk (Nounou, Friesland Campina, Marousi, Greece) and degassed water.

The specific agar is granulated, purified, and free from inhibitors. It is mainly responsible for the bonding that forms between inclusions and background materials. The ingredients of the agar are shown in Table 5.2.1.

Table 5.2.1: List of ingredients composed the agar (M144, HiMedia Laboratories) that was used to produce some of the phantoms.

Ingredients	Gms/Litre
Peptone, special	23000
Corn starch	1000
Sodium chloride	5000
Agar	15000
Final pH (at 25 ^{o}C)	7.3 ± 0.2

Increased dry-weight concentration of agar produces greater stiffness. Silicon dioxide (form: powder, density: 3.44 g/ml at 25 ^{o}C, particle size: <1 μm) and evaporated milk (100 ml of milk includes 4.2 g of fats and 3.5 g of proteins) were added to the phantom to augment the US attenuation and absorption coefficient level. The intended use of Columbia blood agar base (M144, HiMedia Laboratories) that was used for the phantoms production is that it is used as an efficient base for preparation of blood agar, chocolate agar and for preparation of various selective and identification media and isolation of organisms from clinical and non-clinical samples.

The process of producing any of the three different phantom versions was the same as follows: Different quantities of the ingredients were used for each phantom version. First, quantities of granular agar and silicon dioxide were prepared with a precision digital mass balance. For example, for the first phantom version, the volume percentage for agar, silicon dioxide, evaporated milk, and water were 2 % w/v, 1.2 % w/v, 25 % v/v, and 75 % v/v (with an extra 30 % due to evaporation during the heating procedure), respectively. An electronic thermometer (Omega Thermometer, HH806AU, Omega Engineering, Norwalk, Connecticut, USA) was used to measure the temperature. In a single beaker, the appropriate volume of room-

temperature water was added and heated on a magnetic stirrer hot plate until the temperature water reached 50 ^{o}C. Afterwards, the appropriate mass of granular agar was added to the beaker and mixed well using a magnetic stirrer bar as shown in Figure 5.2.1. After 2 minutes, the appropriate mass of silicon dioxide was also added to the beaker. When the two materials were clarified (usually clarification occurs when the temperature rises to 90 ^{o}C), the beaker was removed from the magnetic stirrer and left until the mixture was cooled to 50 ^{o}C. Alongside, the appropriate volume of evaporated milk was added in a different beaker and was slightly boiled to reach around 30 ^{o}C. When the mixture reached 50 ^{o}C and the evaporated milk reached 30 ^{o}C, the evaporated milk was mixed in the mixture and stirred until it was entirely dissolved. At this point, the agar/silica/milk mixture was ready to be poured into the mold for cooling and congealing overnight into a refrigerator. Figure 5.2.2 illustrates the flowchart of the procedure to produce an agar/silicon dioxide/evaporated milk phantom.

As explained above, three phantom versions were designed and used. These phantom versions do not differ in the recipe, but they differ in shape and size and this is due to the different phantom molds that have been designed. The design of the first phantom version included various issues and challenges in the correct measurement of absorption coefficient. Therefore, a new novel mechanical design was designed and 3D-printed in order to estimate the absorption coefficient of any phantom and tissue with the best accuracy and evaluation of results in a very short time. The three different phantom versions are explained and presented in this part of the dissertation.

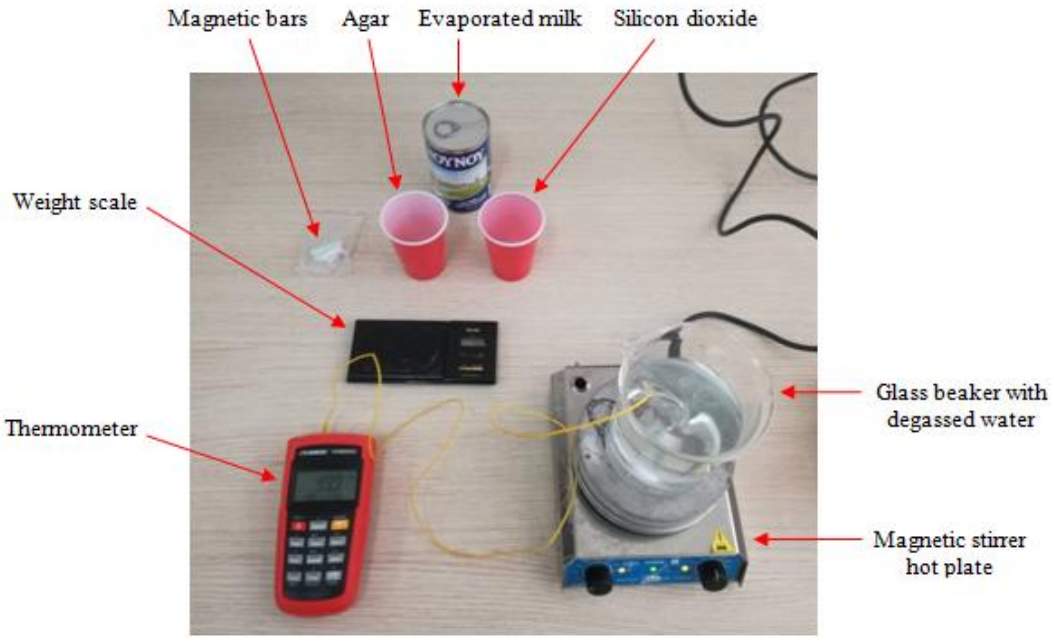

Figure 5.2.1: Procedure to develop agar/silica/milk phantom for the estimation of ultrasonic phantom characteristics.

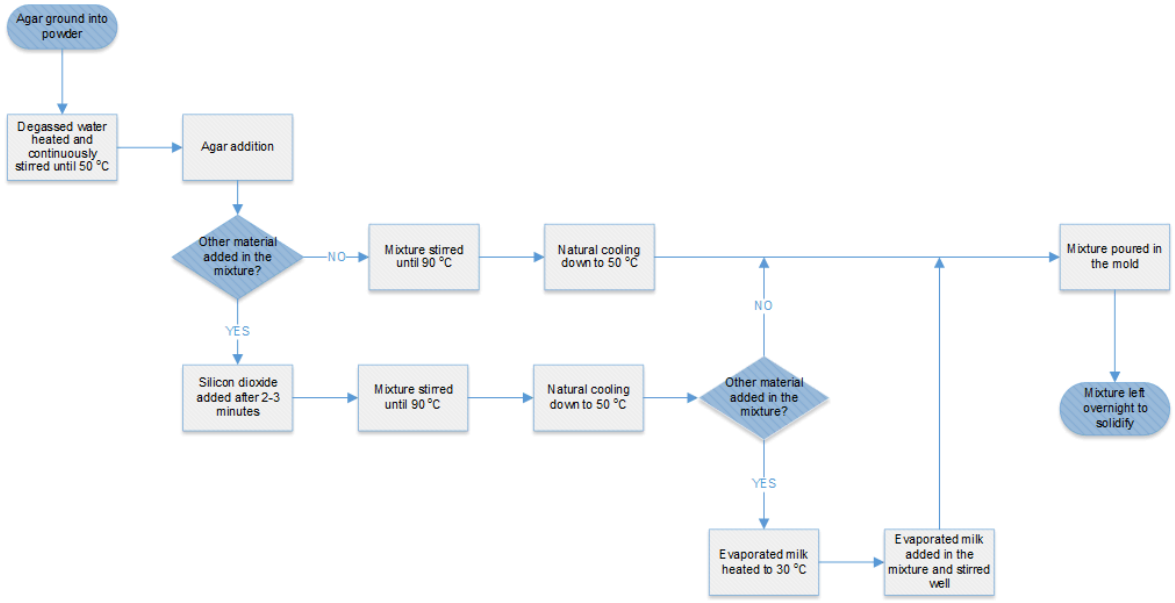

Figure 5.2.2: Flowchart of the procedure to develop an agar/silica/milk phantom.

5.3 Phantom with designed mold version 1

A 3D-printed mold was firstly designed to produce phantoms as an initial idea for trying to measure the absorption coefficient of a phantom with 2 % agar, 1.2 % silicon dioxide, and 25 % evaporated milk. The phantom mold capacity was 0.48 L. After the design was completed, the drawing was sent to a 3D printer (FDM400, Stratasys Ltd.) for production. This 3D printer produces parts made out of ABS. The phantom mold dimensions were 50 mm height, 80 mm width, and 120 mm length. Figure 5.3.1.a illustrates the CAD drawing of the phantom mold (version 1). In order to produce the phantom version 1, the percentage of agar, silicon dioxide, evaporated milk, and water was 2 % w/v, 1.2 % w/v, 25 % v/v, and 75 % v/v, respectively.

The corresponding quantity in grams for agar percentage of 2 % was 9.6 g while for silicon dioxide of 1.2 % was 5.76 g. The corresponding quantity in ml for evaporated milk percentage of 25 % was 120 ml while for distilled water of 75 % was 468 ml. Figure 5.3.1.b shows the phantom mold version 1 prior the production of phantom mixture and Figure 5.3.1.c shows the phantom mold version 1 after filling it with the phantom mixture.

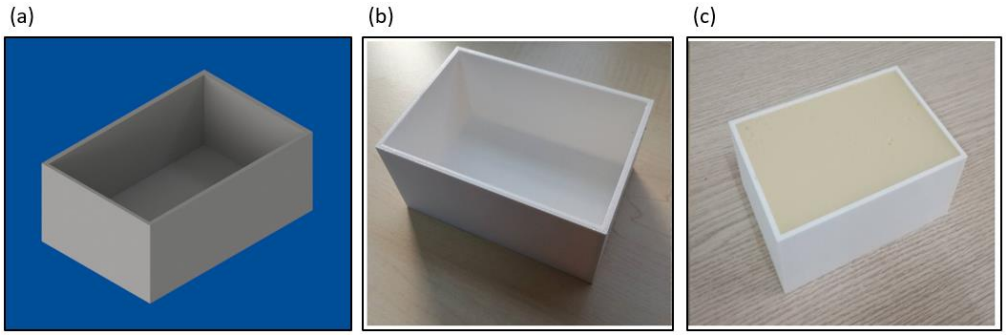

Figure 5.3.1: a) CAD drawing of the phantom mold (version 1) which was initially used to produce phantoms for estimating the ultrasonic absorption coefficient, b) photo of the mold before filling the mixture, and c) after filling the mixture.

5.4 Phantom with designed mold (version 2)

Since the phantom designed mold (version 1) was of large dimensions, it required a longer production time and motion problems have occurred during the experiments since it was difficult to keep it firm in a holder, thus a phantom designed mold (version 2) was designed and produced to overcome these issues. The same procedure was followed to develop another phantom of the same formula but with different quantities, material shape, and size. The mold was designed to produce four phantoms. Multiple phantoms of varying amount of agar, silicon dioxide, and evaporated milk were needed to estimate the appropriate possible ultrasonic parameters. The dimensions of each phantom were 5 cm height, 5 cm width and 5 cm length, thus the phantom mold dimensions were 5 cm height, 10 cm width, and 10 cm length. The phantom mold capacity was 0.5 L (125 ml each phantom). Figure 5.4.1.a illustrates the CAD drawing of the phantom designed mold version 2. Four phantoms were constructed so that the various ultrasonic parameters were calculated and investigated to be as close as possible to the parameters of human tissue. Initially, the concentration of agar and silicon dioxide remained fixed for all four phantoms while the percentage of evaporated milk varied between 0-50 %. The percentages of agar and silicon dioxide were 2 % and 1.2 % respectively. The corresponding quantity in grams for agar percentage of 2 % was 2.5 g while for silicon dioxide of percentage of 1.2 % was 1.5 g. The corresponding quantity in ml for evaporated milk of percentage of 0, 10, 30, and 50 % was 0, 28.8, 86.4, and 144 ml, respectively. Finally, the corresponding quantity in ml for distilled water percentage of 100, 90, 70, and 50 % was 162.5, 146.25, 113.75, and 81.25 ml, respectively. Figure 5.4.1.b shows the phantom mold version 2 prior the production of phantom mixture and Figure 5.4.1.c shows the phantom mold version 2 after filling it with the four different phantom mixtures.

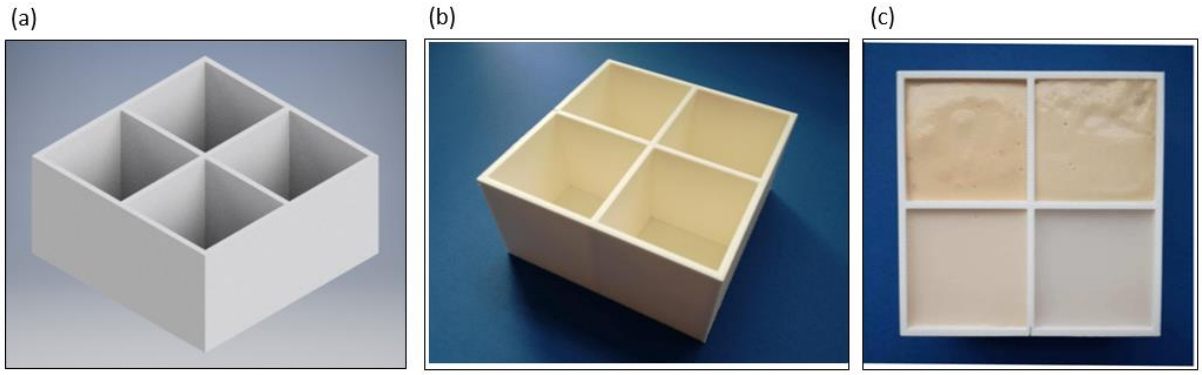

Figure 5.4.1: a) CAD drawing of the phantom mold (version 2) which was used to produce 4 phantoms with different recipe for estimating the ultrasonic absorption coefficient, b) photo of the mold before filling the mixture, and c) after filling the mixture.

5.5 Phantom development with the final version 3D-printed mold

Due to the fact that the phantom dimensions were not adequate to acquire MRI signal resulting in poor image acquisition and there was an alteration of the results, we partially increased the dimensions of the phantom. The new dimensions of each phantom were 8 cm height, 6 cm width and 6 cm length, thus the phantom mold dimensions were 8 cm height, 12 cm width, and 12 cm length. The phantom mold capacity was 1.152 L (288 ml each phantom). Figure 5.5.1.a illustrates the CAD drawing of the phantom mold. All the quantities of materials needed to develop each phantom varied in order to achieve the best parameters. The percentages of agar, silicon dioxide, and evaporated milk varied between a range of 2-12 % w/v (2, 4, 6, 8, 10, 12), 0-8 % w/v (0, 2, 4, 6, 8), and 0-30 % v/v (0, 15, 30), respectively. The corresponding quantity in grams for agar percentage of 2, 4, 6, 8, 10, and 12 % was 5.76, 11.52, 17.28, 23.04, 28.8, and 34.56 g, respectively. In the same way, the corresponding quantity in grams for silicon dioxide percentage of 0, 2, 4, 6, and 8 % was 0, 5.76, 11.52, 17.28, and 23.04 g, respectively while the corresponding quantity in ml for evaporated milk percentage of 0, 15, and 30 % was 0, 43.2, and 86.4 ml, respectively. Finally, the corresponding quantity in ml for distilled water percentage of 100, 85, and 70 % was 0, 28.8, 43.2, 86.4, and 144 ml, respectively. Figure 5.5.1.b shows the phantom mold (final version) prior the production of phantom mixture and Figure 5.5.1.c shows the phantom mold after filling it with the four different phantom mixtures.

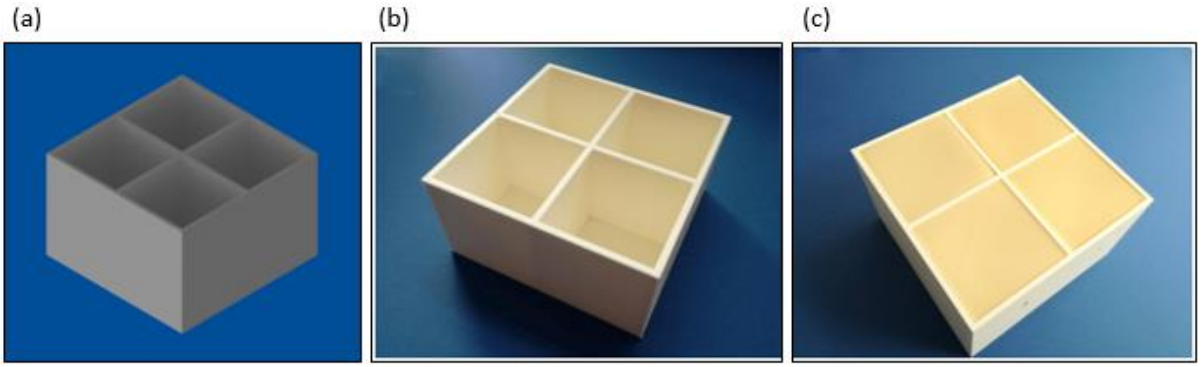

Figure 5.5.1: a) CAD drawing of the phantom mold (final version) which was used to produce 4 phantoms with different recipe for estimating the ultrasonic absorption coefficient, b) photo of the mold before filling the mixture, and c) after filling the mixture.

In Figure 5.5.2, some of the developed phantoms are presented as produced in the phantom mold, while in Figure 5.5.3 the phantoms are showed after their removal from the phantom mold.

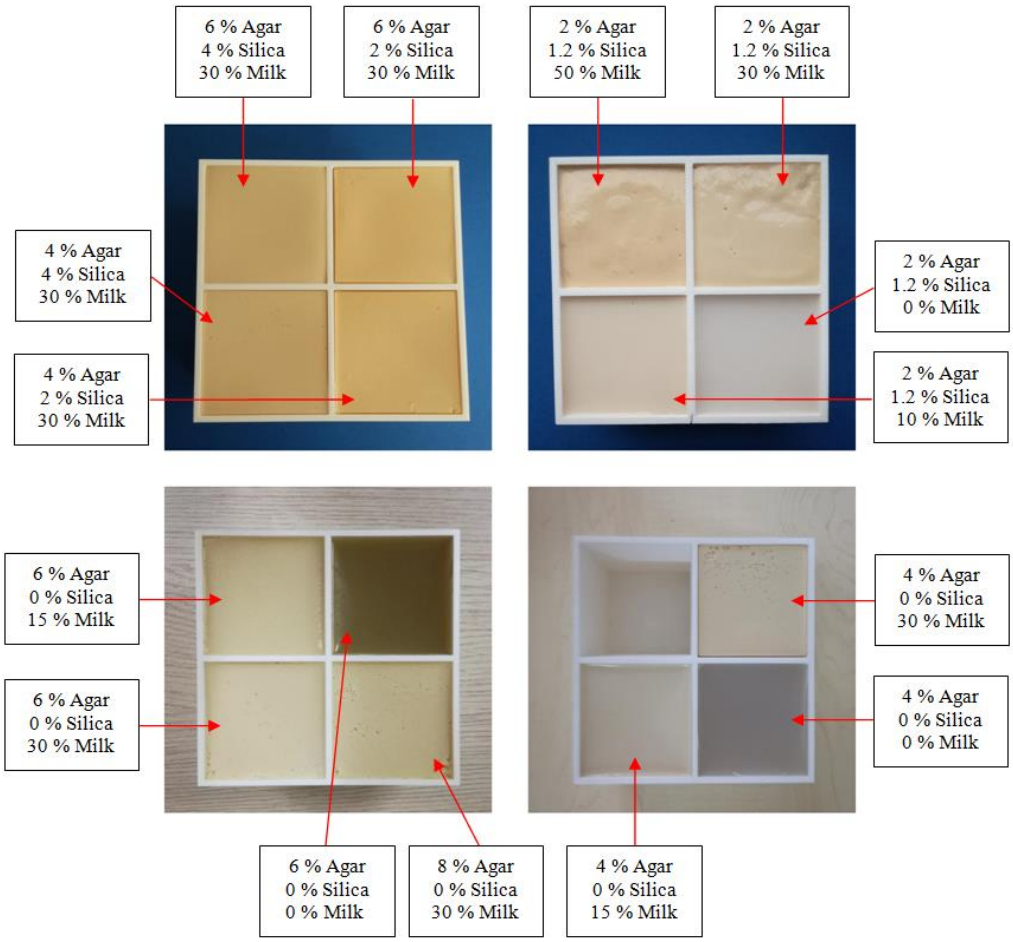

Figure 5.5.2: Phantoms with different percentage of agar, silicon dioxide, and evaporated milk as produced in the phantom mold.

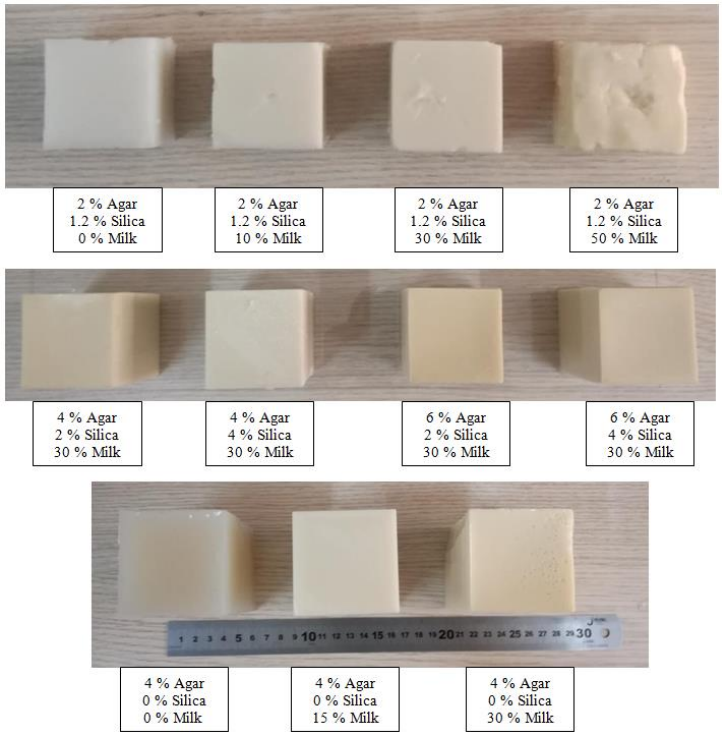

Figure 5.5.3: Phantoms with different agar, silicon dioxide, and evaporated milk concentrations.

5.6 Ultrasound imaging of phantoms with varying agar/silica/evaporated milk concentration

Phantoms are specially designed objects that are scanned or imaged in order to analyze, evaluate and tune the performance of various imaging devices. In the field of therapeutic US, the developed phantoms described in this research can be used to illustrate any change in temperature within the phantom using either MR thermometry or thermocouples.

As has been reported so far, a phantom has been developed to be used in the early stages of the experiments for the evaluation of the transducers. Firstly, US images were obtained to check if the phantom has ultrasonic appearance as soft tissue. From US images with specific methods, ultrasonic parameters can be calculated including speed of sound, attenuation coefficient, backscatter coefficient, depth of penetration, dimensions, and volume measurement.

A diagnostic US device (HD-7XE, Philips, Amsterdam, Netherlands) was used to acquire images of an agar-based phantom that included 4 % agar, 4 % silicon dioxide, and 30 % evaporated milk. Two images were obtained, an image (Figure 5.6.1.a) where the US probe was placed at the top of the phantom and another image (Figure 5.6.1.b) where the US probe

was placed at the bottom of the phantom to check the homogeneous distribution of silicon dioxide.

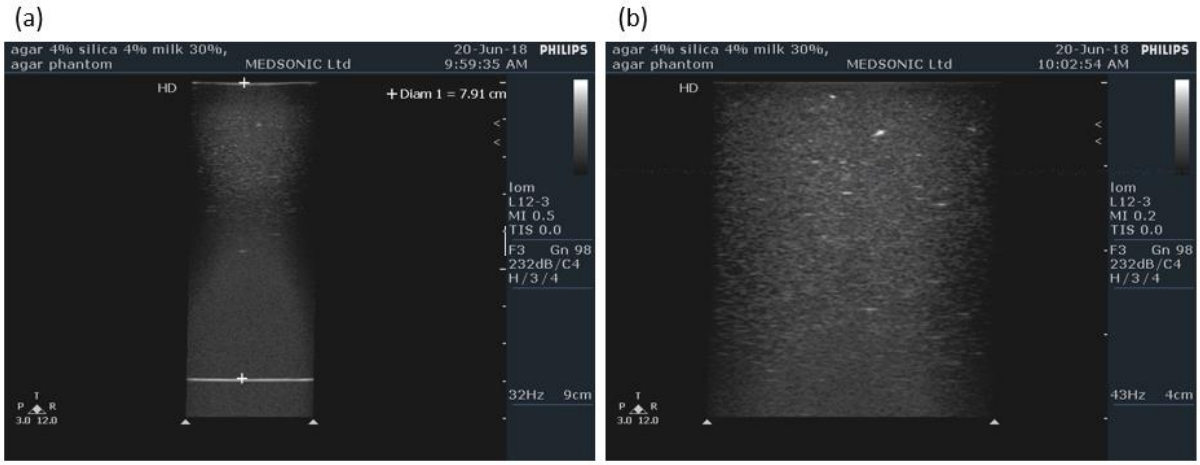

Figure 5.6.1: US image of the phantom (4 % agar, 4 % silicon dioxide, and 30 % evaporated milk). The US probe was placed a) at the top of the phantom, and b) at the bottom. As shown from the images, the height of the phantom was 7.91 cm.

US images of phantoms with the same amount of agar and silicon dioxide but different amount of evaporated milk (0 and 15 %) were also obtained as shown in Figure 5.6.2.

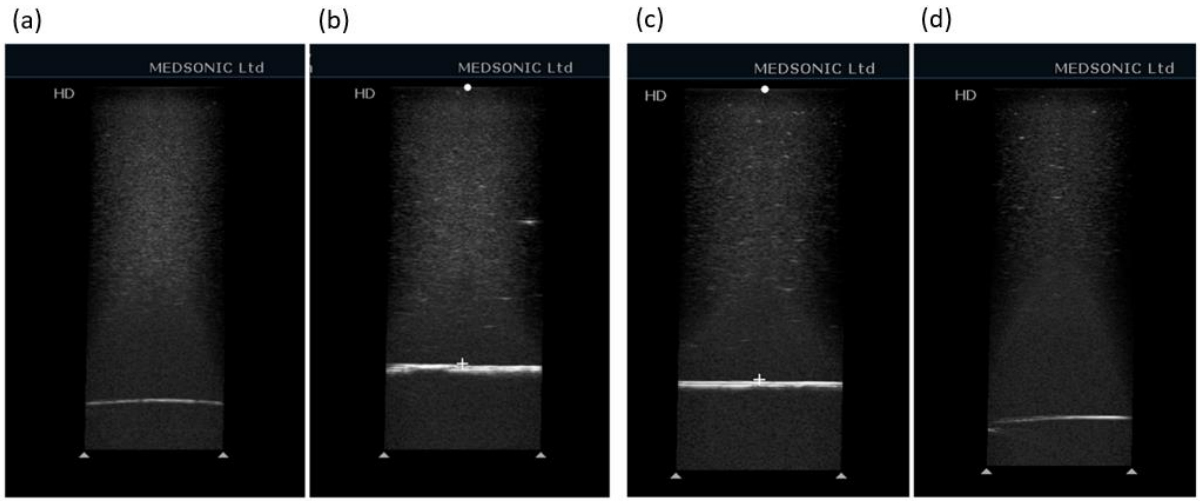

Figure 5.6.2: US images obtained for phantom a) with no evaporated milk concentration and the US probe placed horizontally with the phantom, b) with no evaporated milk concentration and the US probe placed vertically, c) with 15 % evaporated milk concentration and the US probe placed horizontally, and d) with 15 % evaporated milk concentration and the US probe placed vertically with the phantom.

A portable diagnostic US device (UMT-150, Shenzhen Mindray Bio-Medical Electronics Co., Ltd., Shenzhen, P.R. China) was also used to acquire images of phantoms with different agar concentration. US images of phantoms with 30 % evaporated milk and 2, 4 and, 6 % agar concentration were taken as shown in Figure 5.6.3.

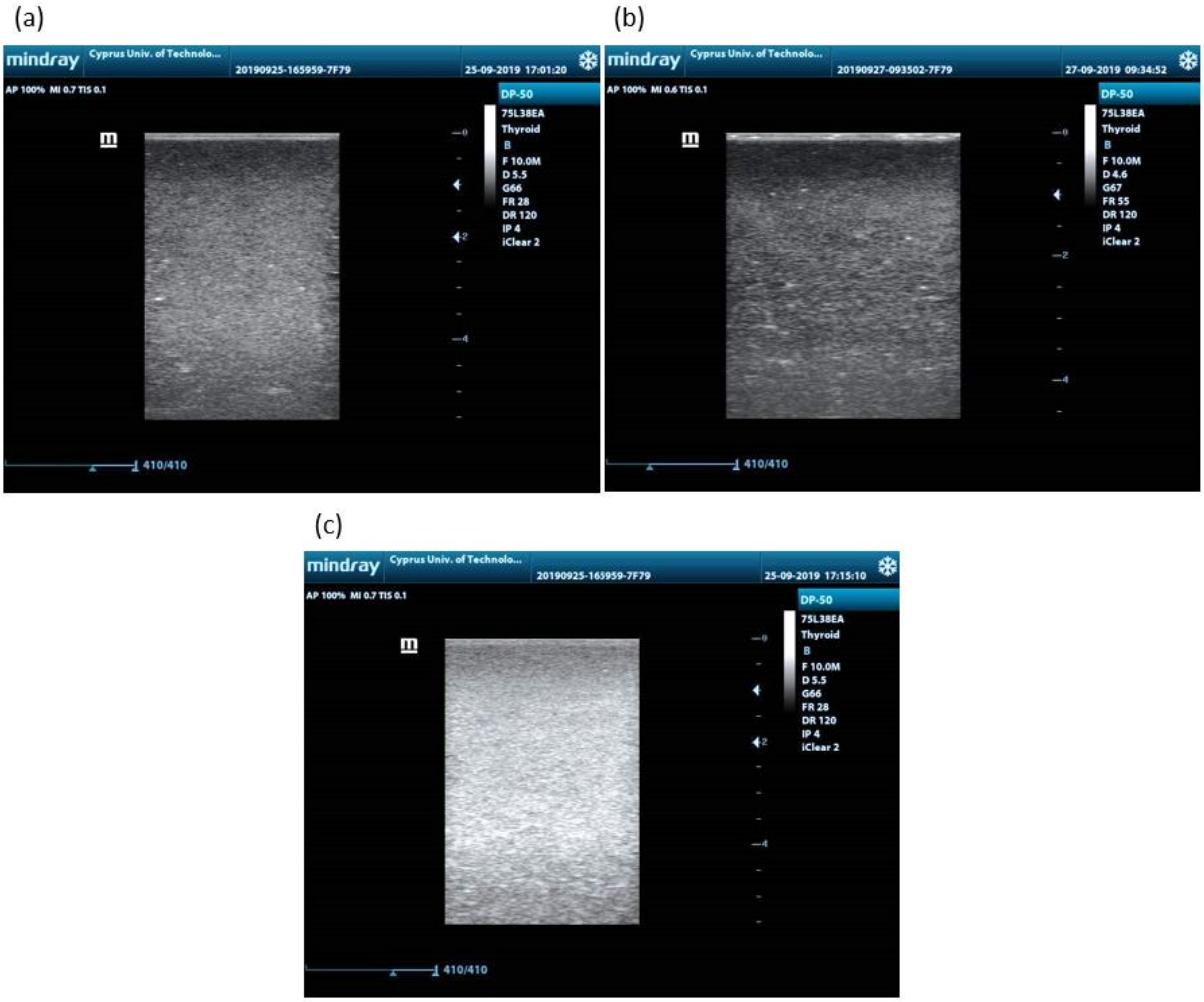

Figure 5.6.3: US image of the phantom with 30 % evaporated milk and a) 2 % agar, b) 4 % agar, and c) 6 % agar.

5.7 MRI imaging and T_1, T_2 relaxation times of agar-based phantoms

MRI images of the mechanical design with the transducer and the phantom were acquired in a 1.5 T MR system (Signa, General Electric, Fairfield, CT, USA) using a GPFLEX coil (USA Instruments, Cleveland, OH, USA). High resolution MR imaging for the phantom was mainly performed to check its homogeneity and visualize the mechanical design. The MRI images were acquired using a Fast Recovery Fast Spin Echo (FRFSE) T_2-weighted sequence with the following parameters: repetition time (TR) = 2200 ms, echo time (TE) = 61.2 ms, slice thickness = 5 mm, matrix = 192 x 192, FOV = 17 cm, number of excitations (NEX) = 1, and echo train length (ETL) = 16. Figure 5.7.1 shows the mechanical design with the transducer and the phantom as placed on the MRI table.

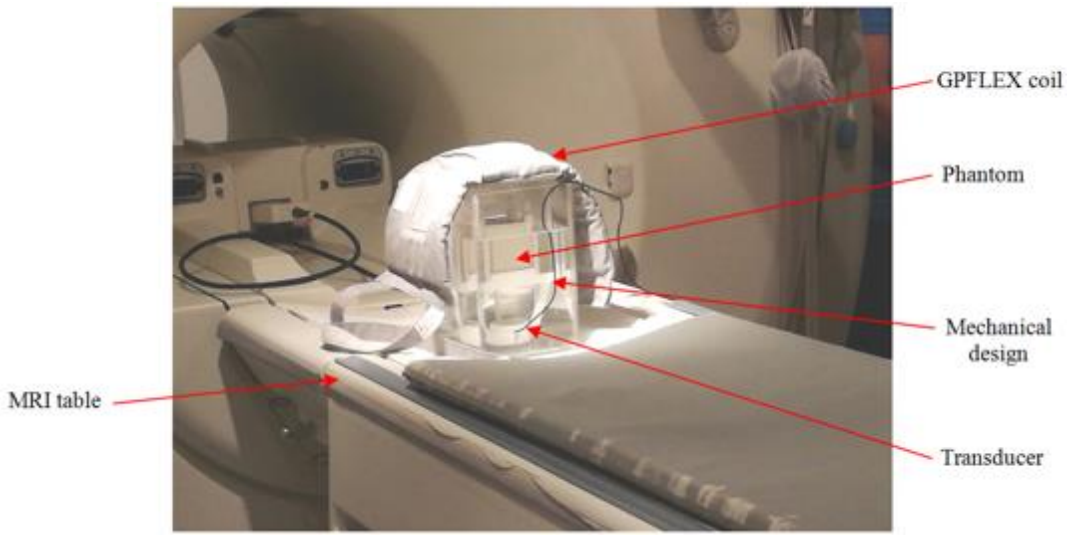

Figure 5.7.1: The mechanical design with the transducer and the phantom as placed on the MRI table.

In Figure 5.7.2, the MR image of the mechanical design, transducer, and phantom is illustrated.

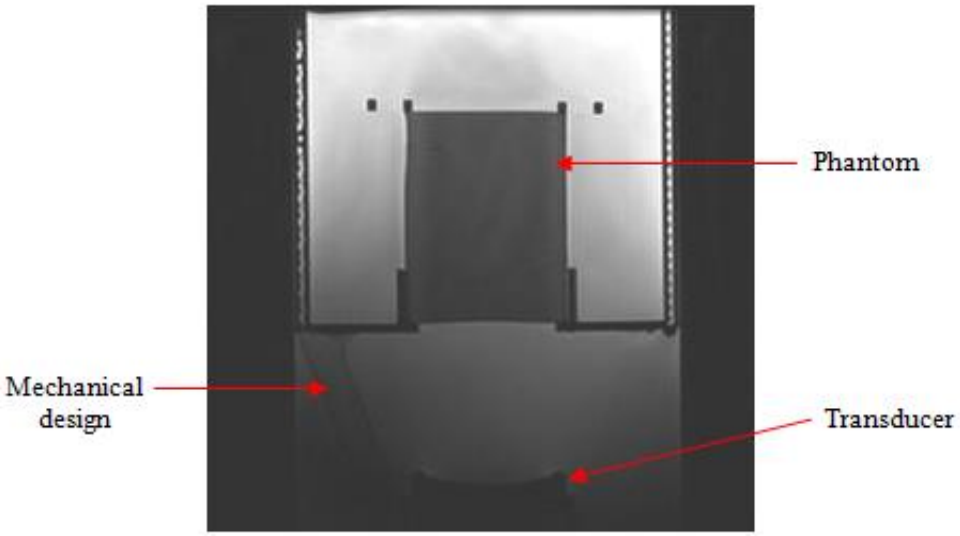

Figure 5.7.2: MRI FRFSE T_2-weighted image of the mechanical design with the 3.2 MHz transducer and the agar-based phantom.

For measuring the spin-lattice relaxation time (T_1), an Inversion Recovery Fast Spin Echo (IR-FSE) sequence was used. In an IR-SE sequence the initial RF pulse inverts the longitudinal magnetization from its equilibrium state by 180^o, with magnitude equal to M_o, around the z-axis. Immediately after application of the inverting pulse, the longitudinal magnetization vector (M_Z) points in the opposite direction and relaxes back to equilibrium at a rate $1/T_1$. After an

inversion time (TI), a second 90^{o} excitation pulse is applied and rotates any longitudinal magnetization. The following equation was used.

$$M_z = M_o(1 - 2e^{\frac{TI}{T_1}}) \quad (5.7.1)$$

Since there is no way of measuring the longitudinal magnetization directly from MRI images, an indirect method was used. Phantom images were acquired at different TIs in order to identify the TI setting for which the signal on magnitude images was nullified. The nulling TI was interpolated by fitting the expression of the above equation to the data and thus the T_1 was calculated.

The T_2 relaxation time was estimated by taking a series of FSE T_2-weighted sequences for different effective echo times. The transverse magnetization was measured in arbitrary units and was then normalized using the factors of the exponential fit described in the following equation.

$$M_{xy} = M_o e^{-\frac{TE}{T_2}} \quad (5.7.2)$$

The T_1 relaxation time of the agar/silica/milk phantom was calculated to be 852 ms and the T_2 relaxation time was 66 ms.

5.8 X-ray imaging of agar-based phantoms

X-ray images of the phantoms including different concentration of agar, silicon dioxide, and evaporated milk were acquired using a portable X-ray system (IMS001, Shenzhen Browiner Tech Co., Ltd., Shenzhen, P.R. China). Figure 5.8.1 shows the X-ray system with the phantoms placed on the CR (Computed Radiography) cassette and the digitize CR reader (Vita Flex, Carestream Health, Inc., Rochester, NY, USA) that was used to transfer the data from the CR cassette to the computer for X-ray image reconstruction. The parameters used for the X-ray images of the phantoms were as follows: tube current = 50 mA, tube voltage = 60 kV, exposure time = 320 ms, and a total of 16 mAs. Some of the phantoms were produced in a different mold with different dimensions (5 cm height, 7 cm wide, and 15 cm long) since they were needed for the thermal conductivity measurements.

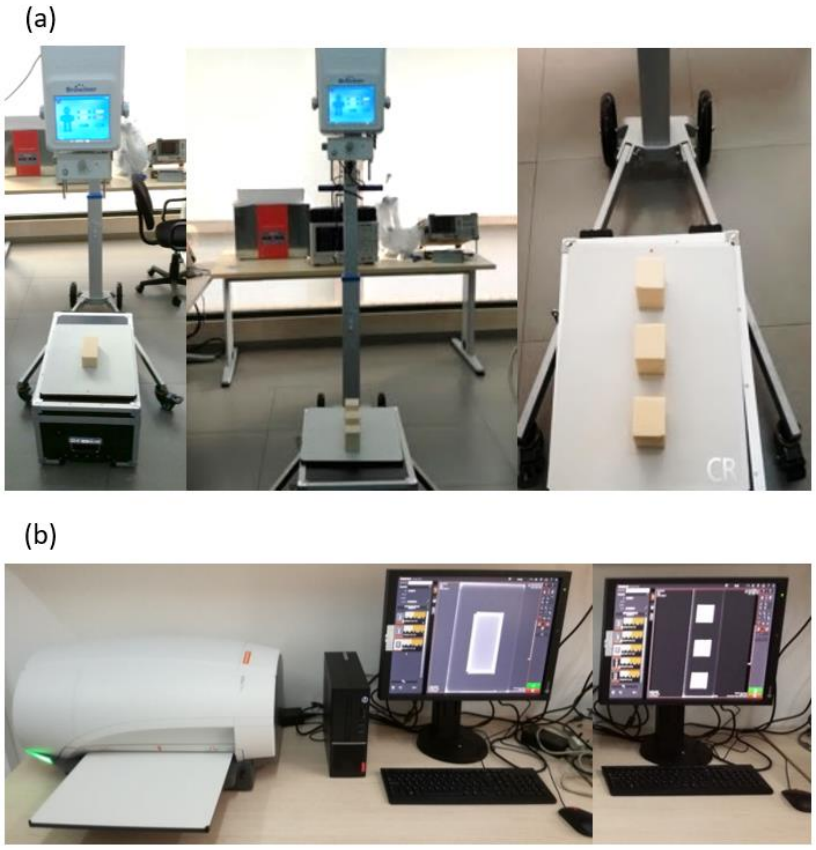

Figure 5.8.1: a) X-ray system with the agar-based phantoms placed on the CR cassette, and b) CR machine that was used to transfer the data from the CR cassette to the computer for X-ray image reconstruction.

Figure 5.8.2 shows the X-ray images of the agar-based phantoms with different concentration of agar, silicon dioxide, and evaporated milk.

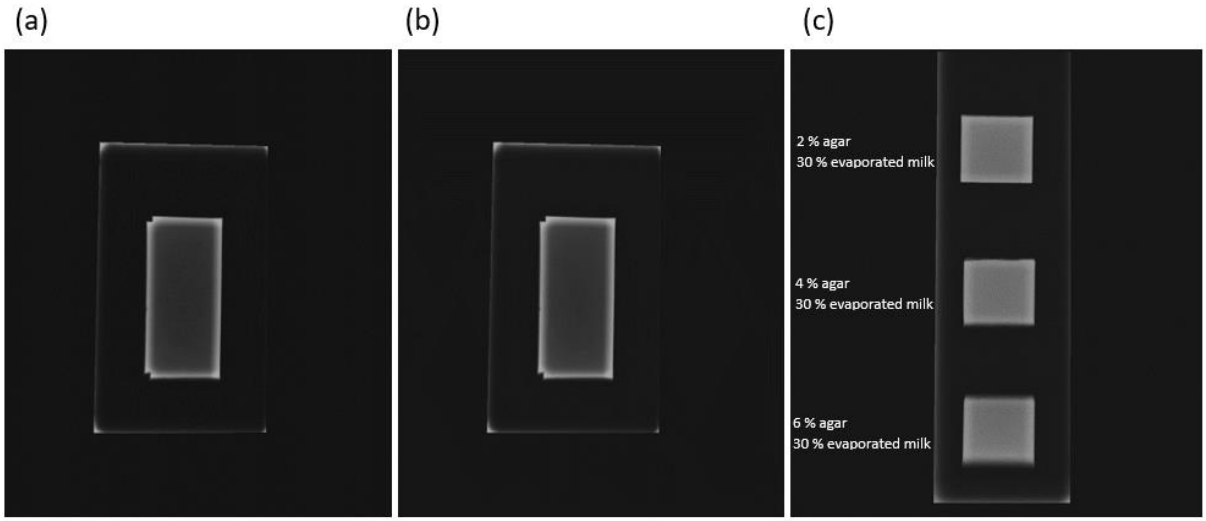

Figure 5.8.2: X-ray image of phantom with a) 4 % agar, b) 6 % agar, and c) 30 % evaporated milk and 2, 4, and 6 % agar.

5.9 Estimation of the density of agar-based phantoms

The mass density of agar-based phantoms with 6 % agar was calculated using the water volume displacement method. A testing tube was filled with a fixed water volume (Figure 5.9.1.a) and then a piece of the phantom was immersed in the tube (Figure 5.9.1.b). The mass of the pieces was calculated using a precision digital mass balance (1479V, Tanita Corporation of America, Inc., USA).

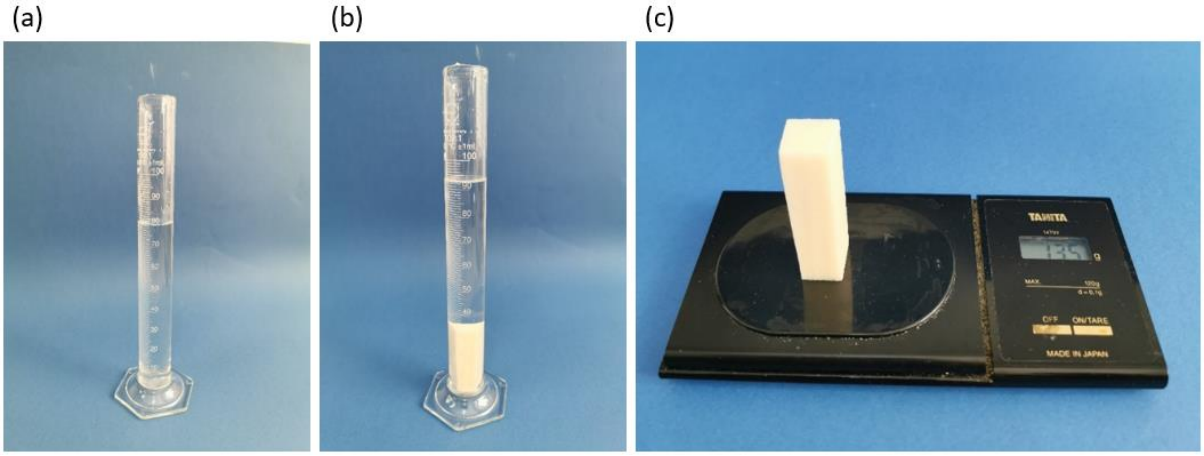

Figure 5.9.1: a) Testing tube with the initial water volume, b) testing tube with the phantom, and c) mass calculation of a piece of the phantom.

The mass of a piece of the phantom was measured to be 13.5 g as shown in Figure 5.9.1.c. The volume without the piece was 79.5 ml. After placement of the piece into the testing tube, the volume with the piece was 92.5 ml. Thus, the density of the phantom with 6 % agar was 1.0385 kg/m^3.

5.10 Estimation of the ultrasonic speed of sound of agar-based phantoms

The propagation speed of the agar-based gel phantoms with different agar concentration was estimated at room temperature. The pulse-echo method was used to estimate the ultrasonic speed of sound. A linear transducer with frequency of 4 MHz was used as a pulser/transmitter and receiver (Panametrics 500PR, Olympus Corp., Tokyo, Japan). A digital oscilloscope (TDS 2012, Tektronix, Inc., Karl Braun Drive, United States) was also used to display and analyze the waveform of the electronic signals. Figure 5.10.1 shows the experimental set-up in order to measure the propagation speed.

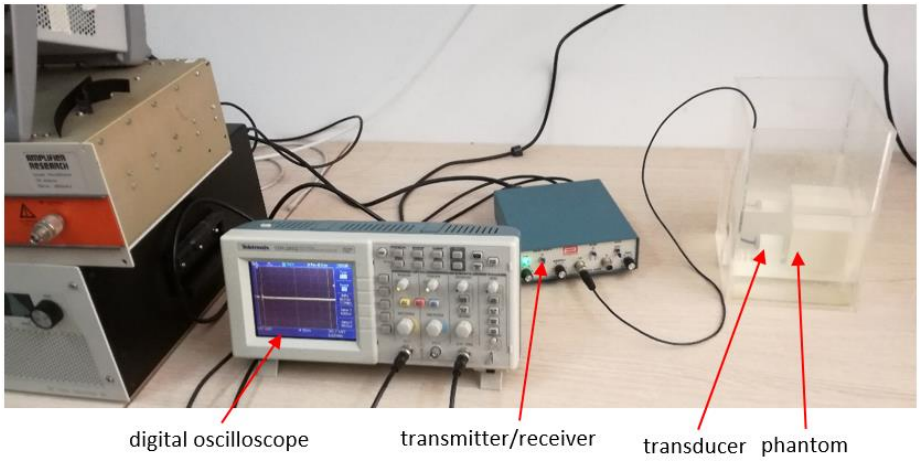

Figure 5.10.1: Experimental set-up in order to measure the speed of sound of the agar-based phantoms.

Figure 5.10.2 shows the ultrasonic speed of sound versus the agar concentration (for n = 10). The thickness of the identical phantoms was 6.6±0.1 cm.

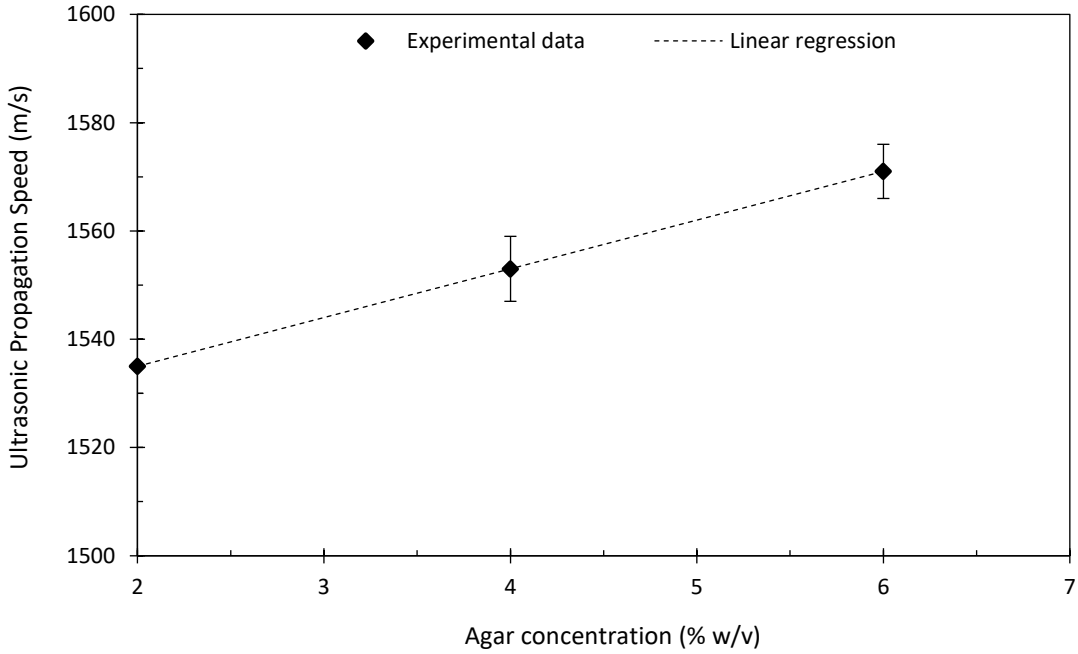

Figure 5.10.2: Ultrasonic speed of sound versus agar concentration. Error bars represent standard deviation.

5.11 Estimation of the thermal properties of agar-based phantoms with varying agar concentration

Thermal conductivity, thermal diffusivity, and specific heat capacity were measured for the phantom with 2, 4, and 6 % agar concentration and 30 % evaporated milk. Silicon dioxide was not added to the phantoms. The thermal conductivity of a material is a measure of its ability

to conduct heat. Thermal diffusivity measures the rate of transfer of heat of a material from the hot end to the cold end. The specific heat capacity of a substance is the heat capacity of a sample of the substance divided by the mass of the sample. Generally, it is the amount of energy that must be added, in the form of heat, to one unit of mass of the substance in order to cause an increase of one unit in its temperature. Thermal diffusivity is given by:

$$\alpha = \frac{k}{\rho c_\rho} \tag{5.11}$$

where k is thermal conductivity, c_ρ is specific heat capacity, and ρ is density. Together, ρc_ρ can be considered as the volumetric heat capacity [242]. A heat transfer analyser (Isomet, model 2104, Applied Precision, Ltd., Bratislava, Slovakia) was used to measure these parameters with a needle probe. For the needle probe, the measurement range was 0.2-1 W/m.K. To correctly measure the thermal conductivity using the needle probe a phantom was developed with the necessary dimensions (5 cm height, 7 cm wide, and 15 cm long). The entire needle was placed in the phantom for correct measurements. The phantom was left two hours in the lab so that its temperature reaches room temperature. This ensured that the measurements were consistent as the probe induces heat to the phantom in order to measure the temperature rate. The device and the experimental procedure that were used to measure the thermal properties are shown in Figure 5.11.1. When the needle probe was inserted in the phantom the device was set-up for the measurement. When the measurement finished, the results appeared in the screen as shown in Figure 5.11.1.b.

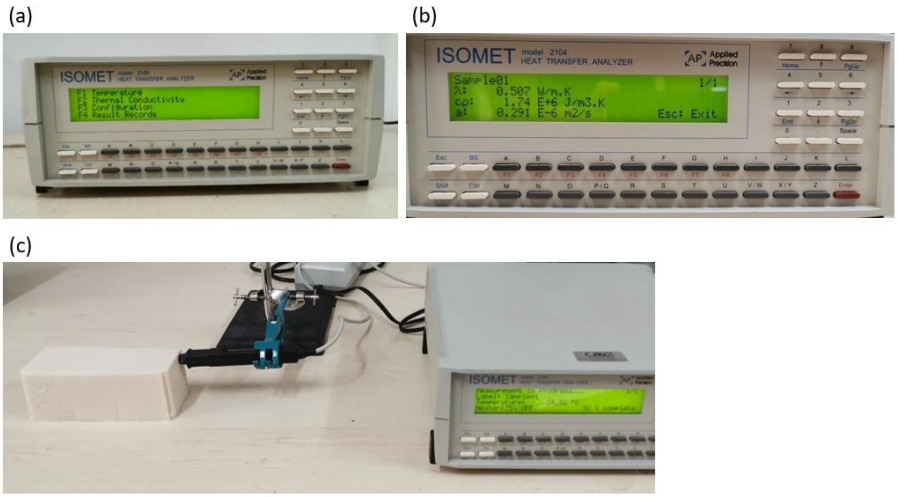

Figure 5.11.1: a) The heat transfer analyzer that was used to measure the thermal properties, b) results of the measurement as appeared in the screen, and c) the needle probe was carefully inserted in the phantom before setting-up the device.

The measurements were performed in four identical phantoms for each different agar concentration. The thermal conductivity of a phantom with 30 % evaporated milk and 2, 4, and 6 % agar were 0.62, 0.5, and 0.55 W/m.K, respectively. The specific heat capacity of a phantom with 30 % evaporated milk and 2, 4, and 6 % agar were constant at 1.75×10^6 J/m^3.K. The thermal diffusivity of a phantom with 30 % evaporated milk and 2, 4, and 6 % agar were 0.36×10^{-6}, 0.29×10^{-6}, and 0.31×10^{-6} m^2/s, respectively. Figure 5.11.2 shows the thermal conductivity and diffusivity versus agar concentration for the phantoms with 30 % evaporated milk and without evaporated milk. Figure 5.11.3 shows the specific heat capacity versus agar concentration.

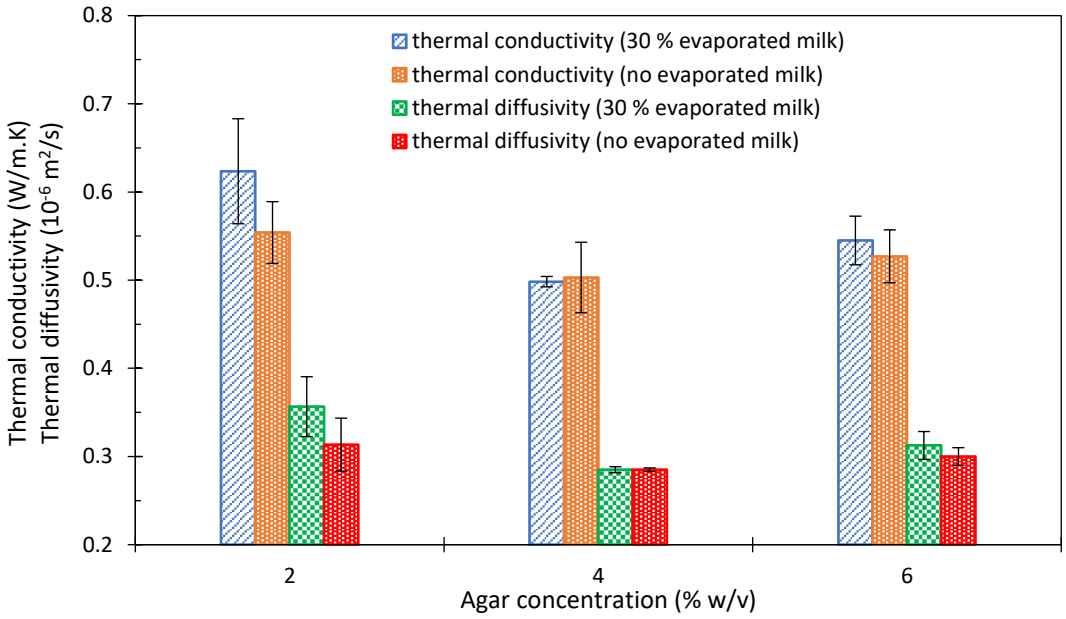

Figure 5.11.2: Thermal conductivity and diffusivity versus agar concentration.

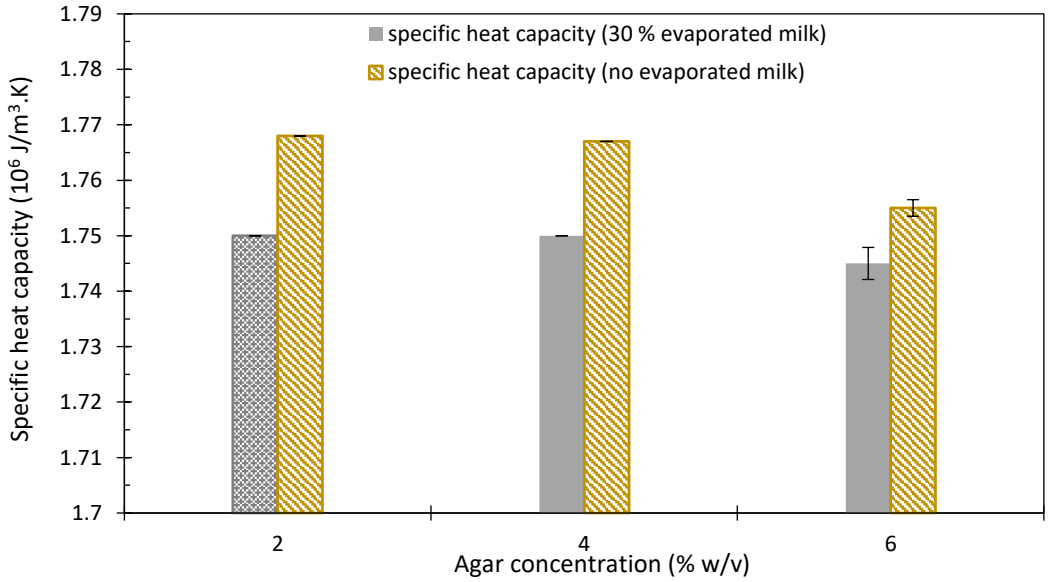

Figure 5.11.3: Specific heat capacity versus agar concentration.

The thermal conductivity, thermal diffusivity, and specific heat capacity of the agar and silicon dioxide were also measured. Figure 5.11.4 shows the experimental set-up that was used to measure the thermal properties of silicon dioxide. A testing tube was used as a container in which the material was placed. A vise was used to secure the needle probe in the material. The same procedure was followed for measurement of the thermal properties of agar.

Figure 5.11.4: Experimental set-up in order to measure the thermal properties of the silicon dioxide and agar.

Table 5.11.1 lists the thermal properties of the agar and silicon dioxide as measured using the heat transfer analyzer.

Table 5.11.1: List of the thermal properties of the agar and silicon dioxide.

Material	**Thermal conductivity λ (W/m.K)**	**Specific heat capacity Cp (10^6 J/m^3.K)**	**Thermal diffusivity a (10^{-6} m^2/s)**
Agar	0.096±0.0008	1.43	0.067±0.0005
Silicon dioxide	0.068±0.0003	1.42	0.048±0.0005

The thermal conductivity versus temperature for the phantoms with 2, 4, and 6 % agar concentration as well as without evaporated milk was also measured using the needle probe of the device as shown in Figure 5.11.5.

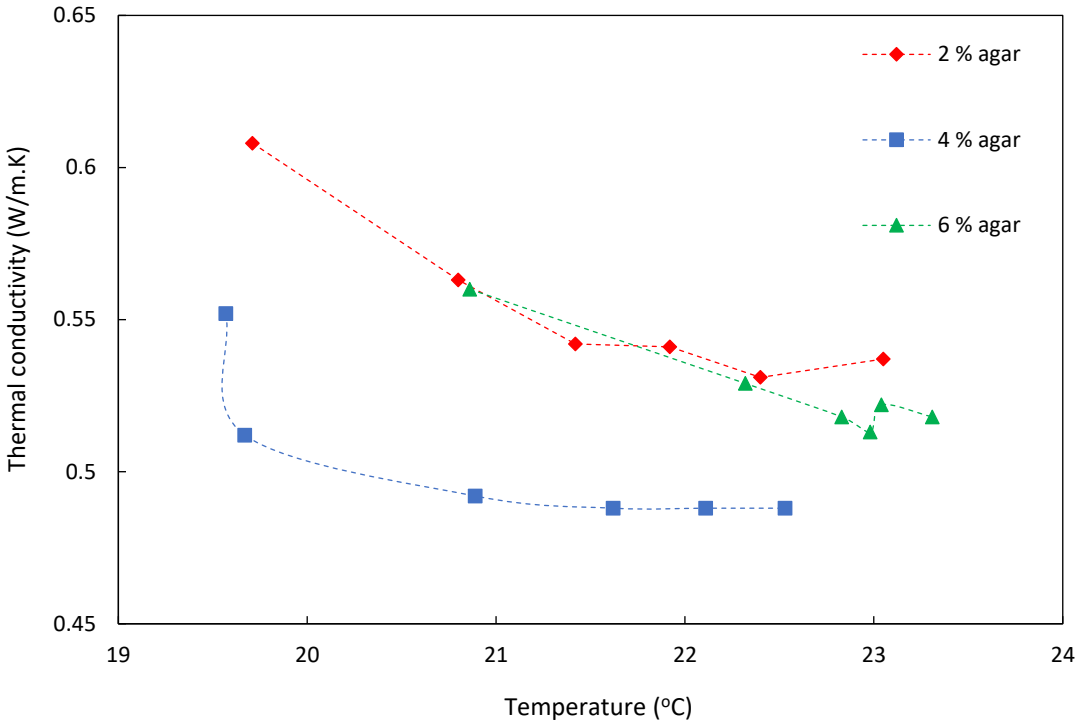

Figure 5.11.5: Thermal conductivity of phantoms with varying agar concentration versus temperature.

6 Estimation of the absorption coefficient of phantoms with varying agar/silica/evaporated milk concentration

6.1 Introduction

MRgFUS surgery is a therapeutic modality that treats patients non-invasively, by employing the thermal bioeffects of US with tissue. The therapeutic effects of US to heat tissue were first suggested in the early 1930s [243]. Between 1930 and 1940, ultrasonic surgery was first suggested after recognizing the potential of FUS in inducing ablative temperatures in tissues. The first FUS system prototype was presented and assessed in a series of animal studies in 1942 [244], whereas subsequent animal studies in the 1940s and 1950s [245] correlated for the first time the effect of sonication dosage to the size of ultrasonic lesion and to histology staining findings.

The investigation of ultrasonic properties such as attenuation and absorption is essential in understanding the physics and mechanisms that control the interaction of MRgFUS with biological tissues and in developing appropriate numerical models of acoustic propagation. Assessment of attenuation and velocity of the ultrasonic beam in tissue is necessary for characterizing acoustic propagation in imaging and therapy purposes, whereas the mechanism of acoustic absorption is important in therapeutic applications because it controls the amount of energy deposition in the form of heat. When short pulses are applied, acoustic absorption becomes the governing property contributing to tissue temperature rise, since the effect of perfusion and conduction is minimized [246]. By minimizing acoustic energy losses due to scattering and reflection, the absorption coefficient approaches the value of attenuation.

One of the most important challenges of MRgFUS is to evaluate heat generation, absorbed energy, and temperature distribution within any biological tissue. This is usually done a priori by performing numerical simulations that require thorough characterization of the aforementioned ultrasonic properties. Experimental methods for estimating the fundamental property of absorption coefficient have been proposed [247].

Initially, the research efforts for measuring absorption coefficient were mainly concentrated in the development of accurate and reliable temperature probes that estimate temperature changes in a liquid media [248]. By knowing the sound intensity of a transducer and the produced temperature change, the absorption coefficient could be determined. Initially, a thermocouple

with galvanometer system was used to measure absorption coefficient [247]. It was found that there are two main phases during the temperature rise immediately after the initiation of the acoustic pulse. During the first phase, the temperature rise is due to the action of viscous forces between the wire of the thermocouple and the medium, while the second phase (linear part) is due to the absorption of sound in the medium [247]. The temperature increase of the thermocouple is independent of the direction of propagation of the US waves, but it is a function of the angle between the direction of propagation of the sound and the thermocouple wire. The absorption coefficient is independent of the intensity of the incident wave and increases as temperature increases [248].

The investigation of the variation of absorption and attenuation coefficient with frequency were conducted to determine any spectral dependence [249]. Experiments were conducted in mice and concluded that the absorption coefficient increased with sonication frequency. An accurate absorption coefficient measurement can be achieved by using a sufficiently small thermocouple thus eliminating motion between the wire and the medium [250]. The ultrasonic beamwidth must be broad enough to completely eliminate conduction effects [247]. The dependence of focal beamwidth on frequency leads to absorption coefficient estimation errors as a result of increased heat diffusion [249].

In 1979, Goss *et al.* [251] identified the magnitude and frequency dependency of ultrasonic absorption coefficient in various biological tissues (brain, heart, kidney, liver, tendon, and testis) using the transient thermoelectric method (TTM). The radiation pressure technique is phase insensitive, frequency independent and much less susceptible to possible errors that arise from phase cancellation artifacts [252]. An automated system for near real-time measurement of absorption coefficient of silicone oil and fresh beef liver was introduced by Duback *et al.* in 1979 [253].

Attempts to investigate the difference between attenuation and absorption coefficients were determined using the TTM method and a new method was proposed by Parker *et al.* in 1983 [254] which was based in temperature decay following a short ultrasonic pulse. Furthermore, the measurement of absorption coefficient is a fundamental measure for hyperthermia treatments [255]. Heat conduction can contribute a significant error to the measurement of the ultrasonic absorption coefficient when using the TTM method [256]. The ultrasonic propagation velocity and absorption coefficient of benzonitrile-isooctane mixture were estimated using a pulse-echo method for various frequencies of range 5-21 MHz [257].

The absorption coefficient in tissue-mimicking polyethylene glycerol material was evaluated using an MRI calorimetry technique [258]. The whole experimental set-up was MR-compatible. Water was placed between a transducer and an agarose gel block and a castor oil was placed just after the agarose gel block. Intensity was measured using a hydrophone. High harmonics are generated by increasing the initial acoustic intensity and thus the thermal transfer effect is enhanced [259]. It was found that the ultrasonic focus moves toward the transducer compared with the geometric focus due to the diffraction of the sound wave. Recently, a parametrical acoustic phase conjugation system was used to eliminate errors for the accurate measurement of absorption coefficient due to the phase cancellation effect [260].

Herein, an improved experimental set-up was designed in order to measure absorption coefficient of small agar-based gel phantoms using the TTM. The whole experimental set-up was MR-compatible. The specific structure of the experimental set-up provides stability both to the transducer and phantom thus eliminating errors rising from motions of the phantom and thermocouple. Moreover, it gives accurate and fast measurement of the rate of temperature changes within the phantom. The transducer holder was coupled to the phantom holder, and then the focal position was accurately determined. Then, the thermocouple was inserted laterally, thus accurately measuring the temperature change. The US beam, focal spot and temperature rise were confirmed using MR thermometry and compared with the thermocouple measurements. An ultrasonic transducer with a broad beamwidth was used in order to eliminate conduction effect. A sufficiently small thermocouple was used to eliminate any possible motion between the transducer and phantom. The main purpose of this new experimental set-up was to minimize any possible error and determine as best as possible the true absorption coefficient of an agar-based gel phantom. Agar-based phantoms are becoming popular recently [261-264] because MRgFUS systems and protocols are easily evaluated using MRI monitoring.

As it is evidenced from the literature, although ultrasonic absorption is the primary tissue parameter that contributes to heat generation, not many research efforts were dedicated towards measuring absorption. This is primarily due to the complexity of the measurement techniques. As a result, the data for agar-based phantoms regarding absorption is limited. In this study [265], the target was to show that the absorption of this type of phantom can be accurately and repeatedly measured and controlled. Absorption measurements were performed extensively between 1950 and 1970 and since then almost no studies appear for the measurement of absorption.

6.2 Materials and methods

6.2.1 Mechanical design of the absorption experimental set-up and temperature measurement

The structure that holds the transducer and phantom was designed to fit in an acrylic water tank. The height of the acrylic water tank was 23 cm, its width was 15 cm and its length was 18 cm. Figure 6.2.1.1 shows the structure that was developed using an ABS 3D printer. The structure included a transducer holder which was placed at the bottom facing upwards (Figure 6.2.1.1.A). The upper part of the structure was coupled to a phantom holder (dimension: 6 cm x 6 cm x 8 cm). The produced phantom is shown in Figure 6.2.1.1.D. The phantom might be moved due to the pressure of the sonication, thus avoiding this motion which can lead to incorrect results, a special holder was added at the top of the structure in order to immobilize the phantom (Figure 6.2.1.1.B). A moveable part with a hole in the middle was inserted around the phantom holder to allow thermocouple insertion at a desired location (Figure 6.2.1.1.C). The fundamental purpose of this structure was to provide stable coupling between the transducer and the phantom. Additionally, the thermocouple can be placed exactly at the ultrasonic focus. The phantom structure was immersed in an acrylic tank (Figure 6.2.1.1.E) which is filled with de-ionized, degassed water. Figure 6.2.1.1.F shows the schematic of the complete experimental setup for the ultrasonic absorption measurement.

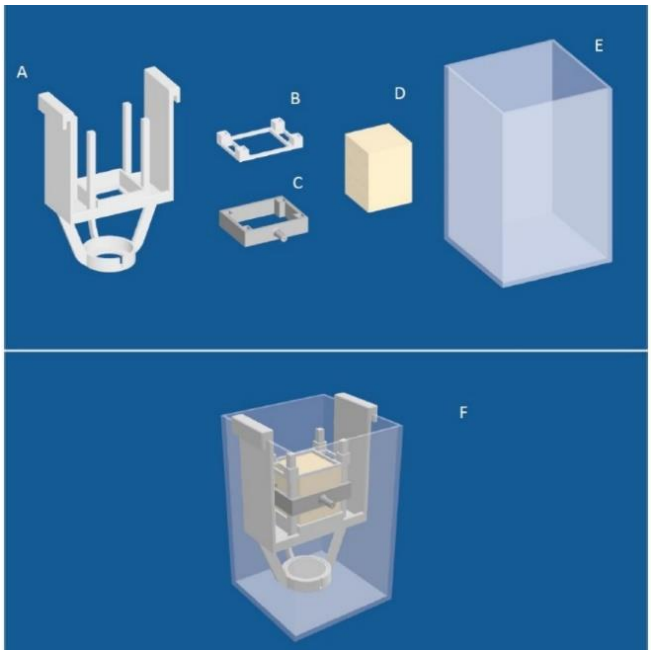

Figure 6.2.1.1: Schematic of the absorption measurement setup. (A) Transducer and sample holder, (B) Structure that secures the sample under test, (C) Phantom, which is produced using a suitable mold, (D) Sample holder, (E) Acrylic tank, (F) Schematic with all components interconnected.

A temperature reader (Omega Thermometer, HH806AU, Omega Engineering) was used. The temperature reader sends the data in a viewing software via a universal serial bus (USB) interface. A 100 μm thick thermocouple (5SC-TT-K-30-36, type K insulated beaded wire, Omega Engineering, Norwalk, Connecticut, USA) was used. A 100 μm optical fiber (10 m long) which is rigid enough was pushed from one end of the phantom, all the way to the other side with the phantom immersed in water. The thermocouple is thin (100 μm) and therefore its size is below the MRI resolution thus no apparent artifact were observed in any of the MRI images. Additionally, the thermocouple junction does not carry electricity and therefore is considered as a passive object in the imaging volume. The thermocouple was attached to the end of the fiber and therefore with this method, the thermocouple reached the other side of the phantom. Then the thermocouple was pulled 3 cm backwards, so that it reaches the focal point. The rate-of-heating was measured 0.5 seconds after the beginning of irradiation to minimize viscous heating and heat conduction errors below [249]. Temperature data was recorded every 0.5 s (this is the fastest provided by this particular reader). Because the thermocouple is so thin, no visible MRI artifacts were noted.

6.2.2 FUS system and sample

The FUS system was composed of a signal generator (HP 33120A, Agilent Technologies, Englewood, Co., USA), an RF amplifier (AR amplifier, research model 75A250M4, 75 watts, 10 kHz-250 MHz, Acoustic Research, Bothell, WA, USA) and a spherically focused transducer (Sonic Concepts, Inc., Seattle, USA). The transducer operates at 0.4 MHz, has focal length of 70 mm and diameter of 40 mm. The -3 dB beamwidth of this transducer was 3.5 mm. Figure 6.2.2.1 shows the schematic of the experimental setup. The FUS system is connected via a cable to the ultrasonic transducer.

A thermocouple was inserted in the sample in order to measure the rate of temperature increase due to the FUS sonication. The thermocouple was placed in the focal position which was 3.5 cm deep (the transducer was 3.5 cm below the phantom).

An agar-based phantom was used to estimate the absorption coefficient. The acoustic absorption can be varied by using different amounts of evaporated milk, which is rich in fats and proteins while scattering US weakly [233]. Scattering was compensated by adding to the mixture appropriate amounts of fine crystalline silica dioxide powder (Sigma Aldrich). The produced sample was isotropic and homogeneous. Another tool to control the absorption was

the agar concentration (M144, HiMedia Laboratories). Experiments in the agar-based phantom were carried out in order to measure the absorption coefficient. The phantom under evaluation was placed on the structure. The transducer was placed on the holder of the structure, which was immersed in the water container, thus providing good acoustical coupling between the phantom and transducer. The water container was filled with de-ionized, degassed water.

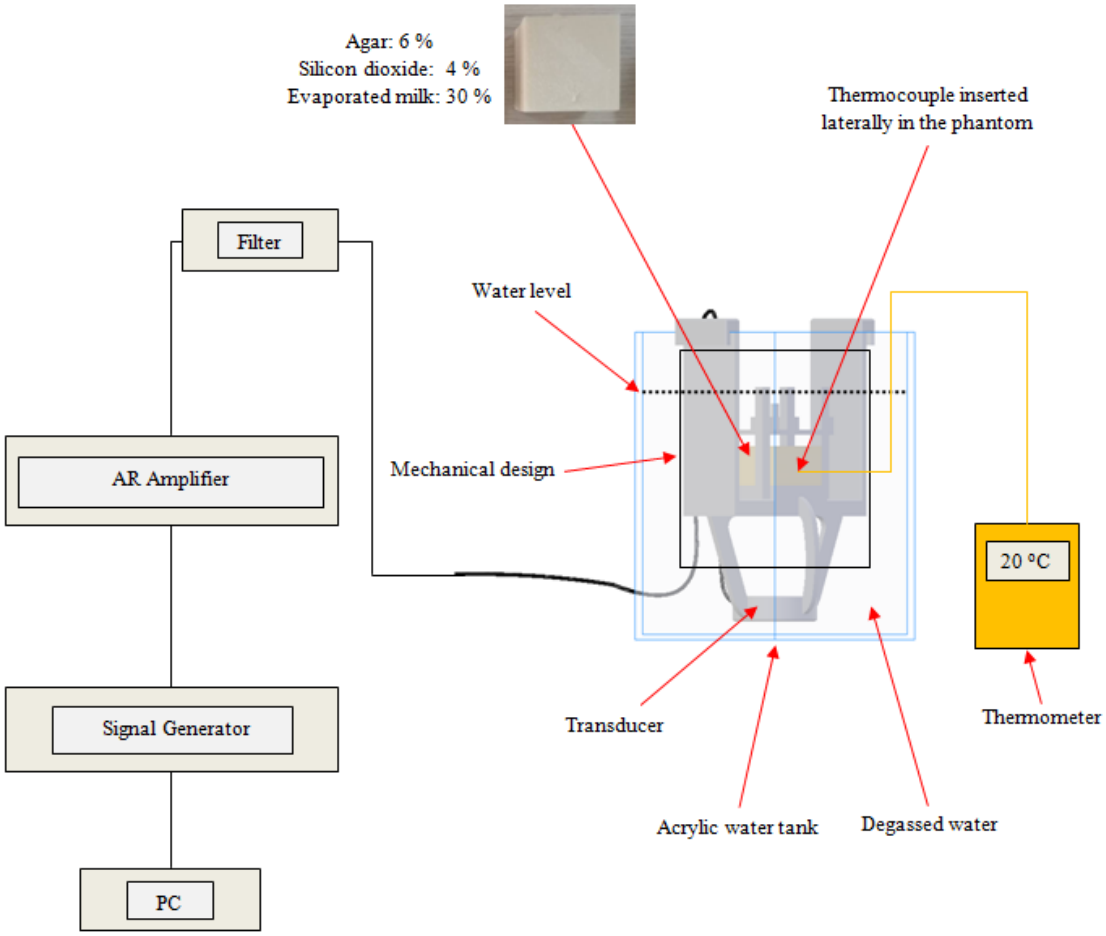

Figure 6.2.2.1: Schematic diagram of the experimental setup.

6.2.3 Absorption estimation and scattering

Inherent to the experimental setup, the so-called TTM [247] was applied to estimate the absorption coefficient of the phantom. It can be shown for any tissue in which no heat is lost by thermal conduction or flow, that the absorption coefficient α (in cm^{-1}) is given by:

$$\rho C_\rho \frac{\partial T}{\partial t} = 2\alpha I = 2\alpha I_o e^{-2\alpha x} \qquad (6.2.3)$$

where ρ is the density, C_ρ, is the heat capacity per unit mass and I_0 is the intensity at the transducer interface, and x is the focal depth. The intensity I at the site of the temperature observation is determined from the free field intensity by correcting for attenuation. The spatial average temporal average intensity was estimated by dividing the applied acoustical power with the beam area. The acoustical power was measured using a radiation force balance instrument (UPM-DT100N, Ohmic Instruments Co.). The acoustical impedance of a similar mixture of agar was found to be 1.64 MRayl [264]. Water has an acoustical impedance of 1.54 MRayl, therefore the reflected intensity in the water-agar interface is 0.01 %. The loss in intensity due to reflection and scattering was considered when estimating the *in-situ* intensity. It was assumed that the correlation between attenuation coefficient and frequency was linear in this agar/silica/milk phantom.

The value of density of the agar mixture was taken to be 1.07 g/cm^3 [264] and the specific heat (mostly dominated by water) to be 4.18 J/g.°C [264]. *dT/dt* is the measured rate of increase of temperature with time. The absorption was assumed to be linearly related to frequency for this type of phantom since this is mostly a water-based phantom. The validity of this assumption could be significant subject of research.

The phantom was exposed to FUS and the absorption coefficient was estimated by measuring *dT/dt* with a thermocouple. In the TTM the derivative of *dT/dt* was evaluated at short time so that the effect of heat conduction can be neglected. Since the conductivity of the agar-based phantom is low (Menikou and Damianou [264]), and the temperature elevation was low (1-3 ^{o}C), the linearity of temperature with time was attained for a long time. Therefore, for the accurate measurement of the slope, the rate of temperature increase was measured at the end of a 60 s pulse. The main source of uncertainty in the measurement of absorption is the placement of the thermocouple. Placement of the thermocouple away from the focus can result to underestimation of absorption. Thus, using a transducer with a wide focal beam reduces the errors due to thermocouple placement. Other small sources of errors are the power measurement and also the assumption that conduction effects are minimal. Scattering was measured using the method described in Menikou and Damianou [157]. The scattering value was needed since, it affects the intensity which is one of the main parameters used in estimating absorption in equation 6.2.3.

6.2.4 MR imaging and MR thermometry

The device was tested in a 1.5 T MR system (Signa Excite, General Electric) using a GPFLEX coil (USA Instruments). MR thermometry data was produced using T_1-weighted spoiled gradient (SPGR) with the following parameters: TR = 38.5 ms, TE = 20 ms, FOV = 21 cm, matrix = 128x128, flip angle = 20º, NEX = 1.

The temperature during the sonication was estimated using the proton resonance frequency shift equation which is described in great detail in Menikou and Damianou [261]. The equation relates the measured phase with the temperature elevation (ΔT). This relationship is given by:

$$\Delta T = \frac{\varphi(T) - \varphi(T_0)}{\gamma \alpha B_0 TE} \tag{6.2.4}$$

where $\varphi(T)$ and $\varphi(T_0)$ are the phases at a starting and final temperature T and T_0 respectively, γ is the gyromagnetic ratio, α is the proton resonant frequency shift coefficient, B_0 is the magnetic field strength and TE is the echo time. The SPGR pulse sequence was used to extract the MRI thermometry maps with a 2 s temporal resolution. All temperature estimations performed using MR thermometry were confirmed by thermocouple measurements. A software was written in MATLAB (Figure 6.2.4.1) to perform the MR thermometry measurements.

Figure 6.2.4.1: Screenshot of the MR thermometry software.

6.2.5 Simulation results for absorption estimation

According to the bioheat transfer equation, in order to estimate the absorption coefficient in a phantom or tissue, the calculation of the transducer beam area was required. The transducer beam area was estimated using a developed HIFU simulator (The MathWorks, Inc., Joshua Soneson, FDA). This specific simulator estimates various transducer features such as pressure, intensity and heating rate. After simulations for the particular transducer (acoustical power of 10 W was chosen as parameter), the graph of intensity of the transducer versus the radial distance was extracted as shown in Figure 6.2.5.1. With simple graphical analysis on the produced graph, the transducer beam area was calculated as follows: from Figure 6.2.5.1 which shows the radial intensity at focus for acoustical power of 10 W at 50 % of the maximum intensity, the radius of the transducer beam was estimated. The maximum intensity at the focus was 17.65 W/cm^2. The 50 % of the intensity was 8.825 W/cm^2. The distance r at 50 % of the maximum intensity was 0.3252 cm. Thus, the area of the transducer beam was calculated as $\pi.r^2 = \pi.(0.3252)^2 = 0.3322$ cm^2 = 33.22 mm^2.

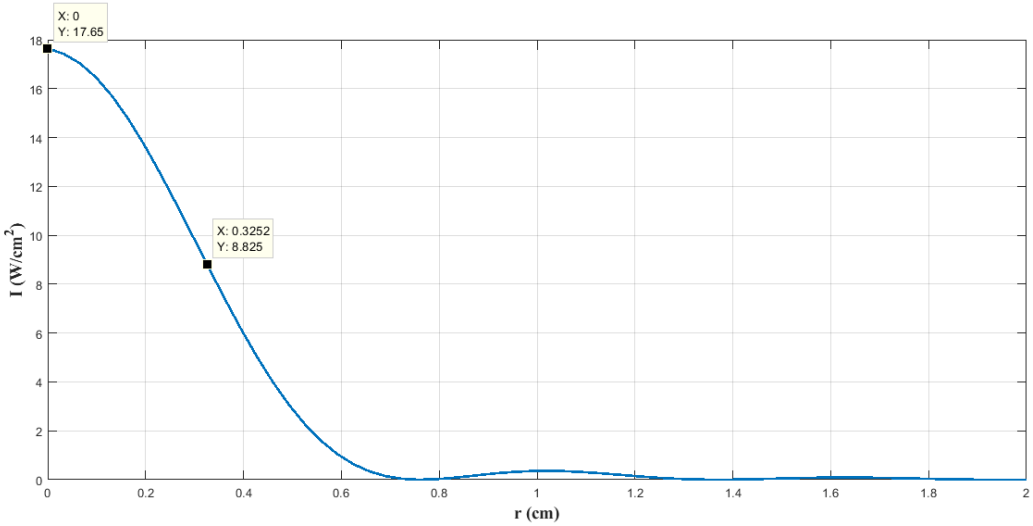

Figure 6.2.5.1: Graphical analysis to estimate the transducer beam area.

6.3 Experimental results

The first step in the experimental efforts was to apply an ultrasonic protocol that produces temperature between 2-3 ^{o}C. This was achieved by using low acoustical power (10 W). Then the thermocouple was inserted precisely at the focal beam. The thermocouple was placed perpendicularly to the beam propagation as shown in Figure 6.3.1.

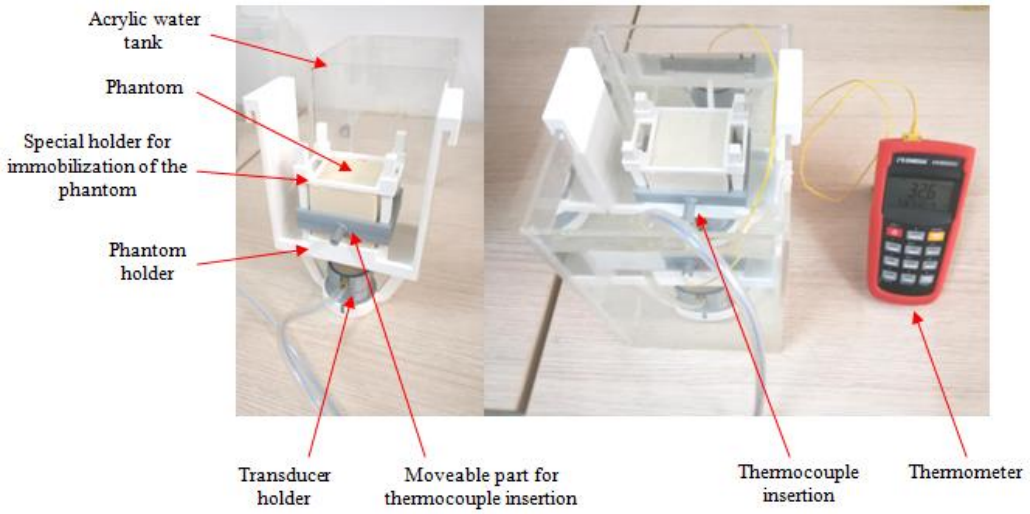

Figure 6.3.1: Experimental setup for measuring the absorption coefficient.

In experiments with the thermocouple being placed parallel to the propagation beam, the temperature elevation was sometimes 50 % lower compared to the perpendicular orientation. Figure 6.3.2 shows the temperature elevation versus time using an acoustical power of 10 W for 60 s. The sample used was a mixture of agar (6 %), silica (4 %), and evaporated milk (30 %). Note that temperature increases linearly with time indicating minimization of conduction. The temperature maintained its linearity for long pulse duration (60 s) because the agar-based phantoms have low conductivity [264]. The maximum temperature was 2.2 ^{o}C and the rate of temperature increase was 0.0366 ^{o}C/s. Based on this temperature the estimated absorption was 0.34 dB/cm-MHz.

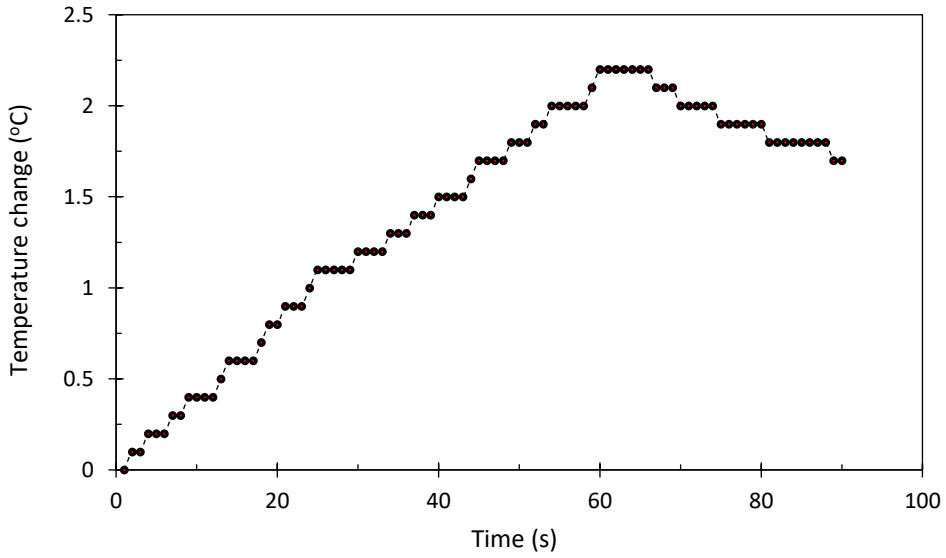

Figure 6.3.2: Temperature change versus time for phantom with 6 % agar, 4 % silicon dioxide, and 30 % evaporated milk concentration.

The same experiment was performed inside the MRI scanner in order to assess the temperature distribution using MR thermometry. Figure 6.3.3 shows a photograph of the experimental setup as placed on the MRI table.

Figure 6.3.3: Photograph of the experimental setup as placed on the bed of the MRI scanner.

Figure 6.3.4 shows an MRI image of the sample as placed in the water tank using SPGR. Note that the entire sample was immersed in water in order to reduce reflections from the sample/air interface which distorted the ultrasonic beam.

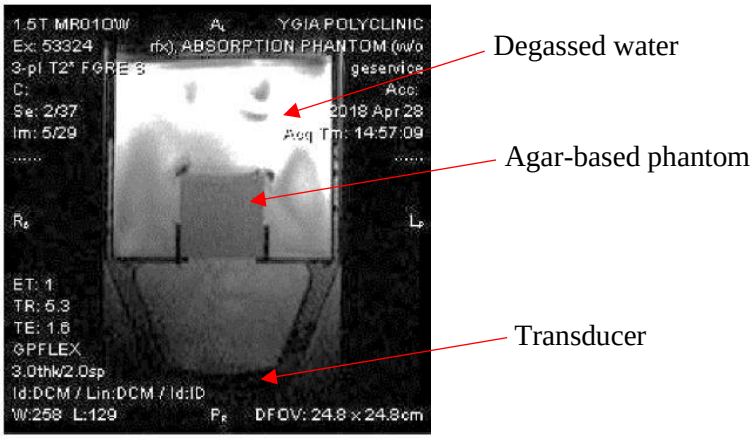

Figure 6.3.4: MRI image of the sample as placed in the water tank using FSE sequence.

Figure 6.3.5 shows the MR thermometry map of the ultrasonic beam on a plane perpendicular to the propagation (coronal plane) using acoustical power of 10 W for 60 s. The maximum temperature was 2.32 ^{o}C, and the rate of temperature increase was 0.0375 ^{o}C/s. The sample

used was an agar mixture of agar (6 %), silica (4 %), and evaporated milk (30 %) Based on this temperature the estimated absorption coefficient was 0.35 dB/cm-MHz.

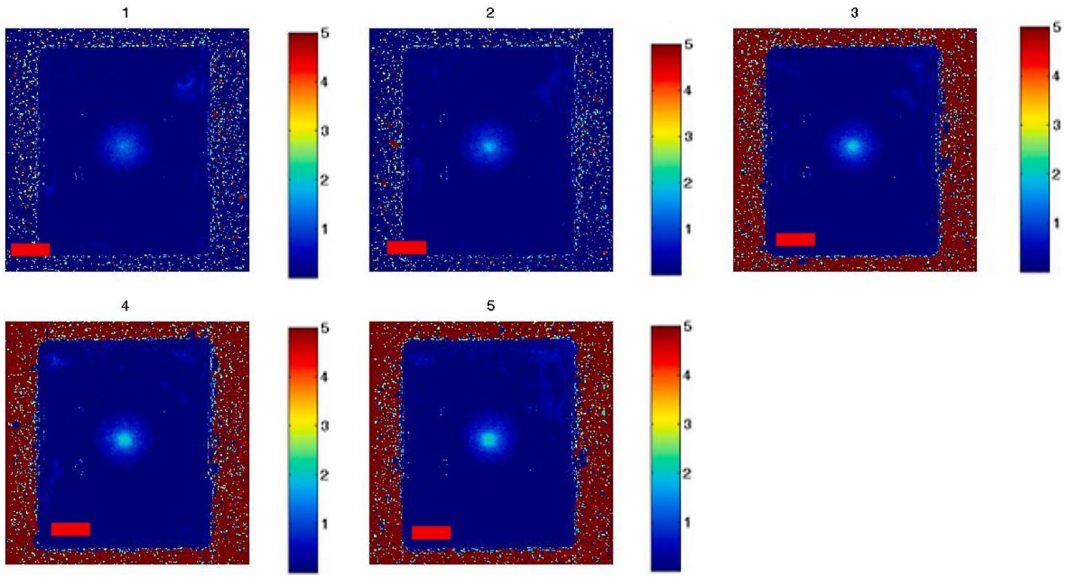

Figure 6.3.5: The MR thermometry map of the ultrasonic beam at a plane perpendicular to the propagation (coronal plane) using acoustical power of 10 W for 60 s. The sample used was a mixture of agar (6 %), silica (4 %), and evaporated milk (30 %). Bar = 10 mm.

Figure 6.3.6 shows the corresponding MR thermometry map beam on a sagittal plane using the same power and duration. The sample used was an agar mixture of agar (6 %), silica (4 %), and evaporated milk (30 %). The maximum temperature was 2.4 ^{o}C. Based on this temperature the estimated absorption was 0.36 dB/cm-MHz.

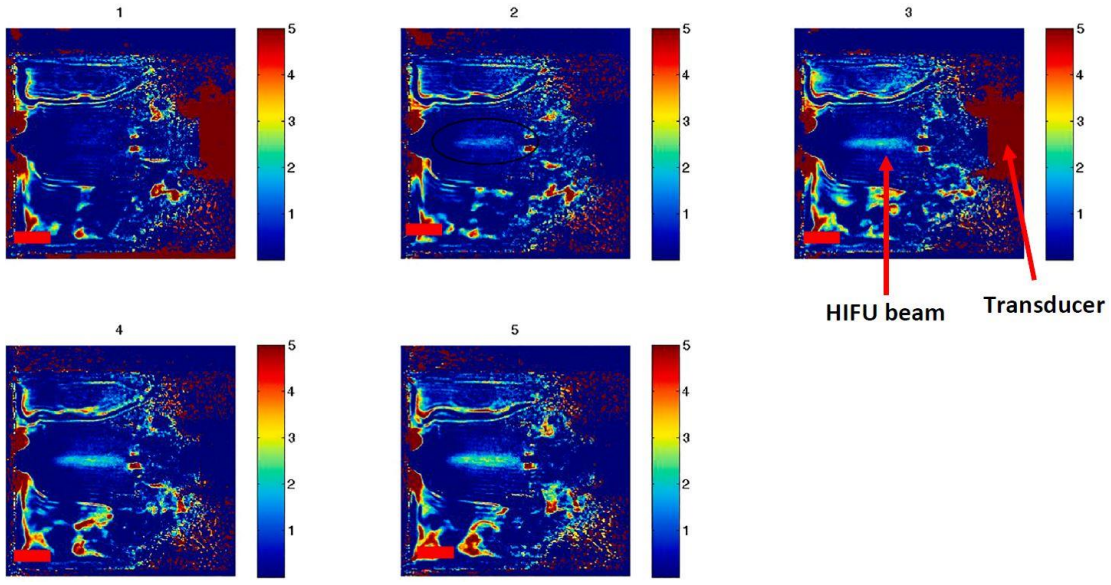

Figure 6.3.6: MR thermometry map beam at a sagittal plane using acoustical power of 10 W for 60 s. The sample used was a mixture of agar (6 %), silica (4 %), and evaporated milk (30 %). Bar = 20 mm.

Initially, ten identical phantoms were produced with the same amount of evaporated milk and silicon dioxide, but the amount of agarose varied in order to observe any change in absorption coefficient value. The mass density (ρ) and the specific heat capacity (C_ρ) were estimated in a previous work by Menikou *et al.* [264]. The mass density was 1.04 g/cm^3 and the specific heat capacity was 4.13 J/g.^{o}C. Using the formula of the TTM, the absorption coefficient was estimated. Table 6.3.1 summarizes the peak temperature change at sonication time of 60 s and the corresponding calculated absorption coefficient for phantom with 4 % silicon dioxide, 30 % evaporated milk and varying agar percentage of 4, 6, 8, 10, and 12 %.

Table 6.3.1: List of peak temperature changes and the estimated absorption coefficient for phantom with 4 % silicon dioxide, 30 % evaporated milk, and different amount of agar.

Agar (%)	Temperature change (^{o}C)	Absorption Coefficient (dB/cm-MHz)
4	2	0.22
6	2.2	0.34
8	2.9	0.40
10	3.1	0.43
12	1.9	0.21

Figure 6.3.7 presents the temperature change with respect to time as recorded using the thermocouple for the phantom with 4 % agar concentration (4 % silicon dioxide and 30 % evaporated milk).

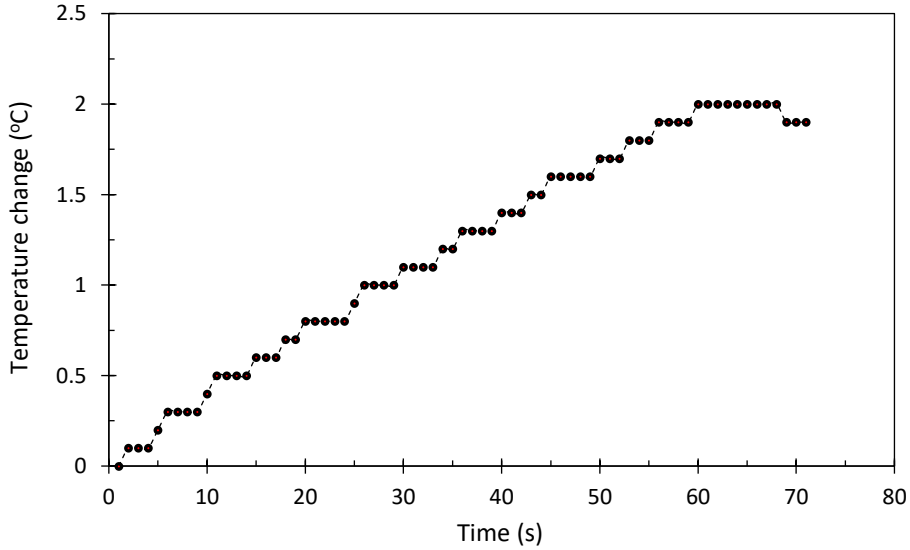

Figure 6.3.7: Temperature change versus time for phantom with 4 % agar, 4 % silicon dioxide, and 30 % evaporated milk concentration.

Figure 6.3.8 shows the absorption coefficient with respect to agar percentage for the phantoms with 4 % silicon dioxide and 30 % evaporated milk.

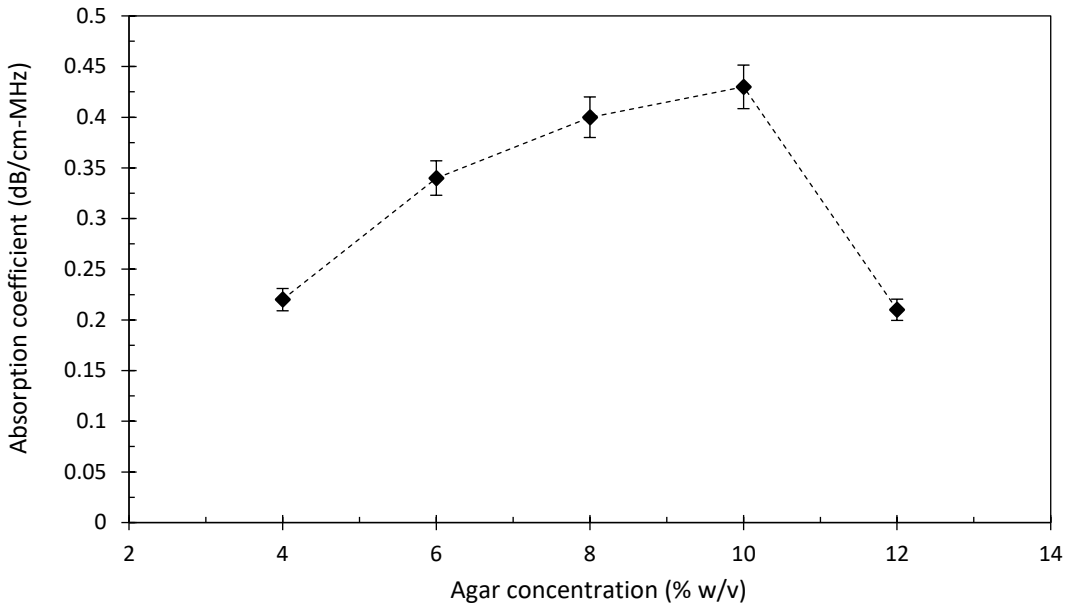

Figure 6.3.8: Absorption coefficient with respect to agar percentage for phantoms (n = 10) with 4 % silicon dioxide and 30 % evaporated milk. Error bars represent standard deviation.

In another recipe with no silicon dioxide and 30 % evaporated milk, the absorption coefficient was also measured. In this recipe, the effect of agar concentration on the absorption coefficient was investigated while the silicon dioxide effect was eliminated. Table 6.3.2 summarizes the temperature change per minute and the corresponding calculated absorption coefficient for a phantom with no silicon dioxide, 30 % evaporated milk and agar percentage of 4, 6, and 8 %.

Table 6.3.2: List of temperature changes and the corresponding absorption coefficient for phantom with no silicon dioxide, 30 % evaporated milk, and different amount of agar.

Agar (%)	Temperature change (°C)	Absorption Coefficient (dB/cm-MHz)
4	1.4	0.15
6	1.5	0.16
8	1.8	0.20

Figure 6.3.9 presents the temperature change with respect to time as recorded using the thermocouple for the phantom with 8 % agar concentration (no silicon dioxide and 30 % evaporated milk).

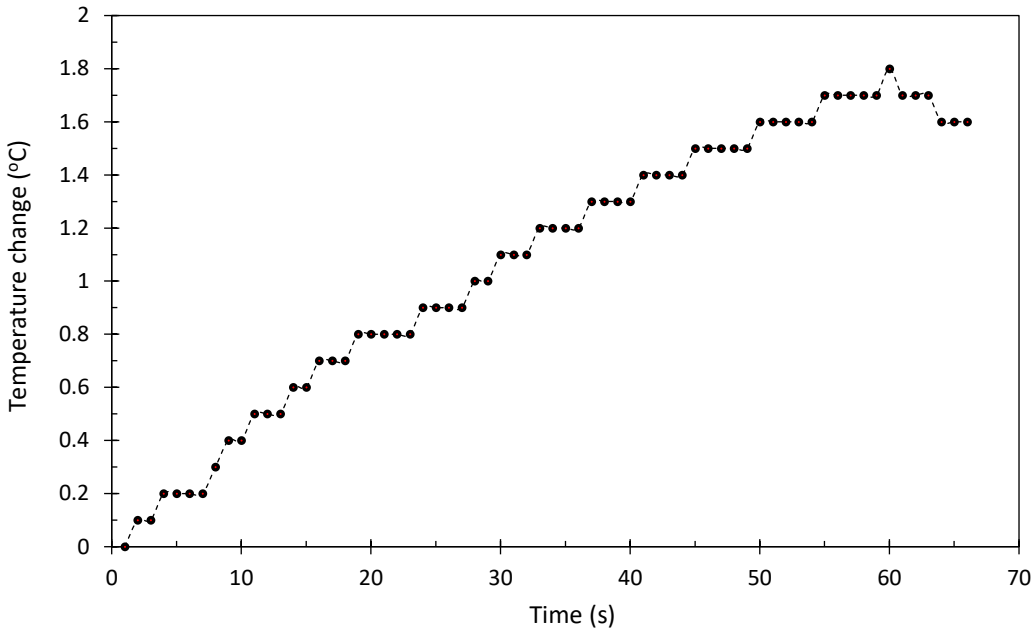

Figure 6.3.9: Temperature change versus time for phantom with 8 % agar, no silicon dioxide, and 30 % evaporated milk concentration.

Figure 6.3.10 shows the absorption coefficient with respect to agar percentage for the phantoms with no silicon dioxide and 30 % evaporated milk.

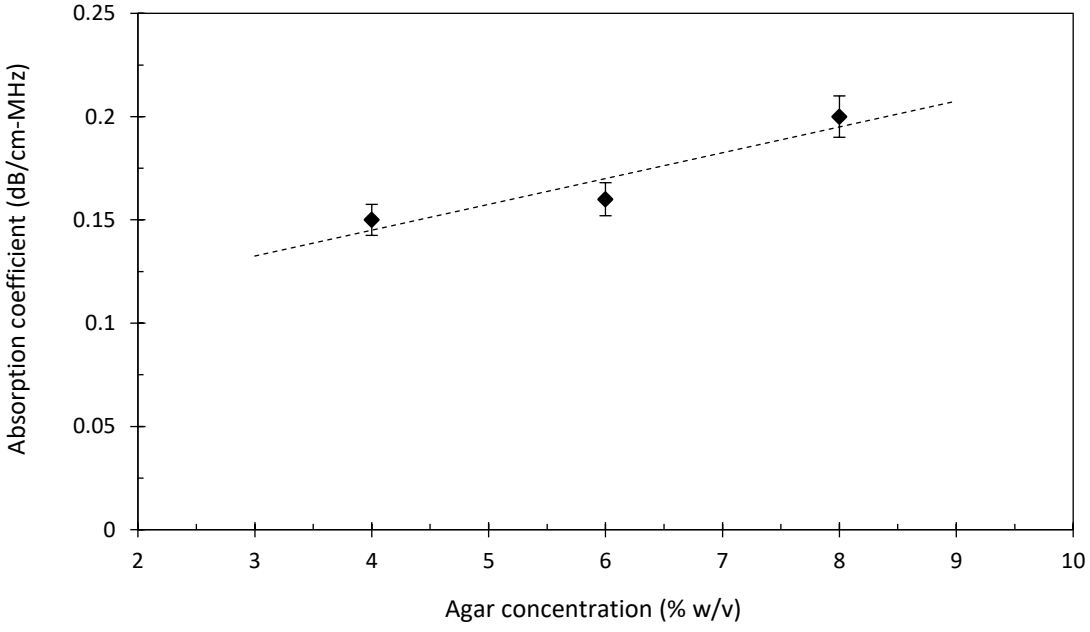

Figure 6.3.10: Absorption coefficient with respect to agar percentage for phantoms (n = 10) with no silicon dioxide and 30 % evaporated milk. Linear fitting was applied to the data. Error bars represent standard deviation.

Repeated measurements were recorded for phantom with 8 % agar, no silicon dioxide, and 30 % evaporated milk. Table 6.3.3 summarizes the temperature change per minute and the corresponding calculated absorption coefficient for the repeated measurements.

Table 6.3.3: List of temperature change and corresponding calculated absorption coefficient for repeated measurements for the phantom with 8 % agar, no silicon dioxide, and 30 % evaporated milk.

Repetition (n)	Temperature change (°C)	Absorption Coefficient (dB/cm-MHz)
1	1.8	0.20
2	1.6	0.174
3	1.3	0.14
4	1.4	0.15
5	1.2	0.13
6	1.2	0.13
7	1.2	0.13

Figure 6.3.11 shows the absorption coefficient for repeated measurements estimated for the phantom with 8 % agar, no silicon dioxide, and 30 % evaporated milk.

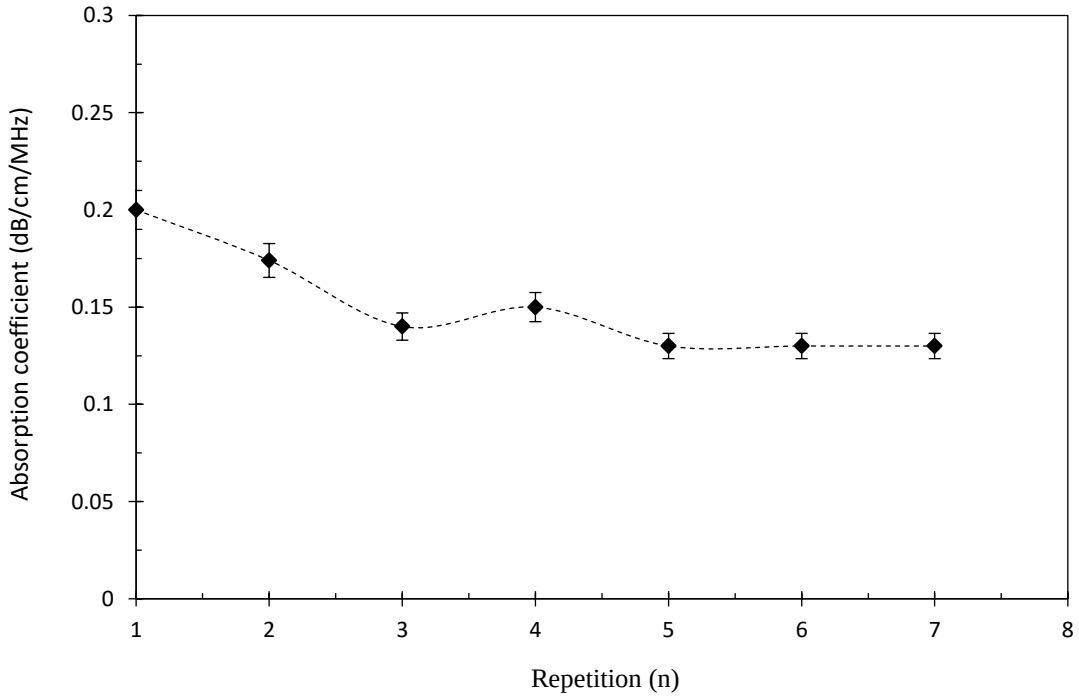

Figure 6.3.11: Absorption coefficient for repeated measurements for the phantom with 8 % agar, no silicon dioxide, and 30 % evaporated milk. Error bars represent standard deviation.

The change in the absorption coefficient relative to the change of evaporated milk concentration has also been investigated. This time, ten identical phantoms with the same amount of agar and silicon dioxide but different amounts of evaporated milk were produced. The absorption coefficient was estimated for phantoms with evaporated milk percentage of 0, 15, and 30 %. It has been observed that although absorption can be increased further with increased evaporated milk concentration, the sample loses its rigidity (it becomes too creamy). Table 6.3.4 summarizes the temperature change per minute and the calculated absorption coefficient for phantom with no silicon dioxide, 4 % agar and evaporated milk percentage of 0, 15, and 30 %.

Table 6.3.4: List of temperature change and the corresponding calculated absorption coefficient for the phantom with no silicon dioxide, 4 % agar, and different amount of evaporated milk.

Evaporated milk (%)	Temperature change (°C)	Absorption Coefficient (dB/cm-MHz)
0	0.6	0.06
15	1.1	0.12
30	1.4	0.15

Figure 6.3.12 shows the temperature change measured with respect to time for the phantom with no silicon dioxide, 4 % agar and 15 % evaporated milk concentration.

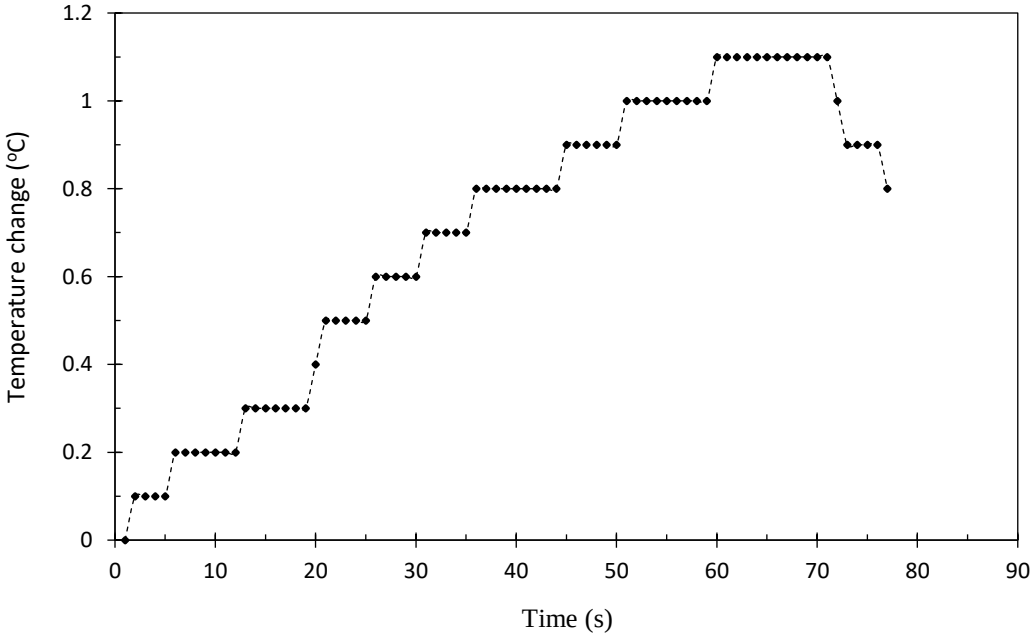

Figure 6.3.12: Temperature change versus time for the phantom with 4 % agar, no silicon dioxide, and 15 % evaporated milk concentration.

Figure 6.3.13 shows the absorption coefficient with respect to evaporated milk percentage for the phantoms with no silicon dioxide and 4 % agar.

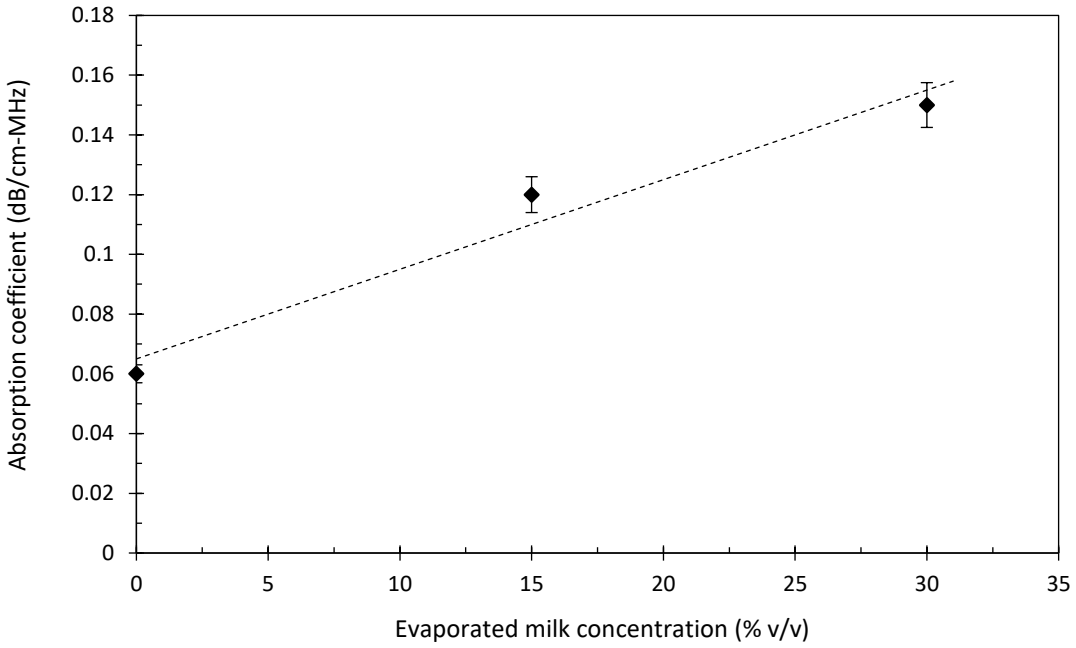

Figure 6.3.13: Absorption coefficient with respect to evaporated milk percentage for the phantom (n = 10) with no silicon dioxide and 4 % agar. Linear fitting was applied to the data. Error bars represent standard deviation.

Table 6.3.5 summarizes the temperature change per minute and the calculated absorption coefficient for phantom with no silicon dioxide, 6 % agar and evaporated milk percentage of 0, 15, and 30 %.

Table 6.3.5: List of temperature change and the corresponding calculated absorption coefficient for the phantom with no silicon dioxide, 6 % agar, and different amount of evaporated milk.

Evaporated milk (%)	Temperature change (°C)	Absorption Coefficient (dB/cm-MHz)
0	0.8	0.085
15	1.2	0.13
30	1.5	0.163

Figure 6.3.14 shows the temperature change with respect to time as recorded using the thermocouple for the phantom with no silicon dioxide, 6 % agar, and 30 % evaporated milk concentration.

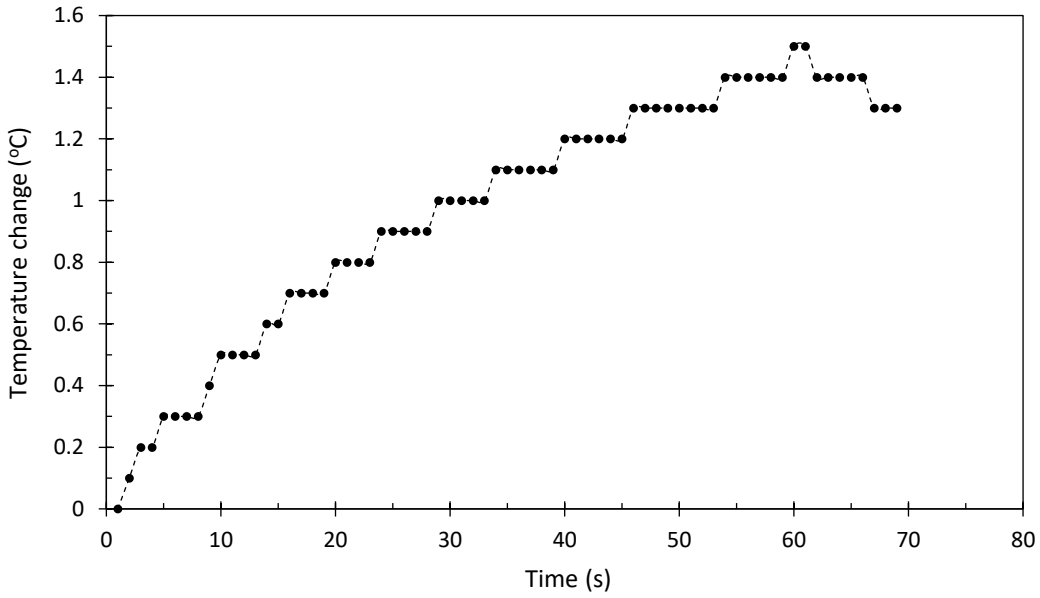

Figure 6.3.14: Temperature change versus time for the phantom with 6 % agar, no silicon dioxide, and 30 % evaporated milk concentration.

Figure 6.3.15 shows the absorption coefficient with respect to evaporated milk percentage for the phantoms with no silicon dioxide and 6 % agar.

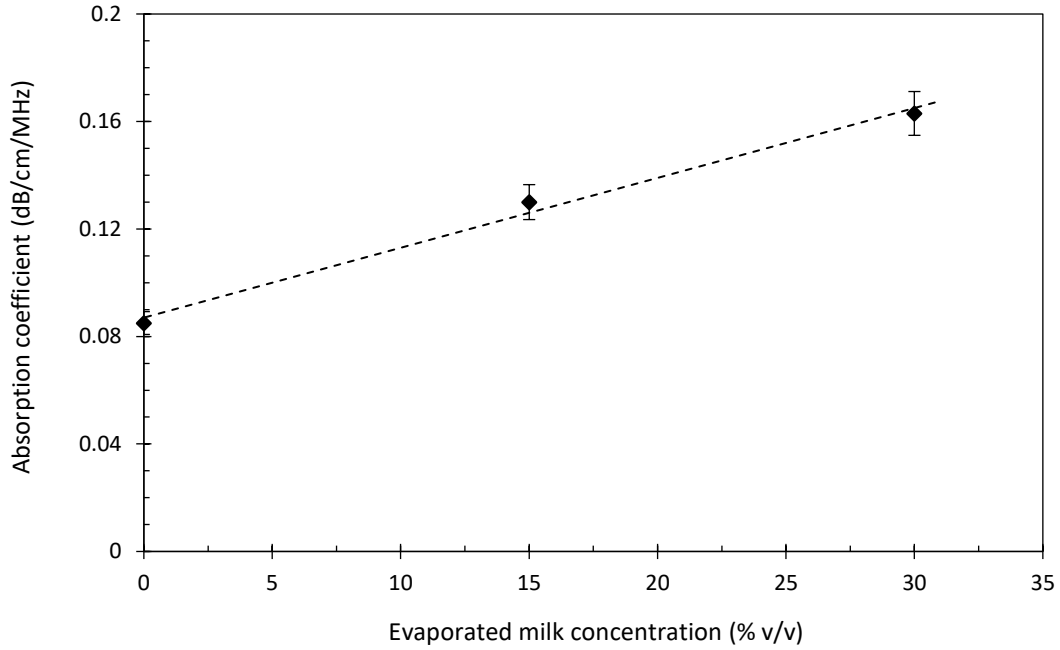

Figure 6.3.15: Absorption coefficient with respect to evaporated milk percentage for the phantoms (n = 10) with no silicon dioxide and 6 % agar. Linear fitting was applied to the data. Error bars represent standard deviation.

Experiments were also conducted in order to investigate the change in the value of the absorption coefficient relative to the change of silicon dioxide concentration. Phantoms (n = 10) with the same amount of agar and evaporated milk but different amount of silicon dioxide were produced. The absorption coefficient was estimated for phantoms with silicon dioxide percentage of 0, 2, 4, 6, and 8 %. Table 6.3.6 summarizes the temperature change per minute and the calculated absorption coefficient for phantoms with 6 % agar, 30 % evaporated milk and silicon dioxide percentage of 0, 2, 4, 6, and 8 %.

Table 6.3.6: Temperature changes and the corresponding calculated absorption coefficient for the phantom with 6 % agar, 30 % evaporated milk, and different amount of silicon dioxide.

Silicon dioxide (%)	Temperature change (°C)	Absorption Coefficient (dB/cm-MHz)
0	1.5	0.163
2	2	0.22
4	2.2	0.34
6	1.4	0.15
8	1.2	0.13

Figure 6.3.16 shows the temperature change with respect to time for the phantoms with 6 % agar, 30 % evaporated milk, and 2 % silicon dioxide concentration.

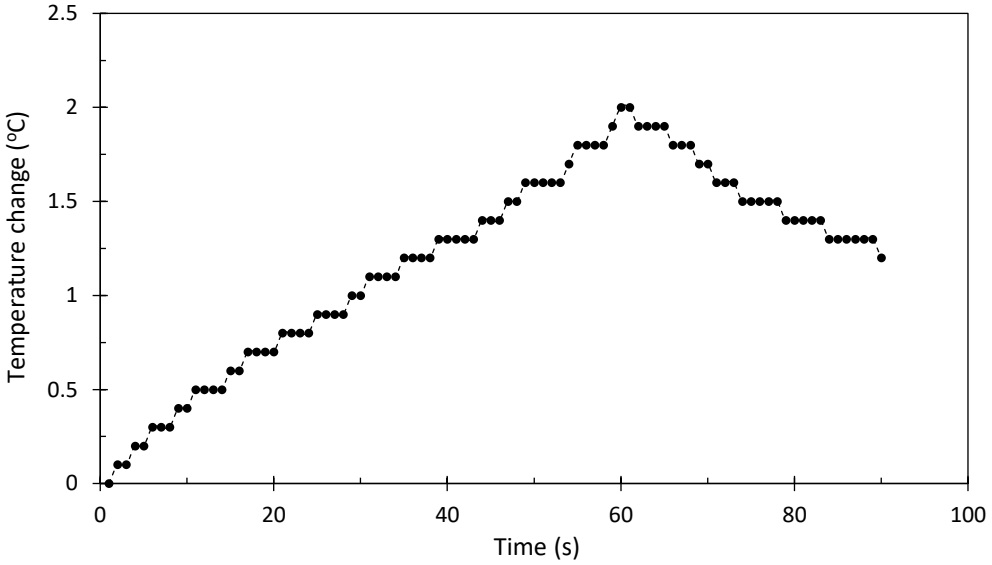

Figure 6.3.16: Temperature change versus time for the phantom with 6 % agar, 30 % evaporated milk, and 2 % silicon dioxide concentration.

Figure 6.3.17 shows the absorption coefficient with respect to silicon dioxide percentage for the phantoms with 30 % evaporated milk and 6 % agar.

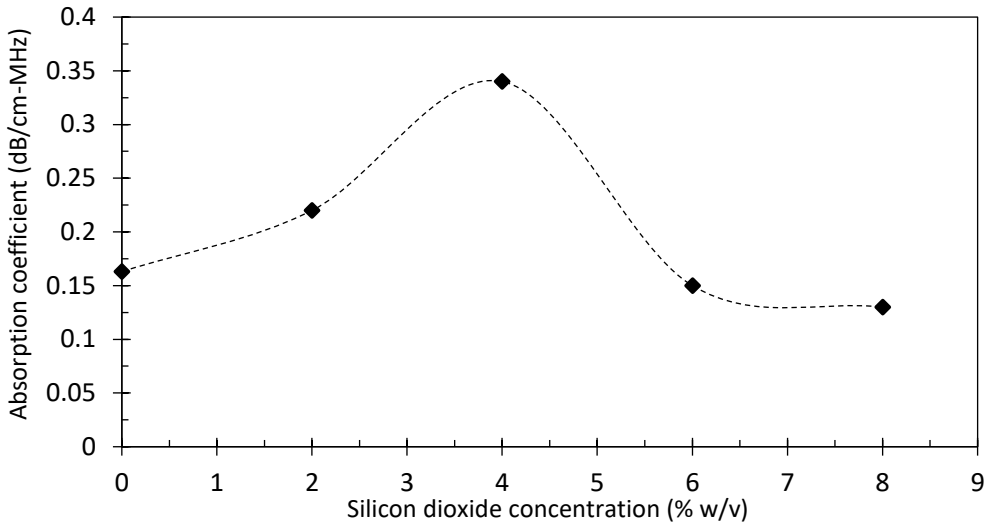

Figure 6.3.17: Absorption coefficient with respect to silicon dioxide percentage for the phantoms (n = 10) with 6 % agar and 30 % evaporated milk. Error bars represent standard deviation.

The absorption coefficient of phantoms (n = 10) with 6 % agar (Merck KGaA, EMD Millipore Corporation) and 4 % silicon dioxide (S5631, Sigma Aldrich) at different days was estimated. The focal depth was 2.5 cm in the phantom. It was observed that the absorption coefficient of the phantom decreases day by day. This decline may be due to the deterioration of the phantom and possible influence of its constituents. At acoustical power of 5 W (linear profile indicating no conduction effect) in the first day, the absorption coefficient was 0.16 dB/cm-MHz and in the seventh day it significantly dropped to 0.088 dB/cm-MHz. Figure 6.3.18 shows the absorption coefficient versus day estimated for the phantom with acoustical power of 5 W.

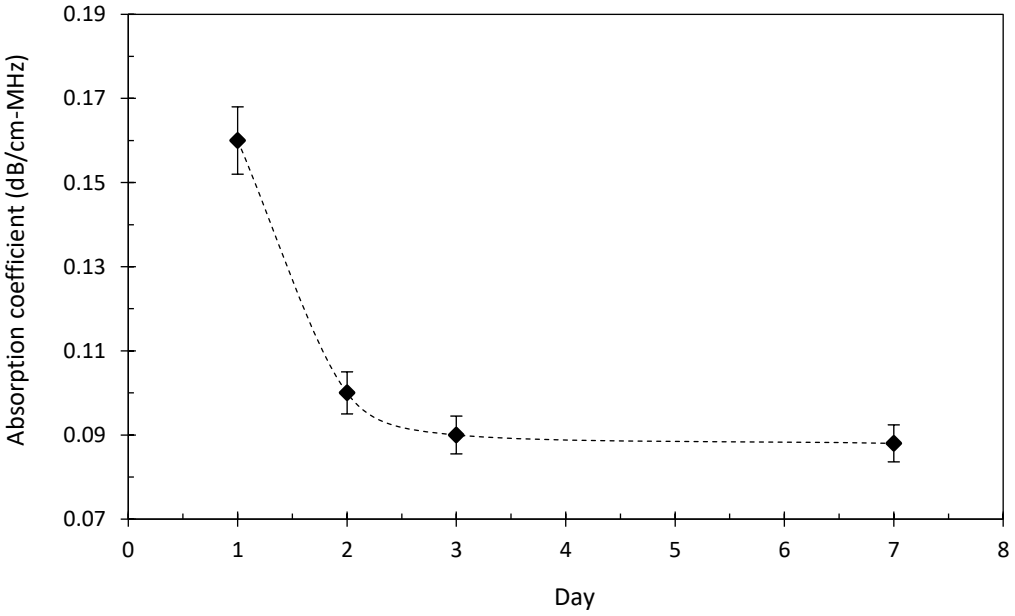

Figure 6.3.18: Absorption coefficient versus day for the phantom at acoustical power of 5 W. Error bars represent standard deviation.

6.4 Conclusions

An improved system for measuring ultrasonic absorption was presented. The sample used for measuring absorption was an agar-based mixture. The mixture included agar, silica and evaporated milk. The produced sample was rigid enough to fit in a holder made out of ABS plastic. The sample was secured by a plastic structure so that motion of the sample was avoided. A structure made out of ABS ensured that the beam was accurately identified so that a thermocouple was precisely placed on the beam. A wide beam transducer (f = 0.4 MHz) was used, so that the effect of conduction was minimized. The orientation of the thermocouple compared to beam played an important role. When the thermocouple was placed parallel to the beam, the measured temperature was lower compared to when it was placed perpendicular. The reason for this, is that with the parallel placement possibly increased reflection occurs and thus the temperature drops. However, this need to be investigated thoroughly in future absorption studies.

A temperature increase between 2 to 2.3 ^{o}C showed a linear increase of temperature with time indicating minimization of thermal conduction. This was achieved using low acoustic power (10 W). The temperature spatial distribution of the setup was estimated using MR thermometry. The MR thermometry was a useful tool for identifying the focal beam. The proper insertion point of the thermocouple was confirmed by MR thermometry. Both thermocouple measurement and MR thermometry revealed the same temperature for a specific ultrasonic protocol (2.2 ^{o}C and 2.3 to 2.4 ^{o}C respectively).

Recently agar-based phantoms are widely used [157,261-264] because they can be easily prepared and effectively mimic soft tissues. Although many thermal and ultrasonic properties [264,266] were measured for agar-based phantoms, data for the very important parameter of ultrasonic absorption is missing and therefore in this dissertation emphasis was given in the measurement of ultrasonic absorption.

As it was already mentioned earlier, not many data exist on the value of the ultrasonic absorption. In the article by Goss *et al.* [251] values of the absorption coefficient of soft tissues (brain, liver, kidney and heart) ranging from 0.024 to 0.028 cm^{-1} at 1 MHz were reported. Therefore, assuming an average absorption of 0.026 cm^{-1}, the desired absorption in dB/cm-MHz is 0.22. Depending on the agar, silica, and evaporated milk concentration the ultrasonic absorption coefficient can vary in the majority of cases below 0.01 cm^{-1}, but in some cases above 0.01 cm^{-1}. The ultrasonic absorption found with 30 % of evaporated milk, 4 % of silica,

and 4 % agar was found to be 0.22 dB/cm-MHz (0.012 cm^{-1}) which is close to the value found in humans [251].

The variation of absorption coefficient with percentage of evaporated milk, agar, and silica was also evaluated. It was found that the absorption of agar-based gels can be best controlled by varying the concentration of agar. The optimum concentration of evaporated milk was 30 % since although absorption can be increased further with increased milk concentration, the sample loses its rigidity (it becomes creamy). Although, silica seems to increase the absorption, its concentration should be limited to 4 % because above this level scattering increases attenuation and thus lowers absorption. Using the optimum recipe for the agar-based phantom (4 % agar, 30 % evaporated milk, and 4 % silica) the absorption coefficient was found to be 0.22 ± 0.02 dB/cm-MHz. Therefore, with a 6.5 % uncertainty, it is believed that the absorption value reported for the optimum recipe of this agar-based phantom is trustworthy.

The absorption coefficient of a phantom of a specific recipe (6 % agar and 4 % silicon dioxide) was measured repeatedly within seven days. The purpose was to investigate any possible change in the absorption coefficient and whether it may change over time. It was concluded that the absorption coefficient of the phantom is significantly lessened the first 1-3 days and then remain stable over time. Therefore, the absorption coefficient of agar-based phantoms needs to be measured within 24 hours.

7. Characterization of a soft tissue-mimicking agar/wood powder material for MRgFUS applications

7.1 Introduction

The need for developing novel diagnostic and therapeutic applications that demonstrate improved safety, efficiency, and specificity towards the battle against serious diseases is a matter of ongoing research. Although phantoms were initially developed, characterized, and calibrated for US imaging applications in the 60s, there is still an undeniable need for developing new phantoms to fill the gap of emerging medical applications. Throughout the years, several efforts have been made by researchers towards developing anthropomorphic phantoms for medical teaching and imaging applications. In the field of HIFU, a reusable TMM that possesses thermal, mechanical, MR, and acoustic properties close to that of soft tissue is of outermost importance.

There are limited commercial phantom options available such as those by ONDA (Onda Corporation) which are useful for MRgFUS systems. Ideally, TMMs should have approximately the same ranges of the speed of sound, attenuation, absorption, and scattering coefficients as soft tissue. These features should be controllable using appropriate additives and the variability of their properties should be small at standard operating conditions.

Different types of phantoms can be found in the literature for reproducing soft tissue using different TMMs. These types of phantoms can be uniform single-component phantoms or more complex ones that mimic the specific anatomy of human tissue [267]. TMMs for MRgFUS applications present different advantages and disadvantages concerning preparation complexity, cost, and acoustic properties.

Gelatin has been widely used as a material to mimic soft tissue for US and MR imaging [268]. Gelatin-based TMMs demonstrate thermal repeatability for low acoustic power, exhibit a nearly linear stress-strain curve, provide a wide range of stiffness that is easily controllable whereas its preparation procedure is simple [269]. However, gelatin-based materials continue to stiffen over time and have a low melting point (45 ^{o}C) making them unsuitable for applications such as HIFU [262]. The attenuation coefficient of gelatin-based TMMs can be controlled by varying the amount of gelatin [270]. Amongst their reported disadvantages is that they are not always homogeneous and are susceptible to microbial and bacterial invasion [271].

Another TMM that is useful for testing MRgFUS applications is polyacrylamide. Polyacrylamide gels can be transparent thus allowing visual observation of the coagulated zone by adding some heat-sensitive contents such as bovine serum albumin (BSA) and egg-white [272-274]. The acoustic attenuation can be adjusted by using materials such as evaporated milk, intralipid, and corn syrup [275]. However, the addition of high concentration of these materials might affect the transparency of polyacrylamide gels. The coagulation temperature of these gels is comparatively higher than that of biological tissues leading to an inaccurate simulation of tissue coagulation during thermal therapies [272]. A serious safety disadvantage of polyacrylamide-based gels is that their main constituent acrylamide monomer is a known neurotoxin which is classified as a carcinogen [274]. This type of gels also exhibits a limited shelf life from several hours when exposed to air to a few weeks when stored in an airtight container [276]. ONDA Corporation produces commercially available polyacrylamide-based phantoms for characterizing ultrasonic protocols. The position and lesion shape evolution in the gel can be observed since it permanently turns opaque when temperature surpasses a threshold of 70 ^{o}C [277]. Therefore, these phantoms are used to perform quality assurance tests on HIFU systems and treatment protocol evaluation. Although polyacrylamide TMMs have a low attenuation coefficient, the addition of glass beads can be used to increase their attenuation coefficient and match the corresponding value of the human liver [273].

N-isopropylacrylamide (NIPAM) gels exhibit higher transparency at room temperature than egg white doped TMMs [278]. A large opacity change can be achieved even with a small temperature change. The formation of thermal lesion is a reversible effect making this type of TMM reusable and ideal to model the therapeutic effects of HIFU. Sun *et al.* [278] investigated only the ability of the NIPAM-based gel to form thermal lesions while it has not been characterized for its acoustical, thermal, and MR properties.

In a recent study by Eranki *et al.* [279], an MR-imageable and HIFU-compatible tissue-mimicking thermochromic acrylamide-based material was presented. Silicon dioxide and BSA were added to enhance ultrasound attenuation and MRI signal changes since the coagulation of BSA causes changes in T_2 relaxation time. A thermochromic ink that changes color based on temperature change after HIFU exposure was also used. The TMM can permanently change color upon heating, thus providing information on ablation volume geometry, spatial targeting accuracy, and quantification of heating. The thermochromic acrylamide-based material is potentially useful for testing MRgFUS applications but its use is hindered by the rather complex and long fabrication procedure.

PVA materials have been also used in MR applications [234] and to mimic breast tissue [280]. PVA is a widely used non-toxic industrial material. The main disadvantage of these materials (in form of pure gel for 1-2 freeze-thaw cycles) is their low acoustic attenuation coefficient which is far lower than the majority of human soft tissue's attenuation coefficient [234]. However, with the addition of additives (enamel paint) and the increase in the number of freeze-thaw cycles, the attenuation can be further increased. The attenuation of a pure PVA-gel with 1 freeze-thaw cycle is stated to be very low at 0.075 dB/cm-MHz and increases to 0.28 dB/cm-MHz when the gel is produced with 4 freeze-thaw cycles [234]. The procedure to manufacture a pure PVA-based TMM is very long and can last for many days depending on the number of freeze-thaw cycles.

Tofu is another material used to develop TMM phantoms. Although Tofu is cheap and it is readily available, it exhibits a lower nonlinearity parameter compared to soft tissue [281]. The acoustic properties of Tofu are not adjustable and vary according to the brand of raw material and extraction method. It has also been reported that Tofu-based TMMs are susceptible to microbial invasion and their shelf life is limited [281]. However, Tofu's absorption and speed characterization replicate adequately the corresponding of human soft tissue.

Agar is also used for the development of phantoms destined for ultrasound imaging and HIFU applications. Agar-based TMMs need to be refrigerated for extending their shelf life and reusability [282]. Agar possesses a higher melting point and superior fracture toughness compared to gelatin gels of similar density and during ultrasound imaging, its echogenicity is similar to human soft tissue [282]. Amongst the advantages of agar against other TMMs is their faster production procedure, and low acoustic scattering coefficient [233,282]. A main limitation of agar is that it tends to be more expensive than gelatin. Agar-based TMMs doped with homogenized whole milk and bovine milk have an attenuation coefficient in the range of 0.35-0.4 dB/cm-MHz while the addition of evaporated milk increases the value to 0.8 dB/cm-MHz [233]. The speed of sound of pure agar-based gel (with 2 % w/v agar) was estimated at 1490 m/s. According to this study [233], more agar percentage results in a higher speed of sound (1512 m/s for 7.5 % w/v agar). An agar-based breast-mimicking material with the addition of silicon dioxide and evaporated milk was proposed for evaluation of FUS systems on patients with breast cancer [266]. Lately, Menikou *et al.* [157] introduced an agar-based head phantom with an attenuation coefficient close to the corresponding human attenuation value for HIFU applications.

There is limited literature on the effects of thermal, acoustic, mechanical, and MR properties of wood powder. The propagation speed and attenuation coefficient of various kinds of wood have been previously measured [283-285]. It has been shown that absorption linearly increases with frequency up to 4 MHz while the propagation speed is dependent on the moisture content of wood [286]. The density of wood powder and water absorption of wood powder composited with bagasse was calculated and compared to other materials [287]. The density of wood powder was found to be 0.42 gr/cm^3 and the water absorption in composite wood powder and bagasse was found to be 13.5 % [287]. In a study by Ababneh [288], it was found that wood blocks (Rhizophora spp) are low-cost, stable over time and possible human breast tissue replicating material for MRI purposes. T_1 and T_2 relaxation times of wood were found to match closely the ones of breast tissue.

The purpose of this part of the dissertation aimed to describe the development of a novel agar-based TMM doped with wood powder and test its suitability as such by characterizing its acoustic, thermal, and MR properties. The idea of using wood powder is to increase the absorption coefficient in a controllable manner with thermal properties similar to soft tissue. The associated T_1 and T_2 relaxation times control the image contrast of the material in conventional MRI sequences. Wood powder is a very attractive additive since it is an abundant industrial furniture waste and most likely free of cost unlike other materials (silicon dioxide, BSA) which are more expensive and require difficult and long production procedures by the manufacturers.

Following test and trial, an appropriate agar concentration was selected to provide moderate strength to the final material in order to resist HIFU forces without cracking. The percentage of agar (2 % w/v) was sufficient to create a compact material. It was chosen to avoid adding preservatives to the recipe to prolong the material's shelf-life since many of them are known of being toxic [289].

7.2 Materials and methods

7.2.1 Soft tissue-mimicking material preparation

The agar was in granular form with a particle size of 1400 μm stated in the manufacturer's datasheet (Merck KGaA, EMD Millipore Corporation). The agar was initially ground to powder using a blender machine to aid mixing in water and result in a homogeneous gel.

Ultrapure degassed/deionized water was slowly heated and continuously stirred using a magnetic stirrer (SBS, A160, Steinberg Systems, Germany) over a period of 10 minutes. The temperature increase was monitored using an electronic thermometer (Omega Thermometer, HH806AU, Omega Engineering). Once the degassed/deionized water reached 50 ^{o}C, 2 % w/v agar was slowly added to mitigate aggregation of the agar in the degassed/deionized water. A certain amount of agar was added to the mixture to achieve a 2 % w/v agar concentration. The wood powder (Swedish pine) was further ground with an average particle size of approximately 150 μm. The average particle size was estimated by quantitative analyzing images collected on a SEM image (FEI, Quanta 200, Hillsboro, Oregon, United States) as shown in Figure 7.2.1.1, using the open-source software Gwyddion [290]. Prior to the SEM investigation, all samples were sputter-coated with a thin (<10 nm) silver layer to reduce electron charging effects. Images were collected at 5 kV to 20 kV accelerating voltages in various magnifications.

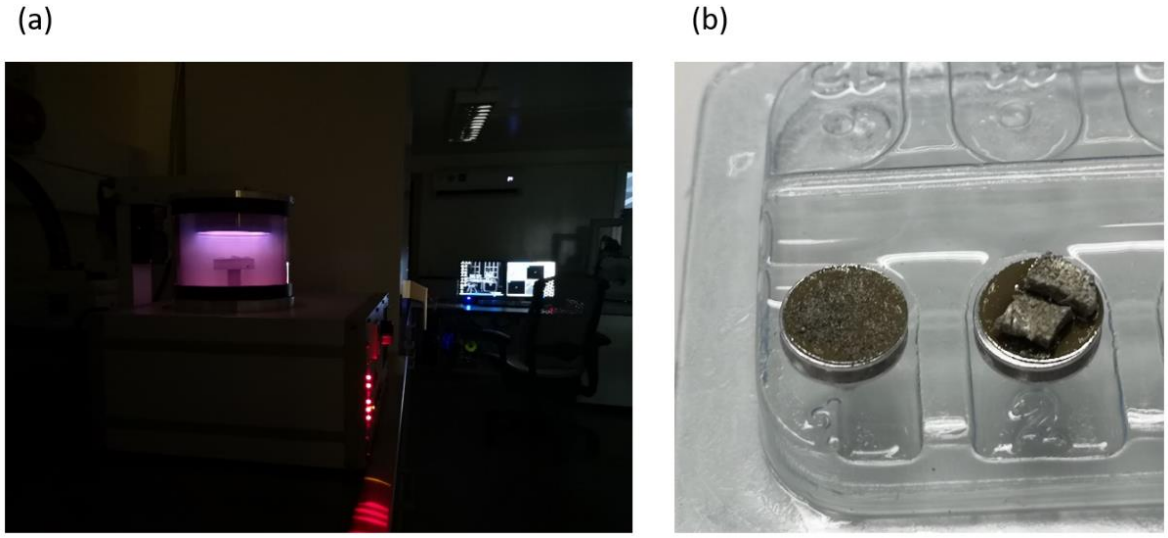

Figure 7.2.1.1: a) The SEM device, and b) the samples (wood powder-left and TMM-right) as positioned on the SEM device.

When agar was completely dissolved in water, a proportionate amount of wood powder (Swedish pine) was added to the mixture so that the w/v concentration of wood powder to be 4 %. The mixture was stirred until the temperature reached 85 ^{o}C. The mixture began to solidify once the temperature dropped (at around 50 ^{o}C). The amount of evaporated water was added to equate the initial mixture volume prior to boiling. The solution was stirred with a low-speed setting to avoid trapping air bubbles in the mixture that would cause serious reflections of the HIFU beam. The whole preparation and development procedure was simple, fast, and lasted around 20-25 minutes for a volume of 300 cm^{3}. The solution was then poured into a mold (6 x

6 x 8 cm^3) and was let to jellify overnight at room temperature. The prepared phantom was tested in ablation experiments within 24 hours after its fabrication.

The wood powder obtained from a carpentry company contained large pieces of particles that may have affected the acoustic properties of the developed TMM and induced susceptibility artifacts in MRI images. It was expected that since wood powder is poor in hydrogen it would appear hypointense in MRI images. The agar/wood powder TMM presented a moderate hardness along with a light brown color as shown in Figure 7.2.1.2.

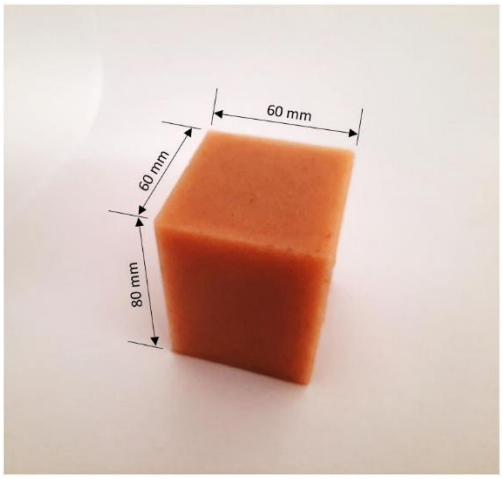

Figure 7.2.1.2: Photo of the developed agar/wood powder-based TMM. The dimensions (as indicated above) have been determined based on the experimental setup that was used to characterize the TMM.

7.2.2 Estimation of the attenuation coefficient

Attenuation measurements were conducted using the through-transmission technique previously described by Madsen *et al.* [291]. The through-transmission technique involved two planar transducers; one for transmitting pulsed US signal and one for receiving it. A special ABS plastic holder that hosts the two transducers, was designed (Inventor Professional 2018, Autodesk, California, USA) and printed using a 3D printer (F270, Stratasys Ltd., Minessota, USA). The ABS holder retained the planar transducers in cylindrical cavities with their active elements facing each other and the sample at fixed positions. Three pairs planar immersion transducers (12 mm diameter, nominal frequency at 1.1, 2 and 3 MHz, Piezotechnologies, Indianapolis, IN, USA) were used. All pairs of transducers have an approximate ± 0.5 MHz bandwidth, thus covering a 1-3 MHz span of frequencies. A pulsed signal was transmitted using a pulser/receiver system (Panametrics 500PR, Olympus Corp.), propagated through a 26 mm sample and received by the receiving transducer which was located 65 mm from the transmitter. The attenuated resulting signal was recorded by the receiver and displayed on a

digital oscilloscope (TDS 2012, Tektronix, Inc.). The sample was positioned in the near field of the emitting transducer. Figure 7.2.2.1 illustrates the experimental setup for the attenuation coefficient measurements.

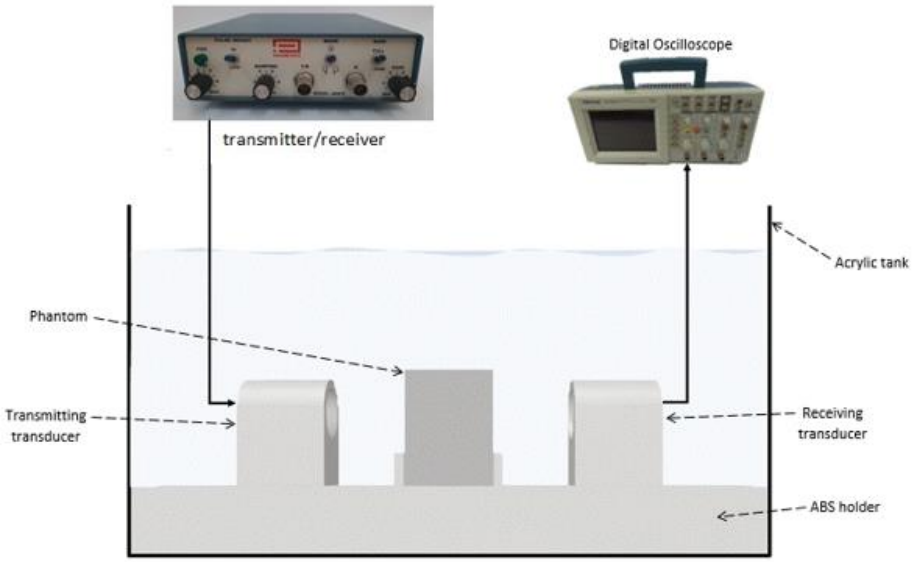

Figure 7.2.2.1: Experimental setup that was used to estimate the attenuation coefficient of the TMM.

The attenuation coefficient was measured over a frequency range of 1.1-3 MHz at room temperature (25 ^{o}C) for five batches of gels. The following equation was used to calculate the attenuation coefficient for each frequency using the through-transmission method and it was modified into equation 1 in units of dB/cm [292].

$$\alpha(f) = \left(\frac{20*\log_{10}\left(\frac{A_S(f)}{A_T(f)}\right)}{\Delta_\chi}\right) + \alpha_w \qquad (8.2.2)$$

where A_s is the reference peak-to-peak voltage without the material, A_r is the resulting peak-to-peak voltage at the receiver side with the addition of the material between the two planar transducers, α_w is the attenuation of water, Δ_χ is the sample's thickness in cm, and f is the transmitting frequency. The attenuation coefficient can be frequency-dependent according to $\alpha = \alpha_o * f^n$, where α is the attenuation coefficient parameter, α_o is the attenuation coefficient at 1 MHz, and n is the power to which frequency is raised in MHz. The impact of temperature on the attenuation coefficient was examined in a temperature range from 25 to 55 ^{o}C for the tested frequency of 1.1 MHz.

7.2.3 Estimation of the absorption coefficient

A method to estimate fast and accurately the absorption coefficient of the material using a novel experimental setup was previously described [265]. According to this methodology, the material was exposed to a FUS beam and the absorption coefficient was determined by measuring the rate of temperature rise using a thermocouple (5SC-TT-K-30-36, type K insulated beaded wire, 100 μm thick, Omega Engineering). For the absorption coefficient measurement, a signal generator (HP 33120A, Agilent Technologies), an RF amplifier (AG1012, T & C Power Conversion, Inc., Humboldt St., Rochester, NY) and a spherically-focused transducer (Sonic Concepts, Inc.) operating at 0.4 MHz (focal length of 70 mm and diameter of 40 mm) were utilized in the experimental setup as described in Chapter 6. A temperature reader (HH806AU, Omega Engineering) was used to record the temperature over time in the TMM. The thermocouple was placed at the focal position which was located 3.5 cm deep from the bottom face of the TMM (the transducer was 3.5 cm below the front surface of the TMM facing upwards). Figure 7.2.3.1 illustrates the schematic diagram (b) and a photo (c) of the experimental setup to estimate the absorption coefficient.

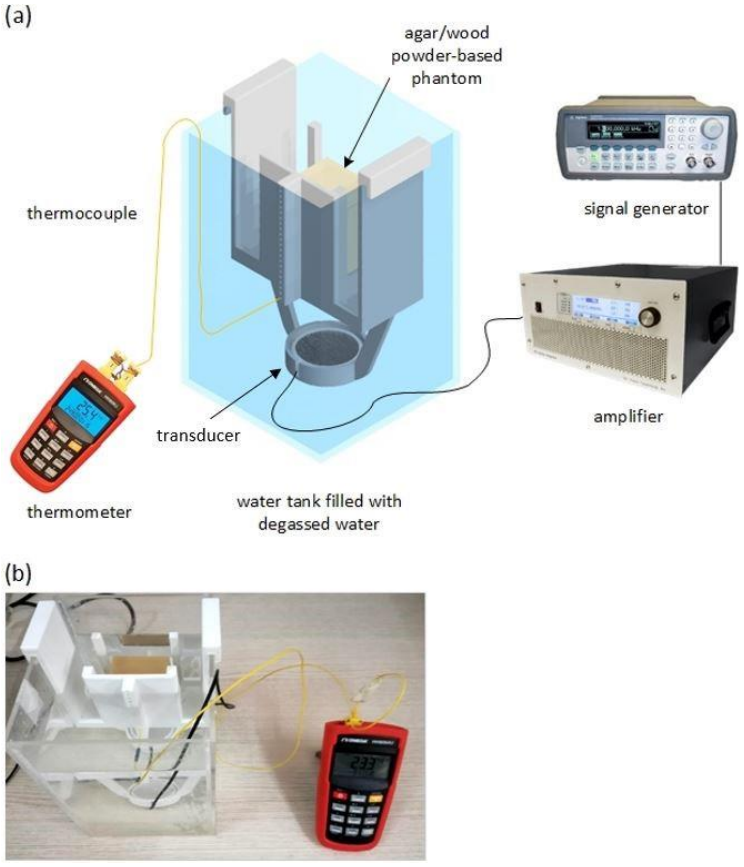

Figure 7.2.3.1: a) Schematic diagram and b) Photo of the experimental setup to measure the absorption coefficient of the TMM.

7.2.4 Estimation of the acoustic propagation speed of the soft tissue-mimicking material using the pulse-echo technique

A pulse-echo measurement immersion technique was employed for estimating the ultrasonic propagation speed of the TMM. The propagation speed was measured in a temperature range of 25 to 55 ^{o}C for the tested frequency of 1.1 MHz. The samples were immersed in a tank filled with degassed/deionized water. This technique involved a single unfocused transducer (the same transmitting transducer that was used for the attenuation measurements) to transmit and receive the reflected ultrasonic signal. The transducer transmitted pulses driven by a Panametrics pulser/receiver system (Panametrics 500PR, Olympus Corp.). A digital oscilloscope (TDS 2012, Tektronix, Inc.) was connected to the pulser/receiver for observing the received signal. A thick sample of 5.8 cm was chosen to increase time difference of echoes and thus derive a more accurate estimation of the ultrasonic propagation speed in the sample. As shown in Figure 7.2.4.1, the signal was transmitted directly in the sample and reflected using a metal reflector. The propagation speed in the sample was estimated by measuring the time difference (Δ_t) between the echoes returning from the interfaces of the sample. Equation 2 was used to estimate the ultrasonic propagation speed (C_s) of the TMM, where d represents the thickness of the sample.

$$C_s = \frac{2d}{\Delta_t} \tag{8.2.4}$$

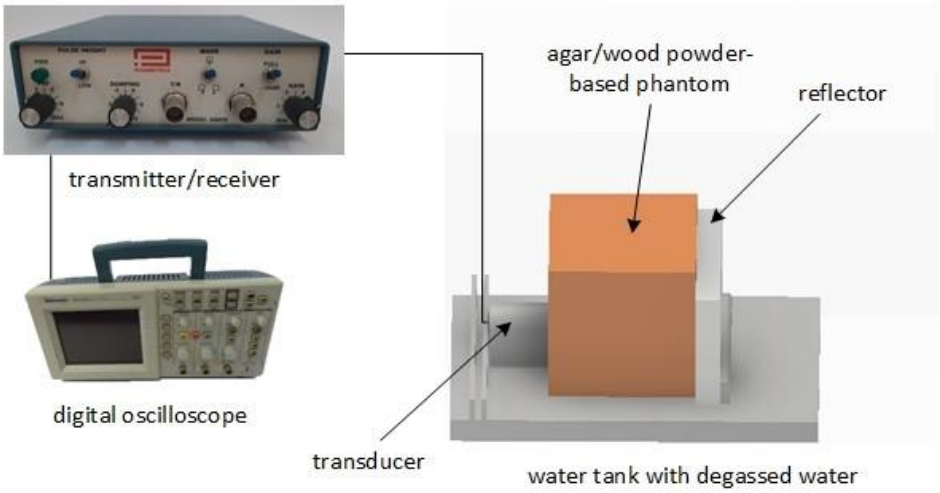

Figure 7.2.4.1: Schematic diagram of the experimental setup to measure the ultrasonic propagation speed of the TMM.

7.2.5 Mass density measurement using the water volume displacement method

Mass density was estimated by measuring the mass and volume of the samples. A 50 mL TMM was prepared and sliced in equal volumes to be placed inside a volumetric tube. Each piece was first weighed with a high precision (±0.01 g) digital scale (1479V, Tanita Corporation of America, Inc.) and then its volume was extracted by measuring water displacement in a volumetric tube. The accuracy of the volumetric tube (±0.1 ml) played an important role in the error of the measurements, therefore large specimens were tested to minimize the fractional error in volume measurements. Five specimens from the same batch were obtained and the average mass density in g/cm^3 was calculated.

7.2.6 Estimation of the soft tissue-mimicking material thermal properties

The thermal properties of the aforementioned TMM were measured using the instrument Isomet (model 2104, Applied Precision, Ltd.). The instrument was used according to the manufacturer's recommendation for estimating thermal conductivity (W/m.K), thermal diffusivity (mm^2/s), and specific heat capacity (kJ/kg.K). The transient method was used to perform the thermal conductivity measurements, which were carried out automatically by a needle sensor. The selected sensor was able to accurately measure in the range of 0.2-1 W/m.K. According to the manufacturer, the accuracy of the device for thermal conductivity measurements was 5 % of reading + 0.001 W/m.K. Thermal diffusivity is derived by dividing conductivity with density whereas specific heat capacity describes how quickly a material reacts to a change in temperature. A spherical volume of the material around the needle probe with a minimum diameter of 5 cm was needed for accurate measurement. Due to this limitation of the system, a specimen of appropriate dimensions (5 cm height, 7 cm wide, and 15 cm long) was prepared. The needle probe was inserted in the TMM and the 3 thermal properties (thermal conductivity, thermal diffusivity, and specific heat capacity) were calculated simultaneously by the device. The procedure was repeated five times and the mean and standard deviation values of each thermal property were deduced.

7.2.7 Experimental setup and HIFU sonication parameters

The absorption experimental setup described previously was used to apply high-power sonication in the phantom. The scope of the high-power sonication was to test the ability of the

phantom to reach high temperatures and create lesions. The phantom was fitted tightly into the holder and a transducer (frequency 2.6 MHz, diameter: 38 mm, focal length: 61 mm, Medsonic Ltd., Limassol, Cyprus) was positioned below the phantom facing upwards for a bottom to top sonication inside an acrylic water tank filled with degassed/deionized water. The experimental HIFU system included a signal generator (HP 33120A, Agilent Technologies), a radio-frequency power amplifier (AG1012, T & C Power Conversion, Inc.), and the spherically-focused transducer. Prior to sonication, the phantom was allowed to reach thermal equilibrium with the degassed/deionized water to minimize conduction effects. During the high-power sonication, a continuous-wave mode of acoustic power of 44 W was applied. The duration of the sonication was 30 s. The transducer position was adjusted in order to focus at 2 cm deep inside the phantom. Post-HIFU, the phantom was dissected to look for a thermal lesion. Multiple lesions were also created in an identical phantom for repeatability purposes.

7.2.8 Temperature measurement using a thermocouple

During a high-power sonication, the temperature change at the focal point of the phantom was recorded. The temperature reader (HH806AU, Omega Engineering) was used to record the temperature change in the phantom. The thermocouple (5SC-TT-K-30-36, type K insulated beaded wire, 100 μm thick, Omega Engineering) was inserted in the sample at the focus which was 2 cm deep. The thermocouple tip was rigid enough and it was inserted from one end of the phantom, all the way to the target with the phantom immersed in degassed/deionized water. The thermocouple tip was selected to be sufficiently thin to reduce possible artifacts. MRI artifacts were also avoided due to the size of the thermocouple. The thermocouple did not carry any electricity and therefore was considered as a passive object in the MR imaging volume. Although the focal length was known, precise localization of the focal point was achieved by changing the position of the thermocouple at low power until the highest temperature change was achieved.

7.2.9 Ultrasound and X-ray imaging

A diagnostic US imaging system (UMT-150, Shenzhen Mindray Bio-Medical Electronics Co., Ltd.) was used to image the TMM in order to check its echogenicity and homogeneity. A homogeneous piece of swine meat was US scanned with the same ultrasonic parameters to be compared with the US image of the TMM. An X-ray image was also acquired using a portable

X-ray system (IMS001, Shenzhen Browiner Tech Co., Ltd.). A CR reader (Vita Flex, Carestream Health, Inc.) was used to digitize the latent image from the CR cassette to the computer for X-ray image reconstruction. The X-ray exposure parameters were as follows: tube current = 50 mA, tube voltage = 60 kV, and an exposure time of 320 ms.

7.2.10 MR imaging and thermometry

High-resolution MR images of the phantom were acquired after HIFU sonication in a 1.5 T MR system (Signa Excite, General Electric) using a GPFLEX coil (USA Instruments). Proton density (PD) MR images were acquired with the following parameters: TR = 2420 ms, TE = 41 ms, receiver bandwidth (rBW) = 15 kHz, matrix = 256 x 256 pixels, slice thickness = 3 mm, NEX = 7, and displayed field of view (DFOV) = 25 x 25 cm^2.

The temperature change in the phantom under HIFU sonication was assessed with MR thermometry. MR thermometry data was produced using single-shot EPI with the following parameters: TR = 80 ms, TE = 25.1 ms, Rbw = 15 kHz, matrix = 64 x 64 pixels, slice thickness = 3 mm, NEX = 1, flip angle = 25^o, and DFOV = 25 x 25 cm^2.

The phantom was sonicated with the same transducer used during the thermocouple's temperature change recordings. Temperature changes were calculated using the proton resonance frequency shift method [264]. The thermometry slice was selected in a plane parallel to the propagation direction. Coronal thermal maps were initially obtained by applying low acoustical power to observe the temperature increase in the phantom and to detect the focal spot of the transducer. When the focal spot was detected, axial thermal maps were recorded to estimate the temperature change and observe the focal beam in the axial plane (parallel to the ultrasonic beam). Following analysis, a single thermal map was produced every 1.65 seconds. The applied acoustical power was 44 W for a sonication time of 30 s using the 2.6 MHz spherical transducer.

7.2.11 T_1 and T_2 Relaxometry

The TMM was scanned in the MRI using the GPFLEX coil (USA instruments) to estimate the relaxation times. The methods to estimate the T_1 and T_2 relaxation times have been previously described in detail by Menikou *et al.* [264]. For measuring the spin-lattice relaxation time (T_1), an IR-FSE sequence with the following acquisition parameters were used: TR = 3000 ms, TE

= 45 ms, slice thickness = 5 mm, NEX = 4, matrix = 256 x 256 pixels, and variable TI = 200, 400, 800, 1200, and 1600 ms.

The T_2 relaxation time was estimated by obtaining a series of FSE sequences for different effective echo times (23, 34, 45, 68, and 101 ms) and by calculating the inverse exponent of the exponential fit. The other MR parameters were: TR = 2500 ms, slice thickness = 5 mm, matrix = 256 x 256 pixels, FOV = 16 cm, NEX = 1, and ETL = 4.

7.3 Results

An agar-based doped with wood powder TMM was prepared following a simple and fast procedure. The gel with 2 % w/v agar and 4 % w/v wood powder was scanned with a US imaging system (UMT-150, Shenzhen Mindray Bio-Medical Electronics Co., Ltd.) in order to demonstrate that wood powder contributes to US scattering. The scattering of the wood powder has been shown to contribute to the absorption and therefore to a total attenuation increase. The TMM appeared homogeneous with increased echogenicity as shown in Figure 7.3.1.a. Figure 7.3.1.b shows the US image of a homogeneous soft tissue (swine meat). The grey texture of the TMM resembled the sonographic appearance of normal soft tissue. Figure 7.3.1.c shows the X-ray image of the TMM.

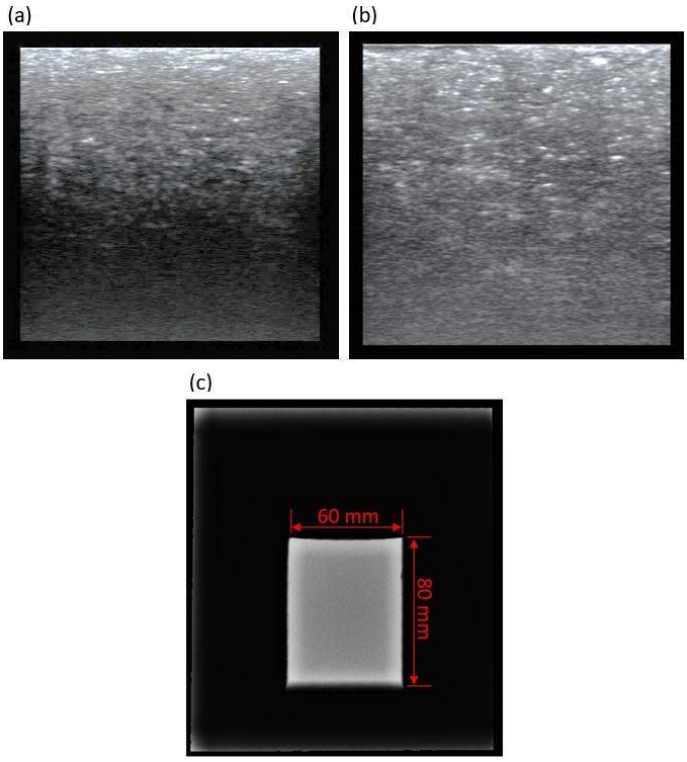

Figure 7.3.1: a) US image of the TMM with 2 % w/v agar and 4 % w/v wood powder, b) US image of a soft tissue (swine meat), and c) X-ray image of the TMM.

SEM images of the wood powder and agar/wood powder TMM are illustrated in Figures 7.3.2 and 7.3.3 at increasing magnifications, respectively. The wood powder particles appear elongated with aspect ratios in the range of 1-5. Statistics on the particle size were extracted by performing line measurements using the open-source software Gwyddion on the long direction of approximately 90 particles (Figure 7.3.4). A range of 20-350 μm was recorded with an average particle size in the ~140 μm range and a standard deviation of ~70 μm.

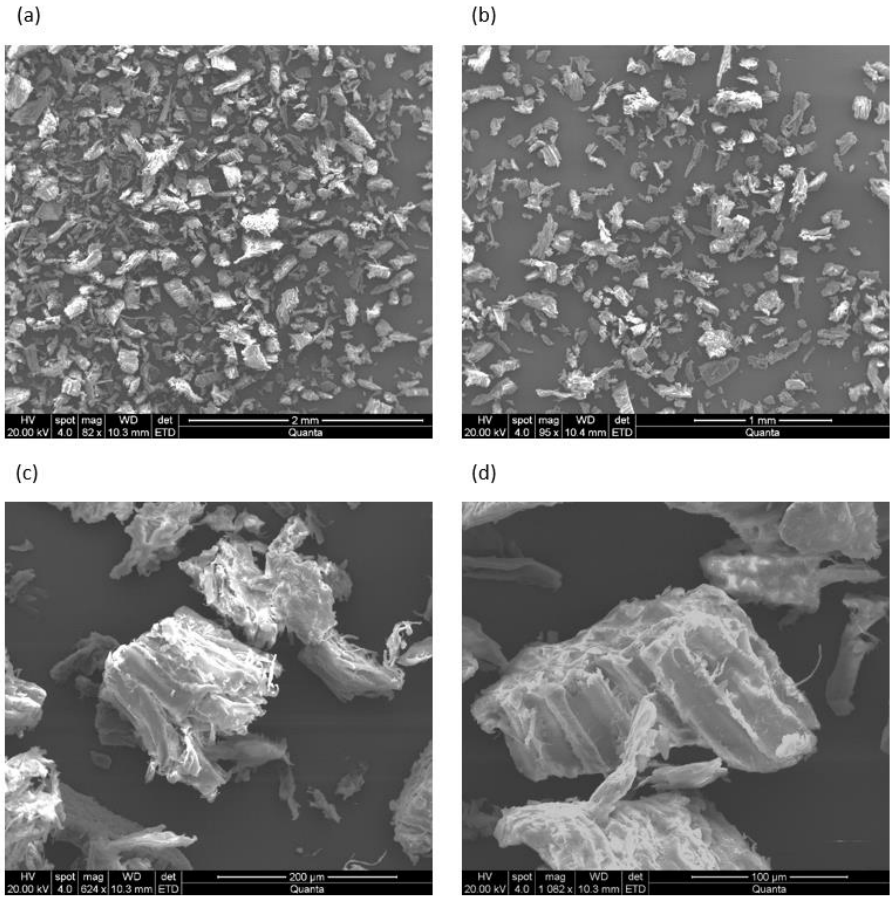

Figure 7.3.2: SEM images of the wood powder particle at magnification of a) 82x, b) 95x, c) 624x, and d) 1082x.

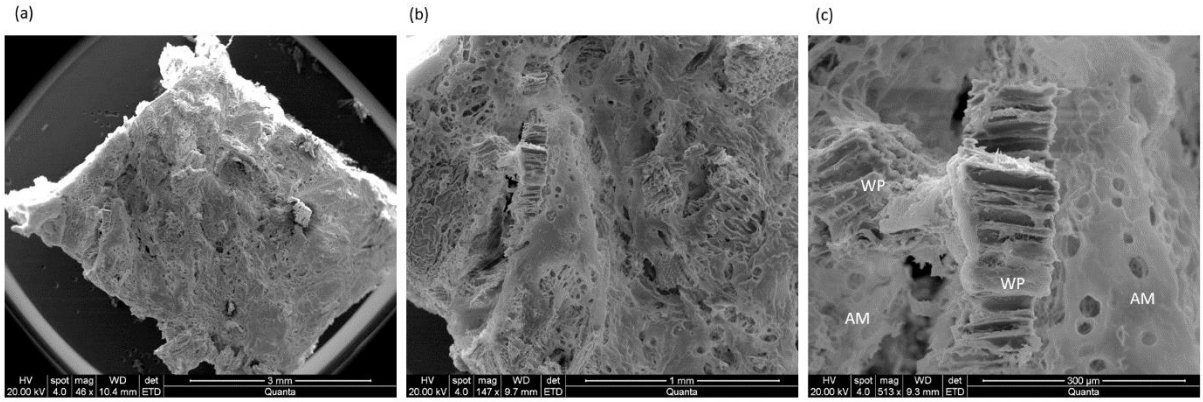

Figure 7.3.3: SEM images of the agar/wood powder TMM at magnification of a) 46x, b) 147x, and c) 513x.

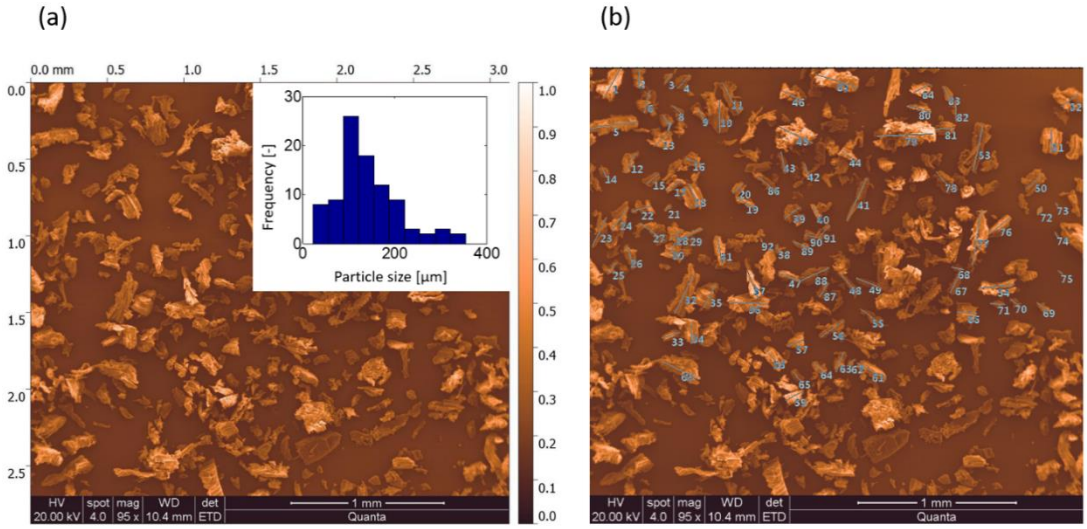

Figure 7.3.4: SEM image of the wood powder a) a histogram of 92 particle length measurements is shown in inset and, b) the selected 92 particles for the estimation of the average wood powder size.

A least mean square fitting was fitted on the attenuation coefficient measurements of various frequencies between 1.1 and 3 MHz. The measured attenuation coefficient (α_o) was 0.48±0.044 dB/cm at 1 MHz which was well within the range of equivalent values of soft tissue [293,294]. A power-law fit was determined on the data and the parameter *n* was found to be 1.059, which for the range of frequencies used in HIFU is safe to assume that the attenuation coefficient of the TMM depends linearly on frequency. Figure 7.3.5 shows the attenuation coefficient as a function of frequency.

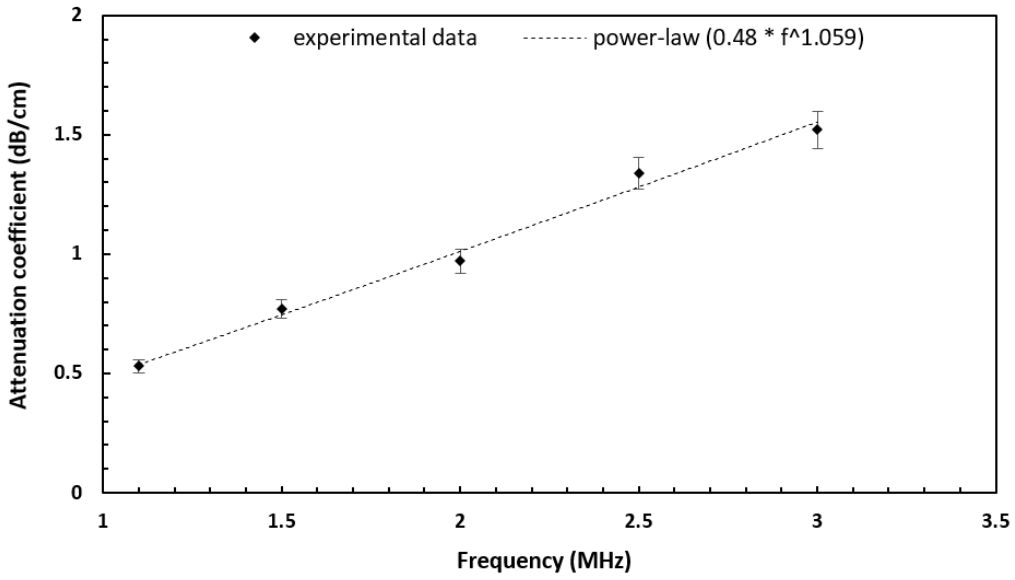

Figure 7.3.5: Attenuation coefficient as a function of frequency for the agar/wood powder-based TMM. The mean and standard deviation are represented by the data points and the error bars respectively.

It was thought that the size of the wood powder particles (<350 µm) played a significant role in the value of the scattering coefficient. Wood powder particles with dimensions of the order

of one wavelength of the sound wave or larger (~ 0.6 mm) are expected to diffract (beam spreading) the acoustic wave rather than scatter the wave in all directions. The attenuation coefficient for a frequency of 1.1 MHz at room temperature was found to be 0.53 dB/cm and the value remained almost unaffected at 37 ^{o}C. At higher temperatures, the attenuation coefficient slightly increased by reaching a value of 0.67 dB/cm at 55 ^{o}C. The effect of temperature on the attenuation coefficient is shown in Figure 7.3.6.

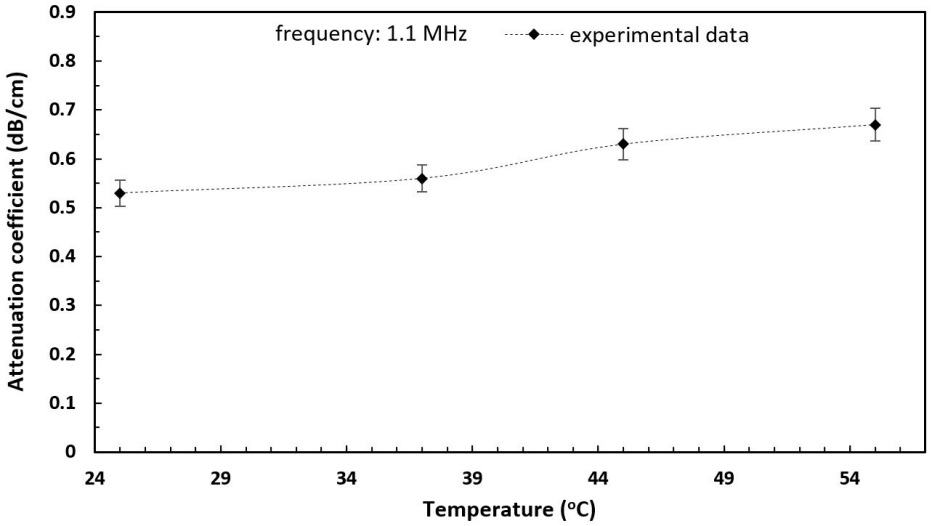

Figure 7.3.6: Attenuation coefficient as a function of temperature for a frequency of 1.1 MHz. The mean and standard deviation are represented by the data points and the error bars respectively.

Acoustic propagation speed and mass density were also assessed. The propagation speed was 1487±5 m/s at room temperature which is a value between the speed of sound of intra-vitam fat (~1480 m/s) [293] and soft tissue (~1540 m/s) [294]. The propagation speed increased from 1487 m/s to 1533 m/s in a temperature range between 25 and 55 ^{o}C as shown in Figure 7.3.7.

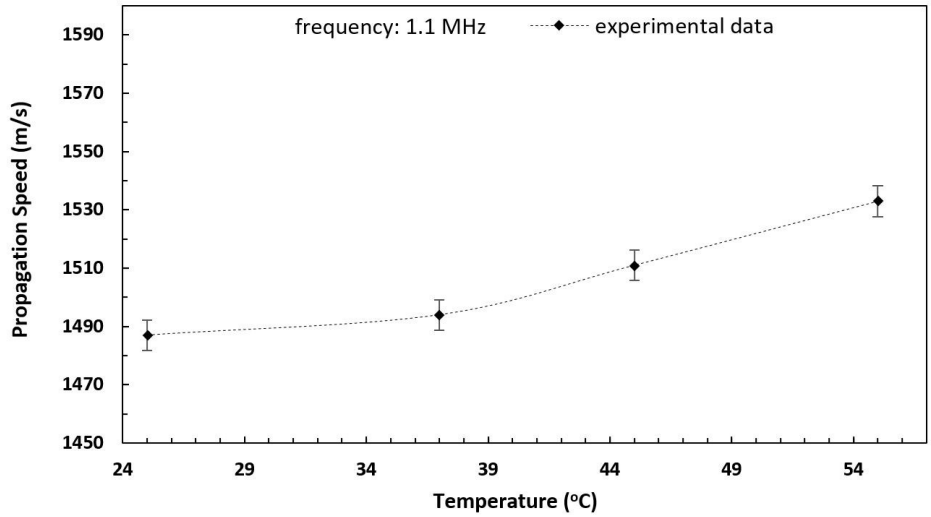

Figure 7.3.7: Propagation speed as a function of temperature for a frequency of 1.1 MHz. The mean and standard deviation are represented by the data points and the error bars respectively.

Density was calculated to be 1060±10 kg/m^3 using the water volume displacement method. Therefore, the acoustic impedance of the TMM was 1.58±0.03 MRayl. This result indicated an acoustic impedance close to that of muscle (1.62 MRayl) [293]. Water has an acoustic impedance of 1.54 MRayl, therefore the reflected intensity in the water/TMM interface was 0.016 %.

The absorption coefficient was estimated by applying an ultrasonic protocol that produces a low-temperature change between 2-3 ^oC, which corresponded to an acoustic power of 1W. During the sonication, the temperature increased linearly with time as expected after eliminating conduction effects. The temperature maintained its linearity (with R-squared of 0.9262) for a long sonication (30 s), which is representative of low conductivity. The maximum temperature recorded was 2.7 °C, and the rate of temperature increase was 0.045 °C/s. Based on the temperature-time gradient, the absorption coefficient was 0.34±0.02 dB/cm-MHz. By subtracting the estimated absorption coefficient from the attenuation coefficient, the remaining value coefficient which is attributed to non-thermal losses is found to be 0.14 dB/cm-MHz (mostly scattering). The reflection coefficient was 0.016 % based on the acoustic impedance measurement.

Thermal properties (thermal conductivity, thermal diffusivity, and specific heat capacity) were assessed by inserting a needle probe in the TMM and allow the appropriate area around the needle probe for accurate measurement. The thermal conductivity, thermal diffusivity, and specific heat capacity were estimated at 0.51±0.005 W/m.K, 0.29±0.0015 mm^2/s, and 1.76±0.001 kJ/(kg.K) respectively.

Temperature change measurements were performed in the phantom using thermocouples. A temperature rise of 63 ^oC was achieved with a HIFU duration of 30 s and 44 W as shown in Figure 7.3.8. After the HIFU exposure, the sonicated area showed some deterioration indicating the extent of the sonicated region. Maximum HIFU temperature changes are far less than the minimum ignition temperature of wood and therefore wood powder is considered a safe material to be used in MRgFUS applications.

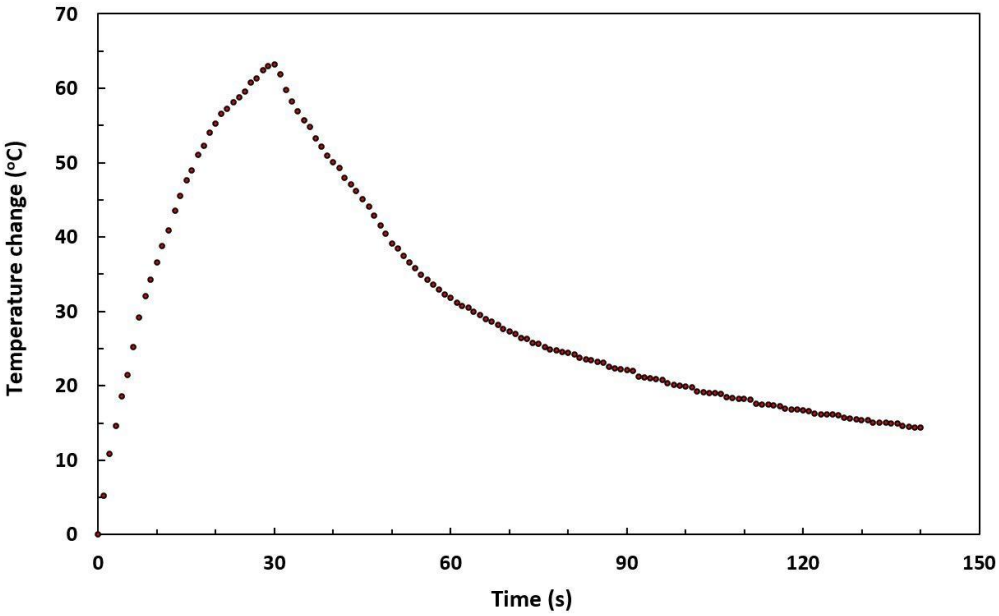

Figure 7.3.8: Temperature change versus time that was recorded using the thermocouple by applying an acoustic power of 44 W for 30 s at a focal depth of 2 cm with the 2.6 MHz spherically-focused transducer.

The TMM was MR imaged using IR-T_1 FSE and T_2-weighted FSE sequences (Figure 7.3.9.a and 7.3.9.b) in order to estimate the T_1 and T_2 relaxation parameters respectively. There were no severe artifacts in the vicinity of the TMM as expected. The best quality images, in terms of signal-to-noise ratio, were taken and provided strong evidence that the TMM contained only MR compatible materials.

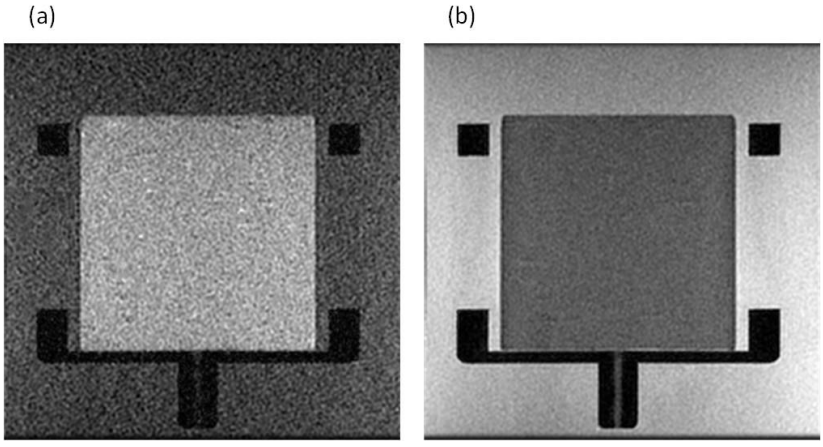

Figure 7.3.9: a) IR-FSE image of the TMM with TR: 3000 ms, TI: 1200 ms, and b) T_2-weighted FSE image with TR: 2500 ms, TE: 68 ms. IR-FSE and T_2-weighted FSE images were acquired with various TI and TE times in order to estimate the T_1 and T_2 relaxation times respectively.

MR thermometry was used to calculate the maximum temperature at the focus for the same sonication protocol that was used to measure the temperature change with the thermocouple

(acoustic power of 44 W for 30 s). Figure 7.3.10 shows the estimated MR thermal maps obtained in a plane parallel to the focal beam at a depth of 2 cm. The sonication was 30 s and MR images were also acquired during the deactivation of the transducer to confirm the temperature drop. EPI sequence was used to obtain 29 MR images within a total MR scanning time of 48 s (1.65 s for each image). However, only 6 out of 29 MR images are presented in the MR thermometry results (4 during sonication and 2 during the cooling-off period). The temperature change as calculated from the thermal map at sonication of 30 s reached a value of 66.4 ^{o}C.

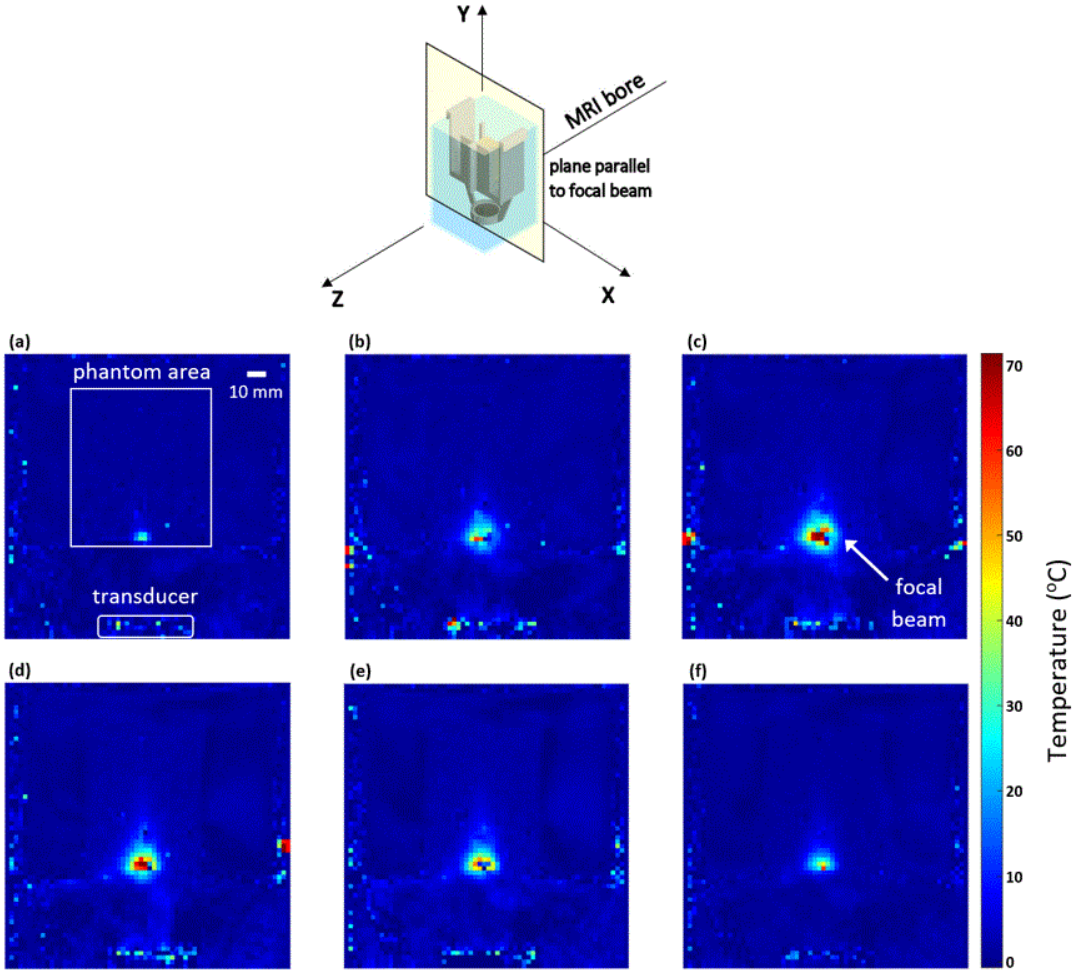

Figure 7.3.10: MR thermal maps obtained in a plane parallel to the beam at a focal depth of 2 cm for sonication time of a) 5 s, b) 15 s, c) 25 s, and d) 30 s and for a cooling time of e) 10 s, and f) 18 s, respectively. The plane of the MR thermometry maps taken in relation to the direction inside the MRI is indicated.

Following image post-processing, the nulling TI was interpolated at 585 ms and the T_1 was estimated at 844 ms. The T_2 relaxation time was found to be 66 ms. The acoustic, MR, and thermal properties of the agar-based doped with wood powder material are summarized in Table 7.3.1 along with the corresponding values of soft tissues and some TMMs.

Table 7.3.1: Summary of the acoustic, MR, and thermal properties of the agar/wood powder-based TMM along with the corresponding values of soft tissues and other TMMs that were found in the literature.

Property	**Value**	
	Agar/wood powder-based	**Soft tissues/other TMMs**
Attenuation coefficient	0.48 ± 0.044 dB/cm-MHz	Fat: 0.48 dB/cm-MHz [293] Liver: 0.5 dB/cm-MHz [294] Pure agar-based phantom (2 % w/v): 0.18 [293] Pure PVA-based phantoms: 0.075-0.28 dB/cm-MHz [234]
Absorption coefficient	0.34 ± 0.02 dB/cm-MHz	Agar (4 %)/silica (4 %)/milk (30 %)-based TMM: 0.22 dB/cm-MHz [265]
Propagation speed at room temperature	1487 ± 5 m/s	Soft tissues: 1478-1595 m/s [267] Intra-vitam fat: 1480 m/s [293] Pure agar-based phantom (2 % w/v): 1490 m/s [233]
Mass density	1060 ± 10 Kg/m^3	Brain, liver, breast: 1040-1060 Kg/ m^3 [296] Muscle: 1090 Kg/ m^3 [296] Agar-based phantoms: 1030 Kg/ m^3 [233]
Acoustic impedance	1.58 ± 0.03 Kg/m^2.s	Muscle: 1.62 MRayl [293] Agar- and polyacrylamide-based phantoms: 1.5-1.66 MRayl [298,300]
Thermal conductivity	0.51 ± 0.005 W/m.K	Non-perfused muscle: 0.5-0.6 W/m.K [301]
Thermal diffusivity	0.29 ± 0.0015 mm^2/s	Agar/silica phantom: 0.12-0.16 mm^2/s [264,302] Acrylamide-based phantom: 0.13-0.14 mm^2/s [279,298]
Specific heat capacity	1.76 ± 0.001 kJ/(kg.K)	Human and animal fat: 1.6-3 kJ/(kg.K) [304]
T_1 relaxation time at 1.5 T	844 ms	Skeletal muscle: 868 ms, heart: 866 ms, liver: 492 ms, kidney: 652 ms [305]
T_2 relaxation time at 1.5 T	66 ms	Skeletal muscle: 47 ms, heart: 57 ms, liver: 43 ms, kidney: 58 ms [305]

A high-resolution PD MR image was obtained after the sonication (Figure 7.3.11.a) and the sonicated area appeared brighter than the non-sonicated area. The TMM was cross-sectioned after the sonication and the sonicated brighter area was visually confirmed (Figure 7.3.11.b). The created lesion as well as its dimensions (length and diameter) are indicated in Figure 7.3.11.b. The length and diameter of the lesion were 14.5 mm and 7.8 mm respectively resulting in a ratio (length to diameter) of 1.85. Six lesions of the same HIFU parameters (44 W acoustic power for 30 s) were created as shown in Figure 7.3.11.c. The mean diameter and length of the lesions were 6.8±0.5 mm and 14.4±1.9 mm respectively.

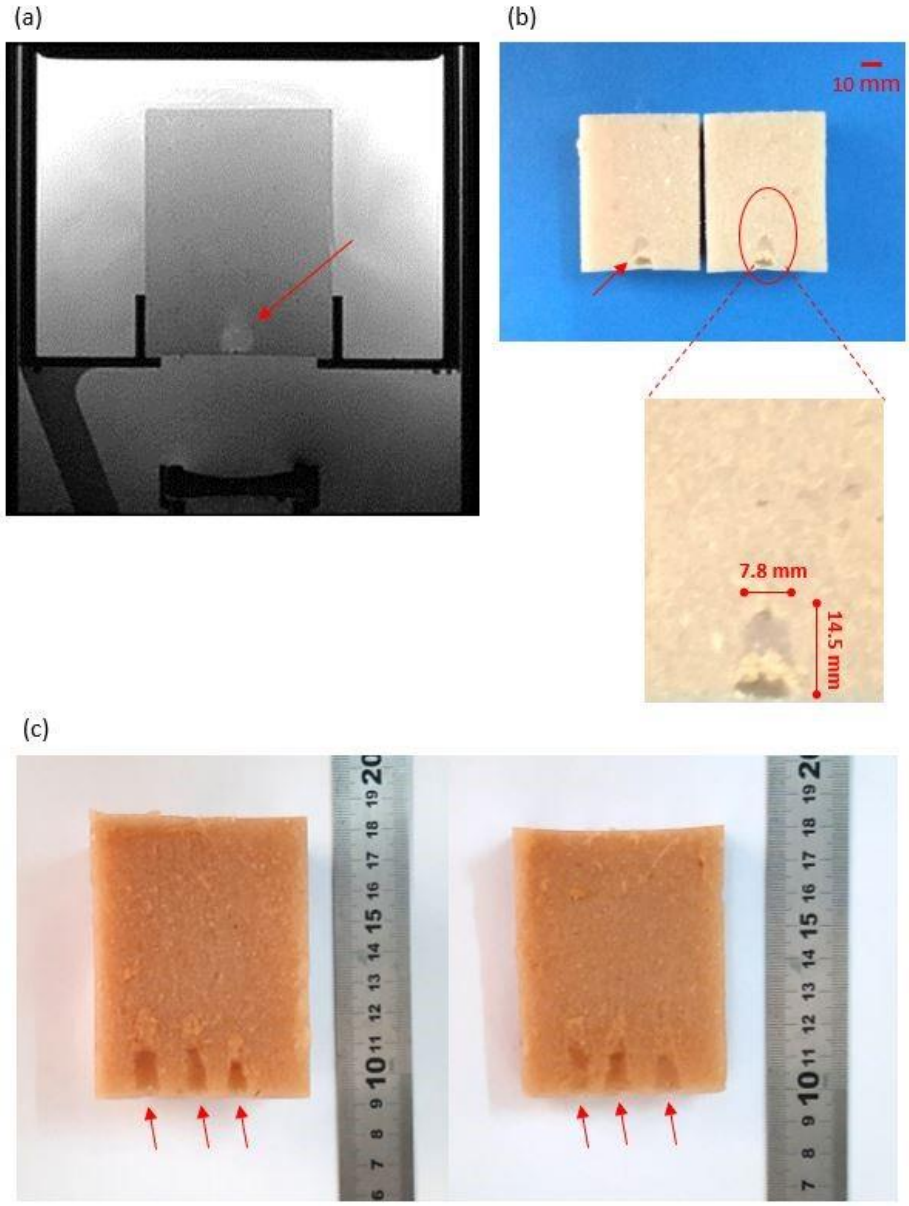

Figure 7.3.11: a) PD MR image of the TMM that was obtained after the sonication of acoustic power of 44 W for 30 s using the 2.6 MHz spherically-focused transducer, and b) Photo of the sonicated area. The TMM was vertically sliced in the middle of the focal spot. A zoomed image of the sonicated area shows the created lesion and its dimensions are indicated, and c) Multiple lesions created in the TMM. The red arrows indicate the lesions.

A focused transducer with a lower frequency (1.1 MHz, diameter: 64 mm, focal length: 63 mm, Medsonic Ltd.) was used to produce a lesion to a greater depth within the phantom. An acoustic power of 37.5 W was applied for 30 s sonication time at a focal depth of 2.5 cm. After the sonication, the phantom was cross-sectioned at 25 mm and a lesion of 18.8 mm length was observed as shown in Figure 7.3.12.

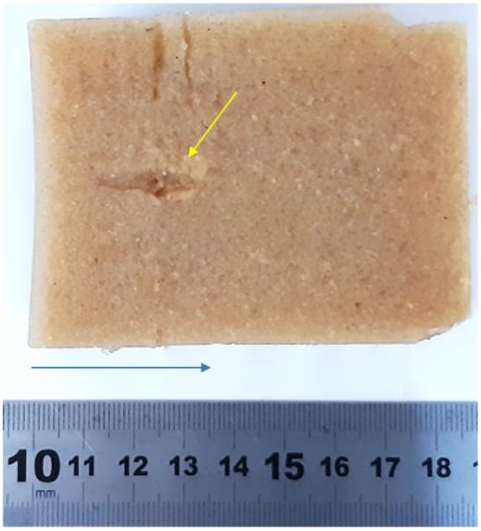

Figure 7.3.12: A lesion was formed on a plane parallel to the ultrasound beam after HIFU exposure at acoustic power of 37.5 W for a sonication time of 30 s using a 1.1 MHz focused transducer at 2.5 cm focal depth. The yellow arrow indicates the lesion and the blue arrow indicates the beam direction.

7.4 Conclusions

In this part, a TMM destined to be used for MRgFUS applications has been characterized for its acoustical, MR, and thermal properties. The TMM was agar-based with the addition of a single material to control both acoustic energy loss mechanisms (absorption and scattering). This easy-to-make agar-based gel with the addition of wood powder is non-toxic, simple and quick to prepare, inexpensive cost, and possesses a high melting temperature point.

The MRI compatibility of the TMM is especially valuable since HIFU treatments are lately performed under MRI guidance [141,205,295]. Powdered wood with low water content produces an MRI signal with an acceptable signal-to-noise ratio. Additionally, changes in magnetic susceptibility at agar gel/wood interfaces, perturb the homogeneity of the local field and may induce artifacts capable of disturbing MR thermometry results. The issues addressed can be avoided by developing in the future a TMM of even smaller wood particles. The particle size of a sample of the wood powder was evaluated using SEM and was estimated to be 139±69 μm with a particle maximum size of 354 μm and a minimum of 22 μm.

Even though Onda Corporation produces phantoms for HIFU applications, the phantoms are expensive and a complex procedure is followed for their production. In addition, these commercial phantoms lack stability when submerged in water because they exhibit reduced rigidity. These disadvantages make them less suitable for some applications. Herein, the proposed MRgFUS TMM has good rigidity, lasts around 10 days stored in the refrigerator at a constant temperature of 4 ^{o}C, whereupon it begins to dry out. However, the life of the TMM can be prolonged by the addition of preservative materials (Thimerosal or Germall-plus). The production cost of the TMM was low, therefore at the end of experimental sessions it was disposed.

The measured attenuation coefficient at 1 MHz was found to be close to fat (0.48 dB/cm-MHz) [293] and liver (0.5 dB/cm-MHz) [294]. A nearly linear frequency dependency of the attenuation coefficient has been demonstrated in a frequency range used mainly in MRgFUS applications. At body temperatures, the attenuation coefficient of the material remained almost constant relative to the same parameter at room temperature. Nevertheless, at higher temperatures, this value has shown a slightly increasing trend. The agar/wood powder TMM (manufactured with only two materials) has higher attenuation than other more complicated TMMs which have been developed and characterized over time such as agar, gelatin with the inclusion of glass bead scatterers (0.35-0.46 dB/cm-MHz) [289] and pure polyacrylamide gels (0.17-0.25 dB/cm-MHz) [293].

The measured absorption coefficient of the prescribed TMM was found to be higher by 0.12 dB/cm-MHz than an optimum recipe (4 % w/v agar, 30 % volume per volume evaporated milk, and 4 % w/v silica) that was proposed in a previous study [265]. The goal was to increase the absorption coefficient as close as possible to 0.5 dB/cm-MHz. It was previously evidenced [265] that the absorption coefficient increases with the increase of agar concentration, evaporated milk, and silicon dioxide (until 4 %). In order to observe the effect of wood powder on the absorption coefficient, a comparison between a TMM with only 2 % agar and one with 2 % agar and 4 % wood powder was performed. The addition of 4 % of wood powder increases the absorption coefficient by 0.11 dB/cm-MHz.

Measurement of the acoustic speed of the soft tissue recipe was in the lower range of biological soft tissues (1478-1595 m/s) [267] and near the value of a head-mimicking phantom that was previously proposed [157]. There has been an increasing trend in the propagation speed relative to the increase in temperature. At high temperatures, the propagation speed was close to the

value of soft tissue. If values closer to 1540 m/s are desired in low room temperatures, an appropriate concentration of an additive (glycerol or milk) can be added.

The mass density of the TMM (1060±10 Kg/m^3) was found to be similar to that of the brain, liver, and breast (1040-1060 Kg/m^3) [296] while it approximated the mass density of muscle (1090 Kg/m^3). Gelatin and polyacrylamide gel TMMs demonstrated mass density values within the range of soft tissues [297-299] and closed values to the proposed TMM. The acoustic impedance was in the range of other agar-based and polyacrylamide-based materials (1.5-1.66 MRayl) [298,300].

The thermal conductivity (0.51±0.005 W/m.K) of the TMM mimics published values for non-perfused soft tissues with the value of non-perfused muscle to be in the range of 0.5-0.6 W/m.K [301]. The thermal diffusivity (0.2935±0.0015 mm^2/s) was more than double compared to agar/silica recipe (0.12-0.16 mm^2/s) [266,302] and acrylamide-based (0.13-0.14 mm^2/s) [279,298] which are similar to the value of water (0.143 mm^2/s) [303]. It is concluded that wood powder also contributes to the increase of the TMM's thermal diffusivity. The high thermal diffusivity shows how quickly the material transfers heat across HIFU temperatures. Specific heat capacity was in the range of the values of human and animal fat [304].

From the US images, it was shown that the addition of wood powder increased the echogenicity of the TMM, such that it closely resembled the US signal generated by real tissues. Additionally, the TMM fulfilled the requirement of being compatible with an MRI scanner. The measured relaxation times T_1 and T_2 were within the range of values found in the literature for soft tissue [305].

MRI and optical images of the TMM indicate that HIFU ablation at high power levels can lead to the formation of focal lesion. The formation of focal lesion in MRI images appears to be hyperintense. The TMM allows the lesions to be optically observed and measured. However, high power sonications cause irreversible damage to the phantom, whilst in low power settings the absence of any material deterioration demonstrated its suitability of being used repeatedly. Additionally, the possibility of inserting thermocouples to measure temperature rise and check transducers' performance without affecting its structural integrity was another feature of the phantom. The temperature rise measured with the thermocouple was confirmed with MR thermometry. Both thermocouple and MR thermometry yielded almost identical temperature change readings for a specific ultrasonic protocol (63 and 66.4 ^{o}C respectively). There is always a possibility that the acoustic field is distorted by the metal-base thermocouple wire, which can

induce a focus shift observed as a peak temperature decrease. Positioning of the thermocouple is done manually and although all possible measures are followed to target the nominal focal region, the procedure is always prone to mispositioning errors. The main advantage of using this method is the relatively low noise of the temperature-time profile compared to MR thermometry. On the other hand, the reliability of MR thermometry results is related to the signal-to-noise ratio of the phase images which is usually limiting since the imaging coils are not optimized for the phantom's geometry. External interferences that induce inhomogeneities to the MR static field are also sources of error in MR thermometry. Mispositioning of single slice MR thermometry especially in the long axis and partial volume effect are also factors that can underestimate peak temperature.

Finally, the length to diameter ratio showed that a good-shaped lesion was created and cavitation was not affecting. The expected focal beam was at a depth of 20 mm. However, the focal beam shifted 10 mm to the front surface of the TMM. Higher penetration of the US beam can be achieved using a transducer with a lower frequency (0.5-1 MHz). This was achieved by using a transducer with lower frequency and lesion was created to a greater depth in the phantom. Multiple lesions were produced indicating repeatability of the lesions' dimensions.

8 Evaluation of the 4-DOF prostate robotic system

8.1 Stages of the evaluation procedure

Simulations were performed to investigate the ultrasonic parameters of two candidate transducers. The power field and thermal effects of the transducers at various acoustic power were investigated in order to select the proper transducer for prostate ablation. The dimensions of the lesions that the transducers can produce at different acoustic power were simulated. The evaluation of the robotic system included the MR compatibility and accuracy of motion. The MR compatibility was checked at various conditions to study the effect of each part of the system on the SNR of the MR images. Evaluation of six different navigation algorithms was performed in order to examine the amount of the transducer's induced heating in the pre-focal region. The delay that is required for complete elimination of the near-field heating was investigated.

Furthermore, in this part the MRI evaluation of the thermal heating of the candidate transducers is described. The FUS system and its composed devices that were used during the evaluation of the transducers are presented. The materials on which the two transducers have been tested are reported (phantoms, excised tissues, small animal). The contents that were used to develop the phantoms, as well as the kind of the excised tissues and animals, are also included. Two different experimental set-ups are illustrated. Both experimental set-ups were used to evaluate the thermal heating of the transducer with a frequency of 4.4 MHz. The first experimental set-up was used for phantoms with large dimensions without knowing the exact location of the focal point, while the second experimental set-up was designed in order to easily locate the focal point and was used for phantoms with smaller dimensions and excised tissues. The 4.4 MHz transducer embedded in the robotic device was also evaluated in excised tissue in the MRI environment. Another experimental set-up was used in order to detect the focal point of the 3.2 MHz transducer in an excised tissue.

Lesions in porcine excised tissues were achieved using an experimental set-up that allows the transducer to be moved manually. Temperature changes were recorded at the focal point in phantoms and excised tissues using a thermocouple and MR thermometry. The temperature elevation at the surface of the 3.2 MHz transducer was also recorded for different HIFU energy in order to check its durability to high intensity. The diameter and length of the lesions from various HIFU parameters were measured and presented versus different acoustical parameters.

MRI images of the experimental set-ups were obtained in order to visualize the set-up, the evaluated transducer, and the material under test. Targeting was confirmed using low-intensity sonications monitored using MR thermometry. After targeting confirmation, the exposure of full-energy sonications in the target area and monitoring in real-time of each sonication was confirmed with MR thermometry. MR thermal maps were obtained to assess the heating of both transducers (4.4 and 3.2 MHz) using the PRFS method for the different experimental set-ups. These maps were obtained in an agar/silica/milk phantom and excised tissues. Temperature changes were recorded through MR thermometry in agar-based gel phantoms and excised tissues for various acoustical parameters. The created lesions were observed using the appropriate MR pulse sequence and they were confirmed by cross-sectioning the excised tissues post-experiment.

The final 4-DOF robotic device with the transducer was evaluated in phantoms and excised tissues. A prostate-mimicking phantom was used and the probe of the device was inserted within the phantom. A number of experimental models (tissue over the transducer, tissue and transducer immersed in a water tank, tissue surrounding the probe) was conducted to create multiple lesions in excised tissues. In all experimental models, acoustic power and sonication time was varied in order to identify the minimum energy needed for the device to ablate tissue. Different grid patterns were performed using the developed software to check the accuracy of the motion of the robotic device (in linear and angular motions) through the produced lesions, as well as the ability of the system to ablate a whole area of interest. In order to achieve a whole area ablation, overlapping lesions were created by setting a particular distance of robotic movement between successive sonications. The size (length and diameter) of the lesions was also calculated by allowing more distance between each sonication site so as to avoid overlapping lesions. The difference between a cavitational and thermal lesion in practice was observed.

The final robotic system was evaluated in a rabbit thigh model in an MRI environment. The rabbit was initially anesthetized and treated using different ultrasonic protocols (acoustic power and sonication time). After the ablation plan, the rabbit was humanely euthanized. The rabbit's thigh was dissected, lesions were observed and their diameter and length were measured. During the MRI experiment, MR thermometry images were acquired during each sonication. The created lesions were observed using high-resolution MR images (PD with fat suppression). Sonications with various acoustic power and sonication time were performed and the

temperature change was recorded. A real-time *in situ* thermal MR thermometry data was obtained and tissue necrosis *ante mortem* was confirmed.

8.2 Simulation results of the candidate transducers

Prior to the evaluation of the candidate transducers in phantoms and excised tissues, an open-source software that was written and developed by Joshua Soneson (HITU simulator, FDA, 2011) was used to simulate the ultrasonic parameters of the two candidate transducers (3.2 and 4.4 MHz). This simulation is a powerful tool that estimates information regarding the power field, mechanical properties, and heating effects of the ultrasonic beam. Using the information estimated by the software, the transducers that were suitable for the robotic device were determined, constructed, and advanced to the evaluation procedure. To estimate the heating effects as accurate as possible, the acoustic properties of the phantom (6 % w/v agar and 30 % v/v evaporated milk) that were measured through a series of experiments, were entered in the software. The materials along with their thicknesses, the distance between them, and the tissue arrangement which were entered as inputs into the software for both transducers are shown in Figure 8.2.1. The red line on the left indicates the ultrasonic transducer element. The light blue-colored strips show the water that was included as the media for the US transmission. The red strip between water demonstrates the tissue. All the parameters that were used for the simulation process are listed in Tables 10.2.1 and 10.2.2 in the appendix section (Simulation parameters and results of the candidate transducers).

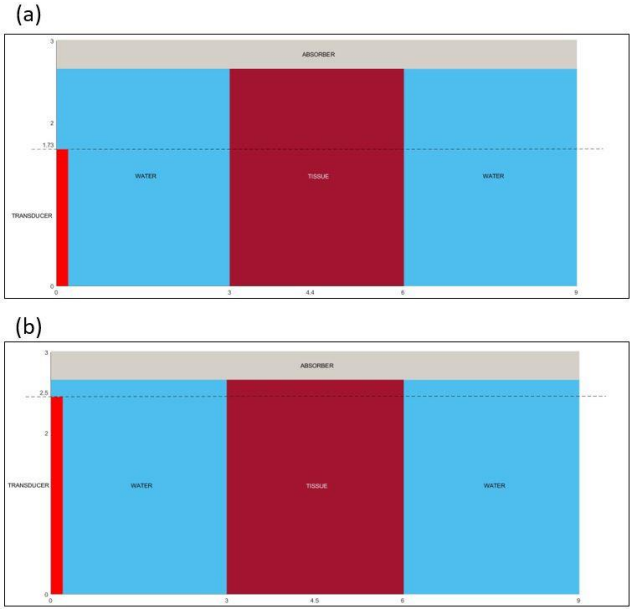

Figure 8.2.1: Material arrangement used in the simulation for the candidate transducer of a) 4.4 MHz, and b) 3.2 MHz.

The simulation extracted data that described the acoustic power, pressure, and temperature on the axial and horizontal plane. This software provided information regarding the size and shape of the transducer which were used for the design of the ultrasonic transducers. Simulations from low to high acoustic power (10, 20, 30, and 50 W) for each transducer were performed. The radial distribution of the first five harmonic pressure amplitudes at Z = 4.045 cm and Z = 4.083 cm for the transducer of 4.4 MHz and 3.2 MHz respectively, is shown in Figure 8.2.2. From the radial distribution, the pressure at the center of the beam for the first harmonic as well as the acoustic intensity were extracted.

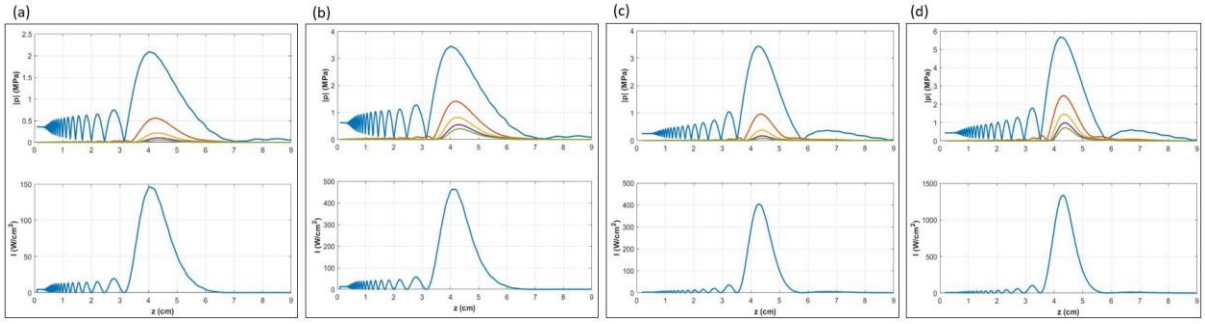

Figure 8.2.2: Radial distribution of the first five harmonic pressure amplitudes of the 4.4 MHz transducer at Z = 4.045 cm and acoustic power of a) 10 W, and b) 30 W and of the 3.2 MHz transducer at Z = 4.083 cm and acoustic power of c) 10 W, and d) 30 W.

Figure 8.2.3 shows the quantitative plot of the US spatial distribution on the axial plane. The vertical scale (*r*) is the diameter of the beam and the lateral axis (*z*) is the sonication depth. This plot shows the prediction of the software application for the size and shape of the ultrasonic beam.

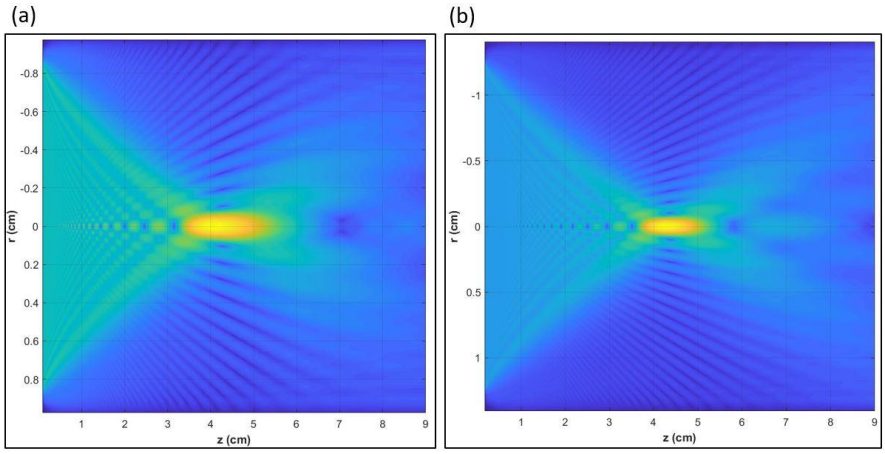

Figure 8.2.3: A qualitative plot of the spatial distribution of the US field of the transducer of a) 4.4 MHz, and b) 3.2 MHz.

Figure 8.2.4 shows the rate at which temperature increases at the focus after the activation of the US for 30 s. When the US was deactivated, the simulation continued to calculate the rate

at which the temperature decreased for 30 s. The temperature was set to begin from a baseline (average normal human body temperature). The thermal dose at 10 W acoustic power is not sufficient to induce lesions for both transducers while the 30 W was shown to create a lesion.

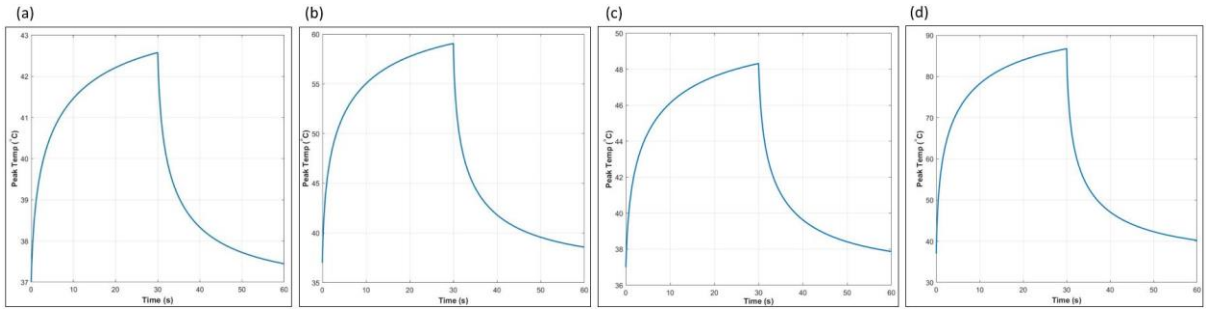

Figure 8.2.4: Temperature with respect to time for activation and deactivation of the 4.4 MHz transducer and acoustic power of a) 10 W, and b) 30 W and of the 3.2 MHz transducer and acoustic power of c) 10 W, and d) 30 W.

Figure 8.2.5 shows the temperature distribution along the beam path at the time when peak temperature occurs. The temperature buildup suggested an estimation for the focus shape and size.

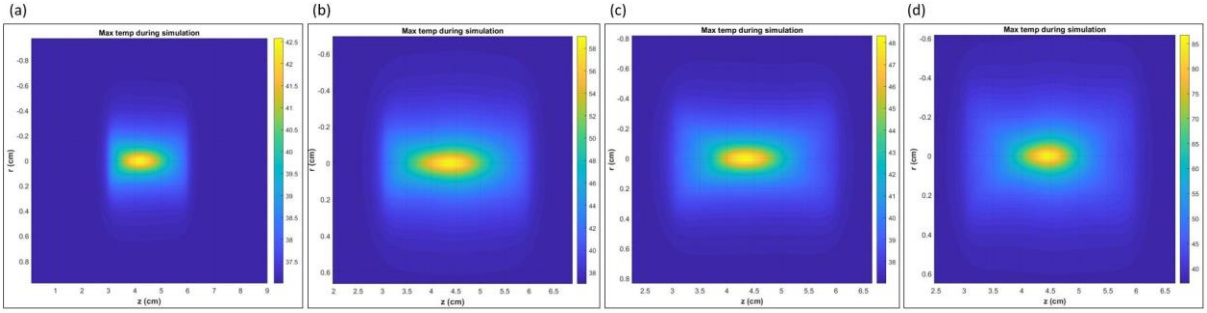

Figure 8.2.5: Temperature distribution at the time peak temperature occurs of the 4.4 MHz transducer and acoustic power of a) 10 W, and b) 30 W and of the 3.2 MHz transducer and acoustic power of c) 10 W, and d) 30 W.

The thermal dose calculation is shown in Figure 8.2.6. The lesion size is calculated by estimating the thermal dose. On the inside of the yellow perimeter, the thermal dose is equal or larger than 240 cumulative equivalent minutes (CEM) which suggests that tissue necrosis occurs.

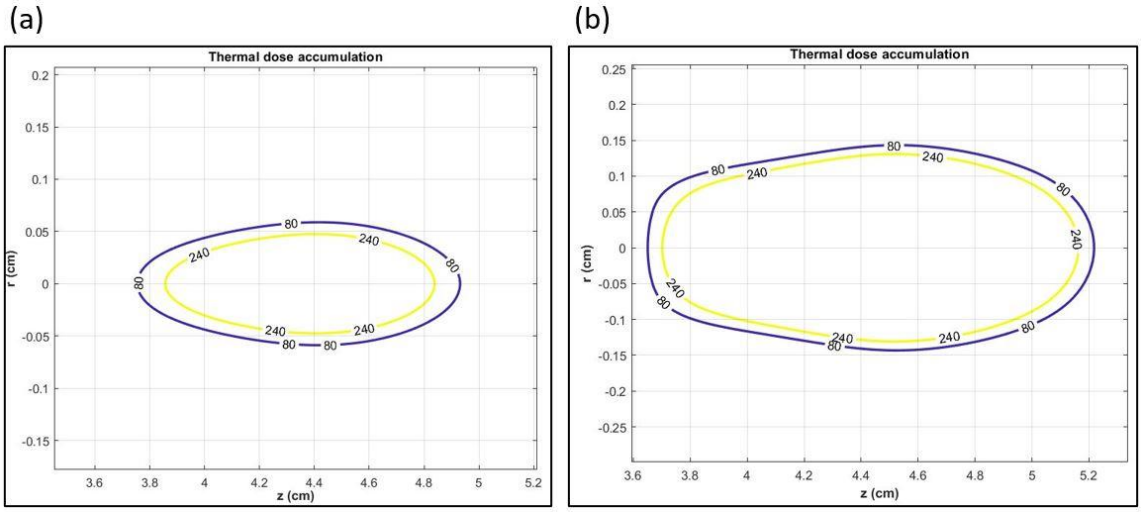

Figure 8.2.6: Thermal dose calculation at the end of the simulation at acoustic power of 30 W and for the transducer of a) 4.4 MHz, and b) 3.2 MHz.

The simulation results for both transducers at acoustic power of 20 and 50 W are included in the appendix section (Simulation parameters and results). All the simulation main results are summarized in Table 8.2.1.

Table 8.2.1: List of the simulation results for the candidate transducers of 4.4 MHz and 3.2 MHz.

Transducer 4.4 MHz					
Acoustic power (W)	**Acoustic pressure (MPa)**	**Intensity (W/cm^2)**	**Temperature change at 30 s (^oC)**	**Lesion diameter (mm)**	**Lesion length (mm)**
10	2.09	146.6	5.6	no lesion	
20	2.874	299.8	12.2	no lesion	
30	3.4	462.5	22.1	1	11.5
50	4.189	814.9	66.2	3.17	19.4
Transducer 3.2 MHz					
Acoustic power (W)	**Acoustic pressure (MPa)**	**Intensity (W/cm^2)**	**Temperature change at 30 s (^oC)**	**Lesion diameter (mm)**	**Lesion length (mm)**
10	3.429	402.3	11.3	no lesion	
20	4.721	842.8	25.9	1.36	9.45
30	5.624	1335	49.7	2.95	16.3
50	6.936	2429	192.4	5.54	22.1

8.3 MR compatibility of the robotic system

The 4-DOF robotic system was tested for MR compatibility. The axes of the robotic device were driven by piezoelectric ultrasonic motors (USR60-S3N, Shinsei Corporation). For each DOF, an angular optical encoder was used (EM1-2-2500-I EM1, US Digital Corporation, Vancouver, WA, USA). The SNR was measured in an agar-based phantom (6 % w/v agar, 30 % v/v evaporated milk) for amplifier and transducer activation for assessing the MR compatibility of the transducer. It was also calculated for different configurations (robotic device in MR bore, connection of robotic device with piezoelectric motors and optical encoders and activation of these devices) in an MR-phantom (cylindrical, SNR 150027, USA Instruments) for evaluating the MR compatibility of the robotic system. The FUS system consisted of a signal generator (HP 33120A, Agilent Technologies), an RF amplifier (Tomco, BT00250-Alpha-CW, Tomco Technologies, Stepney, Australia), and the spherical transducer of 3.2 MHz.

The robotic FUS system was tested in a 1.5 T MR system (Signa, General Electric) using a GPFLEX coil (USA Instruments). Figure 8.3.1 shows the experimental set-up with the transducer and the agar-based phantom on the table of the MRI scanner, that was used to test the MR compatibility of the transducer (activated or not) and the SNR effect after amplifier activation. The RF-coil was placed around the agar-based phantom in order to enhance the MR signal.

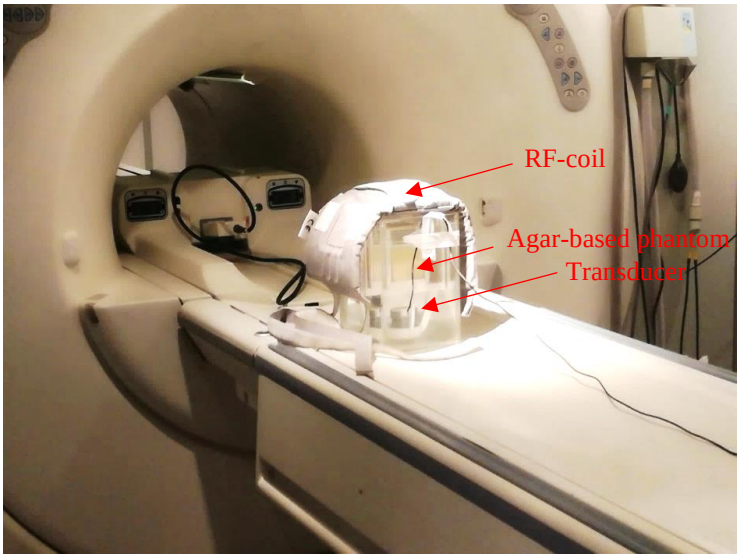

Figure 8.3.1: Experimental set-up to check the MR compatibility of the transducer and amplifier activation.

Figure 8.3.2 illustrates the experimental set-up in the MRI room in order to measure the SNR on the MR-phantom and with the robotic device outside the MR bore (Figure 8.3.2.a), with placement of the robotic device in the bore (Figure 8.3.2.b), with connection of the robotic

device and unshielded cables (Figure 8.3.2.c) and the activation of the motor and encoders. Initially, MR images were acquired with the phantom only in the MR bore. Then the robotic device was placed on the MR table but outside the MR bore (as shown in Figure 8.3.2.a). The robotic device was then placed alongside the phantom as shown in Figure 8.3.2.b. MR images of the phantom were obtained for the following conditions: phantom only and robotic device outside the MR bore, phantom and robotic device (unwired) in the MR bore, phantom and robotic device (wired) in the MR bore but with the deactivated electronic system, and phantom and robotic device (wired) in the MR bore with the activated electronic system.

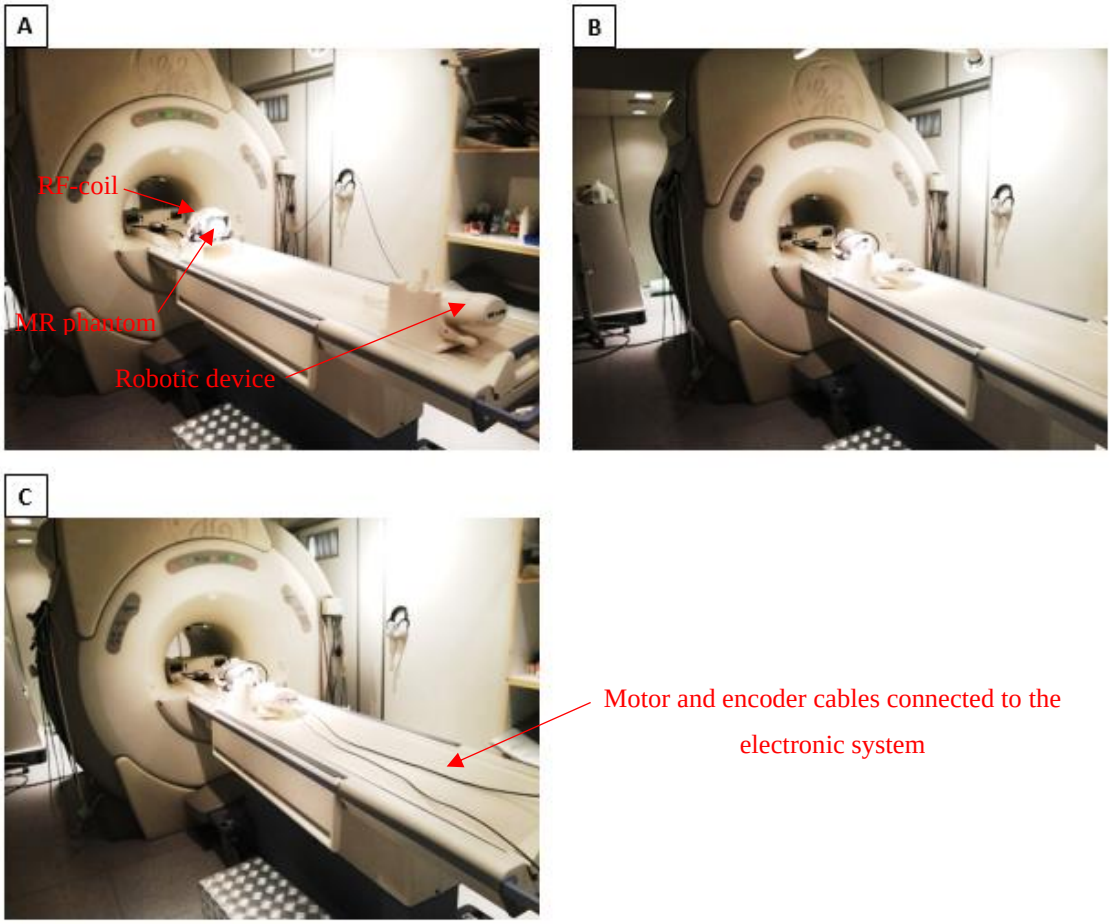

Figure 8.3.2: Experimental set-up in the MR room a) without the robotic device in the MR bore, b) with the robotic device in the MR bore, and c) with the robotic device connected with unshielded cables.

An agar-based phantom was used to test the MR compatibility of the activation of the transducer and amplifier. The SNR was measured under various conditions (electronic system presence or activation and transducer presence or activation) using T_2-weighted FRFSE for high-resolution imaging of the different conditions. The MR thermometry sequences FSPGR and EPI were also obtained and the SNR for the different conditions was compared. The T_2-

weighted FRFSE sequence was used with the following parameters: TR = 2200 ms, TE = 62 ms, FOV = 21 cm, matrix = 256 × 256, flip angle = 90º, and NEX = 3. The FSPGR sequence was used with the following parameters: TR = 40 ms, TE = 20 ms, FOV = 21 cm, matrix = 256 × 256, flip angle = 30º, and NEX = 1. The EPI sequence was used with the following parameters: TR = 80 ms, TE = 19 ms, FOV = 21 cm, matrix = 64 × 64, flip angle = 25º , and NEX = 2. Table 8.3.1 summarizes the different conditions for which the SNR of the agar-based phantom was calculated.

Table 8.3.1: List of the different conditions for which the SNR of the agar-based phantom was measured in order to evaluate the MR compatibility of the transducer.

Nº	Condition
1	Transducer out of MRI room and amplifier power off
2	Transducer in the MRI bore and amplifier power off
3	Transducer in the MRI bore and amplifier power on
4	Transducer in the MRI bore and amplifier activated

An axial T_2-weighted FSPGR image of the experimental set-up was initially obtained as shown in Figure 8.3.3. Coronal MR images of the agar-based phantom taken with T_2-weighted FRFSE, FSPGR, and EPI sequence are shown in Figure 8.3.4, 8.3.5, and 8.3.6 respectively for the different conditions of Table 8.3.1. Figures 8.3.4.a, 8.3.5.a and 8.3.6.a show the T_2-weighted FRFSE, FSPGR, and EPI image of the phantom with the deactivated transducer outside of the MRI room and the amplifier unpowered. Figures 8.3.4.b, 8.3.5.b and 8.3.6.b show the T_2-weighted FRFSE, FSPGR, and EPI image of the phantom with the deactivated transducer in the MR bore and the amplifier unpowered. Figures 8.3.4c, 8.3.5c, and 8.3.6c show the T_2-weighted FRFSE, FSPGR, and EPI image of the phantom with the deactivated transducer in the MR bore and the amplifier powered on. For the T_2-weighted FRFSE sequence, the amplifier was not energized since this sequence is not intended to be used for MR thermometry. Figures 8.3.5.d and 8.3.6.d respectively show the FSPGR and EPI image of the phantom with the activated transducer in the MR bore and the amplifier powered on. The difference between the baseline image (with transducer out of the MRI room and the amplifier unpowered) and the image taken in each different condition is illustrated.

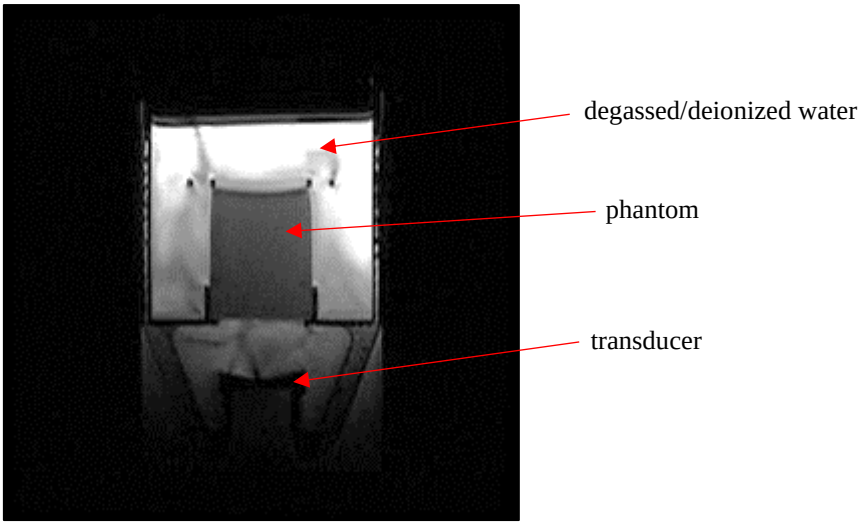

Figure 8.3.3: T_2-FSPGR coronal image of the experimental set-up that was used to investigate the MR compatibility of the transducer.

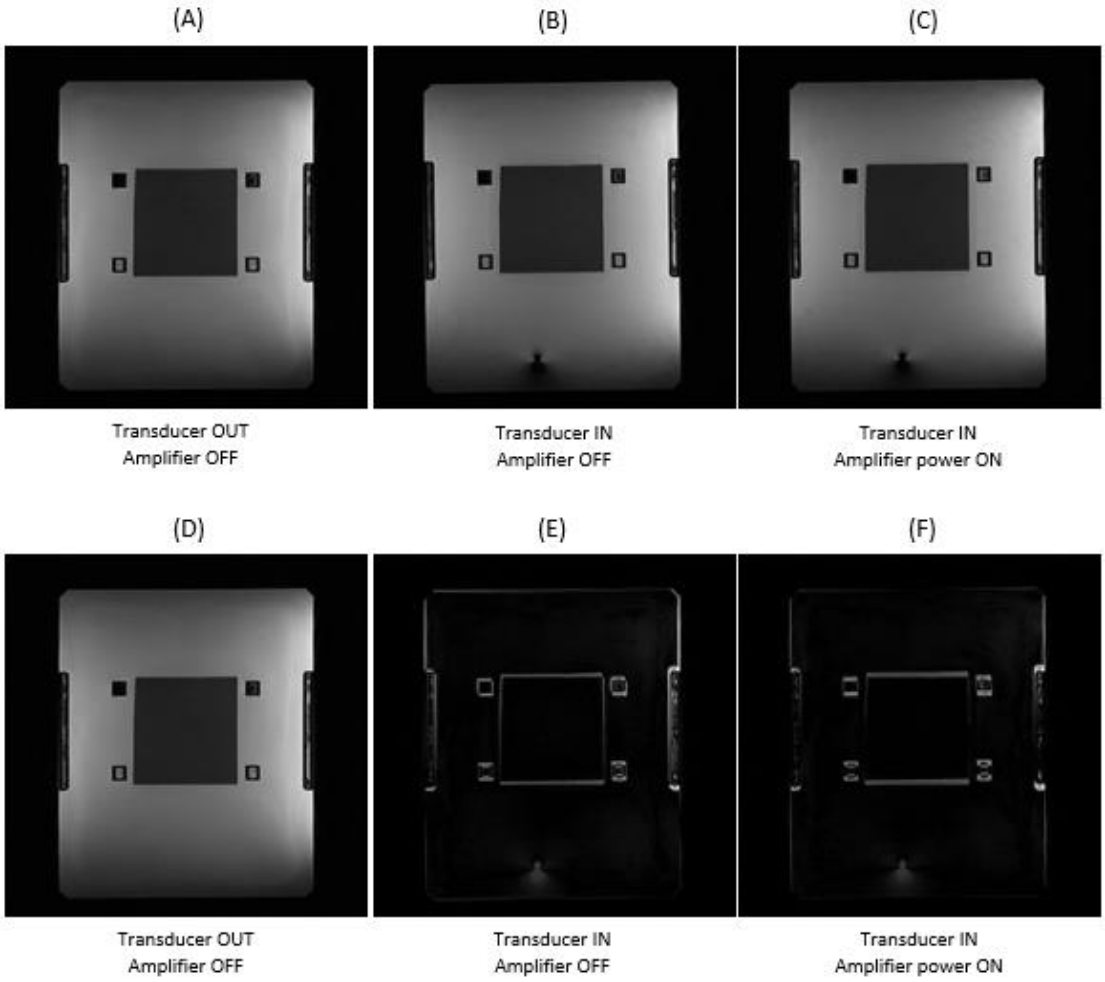

Figure 8.3.4: MR images (top) obtained using T_2-weighted FRFSE sequence for the different conditions and the corresponding differences (bottom) between each condition and the baseline (phantom only and transducer out of the MRI room).

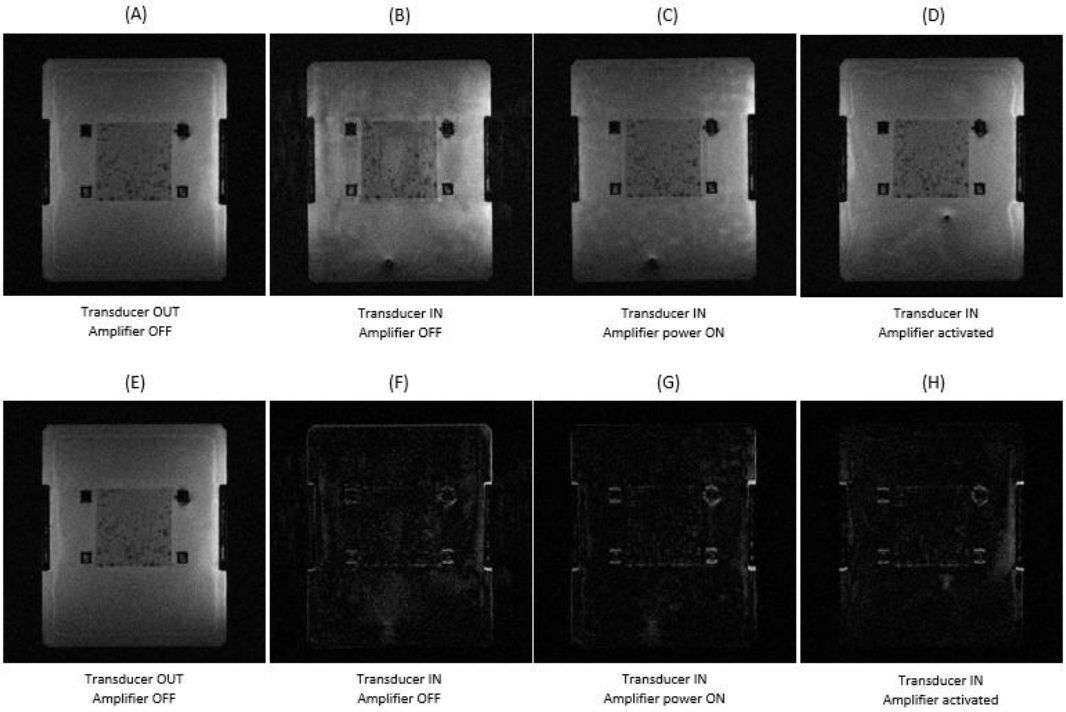

Figure 8.3.5: MR images (top) obtained using FSPGR sequence for the different conditions and the corresponding differences (bottom) between each condition and the baseline (phantom only and transducer out of the MRI room).

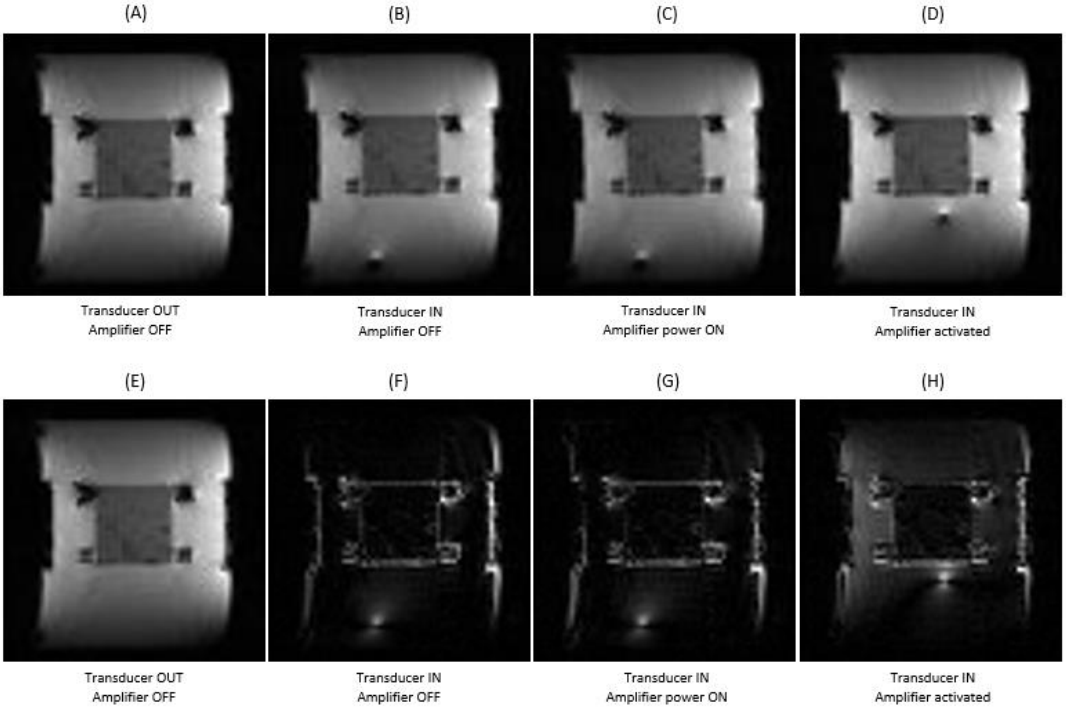

Figure 8.3.6: MR images (top) obtained using EPI sequence for the different conditions and the corresponding differences (bottom) between each condition and the baseline (phantom only and transducer out of the MRI room).

A method in NEMA standard [108] was used to measure the SNR in the phantom for the different configurations. A measurement ROI of at least 75 % of the area of the image of the

signal-producing volume of the phantom was selected. The SNR was calculated by dividing the mean signal of that ROI from the standard deviation of the same area (in pixels) of the noise which was obtained from the subtraction of two acquisition phantom images (at the same slice) as shown in the following equation 8.3.1.

$$\mathrm{SNR} = \sqrt{2}\frac{\mathrm{S_{image1}}}{\mathrm{SD_{|image1-image2|}}} \tag{8.3.1}$$

Figure 8.3.7 shows the SNR measured for the different activations (amplifier and transducer) using T_2-weighted FRFSE, FSPGR, and EPI. The amplifier ON means that the RF amplifier was activated with a DC supply and the transducer ON means that the transducer was activated and sonicated HIFU energy in the agar-based phantom. Transducer out means that the transducer was placed outside the MRI room. When the transducer was not activated without DC supply activation, the SNR was high. When the amplifier was powered on, the SNR dropped slightly meaning that the RF amplifier does not cause significant artifacts to the MR images and it has minimal effect on the SNR. The SNR also decreased slightly when the transducer was activated but it was not significant to affect the MR images and sequences that are usually used for MR thermometry.

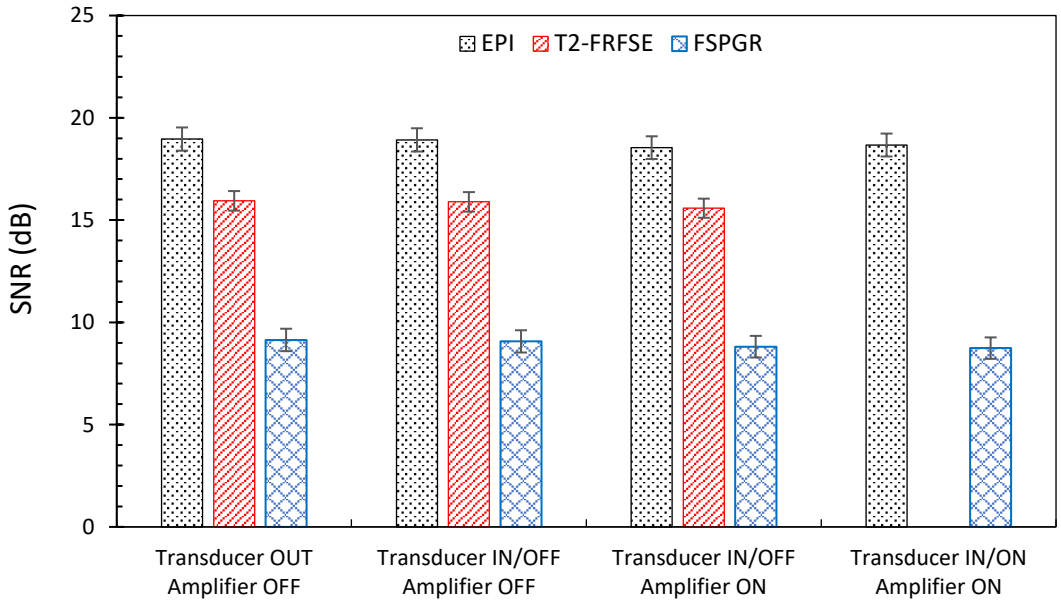

Figure 8.3.7: SNR using T_2-weighted FRFSE sequence measured for different conditions.

The points in the graph of Figure 8.3.8 show the SNR in the agar-based phantom for each sequence and each configuration.

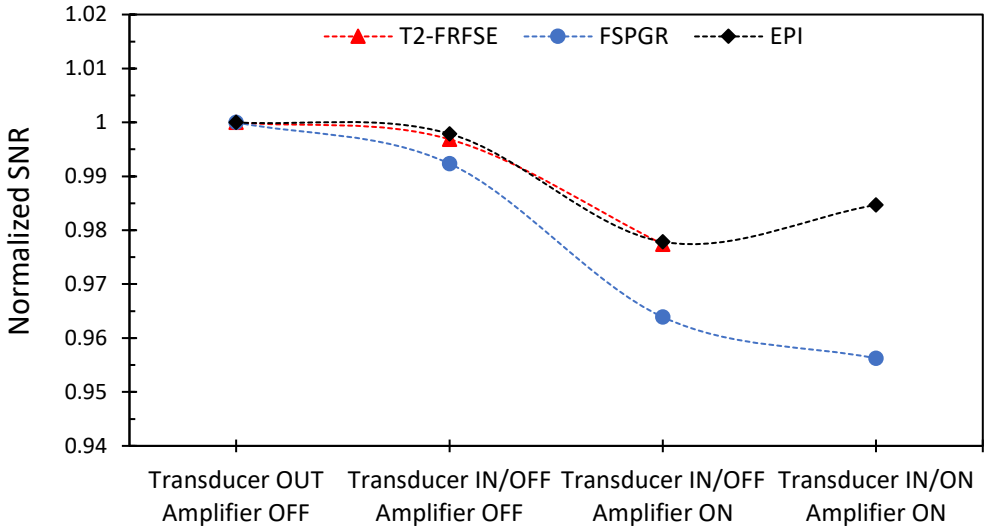

Figure 8.3.8: SNR for three MR imaging protocols with the system in different configurations.

MR images of different pulse sequences were acquired. A T_2-weighted FRFSE sequence was used as a high-resolution image of the different conditions. The MR thermometry sequences FSPGR and EPI were also obtained and the SNR for the different conditions was compared. Table 8.3.2 summarizes the MR pulse sequences used and the different conditions for which the SNR was calculated in order to estimate the SNR of the MR quality assurance phantom. Since during imaging the positioning device was static, the piezoelectric motors were deactivated in all tests. The electronic system that controls the piezoelectric motors and the optical encoders required DC electricity.

Table 8.3.2: List of MR sequences and conditions that were used to calculate SNR.

Nº	**MR sequences**
1	T_2-weighted FRFSE
2	FSPGR
3	EPI
	Conditions
1	Phantom only (baseline image)
2	Robotic device in MR bore (unconnected)
3	Robotic device in MR bore (connected) with deactivated electronic system
4	Robotic device in MR bore (connected) with activated electronic system

MR images of the cylindrical phantom taken with T_2-weighted FRFSE, FSPGR, and EPI are shown for the different conditions in Figure 8.3.9, 8.3.10, and 8.3.11 respectively. The difference between the baseline image (with phantom only) and the image taken in each different condition is also depicted.

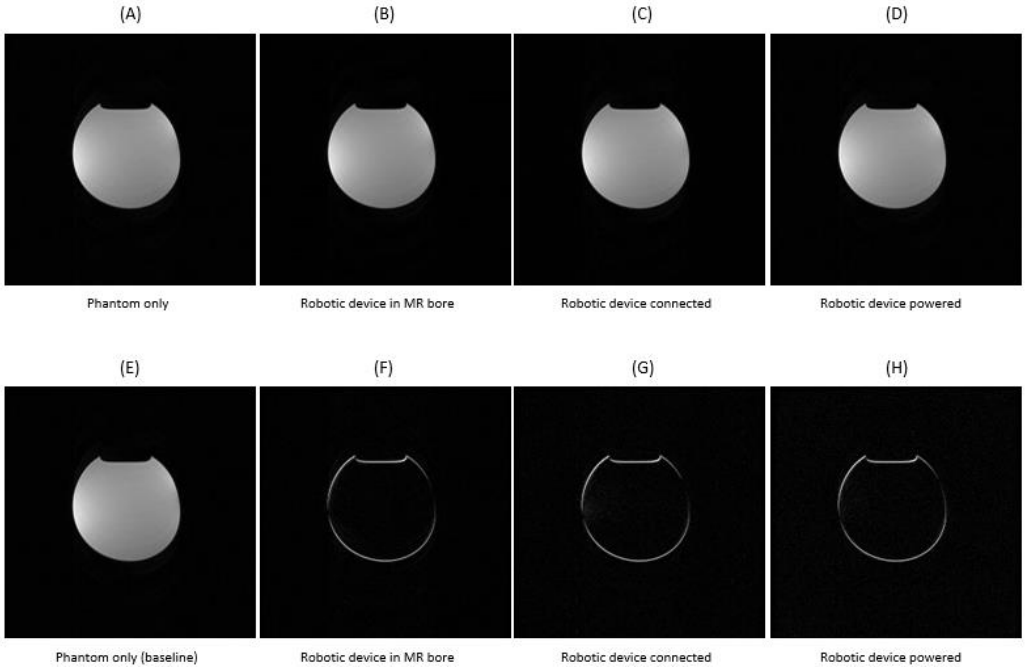

Figure 8.3.9: MR images (top) obtained using T_2-weighted FRFSE sequence for the different conditions and the corresponding differences (bottom) between each condition and the baseline (phantom only).

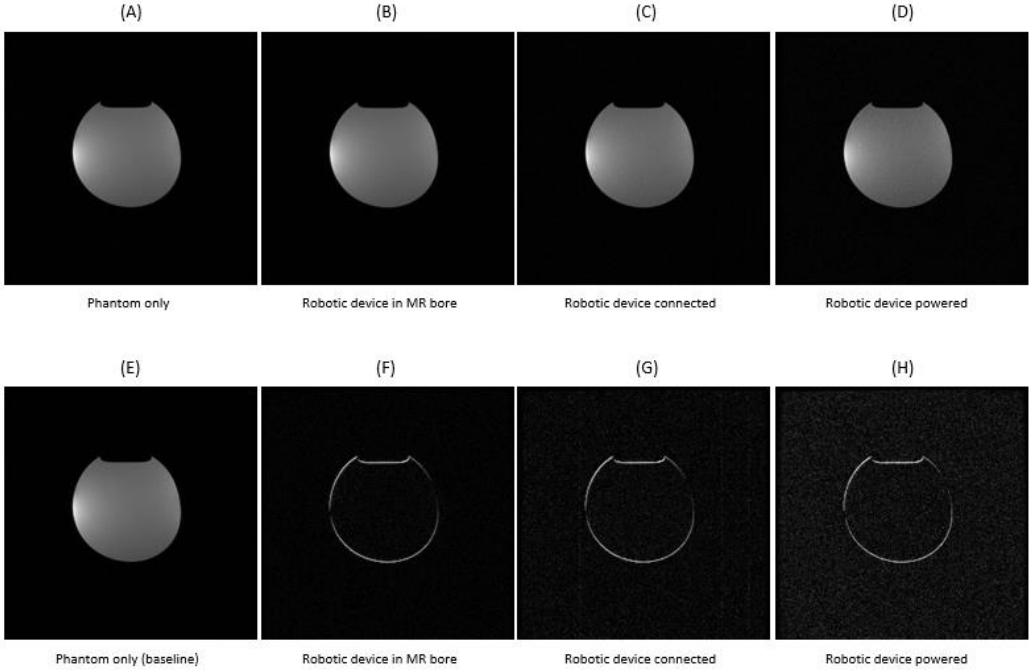

Figure 8.3.10: MR images (top) obtained using FSPGR sequence for the different conditions and the corresponding differences (bottom) between each condition and the baseline (phantom only).

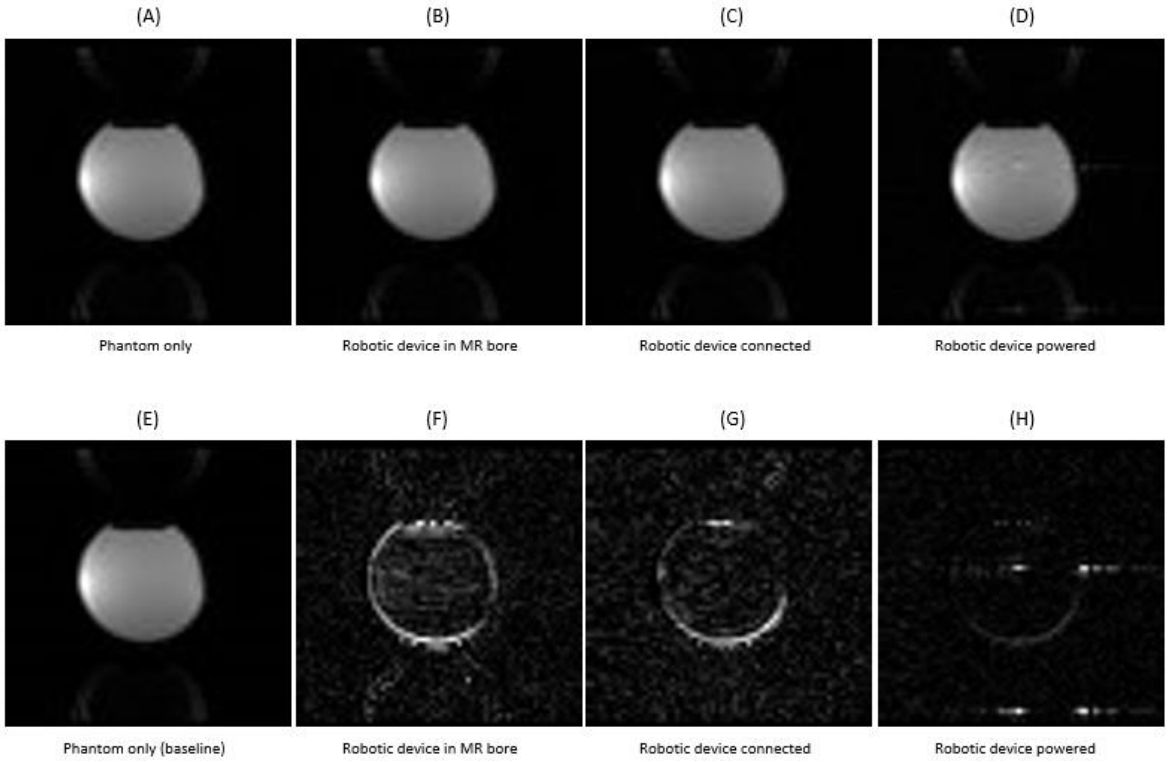

Figure 8.3.11: MR images (top) obtained using the EPI sequence for the different conditions and the corresponding differences (bottom) between each condition and the baseline (phantom only).

Figure 8.3.12 shows the SNR measured for the different conditions using T_2-weighted FRFSE, FSPGR, and EPI sequence.

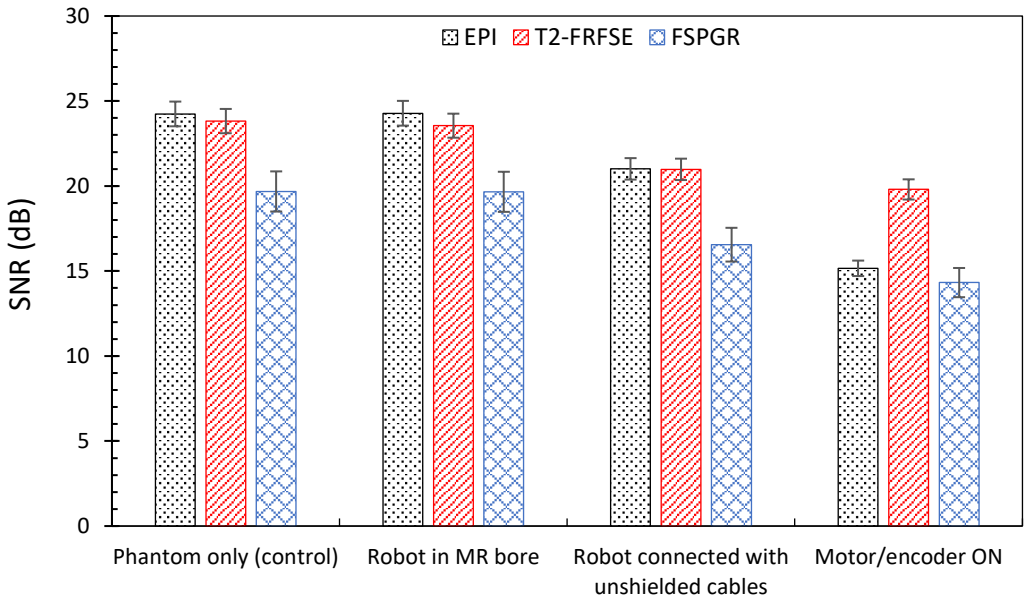

Figure 8.3.12: SNR using T_2-weighted FRFSE sequence measured for different conditions.

Figure 8.3.13 shows the SNR in the phantom for each sequence and each configuration.

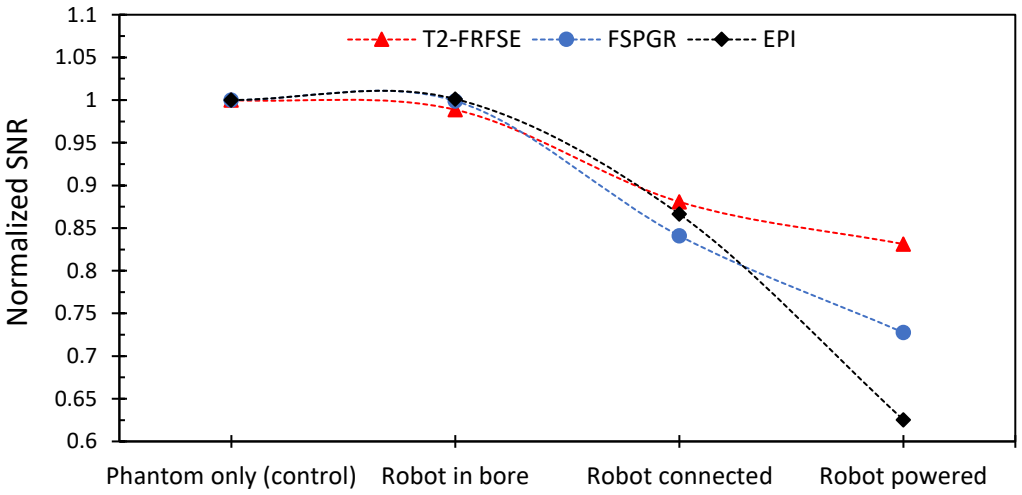

Figure 8.3.13: SNR for three MR imaging protocols with the system in different configurations.

The uniformity of the agar-based phantom for the different configurations was investigated. The non-uniformity index (NUI) is a suitable standardized measure to investigate magnetic field uniformity. Scanning sequences, imaging planes, coils, and the presence of metallic materials can influence MR image uniformity. To evaluate the uniformity of the images, the signal intensity was measured at 5 sample points according to the standardized sample method laid out by NEMA (Figure 8.3.14.a), which allows for a successive NUI calculation of each image. The 5-point measurement was used for each different configuration in order to investigate whether the different conditions of the robotic system affected the uniformity of the phantom. The 5-point measurement was also used for each different configuration and MR sequence (presence of the robotic devices, motors, and encoders) for the MR quality assurance phantom. Figure 8.3.14.b shows the standardized sample method laid out by NEMA in order to calculate the NUI of the MR quality assurance phantom for the different configurations.

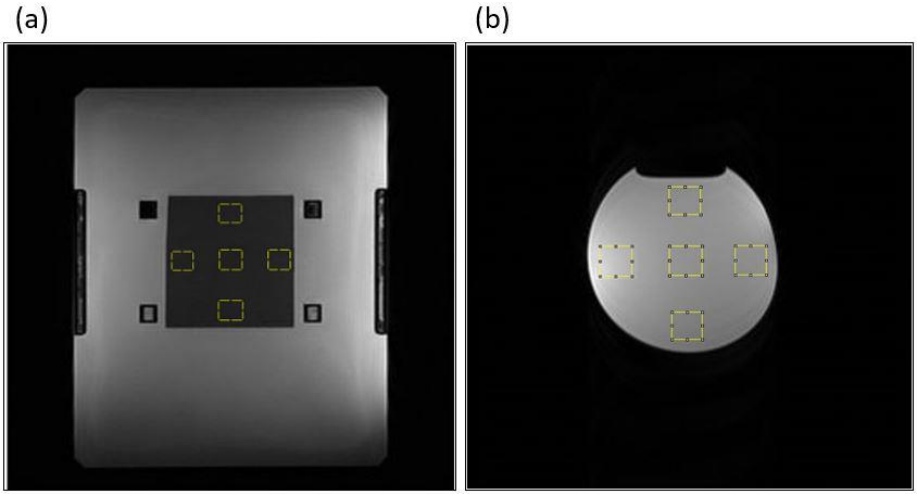

Figure 8.3.14: Standardized 5-point measurement method based on NEMA in order to calculate the NUI of the a) agar-based phantom and b) MR quality assurance phantom for the different configurations.

Figure 8.3.15 shows the NUIs (in %; lower means more uniform) based on 5 sampling points for the different configurations as calculated from the agar-based phantom.

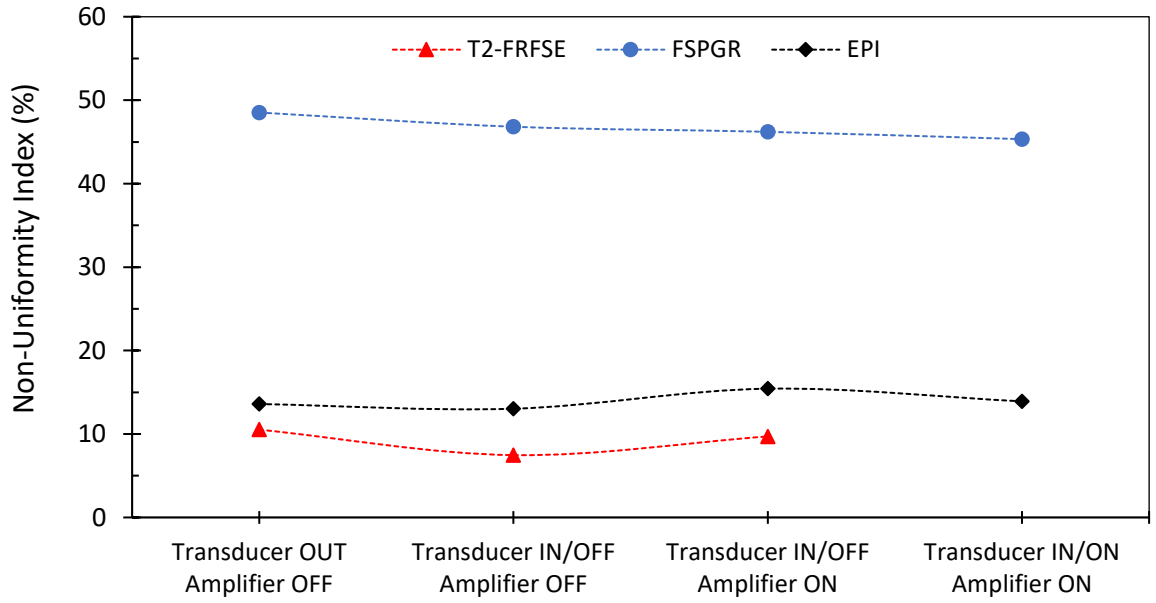

Figure 8.3.15: NUI versus different configurations using three MR sequences for the agar-based phantom.

Figure 8.3.16 shows the NUIs based on 5 sampling points for the different MR sequences and configurations as calculated from the MR quality assurance phantom.

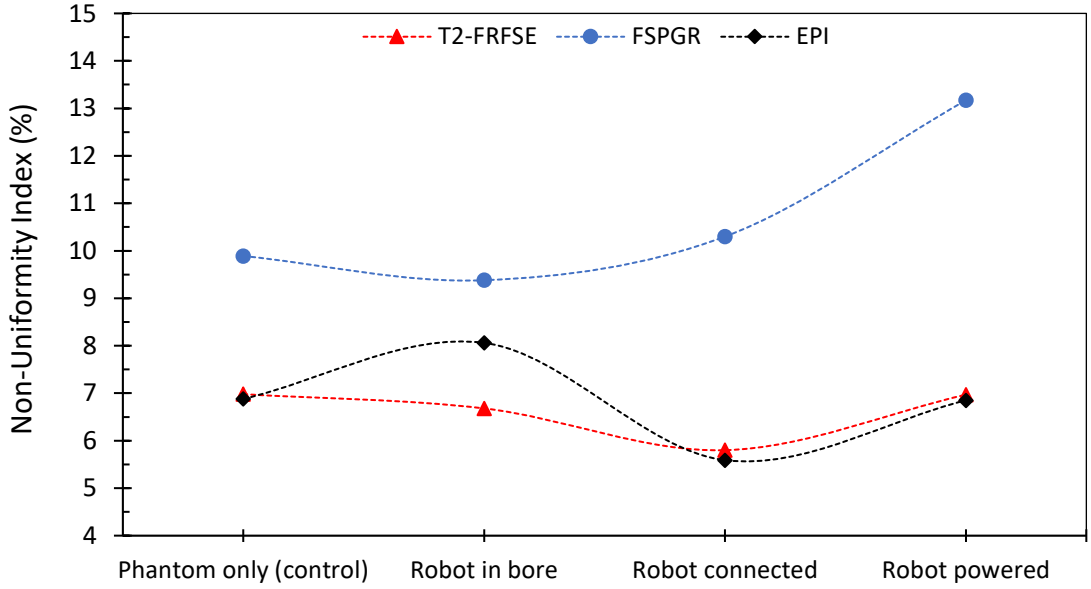

Figure 8.3.16: NUI versus condition for three MR sequences obtained in the MR quality assurance phantom.

8.4 Estimation of the motion accuracy of the robotic system

The accuracy of motion was assayed using digital calipers with specially designed set-ups. The motion and limitations of each stage of the developed 4-DOF prostate robotic device that includes large piezoelectric motors are explained. Special parts were designed in order to secure the digital calipers at fixed positions and obtain accurate measurements. The experimental setup of the evaluation of each stage is also described. The accuracy of the linear motion was estimated at motion steps of 1, 5, 10, 15, and 20 mm. The accuracy of the angular motion was also assessed at step angles of 1, 5, 10, and 15^{o}. The error of both linear and angular motion of the robotic device as well as the speed of each motion were calculated. The accuracy was assessed only for the 2 computer-controlled stages since the Z and Y stages are manually controlled. Besides testing the accuracy of the robot using digital calipers, the accuracy of the motion was evaluated using MR thermometry by acquiring FSPGR images.

The fully assembled 4-DOF robotic device utilising large motors (USR60-S3N, Shinsei Corporation) is shown in Figure 8.4.1.a (front view) and Figure 8.4.1.b (rear view). All components which have been assembled to develop the robotic system are fully described in detail in section 4. X and Θ axes can either be controlled through the software or the manual controls of the electronic system. The height and inclination of the device can only be changed by the hand lever for the Z-axis or the knob for the Φ-axis. Figure 8.4.1.a indicates the computer-controlled X and Θ axes and Figure 8.4.1.b indicates the knob mechanisms which are used to move the robotic device in the Z and Φ direction.

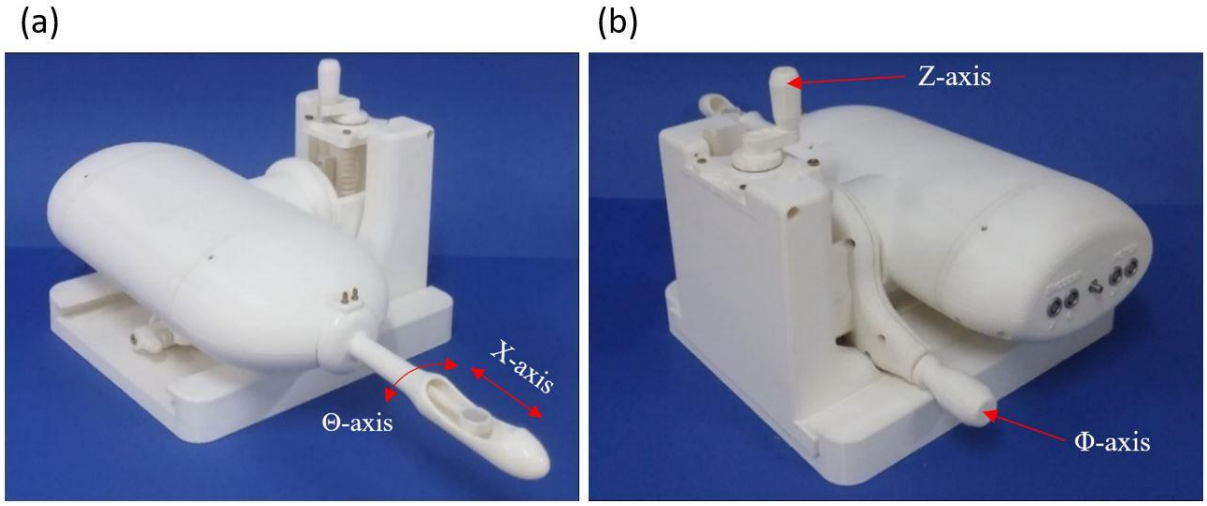

Figure 8.4.1: The 4-DOF robotic system a) front view indicating the 2 computer-controlled axes (X and Θ), and b) rear view indicating the mechanisms of the 2 manual axes (Z and Φ).

There are some dimensional limits due to the geometrical design of the robotic system. The linear axis (X-axis) was designed to move the ultrasonic transducer in forward and backward directions. It has a range of 50 mm. The Z-axis has a range of motion of 60 mm. The Θ-stage has a range of motion of 180^o (90^o CW and 90^o CCW). However, the design of the probe limits the angular movement in a range of motion of 30^o (15^o in each direction).

The motion accuracy of the X-axis was evaluated using a digital caliper (ROHS NORM 2002/95/EC). A specially designed removable setup was developed in order to secure the digital caliper and thus measure more accurately the linear motion of the robotic system. The setup was 3D printed with ABS using a 3D printer (F270, Stratasys Ltd.). Figure 8.4.2 shows the CAD drawing of the robotic device with the extra part that was designed to accurately evaluate the motion of the robotic system. The removable part was easily attached to the robotic device by replacing the probe.

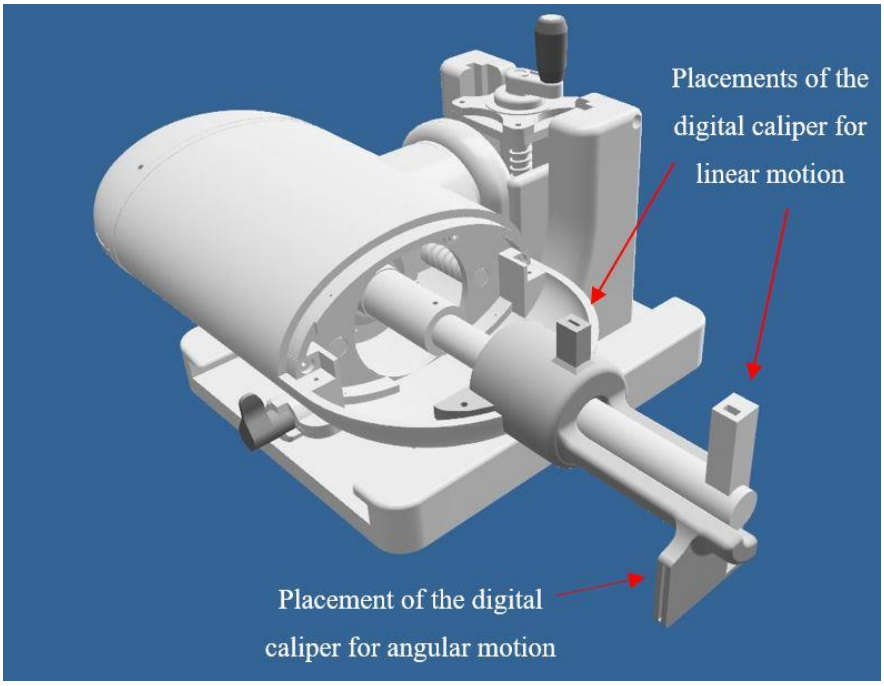

Figure 8.4.2: CAD drawing of the robotic device with the removable part (attached to the probe) that was used to evaluate the linear and angular motion of the robotic device.

Figure 8.4.3.a shows the CAD drawing of the robotic device coupled with the removable part and the digital caliper attached used for estimation of the accuracy of the linear motion while Figure 8.4.3.b shows the corresponding photo.

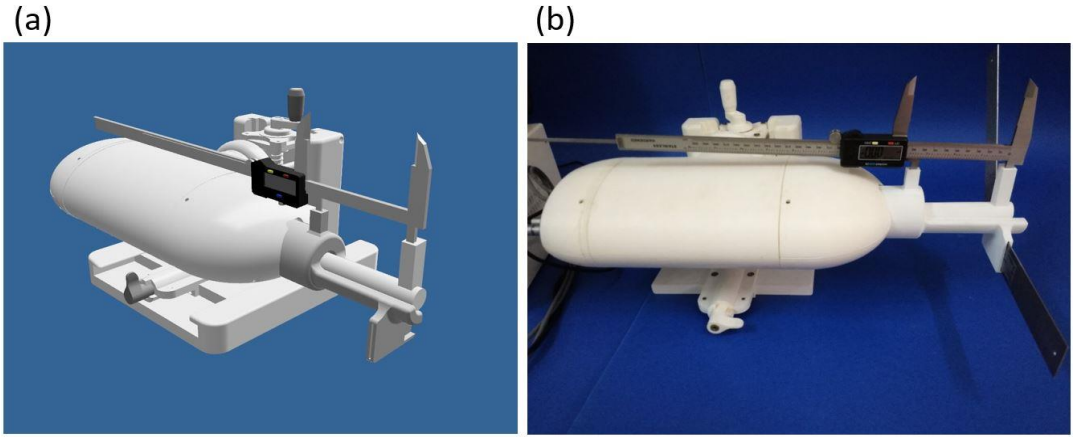

Figure 8.4.3: a) CAD drawing of the robotic device with the digital caliper attached to the removable part for the estimation of the accuracy of the linear motion, and b) Corresponding photo.

The piezoelectric motors and the encoders of the robotic device were connected to the electronic system and consequently to the software. The software provides many capabilities including the motion control of the robotic device. By assessing the precision of the robotic system, the accurate motion of the piezoelectric motors was established. The experimental set-up used to estimate the accuracy of the linear motion is shown in Figure 8.4.4.

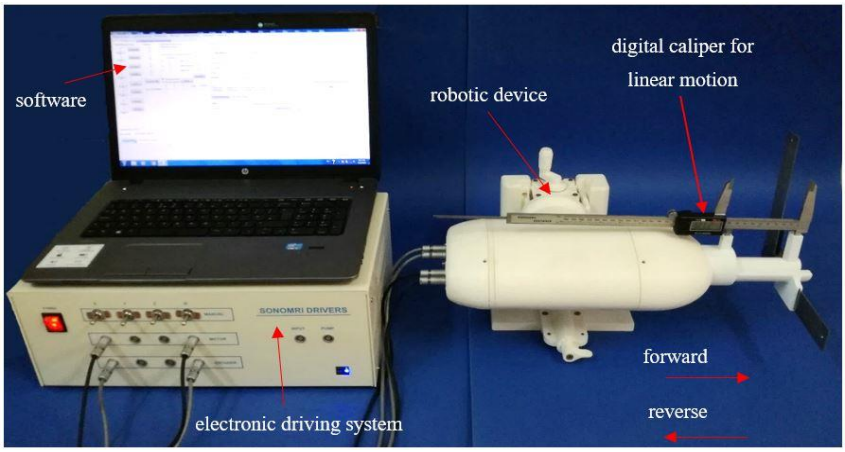

Figure 8.4.4: Experimental setup in order to evaluate the linear motion of the robotic device.

The robot was moved using the software at a certain distance in forward and reverse direction and the actual distance of the motion was recorded using the digital caliper. Motion steps of 1, 5, 10, 15, and 20 mm were evaluated. Accuracy was evaluated as iterative comparison of the distance as set by the software and the distance measured by the caliper. The first step before the evaluation was to calculate the overhead factor that existed due to the piezoelectric motors and this overhead was always subtracted from the final results. Overhead time is the processing time required to send commands to the software. For the linear motion, the overhead factor was 0.1 mm. Figure 8.4.5 shows the distance measurements for 30 repetitions on the X-axis for step movement (forward and reverse) of 1, 5, 10, 15, and 20 mm.

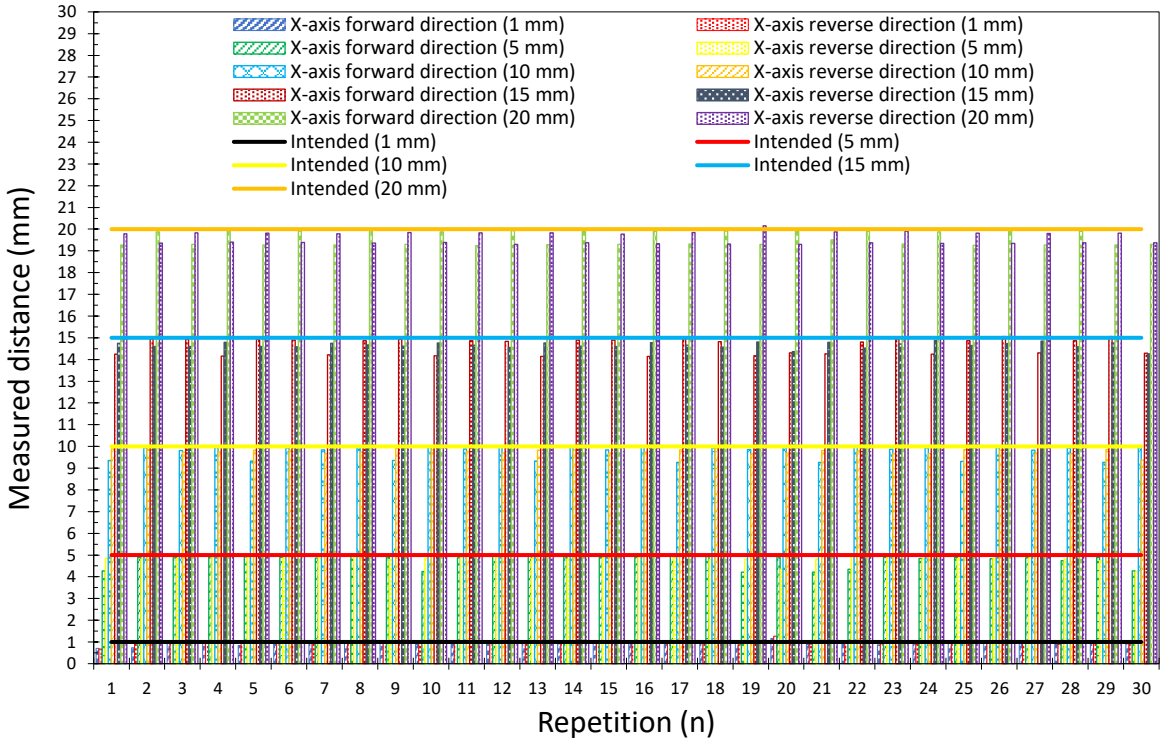

Figure 8.4.5: Distance measurements for 30 repetitions on the X-axis for various movement step in forward and reverse direction. The straight lines indicate the intended distances.

Figure 8.4.6 shows the mean values of the actual measured distance versus the intended distance for the X-axis forward and reverse motion at different step movements.

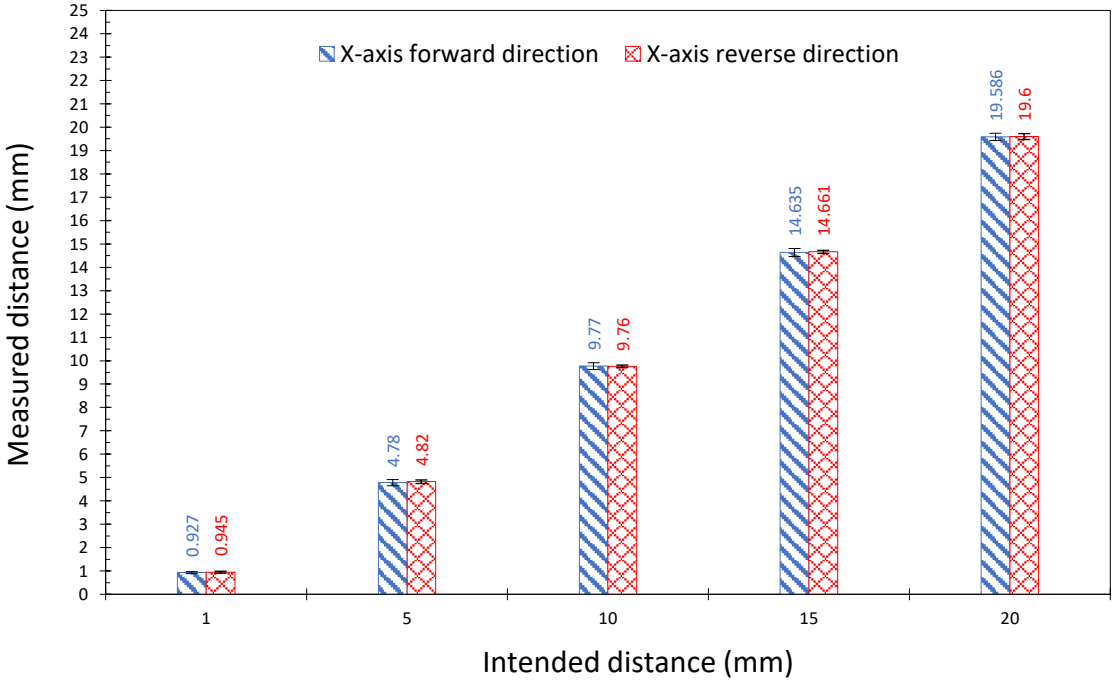

Figure 8.4.6: Mean values of the measured distance versus intended distance for the X-axis forward and reverse motion at different step movements.

The error at each step movement of the robotic device was estimated for the X-axis (forward and reverse) motion. Table 8.4.1 summarizes the error measured at motion steps of 1, 5, 10, 15, and 20 mm for the X-axis forward and reverse directions.

Table 8.4.1: List of error estimated at different motion steps for the X-axis forward and reverse directions.

Step (mm)	Error-forward motion (µm)	Error-forward motion (%)	Error-reverse motion (µm)	Error-reverse motion (%)
1	73	7.3	55	5.5
5	225	4.5	179	3.58
10	233	2.33	237	2.37
15	365	2.43	339	2.26
20	414	2.07	400	2

The speed of the linear motion of the robotic device was also estimated. Motion at varied distances was performed and the time needed to travel that particular distance was measured. The average speed of 1, 5, 10, 15, and 20 mm distances was calculated to be 0.59 mm/s for the forward motion and 0.72 mm/s for the reverse motion. The speed at 1 mm distance was also included in the overall average speed since the robotic device was designed for slow speed to allow encoders to achieve accurate reading. Figure 8.4.7 demonstrates the speed of the linear motion of the robotic system of the forward and reverse direction for varying intended distances.

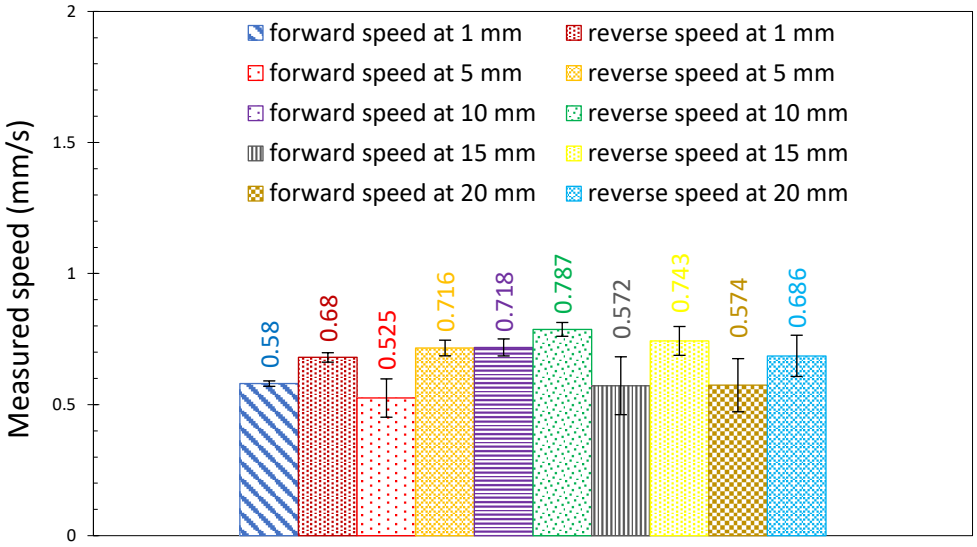

Figure 8.4.7: Measured speed of the linear motion of the robotic system of the forward and reverse direction for varying intended distances.

The accuracy of the angular motion in the Θ-axis was also evaluated. The robot was moved using the software at certain degrees and the actual motion in degrees was measured using another digital caliper which can measure the angle in degrees. A special 3D-printed part was designed to hold the digital caliper and thus accurately measure angular motion. Figure 8.4.8.a shows the CAD drawing of the robotic device with the special part and the digital caliper attached for estimation of the accuracy of the angular motion while Figure 8.4.8.b shows the corresponding photo.

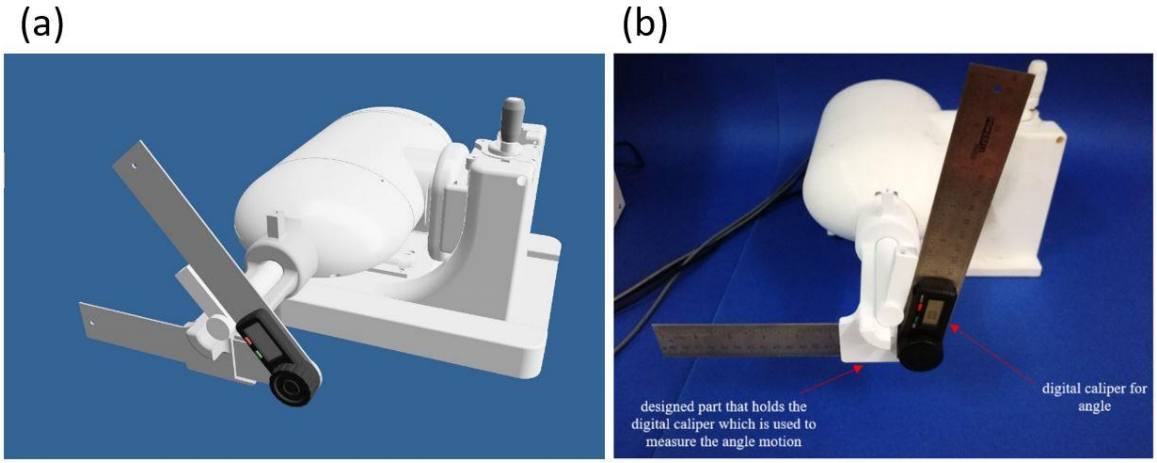

Figure 8.4.8: a) CAD drawing of the robotic device with the digital caliper attached to the special part for the estimation of the accuracy of angular motion, and b) Corresponding photo.

Figure 8.4.9 shows the experimental set-up with the electronic driving system and software. Angle steps of 1, 5, 10, and 15^{o} were evaluated. It was important as a first step before the evaluation to calculate the overhead factor that existed. For the angular motion, the overhead factor was 0.4^{o}. The CW and CCW direction of the robotic device as measured during the evaluation is shown below in Figure 8.4.9.

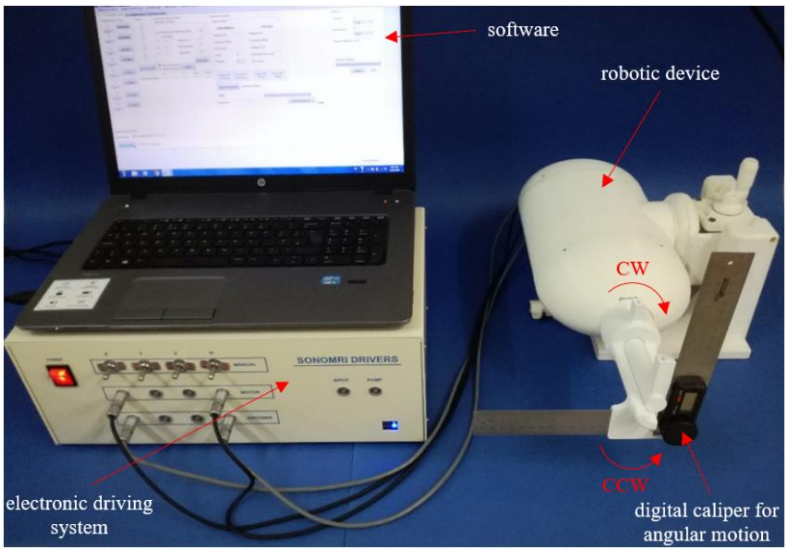

Figure 8.4.9: Experimental setup in order to evaluate the angular motion of the robotic device.

Figure 8.4.10 shows the angle measurements for 30 repetitions on the Θ-axis for angle movement (CW and CCW) of 1, 5, 10, and 15°.

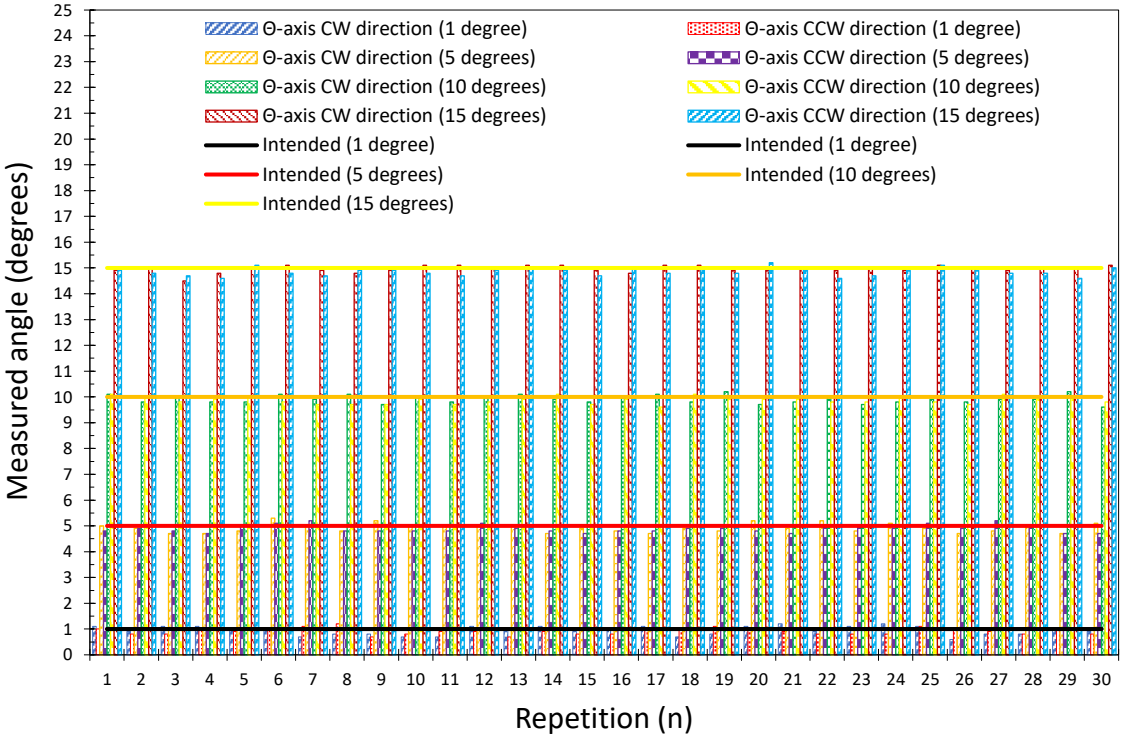

Figure 8.4.10: Angle measurements for 30 repetitions on the Θ-axis for various angle step in CW and CCW direction. The straight lines indicate the intended angles.

Figure 8.4.11 shows the mean values of the actual measured angle versus the intended angle for the Θ-axis CW and CCW motion at different angle movements.

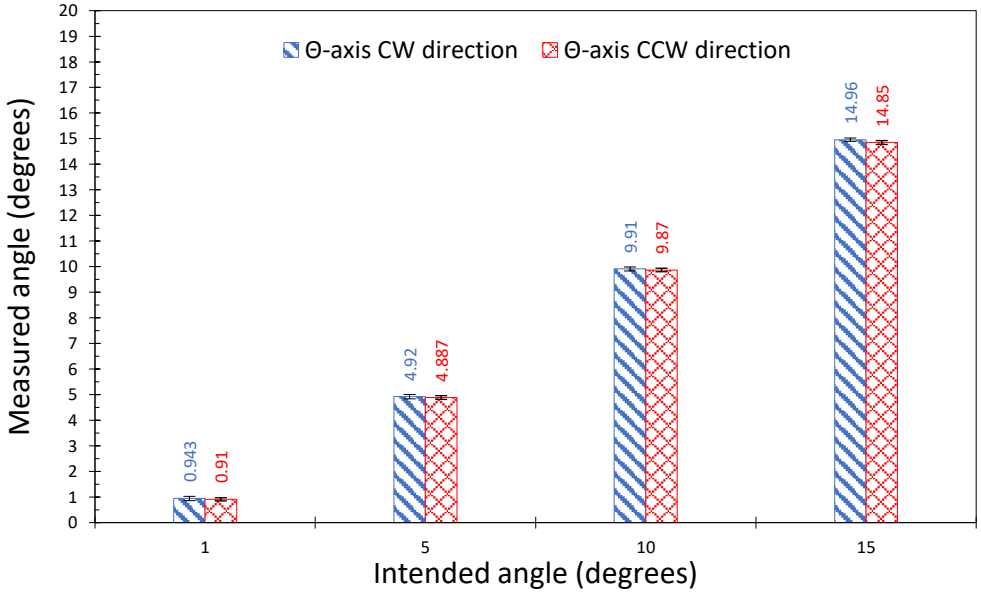

Figure 8.4.11: Mean values of the measured angle versus intended angle for the Θ-axis CW and CCW motion at different angle movements.

The error at each step movement of the robotic device was also estimated for the Θ-axis angular motion. Table 8.4.2 summarizes the error measured at motion steps of 1, 5, 10, and 15° for the Θ-axis CW and CCW directions.

Table 8.4.2: List of error estimated at different angle steps for the Θ-axis CW and CCW directions.

Step (degrees)	Error-CW motion (µm)	Error-CW motion (%)	Error-CCW motion (µm)	Error-CCW motion (%)
1	57	5.7	90	9
5	80	1.6	113	2.27
10	90	0.9	133	1.33
15	37	0.24	147	0.98

The speed of the angular motion of the robotic device was also estimated. The average speed of 1, 5, 10, and 15° was calculated to be 1.33 °/s for the CW direction and 1.37 mm/s °/s for the CCW direction. Figure 8.4.12 demonstrates the speed of the angular motion of the robotic system of the CW and CCW direction for varying intended angle degrees.

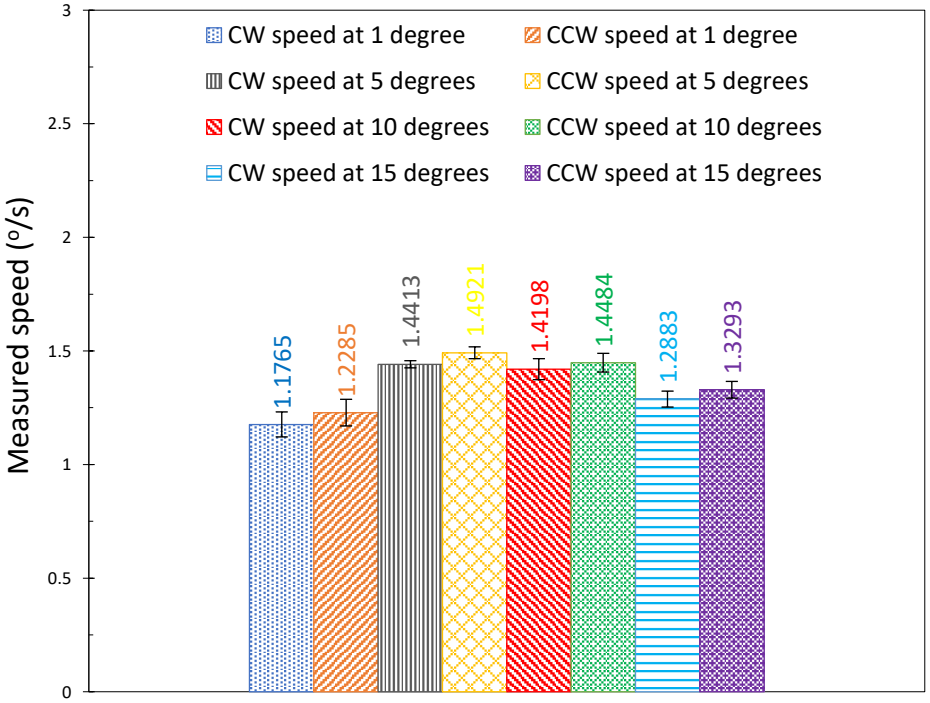

Figure 8.4.12: Measured speed of the angular motion of the robotic system of the CW and CCW direction for varying intended angle degrees.

Besides testing the accuracy of the robot using digital calipers, the accuracy of the motion was also evaluated using MR thermometry by acquiring FSPGR images and observing the ultrasonic beam location in planes perpendicular and parallel to the beam direction. While the robotic device was placed in the MRI bore, low power sonications in linear steps of 10 mm were performed in an agar-based prostate-mimicking phantom and the position of the focal beam (perpendicular to beam direction) was located. The angular motion was also evaluated by observing the ultrasonic beam (parallel to beam direction) through MR thermometry. Prior to the placement of the robotic device in the MRI room, the probe of the robotic device was covered by a medical condom and filled with degassed water using a water pump as shown in Figure 8.4.13.a. Both the 4-DOF robotic device and the agar-based phantom were placed on the scanner table and inside the MRI bore as illustrated in Figure 8.4.13.b.

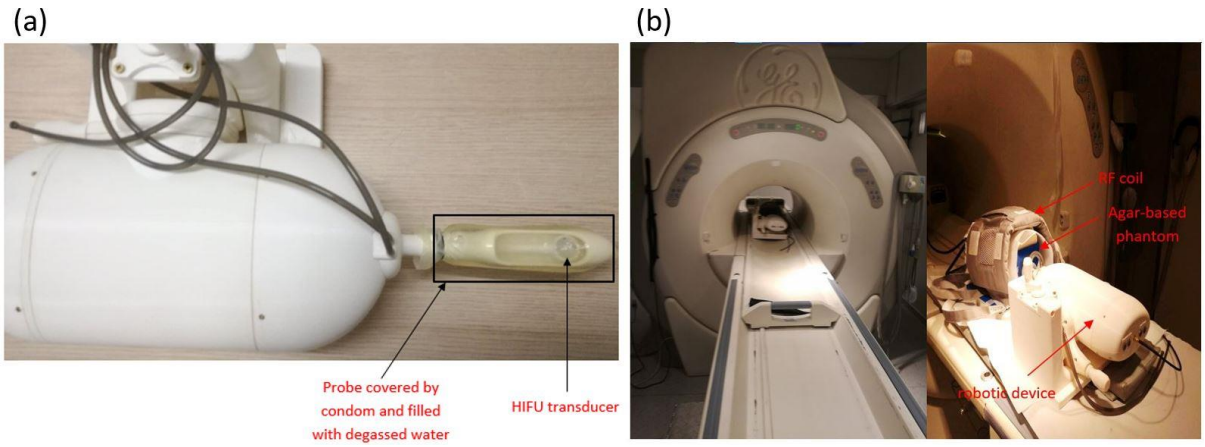

Figure 8.4.13: a) The 4-DOF prostate robotic device with the probe covered by a medical condom and filled with degassed water, and b) Experimental set-up inside the MRI room to evaluate the linear and angular motion of the robotic device using MR thermometry.

The signal generator, amplifier, and driving electronic device remained outside the MRI room and controlled by the software. The robotic device was connected to the drivers' electronic system through four wires, two for X and Θ motor for power supply and 2 for X and Θ encoder for feedback reading. The HIFU transducer of 4.4 MHz was connected to the RF amplifier and signal generator through the penetration panel (Faraday cage). A filter (L8959, Anatech Electronics) was also placed between the connection of the HIFU transducer and the RF amplifier. An RF coil was placed around the agar-based phantom to enhance the MRI signal. The schematic diagram of the experimental set-up is presented in Figure 8.4.14.

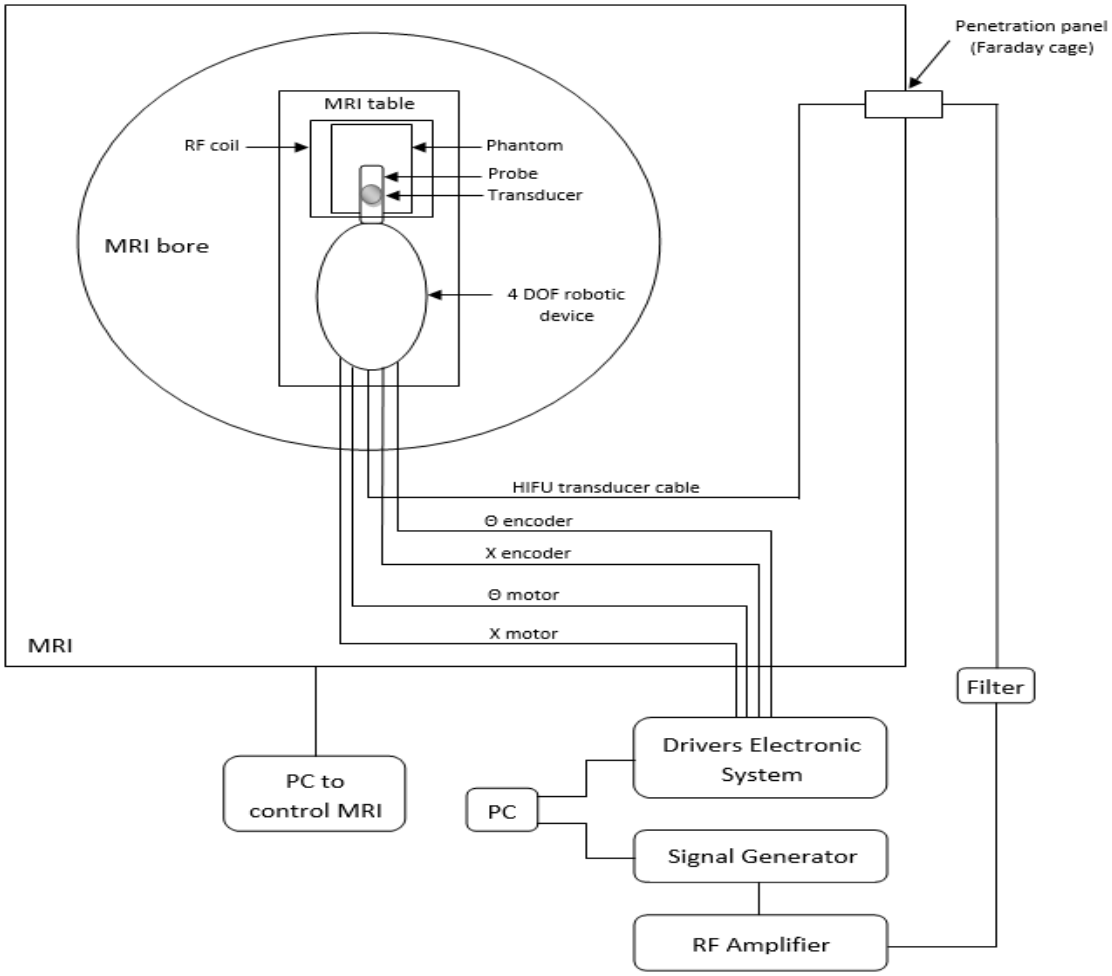

Figure 8.4.14: Schematic diagram of the experiment to evaluate the linear and angular motion of the robotic device using MR thermometry.

Prior to the evaluation of the accuracy motion of the robotic system, T_2-weighted FSE images were acquired to check the coupling between the probe and the prostate-mimicking agar-based phantom. The coupling was observed to be perfect as shown in Figure 8.4.15.

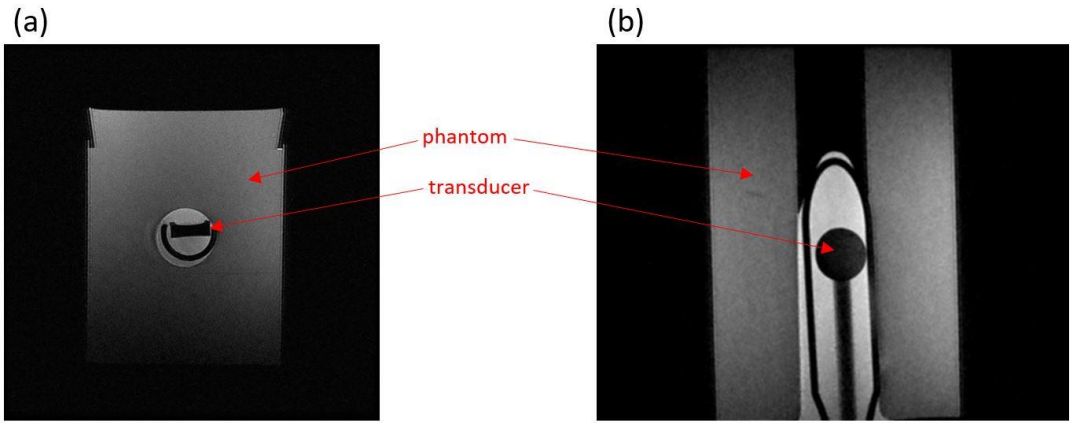

Figure 8.4.15: T_2-weighted FSE image of the probe and rectum-mimicking agar-based phantom, a) axial plane, and b) coronal plane.

FSPGR images were acquired on axial and coronal planes by changing the position of the transducer along the X-axis (Z-axis of MRI) and the angle of the transducer face (Θ-axis). After data acquisition, phase images were reconstructed and unwrapped for further processing using a custom-made MATLAB (MathWorks, Inc., Natick, MA, USA) GUI. The phase difference ΔΦ was calculated by subtracting the 'mask' phase image from the rest of the phase images. An acoustic power of 20 W was applied and a temperature change of 15 ^{o}C was calculated in the agar-based phantom for each movement. A linear grid of four motions of 10 mm step was performed on an axis parallel to the MRI Z-axis and an angular grid of five motions of 10^{o} on an axis parallel to the MRI Y-axis. For each step, six MR images were obtained (each image required 12 s MR scanning). The total sonication time was 36 s and MR images were also obtained during a 36 s cooling time. Figure 8.4.16 presents the temperature maps after data processing as obtained on coronal plane in order to observe the focal beam (perpendicular plane to US beam) while the transducer position was set at a starting position (X = 0 mm) for evaluation of the linear motion.

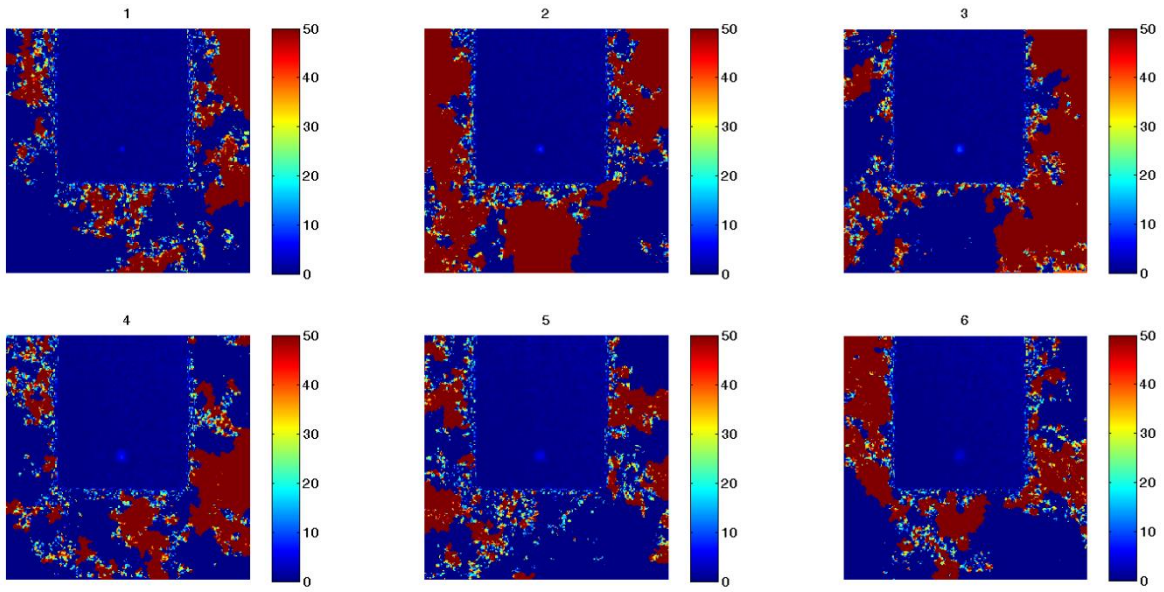

Figure 8.4.16: Temperature maps (coronal plane and perpendicular to beam direction) for sonication time of (1) 12 s, (2) 24 s, (3) 36 s and for a cooling time of (4) 12 s, (5) 24 s, (6) 36 s, X-axis transducer displacement at origin position (X = 0 mm).

Figure 8.4.17 presents the temperature maps after data processing as obtained on axial plane in order to observe the focal beam (parallel plane to US beam) while the transducer position was set at the origin position (Θ = 0^{o}) for evaluation of the angular motion.

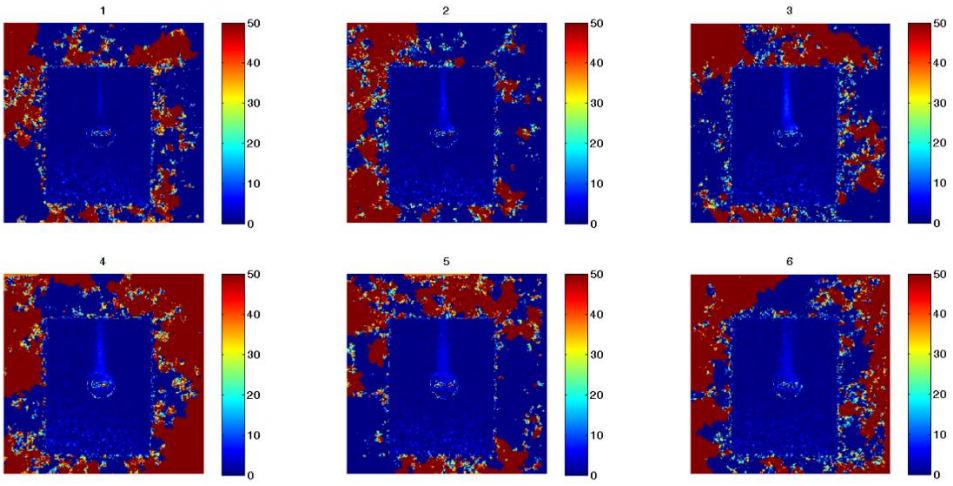

Figure 8.4.17: Temperature maps (axial plane and parallel to beam direction) for sonication time of (1) 12 s, (2) 24 s, (3) 36 s and for a cooling time of (4) 12 s, (5) 24 s, (6) 36 s, Θ-axis transducer displacement at origin position (Θ = 0°).

The two main movements (X and Θ axes) of the robotic device were evaluated through MR thermometry. The focal beam at the original position as well as at different angles in the range of 10 to 40° CW and 10° CCW was observed after acquisition of MRI phase images on the axial plane. MRI images were also obtained on coronal plane to evaluate the accuracy of X-axis movement of the robotic device. The robotic device was moved from 10 to 40 mm using a 10 mm step inside the prostate-mimicking agar-based phantom. In order to estimate the accuracy of the two movements, the MR thermometry images with the highest temperature elevation (at sonication time of 36 s) of each case for both movements (X and Θ axes) were presented in Figures 8.4.18 and 8.4.19, respectively.

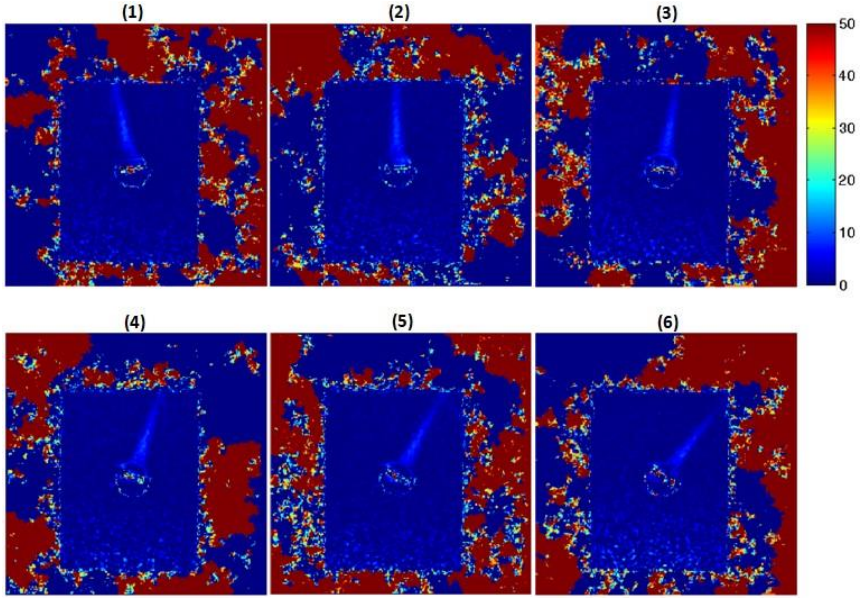

Figure 8.4.18: Temperature maps (axial plane and parallel to beam direction) at sonication time of 36 s for different angles of the transducer; (1) 10 degrees CCW, (2) origin position, (3) 10 degrees CW, (4) 20 degrees CW, (5) 30 degrees CW, and (6) 40 degrees CW.

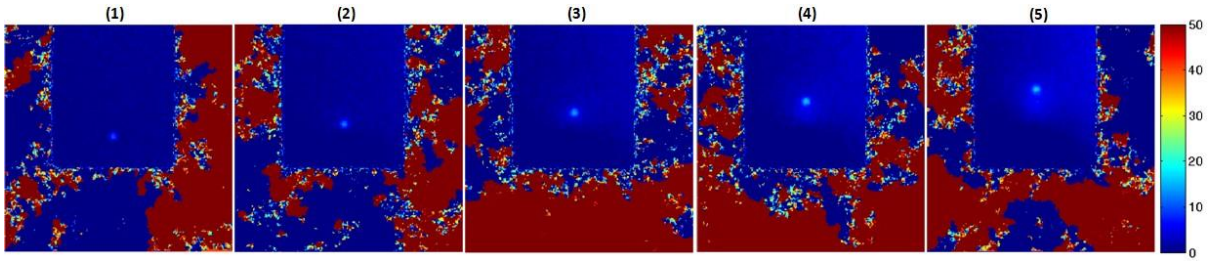

Figure 8.4.19: Temperature maps (coronal plane and perpendicular to beam direction) at sonication time of 36 s for different X-axis position of the transducer; (1) 0 mm, (2) 10 mm forward, (3) 20 mm forward, (4) 30 mm forward, and (5) 40 mm forward.

8.5 Near-field heating of the 3.2 MHz transducer

Evaluation of six different navigation algorithms was performed in order to examine their effect on the amount of the transducer's induced heating in the pre-focal region. Each of the six algorithms (Sequential, Triangular, Spiral, Random, Euler's, Square) was evaluated on an agar-based phantom using movement of the 3.2 MHz transducer in a 10 x 10 sonicated square grid with a 2 mm step, resulting in 100 movements of the transducer. The distance between the transducer and the bottom surface of the phantom was set at 2 cm resulting in a focal depth of 2.5 cm. A thermocouple was inserted in the phantom at 1 cm depth (1.5 cm from the focal plane) to measure induced heating in the near-field region. An acoustical power of 12 W was used for sonication time of 5 s. Different time delays of 0 s (no delay), 10 s, 20 s, 30 s, 40 s, 50 s, and 60 s were used in order to examine the effect of increasing time delay on temperature increase in the pre-focal region using each individual algorithm.

A HIFU procedure for the ablation of a large volume of tissue is highly dependent on the movement of the robotic device carrying the ultrasonic transducer. For the motion algorithm used by the robotic device to be classified as successful, it should be able to visit all cells of the target area and avoid visiting adjacent cells as much as possible in consecutive movements. In the majority of the cases, the robotic devices move using a sequential algorithm [306,307] which is an exception to this rule. The sequential treatment of tissue does not allow surrounding tissue cells to cool down, resulting in the production of excess heating especially in the pre-focal region (near-field). Heating in the near-field is a major drawback for a HIFU procedure since it limits the amount of ultrasonic energy supplied to the focal region affecting maximum tissue ablation and treatment time [308] and can sometimes result in skin burns [309].

The first study that provided a solution for reducing the pre-focal heating proposed using time delays between sonications with a 20 s delay greatly reducing the pre-focal heating [308]. Other

studies showed a variation of time delays between 30-90 s depending on the geometry of the transducer [310], with a 60 s delay completely eliminating pre-focal heating [311]. However, the delays used (20-90 s) increased the treatment time drastically, especially for large ablating targets. Thus, there is a need for new algorithms for controlling the motion of the positioning devices. The goal was to propose non-linear transducer motion algorithms (no motion in a straight line), that completely avoid tissue damage in the pre-focal heating and thus, reduce treatment time.

The HIFU system was composed of a signal generator (HP 33120A, Agilent Technologies) and an RF amplifier (AR amplifier, research model 75A250M4, 75 watts, 10 kHz-250 MHz, Acoustic Research).

An agar-based gel phantom was used as a medium to evaluate the amount of induced near-field heating. The phantom contained de-ionized, degassed water, 6 % w/v agar (Merck KGaA, EMD Millipore Corporation), and 4 % w/v silica (S5631, Sigma Aldrich). The dimensions of the phantom were 8 cm height, 8 cm width, and 8 cm length.

A 3D printed structure was designed to fit in an acrylic water tank in order to hold the phantom. The height of the tank was 18 cm, its width was 25 cm and its length was 35 cm. The holder was printed with ABS and designed such as a thermocouple (5SC-TT-K-30-36, type K insulated beaded wire, Omega Engineering) could be placed at distances of every 5 mm within the phantom. Figure 8.5.1 shows the CAD design of the ABS holder.

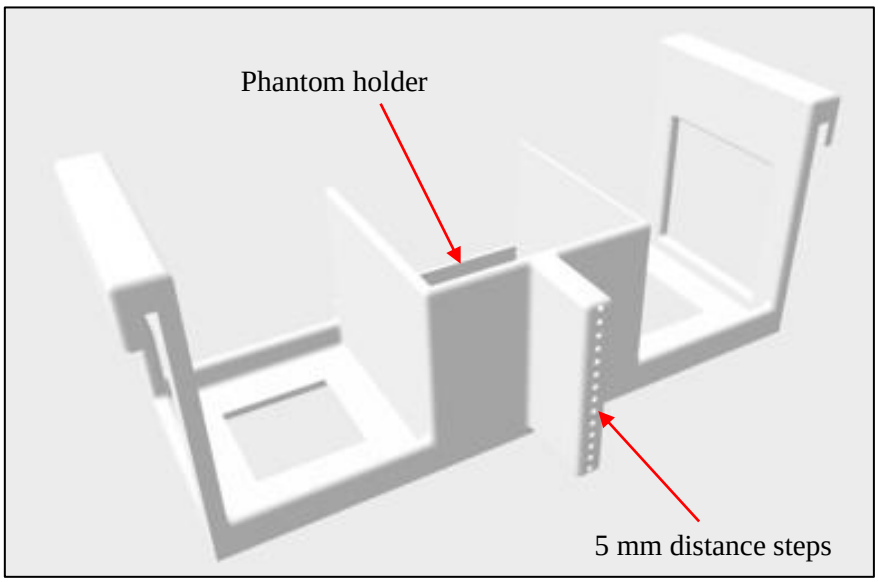

Figure 8.5.1: CAD drawing of the ABS phantom holder.

The transducer was moved by a system of stepping motors (VXM, Velmex Inc., Bloomfield, NY, USA) offering linear movement in X and Y axes. The controlling software was written in Visual Basic .Net (Microsoft, Redmond, Washington, USA) and offered the ability to control the grid size, voltage (acoustic power), sonication time, time delay, and motion algorithm. Figure 8.5.2 shows a screenshot of the controlling software while Figure 8.5.3.a shows a CAD design of the robotic device and the experimental setup. The complete experimental setup is shown in Figure 8.5.3.b.

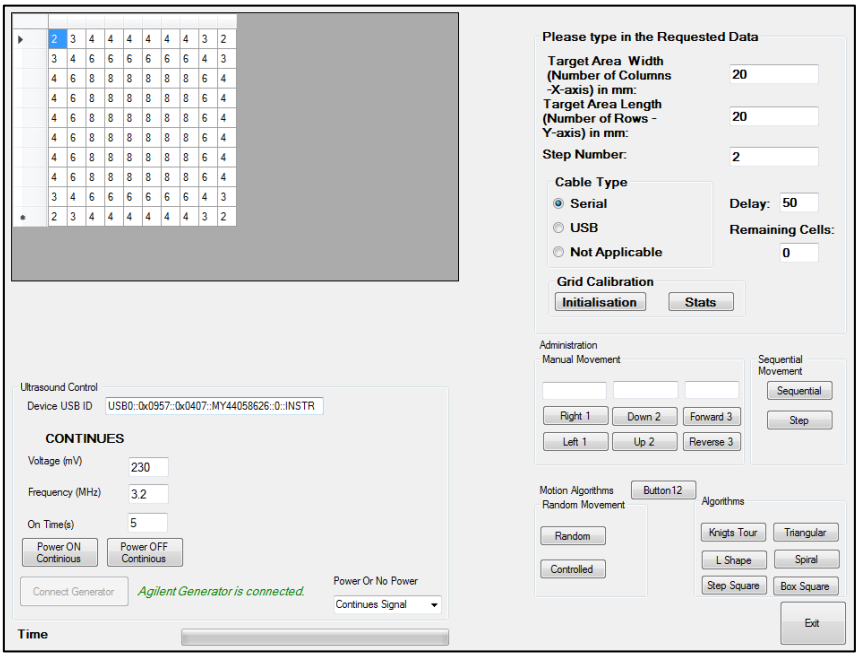

Figure 8.5.2: Software screenshot.

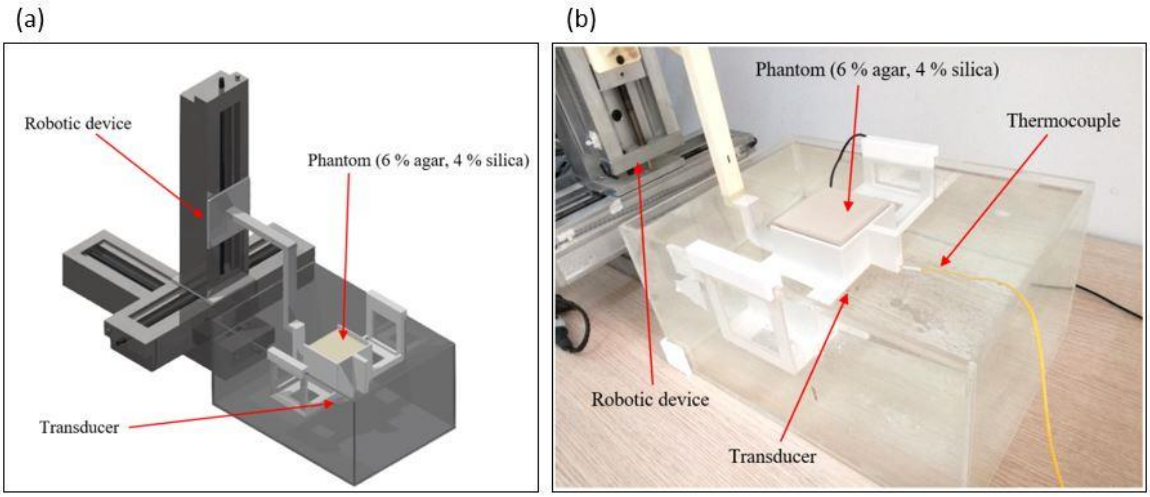

Figure 8.5.3: a) CAD design, and b) Photo of the experimental setup.

The following algorithms were used to evaluate the near-field heating of the transducer:

Sequential: In this algorithm, the transducer moves from left to right in the X-axis and then at the end of the X-axis moves one step down in the Y-axis. Then it starts to move from right to left and the process repeats itself. A conceptual diagram is shown in Figure 8.5.4.a while the sonicated grid is shown in Figure 8.5.5.a.

Triangular: In this algorithm, the movement follows a "V" shape, always advancing the robotic device one column to the right (X-axis) and either moving one row up on the Y-axis or one row down on the Y-axis. A conceptual diagram is shown in Figure 8.5.4.b while the sonicated grid is shown in Figure 8.5.5.b.

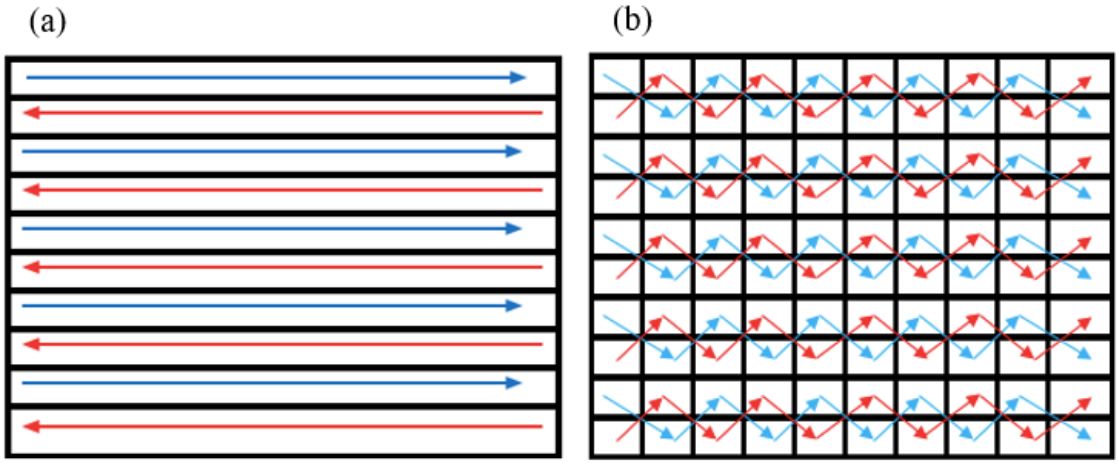

Figure 8.5.4: Conceptual diagram of transducer movement using a) Sequential algorithm, and b) Triangular algorithm.

Spiral: In this algorithm, the movement focuses on the spreading of the visiting cells in a concentric grid in order to reduce the pre-focal heating effect. The sonicated grid is shown in Figure 8.5.5.c.

Random: In this algorithm, random movement depends on the output value of a random function. A random number is generated and checked whether it has already been produced; if not, the positioning device is moved to that location. Otherwise, a new random number is generated. The sonicated grid is shown in Figure 8.5.5.d.

Euler's: In this algorithm, the movement imitates the movement of the "knight" on chess board games. Euler's solution allows "L" shape movement until every "square" of the sonicated grid is visited exactly once. The sonicated grid is shown in Figure 8.5.5.e.

Square: In this algorithm, the motion introduces the concept of concentric "squares". Each square is inside another square with its dimensions reduced by one row and one column. The sonicated grid is shown in Figure 8.5.5.f.

(a)

1	2	3	4	5	6	7	8	9	10
20	19	18	17	16	15	14	13	12	11
21	22	23	24	25	26	27	28	29	30
40	39	38	37	36	35	34	33	32	31
41	42	43	44	45	46	47	48	49	50
60	59	58	57	56	55	54	53	52	51
61	62	63	64	65	66	67	68	69	70
80	79	78	77	76	75	74	73	72	71
81	82	83	84	85	86	87	88	89	90
100	99	98	97	96	95	94	93	92	91

(b)

1	12	3	14	5	16	7	18	9	20
11	2	13	4	15	6	17	8	19	10
21	32	23	34	25	36	27	38	29	40
31	22	33	24	35	26	37	28	39	30
41	52	43	54	45	56	47	58	49	60
51	42	53	44	55	46	57	48	59	50
61	72	63	74	65	76	67	78	69	80
71	62	73	64	75	66	77	68	79	70
81	92	83	94	85	96	87	98	89	100
91	82	93	84	95	86	97	88	99	90

(c)

1	21	41	61	81	2	22	42	62	82
8	28	48	68	88	9	29	49	69	3
87	73	93	14	34	54	74	94	89	23
67	53	77	97	18	38	58	15	10	43
47	33	57	20	40	60	78	35	30	63
27	13	37	99	100	80	98	55	50	83
7	92	17	79	59	39	19	75	70	4
86	72	96	76	56	36	16	95	90	24
66	52	32	12	91	71	51	31	11	44
46	26	6	85	65	45	25	5	84	64

(d)

100	45	88	84	58	47	26	59	64	83
92	63	12	65	42	75	50	99	19	1
70	39	17	95	38	77	40	60	86	16
7	91	18	61	24	6	8	72	66	32
15	35	49	80	27	73	90	76	51	97
10	94	98	41	20	69	4	28	22	3
13	37	29	81	56	30	2	96	53	82
74	5	57	71	85	9	23	52	33	44
78	21	68	89	46	31	62	79	48	55
93	54	67	36	87	34	43	11	25	14

(e)

1	4	31	24	51	6	65	10	53	8
32	23	2	5	64	25	52	7	68	11
3	30	33	50	27	66	69	84	9	54
22	49	28	63	46	85	26	67	12	83
29	34	47	78	61	70	95	82	55	72
48	21	62	45	90	81	86	71	96	13
35	44	79	60	77	94	91	100	73	56
20	41	38	89	80	87	76	93	14	97
39	36	43	18	59	92	99	16	57	74
42	19	40	37	88	17	58	75	98	15

(f)

1	21	37	53	65	77	85	93	97	2
99	5	25	41	57	69	81	89	6	22
95	91	9	29	45	61	73	10	26	38
87	83	75	13	33	49	14	30	42	54
79	71	63	51	17	18	34	46	58	66
67	59	47	35	19	20	50	62	70	78
55	43	31	15	52	36	16	74	82	86
39	27	11	76	64	48	32	12	90	94
23	7	92	84	72	60	44	28	8	98
3	100	96	88	80	68	56	40	24	4

Figure 8.5.5: Transducer movement with each algorithm, a) Sequential, b) Triangular, c) Spiral, d) Random, e) Euler's, f) Square.

For each algorithm, an acoustical power of 12 W for a sonication time of 5 s was used with different time delays of 0 s (no delay), 10 s, 20 s, 30 s, 40 s, 50 s, and 60 s. Temperature change versus time at the near-field was recorded for each time delay and algorithm. Temperature change versus time using different time delays is shown for Sequential, Triangular, Spiral, Random, Euler's, and Square algorithms respectively on Figure 8.5.6.a, b, and Figure 8.5.7.a, b, c, and d.

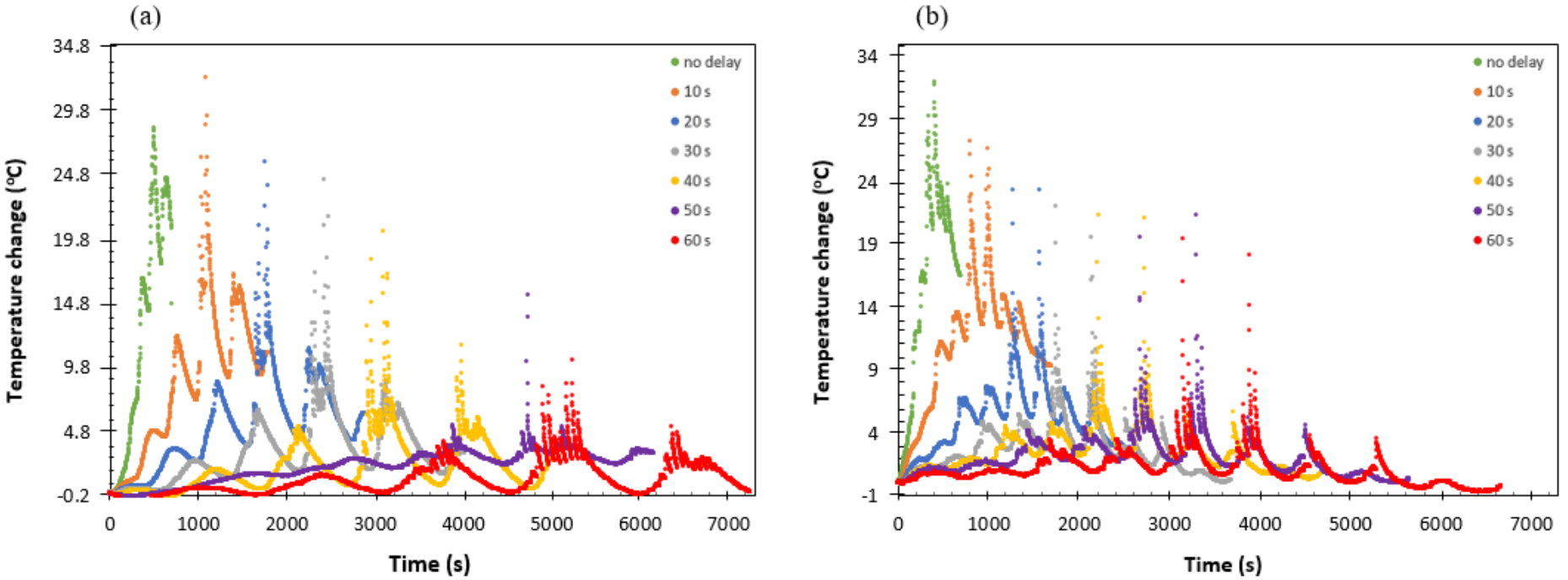

Figure 8.5.6: Temperature change versus time at near-field (1 cm depth) for sonication in a 10 x 10 grid using acoustical power of 12 W at focal depth = 2.5 cm, for sonication time of 5 s and varying time delays using a) Sequential algorithm, and b) Triangular algorithm.

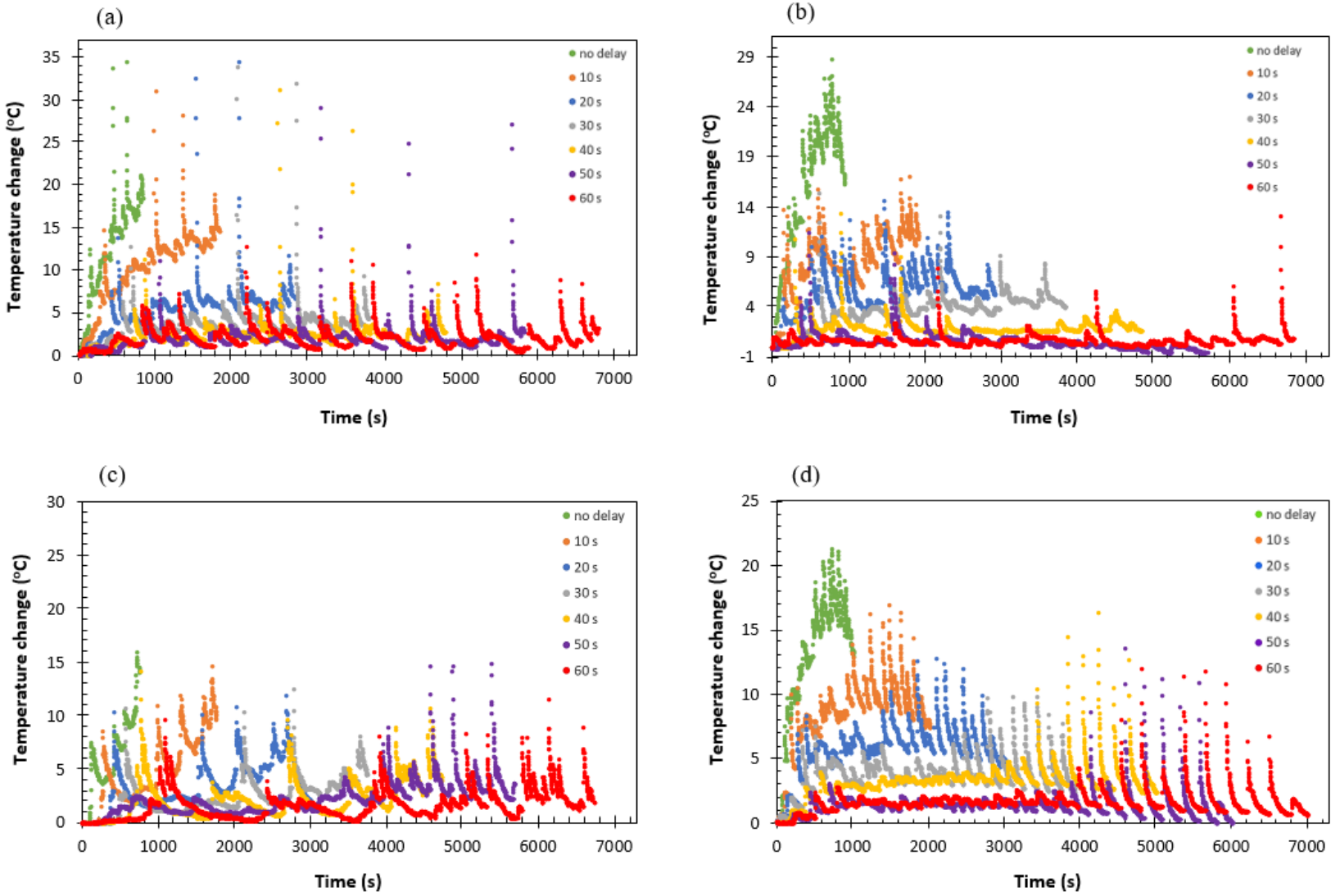

Figure 8.5.7: Temperature change versus time at near-field (1 cm depth) for sonication in a 10 x 10 grid using acoustical power of 12 W at focal depth = 2.5 cm, for sonication time of 5 s and varying time delays using a) Spiral algorithm, b) Random algorithm, c) Euler's algorithm, and d) Square algorithm.

The peak temperature change for each time delay and algorithm is shown in Table 8.5.1.

Table 8.5.1: Peak temperature change at near-field for sonication in a 10 x 10 grid using acoustical power of 12 W at focal depth = 2.5 cm, for sonication time of 5 s using different motion algorithms and varying time delays.

Algorithm	**Time delay**						
	0 s	10 s	20 s	30 s	40 s	50 s	60 s
	Temperature (ºC)						
Sequential	28.4	32.4	25.8	24.4	20.4	15.4	10.4
Triangular	32	27.2	23.4	22.1	21.3	21.4	19.5
Spiral	34.5	31.1	34.5	34	31.2	29.1	12.7
Random	28.9	17.1	14.6	15.4	13.4	11.4	13.1
Euler's	16	14.7	11.9	12.5	14.3	15	11.5
Square	21.3	16.9	12.8	9.8	16.3	13.6	12

The average temperature change for each different time delay and algorithm is shown in Table 8.5.2 and on average, it decreased with increasing time delay.

Table 8.5.2: Average temperature change at near-field for sonication in a 10 x 10 grid using acoustical power of 12 W at focal depth = 2.5 cm, for sonication time of 5 s using different motion algorithm and varying time delays.

Algorithm	**Time delay**						
	0 s	10 s	20 s	30 s	40 s	50 s	60 s
	Temperature (ºC)						
Sequential	11.5	8.4	5	3.08	2.05	2.05	1.04
Triangular	15.3	10.6	4.83	2.69	2.41	1.98	1.12
Spiral	11.97	10.14	5.37	3.66	2.45	1.97	2.11
Random	15.45	8.55	5.53	3.59	1.9	0.6	0.73
Euler's	5.88	4.68	3.39	2.38	2.17	2.26	1.68
Square	12.8	8.5	5.8	3.8	3.28	1.4	1.7

The time taken for robot movement was calculated for all six algorithms to examine the effect on total treatment time. Table 8.5.3 shows the total treatment time needed for each algorithm for complete elimination (<3 ^{o}C) of near-field heating.

Table 8.5.3: Total time needed for treatment using each algorithm for complete reduction in near-field heating.

Algorithm	Robot time (s)	Time delay for elimination of near-field heating (s)	Sonication time (s)	Scanning time (s)	Total time (s) = Robot time+ Scanning time+ Sonication time	Total time (min)
Sequential	102	40	500	4000	4602	76.7
Triangular	162	30	500	3000	3662	61
Spiral	297	40	500	4000	4797	79.95
Random	359-411	40	500	4000	4859-4911	80.9-81.9
Euler's	195	30	500	3000	3695	61.6
Square	466	50	500	5500	5966	99.4

8.6 Evaluation of the candidate transducers in agar-based phantoms

8.6.1 Evaluation of the 4.4 MHz transducer in phantoms

Agar-based gel phantoms with different quantities were used to evaluate the thermal heating of the transducers. The phantom and the transducer under evaluation having frequency of 4.4 MHz were placed in a structure (version 1) that was initially designed for evaluation purposes. The structure was designed and set-up so that the focal point of the transducer was located at a depth of 1.5 cm within the phantom. The phantom contained de-ionized, degassed water, 2 % agar, 1.2 % silicon dioxide, and 25 % evaporated milk. Figure 8.6.1.1.a shows the parts of the experimental set-up as well as the phantom while Figure 8.6.1.1.b shows the experimental set-up. The structure was placed in a 1.5 T MR system (Signa Excite, General Electric) surrounded by a GPFLEX coil (USA Instruments). Figure 8.6.1.1.c illustrates the acrylic water tank with the structure on the MRI table.

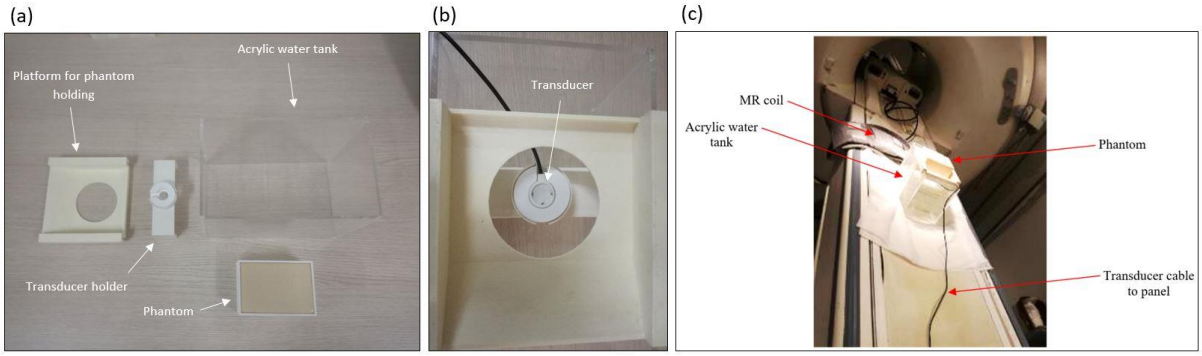

Figure 8.6.1.1: a) Parts of the experimental set-up and the phantom, b) Experimental set-up with the 4.4 MHz transducer, and c) The acrylic water tank with the structure (version 1) as illustrated in the MRI room.

The phantom and the 4.4 MHz transducer under evaluation were placed in another updated structure (version 2) which provided stability for accurate results and precise thermocouple insertion. The transducer was placed in the holder of the structure, which was immersed in the water container, thus providing good acoustical coupling between the phantom and the transducer. The water container was filled with de-ionized/degassed water. The structure that hosted the transducer and the phantom was designed to fit in an acrylic water tank. The transducer holder was adjusted so as the focal depth was at 2 cm. The temperature change at the focal point was measured using a thermocouple as shown in Figure 8.6.1.2.a. Figure 8.6.1.2.b shows the experimental setup as placed on the MRI table.

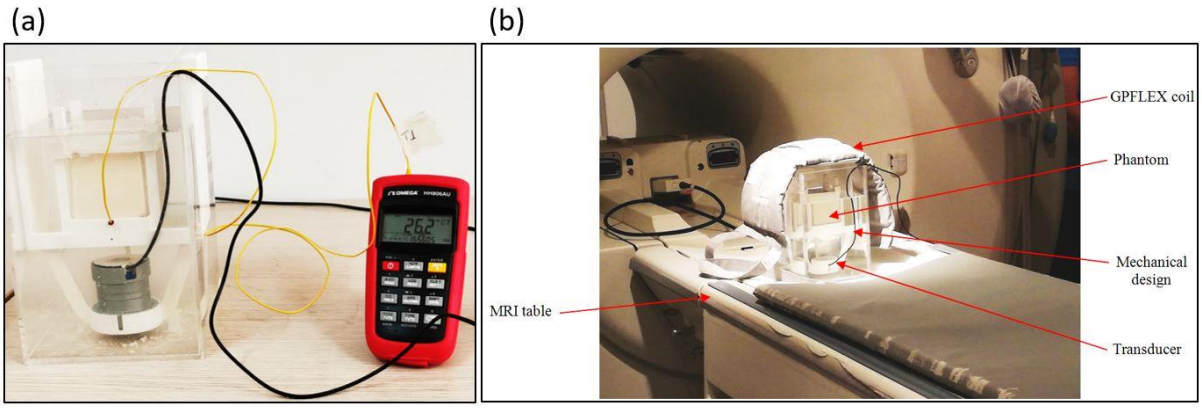

Figure 8.6.1.2: a) Experimental set-up in order to measure the temperature change in the phantom using a thermocouple, and b) The acrylic water tank with the updated structure (version 2) as illustrated in the MRI room.

T_2-weighted FSPGR images of the experimental set-up (version 2) with the phantom were obtained as shown in Figure 8.6.1.3. The MR images were usually taken prior to the experiments in order to check the image quality, the phantom homogeneity and whether the image was sufficient for MR thermometry post-processing. Moreover, the experimental set-up was checked for possible movement of any of its part including the phantom.

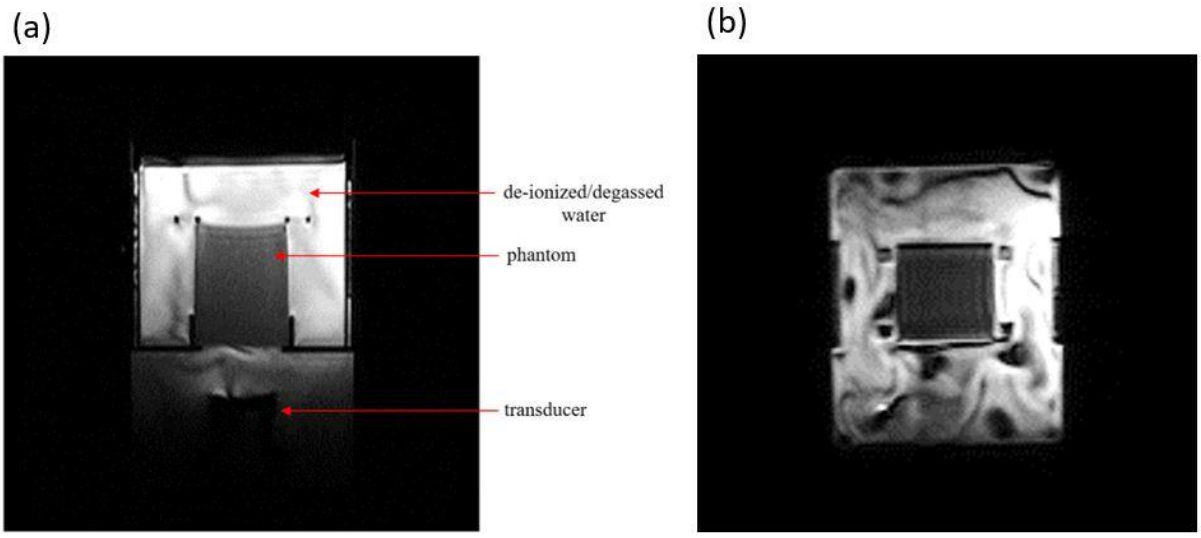

Figure 8.6.1.3: T_2-weighted FSPGR echo image of the experimental set-up for the evaluation of the 4.4 MHz transducer, a) axial plane, and b) coronal plane.

The temperature change at a depth of 1.5 and 2.5 cm in the phantom was recorded using a thermocouple (thickness 100 μm) by applying different acoustical power. Figure 8.6.1.4 and 8.6.1.5 shows the temperature elevation versus exposure time for acoustical power of 10 and 15 W as recorded at depth of 2.5 and 1.5 cm, respectively. The temperature change at the lower depth was higher due to the attenuation parameter. The attenuation of the US beam decreases as the travelling distance of the US beam in the phantom decreases.

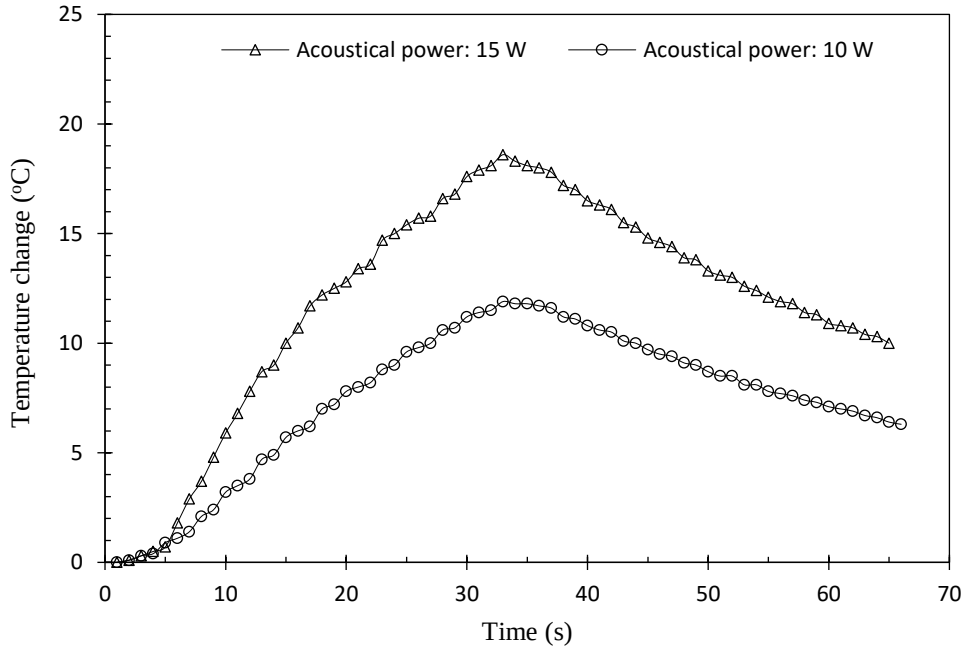

Figure 8.6.1.4: Temperature change versus time for acoustical power of 10 and 15 W as recorded at depth of 2.5 cm using the 4.4 MHz transducer.

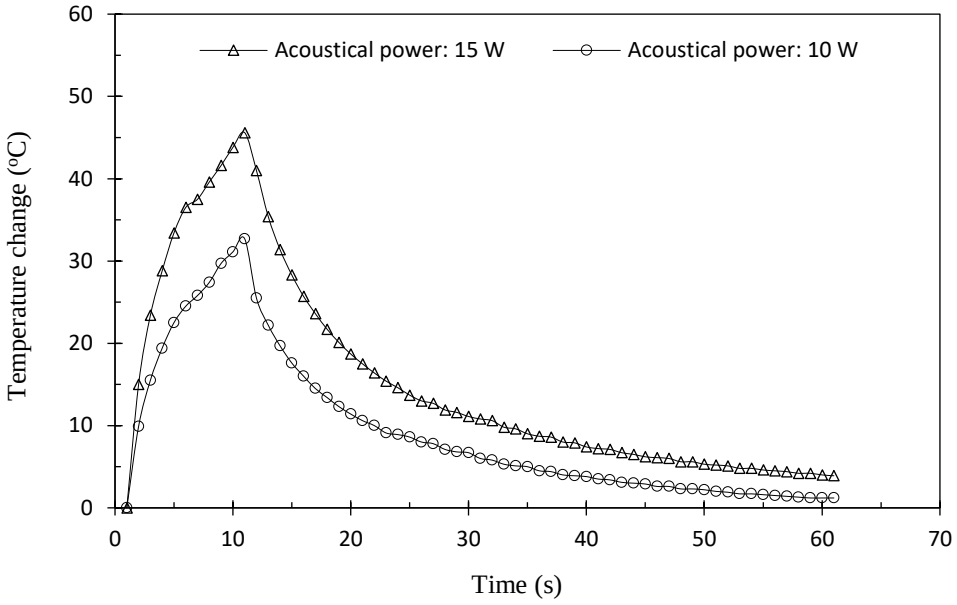

Figure 8.6.1.5: Temperature change versus time for acoustical power of 10 and 15 W as recorded at depth of 1.5 cm using the 4.4 MHz transducer.

The temperature change at the focal point in the phantom was also recorded using the thermocouple with the experimental set-up (version 2). The thermocouple was placed 2 cm deep in the phantom. The exposure time was 60 s and an acoustic power of 8.2 W was applied. The temperature change profile is shown in Figure 8.6.1.6.

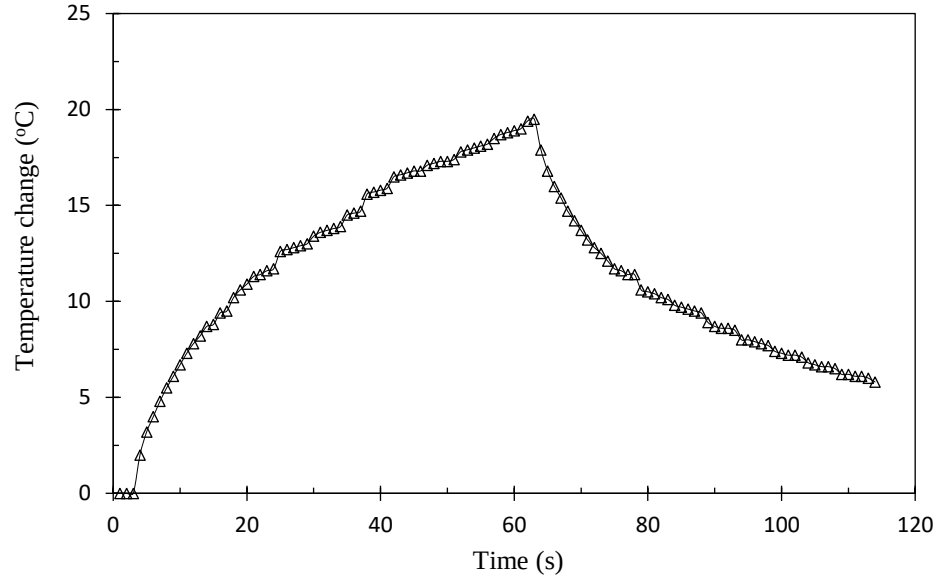

Figure 8.6.1.6: Temperature change versus time obtained using the 4.4 MHz transducer and acoustic power of 8.2 W at depth of 2 cm.

The temperature change at the focal point in the agar-based gel prostate-mimicking phantom was recorded using the thermocouple while the transducer was housed in the probe of the robotic device. An exposure time of 36 s was used and different acoustical power was applied.

Figure 8.6.1.7 shows the change of temperature versus acoustical power for sonication exposure of 36 s.

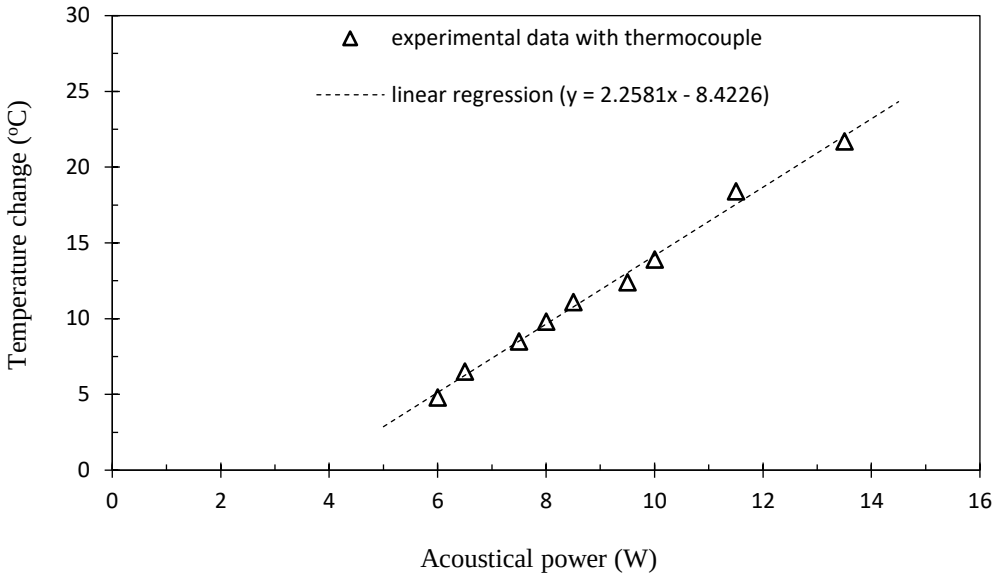

Figure 8.6.1.7: Temperature change versus acoustical power for sonication of 36 s at depth of 2 cm using the 4.4 MHz transducer.

MR thermometry data was acquired using the experimental set-up (version 1). The sonication time was 36 s while MR images were also obtained during 36 s cooling time. Acoustical power of 10.6 W was applied for both axial and coronal planes. A FSPGR image was obtained every 12 s of a total of 72 s (totally 6 MR images). The focal point was set to be 1.5 cm deep in the phantom. Figure 8.6.1.8 and 8.6.1.9 presents the temperature maps that were produced after data processing and obtained at acoustical power of 10.6 W on axial and coronal plane, respectively.

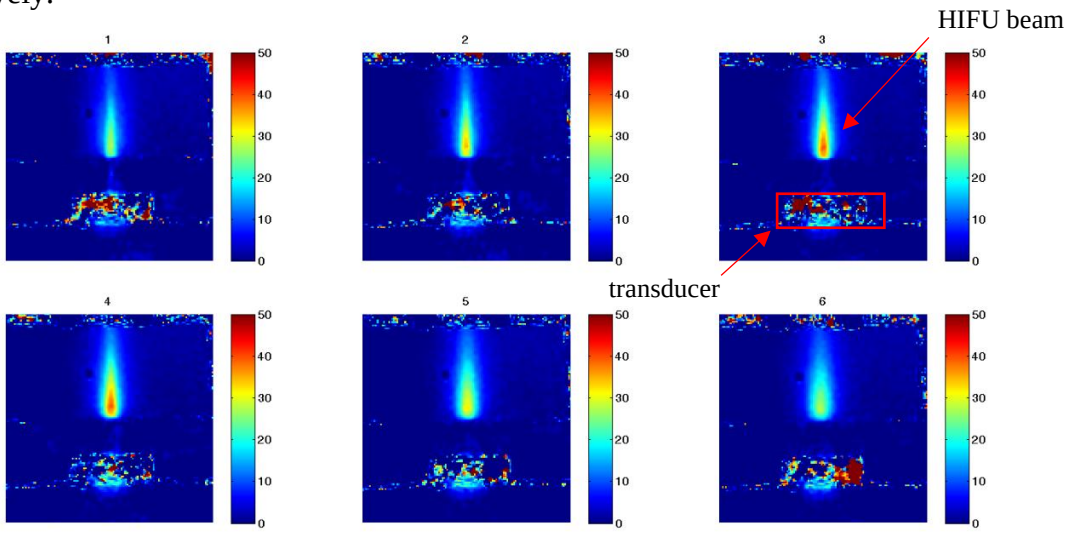

Figure 8.6.1.8: Temperature maps (axial plane) for sonication time of 12 s, 24 s, 36 s and cooling time of 12 s, 24 s, and 36 s. The acoustical power was 10.6 W and the focal depth was 1.5 cm using the 4.4 MHz. The temperature change at 36 s was 40.8 °C.

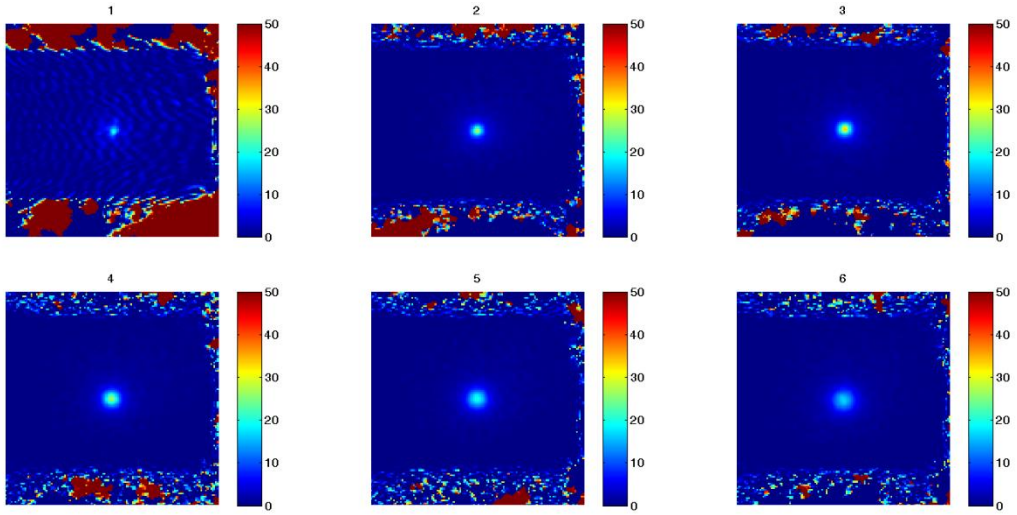

Figure 8.6.1.9: Temperature maps (coronal plane) for sonication time of 12 s, 24 s, 36 s and cooling time of 12 s, 24 s, and 36 s. The acoustical power was 10.6 W and the focal depth was 1.5 cm using the 4.4 MHz. The temperature change at 36 s was 41.3 ^{o}C.

Figure 8.6.1.10 illustrates the temperature change with respect to the longitudinal distance of various sonication and cooling time of the transducer. Thermal focus formed 6-7 mm inside the phantom adding up to 26-27 mm of focal length.

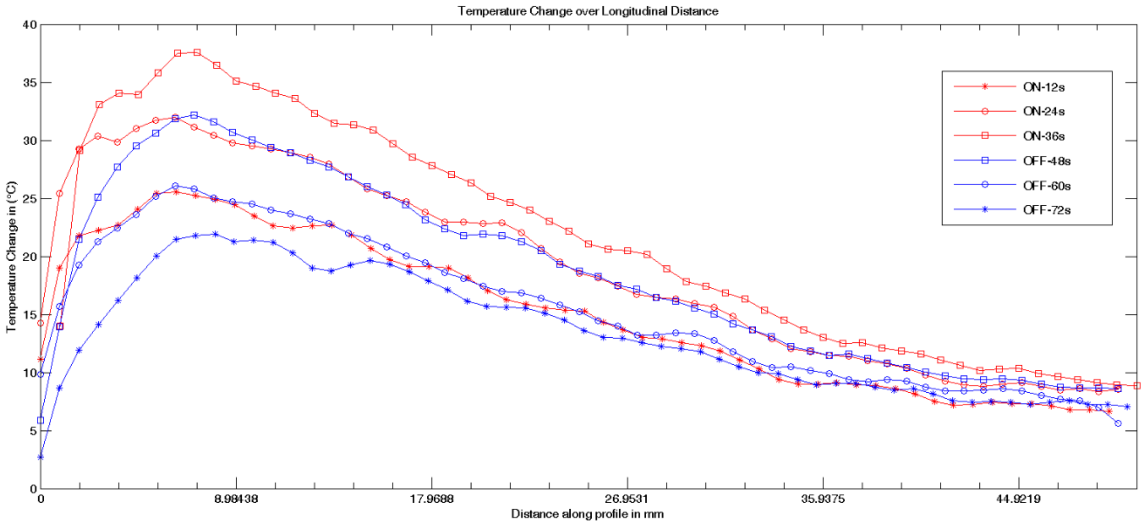

Figure 8.6.1.10: Temperature profiles of various sonication and cooling time of the 4.4 MHz transducer.

MR thermometry data were also obtained using the experimental set-up (version 2). The sonication time was 60 s while an acoustical power of 18 W was applied for both axial and coronal planes. FSPGR pulse sequence was used to obtain the MRI images which were later used for MR thermometry post-processing. The focal point was set to be 2.5 cm deep in the

phantom. Figure 8.6.1.11 and 8.6.1.12 shows the temperature maps that were produced after data processing and obtained on axial and coronal planes, respectively. Figure 8.6.1.13 shows the temperature change versus time measured for exposure of 60 s for the coronal plane MR images acquisition.

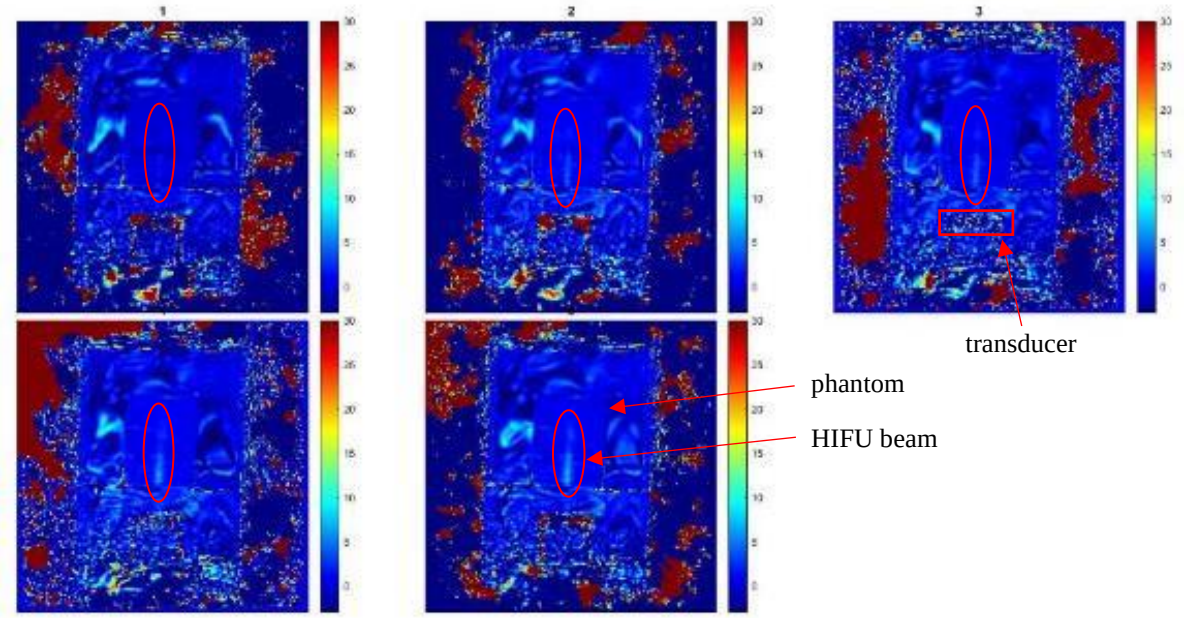

Figure 8.6.1.11: Temperature maps (axial plane) recorded using the 4.4 MHz transducer (P_a = 18 W, depth = 2.5 cm) for sonication time of 12 s, 24 s, 36 s, 48 s, and 60 s. The peak temperature change was 7 ^{o}C.

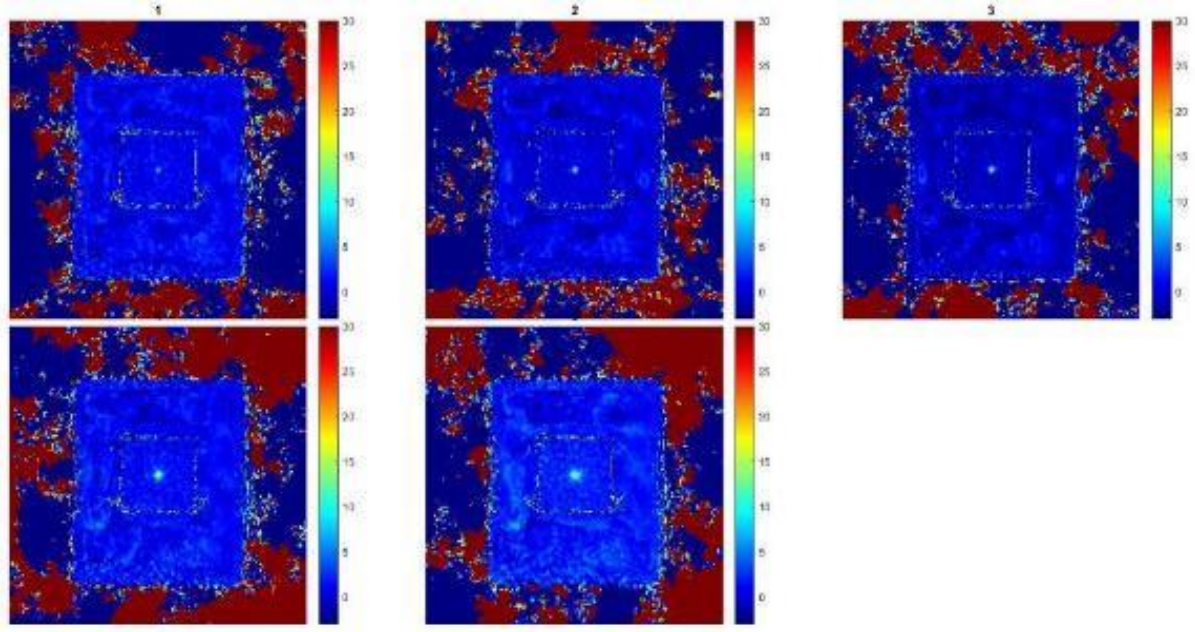

Figure 8.6.1.12: Temperature maps (coronal plane) recorded using the 4.4 MHz transducer (P_a = 18 W, depth = 2.5 cm) for sonication time of 12 s, 24 s, 36 s, 48 s, and 60 s. The peak temperature change was 22.91 ^{o}C.

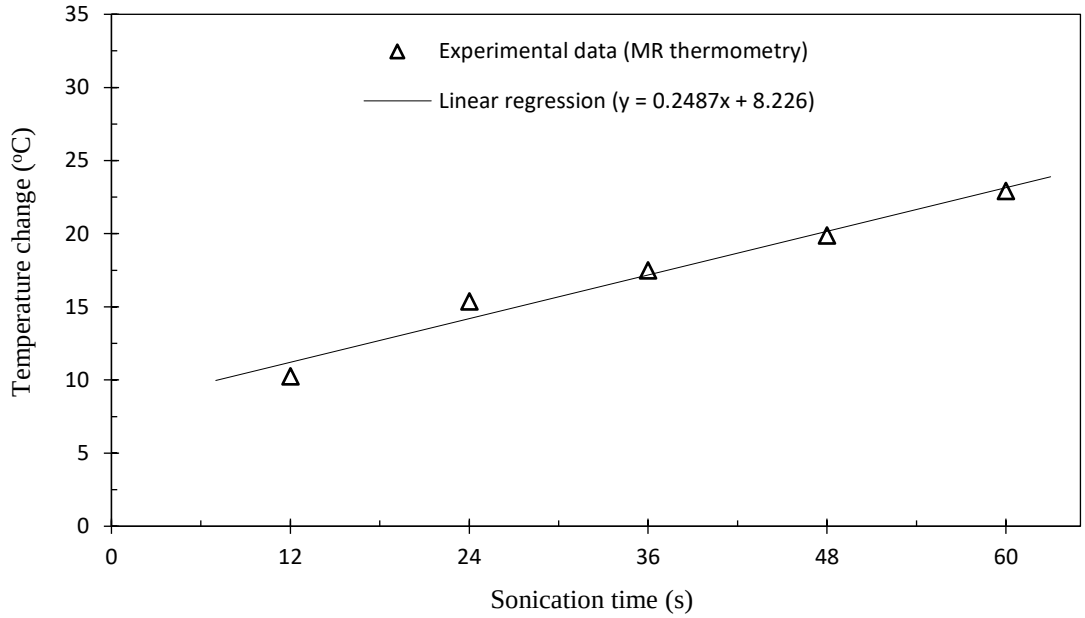

Figure 8.6.1.13: Temperature change versus sonication time as calculated from the coronal plane MR images acquisition at acoustical power of 18 W and depth of 2.5 cm using the 4.4 MHz transducer.

8.6.2 Evaluation of the 3.2 MHz transducer in phantoms

The 3.2 MHz transducer was initially evaluated in a prostate-mimicking agar-based phantom (6 % agar and 4 % silica) while it was housed in the probe of the robotic device. A thermocouple was placed 4.5 cm deep in the phantom. Measurements for acoustic power of 9, 18, and 24 W were performed. Then the thermocouple was placed 0.5 cm deep in the phantom and measurements were obtained for the same acoustic power while the sonication for all the measurements was 60 s. Figure 8.6.2.1 shows the experimental set-up with the prostate-mimicking agar-based phantom.

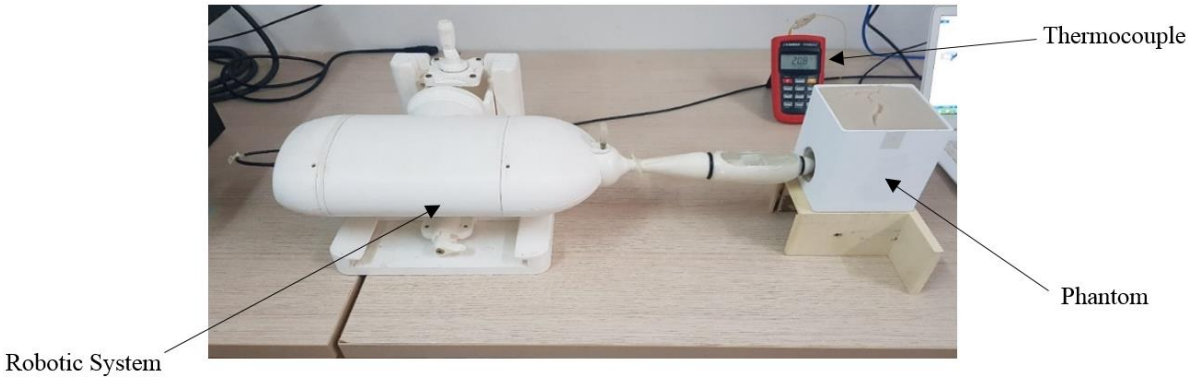

Figure 8.6.2.1: Experimental set-up to evaluate the thermal heating of the 3.2 MHz transducer.

Figure 8.6.2.2.a and 8.6.2.2.b shows the temperature change versus exposure time for acoustical power of 9, 18, and 24 W as recorded at a depth of 4.5 and 0.5 cm, respectively. Temperatures at the focal point of 4.5 cm were significantly higher.

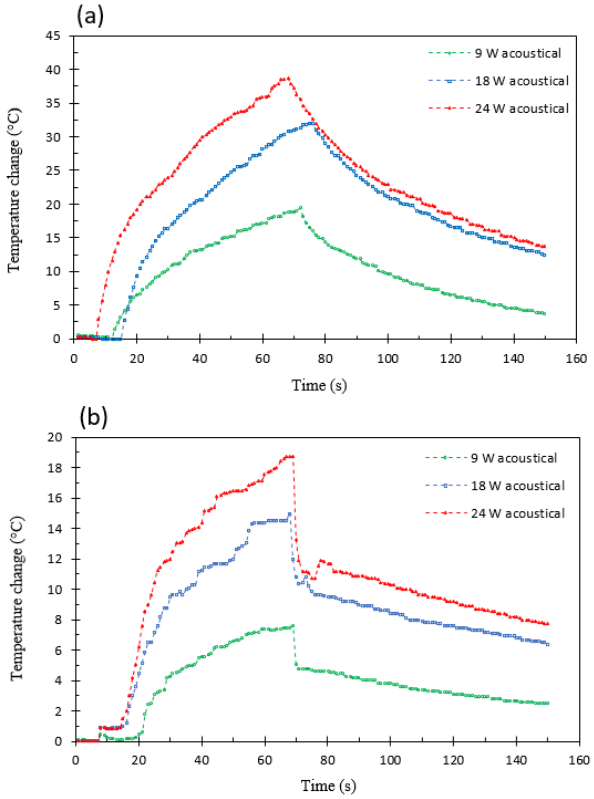

Figure 8.6.2.2: Temperature change versus time in the rectum-mimicking agar-based phantom as recorded at focal depth of a) 4.5 cm, and b) 0.5 cm using the 3.2 MHz transducer.

Table 8.6.2.1 shows the parameters and the maximum temperature achieved for each acoustic power at a different focal depth.

Table 8.6.2.1: List of parameters and maximum temperature achieved for different acoustic power and focal depth in the phantom using the 3.2 MHz transducer.

Acoustic power (W)	Focal depth (cm)	Temperature change at sonication of 60 s (°C)
9	4.5	19.4
18		32
24		38.6
9	0.5	7.6
18		15
24		18.7

8.7 Evaluation of the candidate transducers in excised tissues

8.7.1 Evaluation of the 4.4 MHz transducer in excised tissues

The transducer with an operating frequency of 4.4 MHz was used to evaluate its thermal heating in freshly excised tissue (piece of beef with dimensions of 7 cm x 8 cm x 4 cm) as well as to check the coupling of the transducer with the testing sample. Figure 8.7.1.1.a shows the robotic device with the piece of beef placed on the probe of the robotic device in the MRI room while it was covered with an MR coil. MR images of the freshly excised beef were obtained on axial and coronal plane after a sonication of 36 s and 12 s cooling time. An MR image at that sonication time was only obtained for both planes by applying an acoustic power of 24 W. T_2-weighted FSPGR echo images of the freshly excised beef after the sonication of 36 s in coronal and axial plane are shown in Figures 8.7.1.1.b and 8.7.1.1.c, respectively. The formed lesion was observed in both planes.

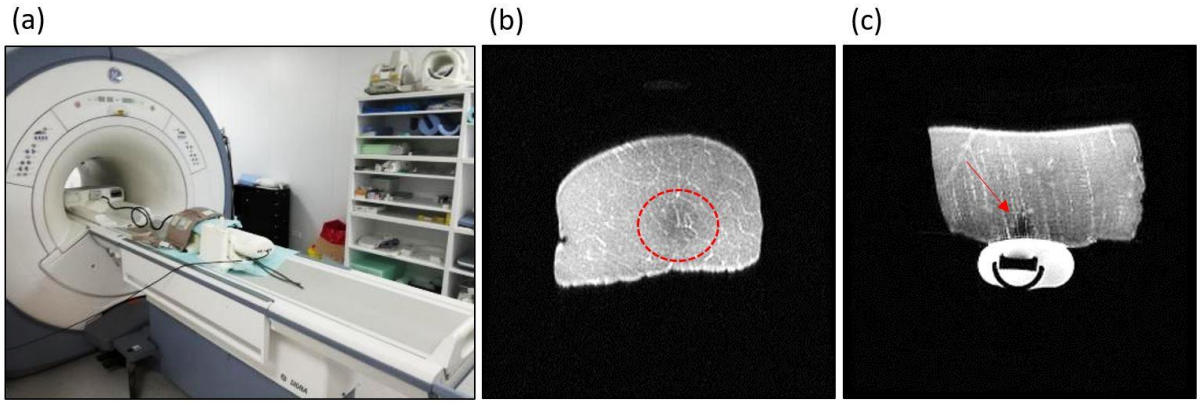

Figure 8.7.1.1: a) The prostate robotic device with the piece of beef under the MR coil as illustrated in the MRI room, b) T_2-weighted FSPGR image of the piece of beef obtained in coronal plane (perpendicular to beam direction). The red circle indicates the lesion, and c) T_2-weighted FSPGR image of the piece of beef obtained in axial plane. The red arrow indicates the lesion.

Figure 8.7.1.2.a and 8.7.1.2.b shows the MR thermometry temperature map of the piece of beef that was obtained after a sonication of 36 s and 12 s cooling time on coronal and axial plane, respectively. A T_2-weighted FSPGR sequence was used to obtain these MR images. The ultrasonic energy (864 J) that was applied to the excised tissue created a lesion at the interface. Figure 8.7.1.2.c shows the formed lesion having a diameter of 10 mm and a length of 20 mm. One of the disadvantages of this transducer was the poor penetration of the ultrasonic beam in

the tissue. Another disadvantage was the heating of the element at high power sonication for long periods.

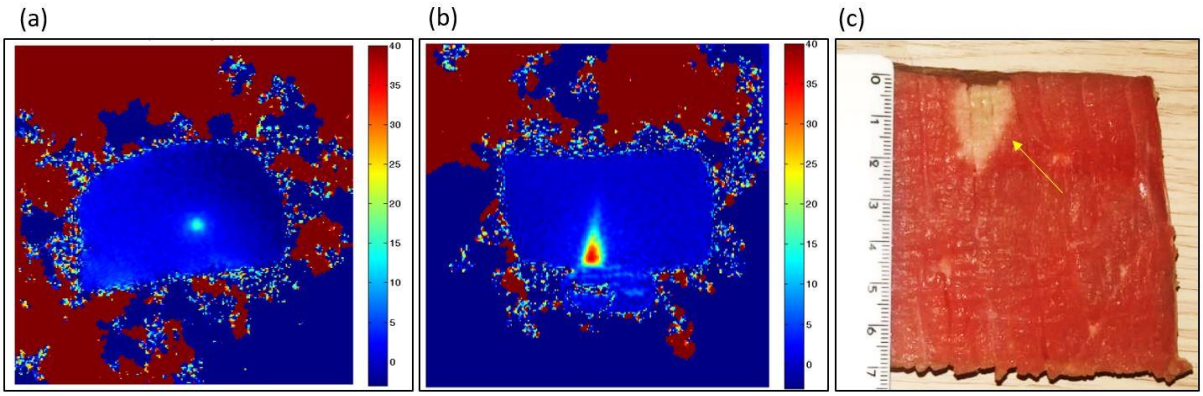

Figure 8.7.1.2: Temperature maps obtained after sonicating the piece of beef for 36 s and left it to cool down for 12 s in a) coronal plane, and b) axial plane. The applied acoustical power was 24 W and the focal depth was 1.5 cm using the 4.4 MHz transducer. c) Vertical middle cross-section of the formed lesion. The yellow arrow indicates the lesion.

A lesion was also achieved in a porcine excised tissue. The tissue was placed carefully above the probe and different sonication parameters were tested to achieve necrosis in the tissue. The necrosis was achieved with an acoustic power of 25 W and a sonication time of 60 s. Figure 8.7.1.3 shows the necrosis that was achieved after cross-sectioning. The diameter of the lesion was 5 mm and its length was 10 mm.

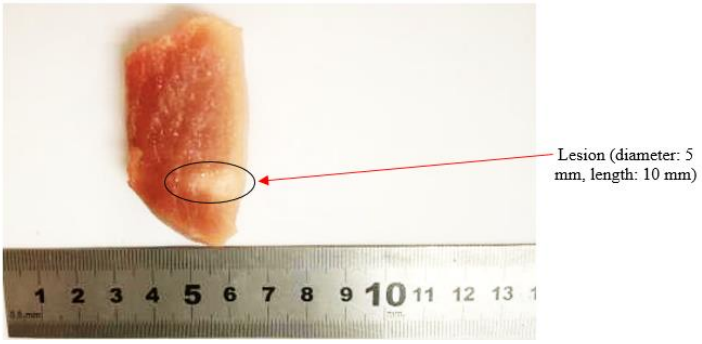

Figure 8.7.1.3: Vertical middle cross-section of the excised tissue. A lesion was achieved by applying acoustic power of 25 W for an exposure time of 60 s using the 4.4 MHz transducer at a focal depth of 2 cm. The red arrow indicates the formed lesion.

8.7.2 Evaluation of the 3.2 MHz transducer in excised tissues

A specially designed set-up was used to detect the focal point of the transducer in an excised tissue. The focus is usually shifted in some materials and a procedure was followed to detect the exact focal point after that shift. The thermocouple was inserted in the tissue at different locations with a 5 mm step. The distance from the surface of the transducer to the front face of

the tissue was set at 2 cm, thus expecting to find the focal depth at 2 cm. Figure 8.7.2.1.a shows the CAD design of the experimental set-up and Figure 8.7.2.1.b shows the experimental set-up that was used to locate the focal point of the transducer in the excised tissue.

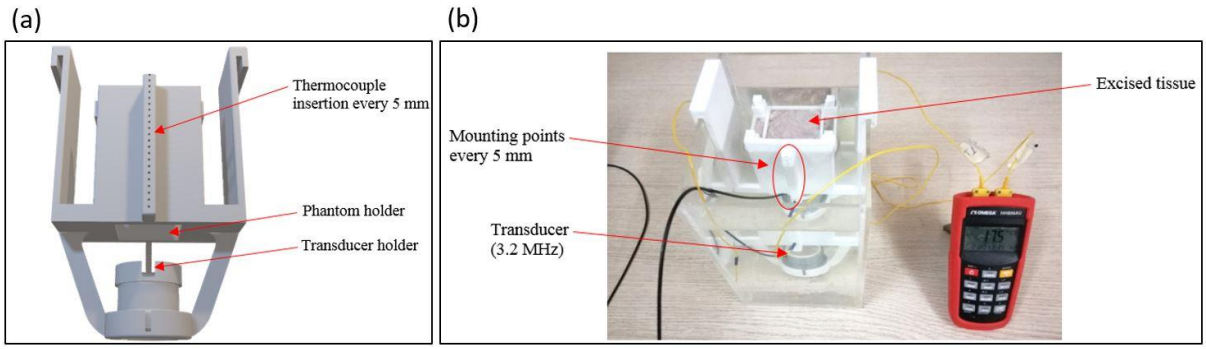

Figure 8.7.2.1: a) CAD design and b) Photo of the experimental set-up used for the measurement of temperature elevation at different depths in the excised tissue.

The thermocouple was inserted in the tissue at different locations of 5 mm step. The change of temperature was measured for each of the locations for a sonication time of 30 s and acoustic power of 15 W. The temperature sampling rate was 1 s. Figure 8.7.2.2 illustrates the change of temperature versus the depth in the tissue. The focal depth of the transducer was calculated to be at 2 cm. There was a large increase in temperature at the interface (5 mm) which created a lesion. This temperature increase was probably due to reflection of the ultrasonic beam between the tissue interface and the deionized/degassed water.

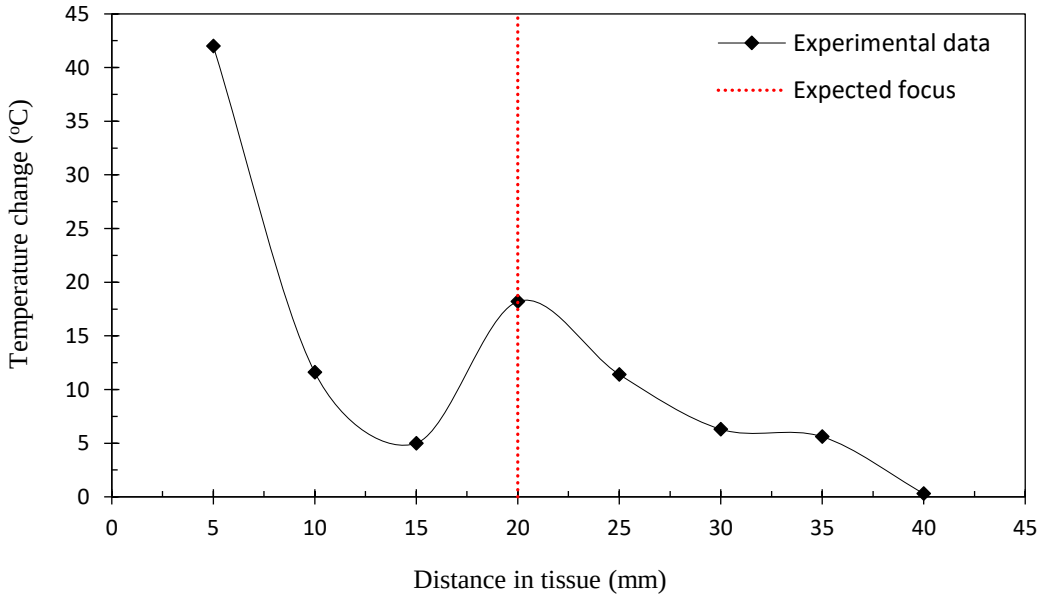

Figure 8.7.2.2: Temperature change versus distance in tissue at acoustic power of 15 W and exposure of 30 s using the 3.2 MHz transducer.

Sonication was performed while the thermocouple was placed at a distance of 5 mm in order to record the temperature change for lesion formation at acoustical power of 15 W for a sonication time of 30 s. Figure 8.7.2.3 illustrates the temperature change versus time at that depth.

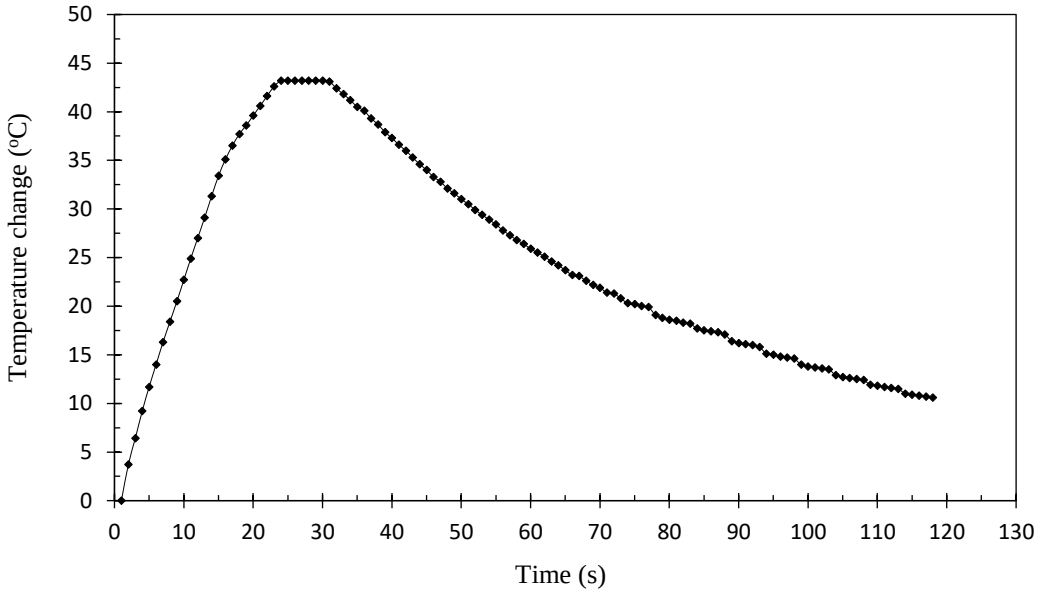

Figure 8.7.2.3: Temperature change versus time for acoustic power of 15 W, exposure of 30 s, and focal depth of 2 cm using the 3.2 MHz transducer. The thermocouple was placed at the 5 mm depth.

Figure 8.7.2.4 shows the lesion formed at the interface of the excised tissue and after a vertical cross-section to expose its length. The diameter and length of the formed lesion was measured at 11 and 19 mm respectively.

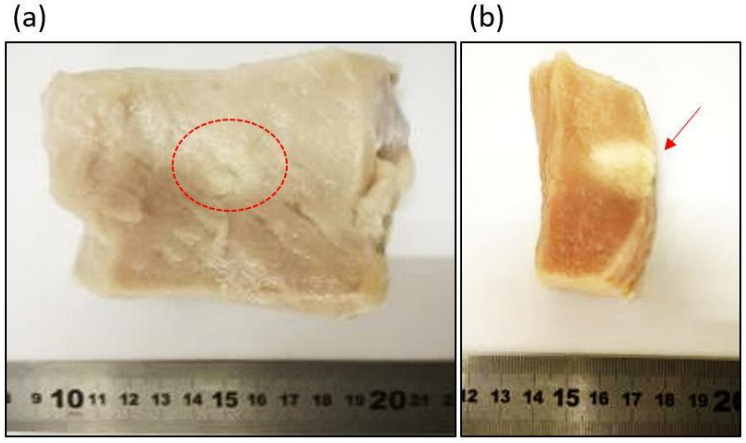

Figure 8.7.2.4: a) Lesion formed at the interface at acoustical power of 15 W for sonication time of 30 s using the 3.2 MHz transducer at a focal depth of 2 cm, and b) Vertical middle cross-section of the lesion. The red circle and arrow indicate the formed lesion.

A specially designed set-up was used to create manually multiple lesions at different locations in the excised tissue, for different acoustical power and sonication time using the 3.2 MHz

transducer. The experimental set-up (Figure 8.7.2.5) was designed so that the distance of the surface of the transducer to the top surface of the tissue and the location of the HIFU beam could be manually adjusted.

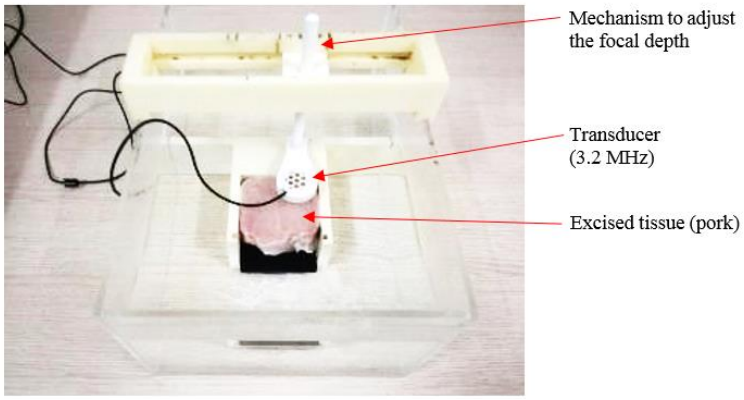

Figure 8.7.2.5: Experimental set-up used for tissue manual multiple ablations.

Multiple ablations were performed in porcine excised tissues with varying acoustic power and sonication time. The purpose of the multiple ablations was to evaluate the focused transducer at different focal depths, observe and measure the shape and size of the formed lesions and detect the minimum ultrasonic energy needed to create a thermal lesion. Figure 8.7.2.6.a shows the vertical cross-section of the lesions acquired at each location while figure 8.7.2.6.b shows the corresponding sonication parameters (acoustical power, sonication time) that was applied for each lesion formation.

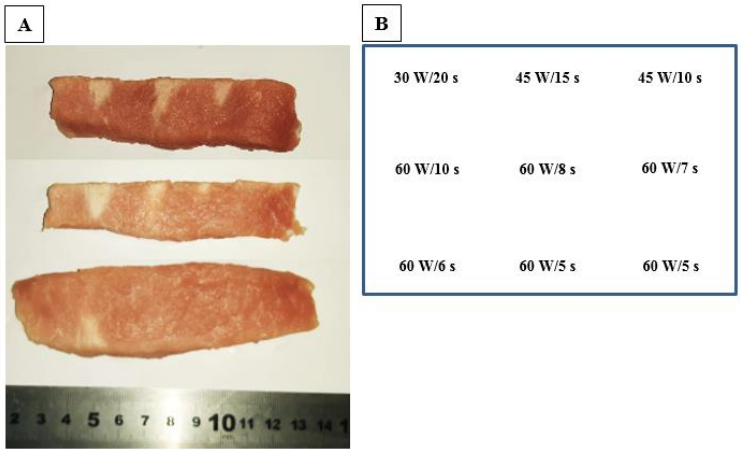

Figure 8.7.2.6: a) Vertical cross-section of lesions formed at different locations and focal depth (first row at 2 cm, second row at 3 cm, and third row at 4 cm) in an excised tissue, and b) Sonication parameters used for each ablation.

Table 8.7.2.1 lists the diameter and length of each formed lesion by applying different acoustical power. The energy needed to create a lesion was 360 J and was surprisingly not sensitive to depth. In some sonications, the ratio of lesion length to diameter was good (10 s sonication).

Table 8.7.2.1: Lesion dimensions formed by applying different sonication parameters.

Acoustic power (W)	HIFU exposure time (s)	Energy (J)	Depth (cm)	Lesion diameter (mm)	Lesion length (mm)
30	20	600	2	10.3	13.95
45	15	675		12.8	18.6
45	10	450		8.6	16.5
60	10	600	3	11.4	18.1
60	8	480		6.9	8.85
60	7	420		5.5	4.2
60	6	360	4	9.8	11.5
60	5	300		no lesion	no lesion
60	5	300		no lesion	no lesion

Figure 8.7.2.7 shows the lesion diameter and length versus sonication time for exposure at a constant acoustic power of 60 W and focal depth of 3 cm.

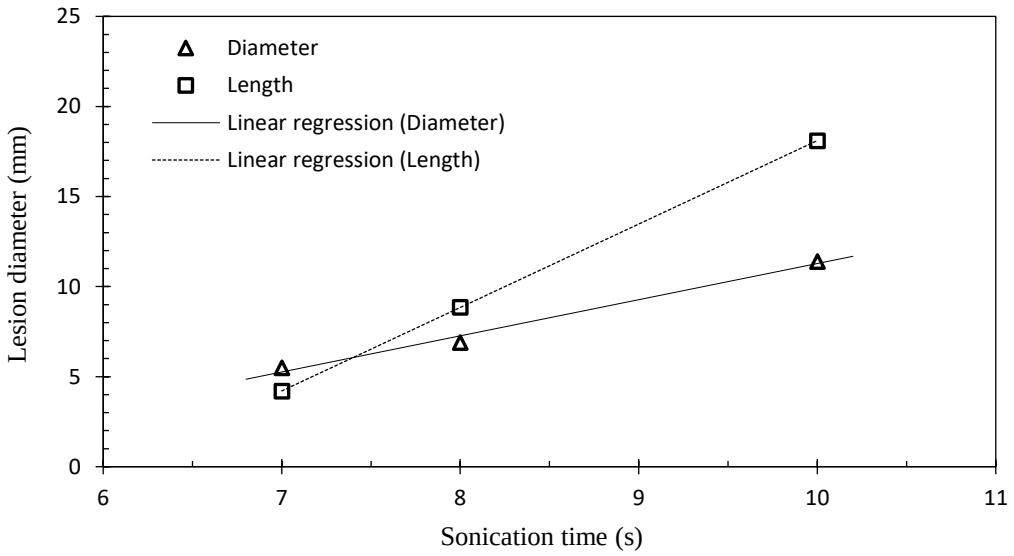

Figure 8.7.2.7: Lesion diameter and length versus time at acoustic power of 60 W and focal depth of 3 cm.

Another excised tissue was used in order to create discrete ablations at different locations (nine lesions) by sonicating with the same ultrasonic energy for repeatability purposes. The acoustic power applied was 60 W and the sonication time was 6 s. The focal depth was 3 cm. Figure 8.7.2.8.a shows the lesions formed at the interface after the multiple sonications, while Figure 8.7.2.8.b shows the axial cross-section of the lesions.

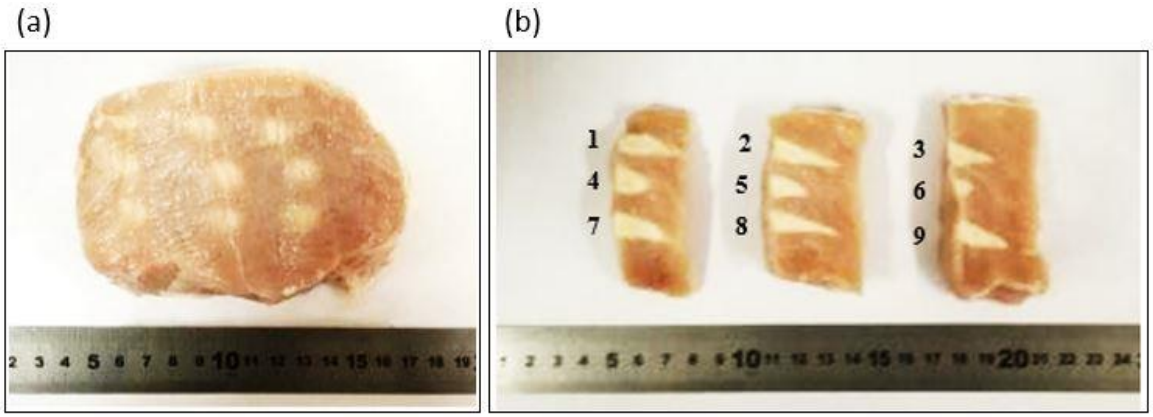

Figure 8.7.2.8: a) Induced lesion at the interface in *ex vivo* excised tissue resulting from sonication time of 6 s and acoustic power of 60 W at a plane perpendicular to the beam direction, and b) Axial section of the formed lesions.

Table 8.7.2.2 lists the diameter and length of the lesions created after applying sonication time of 6 s and acoustical power of 60 W. Energy of 360 J was also sufficient to create necrosis. Six out of nine lesions had a high ratio of lesion length to diameter. In one case, a lesion was created with a very low ratio indicating possible existence of air at that location. The repeatability of the lesion diameter was extremely good.

Table 8.7.2.2: List of diameter and length of lesions measured for sonication time of 6 s, acoustical power of 60 W, focal depth 3 cm, and total ultrasonic energy of 360 J.

Nº (from figure 8.7.2.8)	**Lesion diameter (mm)**	**Lesion length (mm)**	**Ratio (length to diameter)**
1	8.65	19.9	2.3
2	7.8	22.85	2.93
3	7.8	17	2.18
4	7.8	12.2	1.56
5	8	15.45	1.93
6	8	7	0.88
7	8.2	17.8	2.17
8	8.8	24.7	2.81
9	8.8	18.6	2.11
Average	**8.2**	**17.3**	**2.1**

The ideal scenario in an MRgFUS treatment is to apply multiple sonications so that a necrotic region will be created with the least sonication time. Low sonication time provides many advantages both to the system and treatment procedure. The temperature of the focused transducer's element increases during activation. This increases the possibility of creating irreversible damage to the element (mostly cracking), and rockets the treatment time of the entire procedure. A desirable sonication time is less than 5 s. For that reason, an excised tissue was ablated at multiple locations with an acoustic power of 70 W and sonication time of 5 s. The focal depth was 3 cm. Figure 8.7.2.9.a shows the lesions formed at the interface after the multiple sonications while Figure 8.7.2.9.b shows the axial cross-section of the lesions.

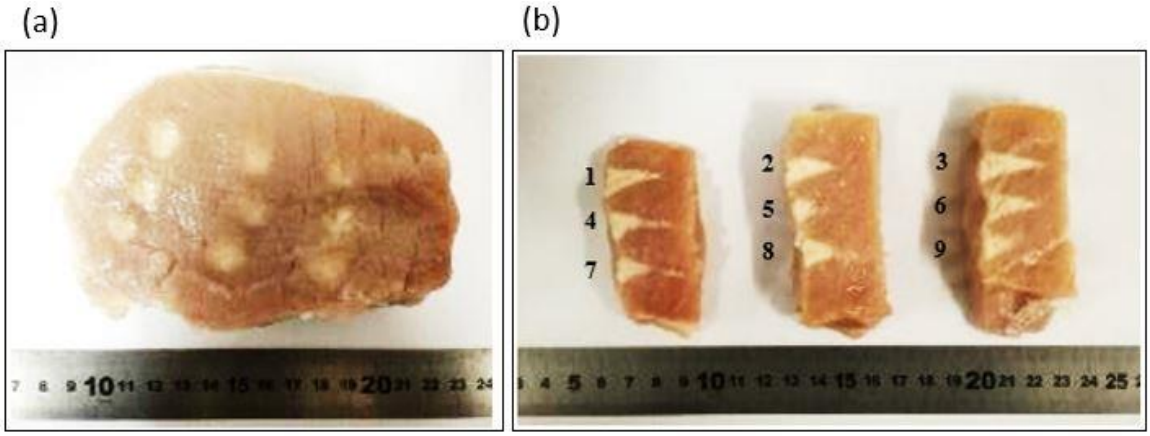

Figure 8.7.2.9: a) Induced lesion at the interface in *ex vivo* excised tissue resulting from sonication time of 5 s and acoustic power of 70 W, and b) Axial section of the formed lesions.

Table 8.7.2.3 lists the diameter and length of the lesions created after applying sonication time of 5 s and acoustical power of 70 W. The energy needed to create a lesion was 350 J. Shortest time to create a lesion for all cases was 5 s. In most of the cases, the ratio of lesion length to diameter was good. The repeatability of the lesions' diameter was also good. However, the lesion length varied due to possible air bubbles and creation of cavitation. Moreover, at some locations in the tissue there was no good homogeneity thereby leading to a possible influence of the ultrasonic beam. Also, the top surface of the tissue was not completely flat. These were some of the reasons for the variation of the lesions' length.

Table 8.7.2.3: List of diameter and length of lesions measured for sonication time of 5 s, acoustical power of 70 W, focal depth 3 cm, and total ultrasonic energy of 350 J.

Nº (from figure 8.7.2.9)	**Lesion diameter (mm)**	**Lesion length (mm)**	**Ratio (length to diameter)**
1	8.7	19.5	2.24
2	8.7	16.9	1.94
3	6.7	21.3	3.18
4	8.8	19.5	2.22
5	8.8	8.9	1.01
6	6.2	17	2.74
7	8.8	10.7	1.22
8	8.85	9.4	1.06
9	8.85	11.10	1.25
Average	**8.3**	**14.9**	**1.8**

Figure 8.7.2.10 shows the lesion diameter and length versus energy at a focal depth of 3 cm.

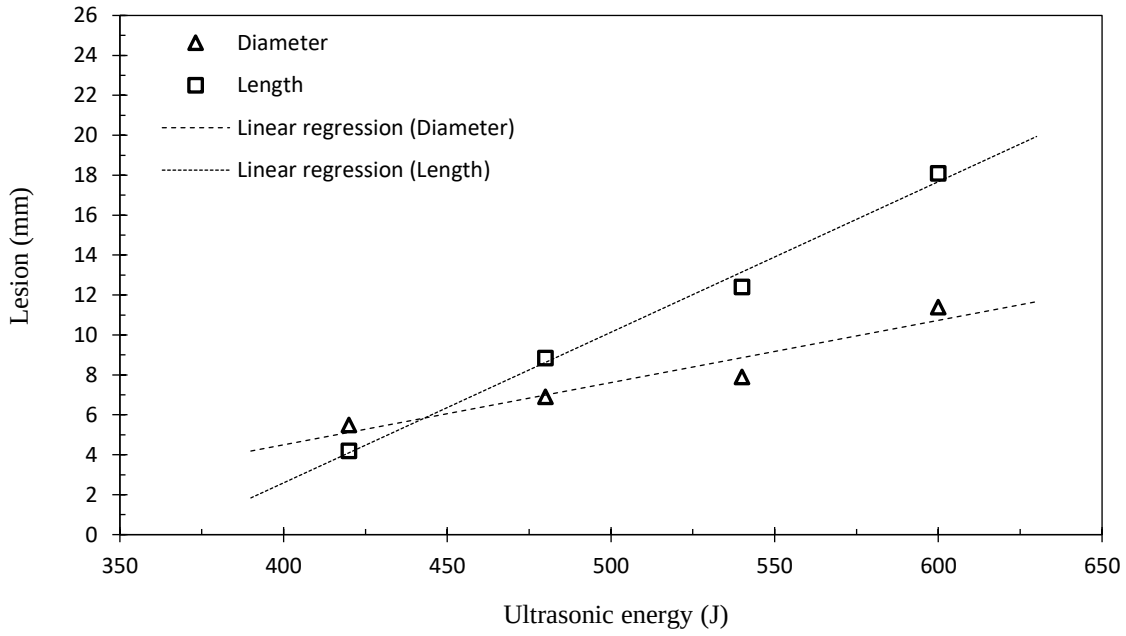

Figure 8.7.2.10: Lesion diameter and length versus ultrasonic energy at a focal depth of 3 cm.

8.7.3 Evaluation of the 3.2 MHz transducer in excised tissues using MR thermometry

The experimental set-up was transferred to the MRI room to evaluate the thermal heating of the transducer using MR thermometry. Figure 8.7.3.1 shows the experimental set-up that was used to create multiple lesions in a porcine excised tissue in the MRI room.

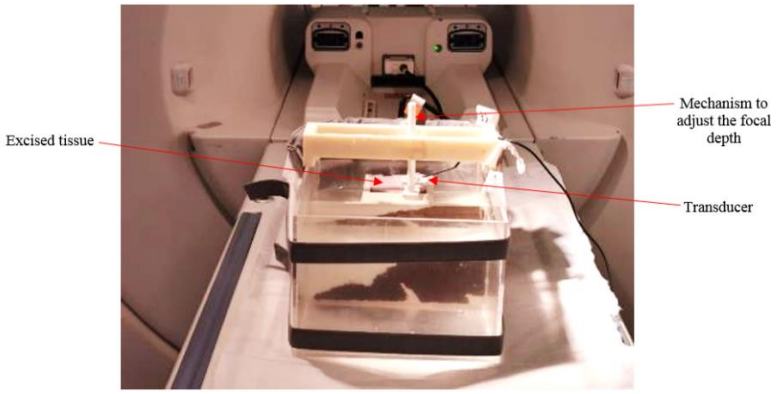

Figure 8.7.3.1: Experimental set-up as illustrated in the MRI room.

T_2-FSPGR images were acquired on axial and coronal planes in order to visualize the experimental set-up, check whether the MR image quality was sufficient for MR thermometry post-processing, as well as checking for possible movement of any part of the experimental set-up including the excised tissue and transducer. Figure 8.7.3.2.a and 8.7.3.2.b show the axial and coronal T_2-FSPGR MR image of the experimental set-up that was used to create necrosis at different locations in the excised tissue.

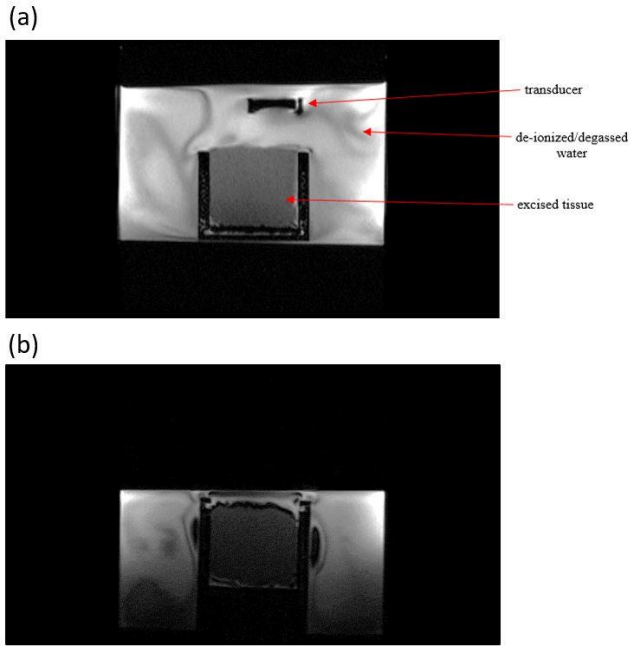

Figure 8.7.3.2: T_2-FSPGR echo image of the experimental set-up, a) axial plane, and b) coronal plane.

Lesions in excised tissue were created for various acoustical power and sonication time. Instead of using the T_2-FSPGR sequence, a single-shot EPI sequence was used which allows acquisition of an MR image at every around 1 s.

MRI signals were acquired on axial and coronal planes using different MR parameters. Table 8.7.3.1 summarizes the main HIFU and MR parameters that were used for the single-shot EPI MR sequences as well as the calculated maximum temperature change during sonication. The following parameters for all cases were: ETL = 1, flip angle = 25 º, FOV = 15 cm, delay = 1000 ms, TR = 80 ms, TE = 25.5 ms, and acquisition matrix = 64 x 64. Initially, the focal point of the transducer was adjusted at 2 cm deep in the tissue and later was set-up at 3 cm. The MR thermometry software provided data, calculated the temperature change during the sonication, and plotted a profile of temperature change versus post mask elapsed time.

Table 8.7.3.1: List of HIFU and main MR parameters that were used to create lesions and obtain the MR data.

Plane	Depth (cm)	P_a (W)	Time of sonication (s)	Time of MR images acquisition (s)	Slice thickness (mm)	Number of averages	ΔT (ºC)
coronal	2	29	20	35	3	2	7.7
axial		43	10	28	2	4	38.2
coronal		29	10	16	3		7
axial		43	10	27	2		52.6
axial		57	5	28	2		39.5
coronal	3	29	10	12	3		10
axial		57	10	28	2		55.8
axial		57	8	28	2		42.3
axial		57	5	28	2		28.9

Figure 8.7.3.3 shows the temperature maps produced after data processing using the 3.2 MHz transducer. In the beginning, since the location of the transducer beam was not accurately known, coronal plane MR images were acquired during a low acoustic power sonication to detect the focal beam (indicated as a spot). Thus, with more accuracy, the axial section of the beam was detected through MR thermometry. The thermal maps were produced on coronal plane while low acoustical power of 29 W was applied for exposure of 10 s.

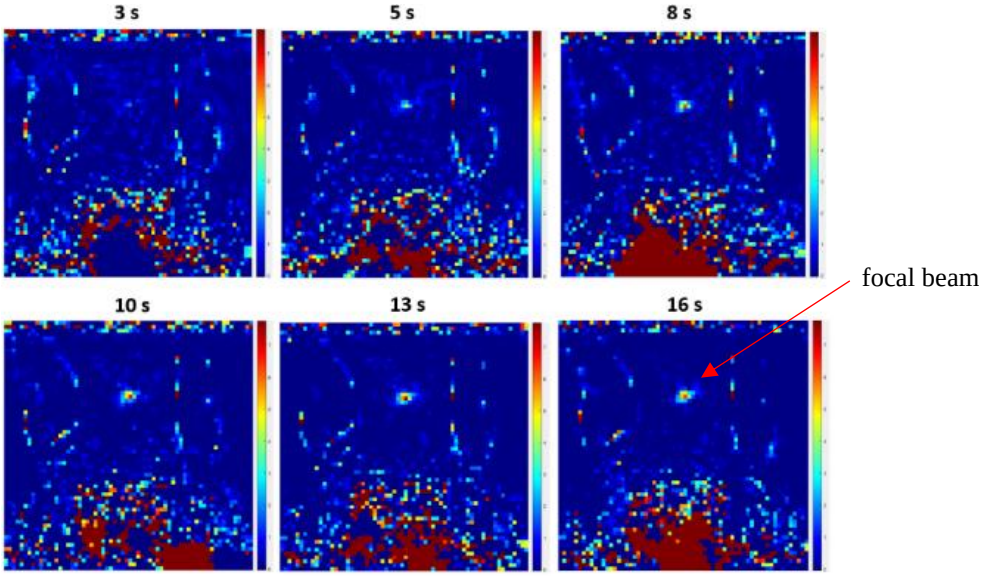

Figure 8.7.3.3: Temperature maps (coronal plane, perpendicular to US beam) recorded using single-shot EPI sequence and the 3.2 MHz transducer (P_a = 29 W, depth = 2 cm) for 10 s and cooling time of 6 s (total MRI scan of 16 s). MR parameters: NEX = 4, TR = 80 ms, TE = 25.5 ms, acquisition time of each image = 1.3 s, slice thickness = 3 mm. The peak temperature change was 7 ºC.

Thermal maps were obtained on axial plane in order to observe the transducer beam. Figure 8.7.3.4 shows the temperature maps at acoustical power of 43 W for exposure of 10 s and cooling time of 18 s.

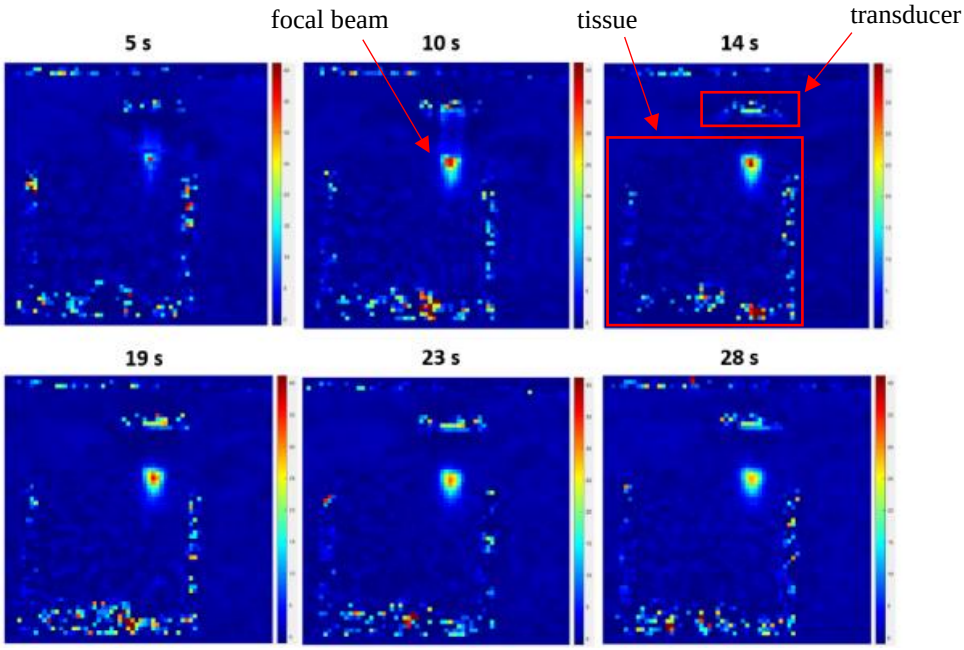

Figure 8.7.3.4: Temperature maps (axial plane) recorded using single-shot EPI sequence and the 3.2 MHz transducer (P_a = 43 W, depth = 2 cm) for 10 s and cooling time of 18 s (total MRI scan of 28 s). MR parameters: NEX = 4, TR = 80 ms, TE = 25.5 ms, acquisition time of each image = 1.7 s, slice thickness = 2 mm. The peak temperature change was 38.2 ºC.

Figure 8.7.3.5 shows the temperature maps at acoustical power of 57 W for exposure of 10 s and cooling time of 18 s.

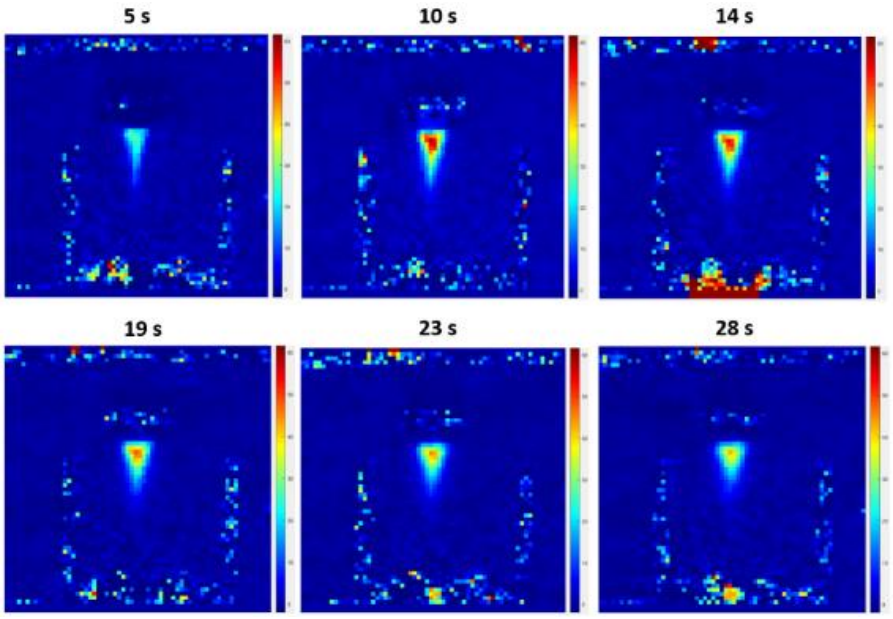

Figure 8.7.3.5: Temperature maps (axial plane) recorded using single-shot EPI sequence and the 3.2 MHz transducer (P_a = 57 W, depth = 3 cm) for 10 s and cooling time of 18 s (total MRI scan of 28 s). MR parameters: NEX = 4, TR = 80 ms, TE = 25.5 ms, acquisition time of each image = 1.04 s, slice thickness = 2 mm. The peak temperature change was 55.8 ^{o}C.

The corresponding temperature change versus time profile (Figure 8.7.3.6) was extracted directly from the MR thermometry software.

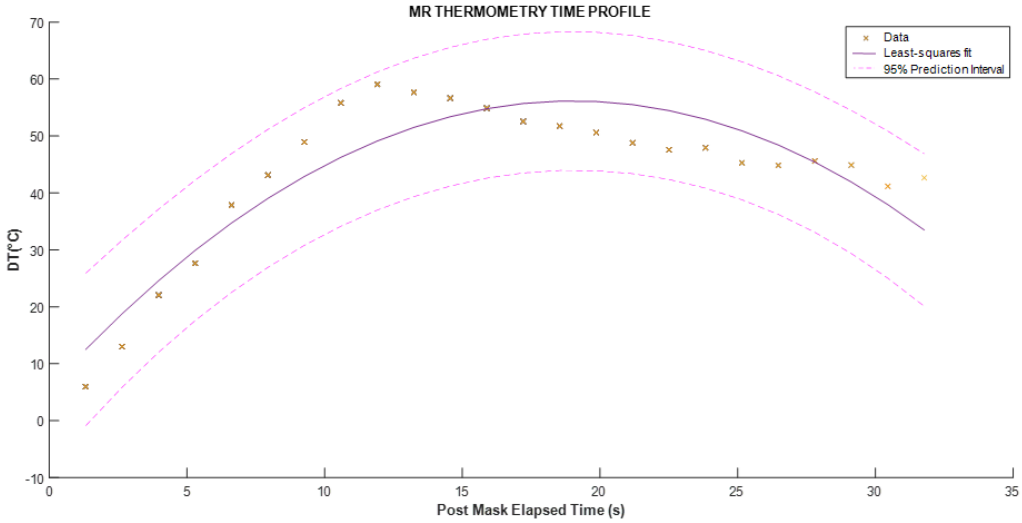

Figure 8.7.3.6: Temperature change versus post mask elapsed time as calculated from the above axial plane MR images with acoustical power of 57 W.

Figure 8.7.3.7 shows PD with fat suppression MR images obtained on coronal plane at different slice locations. The lesions were clearly observed and the ultrasonic parameters of the lesions are noted in each lesion. Lesions were created with a minimum ultrasonic energy of 285 J. After the MRI experiment, the excised tissue was cross-sectioned in order to measure the dimensions of each lesion as illustrated in Figure 8.7.3.7.d. Figure 8.7.3.7.e shows the corresponding parameters (acoustic power and sonication) that were used for each lesion.

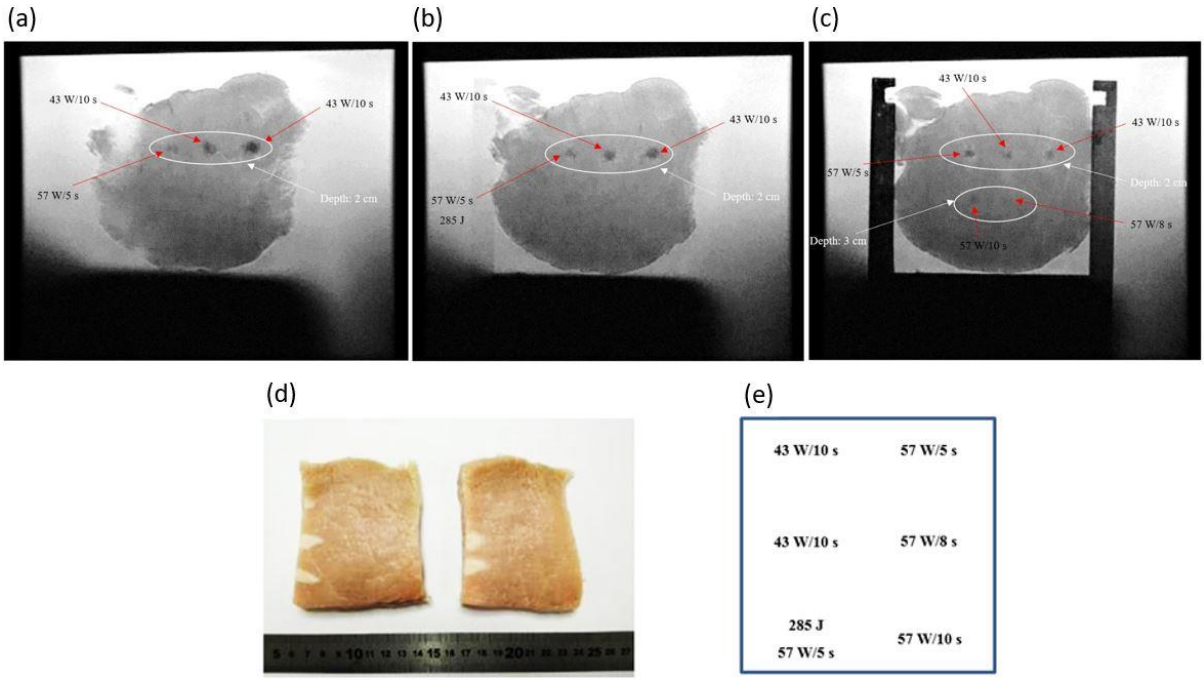

Figure 8.7.3.7: High-resolution PD with fat suppression MR image (coronal plane) obtained after the multiple HIFU sonications at slice location of a) 41.2 mm, b) 44.2 mm, and c) 47.2 mm. d) Vertical cross-section of lesions formed at different locations of the excised tissue, and e) Sonication parameters used for each ablation.

Table 8.7.3.2 lists the diameter and length of each lesion as measured after the axial cross-section of the excised tissue. At 2 cm focal depth, 285 J were needed to create a lesion whereas 456 J were needed at 3 cm focal depth.

Table 8.7.3.2: List of diameter and length of created lesions as measured for the varying HIFU exposure and acoustic power.

Acoustic power (W)	HIFU exposure time (s)	Energy (J)	Depth (cm)	Lesion diameter (mm)	Lesion length (mm)
43	10	430	2	5.8	7
43	10	430		8.6	14.8
57	5	285		8	16.9
57	10	570	3	10.4	15.3
57	8	456		9.4	11.8
57	5	285		no lesion	no lesion

8.8 Evaluation of the robotic system in excised tissues

The robotic system was evaluated in excised tissues using three different experimental models. The difference between the models was in the coupling technique. Initially, the robotic system was evaluated whith the excised tissue placed over the transducer. At a later stage, both the probe and excised tissue were immersed in degassed water and at last, the excised tissue was pierced and the probe was placed in the center of the tissue. Multiple lesions were performed by applying grid patterns of different ultrasonic energy.

8.8.1 Excised tissue over the probe

A plastic structure was used to support the excised tissue over the probe. The distance between the transducer and the bottom surface of the excised tissue was 0.5 cm. The software was used to control the frequency, acoustic power, sonication time, and the step between each sonication. A 1 x 3 grid pattern was performed with a 10 mm step while a cooling period sufficient for the temperature of the excised tissue to drop to 24 °C was used. The sonication time was 30 s and the acoustical power 24 W. Figure 8.8.1.1 shows the experimental set-up with the excised tissue placed above the probe.

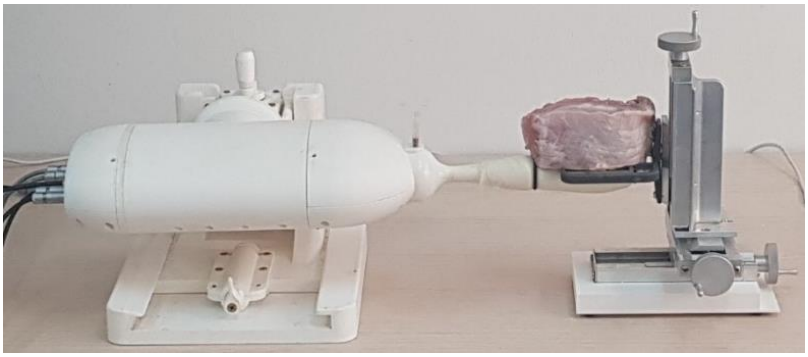

Figure 8.8.1.1: Experimental set-up with the excised tissue placed above the probe.

Figure 8.8.1.2 shows the necrosis achieved in the excised tissue. It can be seen that one lesion was formed with shorter length than the other lesions indicating the presence of cavitation due to possible air trapped in the tissue or poor coupling of the medical condom covering the probe with the tissue. Another possible reason could be the condom's material thereby leading to a possible influence of the ultrasonic beam.

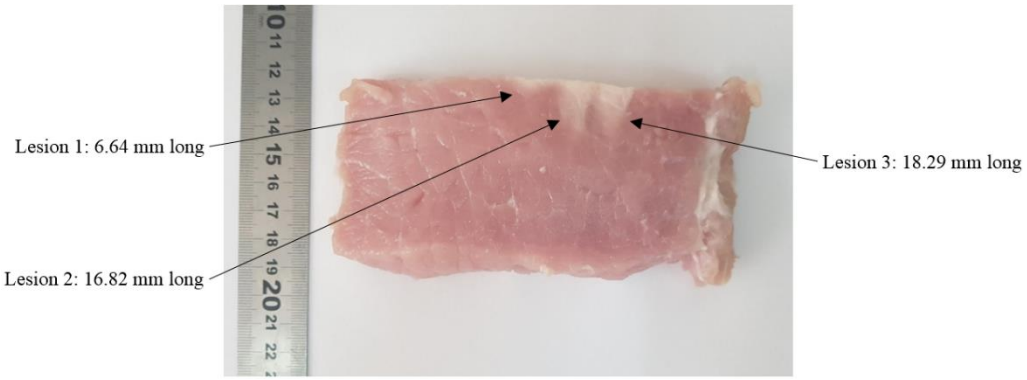

Figure 8.8.1.2: Vertical cross-section of the formed lesions (acoustic power of 24 W, 30 s sonication time, 10 mm step, and focal depth of 45 mm).

8.8.2 Excised tissue and probe both immersed in degassed water

A 3D-printed structure supported the excised tissue in a water acrylic tank next to the transducer. The distance between the transducer and the surface of the tissue was 0.5 cm. Twenty similar pieces of excised tissue were ablated. Multiple ablations were performed where the medical condom did not cover the probe and there was direct conduct of the transducer with the degassed water. Figure 8.8.2.1 shows the experimental set-up that was used for the multiple ablations using this placement technique.

Figure 8.8.2.1: Experimental set-up when both the excised tissue and probe were immersed in degassed water.

Table 10.3.1 in the appendix section (Multiple ablations in excised tissues using the robotic system and the 3.2 MHz transducer) lists the parameters, length, and diameter of the formed lesions at different acoustic power, sonication time, and grid pattern. In some cases, where the excised tissues were homogeneous, repeatability of the results was achieved. In some other cases, the length varied indicating the presence of air bubbles in the tissue. Figure 8.8.2.2 shows

the axial cross-section of discrete lesions created after applying a 3 x 1 grid pattern, acoustic power of 22.5 W, and sonication time of 30 s. The average diameter and length of the formed lesions was 17.60 mm x 12.74 mm and 23.94 mm, respectively.

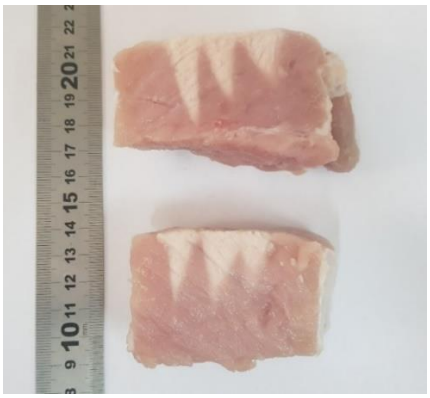

Figure 8.8.2.2: Vertical cross-section of the formed lesions (acoustic power of 22.5 W, 30 s sonication time, 10 mm step, 3 x 1 grid pattern, and focal depth of 45 mm).

Overlapped lesions were created with a grid pattern of 5 (linear) x 5 (angular) at step movement of 3 mm and 5° respectively. Figure 8.8.2.3.a shows the vertical cross-section of the overlapped lesions created after applying acoustic power of 30 W for sonication time of 10 s. The average length of the overlapped lesions was 32.81 mm and the ablated area was 29.18 mm x 20.27 mm. Discrete lesions were also formed to evaluate the thermal heating of the transducer and the accurate movement of the robotic device. The grid pattern was 5 (linear) x 5 (angular) at step movement of 5 mm and 8° respectively. Figure 8.8.2.3.b shows the vertical cross-section of the formed discrete lesions by applying acoustic power of 38.4 W for sonication time of 5 s. The average length of the discrete lesions was 31.11 mm.

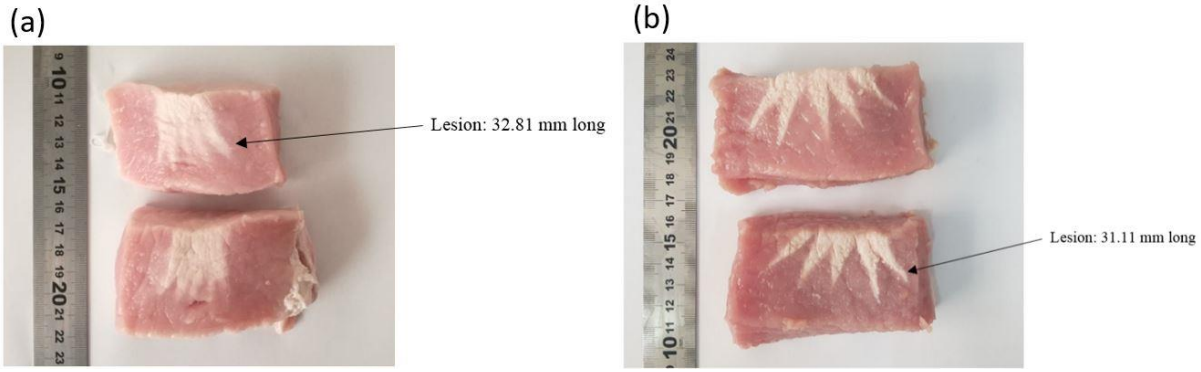

Figure 8.8.2.3: a) Vertical cross-section of the formed overlapped lesions (acoustic power of 30 W, 10 s sonication time, 120 s cooling time, 3 mm linear step and 5° angular step, 5 x 5 grid pattern, and focal depth of 45 mm), and b) Vertical cross-section of the formed discrete lesions (acoustic power of 38.4 W, 5 s sonication time, 120 s cooling time, 5 mm linear step and 8° angular step, 5 x 5 grid pattern, and focal depth of 45 mm).

8.8.3 Excised tissue surrounding the probe

The excised tissue was pierced at the center and the probe was placed within the tissue as shown in Figure 8.8.3.1. The distance between the transducer and the surface of the tissue was 0.5 cm. Seven similar pieces of excised tissue were used for ablation on both sides. Table 10.3.2 in the appendix section (Multiple ablations in excised tissues using the robotic system and the 3.2 MHz transducer) lists the parameters, length, and diameter of the formed lesions at different acoustic power, sonication time, and grid pattern.

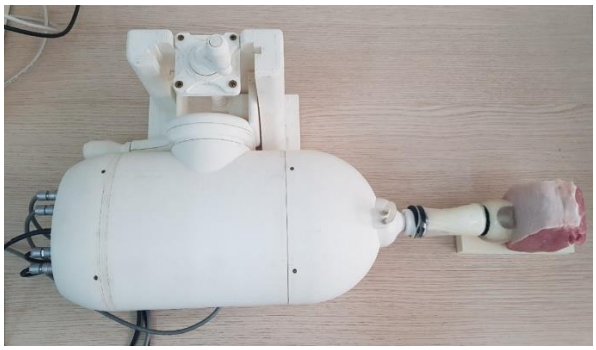

Figure 8.8.3.1: Experimental set-up with the excised tissue pierced and the probe inserted in the center of the tissue.

Figure 8.8.3.2 shows the vertical cross-section of the overlapped lesions created with an acoustic power of 30 W, sonication time of 10 s, and an angular step of 5°. The length of the lesion was 24.26 mm and the ablated area was 22.57 mm x 18.81 mm.

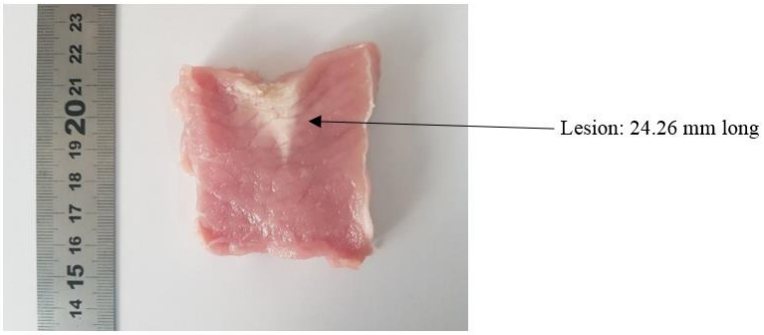

Figure 8.8.3.2: Vertical cross-section of the formed overlapped lesions (acoustic power of 30 W, 30 s sonication time, 120 s cooling time, 5 mm linear step and 5° angular step, 3 x 3 grid pattern, and focal depth of 45 mm).

8.9 SEM characterization of thermal and cavitational lesions

SEM is a very powerful technique for visualizing the surface of 3D samples in microscopic level. The preparation of biological samples is complex, and requires caution to avoid changes in the sample's appearance leading to false impression of how the sample looks.

Two lesions, one cavitational and one thermal were formed on a porcine tissue by applying acoustical power of 78 W for sonication time of 10 s. The lesions were both produced on the same tissue so as to investigate their microscopic differences through SEM analysis. The diameter and length of the formed thermal lesion was 3 and 10.6 mm, respectively. The diameter and length of the formed cavitational lesion was 9 and 12.2 mm, respectively. Figure 8.9.1 shows the lesions that were produced for the SEM analysis.

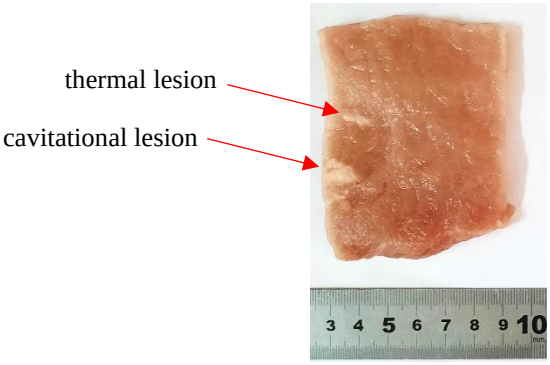

Figure 8.9.1: Thermal and cavitational lesion that were investigated in microscopic level using SEM analysis.

The procedure initiated with a careful preparation of the samples. The lesions were cut/separated from the tissue, but a small margin of healthy tissue remained to be SEM imaged and compared with the necrotic area. Afterwards, the samples were mounted using sticky conducting tapes on the sample mounts and sputter-coated with a thin (<10 nm) silver layer to reduce electron charging effects. The sputter coating was needed to increase the SNR during SEM imaging and produce higher quality images. This was achieved by using a sputter deposition system which ensured that the SEM electrons were ground, and it also prevented charging artefacts. Images were collected at 20 kV accelerating voltages in various magnifications. Figure 8.9.2 shows the SEM images at low magnification of the thermal lesion.

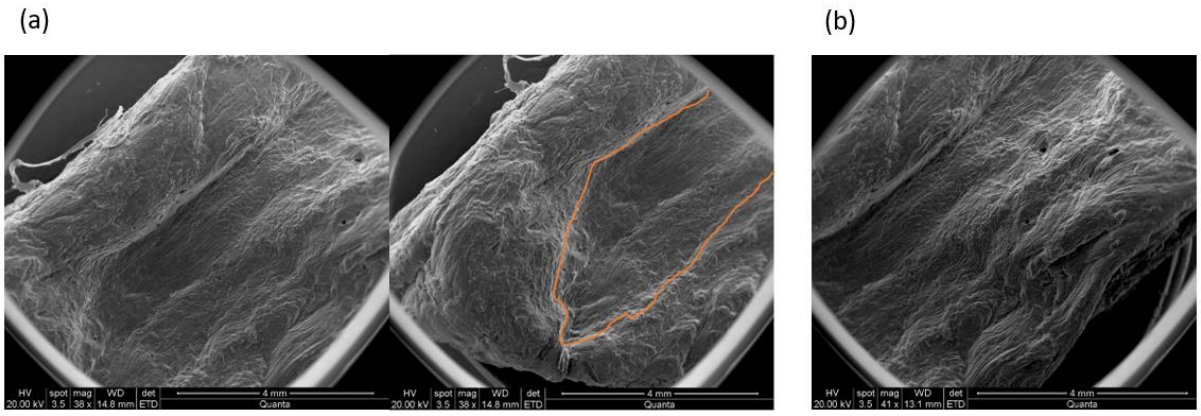

Figure 8.9.2: SEM images of a thermal lesion at magnification of a) 38x (on the right image the margins of the lesion are indicated), and b) 41x.

Figure 8.9.3 shows the SEM images at higher magnification of the thermal lesion.

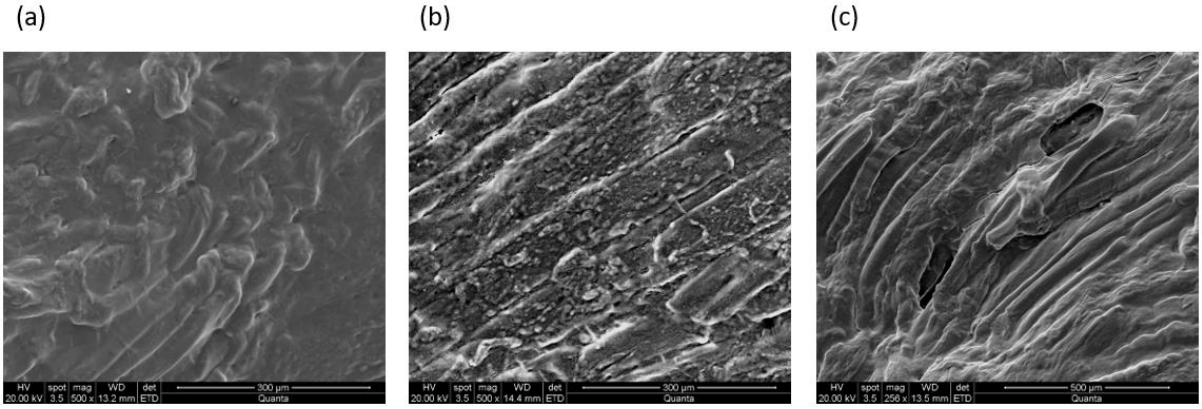

Figure 8.9.3: SEM images a) outside of the thermal lesion (500x magnification), b) within thermal lesion (500x magnification), and c) within thermal lesion where some voids were observed (256x magnification).

Back-scattered electron (BSE) microscopy images were also acquired and showed higher contrast among regions with different phases/densities of the lesions. Figure 8.9.4 shows the BSE images at low and high magnification of the thermal lesion.

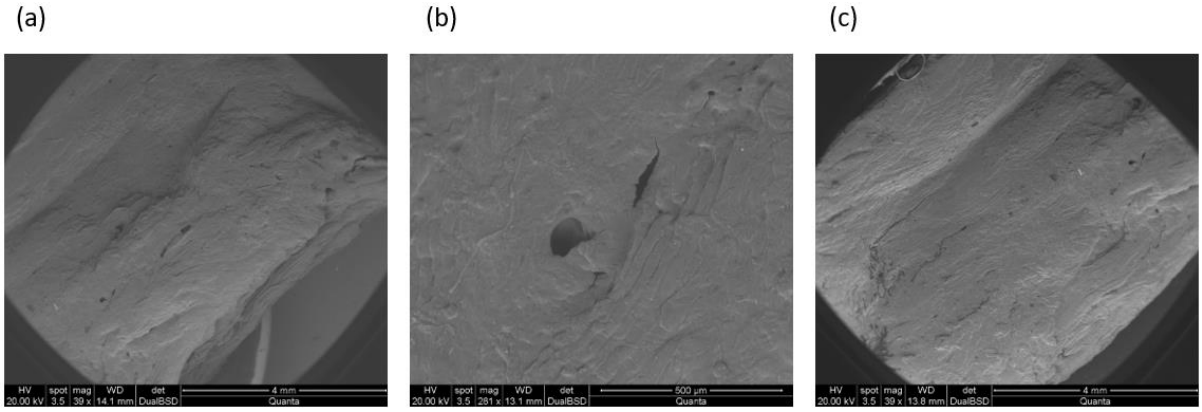

Figure 8.9.4: BSE images of a thermal lesion a) outside of the thermal lesion at magnification of a,c) 38x, and b) 281x.

Figure 8.9.5 shows the SEM images at low magnification of the cavitational lesion.

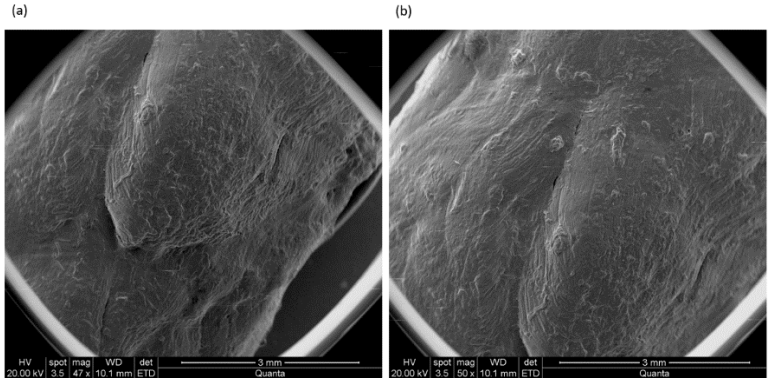

Figure 8.9.5: SEM images of a cavitational lesion at magnification of a) 47x, and b) 50x.

Figure 8.9.6 shows the BSE images of low and high magnification of the cavitational lesion.

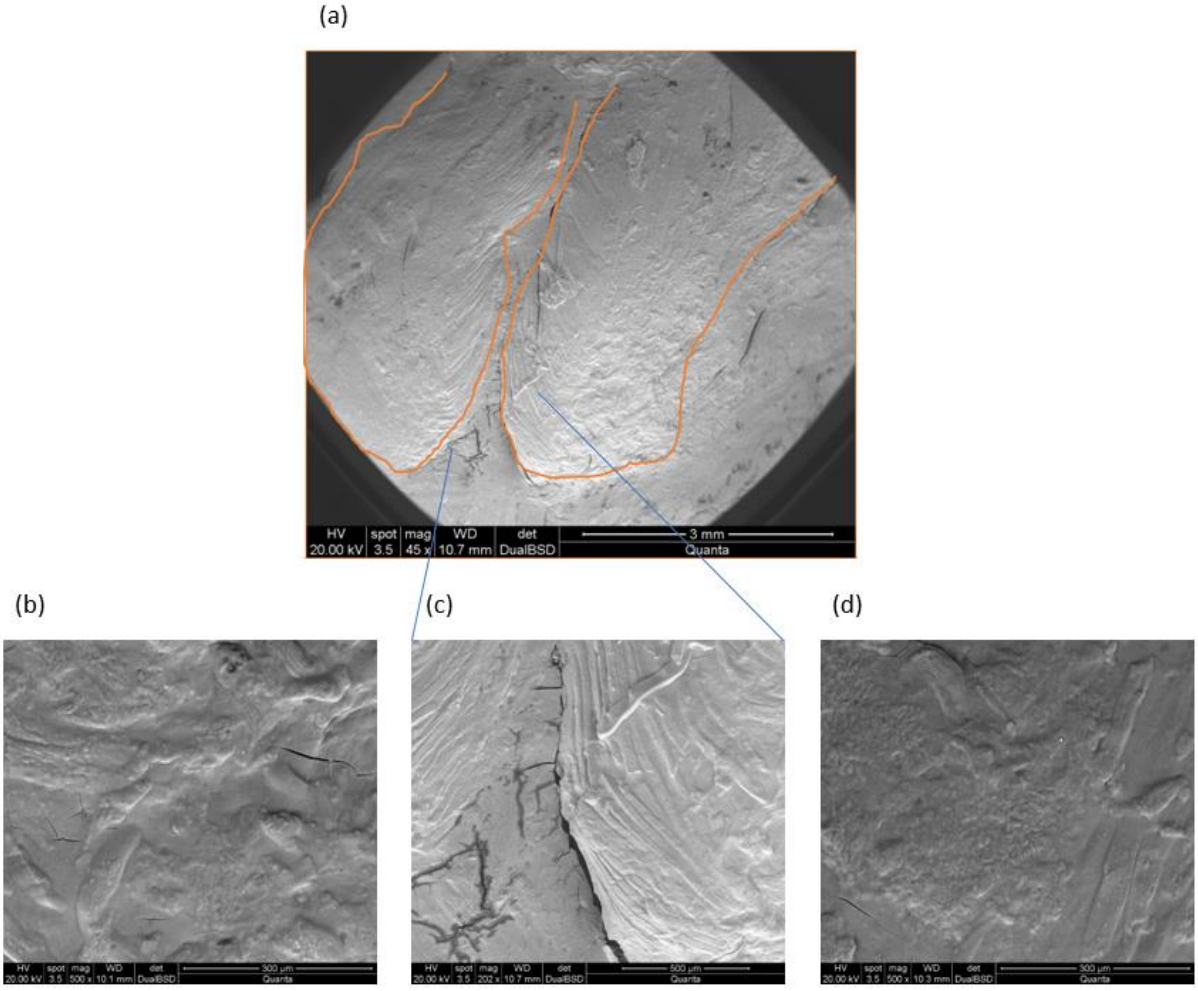

Figure 8.9.6: BSE images of a cavitational lesion at magnification of a) 45x, b) 500x (interface), c) 202x, and d) 500x.

8.10 Evaluation of the robotic system in small animal (healthy rabbit) using MR thermometry

The robotic system was evaluated on a rabbit in the MRI environment (1.5 T, Signa Excite, General Electric). The thigh of the rabbit was ablated using the 4-DOF robotic device. The thigh of the rabbit was placed above the probe (which was covered with a medical condom and filled with degassed water). MR thermometry images were acquired during sonication and necrosis was observed post-treatment using high-resolution images. Sonications were performed and the temperature change was recorded. A real-time *in situ* thermal MR thermometry data was obtained and tissue necrosis *ante mortem* was confirmed. The evaluation of the robotic system was conducted in Ygia Polyclinic Private Hospital. The following devices along with the robotic system were used: signal generator (HP 33120A, Agilent Technologies),

amplifier (AR amplifier, research model 75A250M4, 75 watts, 10 kHz-250 MHz, Acoustic Research) and GPFLEX coil (USA Instruments).

Figure 8.10.1.a illustrates the robotic system after its placement on the MRI table and its connection with the electronic system. Figure 8.10.1.b is a closer view of the 4-DOF robotic system in the MRI room. Figure 8.10.1.c shows the placement of the rabbit on the robotic device by the veterinarian and Figure 8.10.1.d shows the placement of the robotic device with the rabbit in the MR bore. The experiment was approved by the authorities of the Veterinary Services, Ministry of Agriculture. A locally bred rabbit (purchased from an accredited farm; S. Ioannou-CY.EXP.111) was examined, weighed, and anesthetized (see anesthesia record in Table 8.9.1). The thighs of the rabbit were depilated (VEET, Reckitt Benkiser, UK) shaved, and the rabbit was placed on a platform with its thigh coupled with the probe which housed the transducer and was filled with degassed water. US gel was used as a coupling material between the medical condom that was fitted on the probe and the rabbit's thigh.

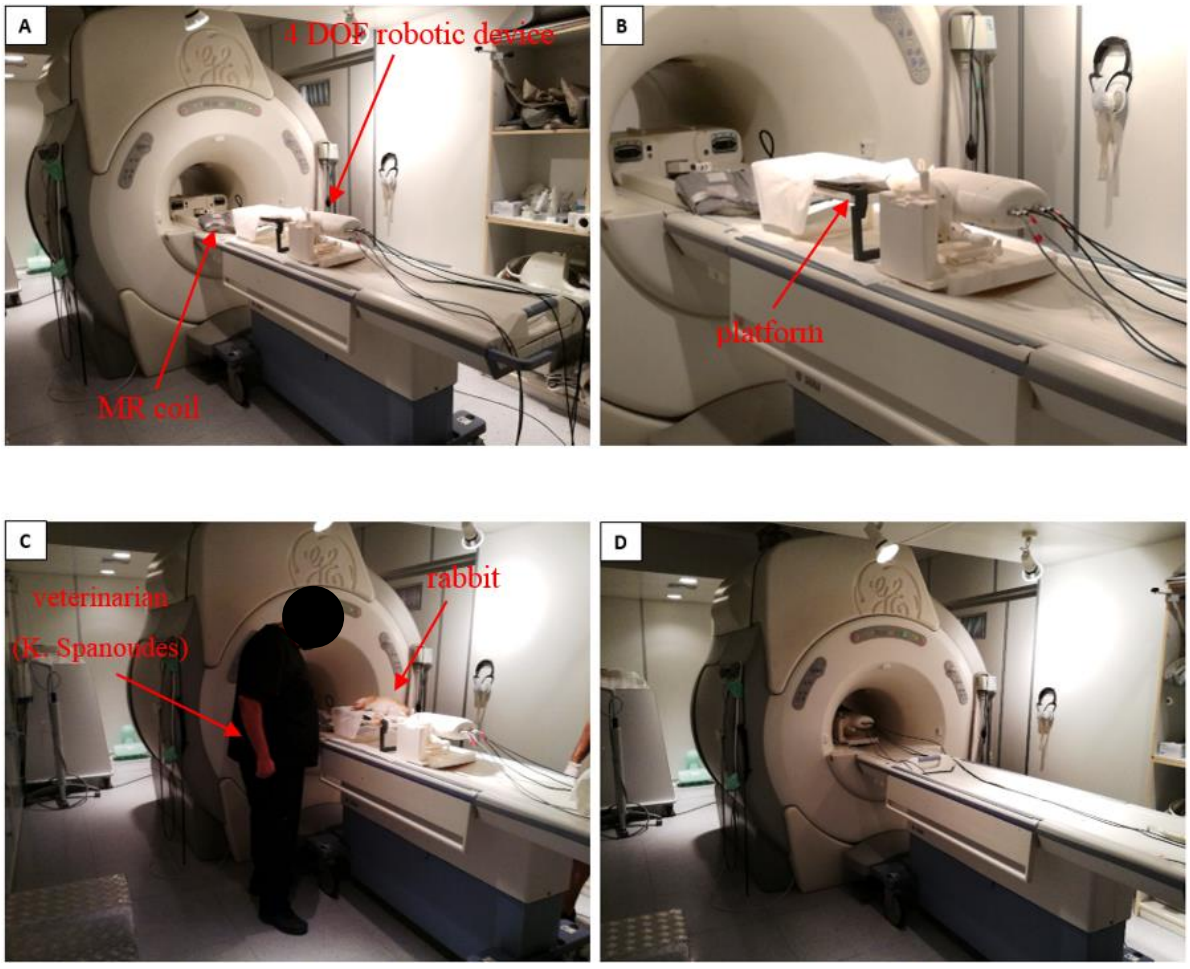

Figure 8.10.1: Photos of the 4-DOF robotic device and the rabbit during their placement in the MRI room.

Table 8.10.1: Anaesthesia record for the evaluation of the robotic system in the rabbit.

Date	**Time**
23/06/2020	18:20
Species	Rabbit
Sex	F
Age	Adult
Weight (Kg)	2.8
Study	CY/EXP/PR.L7/2019
Time	**Anesthesia**
18:25	medetomidine 0.75 mg + Ketamine 25 mg SC
19:05	medetomidine 1.5 mg + Ketamine 50mg SC
19:35	medetomidine 0.75 mg + Ketamine 25 mg SC
20:00	medetomidine 0.75 mg + Ketamine 25 mg SC
20:35	medetomidine 0.75 mg + Ketamine 25 mg SC
Euthanasia	20.50 1 ml T61

Time	**Heart Rate**	**Resp. Rate**	**Urination (0 to 3)**	**Absence of Movement /Pedal Reflex**	**Temp. (°C)**
18:30	100	90	3	Absent	n/a
18:45	96	88	0	Absent	n/a
19:00	96	88	0	Absent	n/a
19:30	88	82	0	Absent	n/a
20:00	90	86	2	Absent	n/a
20:30	90	90	0	Absent	n/a
20:45	88	82	0	Absent	n/a

Sagittal (Figure 8.10.2) and coronal (Figure 8.10.3) T_2-weighted FRFSE images were initially obtained for localization and inspection of the coupling of the rabbit's thigh with the robotic device. Main parameters used to obtain the high-resolution MR images were the following: TE = 68.7 ms, TR = 2300 ms, number of averages = 2, ETL = 16, FOV = 20 cm, slice thickness = 3 mm, matrix = 256 x 256, and flip angle = 90º.

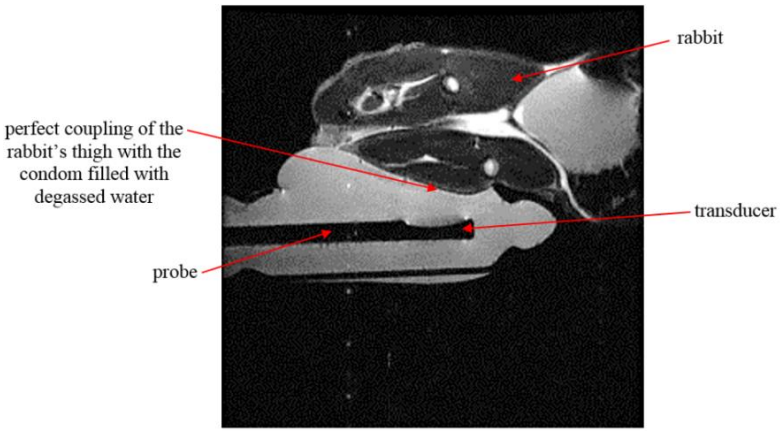

Figure 8.10.2: T_2-weighted FRFSE image (sagittal plane) of the probe of the 4-DOF robotic device and the rabbit.

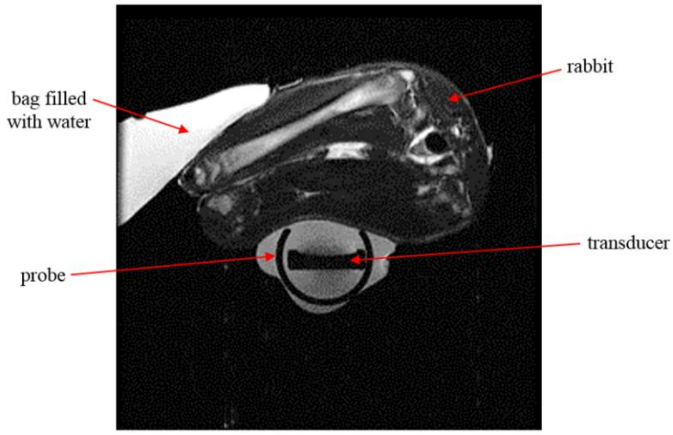

Figure 8.10.3: T_2-weighted FRFSE image (coronal plane) of the probe of the 4-DOF robotic device and the rabbit.

The rabbit was placed on a platform (as shown in Figure 8.10.1.c) so that its right thigh was sonicated. The focal depth in the rabbit's thigh was adjusted to be 2 cm. MR thermometry images were obtained in coronal and axial planes in order to monitor the temperature change in the rabbit's thigh. For coronal plane, acoustic power of 8.6 W and 22.5 W was applied to the rabbit for 30 s sonication time. The total MR scanning was 61 s for the coronal plane MR images (33 images were obtained during each MR scanning, 1.85 s for each image) and 88 s for the axial plane images (33 images were obtained during each MR scanning, 2.67 s for each image). Only 6 out of 33 images are presented in the MR thermometry results (1 image for every 10 s of the MR scanning). Figure 8.10.4 shows the temperature maps produced after data processing and which were obtained on coronal plane for acoustic power of 8.6 W using single-shot EPI multiphase sequence. Main parameters used to obtain the coronal plane MR images were: TE = 22 ms, TR = 200 ms, number of averages = 4, ETL = 1, FOV = 20 cm, slice thickness = 5 mm, matrix = 64x64, and flip angle = 25^o. Main parameters that were used to obtain the axial plane MR images were:

TE = 24 ms, TR = 200 ms, number of averages = 8, ETL = 1, FOV = 20 cm, slice thickness = 2 mm, matrix = 64x64, and flip angle = 25º.

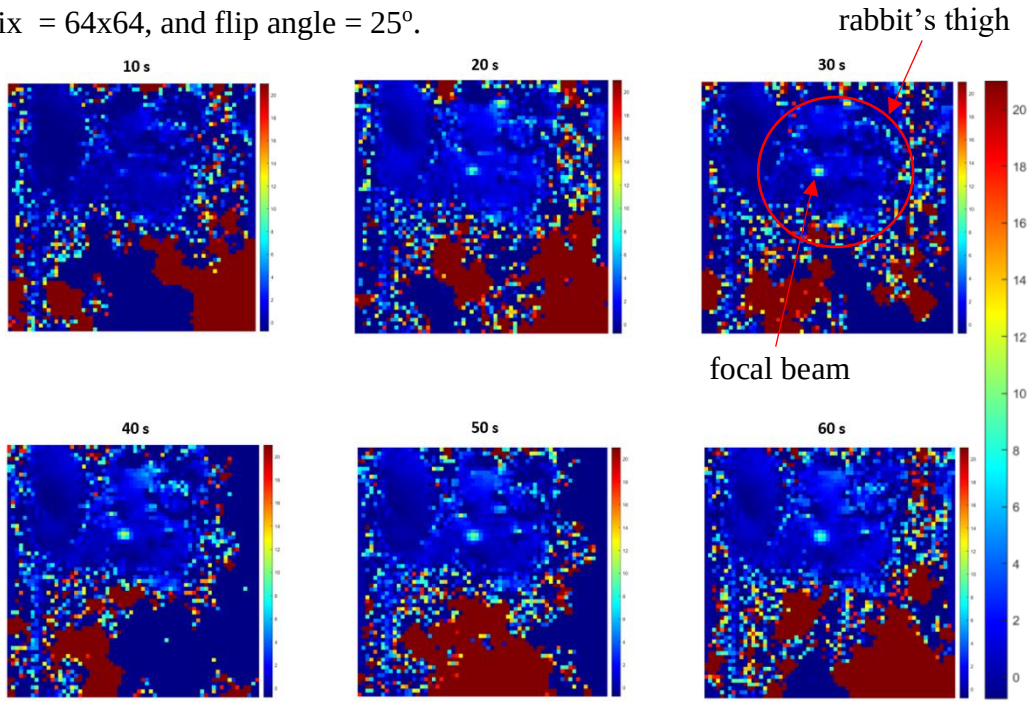

Figure 8.10.4: Temperature maps (coronal plane) recorded using single-shot EPI sequence at acoustic power of 8.6 W for sonication of 10 s, 20 s, 30 s and cooling time of 10 s, 20 s, and 30 s (2 cm focal depth, 1.85 s acquisition time for each image, plane perpendicular to the US beam). The temperature change recorded at 30 s was 13.2 ºC.

Figure 8.10.5 shows the temperature maps produced after data processing and obtained on coronal plane for acoustic power of 22.5 W using the EPI single-shot sequence.

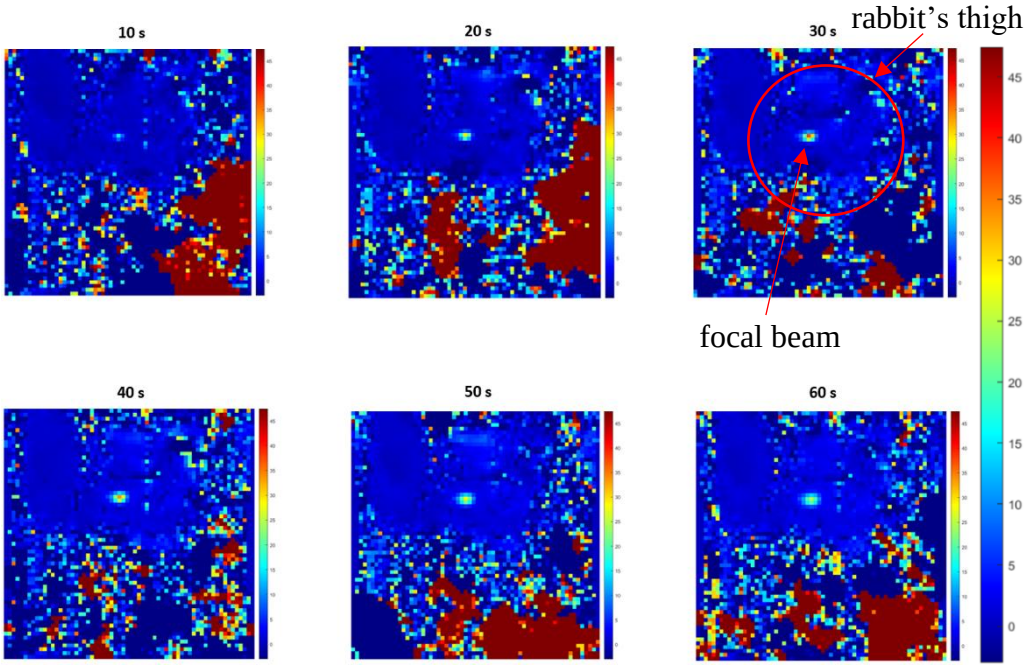

Figure 8.10.5: Temperature maps (coronal plane) recorded using single-shot EPI sequence at acoustic power of 22.5 W for sonication of 10 s, 20 s, 30 s and cooling time of 10 s, 20 s, and 30 s (2 cm focal depth, 1.85 s acquisition time for each image, plane perpendicular to the US beam). The temperature change recorded at 30 s was 39.3 ºC.

Figure 8.10.6 shows the temperature maps produced after data processing and which were obtained on axial plane for acoustic power of 22.5 W using the EPI single-shot sequence.

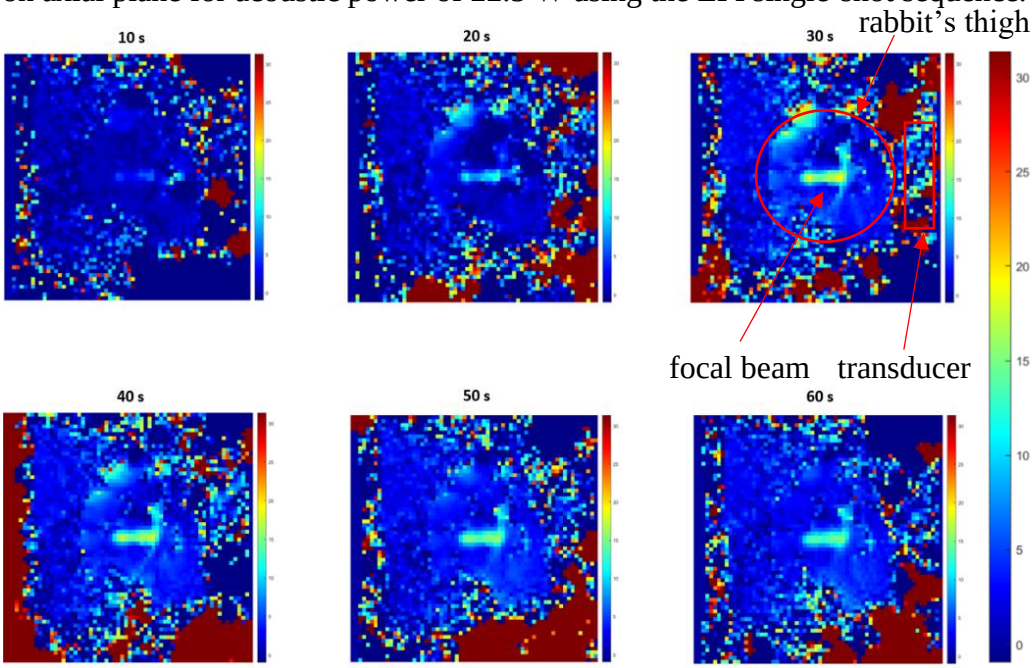

Figure 8.10.6: Temperature maps (axial plane) recorded using single-shot EPI sequence at acoustic power of 22.5 W for sonication of 10 s, 20 s, 30 s and cooling time of 10 s, 20 s, and 30 s (2 cm focal depth, 2 mm slice thickness, 2.67 s acquisition time for each image). The temperature change recorded at 30 s was 19.3 ^{o}C.

After the sonication, PD with fat suppression MR images were acquired on sagittal and coronal planes in order to detect and measure possible necrotic area. Necrosis was observed as shown in Figure 8.10.7. The dimensions of the ablated area in the vertical and horizontal directions are also indicated.

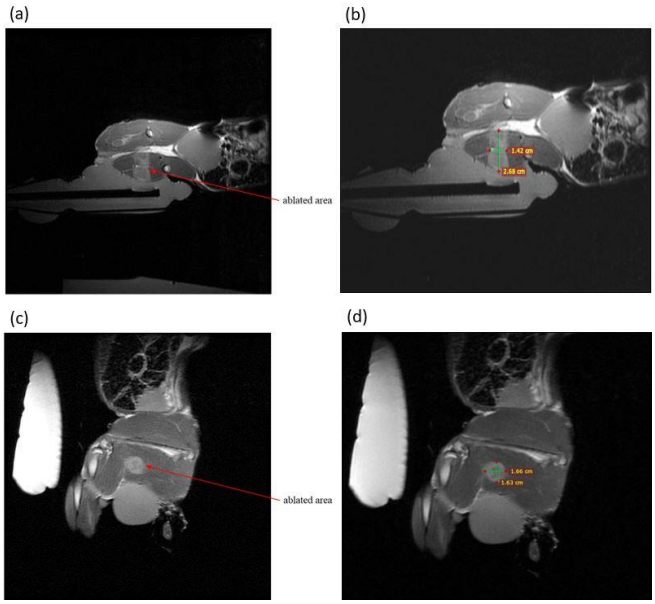

Figure 8.10.7: PD images with fat suppression that were obtained after completion of the ablation in a) sagittal plane and c) coronal plane. Measurement of the ablated area in sagittal (b) and coronal (d) plane was performed using an imaging open source DICOM software tool (RadiAnt DICOM viewer).

The right thigh of the rabbit was dissected after euthanasia to detect and measure the ablated area. Figure 8.10.8 demonstrates the lesion appearance above and below the skin on the inner and outer side, which was in proximity to the transducer. After muscle exposure, a more clear view of the lesions was seen. The lesion on the outer side of the thigh (Figure 8.10.9.c, 10 mm diameter) contained two smaller lesions (3 mm diameter each). Those lesions possibly corresponded to different ablations. The overall 10 mm diameter lesion corresponded to the cumulative tissue damage after all ablations. The lesion appearance on the inner thigh had an oval shape, as opposed to the round-shape appearance on the outer side.

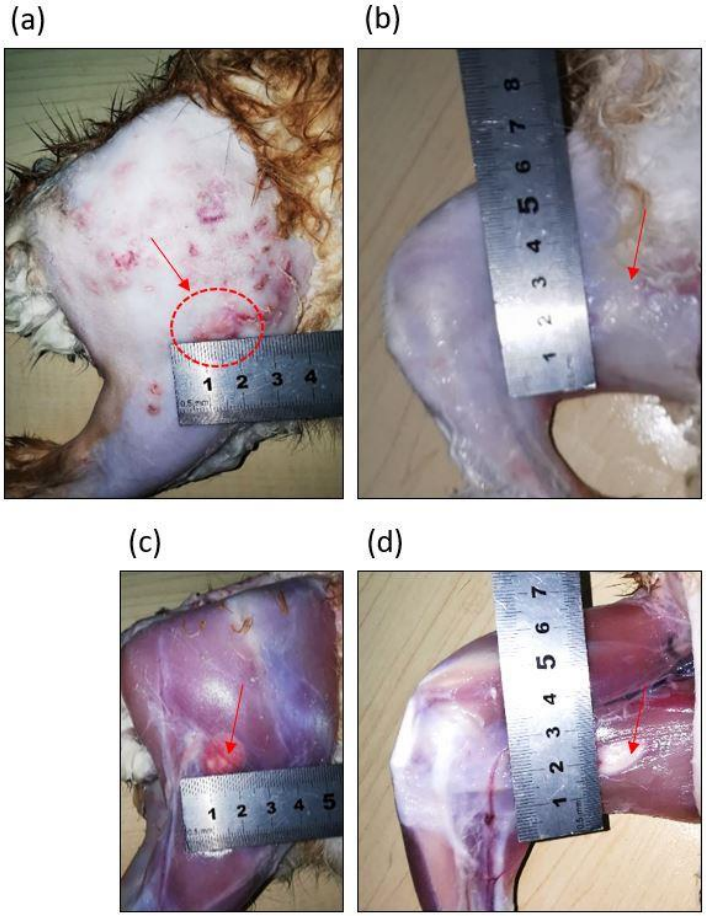

Figure 8.10.8: a) Macroscopic appearance of the outer side of the right thigh (lesion of 10 mm diameter), b) Macroscopic appearance of the inner side of the right thigh (lesion of 10 mm diameter), c) Macroscopic appearance of the outer side of the right thigh after muscle exposure (lesion of 10 mm diameter). Two round lesions of 3 mm diameter appear within the lesion area, and d) Macroscopic appearance of the inner side of the right thigh after muscle exposure (lesion of 15 mm length and 10 mm width). The lesion appears in a plane perpendicular to the beam. The red arrows indicate the formed lesion.

Figure 8.10.9 demonstrates the dissected tissue from the lesion site, which had a length of 24 mm. The ablated area was running throughout the thigh, from the outer to the inner side.

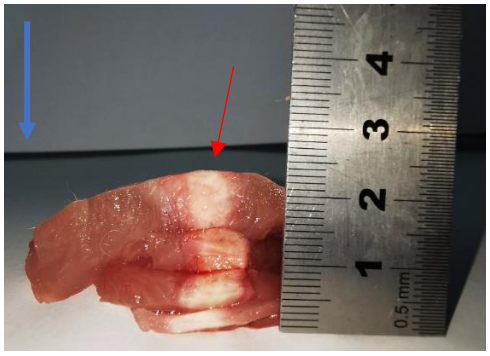

Figure 8.10.9: Macroscopic appearance of the lesion after dissection. The lesion appears in a plane parallel to the beam. The red arrow indicates the lesion (24 mm length) and the blue arrow indicates the beam direction.

Table 8.10.2 summarizes the parameters used for each sonication, the temperature change recorded from the MR thermometry results, and the dimensions of the ablation after the dissection of the rabbit's thigh.

Table 8.10.2: List of sonication parameters, dimensions of each lesion, and temperature change.

Sonication Nº	**Plane**	**Acoustic power (W)**	**Sonication time (s)**	**Length (mm)**	**Diameter (mm)**	**Temperature (ºC)**
1	coronal	8.6	30	24	10	13.2
2	coronal	22.5				39.3
3	axial					18.2
4	axial					19.3

9 Discussion and future perspectives

9.1 Discussion

The aim of this dissertation was to evaluate a MRgFUS 4-DOF robotic system that is intended to be used primarily for the treatment of PC or treatment of BPH. The process consisted of various methods to perform a complete evaluation of the robotic system such as focused ultrasound transducer evaluation in phantoms and excised tissues, evaluation of MR compatibility and accuracy of motion, near-field heating investigation and evaluation of the entire robotic system in the MRI environment in phantoms, excised tissues, and a small animal (preclinical stage).

The prostate gland is an integral part of the reproductive system in the male body and despite its small size, it still forms as the most important accessory male gland. However, it is usually affected by diseases including PC and non-cancerous diseases such as prostatitis and BPH. PIN and PIA diseases are also non-cancerous but, in some cases, may develop PC. Non-cancerous diseases influence the QOL of men and in many cases have to be treated.

Ultrasonic characteristics that were measured by other researchers [34,35] were important for the correct evaluation of the focused transducer. TMMs were developed to possess ultrasonic characteristics as close as possible to those of the human prostate, as found in the literature.

The two commercial transrectal devices that were approved for PC treatments and used by hospitals still have limitations mostly due to the image guidance and treatment feedback. Despite their advanced US softwares, the temperature change in the prostate is unknown during the procedure. Moreover, patients do not prefer HIFU treatment because of the high cost. The ExAblate transrectal system seems a promising system and is in the phase of clinical trials but there are still doubts about its cost since it uses a multi-element (1000) focused transducer which increases its price. A transurethral device (Tulsa-pro) has also been developed using MRI guidance and thus provides real-time temperature change feedback. However, this device uses transducer with planar elements and the treatment follows the ablation of a part of the prostate where the tumor exists, thereby in case of secondary small tumors there is a high possibility of ablating healthy prostate area. Furthermore, the clinical trials performed using the Sonablate and Ablatherm transrectal devices were promising and follow-up observations had shown complete PC treatment, with the appearance of some side effects. However, in many studies with these devices, it is not clear whether the devices precisely target and destroy PC

cells, or they also destroy surrounding healthy tissue. In preclinical studies, HIFU technology has been tested mainly in rats (small available area to be ablated) and in rare cases in dogs, while in this study the proposed robotic device has been tested in rabbits.

Agar/silica/milk TMMs were developed and used in the evaluation procedure of the thermal heating of the candidate transducers. Different types of TMMs (agar-based, PVC, PVA, NIPAM-based, PDMS, zerdine) are widely used to evaluate HIFU systems, with the phantoms developed herein undeniably being an integral part of this study. Prior the evaluation of the focused transducers and the robotic device, the phantoms were US imaged in order to check the homogeneity and echogenicity of the different concentrations of the silicon dioxide added. The silicon dioxide enhanced the scattering of the phantoms, as visualized from the US images. In addition, MR images were acquired to confirm that the phantoms were homogeneous and MR compatible. X-ray images were obtained entirely for observing how the agar/silica/milk phantoms look like under exposure to X-ray beam. No differences were observed between the different phantom recipes under the X-ray exposure. The mass density of an agar-based phantom was measured using the water volume displacement method and found to be 1.0385 kg/m^3. Another significant ultrasonic measurement of the developed agar-based TMMs was the speed of sound. The agar concentration was varied and the speed of sound was found in the range of 1535-1571 m/s. It resulted that the speed of sound of the agar-based phantoms increases with increasing agar concentration. The thermal properties of the agar-based TMMs were also estimated for varying agar concentration and the effect of evaporated milk on the thermal conductivity, diffusivity, and specific heat capacity was investigated. For TMMs with 2 and 6 % agar, the addition of evaporated milk increases the thermal conductivity and diffusivity, while for 4 % agar there is no significant difference. On the other hand, the addition of evaporated milk decreases the specific heat capacity of the agar-based TMMs. By changing the amount of agar from 2 to 4 %, the thermal conductivity and diffusivity of the TMMs with and without evaporated milk decreases while from 4 to 6 % it increases. This could be a result of density changes of the phantom that might be created with the addition of high agar concentration (>4 %). Therefore, the density change leads to increased thermal conductivity. Moreover, the change in the agar concentration results in an insignificant decrease of the specific heat capacity of the agar-based TMMs. The thermal conductivity, diffusivity, and specific heat capacity of agar and silicon dioxide were also measured. The agar has higher thermal properties than silicon dioxide with significant difference in thermal conductivity and diffusivity. It was also shown that temperature plays a major role in the thermal conductivity

of the agar-based TMMs. As the temperature of the agar-based TMM increases there is a decline in the value of thermal conductivity.

Since TMMs are crucial in the HIFU field, there was a need to develop a new TMM by replacing the silicon dioxide, which was used as scattering material, with a new material in order to reduce the thermal conductivity. An agar-based TMM doped with wood powder destined for evaluation of MRgFUS protocols was presented and characterized for its acoustical, MR, and thermal properties. The TMM was agar-based with the addition of a single material to control both acoustic energy loss mechanisms (absorption and scattering). This easy-to-make agar-based gel with the addition of wood powder was non-toxic, simple and easy to prepare, inexpensive, and possessed a high melting temperature point. The main objective of the study was to investigate the suitability of wood powder as an inexpensive alternative in replacing other added materials that have been suggested in previous studies for controlling the ultrasonic properties of TMMs. The characterization procedure involved a series of experiments designed to estimate the acoustic (attenuation coefficient, absorption coefficient, propagation speed, and impedance), thermal (conductivity, diffusivity, specific heat capacity), and MR properties (T_1 and T_2 relaxation times) of the wood-powder doped material. As expected, the developed TMM (2 % w/v agar and 4 % w/v wood powder) demonstrated MRI compatibility. The acoustic attenuation coefficient of the proposed material was measured over the frequency range of 1.1-3 MHz and found to be nearly proportional to frequency. The measured attenuation coefficient was 0.48 dB/cm at 1 MHz which was well within the range of soft tissue. Temperatures over 37 ^{o}C proved to increase marginally the attenuation coefficient. Following the transient thermoelectric method, the acoustic absorption coefficient was estimated at 0.34 dB/cm-MHz. The estimated propagation speed (1487 m/s) was within the range of soft tissue at room temperature, while it significantly increased with higher temperature. The material possessed an acoustic impedance of 1.58 MRayl which was found to be comparable to the corresponding value of muscle tissue. The thermal conductivity of the material was estimated at 0.51 W/m.K. Furthermore, the measured relaxation times T_1 (844 ms) and T_2 (66 ms) were within the range of values found in the literature for soft tissue. The phantom was tested for its suitability for evaluating MRgFUS thermal protocols. High acoustic energy was applied and temperature change was recorded using thermocouples and MR thermometry. MR thermal maps were acquired using single-shot EPI sequence. The TMM matched adequately the acoustic and thermal properties of human tissues and through a series of experiments, it was proven that wood concentration enhances acoustic absorption.

Experiments using MR thermometry demonstrated the usefulness of this phantom to evaluate ultrasonic thermal protocols by monitoring peak temperatures in real-time. Thermal lesions formed above an ultrasonic energy threshold were observed in both high-resolution MR images and visual dissections of the proposed TMM.

An improved system for measuring ultrasonic absorption was presented. The system was used to estimate the absorption coefficient of agar-based mixtures having varying concentration of agar, silicon dioxide, and evaporated milk. It was found that the absorption of agar-based gels can be best controlled by varying the concentration of agar. The increase of concentration of agar and evaporated milk results in an increase of the absorption coefficient of the agar-based TMMs. Although, silica seems to increase the absorption, its concentration should be limited to 4 % because above this level, scattering increases attenuation and thus lowers absorption. Using the optimum recipe for the agar-based phantom (4 % agar, 30 % evaporated milk and 4 % silica), the absorption coefficient was found to be 0.22 ± 0.02 dB/cm-MHz which is close to the value found in humans [251]. The absorption coefficient of a phantom with 6 % agar and 4 % silicon dioxide was measured repeatedly over seven days. The purpose was to investigate any possible change in the absorption coefficient and whether it changes over time. It was concluded that the absorption coefficient of the phantom is significantly lessened the first 1-3 days and then remains stable over time. Therefore, the absorption coefficient of agar-based phantoms needs to be measured within 24 hours.

A new prototype version of the robot was derived from a previous older version [19] having many modifications including the addition of Y and Φ axes. The previous older version included 2-DOF. In this robotic device, manual adjustment of the Y, Z, and Φ-axis was preferable after physicians' suggestions. The speed reduction resulting from the mechanisms, provided an easy to control motion with minimal effort. The addition of another 1-DOF manual axis enabled the user to adjust the probe accordingly, so that the patient would maintain a comfortable posture for the probe insertion; an important aspect as the patient must remain motionless during the entire treatment. The Y, Z, and Φ axes were operated manually by levers and knobs as they were designed to allow the appropriate placement of the device. These axes were used to set the insertion path of the probe, with regards to each patient's rectum anatomy. The proposed device is small enough to fit in any MRI bore that performs MR patient imaging. It is also compact while covers were used to hide the inside mechanisms thereby giving a more aesthetic and professional appearance. The PC treatment with this device is performed endorectally which allows the focused transducer to be next to the prostate. It was made out of

ABS plastic and the motion of every computer-controlled axis was activated by non-magnetic piezoelectric motors. The device includes the following axes: X-axis with a range of 50 mm, Θ-axis with a range of 180^{o} (90^{o} CW and 90^{o} CCW), Z-axis with a range of 60 mm, Φ-axis with a range of 90 ^{o}. However, the design of the probe limits the angular movement in a range of motion of 30^{o} (15^{o} on each direction).

The diameter of the 4.4 MHz transducer was smaller thus having the advantage of reducing the size of the probe but it also has the disadvantage of not achieving enough ultrasonic penetration in the phantom and tissue due to its higher frequency. On the other end, the diameter of the 3.2 MHz transducer was larger thus increasing the size of the probe however having a lower frequency of resonance results in better penetration of the HIFU energy and better focusing. Moreover, the 3.2 MHz transducer was more resistant to high power sonications and despite the many experiments that had been performed, it did not present any defects. For those reasons, the transducer of 3.2 MHz was selected for the robotic device in order to proceed to the evaluation procedure with this transducer.

The MR compatibility of the activation of the transducer and RF amplifier was evaluated in an agar-based phantom. The SNR was measured under various conditions (electronic system presence or activation, and transducer presence or activation) using three different MR sequences (T2-FRFSE, FSPGR, EPI). The SNR was maximum when all components were deactivated. There was some decrease in the SNR when the RF amplifier was activated while there was a higher decrease in the SNR when the transducer was activated.

It resulted that the piezoelectric motors and optical encoders of the robotic device are MR compatible under high resolution sequences and MR thermometry imaging sequences. The SNR in the MR quality assurance phantom was calculated for different configurations. There was some decrease in the SNR when a motor or encoder or the transducer was activated. It was shown that the SNR does not change dramatically from the control condition with the phantom present in the MR bore or with presence of the electronic system (activated or not). The highest reduction of the SNR was calculated with EPI sequence with a reduction of around 9 dB. The SNR using T2-FRFSE and FSPGR dropped slightly with each configuration. Both motors and encoders did not cause dramatic reduction in the SNR for all MR sequences. As a consequence, both FSPGR and EPI can be used to obtain MR data for MR thermometry since the robotic system does not significantly affect the SNR. However, an attempt to obtain MR images during motion of the robotic system introduced extensive noise on the encoder signal line, resulting in device malfunction.

The NUI of the agar-based phantom under various conditions was estimated. The uniformity of the agar-based phantom for all MR sequences remained almost stable with each configuration. The agar-based phantom for the FSPGR sequence showed high NUI meaning that the signal in the phantom was affected. However, the T2-FRFSE and EPI sequence showed low NUI meaning that the agar-based phantom was uniform and the signal did not significantly change using these sequences. Thus, EPI sequence can be used for MR thermometry even if the phantom is not completely uniform or the signal is not excellent.

The NUI of the MR quality assurance phantom for the different MR sequences and configurations was also calculated. At the control condition with the phantom only, the minor drop in the uniformity of the phantom was possibly due to poor transmission of the RF-coil. The uniformity of the phantom showed the same behavior for the T2-FRFSE and EPI sequences. The uniformity of the phantom did not show any change using the T2-FRFSE and EPI sequence. However, the uniformity of the phantom using FSPGR sequence significantly decreased upon activation of the motors and encoders. Overall, the presence of the robotic device in the MR bore, its connection to the electronic system and the activation of electronics did not significantly affect the SNR and uniformity of the MR-phantom.

To sum up, the activation of the amplifier, transducer, piezoelectric motors and optical encoders did not affect the quality of MR images. Since the quality of the MR images was not affected more than expected, electromagnetic shielding was not necessary.

Furthermore, the accuracy of the motion of the 4-DOF robotic system was evaluated. The accuracy of the motion was evaluated at step movements of 1, 5, 10, 15, and 20 mm for linear motion (X-axis) and 1, 5, 10, and 15^{o} for angular motion (Θ-axis) using digital calipers and a specially designed setup. The evaluation of the 2 additional axes (Z and Φ-axis) was not performed since these axes are manually controlled.

The error at each step movement of the robotic device was estimated for both linear (forward and reverse) and angular (CW and CCW) motion. Regarding linear motion, a step movement of 1 mm resulted in slightly higher (7.3 %) error in forward motion than reverse (5.5 %) and it was the highest error of all moving steps of the linear PC-controlled motion. Step movement of 5 mm also resulted in slightly higher error(4.5 %) in forward direction than reverse (3.58 %) while at step movement of 10, 15, and 20 mm the error between the forward and reverse direction was approximately the same (2-3 %). Therefore, for the 1 mm linear motion, the maximum error was 73 μm (forward direction). For 5 mm the maximum error was 225 μm

while for 10 mm it was 237 μm for the same axis. For 15 and 20 mm, the maximum error was 365 μm and 414 μm for the reverse direction, respectively.

Moreover, the speed of motion of the linear axis of the robotic device in both directions (forward and reverse) was calculated. The speed motion of the forward direction was slower (0.59 mm/s) than that of the reverse (0.72 mm/s). Overall, the speed of linear motion of the robotic device was slow allowing for more accurate motion. The speed of each piezoelectric motor depends mainly on the corresponding drivers (D6060, Shinsei Corporation) of the motors thus each driver can control the motors at different speeds.

The accuracy of the angular motion was also assessed with a specially designed 3D-printed part. A digital caliper which measures angular motion was used. The error of angular motion in the CCW direction was higher than the error in the CW direction for angular steps of 1, 5, 10, and 15^{o}. The maximum percentage error occurred at the 1^{o} angular step (9 %), concluding that as the angular step increases the error decreases.

Moreover, for the 1^{o} step the maximum error was 0.09^{o}, for the 5^{o} step was 0.113^{o}, for the 10^{o} step was 0.133^{o} and for the 15^{o} was 0.147^{o} in the CCW direction. The speed of the angular motion was 1.33 ^{o}/s in the CW direction and 1.37 ^{o}/s in the CCW direction. Since the angular speed was slower, the issue that was previously observed with the inaccuracy of the angular motion at low angle steps (<5^{o}) has been overcome.

The accuracy of the motion was also evaluated using MR thermometry by acquiring FSPGR images and observe the ultrasonic beam location in planes perpendicular and parallel to the beam direction.

Six algorithms (Sequential, Triangular, Spiral, Random, Euler's, Square) were used with different time delays of 0 s (no delay), 10 s, 20 s, 30 s, 40 s, 50 s, and 60 s to examine their effect on the variation of the transducer's induced heating in the pre-focal region. Temperature change versus time was recorded for each different time delay. Peak temperature change did not show any specific trend mostly because it was dependent on the location of the thermocouple (i.e. largest temperature recorded at the closest location of the transducer to the thermocouple).

The average temperature change for each different time delay and algorithm on average decreased with increasing time delay. With no time delay between sonications, all algorithms except Euler's, produced severe average heating of more than 10 ^{o}C in the pre-focal region. Amongst these five algorithms, Random algorithm induced the highest average temperature

change and Sequential the lowest. Euler's algorithm resulted in an average temperature change of far less than 10 ^{o}C (moderate heating). A time delay of 10 s produced severe heating in all algorithms except Euler's, with Triangular resulting in the highest average temperature change. The time delay of 10 s using Euler's algorithm turned out to be adequate for a near-field heating elimination of less than 5 ^{o}C. Moderate heating (3-7 ^{o}C) was induced in all algorithms at 20 s time delay. At 30 s time delay, Euler's and Triangular algorithms were the first to eliminate (< 3 ^{o}C) pre-focal heating, with the rest of the algorithms still inducing moderate heating. Pre-focal heating was eliminated at 40 s delay in all algorithms except Square which still induced slightly moderate heating. The pre-focal temperature increase was eliminated for all algorithms at 50 and 60 s delay, with Random resulting in the lowest and Euler's algorithm in the greatest. Generally, a 40 s time delay results in safe temperatures in the near-field region using the transducer of 3.2 MHz for prostate ablation.

The time taken for robot movement was calculated for all six algorithms to examine the effect on total treatment time. Assuming a 40 s delay and a 5 s sonication time using a 10 x 10 grid (100 movements), the total treatment time was 76.7 minutes for sequential algorithm, 77.7 minutes for triangular algorithm, 79.95 minutes for spiral algorithm, 80.9-81.9 minutes for random algorithm, and 78.25 minutes for Euler's algorithm. However, 30 s time delay was found satisfactory for completely eliminating pre-focal heating using Triangular and Euler's algorithm and thus their total time was reduced to 61 and 61.6 minutes respectively. Square needed a total of 82.77 minutes; however, it still induced moderate heating. For complete elimination of the near-field heating, a 50 s time delay was needed, increasing the total treatment time to 99.4 minutes.

Experiments have shown that phantoms are ideal for multiple sonications and many results can be acquired since they are able to withstand high temperatures. However, excised tissues and the particular set-up that was used for the experiments, provided the possibility of lesion formation in several locations using varied HIFU protocols. The first experimental set-up (version 1) was used for phantom experiments but due to structural shortcomings it was replaced with another experimental set-up (version 2).

The experimental set-up that was used in order to detect the focal point in a porcine excised tissue was important since it provided the potential of recording the temperature change using a thermocouple at every 5 mm distance. The focal point of the transducer of 3.2 MHz in the excised tissue was found at 2 cm as expected, however there was also an increase of temperature at the interface. A lesion was formed with 15 W acoustic power for 30 s sonication.

Therefore, the transducer of 3.2 MHz was capable to induce lesions even with low acoustic power and sonication time.

At focal depth of 2 cm, 285 J were needed to create lesion using sonication time of 5 s (shortest sonication time that created a lesion of 8 mm diameter and 16.9 mm length). At 3 and 4 cm focal depth, 360 J were needed to create lesion using sonication time of 20 and 5 s, respectively. Moreover, in some sonications the ratio of lesion length to diameter was good (10 s sonication). Overall, the 3.2 MHz transducer can create lesions at focal depth up to 4 cm for sonication time of 5 s.

A minimum product (energy) of 350 J was sufficient to create a lesion in just 5 s when the focal length was set at 3 cm in the tissue. In most cases where the excised tissues were homogeneous, repeatability of the results was achieved. Most of the lesions showed good ratio of lesion length to diameter. Possible reasons resulting in low ratio of lesion length to diameter were the presence of cavitation due to possible air in the excised tissue, poor homogeneity at varied locations in the tissue and the top surface of the tissue not being completely flat. These issues could influence the ultrasonic beam and therefore the formation of lesions. The lesions formed with 5 s sonication penetrated the tissue with an average length of around 1.5 cm, thus a pulse sonication of 5 s and energy of 350 J is advised for lesion creation with this transducer. It seems that at focal depth of 3 cm and the same acoustical power, as the pulse duration decreases and therefore the energy decreases, the lesion diameter also declines and the lesion penetrates deeper in the tissue (increase of lesion length).

The experimental set-up that was used in order to create lesions in excised tissues has the ability of adjusting the depth of the focal point in the tissue while the location of the HIFU beam can be manually adjusted. The evolution of the experimental set-ups was performed to result in an experimental set-up that provided stability for the testing materials (phantoms and excised tissues) and the exact location of the focal point was known for thermocouple measurements.

The diameter and length of a lesion increases as long as the acoustical power increases. However, the diameter and length of a lesion drops as the depth increases, mainly due to the attenuation. All the experimental set-ups were MR compatible without affecting the MR signal.

MR images of the experimental set-ups were acquired using a T2-weighted FSPGR sequence in order to visualize the experimental set-up, evaluated transducer and testing material. The resolution of the T2-weighted FSPGR sequence was sufficient and the contrast between the testing material and the degassed/deionized water was ideal for MR imaging of the

experimental set-up. The transducer was also clearly visible in the MR images without distorting them.

MR thermal maps were produced using MR thermometry. Initially, MR data was acquired on coronal and axial planes after sonicating phantoms using the transducer of 4.4 MHz. T2-weighted FSPGR was used to obtain the data. By selecting this sequence, it was possible to obtain an MR image every 12 s for sonication of 60 s. Temperature change from each image was calculated. The peak temperature at acoustical power of 18 W, sonication of 60 s, and focal depth of 2.5 cm was around 23 ºC.

MR thermal maps were also obtained in excised tissues using both the transducer of 4.4 MHz and 3.2 MHz. Lesions with various HIFU parameters were produced using the transducer of 3.2 MHz. For each HIFU sonication, an MR map on axial plane was obtained in order to visualize the HIFU beam and obtain feedback of temperature changes during sonication and cooling time. A single-shot EPI pulse echo sequence was later used which was able to obtain an MR image every around 1 s.

The robotic system was evaluated in an agar-based rectum-mimicking phantom and in excised tissues using three different experimental models (excised tissue over the probe, excised tissue and probe both immersed in degassed water, and excised tissue surrounding the probe). During evaluation in the agar-based rectum-mimicking phantom, the minimum temperature at the focal point (4.5 cm) was 47.3 °C for an acoustical power of 9 W while the maximum temperature was 66.2 °C for an acoustical power of 24 W. Resepectively, the minimum temperature at the probe-phantom interface (0.5 cm) was 37 °C for an acoustical power of 9 W while the maximum temperature was 49.1 °C for an acoustical power of 24 W.

During the evaluation where the excised tissue was over the probe, lesions' creation was problematic. Most of the trials failed while cases where lesions were formed, they were superficial with no depth penetration. Possible reasons were the inadequate coupling between excised tissue and medical condom and the presence of cavitation due to possible air in the excised tissue. After a successful trial (acoustical power of 24 W and sonication time of 30 s), a grid pattern of 1 x 3 was performed and the average diameter and length of the formed lesions were 14.79 mm x 18.32 mm and 13.9 mm, respectively.

The robotic system was evaluated with the excised tissue and probe both immersed in a water tank filled with degassed water. Repeatability of the lesions's shape and size was achieved. Most of the lesions showed good ratio of length to diameter. The maximum lesion length was

33.65 mm and was achieved for an acoustical power of 38.4 W with sonication time of 5 s. The minimum lesion length was 19.94 mm for an acoustical power of 22.5 W with sonication time of 30 s. Some of the cases failed due to the presence of air bubbles in the excised tissues.

The last technique to evaluate the robotic system, which is closer to the real treatment style, was performed after piercing the excised porcine tissue at the center (mimicking rectum) and placing the probe in the center. Most of the trials were successful but some of the cases failed due to the presence of air bubbles. A lesion with maximum length of 41.2 mm was achieved for an acoustical power of 28.5 W and sonication time of 30 s, while the minimum lesion length was 4.85 mm for an acoustical power of 25.5 W and sonication time of 15 s.

Finally, the *in-vivo* efficiency of the 4-DOF robotic system was evaluated in small animal (healthy rabbit) under MRI guidance. During the experiment, there was no indication of animal suffering and the animal remained in deep general anesthesia until euthanasia. High-resolution MR images were taken prior the treatment and a perfect coupling between the probe (covered with a medical condom and filled with degassed water) and the rabbit's thigh was confirmed. MR thermometry was acquired on coronal and axial planes indicating the temperature change induced by the ultrasonic beam. MR thermometry images were successfully obtained under respiratory motion and blood flow. During the MR thermometry, profiles of the temperature change versus sonication time were also acquired. Tissue ablation remained in the targeted zone, without tissue damage in other areas, suggesting no unwanted side-effects. Post-treatment, PD MR images with fat suppression were obtained on sagittal and coronal planes in order to respectively visualize the diameter and length of the ablated area . The total ablated area of the diameter as calculated from the MR images was around 270 mm^2 (16.6 mm x 16.3 mm) while the length was 26.8 mm. Finally, the right thigh of the rabbit was dissected after euthanasia and the ablated area was detected and measured (10 mm diameter and 24 mm length).

9.2 Future perspectives and suggestions for improvements

The main scope of this dissertation was the evaluation of a 4-DOF robotic system for the treatment of PC at early stage. Another important point of the research was the investigation of TMMs and the measurement of their acoustic and thermal parameters. Emphasis was given on the estimation of the ultrasonic absorption coefficient by introducing a new, simple and fast method. Although the measurements were performed on TMMs, some of the future studies

include the absorption measurement of freshly excised tissues using this simple to use experimental setup which provides accurate measurement of the absorption coefficient. It is highly desirable to measure the absorption of brain, prostate, and fibroid tissues due to the current clinical efforts for these tissues.

Further, a new TMM containing agar and wood powder has been proposed. The TMM has the ability to model the formation of thermal lesions above the temperature threshold which is still unknown. In the future, when the threshold is determined it will be possible to estimate the ultrasonic energy that is needed to produce a lesion in the TMM. Future studies will entail adding materials to change the agar/wood powder TMM properties to match the properties of specific tissues of interest.

Some modifications and suggestions regarding the 4-DOF robotic system include the insertion of special registration marks at fixed positions within the probe for faster recognition of the transducer through the MR images and better treatment plan. Also, the transducer of the robotic device will be more efficient with the development of a professional cooling device which will be a part of the entire system. The cooling system is required to circulate the degassed water within the probe so as to achieve transducer cooling during sonications and avoid unwanted heating of the rectum wall. In addition, the next step of the evaluation procedure is the acquisition of a regulatory approval for performing preclinical trials in dogs for treating dogs' prostate which has similar characteristics to male human. At a later stage, it will be feasible to receive regulatory approval for performing clinical trials.

10 Appendix

10.1 Summarize of the review of clinical studies of the existing HIFU devices

Table 10.1.1 lists the researchers of all-important clinical studies, the devices that were used, patients involved in the studies, and the main outcomes and conclusions of their studies.

Table 10.1.1: List of studies performed using focal therapies including the existing HIFU devices (Sonablate and Ablatherm).

Author	Reference	Treatment	HIFU device	Patients	Conclusions
Fegoun *et al.*	[191]	HIFU	Ablatherm	12 patients received prostate hemi-ablation	2 men died, 58 % of the patients showed no evidence of disease at 10-years follow-up
Perera *et al.*	[50]	cryotherapy, HIFU, photodynamic therapy, laser, irreversible electroporation, local brachytherapy, and RF ablation	NM[1]	NM	advantages, disadvantages, and side effects were reported for each treatment type
Topazio *et al.*	[192]	salvage HIFU	Ablatherm	1 patient	there was no evidence of fistula at 24 months follow-up
Poissonier *et al.*	[193]	HIFU	Ablatherm	227 patients	negative post-HIFU biopsies in 196 patients, side effects such as bladder neck and urethral stenosis were observed, the 5-year disease-free survival rate was 66 %

[1] Not Mentioned

Thuroff *et al.*	[195]	HlFU	Ablatherm	704 patients (78.5 % intermediate or high-risk disease)	cancer specific survival rate of 99 %, metastasis-free survival of 95 %, 10-year salvage treatment-free rates of 98 % for low-risk, 72 % for intermediate-risk and 68 % for high-risk respectively, side effects were observed including incontinence, obstruction, infection, rectourethral fistula formation, and perineal pain
Blana *et al.*	[8]	HlFU	Ablatherm	140 patients	prostate biopsies were negative in 86.4 % of patients, the biochemical failure-free survival rates at 5 and 7 years were 77 % and 69 % respectively, the actuarial disease-free at 5 and 7 years were 66 % and 59 % respectively, side effects: 132 patients developed continent, 7 with incontinence grade I, 1 with incontinence grade II, 10 developed urinary infection, urinary obstruction was observed in 19 patients and 8 developed pelvic pain
Uchida *et al.*	[196]	HlFU	Sonablate	181 patients	prostate was treated in 1 (156 patients), 2 (22 patients) and 3 (1 patient) HIFU sessions, the median time of treatment was 152 minutes, side effects were appeared, 39 patients with urethral stricture, 11 with epididymitis, 2 with rectourethral fistula and a transient grade I was observed in 1 patient
Madersbacher *et al.*	[197]	HlFU	NM	10 patients	HIFU completely treated 3 out of 10 tumors and destroyed a mean of 53 % of the total tumor in the other 7 patients
Muto *et al.*	[198]	HlFU	Sonablate 500	70 patients received whole-gland treatment compared to 29 men who had the	2-year biochemical disease-free survival rates in patients with low, intermediate, and high-risk were 85.9 %, 50.9 %, and 0 % respectively, a 12-months follow-up showed negative biopsy

				transitional zones spared on the unaffected site	rate of 81.6 %, 76.5 % in patients receiving focal therapy and 84.4 % in patients with whole therapy
Ahmed *et al.*	[199]	HlFU	NM	20 patients received HIFU hemi-ablation	6 months follow-up showed negative biopsy rate of 89 %
Thuroff *et al.*	[200]	HlFU	Ablatherm	NM	87 % of the patients showed negative biopsy with 92 %, 86 %, and 82 % in the low, intermediate, and high-risk groups respectively
Asimakopoulos *et al.*	[201]	HlFU	Ablatherm	19 patients	17 out of 19 patients (89.5 %) received successful treatment, side effects: acute urinary retention and stress urinary incontinence
Chaussy *et al.*	[202]	HlFU	Ablatherm	184 patients (232 sessions, mean duration 90 minutes, 2.25 MHz or 3 MHz, 50 W and penetration depth of 25 mm)	80 % of patients were cancer-free after follow-up and no side effects were observed
Crouzet *et al.*	[203]	HlFU	Sonablate and Ablatherm	880 patients	free-survival rates were around 70 % and negative post-operative prostate biopsies were almost 85 %
Challacombe *et al.*	[204]	HlFU	Ablatherm	43 patients; primary HIFU treatment (31), salvage HIFU treatment (12)	mean treatment time in the primary group was 71.1 minutes and in salvage was 63.3 minutes, in the primary group there were 13 failures and in the salvage 5 failures using the Phoenix definition, in the primary group there were 21 failures and in the salvage 8 using the FDA trial endpoint, side effects: 2 patients developed urethral strictures in the primary group and 1 patient in the salvage group developed urethral stricture and 2 prostatorectal fistulas

Blana *et al.*	[205]	HlFU	Ablatherm	146 patients	93.4 % of patients showed negative control cancer biopsies, 12 % developed transurethral resection due to obstruction, 47.3 % with erectile function and 1 patient with rectourethral fistula while no stress incontinence was noted
Rove *et al.*	[206]	HlFU	comparison of Ablatherm and Sonablate	301 patients	the negative biopsy rates after 3 months ranged from 80 % to 90 % using the ablatherm device while for Sonablate they ranged from 64 % to 87 %, the disease-free rate for Ablatherm was 77 % at 5-years follow-up (for 120 patients) whereas for Sonablate it was 78 % (for 181 patients)
Ahmed *et al.*	[13]	HlFU	Sonablate	172 patients	urethral stricture was lower in patients with suprapubic catheter than those with urethral catheters, side effects: epididymitis, potency and mild stress urinary incontinence, there was no evidence of cancer after 1 HIFU session in 92.4 % of patients
Chalasani *et al.*	[207]	HlFU	Sonablate	1 patient	The patient developed prostatorectal fistula and histological changes of dense fibrosis were observed at the treated area
Blana *et al.*	[208]	HlFU	Ablatherm	223 patients (174 received only 1 treatment and 49 received second treatment)	side effects: urinary tract infection, chronic pelvic pain, infravesical obstruction, stress incontinence and impotence
Robison *et al.*	[209]	HlFU	NM	1 patient	side effects: urinary retention, urinary tract infections and intermittent stress, a new side effect was appeared (pubic bone osteomyelitis stemming)

Shoji *et al.*	[210]	HlFU	Sonablate 500	44 patients (3 HIFU sessions needed to cover the prostate treated area)	prostate swelling and intraprostatic point shift were measured, during session 1 it was found the most prostate swelling and intraprostatic point shifts
Ripert *et al.*	[211]	salvage EBRT after HIFU failure	Ablatherm	60 patients (69 HIFU procedures, 48 in first line and 12 in second line)	35 patients who treated in first line showed HIFU failure and the overall disease-free survival rate was 83.3 % at 36.5 months follow-up
Komura *et al.*	[212]	HlFU	Sonablate	171 patients (52 with low-risk, 47 intermediate-risk and 72 high-risk)	after median follow-up time of 43 months, 44 and 36 patients experienced biochemical failure using the Stuttgart and Phoenix definitions respectively, the overall and cancer specific survival rates at 5-years were 98.8 % and 100 % respectively
Uchida *et al.*	[213]	HlFU	Sonablate 200	20 patients (28 HIFU procedures)	side effects: 1 patient developed rectourethral fistula, 2 appeared with urethral stricture and 1 underwent transurethral resection
Uchida *et al.*	[214]	HlFU	Sonablate	63 patients	the overall biochemical disease-free rate was 75 %, 55 patients were cancer-free
Mearini *et al.*	[215]	HlFU	Sonablate 500	30 patients (before HIFU and 3-6 months after surgery, patients underwent urodynamic study)	improvement in bladder outlet, maximum flow at uroflowmetry and decrease in postvoid residual
Song *et al.*	[216]	HlFU	Ablatherm	13 patients	the overall biochemical recurrence-free rate was 53.8 % and the complication rate was evaluated at 38.5 %

10.2 Simulation parameters and results of the candidate transducers

Table 10.2.1 lists the parameters that were entered as inputs into the software for the transducer of 4.4 MHz.

Table 10.2.1: List of the simulation parameters for the candidate transducer of 4.4 MHz.

	Parameter	**Variable**	**Value**	**Unit**
Transducer	Frequency	Tx.f	4.4e6	Hz
	Inner radius	a_1	0	cm
	Outer radius	a_2	0.865	cm
	Focusing depth	Tx.d	4.4	cm
	Power	Tx.P	10, 20, 30, 50	W
Computational domain	Starting point	z_start	$d-\sqrt{d^2-a_2^2}$	cm
	Max axial distance	Grid.Z	9	cm
	Number of harmonics	Grid.KK	128	-
	Radial grid density	ppw_r	12	-
	Axial grid density	ppw_z	10	-
Hydrophone	Element diameter	hd	0.2	mm
Graphical output	Axial locations	z_output	4.045-4.086	cm
Material	Number of layers	II	3	-
Material 1	Material transition distance	Layer(1).z	0	cm
	Small-signal sound speed	Layer(1).c	1482	m/s
	Mass density	Layer(1).rho	1000	Kg/m^3
	Attenuation at 1 MHz	Layer(1).alpha	15	dB/m
	Fraction due to absorption	Layer(1).fraction	0	-

	Exponent of attenuation power law	Layer(1).eta	2	-
	Nonlinear parameter	Layer(1).beta	3.5	-
	Heat capacity	Layer(1).Cp	4180	J/kg/K
	Thermal conductivity	Layer(1).kappa	0.6	W/m/K
	Perfusion rate	Layer(1).w	0	$Kg/m^3/s$
Material 2	Material transition distance	Layer(2).z	3	cm
	Small-signal sound speed	Layer(2).c	1629	m/s
	Mass density	Layer(2).rho	1000	Kg/m^3
	Attenuation at 1 MHz	Layer(2).alpha	10	dB/m
	Fraction due to absorption	Layer(2).fraction	0.9	-
	Exponent of attenuation power law	Layer(2).eta	1	-
	Nonlinear parameter	Layer(2).beta	4.5	-
	Heat capacity	Layer(2).Cp	4180	J/kg/K
	Thermal conductivity	Layer(2).kappa	0.6	W/m/K
	Perfusion rate	Layer(2).w	20	$Kg/m^3/s$
Material 3	Material transition distance	Layer(3).z	6	cm
	Small-signal sound speed	Layer(3).c	1482	m/s
	Mass density	Layer(3).rho	1000	Kg/m^3
	Attenuation at 1 MHz	Layer(3).alpha	15	dB/m
	Fraction due to absorption	Layer(3).fraction	0	-
	Exponent of attenuation power law	Layer(3).eta	2	-
	Nonlinear parameter	Layer(3).beta	3.5	-
	Heat capacity	Layer(3).Cp	4180	J/kg/K

	Thermal conductivity	Layer(3).kappa	0.6	W/m/K
	Perfusion rate	Layer(3).w	0	$Kg/m^3/s$
Thermal heating	Sonication duration	t_h	30	sec
	Cooling duration	t_c	30	sec
	Baseline temperature	Teq	37	ºC
	Dose threshold for safety	safety	80	CEM_{43}
	Dose threshold for efficacy	efficacy	240	CEM_{43}

Table 10.2.2 lists the parameters that were entered as inputs into the software for the transducer of 3.2 MHz.

Table 10.2.2: List of the simulation parameters for the candidate transducer of 3.2 MHz.

	Parameter	**Variable**	**Value**	**Unit**
Transducer	Frequency	Tx.f	3.2e6	Hz
	Inner radius	a_1	0	cm
	Outer radius	a_2	1.25	cm
	Focusing depth	Tx.d	4.5	cm
	Power	Tx.P	10, 20, 30, 50	W
Computational domain	Starting point	z_start	$d - \sqrt{d^2 - a_2^2}$	cm
	Max axial distance	Grid.Z	12	cm
	Number of harmonics	Grid.KK	128	-
	Radial grid density	ppw_r	12	-
	Axial grid density	ppw_z	10	-
Hydrophone	Element diameter	hd	0.2	mm
Graphical output	Axial locations	z_output	4.277-4.314	cm

Material	Number of layers	II	3	-
Material 1	Material transition distance	Layer(1).z	0	cm
	Small-signal sound speed	Layer(1).c	1482	m/s
	Mass density	Layer(1).rho	1000	Kg/m^3
	Attenuation at 1 MHz	Layer(1).alpha	15	dB/m
	Fraction due to absorption	Layer(1).fraction	0	-
	Exponent of attenuation power law	Layer(1).eta	2	-
	Nonlinear parameter	Layer(1).beta	3.5	-
	Heat capacity	Layer(1).Cp	4180	J/kg/K
	Thermal conductivity	Layer(1).kappa	0.6	W/m/K
	Perfusion rate	Layer(1).w	0	$Kg/m^3/s$
Material 2	Material transition distance	Layer(2).z	3	cm
	Small-signal sound speed	Layer(2).c	1629	m/s
	Mass density	Layer(2).rho	1000	Kg/m^3
	Attenuation at 1 MHz	Layer(2).alpha	10	dB/m
	Fraction due to absorption	Layer(2).fraction	0.9	-
	Exponent of attenuation power law	Layer(2).eta	1	-
	Nonlinear parameter	Layer(2).beta	4.5	-
	Heat capacity	Layer(2).Cp	4180	J/kg/K
	Thermal conductivity	Layer(2).kappa	0.6	W/m/K
	Perfusion rate	Layer(2).w	20	$Kg/m^3/s$
Material 3	Material transition distance	Layer(3).z	6	cm
	Small-signal sound speed	Layer(3).c	1482	m/s
	Mass density	Layer(3).rho	1000	Kg/m^3
	Attenuation at 1 MHz	Layer(3).alpha	15	dB/m

	Fraction due to absorption	Layer(3).fraction	0	-
	Exponent of attenuation power law	Layer(3).eta	2	-
	Nonlinear parameter	Layer(3).beta	3.5	-
	Heat capacity	Layer(3).Cp	4180	J/kg/K
	Thermal conductivity	Layer(3).kappa	0.6	W/m/K
	Perfusion rate	Layer(3).w	0	$Kg/m^3/s$
Thermal heating	Sonication duration	t_h	30	sec
	Cooling duration	t_c	30	sec
	Baseline temperature	Teq	37	ºC
	Dose threshold for safety	safety	80	CEM_{43}
	Dose threshold for efficacy	efficacy	240	CEM_{43}

The radial distribution of the first five harmonic pressure amplitudes at Z = 4.056 cm (for 20 W), Z = 4.086 cm (for 50 W) for the transducer of 4.4 MHz, and at Z = 4.3 cm (for 20 W), Z = 4.277 cm (for 50 W) for the transducer of 3.2 MHz is shown in Figure 10.2.1. From the radial distribution, the pressure at the center of the beam for the first harmonic as well as the acoustic intensity were extracted.

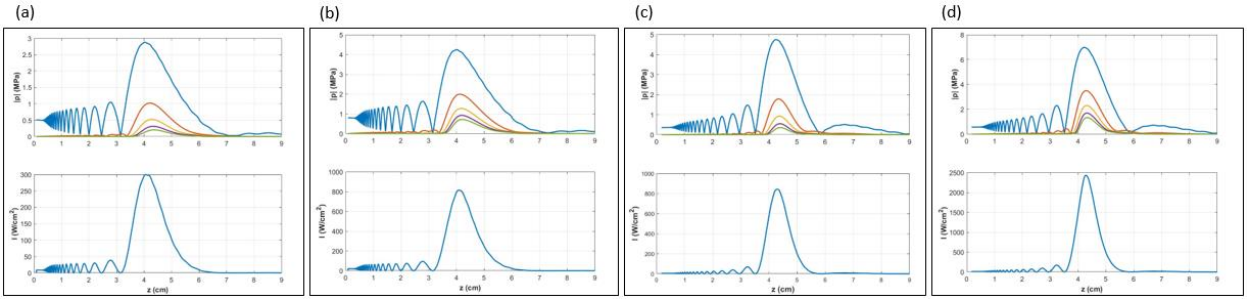

Figure 10.2.1: Radial distribution of the first five harmonic pressure amplitudes of the 4.4 MHz transducer at acoustic power of a) 20 W, and b) 50 W and of the 3.2 MHz transducer at acoustic power of c) 20 W, and d) 50 W.

Figure 10.2.2 shows the quantitative plot of the US spatial distribution on the axial plane. The vertical scale (*r*) is the diameter of the beam and the lateral axis (*z*) is the sonication depth. This plot shows the prediction of the software application for the size and shape of the ultrasonic beam.

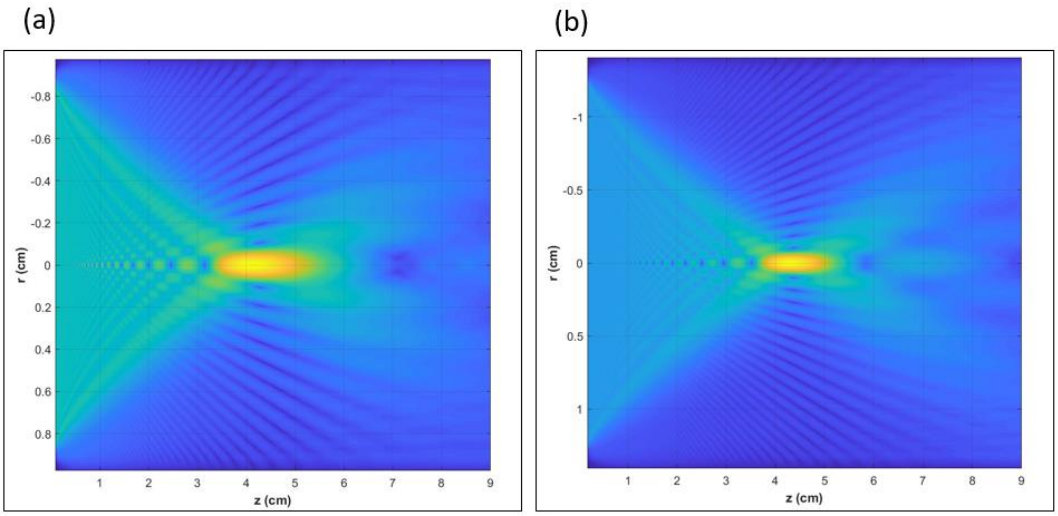

Figure 10.2.2: A qualitative plot of the spatial distribution of the US field of the transducer of a) 4.4 MHz, and b) 3.2 MHz.

Figure 10.2.3 shows the rate at which the temperature increases at the focus after activation of the transducer for 30 s. When the transducer was deactivated the simulation continued to calculate the rate at which the temperature decreased for 30 s. The temperature was set to begin from a baseline (average normal human body temperature). The thermal dose at 20 W acoustic power for the 4.4 MHz transducer is not sufficient to induce lesions while this power induces lesions with the 3.2 MHz transducer. The acoustic power of 50 W is sufficient to induce lesions for both transducers, but the produced lesion using the 3.2 MHz transducer has more homogeneous cigar-shape.

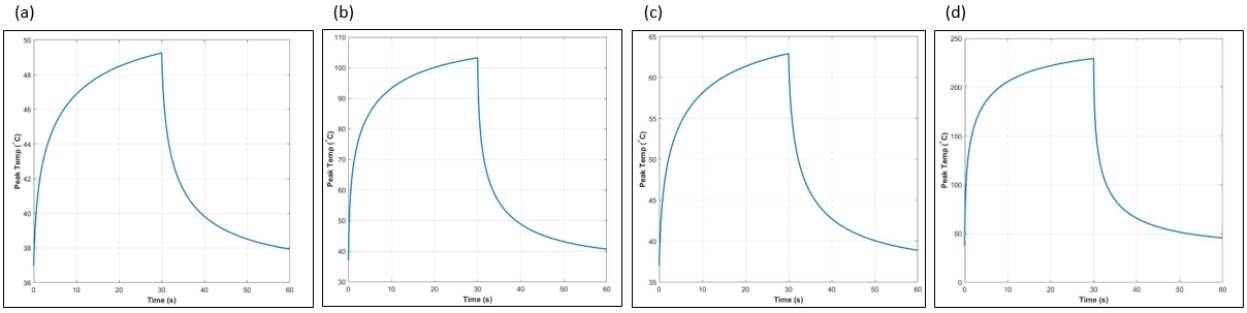

Figure 10.2.3: Temperature with respect to time for activation and deactivation of the 4.4 MHz transducer and acoustic power of a) 20 W, and b) 50 W and of the 3.2 MHz transducer and acoustic power of c) 20 W, and d) 50 W.

Figure 10.2.4 shows the temperature distribution along the beam path at the time when the peak temperature occurs. The temperature buildup suggested an estimation for the focus shape and size.

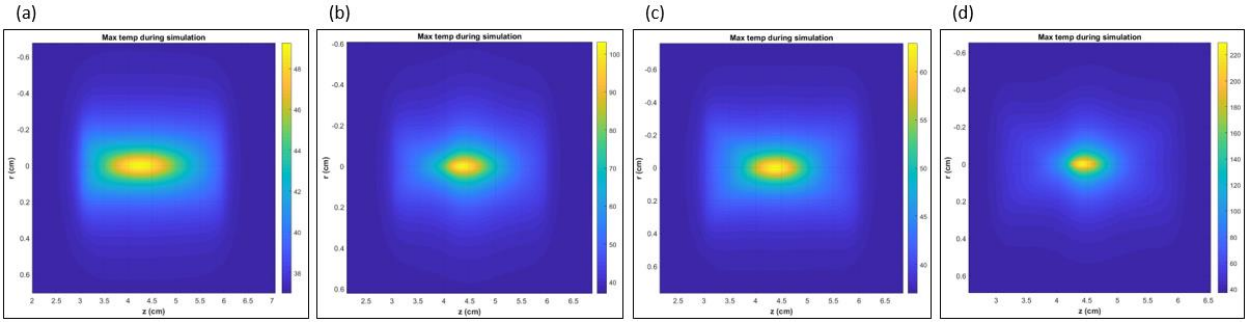

Figure 10.2.4: Temperature distribution at the time peak temperature occurs of the 4.4 MHz transducer and acoustic power of a) 20 W, and b) 50 W and of the 3.2 MHz transducer and acoustic power of c) 20 W, and d) 50 W.

The thermal dose calculation is shown in Figure 10.2.5. The lesion size is calculated by estimating the thermal dose. On the inside of the yellow perimeter, the thermal dose is equal or larger than 240 cumulative equivalent minutes (CEM) which suggests that tissue necrosis occurs.

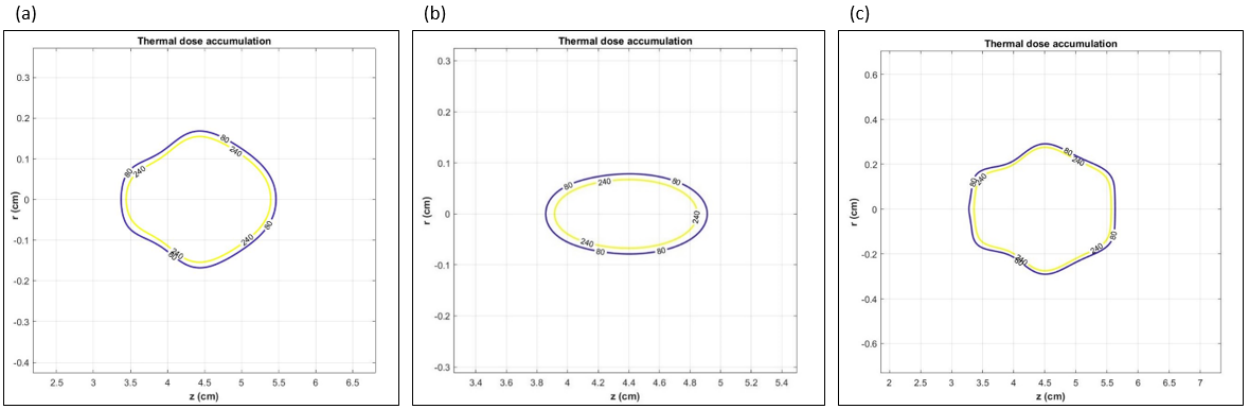

Figure 10.2.5: Thermal dose calculation at the end of the simulation at acoustic power of b) 20 W for the 3.2 MHz transducer and at acoustic power of 50 W for the transducer of a) 4.4 MHz, and c) 3.2 MHz.

10.3 Multiple ablations in excised tissues using the robotic system and the 3.2 MHz transducer

Table 10.3.1 lists the parameters, length, and area of the formed lesions at different acoustic power, sonication time, and grid pattern that were used for the evaluation of the robotic system with the excised tissue and probe both immersed in degassed water. Table 10.3.2 lists the ultrasonic parameters that were used for the evaluation of the robotic system with the probe placed in the center of the excised tissue (after being pierced at the center) as well as the length and area of the formed discrete or overlapping lesions.

Table 10.3.1: List of acoustical parameters, length and area of lesions (with the excised tissue and probe both immersed in degassed water).

Experiment Nº	Acoustical power (W)	Step (mm/degrees)	Grid pattern	Sonication time (s)	Average lesion length (mm)	Average lesion area (mm^2)
1	22.5	10 mm	3 x 1	30	23.94	17.60 x 12.74
2					22.8	14.78 x 12.09
3					19.94	9.67 x 9.63
4		5 mm linear	3 (linear) x 3 (angular)		21.37	28.04 x 15.07
5		10° angular	6 (linear) x 3 (angular)		23.01	36.89 x 16.33
6		5 mm linear 8° angular	5 (linear) x 5 (angular)		23.32	34.08 x 17.42
7	16.5				24.46	37.25 x 21.21
8	22.5			20	32.01	30.03 x 17.82
9	16.5				28.49	23.14 x 17.80
10					31.93	30.35 x 16.53
11	21				23.08	31.77 x 19.21
12	30	5 mm linear 5° angular		10	32.81	29.18 x 20.27
13		5 mm linear			32.63	26.72 x 20.90
14	31.5	8° angular		5	27.14	2.34 each discrete lesion
15		3 mm linear			24.77	19.04 x 12.91

		5° angular				
16	38.4	3 mm linear 5° angular			33.65	16.92 x 15
17	38.4	3 mm linear 8° angular			31.11	35.49 x 17.70
18	29.1	3 mm linear 5° angular	5 (linear) x 4 (angular	8	22.93	25.77 x 23.06
19	29.1		5 (linear) x 5 (angular		22.30	22.33 x 21.28
20	29.1				22.36	31 x 19.47

Table 10.3.2: List of acoustical parameters, length and area of lesions (with the excised tissue surrounding the probe).

Experiment Nº	**Acoustical power (W)**	**Step (mm/degrees)**	**Grid pattern**	**Sonication time (s)**	**Lesion length (mm)**	**Lesion area (mm^2)**
1	30	-	1 x 1	15	21.57	5.10 x 5.10
2		-			12.52	8.09 x 8.09
3		10 mm	2 x 1		1^{st} lesion: 14.36 2^{nd} lesion: 12.53	1^{st} lesion: 8.38 x 8.38 2^{nd} : lesion: 8.34 x 8.34
4	25.5	12 mm			1^{st} lesion: 18.20 2^{nd} lesion: 11.91	1^{st} lesion: 8.23 x 8.24 2^{nd} : lesion: 8.24 x 8.23

5					1st lesion: 4.85 2nd lesion: 14.34	1st lesion: 8.25 x 8.22 2nd : lesion: 8.23 x 8.24
6					1st lesion: 27.46 2nd lesion: 15.94	1st lesion: 8.4 x 8.41 2nd : lesion: 8.39 x 8.4
7					1st lesion: 12.41 2nd lesion: 19.11	1st lesion: 8.39 x 8.38 2nd : lesion: 8.39 x 8.4
8	30	6.5 mm			1st lesion: 5.26 2nd lesion: 6.37	1st lesion: 10.58 x 10.58 2nd : lesion: 8.60 x 8.60
9		24.5 mm		30	1st lesion: 21.07 2nd lesion: 13.86	1st lesion: 9.50 x 9.50 2nd : lesion: 10.11 x 10.11
10		30 mm			1st lesion: 25.82 2nd lesion: 22.58	1st lesion: 10.71 x 10.71 2nd : lesion: 8.12 x 8.12
11		5 mm (linear) x 5° (angular)	3 (linear) x 3 (angular)		24.26 (average)	22.57 x 18.81
12	28.5	5 mm (linear) x 5° (angular)	3 (linear) x 3 (angular)	20	13.70 (average)	25.07 x 15.52
13				30	41.19 (average)	24.85 x 17.33
14	23.1				21.35 (average)	23.54 x 18.20

10.4 Journal Publications and Conferences

A. Journal Publications with peer review process:

1. **T. Drakos**, M. Giannakou, G. Menikou, G. Constantinides, C. Damianou, "Characterization of a soft tissue-mimicking agar/wood powder material for MRgFUS applications", *Ultrasonics* 113 (2021) 1-13, doi: 10.1016/j.ultras.2021.106357.

2. A. Antoniou, **T. Drakos**, M. Giannakou, N. Evripidou, L. Georgiou, T. Christodoulou, N. Panayiotou, C. Ioannides, N. Zamboglou, C. Damianou, "Simple methods to test the accuracy of MRgFUS robotic systems", *Int J Med Robot.* 17 (2) (2021) 22:e2287, 1-10, doi: 10.1002/rcs.2287.

3. A. Filippou, **T. Drakos**, M. Giannakou, N. Evripidou, C. Damianou, "Experimental evaluation of the near-field and far-field heating of focused ultrasound using the thermal dose concept", *Ultrasonics* 116 (4) (2021) 1-10, doi: 10.1016/j.ultras.2021.106513.

4. **T. Drakos**, M. Giannakou, G. Menikou, A. Filippou, N. Evripidou, K. Spanoudes, L. Ioannou, C. Damianou, "MRI-guided focused ultrasound robotic system for preclinical use", *J Vet Med Animal Sci.* 4 (1) (2020) 1049, 1-11.

5. **T. Drakos**, A. Antoniou, N. Evripidou, T. Alecou, M. Giannakou, G. Menikou, G. Constantinides, C. Damianou, "Ultrasonic attenuation of an agar, silicon dioxide, and evaporated milk gel phantom", *J Med Ultrasound* (2021) 1-11, doi: 10.4103/JMU.JMU_145_20.

6. M. Giannakou, **T. Drakos**, G. Menikou, N. Evripidou, A. Filippou, K. Spanoudes, L. Ioannou, C. Damianou, "Magnetic resonance image-guided focused ultrasound robotic system for transrectal prostate cancer therapy", *Int J Med Robot.* (2021) 1-15, doi: 10.1002/rcs.2237.

7. K. Spanoudes, N. Evripidou, M. Giannakou, **T. Drakos**, G. Menikou, C. Damianou, "A high intensity focused ultrasound system for veterinary oncology applications", *J Med Ultrasound* (2021) 1-8, doi: 10.4103/JMU.JMU_130_20.

8. **T. Drakos**, M. Giannakou, G. Menikou, C. Damianou, "MRI-guided focused ultrasound positioning system for preclinical studies in small animals", *J Ultrasound Med.* 9999 (2020) 1-10, doi: 10.1002/jum.15514.

9. **T. Drakos**, M. Giannakou, G. Menikou, C. Ioannides, C. Damianou, "An improved method to estimate ultrasonic absorption in agar-based gel phantom using thermocouples and MR thermometry", *Ultrasonics* 103 (2020) 1-8, doi: 10.1016/j.ultras.2020.106089.

10. E. Epaminonda, **T. Drakos**, C. Kalogirou, M. Theodoulou, C. Yiallouras, C. Damianou, "MRI guided focused ultrasound robotic system for the treatment of gynaecological tumors", *Int J Med Robot.* 12 (1) (2016) 46-52, doi: 10.1002/rcs.1653.

The following above-mentioned publications have evolved from my doctoral dissertation: A1, A6, A9.

B. Conferences:

1. M. Giannakou, **T. Drakos**, N. Evripidou, G. Menikou, C. Damianou. "MRI guided positioning device using focused ultrasound for treatment of prostate cancer". 7th International Symposium on Focused Ultrasound, Virtual Meeting, Gyeongju, South Korea, 9-13 November 2020.

2. M. Giannakou, **T. Drakos**, N. Evripidou, G. Menikou, A. Filippou, C. Damianou, G. Evripidou. "Pre-clinical MRI guided robotic device using focused ultrasound". 7th International Symposium on Focused Ultrasound, Virtual Meeting, Gyeongju, South Korea, 9-13 November 2020.

3. K. Spanoudes, N. Evripidou, M. Giannakou, **T. Drakos**, G. Menikou, C. Damianou. "A High Intensity Focused Ultrasound System for veterinary oncology patients". 7th International Symposium on Focused Ultrasound, Virtual Meeting, Gyeongju, South Korea, 9-13 November 2020.

4. **T. Drakos**, M. Giannakou, G. Menikou, G. Constantinides, C. Damianou. "Characterization of an agar/wood powder soft tissue-mimicking material for MRgFUS therapies". 12th Annual Scientific Symposium, Ultrahigh Field Magnetic Resonance: Clinical Needs, Research Promises and Technical Solutions, Berlin, Germany, 2-3 September 2021.

References

[1] P. Pavlou, A. Demetriou, "Cyprus Cancer Registry", *Ministry of Health*, Nicosia, 2016.

[2] E. Crocetti, "Epidemiology of prostate cancer in Europe", EU Science Hub, *Centre for Parliamentary Studies*, 2015, Retrieved from https://ec.europa.eu/jrc/en/publication/epidemiology-prostate-cancer-europe

[3] Cancer.Net, "Prostate Cancer: Statistics", *American Society of Clinical Oncology*, 2020, Retrieved from https://www.cancer.net/cancer-types/prostate-cancer/statistics

[4] Urologic Oncology Program, "Hormone therapy and prostate cancer: A patient guide", *UCSF Helen Diller Comprehensive Cancer Center*, University of California, San Francisco, 2012.

[5] NCCN guidelines for patients, "Prostate Cancer", *National Comprehensive Cancer Network Foundation*, Plymouth, PA, USA, 2019.

[6] C. P. Filson, L. S. Marks, M. S. Litwin, "Expectant Management for men with early stage prostate cancer", *CA Cancer J Clin* 65(4) (2015) 264-282, doi: 10.3322/caac.21278

[7] A. Kulik, M. Dabkowski, "Prostate cancer radiotherapy", *Wspolczesna Onkologia* 15(5) (2011) 317-322, doi: 10.5114/wo.2011.25661

[8] A. Blana, F. J. Murat, B. Walter, S. Thuroff, W. F. Wieland, C. Chaussy, A. Gelet, "First analysis of the long-term results with transrectal HIFU in patients with localised prostate cancer", *Eur Urol.* 53(6) (2008) 1194-1203, doi: 10.1016/j.eururo.2007.10.062

[9] M. Johannsen, U. Gneveckow, K. Taymoorian, B. Thiesen, N. Waldofner, R. Scholz, K. Jung, A. Jordan, P. Wust, S. A. Loening, "Morbidity and quality of life during thermotherapy using magnetic nanoparticles in locally recurrent prostate cancer: results of a prospective phase I trial", *Int J Hyperthermia* 23(3) (2007) 315-323, doi: 10.1080/02656730601175479

[10] F. Ting, M. Tran, M. Bohm, A. Siriwardana, P. J. Van Leeuwen, A. M. Haynes, W. Delprado, R. Shnier, P. D. Stricker, "Focal irreversible electroporation for prostate cancer: functional outcomes and short-term oncological control", *Prostate Cancer Prostatic Dis* 19(1) (2016) 46-52, doi: 10.1038/pcan.2015.47

[11] J. T. Polascik, V. Mouraviev, "Focal therapy for prostate cancer", *Current Opinion in Urology* 18 (2008) 269-274, 2008.

[12] E. Zacharakis, H. U. Ahmed, A. Ishaq, R. Scott, R. Illing, A. Freeman, C. Allen, M. Emberton, "The feasibility and safety of high-intensity focused ultrasound as salvage therapy for recurrent prostate cancer following external beam radiotherapy", *BJU Int.* 12(7) (2008) 786-792, doi: 10.1111/j.1464-410X.2008.07775.x

[13] H. U. Ahmed, E. Zacharakis, T. Dudderidge, J. N. Armitage, R. Scott, J. Calleary, R. Illing, A. Kirkham, A. Freeman, C. Ogden, C. Allen, M. Emberton, "High-intensity-focused ultrasound in the treatment of primary prostate cancer: the first UK series", *Br J Cancer* 101(1) (2009) 19-26, doi: 10.1038/sj.bjc.6605116

[14] Y. Hsiao, S. Kuo, H. Tsai, M. Chou, G. Yeh, "Clinical application of high-intensity focused ultrasound in cancer therapy", *J Cancer* 7(3) (2016) 225-231, doi: 10.7150/jca.13906

[15] A. Di Mari, S. R. Giuliano, E. Lanteri, V. Pumo, F. Romano, G. Trombatore, A. Bucolo, P. Tralongo, "Clinical use of high-intensity focused ultrasound in the management of different solid tumors", *WCRJ* 1(3) (2014) e295.

[16] N. T. Sanghvi, R. S. Foster, R. Bihrle, R. Casey, T. Uchida, M. H. Phillips, J. Syrus, A. V. Zaitsev, K. W. Marich, F. J. Fry, "Noninvasive surgery of prostate tissue by high intensity focused ultrasound: an updated report", *Eur J Ultrasound* 9(1) (1999) 19-29, doi: 10.1016/s0929-8266(99)00010-5

[17] J. C. Rewcastle, "High intensity focused ultrasound for prostate cancer: a review of the scientific foundation, technology and clinical outcomes", *Technol Cancer Res Treat.* 5(6) (2006) 619-625, doi: 10.1177/153303460600500610

[18] C. G. Trumm, A. Napoli, M. Peller, D-A. Clevert, R. Stahl, M. Reiser, M. Matzko, "MR-guided focused ultrasound. Current and future applications", *Radiologe 53(3) (2013)* 200-208, doi: 10.1007/s00117-012-2417-x

[19] C. Yiallouras, N. Mylonas, C. Damianou, "MRI-compatible positioning device for guiding a focused ultrasound system for transrectal treatment of prostate cancer", *Int J Comput Assist Radiol Surg.* 9(4) (2014) 745-753, doi: 10.1007/s11548-013-0964-x

[20] M. Li, D. Mazilu, A. Kapoor, K. A. Horvath, "MRI compatible robot systems for medical intervention", *Advances in Robot Manipulators* (2010) 443-458, doi: 105772/9675

[21] B. G. Timms, "Anatomical perspectives of prostate development", Prostate: Basic and Clinical Aspects, *Naz RK, ed., CRC Press* (1997) 36.

[22] M. Mitterberger, W. Horninger, F. Aigner, G. M. Pinggera, I. Steppan, P. Rehder, F. Frauscher, "Ultrasound of the prostate", *Cancer Imaging 10(1) (2010)* 40-48, doi: 10.1102/1470-7330.2010.0004

[23] C. H. Lee, O. Akin-Olugbade, A. Kirschenbaum, "Overview of prostate anatomy, histology, and pathology", *Endocrinol Metab Clin North Am 40(3) (2011)* 565-575, doi: 10.1016/j.ecl.2011.05.012

[24] National Cancer Institute, "Lobes of the Prostate", *SEER Training Modules*, 2018, Retrieved from https://training.seer.cancer.gov/prostate/anatomy/lobes.html.

[25] A. Bhavsar, S. Verma, "Anatomic Imaging of the Prostate" *BioMed Res Int.* (2014) 728539, doi: 10.1155/2014/728539

[26] M. Ashford, "What Does the Prostate Gland Do?", *Life science*, 2010, Retrieved from: https://www.livescience.com/32751-what-does-the-prostate-gland-do.html.

[27] D. Sadava, H. C. Heller, G. H. Orians, W. K. Purves, D. M. Hillis, Life: The Science of Biology, Eighth Edition, Freeman, 2008.

[28] M. K. Brawer, Prostate Specific Antigen, *Informa Healthcare* (2001) 344.

[29] A. U. Hassan, G. Hassan, Z. Rasool, Zubeida, "Aims and objectives of histological studies of prostate", *Universal Journal of Clinical Medicine* 1(2) (2013) 13-21, doi: 10.13189/ujcm.2013.010201

[30] T. H. van der Kwast, C. Lopes, C. Santonja, C-G. Pihl, I. Neetens, P. Martikainen, S. Di Lollo, L. Budendorf, R. F. Hoedemaeker, "Guidelines for processing and reporting of prostatic needle biopsies", *J Clin Pathol. 56(5) (2003)* 336-340, doi: 10.1136/jcp.56.5.336

[31] J. C. Kim, "Computed Tomography of the prostate," *Vogl T.J., Clauß W., Li GZ., Yeon K.M. (eds) Computed Tomography* (1996) 178-186, doi: 10.1007/978-3-642-79887-0_22

[32] Male Imaging: The prostate case 1, Retrieved from: http://mycourses.med.harvard.edu/vp_view.asp?tracking=N&case_id=%7B06DE39EB%2DE91D%2D49E6%2D9B8C%2DB8EC4CF18BBF%7D&encounter_id=&section_id=&task=reviewcase

[33] S. S. Taneja, "Imaging in the diagnosis and management of prostate cancer", *Rev Urol.* 6(3) (2004) 101-113.

[34] V. Suomi, B. Treeby, J. Jaros, J. Saunavaara, A. Kiviniemi, R. Blanco, "The effect of tissue physiological variability on transurethral ultrasound therapy of the prostate", *40th Annual International Conference of the IEEE Engineering in Medicine and Biology Society* (2018) 5701-5704, doi: 10.1109/EMBC.2018.8513548

[35] Cedric M. J. de Bazelaire, G. D. Duhamel, N. M. Rofsky, D. C. Alsop, "MR imaging relaxation times of abdominal and pelvic tissues measured in vivo at 3.0 T: preliminary results", *Radiology* 230(3) (2004) 652-659, doi: 10.1148/radiol.2303021331

[36] S. K. Almugbel, F. K. B. Alanezi, F. M. Alhoshan, R. O. Alkhalifa, A. H. Alkhzaim, M. Almohideb, "Classification and treatment of prostatitis: a review of literature", *Int J Community Med Public Health* 5(11) (2018) 6, doi: 10.18203/2394-6040.ijcmph20184247

[37] J. N. Krieger, L. Nyberg Jr, J. C. Nickel, "NIH consensus definition and classification of prostatitis", *JAMA* 282(3) (1999) 236-237, doi: 10.1001/jama.282.3.236

[38] Benign Prostatic Hyperplasia (BPH), "What is benign prostatic hyperplasia (BPH)", Urology Care Foundation, 2020, Retrieved from: https://www.urologyhealth.org/urology-a-z/b/benign-prostatic-hyperplasia-(bph)

[39] N. Nagar, "Benign Prostatic Hyperplasia: updated review," Praveen R. Int. Res. J. Pharm. 4(8) (2013) 45-51, doi: 10.7897/2230-8407.04808

[40] S. J. Berry, D. S. Coffey, P. C. Walsh, L. L. Ewing, "The development of human benign prostatic hyperplasia with age", *J Urol* 132(3) (1984) 474-479, doi: 10.1016/s0022-5347(17)49698-4

[41] J. Adams, "The case of scirrhous of the prostate gland with corresponding affliction of the lymphatic glands in the lumbar region and in the pelvis", *The Lancet* 1 (1853) 393.

[42] H. H. Young, "The early diagnosis and radical cure of carcinoma of the prostate: being a study of 40 cases and presentation of a radical operation which was carried out in four cases", *J Urol.* 167(2 Pt 2) (1905) 939-946.

[43] C. Huggins, C. V. Hodges, "Studies on prostate cancer. I. The effects of castration, of estrogen and androgen injection on serum phosphatases in metastatic carcinoma of the prostate", *CA cancer J Clin.* 22(4) (1972) 232-240, doi: 10.3322/canjclin.22.4.232

[44] A. V. Schally, A. J. Kastin, A. Arimura, "Hypothalamic follicle-stimulating hormone (FSH) and luteinizing hormone (LH)-regulating hormone: structure, physiology, and clinical studies", *Fertil Steril.* 22(11) (1971) 703-721.

[45] G. Tolis , D. Ackman, A. Stellos, A. Mehta, F. Labrie, A. T. Fazekas, A. M. Comaru-Schally, A. V. Schally, "Tumor growth inhibition in patients with prostatic carcinoma treated with luteinizing hormone-releasing hormone agonists", *Proc Natl Acad Sci USA* 79(5) (1982) 1658-1662, doi: 10.1073/pnas.79.5.1658

[46] W. W. Scott , D. E. Johnson , J. E. Schmidt, R. P. Gibbons, G. R. Prout, J. R. Joiner, J. Saroff, G. P. Murphy, "Chemotherapy of advanced prostatic carcinoma with cyclophosphamide or 5-fluorouracil: results of first national randomized study", *J Urol.* 114(6) (1975) 909-911, doi: 10.1016/s0022-5347(17)67172-6

[47] P. C. Walsh, H. Lepor, J. C. Eggleston, "Radical prostatectomy with preservation of sexual function: anatomical and pathological considerations", *Prostate* 4(5) (1983) 473-485, doi: 10.1002/pros.2990040506

[48] S. R. Denmeade, J. T. Isaacs, "A history of prostate cancer treatment" *Nat Rev Cancer* 2(5) (2002) 389-396, doi: 10.1038/nrc801

[49] H. J. Jewett, "The present status of radical prostatectomy for stages A and B prostatic cancer", *Urol Clin North Am.* 2(1) (1975) 105-124.

[50] M. Perera, N. Krishnananthan, U. Lindner, N. Lawrentschuk, "An update on focal therapy for prostate cancer", *Nat Rev Urol.* 13(11) (2016) 641-653, doi: 10.1038/nrurol.2016.177

[51] Prostate Cancer Foundation, "Gleason Score and Grade Group", 2020, Retrieved from: https://www.pcf.org/about-prostate-cancer/diagnosis-staging-prostate-cancer/gleason-score-isup-grade/

[52] K. H. Hammerich, G. E. Ayala, T. M. Wheeler, "Anatomy of the prostate gland and surgical pathology of prostate cancer", *Cambridge University Press* (2008) 1-14, doi: 10.1017/CB09780511551994.003

[53] R. Siegel, K. D. Miller, A. Jemal, "Cancer statistics, 2019", *CA Cancer J Clin* 69(1) (2019) 9-34, doi: 10.3322/caac.21551

[54] R. Siegel, E. Ward, O. Brawley, A. Jemal, "Cancer statistics", *CA Cancer J Clin* 61 (4) (2011) 212-236, doi: 10.3322/caac.20121

[55] R. Gulati, E. M. Wever, A. Tsodikov, D. F. Penson, L. Y. Inoue, J. Katcher, S. Lee, E. Heijnsdijk, G. Draisma, H. J. de Koning, R. Etzioni, "What if I don't treat my PSA-detected prostate cancer? Answers from three natural history models", *Cancer Epidemiol Biomarkers Prev* 20(5) (2011) 740-750, doi: 10.1158/1055-9965

[56] A. Jemal, R. Siegel, J. Xu, E. Ward, "Cancer Statistics, 2010", *CA Cancer J Clin* 60 (5) (2010) 277, doi: 10.3322/caac.20073

[57] A. B. Reed, D. J. Parekh, "Biomarkers for prostate cancer detection", *Expert Review of Anticancer Therapy 10(1) (2010)* 103-114, doi: 10.1586/ERA.09.168

[58] G. Chodak, "Prostate cancer: epidemiology, screening, and biomarkers", *Rev Urol.* 8(Suppl 2) (2006) S3-S8.

[59] C. K. Gwede, J. Pow-Sang, J. Seigne, R. Heysek, M. Helal, K. Shade, A. Cantor, P. B. Jacobsen, "Treatment decision-making strategies and influences in patients with localized prostate carcinoma", *Cancer* 104(7) (2005) 1381-1390, doi: 10.1002/cncr.21330

[60] R. Harris, K. Lohr, "Screening for prostate cancer: an update of the evidence for the U.S. preventive services task force", *Annuals of Internal Medicine* 137(11) (2002) 917-929.

[61] H. U. Ahmed, C. Moore, M. Emberton, "Minimally-invasive technologies in uro-oncology: the role of cryotherapy, HIFU and photodynamic therapy in whole gland and focal therapy of localised prostate cancer", *Surgical Oncology* 18(3) (2009) 219-232, doi: 10.1016/j.suronc.2009.02.002

[62] U. Lindner, N. Lawrentschuk, J. Trachtenberg, "Image guidance for focal therapy of prostate cancer" *World J Urol* 28(6) (2010) 727-734, doi: 10.1007/s00345-010-0604-9

[63] J. F. Ward, "Contemporary outcomes of focal therapy in prostate cancer: what do we know so far", *World J Urol* 28(5) (2010) 593-597, doi: 10.1007/s00345-010-0584-9

[64] C. Chaussy, S. Thuroff, "High-intensity focused ultrasound in the management of prostate cancer", *Expert Review of Medical Devices* 7(2) (2010) 209-217, doi: 10.1586/erd.09.66

[65] N. Howlader, A. M. Noone, M. Krapcho, N. Neyman, R. Aminou, W. Waldron, S. F. Altekuse, C. L. Kosary, J. Ruhl, Z. Tatalovich, H. Cho, A. Mariotto, M. P. Eisner, D. R. Lewis, H. S. Chen, E. J. Feuer, K. A. Cronin, B. K. Edwards, "Contents of the SEER Cancer Statistics Review (CSR)", *SEER Cancer Statistics Review, 1975-2008*, National Cancer Institute, Eds. (2011), Bethesda, MD, Retrieved from: http://seer.cancer.gov/csr/1975_2008/

[66] The Global Cancer Observatory, Cyprus (Source: Globocan 2020), International Agency for Research on Cancer (World Health Organization), Retrieved from: https://gco.iarc.fr/today/data/factsheets/populations/196-cyprus-fact-sheets.pdf

[67] American Cancer Society, "About Prostate Cancer", 2019, Retrieved from: https://www.cancer.org/content/dam/CRC/PDF/Public/8793.00.pdf

[68] H. A. Gay, J. M. Michalski, "Radiation therapy for prostate cancer", *Mo Med* 115(2) (2018) 146-150.

[69] G. Mitchell, "The rationale for fractionation in radiotherapy", *Clin J Oncol Nurs.* 17(4) (2013) 412-417, doi: 10.1188/13.CJON.412-417

[70] S. R. Mehta, V. Suhag, M. Semwal, N. Sharma, "Radiotherapy: Basic Concepts and recent advances", *Med J Armed Forces India* 66(2) (2010) 158-162, doi: 10.1016/S0377-1237(10)80132-7

[71] Carl J. Ross Jr, "Proton beam radiation therapy of prostate cancer-history, results, and future directions", *Translational Cancer Research* 1(3)(2012) 173-183, doi: 10.3978/j.issn.2218-676X.2012.10.06

[72] S. Abel, S. Lee, E. B. Ludmir, V. Verma, "Principles and applications of stereotactic radiosurgery and stereotactic body radiation therapy", *Hematol Oncol Clin North Am. 33(6) (2019)* 977-987, doi: 10.1016/j.hoc.2019.08.007

[73] R. Nader, Joelle El. Amm, J. B. Aragon-Ching, "Role of chemotherapy in prostate cancer", *Asian J Androl.* 20(3) (2018) 221-229, doi: 10.1403/aja.aja_40_17

[74] M. A. Cheever, C. S. Higano, "PROVENGE (Sipuleucel-T) in prostate cancer: The first FDA approved therapeutic cancer vaccine", *Clin Cancer Res.* 17(11) (2011) 3520-3526, doi: 10.1158/1078-0432.CCR-10-3126

[75] National Institute for Health and Clinical Excellence, "Review of clinical guidelines (CG58)-Prostate cancer: diagnosis and treatment", National Collaborating Centre for Cancer, 2008, Retrieved from: https://www.nice.org.uk/guidance/cg58/documents/prostate-cancer-review-decision2

[76] N. McDannold, M. Moss, R. Killiany, D. L. Rosene, Randy L. King, Ferenc A. Jolesz, K. Hynynen, "MRI-guided focused ultrasound surgery in the brain: tests in a primate model", *Magn Reson Med.* 49(6) (2003) 1188–1191, doi: 10.1002/mrm.10453

[77] C. Damianou, M. Pavlou, O. Velev, K. Kyriakou, M. Trimikliniotis, "High intensity focused ultrasound ablation of kidney guided by MRI" *Ultrasound Med Biol.* 30(3) (2004) 397–404, doi: 10.1016/j.ultrasmedbio.2003.10.018

[78] H. Furusawa, K. Namba, S. Thomsen, F. Akiyama, A. Bendet, C. Tanaka, Y. Yasuda, H. Nakahara, "Magnetic resonance-guided focused ultrasound surgery of breast cancer: reliability and effectiveness", *J Am Coll Surg.* 203(1) (2006) 54–63, doi: 10.1016/jamcollsurg.2006.04.002

[79] M. Z. Mahmoud, M. Alkhorayed, K. S. Alzimami, M. S. Aljuhani, A. Sulieman, "High-intensity focused ultrasound (HIFU) in uterine fibroid treatment: review study ", *Pol J Radiol.* 79 (2014) 384-390, doi: 10.12659/PJR.891110

[80] C. Li, G. Xu, Z. Jiang, J. Li, G. Luo, H. Shan, R. Zhang, Y. Li, "Analysis of clinical effect of high-intensity focused ultrasound on liver cancer", *World J Gastroenterol.* 10(15) (2004) 2201-2204, doi: 10.3748/wjg.v10.i15.2201

[81] M. Rohani, A. Fasano, "Focused ultrasound for essential tremor: review of the evidence and discussion of current hurdles ", *Tremor Other Hyperkinet Mov (N Y).* 7 (2017) 462, doi: 10.7916/D8Z89JN1

[82] E. S. Ebbini, G. ter Haar, "Ultrasound-guided therapeutic focused ultrasound: current status and future directions", *Int J Hyperthermia.* 31(2) (2015) 77–89, doi: 10.3109/02656736.2014.995238

[83] K. Hynynen, B. A. Lulu, "Hyperthermia in cancer treatment", *Invest Radiol.* 25(7) (1990) 824–834, doi: 10.1097/00004424-199007000-00014

[84] Focused Ultrasound, "State of the field 2019", *Focused Ultrasound Foundation*, 2019, Retrieved from: http://www.fusfoundation.org/images/pdf/FUSF_State_of_the_Field_Report_2019.pdf

[85] USHIFU, "Clinical Information about HIFU in the U.S", 2012, Retrieved from: https://web.archive.org/web/20090807071512/http:/www.ushifu.com/index.php?option=com_content&view=article&id=3&Itemid=3

[86] K. Hynynen, C. Damianou, A. Darkazanli, E. Unger, M. Levy, J. F. Schenck, "On-line MRI monitored noninvasive ultrasound surgery", *14th Annual International Conference of the IEEE Engineering in Medicine and Biology Society*, Paris, 1992, 350-351, doi: 10.1109/IEMBS.1992.5760999

[87] Espacenet, Patent search (US5247935), "Magnetic resonance guided focused ultrasound surgery", 1992, Retrieved from: https://worldwide.espacenet.com/publicationDetails/biblio?CC=US&NR=5247935&KC=&FT=E&locale=en_EP

[88] Premarket Approval (PMA), "PMA P150038 ExAblate Neuro, MR-guided focused ultrasound system, InSightec (PMA P150038)", *FDA, US Food and Drug Administration*, 2016, Retrieved from: https://www.accessdata.fda.gov/scripts/cdrh/cfdocs/cfpma/pma.cfm?id=P150038

[89] K. Hynynen, Ryan M. Jones, "Image-guided ultrasound phased arrays are a disruptive technology for non-invasive therapy", *Phys Med Biol.* 61(17) (2016) R206-248, doi: 10.1088/0031-9155/61/17/R206

[90] Focused Ultrasound Foundation, "An overview of the biological effects of focused ultrasound", 2015, Retrieved from: https://www.fusfoundation.org/images/pdf/Bioeffects_Paper_July_2015.pdf

[91] Wikiwand, "High-intensity focused ultrasound", 2008, Retrieved from: https://www.wikiwand.com/en/High-intensity_focused_ultrasound

[92] T. Barrett, "What is multiparametric-MRI of the prostate and why do we need it? ", *Imaging Med*. 7(1) (2015) 13-17.

[93] H. U. Ahmed, A. E. Bosaily, L. C. Brown, R. Gabe, R. Kaplan, M. K. Parmar, Y. Collaco-Moraes, K. Ward, R. G. Hindley, A. Freeman, A. P. Kirkham, R. Oldroyd, C. Parker, M. Emberton, "Diagnostic accuracy of multi-parametric MRI and TRUS biopsy in prostate cancer (PROMIS): a paired validating confirmatory study", *Lancet.* 389(10071) (2017) 815-822, doi: 10.1016/S0140-6736(16)32401-1

[94] M. Chen, W. Zhan, B. Han, X. Fei, X. Jin, W. Chai, D. Wang, K. Shen, W. Wang, "Accuracy of physical examination, ultrasonography, and magnetic resonance imaging in predicting response to neo-adjuvant chemotherapy for breast cancer", *Chin Med J (Engl).* 125(11) (2012) 1862-1866.

[95] B. S. Kim, B. I. Moon, E. S. Cha, "A comparative study of breast-specific gamma imaging with the conventional imaging modality in breast cancer patients with dense breasts ", *Ann Nucl Med.* 26(10) (2012) 823-829, doi: 10.1007/s12149-012-0649-5

[96] A. Ziadloo, S. Vaezy, "Real-time 3D image-guided HIFU therapy ", *Annu Int Conf IEEE Eng Med Bio Soc.* (2008) 4459-4462, doi: 10.1109/IEMBS.2008.4650201

[97] V. Rieke, K. B. Pauly, "MR Thermometry ", *J Magn Reson Imaging.* 27(2) (2008) 376-390, doi: 10.1002/jmri.21265.

[98] J. De Poorter, C. De Wagter, Y. De Deene, C. Thomsen, F. Stahlberg, E. Achten, "Noninvasive MRI thermometry with the proton resonance frequency (PRF) Method: in vivo results in human muscle ", *Magn Reson Med.* 33(1) (1995) 74-81, doi: 10.1002/mrm.1910330111

[99] V. A. Salgaonkar, P. Prakash, V. Rieke, E. Ozhinsky, J. Plata, J. Kurhanewicz, I. J. Hsu, C. J. Diederich, "Model-based feasibility assessment and evaluation of prostate hyperthermia with a commercial MR-guided endorectal HIFU ablation array", *Med. Phys.* 41(3) (2014) 033301, doi: 10.1118/1.4866226

[100] K. Chinzei, N. Hata, F. A. Jolesz, R. Kikinis, "MR compatible surgical assist robot: system integration and preliminary feasibility study ", *Med Image Comput Comput Assist Interv* 1935 (2000) 921-930, doi: 10.1007/978-3-540-40899-4_95

[101] G. S. Fischer, A. Krieger, I. Iordachita, C. Csoma, L. L. Whitcomb, F. Gabor, "MRI compatibility of robot actuation techniques-a comparative study ", *Med Image Comput Comput Assist Interv.* 11(Pt 2) (2008) 509-517, doi: 10.1007/978-3-540-85990-1_61

[102] L. Bendel, F. G. Shellock, M. Seckel, “The effect of mechanical deformation on magnetic properties of MRI artifacts of type 304 and 316L stainless steel “, *J. Magn. Reason. Imaging.* 7(6) (1997) 1190-1173, doi: 10.1002/jmri.1880070635

[103] C. Damianou, M. Giannakou, C. Yiallouras, G. Menikou, “The role of three-dimensional printing in magnetic resonance imaging-guided focused ultrasound surgery “, *Digit Med.* 4(1) (2018) 22-26, doi: 10.4103/digm.digm_48_17

[104] R. Chopra, L. Curiel, R. Staruch, L. Morrison, K. Hynynen, “An MRI-compatible system for focused ultrasound experiments in small animal models “, *Med. Phys.* 36(5) (2009) 1867-1874, doi: 10.1118/1.3115680

[105] C. Yiallouras, C. Damianou, “Review of MRI positioning devices for guiding focused ultrasound systems “, *Int. J. Med. Rob. Comput. Assisted Surg.* 11(2) (2015) 247-255, doi: 10.1002/rcs.1601

[106] Technical Report, “Establishing safety and compatibility of passive implants in the magnetic resonance (MR) environment “, *Food and Drug Administration*, 2014.

[107] Technical Report ASTM F2503-13. “Standard practice for marking medical devices and other items for safety in the magnetic resonance environment “, *ASTM International*, West Conshohocken, PA, 2013, Retrieved from: http://www.astm.org/cgi-bin/resolver.cgi?F2503-13

[108] NEMA Standards Publication MS 1-2008, “Determination of Signal-to-Noise-Ratio (SNR) in Diagnostic Magnetic Resonance Imaging “, *National Electrical Manufacturers Association (NEMA)*, 2008, Retrieved from: http://mriquestions.com/uploads/3/4/5/7/34572113/nema_snr_standards_2008.pdf

[109] D. Stoianovici, D. Song, D. Petrisor, D. Ursu, D. Mazilu, M. Mutener, M. Schar, A. Patriciu, “MRI Stealth robot for prostate interventions “, *Minim Invasive Ther Allied Technol.* 16(4) (2007) 241-248, doi: 10.1080/13645700701520735

[110] A. Krieger, S. Song, N. B. Cho, I. Iordachita, P. Guion, G. Fichtinger, L. L. Whitcomb, “Development and evaluation of an actuated MRI-compatible robotic system for MRI-guided prostate intervention “, *IEEE ASME Trans Mechatron.* 18(1) (2012) 273-284, doi: 10.1109/TMECH.201132163523.

[111] H. Elhawary, A. Zivanovic, M. Rea, B. Davies, C. Besant, D. McRobbie, N. de Souza, I. Young, M. Lamperth, “The feasibility of MR-image guided prostate biopsy using piezoceramic motors inside or near to the magnet isocentre“, *Med Image Comput Comput Assist Interv.* 9(Pt 1) (2006) 519-526, doi: 10.1007/11866565_64

[112] J. Harja, J. Tikkanen, H. Sorvoja, R. Myllyla, “Magnetic resonance imaging-compatible, three-degrees-of-freedom joystick for surgical robot “, *Int J Med Robotics Comput Assist Surg.* 3(4) (2007) 365-371, doi: 10.1002/rcs.159

[113] Y. Wang, G. A. Cole, H. Su, J. G. Pilitsis, G. S. Fischer, “MRI compatibility evaluation of a piezoelectric actuator system for a neural interventional robot “, *Annu Int Conf IEEE Eng Med Soc.* (2009) 6072-6075, doi: 10.1109/IEMBS.2009.5334206

[114] A. Kapoor, B. Wood, D. Mazilu, K. A. Horvath, M. Li, “MRI-compatible hands-on cooperative control of a pneumatically actuated robot “, *IEEE Int Conf Robot Autom.* (2009) 2681-2686, doi: 10.1109/ROBOT.2009.5152541

[115] N. V. Tsekos, A. Ozcan, E. Christoforou, “A prototype manipulator for magnetic resonance-guided interventions inside standard cylindrical magnetic resonance imaging scanners “, *J Biomech Eng.* 127(6) (2005) 972-980, doi: 10.1115/1.2049339

[116] F. Tajima, K. Kishi, K. Nishizawa, K. Kan, Y. Nemoto, H. Takeda, S. Umemura, H. Takeuchi, M. G. Fujie, T. Dohi, K. Sudo, S. Takamoto, “Development of MR compatible surgical manipulator toward a unified support system for diagnosis and treatment of heart disease“, *Med Image Comput Comput Assist Interv.* 2488 (2002) 83-90, doi: 10.1007/3-540-45786-0_11

[117] Y. Koseki, T. Washio, K. Chinzei, H. Iseki, “Endoscope manipulator for trans-nasal neurosurgery, optimized for and compatible to vertical field open MRI “, *Med Image Comput Comput Assist Interv.* 2488 (2002) 114-121, doi: 10.1007/3-540-45786-0_15

[118] K. D. Price, V. W. Sin, C. Mougenot, S. Pichardo, T. Looi, A. C. Waspe, J. M. Drake, “Design and validation of an MR-conditional robot for transcranial focused ultrasound surgery in infants“, *Med. Phys.* 43(9) (2016) 4983, doi: 10.1118/1.4955174

[119] T. Mashimo, S. Toyama, “MRI-compatibility of a manipulator using a spherical ultrasonic motor “, *12th IFToMM World Congress*, Besancon (France), 2007.

[120] E. Hempel, H. Fischer, L. Gumb, T. Hohn, H. Krause, U. Voges, H. Breitwieser, B. Gutmann, J. Durke, M. Bock, A. Melzer, "An MRI-compatible surgical robot for precise radiological interventions", *Comput Aided Surg.* 8(4) (2003) 180-191, doi: 10.3109/10929080309146052

[121] R. Gassert, A. Yamamoto, D. Chapuis, L. Dovat, H. Bleuler, E. Burdet, "Actuation methods for applications in MR environments", *Magn Reson Eng.* 29B(4) (2006) 191-209, doi: 10.1002/cmr.b.20070

[122] V. Hartwig, N. Vanello, G. Gaeta, N. Sgambelluri, E. P. Scilingo, A. Bicchi, "Design of fMRI Compatible Actuators", *TOUCH-HapSys*, 2003.

[123] M. A. Tavallaei, P. M. Johnson, J. Liu, M. Drangova, "Design and evaluation of an MRI-compatible linear motion stage", *Med Phys.* 43(1) (2016) 62, doi: 10.1118/1.4937780

[124] R. Salomir, L. Petrusca, V. Auboiroux, A. Muller, M. Vargas, D. R. Morel, T. Goget, R. Breguet, S. Terraz, J. Hopple, X. Montet, C. D. Becker, M. Viallon, "Magnetic resonance-guided shielding of prefocal acoustic obstacles in focused ultrasound therapy: application to intercostal ablation in liver", *Invest Radiol.* 48(6) (2013) 366-380, doi: 10.1097/RLI.0b013e31827a90d7

[125] L. Kuo, L. Chiu, W. Lin, J. Chen, G. Dong, S. Chen, G. Chen, "Development of an MRI-compatible high-intensity focused ultrasound phased array transducer dedicated for breast tumor treatment", *IEEE Trans Ultrason Ferroelectr Freq Control.* 65(8) (2018) 1423-1432, doi: 10.1109/TUFFC.2018.2841418

[126] C. Bing, J. Nofiele, R. Staruch, M. Ladouceur-Wodzak, Y. Chatzinoff, A. Ranjan, R. Chopra, "Localised hyperthermia in rodent models using an MRI-compatible high-intensity focused ultrasound system", *Int J Hyperthermia.* 31(8) (2015) 813-822, doi: 10.3109/02656736.2015.1094833

[127] T. Azuma, K. Sasaki, K. Kawabata, A. Osada, H. Itagaki, K. Komura, T. Takahashi, K. Ishida, Y. Satoh, S. Umemura, "MRI-compatible ultrasonic probe for minimally invasive therapy", IEEE Ultrasonics Symposium 2 (2002) 1465-1468, doi: 10.1109/ULTSYM.2002.1192573

[128] M. Yiannakou, G. Menikou, C. Yiallouras, C. Ioannides, C. Damianou, "MRI guided focused ultrasound robotic system for animal experiments", *Int. J. Med. Robotics Comput. Assist. Surg.* 13(4) (2017), doi: 10.1002/rcs.1804

[129] K. Chinzei, R. Kikinis, F. A. Jolesz, "MR compatibility of mechatronic devices: design criteria", *Med Image Comput Comput Assist Interv.* 1679 (1999) 1020-1030, doi: 10.1007/10704282_111

[130] T. Wu, J. P. Felmlee, "A quality control program for MR-guided focused ultrasound ablation therapy", *J. Appl. Clin. Med. Phys.* 3(2) (2002) 162-167, doi: 10.1120/jacmp.v3i2.2584

[131] H. E. Cline, J. F. Schenck, K. Hynynen, R. D. Watkins, S. P. Souza, F. A. Jolesz, "MR-Guided Focused Ultrasound Surgery", *J Comput Assist Tomogr.* 16 (1992) 956–965.

[132] K. Hynynen, A. Darkazanli, C. A. Damianou, E. Unger, J. F. Schenck, "The usefulness of a contrast agent and gradient-recalled acquisition in a steady-state imaging sequence for magnetic resonance imaging-guided noninvasive ultrasound surgery", *Invest. Radiol.* 29(10) (1994) 897–903, doi: 10.1097/00004424-199410000-00006

[133] W. R. Cline H, Ettinger R, Rohling K, "Magnetic resonance guided focused ultrasound surgery", *General Electric Company*, assignee, US Patent (US5247935), 1993.

[134] R. Gassert, E. Burdet, K. Chinzei, "MRI-compatible robotics", *IEEE Eng. Med. Biol. Mag.* 27(3) (2008) 12–14, 2008, doi: 10.1109/EMB.2007.910273

[135] J. F. Schenck, "The role of magnetic susceptibility in magnetic resonance imaging: MRI magnetic compatibility of the first and second kinds", *Med Phys.* 23(6) (1996) 815-850, doi: 10.1118/1.597854

[136] T. Drakos, M. Giannakou, G. Menikou, C. Damianou, "Magnetic resonance imaging-guided focused ultrasound positioning system for preclinical studies in small animals", *J Ultrasound Med.* 9999 (2020) 1-10, doi: 10.1002/jum.15514

[137] R. Ettinger, R. Watkins, K. Rohling, "Magnetic resonance guided focused ultrasound therapy system with inclined track to move transducers in a small vertical space", *General Electric Company*, assignee, US Patent (US 5275165), 1994.

[138] H. Cline, K. Rohling, W. Abeliing, "Mechanical positioner for magnetic resonance guided ultrasound therapy", *General Electric Company*, assignee, US Patent (US5443068), 1995.

[139] O. Yehezkeli, D. Freundlich, N. Magen, "Mechanical positioner for MRI guided ultrasound therapy system", *InSightec-Tx-Sonics LTD*, assignee (WO0209812), 2002.

[140] C. M. C. Tempany, E. A. Stewart, N. McDannold, B. J. Quade, F. A. Jolesz, K. Hynynen, "MR imaging-guided focused ultrasound surgery of uterine leiomyomas: a feasibility study", *Radiology* 226(3) (2003) 897–905, doi: 10.1148/radiol.2271020395

[141] E. A. Stewart, J. Rabinovici, C. M. C. Tempany, Y. Inbar, L. Regan, B. Gastout, G. Hesley, H. S. Kim, S. Hengst, W. M. Gedroye, "Clinical outcomes of focused ultrasound surgery for the treatment of uterine fibroids", *Fertil Steril.* 85(1) (2006) 22-29, doi: 10.1016/j.fertnstert.2005.04.072

[142] H. S. Kim, J.H. Baik, L. D. Pham, M. A. Jacobs, "MR-guided high-intensity focused ultrasound treatment for symptomatic uterine leiomyomata: long-term outcomes", *Acad. Radiol.* 18(8) (2011) 970–976, doi: 10.1016/j.acra.2011.03.008

[143] M. A. Behera, M. Leong, L. Johnson, H. Brown, "Eligibility and accessibility of magnetic resonance-guided focused ultrasound (MRgFUS) for the treatment of uterine leiomyomas", *Fertil Steril.* 94(5) (2010) 1864-1868, doi: 10.1016/j.fertnstert.2009.09.063

[144] C. Zini,E. Hipp, S. Thomas, A. Napoli, C. Catalano, A. Oto, "Ultrasound- and MR-guided focused ultrasound surgery for prostate cancer", *World J. Radiol.* 4(6) (2012) 247-252, doi: 10.4329/wjr.v4.i6.247

[145] A. Napoli, M. Anzidei, C. De Nunzio, G. Cartocci, V. Panebianco, C. De Dominicis, C. Catalano, F. Petrucci, C. Leonardo, "Real-time magnetic resonance-guided high-intensity focused ultrasound focal therapy for localised prostate cancer: Preliminary experience", *Eur Urol.* 63(2) (2013) 395–398, doi: 10.1016/j.eururo.2012.11.002

[146] E. C. Gombos, D. F. Kacher, H. Furusawa, K. Namba, "Breast focused ultrasound surgery with magnetic resonance guidance", *Top. Magn Reson Imaging.* 17(3) (2006) 181-188, doi: 10.1097/RMR.0b013e318033789f

[147] M. Peek, F. Wu, "High-intensity focused ultrasound in the treatment of breast tumors", *Ecancermedicalscience* 12 (2018) 794, doi: 10.3332/ecancer.2018.794

[148] D. Gianfelice, A. Khiat, Y. Boulanger, M. Amara, A. Belblidia, "Feasibility of magnetic resonance imaging-guided focused ultrasound surgery as an adjunct to tamoxifen therapy in high-risk surgical patients with breast carcinoma", *J Vasc Interv Radiol.* 14(10) (2003) 1275-1282, doi: 10.1097/01.rvi.00000900.73329.a2

[149] A. Okada, T. Murakami, K. Mikami, H. Onishi, N. Tanigawa, T. Marukawa, H. Nakamura, "A case of hepatocellular carcinoma treated by MR-guided focused ultrasound ablation with respiratory gating", *Magn Reson Med Sci.* 5(3) (2006) 167-171, doi: 10.2463/mrms.5.167

[150] D. Kopelman, Y. Inbar, A. Hanannel, G. Dank, D. Freundlich, A. Perel, D. Castel, A. Greenfeld, T. Salomon, M. Sareli, A. Valeanu, M. Papa, "Magnetic resonance-guided focused ultrasound surgery (MRgFUS). Four ablation treatments of a single canine hepatocellular adenoma", *HPB (Oxford).* 8(4) (2006) 292-298, doi: 10.1080/13651820500465212

[151] A. Napoli, M. Anzidei, B. C. Marincola, G. Brachetti, F. Ciolina, G. Cartocci, C. Marsecano, F. Zaccagna, L. Marchetti, E. Cortesi, C. Catalano, "Primary pain palliation and local tumor control in bone metastases treated with magnetic resonance-guided focused ultrasound", *Invest Radiol.* 48(6) (2013) 351-358, doi: 10.1097/RLI.0b013e318285bbab

[152] J. E. Lee, S. Yoon, K. A. Kim, J. T. Lee, L. Shay, K. S. Lee, "Successful use of magnetic resonance-guided focused ultrasound surgery for long-term pain palliation in a patient suffering from metastatic bone tumor", *J Korean Soc Radiol.* 65(2) (2011) 133-138, doi: 10.3348/jksr.2011.65.2.133

[153] D. Kopelman, Y. Inbar, A. Hanannel, R. M. Pfeffer, O. Dogadkin, D. Freundlich, B. Liberman, R. Catane, "Magnetic resonance guided focused ultrasound surgery. Ablation of soft tissue at bone-muscle interface in a porcine model", *Eur J Clin Invest.* 38(4) (2008) 268-275, doi: 10.1111/j.1365-2362.2008.01931.x

[154] R. Catane, A. Beck, Y. Inbar, T. Rabin, N. Shabshin, S. Hengst, R. M. Pfeffer, A. Hanannel, O. Dogadkin, B. Liberman, D. Kopelman, "MR-guided focused ultrasound surgery (MRgFUS) for the palliation of pain in patients with bone metastases - preliminary clinical experience", *Ann Oncol.* 18(1) (2007) 163-167, doi: 10.1093/annonc/mdl335

[155] C. Damianou, K. Ioannides, V. Hadjisavvas, N. Mylonas, A. Couppis, D. Iosif, "In vitro and in vivo brain ablation created by high-intensity focused ultrasound and monitored by MRI", *IEEE Trans Ultrason Ferroelectr Freq Control.* 56(6) (2009) 1189-1198, doi: 10.1109/TUFFC.2009.1160

[156] N. Mylonas, C. Damianou, "MR compatible positioning device for guiding a focused ultrasound system for the treatment of brain deseases", *Int J Med Robot.* 10(1) (2014) 1-10, doi: 10.1002/rcs.1501

[157] G. Menikou, T. Dadakova, M. Pavlina, M. Bock, C. Damianou, "MRI compatible head phantom for ultrasound surgery", *Ultrasonics* 57 (2015) 144-152, doi: 10.1016/j.ultras.2014.11.004

[158] Multi-modal high intensity focused ultrasound ablation platform, *Sonacare Medical*, 2017, Retrieved from: https://www.temasinergie.it/wp-content/uploads/temasinergie2.com/2017/09/MKP-065-ROW-Product-Brochure.pdf

[159] Sonablate vs Ablatherm Comparison Guide, *Sonacare Medical*, 2017, Retrieved from: https://sonacaremedical.com/images/USA/Brochures/MK-217-Sonablate_Vs_Ablatherm.pdf

[160] Non-invasive treatment for prostate cancer, *Ablatherm HIFU*, 2017, Retrieved from: http://www.edap-tms.com/en/products-services/prostatecancer/ablatherm-hifu

[161] Robot-Assisted Prostate Tumorectomy, *Ablatherm HIFU*, 2017, Retrieved from: http://www.edap-tms.com/en/products-services/prostatecancer/focal-one.

[162] V. A. Salgaonkar, V. Rieke, P. Prakash, J. Plata, "MRI-guided ultrasound hyperthermia for prostate cancer", Retrieved from: acoustics.org/pressroom/httpdocs/166th/4pBA2-Salgaonkar.html.

[163] V. Rieke, "MR-guided focused ultrasound (MRgFUS) research at China basin", *Department of Radiology and Biomedical Imaging*, University of California, San Francisco, 2017, Retrieved from: https://radiology.ucsf.edu/mr-guided-focused-ultrasound-mrgfus-research-china-basin.

[164] C. J. Diederich, W. H. Nau, A. Kinsey, T. Ross, J. Wootton, T. Juang, K. Buts-Pauly, V. Rieke, J. Chen, D. M. Bouley, G. Sommer, "Catheter-based ultrasound devices and MR thermal monitoring for conformal prostate thermal therapy", *Annu Int Conf IEEE Eng Med Biol Soc.* (2008) 3664-3668, doi: 10.1109/IEMBS.2008.4650002

[165] A. B. Ross, C. J. Diederich, W. H. Nau, H. Gill, D. M. Bouley, B. Daniel, V. Rieke, R. K. Buuts, G. Sommer, "Highly directional transurethral ultrasound applicators with rotational control for MRI-guided prostatic thermal therapy", *Phys Med Biol.* 49(2) (2004) 189-204, doi: 10.1088/0031-9155/49/2/002.

[166] R. Chopra, N. Baker, V. Choy, A. Boyes, K. Tang, D. Bradwell, M. J. Bronskill, "MRI-compatible transurethral ultrasound system for the treatment of localized prostate cancer using rotational control", *Med Phys.* 35(4) (2008) 1346-1357, doi: 10.1118/1.2841937

[167] R. Chopra, M. Burtnyk, W. A. N'djin, M. Bronskill, "MRI-controlled transurethral ultrasound therapy for localised prostate cancer", *Int J Hyperthermia* 26(8) (2010) 804-821, doi: 10.3109/02656736.2010.503670

[168] K. Siddiqui, R. Chopra, S. Vedula, L. Sugar, M. Haider, A. Boyes, M. Musquera, M. Bronskill, L. Klotz, "MRI-guided transurethral ultrasound therapy of the prostate gland using real-time thermal mapping: initial studies", *Urology.* 76(6) (2010) 1506-1511, doi: 10.1016/j.urology.2010.04.046

[169] C. J. Diederich, E. C. Burdette, "Transurethral ultrasound array for prostate thermal therapy: initial studies", *IEEE Transactions on Ultrasonics, Ferroelectrics, and Frequency Control* 43(6) (1996) 1011-1022, doi: 10.1109/58.542046

[170] M. Mueller-Wolf, M. Rothke, B. Hadaschik, S. Pahernik, J. Chin, J. Relle, M. Burtnyk, S. Dubler, J. Motsch, M. Hohenfellner, H. Schlemmer, D. Bonekamp, "Transurethral MR-thermometry guided ultrasound ablation of the prostate-The Heidelberg experience during phase I of the TULSA-PRO device trial", *MAGNETOM Flash* 66(3) (2016) 130-137.

[171] J. L. Chin, M. Billia, J. Relle, M. C. Roethke, I. V. Popeneciu, T. H. Kuru, G. Hatiboglu, M. B. Mueller-Wolf, J. Motsch, C. Romagnoli, Z. Kassam, C. C. Harle, J. Hafron, K. R. Nandalur, B. A. Chronik, M. Burtnyk, H. Schlemmer, S. Pahernik, "Magnetic resonance imaging-guided transurethral ultrasound ablation of prostate tissue in patients with localized prostate cancer: a prospective phase 1 clinical trial", Eur Urol. 70(3) (2016) 447-455, doi: 10.1016/j.eururo.2015.12.029

[172] K. Ishida, J. Kubota, T. Mitake, R. F. Carlson, R. Seip, N. Sanghvi, T. Azuma, K. Sasaki, K. Kawabata, S. Umemura, "Development and animal experiment of variable focusing HIFU system for prostate cancer treatment", *Research & Development Center, Hitachi Medical Corporation*, 2003.

[173] K. Sasaki, M. S. Medan, T. Azuma, K. Kawabata, M. Shimoda, S. Umemura, "Effect of echo-guided high-intensity focused ultrasound ablation on localized experimental tumors", *J Vet Med Sci.* 68(10) (2006) 1069-1074, doi: 10.1292/jvms.68.1069

[174] S. Umemura, K. Sasaki, K. Kawabata, T. Azuma, N. T. Sanghvi, "Coagulation of swine liver and canine prostate with prototype split-focus transducer", *1999 IEEE Ultrasonics Symposium, Proceedings, International Symposium (Cat. No. 99CH37027), Caesars Tahoe*, NV, 2 (1999) 1439-1442, doi: 10.1109/ULTSYM.1999.849267

[175] R. Bihrle, R. S. Foster, N. Sanghvi, F. Fry, J. P. Donohue, "Transrectal high intensity focused ultrasound subtotal ablation of the prostate in a canine model", *J Urol.* 153 (Suppl.) (1995) 435A.

[176] R. Yang, C. R. Reilly, F. J. Rescorla, P. R. Faught, N. T. Sanghvi, F. J. Fry, T. D. Franklin Jr, L. Lumeng, J. L. Grosfeld, "High-intensity focused ultrasound in the treatment of experimental liver cancer", *Arch Surg.* 126(8) (1991) 1002-1009, doi: 10.1001/archsurg.1991.01410320088012

[177] X. Huang, F. Yuan, M. Liang, H. Lo, M. L. Shinohara, C. Robertson, P. Zhong, "M-HIFU inhibits tumor growth, suppresses STAT3 activity and enhances tumor specific immunity in a transplant tumor model of prostate cancer", *PLoS One* 7(7) (2012) e41632. doi: 10.1371/journal.pone.0041632

[178] M. Hoogenboom, M. J. van Amerongen, D. C. Eikelenboom, M. Wassink, M. H. den Brok, C. H. de Kaa, E. Dumont, G. J. Adema, A. Heerschap, J. J. Futterer, "Development of a high-field MR-guided HIFU setup for thermal and mechanical ablation methods in small animals", *J Ther Ultrasound* 3 (14) (2015), doi: 10.1186/s40349-015-0035-6.

[179] J. Y. Chapelon, J. Margonari, F. Vernier, F. Gorry, R. Ecochard, A. Gelet, "In vivo effects of high-intensity ultrasound on prostatic adenocarcinoma Dunning R3327", *Cancer Res.* 15(52) (1992) 6353-6357.

[180] R. Bihrle, R. Foster, N. T. Sanghvi, F. J. Fry, J. P. Donohue, "High-intensity focused ultrasound in the treatment of prostatic tissue", *Supplement to Urology.* 43 (2) (1994) 21-26.

[181] G. O. Oosterhof, E. B. Cornel, G. A. Smits, F. M. Debruyne, J. A. Schalken, "Influence of high-intensity focused ultrasound on the development of metastases", *Eur Urol.* 32(1) (1997) 91-95.

[182] A. Gelet, J.Y. Chapelon, J. Margonari, Y. Theillere, F. Gorry, D. Cathignl, E. Blanc, "Prostatic tissue destruction by high-intensity focused ultrasound: experimentation on canine prostate", *J Endourol.* 7(3) (1993) 249-253, doi: 10.1089/end.1993.7.249

[183] J. Lu, Z. Ye, W. Wang, Z. Chen, Y. Zhang, W. Hu, "Experimental study on the effect of high-intensity focused ultrasound (HIFU) using Sonablate-500 in the ablation of canine prostate", *J. Huazhong Univ. Sc. Technol.* 27(2) (2007) 193-196, doi: 10.1007/s11596-007-0223-x

[184] W. E. Moore, R. Lopez, D. E. Matthews, P. W. Sheets, M. R. Etchison, A. S. Hurwitz, A. A. Chalian, F. J. Fry, D. W. Vane, J. L. Grosfeld, "Evaluation of high-intensity therapeutic ultrasound irradiation in the treatment of experimental hepatoma", *J Pediatr Surg.* 24(1) (1989) 30-33, doi: 10.1016/S0022-3468(89)80295-7

[185] W. W. Roberts, "Development and translation of histotripsy: current status and future directions", *Curr Opin Urol.* 24(1) (2014) 104-110, doi: 10.1097/MOU.0000000000000001

[186] G. R. Schade, J. Keller, K. Ives, X. Cheng, T. J. Rosol, E. Keller, W. W. Roberts, "Histotripsy focal ablation of implanted prostate tumor in an ACE-1 canine cancer model", *J Urol.* 188(5) (2012) 1957-1964, doi: 10.1016/j.juro.2012.07.006.

[187] S. E. Darnell, T. L. Hall, S. A. Tomlins, X. Cheng, K. A. Ives, W. W. Roberts, "Histotripsy of the prostate in a canine model: characterization of post-therapy inflammation and fibrosis", *J Endourol.* 29(7) (2015) 810-815, doi: 10.1089/end.2014.0585

[188] T. Uchida, M. Muramoto, H. Kyunou, M. Iwamura, S. Egawa, K. Koshiba, "Clinical outcome of high-intensity focused ultrasound for treating benign prostatic hyperplasia: preliminary report", *Urology.* 52(1) (1998) 66-71, doi: 10.1016/s0090-4295(98)00118-6

[189] L.D. Sullivan, M. G. McLoughlin, L. G. Goldenberg, M. E. Gleave, K. W. Marich, "Early experience with high-intensity focused ultrasound for the treatment of benign prostatic hypertrophy", *Br J Urol.* 79(2) (1997) 172-176, doi: 10.1046/j.1464-410x.1997.03235.x

[190] N. T. Sanghvi, F. J. Fry, R. Bihrle, R. S. Foster, M. H. Phillips, J. Syrus, A. V. Zaitsev, C. W. Hennige, "Noninvasive surgery of prostate tissue by high intensity focused ultrasound", *IEEE Transactions on Ultrasonics, Ferroelectrics, and Frequency Control* 3(6) (1996) 1099-1110, doi: 10.1109/58.542053

[191] A. B. El Fegoun, E. Barret, D. Prapotnich, S. Soon, X. Cathelineau, F. Roset, m. Galiano, R. Sanchez-Salas, G. Vallancien, "Focal therapy with high-intensity focused ultrasound for prostate cancer in the elderly. A

feasibility study with 10 years follow-up“, *Int Braz J Urol.* 37(2) (2011) 213-219, doi: 10.1590/s1677-55382011000200008

[192] L. Topazio, C. Perugia, E. Finazzi-Agro, “Conservative treatment of a recto-urethral fistula due to savage HIFU for local recurrence of prostate cancer, 5 years after radical prostatectomy and external beam radiotherapy“, *BMJ Case Reports*, 2012, doi: 10.1136/bcr.03.2012.6115

[193] L. Poissonnier, J. Chapelon, O. Rouviere, L. Curiel, R. Bouvier, X. Martin, J. M. Dubernard, A. Gelet, “Control of prostate cancer by transrectal HIFU in 227 patients“, *Eur Urol.* 51(2) (2007) 381-387, doi: 10.1016/j.eururo.2006.04.012

[194] H. Ide, T. Nakagawa, Y. Terado, M. Yasuda, Y. Kamiyama, S. Muto, S. Horie, “DNA damage response in prostate cancer cells after high-intensity focused ultrasound (HIFU) treatment“, *Anticancer Res.* 28(2A) (2008) 639-643.

[195] S. Thuroff, C. Chaussy, “Evolution and outcomes of 3 MHz high intensity focused ultrasound therapy for localized prostate cancer during 15 years“, *J Urol.* 190(2) (2013) 702-710, doi: 10.1016/j.juro.2013.02.010

[196] T. Uchida, H. Ohkusa, H. Yamashita, S. Shoji, Y. Nagata, T. Hyodo, T. Satoh, “Five years experience of transrectal high-intensity focused ultrasound using the Sonablate device in the treatment of localized prostate cancer“, *Int J Urol.* 13(3) (2006) 228-233, doi: 10.1111/j.1442-2042.2006.01272.x

[197] S. Madersbacher, M. Pedevilla, L. Vingers, M. Susani, M. Marberger, “Effect of high-intensity focused ultrasound on human prostate cancer in vivo“, *Cancer Res.* 55(15) (1995) 3346-3351.

[198] S. Muto, T. Yoshii, K. Saito, Y. Kamiyama, H. Ide, S. Horie, “Focal therapy with high-intensity-focused ultrasound in the treatment of localized prostate cancer“, *Jpn J Clin Oncol.* 38(3) (2008) 192-199, doi: 10.1093/jjco/hym173

[199] H. U. Ahmed, A. Freeman, A. Kirkham, M. Sahu, R. Scott, C. Allen, J. Van der Meulen, M. Emberton, “Focal therapy for localized prostate cancer: a phase I/II trial“, *J Urol.* 185(4) (2011) 1246-1254, doi: 10.1016/j.juro.2010.11.079

[200] S. Thuroff, C. Chaussy, G. Vallancien, W. Wieland, H. J. Kiel, A. Le Duc, F. Desgrandchamps, J. De La Rosette, A. Gelet, “High-intensity focused ultrasound and localized prostate cancer: efficacy results from the European multicentric study“, *J Endourol.* 17(8) (2003) 673-677, doi: 10.1089/089277903322518699

[201] A. D. Asimakopoulos, R. Miano, G. Virgili, G. Vespasiani, E. F. Agro, “HIFU as salvage first-line treatment for palpable, TRUS-evidenced, biopsy-proven locally recurrent prostate cancer after radical prostatectomy: a pilot study“, *Urol Oncol.* 30(5) (2012) 577-583, doi: 10.1016/j.urolonc.2010.08.019

[202] C. Chaussy, S. Thuroff, “High-intensity focused ultrasound in prostate cancer: results after 3 years“, *Mol Urol.* 4(3) (2000) 179-182.

[203] S. Crouzet, F. J. Murat, G. Pasticier, P. Cassier, J. Y. Chapelon, A. Gelet, “High intensity focused ultrasound (HIFU) for prostate cancer: current clinical status, outcomes and future perspectives“, *Int J Hyperthermia.* 26(8) (2010) 796-803, doi: 10.3109/02656736.2010.498803

[204] B. J. Challacombe, D. G. Murphy, R. Zakri, D. J. Cahill, “High-intensity focused ultrasound for localized prostate cancer: initial experience with a 2-year follow-up“, *BJU Int.* 104(2) (2009) 200-204, doi: 10.1111/j.1464-410X.2009.08355.x

[205] A. Blana, B. Walter, S. Rogenhofer, W. F. Wieland, “High-intensity focused ultrasound for the treatment of localized prostate cancer: 5-year experience“, *Urology.* 63(2) (2004) 297-300, doi: 10.1016/j.urology.2003.09.020

[206] K. O. Rove, K. F. Sullivan, E. D. Crawford, “High-intensity focused ultrasound: ready for primetime“, *Urol Clin North Am.* 37(1) (2010) 27-35, doi: 10.1016/j.ucl.2009.11.010

[207] V. Chalasani, C. H. Martinez, A. K. Williams, K. Kwan, J. L. Chin, “Histological changes in the human prostate after radiotherapy and salvage high intensity focused ultrasound“, *Can Urol Assoc J.* 4(4) (2010) E100-102.

[208] A. Blana, S. Rogenhofer, R. Ganzer, P. J. Wild, W. F. Wieland, B. Walter, “Morbidity associated with repeated transrectal high-intensity focused ultrasound treatment of localized prostate cancer“, *World J Urol.* 24(5) (2006) 585-590, doi: 10.1007/s00345-006-0107-x

[209] C. M. Robison, R. A. Gor, M. J. Metro, “Pubic bone osteomyelitis after salvage high-intensity focused ultrasound for prostate cancer“, *Curr Urol.* 7(3) (2013) 149-151, doi: 10.1159/000356268

[210] S. Shoji, T. Uchida, M. Nakamoto, H. Kim, A. L. de Castro Abreu, S. Leslie, Y. Sato, I. S. Gill, O. Ukimura, "Prostate swelling and shift during high intensity focused ultrasound: implication for targeted focal therapy", *J Urol.* 190(4) (2013) 1224-1232, doi: 10.1016/j.juro.2013.03.116

[211] T. Ripert, Y. Bayoud, R. Messaoudi, J. Menard, M. Azemar, F. Duval, T. D. Nguyen, F. Staerman. "Salvage radiotherapy after high-intensity focused ultrasound treatment for localized prostate cancer: feasibility, tolerance and efficacy", *Can Urol Assoc J.* 6(5) (2012) E179-183, doi: 10.5489/cuaj.10137

[212] K. Komura, T. Inamoto, T. Takai, T. Uchimoto, K. Saito, N. Tanda, J. Kono, K. Minami, H. Uehara, Y. Fujisue, K. Takahara, H. Hirano, H. Nomi, T. Watsuji, S. Kiyama, H. Azuma, "Single session of high-intensity focused ultrasound for localized prostate cancer: treatment outcomes and potential effect as a primary therapy", *World J Urol.* 32(5) (2014) 1339-1345, doi: 10.1007/s00345-013-1215-z

[213] T. Uchida, N. T. Sanghvi, T. A. Gardner, M. O. Koch, D. Ishii, S. Minei, T. Satoh, T. Hyodo, A. Irie, S. Baba, "Transrectal high-intensity focused ultrasound for treatment of patients with stage T1b-2n0m0 localized prostate cancer: a preliminary report", *Urology.* 59(3) (2002) 394-398, doi: 10.1016/s0090-4295(01)01624-7

[214] T. Uchida, H. Ohkusa, Y. Nagata, T. Hyodo, T. Satoh, A. Irie, "Treatment of localized prostate cancer using high-intensity focused ultrasound", *BJU Int.* 97(1) (2006) 56-61, doi: 10.1111/j.1464-410X.2006.05864.x

[215] L. Mearini, E. Nunzi, S. Giovannozzi, L. Lepri, C. Lolli, A. Giannantoni, "Urodynamic evaluation after high-intensity focused ultrasound for patients with prostate cancer", *Prostate Cancer* (2014) 462153, doi: 10.1155/2014/462153

[216] W. Song, U. S. Jung, Y. S. Suh, H. J. Jang, H. H. Sung, H. G. Jeon, B. C. Jeong, S. I. Seo, S. S. Jeon, H. Y. Choi, H. M. Lee, "High-intensity focused ultrasound as salvage therapy for patients with recurrent prostate cancer after radiotherapy", *Korean J Urol.* 55(2) (2014)91-96, doi: 10.4111/kju.2014.55.2.91

[217] M.R. Da Rosa, J. Trachtenberg, R. Chopra, M.A. Haider, "Early experience in MRI-guided therapies of prostate cancer: HIFU, laser and photodynamic treatment", *Cancer Imaging.* 11(1A) (2011) S3-S8, doi: 10.1102/1470-7330.2011.9003

[218] S. T. Chang, A. C. Westphalen, P. Jha, A. J. Jung, P. R. Carroll, J. Kurhanewicz, F. V. Coakley, "Endorectal MR imaging and MR spectroscopic imaging of prostate cancer: developing selection criteria for MR-guided focal therapy", *J Magn Reson Imaging.* 39(3) (2014) 519-525, doi: 10.1002/jmri.24187

[219] U. Lindner, S. Ghai, P. Spensieri, E. Hlasny, T. H. Van Der Kwast, S. A. McCluskey, M. A. Haider, W. Kucharczyk, J. Trachtenberg, "Focal magnetic resonance guided focused ultrasound for prostate cancer: Initial North American experience", *Can Urol Assoc J.* 6(6) (2012) E283-286, doi: 10.5489/cuaj.12218

[220] L. Dickinson, Y. Hu, H. U. Ahmed, C. Allen, A. P. Kirkham, M. Emberton, D. Barratt, "Image-directed, tissue-preserving focal therapy of prostate cancer: a feasibility study of a novel deformable magnetic resonance-ultrasound (MR-US) registration system", *BJU Int.* 112(5) (2013) 594-601, doi: 10.1111/bju.12223

[221] N. McDannold, H. Ziso, B. Assif, A. Hananel, N. Vykhodtseva, P. Gretton, M. Pilatou, S. Haker, C. Tempany, "MRI-guided focused ultrasound (MRgFUS) system for thermal ablation of prostate cancer: pre-clinical evaluation in canines", *Proc. SPIE 7181, Energy-based Treatment of Tissue and Assessment V*, 71810H, 2009, doi: 10.1117/12.811178

[222] J. Chen, B. L. Daniel, C. J. Diederich, D. M. Bouley, M. J. van den Bosch, A. M. Kinsey, G. Sommer, K. B. Pauly, "Monitoring prostate thermal therapy with diffusion- weighted MRI", *Magn Reson Med.* 59(6) (2008) 1365-1372, doi: 10.1002/mrm.21589

[223] J. D. Hazle, C. J. Diederich, M. Kangasniemi, R. E. Price, L. E. Olsson, R. J. Stafford, "MRI-guided thermal therapy of transplanted tumors in the canine prostate using a directional transurethral ultrasound applicator", *J Magn Reson Imaging.* 15(4) (2002) 409-417, doi: 10.1002/jmri.10076

[224] X. Chen, D. Cvetkovic, C. Ma, L. Chen, "Quantitative study of focused ultrasound enhanced doxorubicin delivery to prostate tumor in vivo with MRI guidance", *Med Phys.* 39(5) (2012) 2780-2786, doi: 10.1118/1.4705346

[225] A. I. So, "HIFU ablation is not a proven standard treatment for localized prostate cancer", *Can Urol Assoc J.* 5(6) (2011) 424-426, doi: 10.5489/cuaj.11232

[226] O. Rouviere, "Imaging techniques for local recurrence of prostate cancer: for whom, why and how? ", *Diagn Interv Imaging.* 93(4) (2012) 279-290, doi: 10.1016/j.diii.2012.01.012

[227] C. Tempany, S. Straus, N. Hata, S. Haker, "MR-guided prostate interventions", *J Magn Reson Imaging.* 27(2) (2008) 356-367, doi: 10.1002/jmri.21259

[228] B. G. Muller, J. J. Futterer, R. T. Gupta, A. Katz, A. Kirkham, J. Kurhanewicz, J. W. Moul, P. A. Pinto, A. R. Rastinehad, C. Robertson, J. de la Rosette, R. Sanchez-Salas, J. S. Jones, O. Ukimura, S. Verma, H. Wijkstra, M. Marberger, "The role of magnetic resonance imaging (MRI) in focal therapy for prostate cancer: recommendations from a consensus panel", *BJU Int.* 113(2) (2014) 218-227, doi: 10.1111/bju.12243

[229] M. I. Resnick, E. D. Crawford, M. E. Gleave, J. Lynch, J. P. Mulhall, K. Pummer, G. Vallancien, "Therapeutic strategies for localized prostate cancer I: surgery, ultrasound, adjuvant and neoadjuvant therapy", *Rev Urol.* 2 (Suppl 4) (2000) S23-S29.

[230] A. I. Farrer, H. Odéen, J. de Bever, B. Coats, D. L. Parker, A. Payne, D. A. Christensen, "Characterization and evaluation of tissue-mimicking gelatin phantoms for use with MRgFUS", *J Ther Ultrasound.* 3 (2015) 9, doi: 10.1186/s40349-015-0030-y.

[231] R. 0. Bude, R. S. Adler, "An easily made, low-cost, tissue-like ultrasound phantom material", *J Clin Ultrasound.* 23(4) (1995) 271-273, doi: 10.1002/jcu.1870230413

[232] J. C. Blechinger, E. L. Madsen, G. R. Frank, "Tissue-mimicking gelatin-agar gels for use in magnetic resonance imaging phantoms", *Med Phys.* 15(4) (1988) 629-636, doi: 10.1118/1.596219

[233] E. L. Madsen, G. R. Frank, F. Dong, "Liquid or solid ultrasonically tissue-mimicking materials with very low scatter", *Ultrasound Med Biol.* 24(4) (1998) 535-542, doi: 10.1016/s0351-5629(98)00013-1

[234] K. Surry, H. Austin, A. Fenster, T. M. Peters, "Poly(vinyl alcohol) cryogel phantoms for use in ultrasound and MR imaging", *Phys Med Biol.* 49(24) (2004) 5529-5546, doi: 10.1088/0031-9155/49/24/009

[235] N. Hungr, J. Long, V. Beix, J. Troccaz, "A realistic deformable prostate phantom for multimodal imaging and needle-insertion procedures". *Med Phys.* 39(4) (2012) 2031-2041, doi: 10.1118/1.3692179

[236] F. Ayers, A. Grant, D. Kuo, D. J. Cuccia, A. J. Durkin, "Fabrication and characterization of silicone-based tissue phantoms with tunable optical properties in the visible and near infrared domain". *Proc. SPIE 6870, Design and performance validation of phantoms used in conjunction with optical measurements of tissue*, 687007, 2008, doi: 10.1117/12.764969

[237] A. Steinmann, R. J. Stafford, G. Sawakuchi, Z. Wen, L. Court, C. D. Fuller, D. Followill, "Developing and characterizing MR/CT-visible materials used in QA phantoms for MRgRT systems", *Med Phys.* 45(2) (2018) 773-782, doi: 10.1002/mp.12700

[238] K. Zell, J. I. Sperl, M. W. Vogel, R. Niessner, C. Haisch, "Acoustical properties of selected tissue phantom materials for ultrasound imaging", *Phys Med Biol.* 52(20) (2007) N475-484, doi: 10.1088/0031-9155/52/20/N02

[239] A. Partanen, C. Mougenot, T. Vaara, "Feasibility of agar-silica phantoms in quality assurance of MRgHIFU", *AIP Conference Proceedings* 1113 (1) (2009), doi: 10.1063/1.3131434

[240] M. M. Burlew, E. L. Madsen, J. A. Zagzebski, R. A. Banjavic, S. W. Sum, "A new ultrasound tissue-equivalent material", *Radiology.* 134(2) (1980) 517-520, doi: 10.1148/radiology.134.2.7352242

[241] M. D. Mitchell, H. L. Kundel, L. Axel, P. M. Joseph, "Agarose as a tissue equivalent phantom material for NMR imaging", *Magn Reson Imaging* 4(3) (1986) 263–266, doi: 10.1016/0730-725x(86)91068-4

[242] K. Kochanowski, W. Oliferuk, Z. Plochocki, A. Adamowicz, "Determination of thermal diffusivity of austenitic steel using pulsed infrared thermography", *Arch of Metall Mater.* 59(3) (2014) 893-897, doi: 10.2478/amm-2014-0151

[243] H. Freundlich, K. Söllner, F. Rogowski, "Some biological effects of ultrasound", *Klin. Wochenschr* 11 (1932) 1512-1513.

[244] J.G. Lynn, R. L. Zwemer, A. J. Chick, A. F. Miller, "A new method for the generation and use of focused ultrasound in experimental biology", *J. Gen Physiol.* 26 (2) (1942), 179-193, doi: 10.1085/jgp.26.2.179

[245] W.J Fry, J. W. Barnard, F. J. Fry, R. F. Krumins, J. F. Brennan, "Ultrasonic lesions in the mammalian central nervous system", *Science.* 122(3168) (1955) 517-518.

[246] C. A. Damianou, N. T. Sanghvi, F. J. Fry, R. Maass-Moreno, "Ultrasonic attenuation and absorption dependence on temperature and thermal dose in dog soft tissues", *J Acoust Soc Am.* 102(1) (1997) 628-634, doi: 10.1121/1.419737

[247] W. J. Fry, R. B. Fry, "Determination of absolute sound levels and acoustic absorption coefficients by thermocouple probes-experiment", *J Acoust Soc Am.* 26(3) (1954) 311-317, doi: 10.1121/1.1907333

[248] F. Dunn, "Temperature and amplitude dependence of acoustic absorption in tissue", *J Acoust Soc Am.* 14(10) (1962) 1545-1547, doi: 10.1121/1.1909039

[249] S. A. Goss, L. A. Frizzell, F. Dunn, "Frequency dependence of ultrasonic absorption in mammalian testis", *J Acoust Soc Am.* 63(4) (1978) 1226-1229, doi: 10.1121/1.381811

[250] J. K. Brady, S. A. Goss, R. L. Johnston, W. D. O'Brien, Jr., F. Dunn, "Ultrasonic propagation properties of mammalian", *J Acoust Soc Am.* 60(6) (1976), 1407-1409, doi: 10.1121/1.381235

[251] S. A. Goss, L. A. Frizzell, F. Dunn, "Ultrasonic absorption and attenuation in mammalian tissues", *Ultrasound Med Biol.* 5(2) (1979) 181-186, doi: 10.1016/0301-5629(79)90086-3

[252] L. A. Frizzell, C. A. Linke, E. L. Carstensen, C. W. Fridd, "Thresholds for focal ultrasonic lesions in rabbit kidney, liver, and testicle", *IEEE Trans Biomed Eng.* 24 (4) (1977) 393-396, doi: 10.1109/TBME.1977.326151

[253] D. W. Duback, L. A. Frizzell, W. D. O'brien, Jr, "An automated system for measurement of absorption coefficients using the transient thermoelectric". *Ultrasonics Symposium* (1979) 388-391, doi: 10.1109/ULTSYM.1979.197227

[254] K. J. Parker, "Ultrasonic attenuation and absorption in liver tissue", *Ultrasound Med Biol.* 9(4) (1983) 363-369, doi: 10.1016/0301-5629(83)90089-3

[255] R. Braakman, P. van der Valk, J. L. van Delft, D. de Wolff-Rouendaal, J. A. Oosrerhuis, "The effects of ultrasonically induced hyperthermia on experimental tumors in the rabbit", *Invest Ophthalmol Vis Sci.* 30(5) (1989) 835-844.

[256] J. L. Drewniak, L. A. Frizzell, F. Dunn. "Errors resulting from finite beamwidth and sample dimensions in the determination of the ultrasonic absorption", *J Acoust Soc Am.* 88(2) (1990) 967-977, doi: 10.1121/1.399747

[257] T. Hornowski, "Ultrasonic absorption coefficient and propagation velocity in critical benzonitrile-isooctane", *Acta Physica Polonica A* 82(6) (1992) 961-966, doi: 10.12693/APhysPolA.82.961

[258] Y. Wang, D. B. Plewes, "An MRI calorimetry technique to measure tissue ultrasound absorption", *Magn Reson Med.* 42(1) (1999) 158-166, doi: 10.1002/(sici)1522-2594(199907)42:1<158::aid-mrm21>3.0.co;2-v

[259] X. Liu, J. Li, X. Gong, D. Zhang, "Nonlinear absorption in biological tissue for high intensity focused ultrasound", *Ultrasonics* 44 (2006) e27-30, doi: 10.1016/j.ultras.2006.06.035

[260] N. V. Smagin, L. M. Krutyansky, A. P. Brysev, F. V. Bunkin, "Measurement of acoustic absorption coefficient of biological phantoms and tissues using phase conjugation of ultrasonic waves", *European Acoustics Association*, Forum Acusticum, 2011.

[261] B. Dumire, J. C. Kucewicz, S. B. Mitchell, L. A. Crum, K. M. Sekins, "Characterizing an agar/gelatin phantom for image guided dosing and feedback control of high-intensity focused ultrasound", *Ultrasound Med Biol.* 39(2) (2013) 300–311, doi: 10.1016/j.ultrasmedbio.2012.09.016

[262] A. Dabbagh, B. Abdullah, C. Ramasindarum, N. Kasim, "Tissue-mimicking gel phantoms for thermal therapy studies", *Ultrason Imaging.* 36(4) (2014) 291-316, doi: 10.1177/0161734614526372

[263] J. Kim, M. Kim, Y. Park, K. Ha. "Development of an agar phantom adaptable for visualization of thermal distribution caused by focused ultrasound", *IEEE International Ultrasonics Symposium*, Orlando, FL, 2011, 1372-1375, doi: 10.1109/ULTSYM.2011.0339

[264] G. Menikou, C. Damianou, "Acoustic and thermal characterization of agar based phantoms used for evaluating focused ultrasound exposures", *J Ther Ultrasound.* 5 (2017) 14, doi: 10.1186/s40349-017-0093-z

[265] T. Drakos, M. Giannakou, G. Menikou, C. Ioannides, C. Damianou, "An improved method to estimate ultrasonic absorption in agar-based gel phantom using thermocouples and MR thermometry", *Ultrasonics* 103 (2020) 106089, doi: 10.1016/j.ultras.2020.106089

[266] G. Menikou, M. Yiannakou, C. Yiallouras, C. Ioannides, C. Damianou, "MRI-compatible breast/rib phantom for evaluating ultrasonic thermal exposures", *Int J Med Robot.* 14 (1) (2018), doi: 10.1002/rcs.1849

[267] M. O. Culjat, D. Goldenberg, P. Tewari, R. S. Singh, "A review of tissue substitutes for ultrasound imaging", *Ultrasound Med Biol.* 36(6) (2010) 861-873, doi: 10.1016/j.ultrasmedbio.2010.02.012

[268] L. Hofstetter, L. Fausett, A. Mueller, H. Odeen, A. H. Payne, D. A. Christensen, D. L. Parker, "Development and characterization of a tissue mimicling psyllium husk gelatin phantom for ultrasound and magnetic resonance imaging", *Int J Hyperthemia.* 37(1) (2020) 283-290, doi: 0.1080/02656736.2020.1739345

[269] T. J. Hall, M. Bilgen, M. F. Insana, T. A. Krouskop, "Phantom Materials for Elastography", *IEEE Trans Ultrason, Ferroelectr, Freq Control.* 44(6) (1997) 1355-1365, doi: 10.1109/58.656639

[270] J. R. Cook, R. R. Bouchard, S. Y. Emelianov, "Tissue-mimicking phantoms for photoacoustic and ultrasound imaging", *Biomed. Opt. Express* 2(11) (2011) 3193-3206, doi: 10.1364/BOE.2.003193

[271] E. L. Madsen, J. A. Zagzebski, R. A. Banjavie, R. E. Jutila, "Tissue mimicking materials for ultrasound phantoms", *Med Phys.* 5(5) (1978) 391-394, doi: 10.1118/1.594483

[272] K. Takegami, Y. Kaneko, T. Watanabe, T. Maruyama, Y. Matsumoto, H. Nagawa, "Polyacrylamide gel containing egg white as new model for irradiation experiments using focused ultrasound", *Ultrasound Med Biol.* 30(10) (2004) 1419-1422, doi: 10.1016/j.ultrasmedbio.2004.07.016

[273] J. M. Choi, S. R. Guntur, K. I. Lee, D. G. Paeng, A. Coleman, "A tissue mimicking polyacrylamide hydrogel phantom for visualizing thermal lesions generated by high intensity focused ultrasound", *Ultrasound Med Biol.* 39(3) (2013) 439-448, doi: 10.1016/j.ultrasmedbio.2012.10.002

[274] C. Lafon, V. Zderic, M. L. Noble, J. C. Yuen, P. J. Kaczkowski, O. A. Sapozhnikov, F. Chavrier, L. A. Crum, S. Vaezy, "Gel phantom for use in high-intensity focused ultrasound dosimetry", *Ultrasound Med Biol.* 31(10) (2005) 1383-1389, doi: 10.1016/j.ultrasmedbio.2005.06.004

[275] M. McDonald, S. Lochhead, R. Chopra, M. Bronskill, "Multi-modality tissue-mimicking phantom for thermal therapy", *Phys Med Biol.* 49(13) (2004) 2767-2778, doi: 10.1088/0031-9155/49/13/001

[276] M. Bini, A. Ignesti, L. Millanta, R. Olmi, N. Rubino, R. Vanni, "The polyacrylamide as a phantom material for electromagnetic hyperthermia studies", *IEEE Trans Biomed Eng.* 31(3) (1984) 317-322, doi: 10.1109/TBME.1984.325271

[277] ONDA Corporation, HIFU Phantom Gel, 2012, Retrieved from: http://www.ondacorp.com/images/brochures/Onda_GelPhantom_DataSheet.pdf

[278] M. Sun, J. Shieh, C. Lo, C. Chen, B. Chen, C. Huang, W. Chen, "Reusable tissue-mimicking hydrogel phantoms for focused ultrasound ablation", *Ultrason Sonochem.* 23 (2015) 399-405, doi: 10.1016/j.ultsonch.2014.10.008

[279] A. Eranki, A. S. Mikhail, A. H. Negussie, P. S. Katti, B. J. Wood, A. Partanen, "Tissue-mimicking thermochronic phantom for characterization of HIFU devices and applications", *Int J Hyperthermia.* 36(1) (2019) 517-528, doi: 10.1080/02656736.2019.1605458

[280] W. Xia, D. Piras, M. Heijblom, W. Steenbergen, T. G. van Leeuwen, S. Manohar, "Poly(vinyl alcohol) gels as photoacoustic breast phantoms revisited", *J Biomed Opt.* 16(7) (2011) 075002, doi: 10.1117/1.3597616

[281] G. Wojcik, T. Szabo, J. Mould, L. Carcione, F. Clougherty, "Nonlinear pulse calculations and data in water and a tissue mimic", *Proceedings of the IEEE Ultrasonics Symposium* 2 (1999) 1521-1526, doi: 10.1109/ULTSYM.1999.849286

[282] M. Earle, G. De Portu, E. De Vos, "Agar ultrasound phantoms for low-cost training without refrigeration", *Afr J Emerg Med.* 6(1) (2016) 18-23, doi: 10.1016/j.afjem.2015.09.003

[283] R. Concalves, A. J. Trinca, G. C. dos Santos Ferreira, "Effect of coupling media on velocity and attenuation of ultrasonic waves in Brazilian wood", *J Wood Sci.* 57 (2011) 282-287, doi: 10.1007/s10086-011-1177-y

[284] H. Berndt, G. C. Johnson, "Examination of wave propagation in wood from a microstructural perspective", *Review of Progress in Quantitative Nondestructive Evaluation* 14 (1995) 1661-1668, doi: 10.1007/978-1-4615-1987-4_213

[285] F. Liu, P. Xu, H. Zhang, C. Guan, D. Feng, X. Wang, "Use of time-of-flight ultrasound to measure wave speed in poplar seedlings", *Forests* 10(8) (2019) 17, doi: 10.3390/f10080682

[286] H. Sakai, K. Takagi, A. Minanisawa, "Ultrasonic properties in woods", *Jpn J Appl Phys.* 27 (1988) 55-57.

[287] E. Y. Sari, P. Nasution, F. Ramdhan, "Characteristics of physical properties of wood powder composites and bagasseas construction materials of ship", *SPERMONDE* 5(1) (2019) 11-15, doi: 10.20956/jiks.v5i1.7038

[288] B. Ababneh, A. A. Tajuddin, R. Hashim, I. L. Shuaib, S. M. Isa, A. AL-Jarrah, "Evaluation of the relaxation times for Rhizophore app. Wood as human tissue equivalent for MRI breast phantom", *Asian J Appl Sci.* 3(6) (2015) 759-764

[289] E. L. Madsen, M. A. Hobson, H. Shi, T. Varghese, G. R. Frank, "Tissue-mimicking agar/gelatin materials for use in heterogeneous elastography phantoms", *Phys Med Biol.* 50(23) (2005) 5597-5618, doi: 10.1088/0031-9155/50/23/013

[290] D. Nečas, P. Klapetek, "Gwyddion: an open-source software for SPM data analysis", *Cent Eur J Phys.* 10(1) (2012) 181-188.

[291] E. L. Madsen, J. A. Zagzebski, G. R. Frank, "Oil-in-gelatin dispersions for use as ultrasonically tissue-mimicking materials", *Ultrasound Med Biol.* 8(3) (1982) 277-287, doi: 10.1016/0301-5629(82)90034-5

[292] A. Keshavarzi, S. Vaezy, P. J. Kaczkowski, G. Keilman, R. Martin, E. Y. Chi, R. Garcia, V. Y. Fujimoto, "Attenuation coefficient and sound speed in human myometrium and uterine fibroid tumors", *J Ultrasound Med.* 20(5) (2001) 473-480, doi: 10.7863/jum.2001.20.5.473

[293] A. Cafarelli, A. Verbeni, A. Poliziani, P. Dario, A. Menciassi, L. Ricotti, "Tuning acoustic and mechanical properties of materials for ultrasound phantoms and smart substrates for cell cultures", *Acta Biomater.* 49 (2016) 368-378, doi: 10.1016/j.actbio.2016.11.049

[294] S. Mueller, L. Sandrin, "Liver stiffness: a novel parameter for the diagnosis of liver disease", *Hepat Med.* 2 (2010) 49-67, doi: 10.2147/hmer.s7394

[295] J. W. Elias, D. Huss, T. Voss, J. Loomba, M. Khaled, E. Zadicario, "A pilot study of focused ultrasound thalamotomy for essential tremor", *N Engl J Med.* 369(7) (2013) 640-648, doi: 10.1056/NEJMoa1300962

[296] A. P. Hasgall, F. Gennaro, C. Baumgartner, E. Neufeld, C. M. Gosselin, D. Payne, "IT'IS Database for thermal and electromagnetic parameters of biological tissues", Version 2.6, 2012, Retrieved from: www.itis.ethz.ch/database

[297] Z. Bu-Lin, H. Bing, K. Sheng-Li, Y. Huang, W. Rong, L. Jia, "A polyacrylamide gel phantom for radiofrequency ablation", *Int J Hyperthermia.* 24(7) (2008) 568-576, doi: 10.1080/02656730802104732

[298] C. Lafon, J. P. Kaczkowski, S. Vaezy, M. Noble, A. O. Sapozhnikov, "Development and characterization of an innovative synthetic tissue-mimicking material for high intensity focused ultrasound (HIFU) exposures", *IEEE Ultrasonics Symposium*, Atlanta, 2001, doi: 10.1109/ULTSYM.2001.991957

[299] P. M. Robinson, J. M. Richardson, L. J. Green, W. A. Preece, "New materials for dielectric simulation of tissues", *Phys Med Biol.* 36(12) (1991) 1565-1571, doi: 10.1088/0031-9155/36/12/002

[300] P. C. Labuda, C. C. Church, "Augmentation of HIFU-induced heating with fibers embedded in a phantom", *Ultrasound Med Biol.* 37(3) (2011) 442-449, doi: 10.1016/j.ultrasmedbio.2010.12.010

[301] J. Crezee, J. J. Lagendijk, "Temperature uniformity during hyperthermia: the impact of large vessels", *Phys Med Biol.* 37(6) (1992) 1321-1337, doi: 10.1088/0031-9155/37/6/009

[302] Y. C. Lai, E. D. Kruse, F. C. Caskey, N. D. Stephens, L. P. Sutcliffe, W. K. Ferrara, "Noninvasive thermometry assisted by a dual-function ultrasound transducer for mild hyperthermia", IEEE Trans Ultrason, Ferroelectr, Freq Control. 57(12) (2010) 2671-2684, doi: 10.1109/TUFFC.2010.1741

[303] J. Blumm, A. Lindemann, "Characterization of the thermophysical properties of molten polymers and liquids using the flash technique", *High Temp High Press* 35(6) (2003) 627-632, doi: 10.1118/1.595535

[304] K. Giering, I. Lamprecht, O. Minet, "Specific heat capacities of human and animal tissues", *Proc. SPIE 2624, Laser-Tissue Interaction and Tissue Optics* (1996), doi: 10.1117/12.229547

[305] A. P. Bottomley, H. T. Foster, E. R. Argersinger, M. L. Pfeiffer, "A review of normal tissue hydrogen NMR relaxation times and relaxation mechanisms from 1-100 MHz: dependence on tissue type, NMR frequency, temperature, species, excision and age", *Med Phys.* 11(4) (1984) 425-448, doi: 10.1118/1.595535

[306] C. Damianou, K. Ioannides, M. Milonas, "Positioning device for MRI-guided high intensity focused ultrasound system", *Int J Comput Assist Radiol Surg.* 2(6) (2008) 335–345, doi: 10.1007/s11548-007-0145-x

[307] K. Hynynen, O. Pomeroy, D.N. Smith, P.E. Huber, N.J. McDannold, J. Kettenbach, J. Baum, S. Singer, F.A. Jolesz, "MR imaging-guided focused ultrasound surgery of fibroadenomas in the breast: a feasibility study", *Radiology* 219(1) (2001) 176–185, doi: 10.1148/radiology.219.1.r01ap02176

[308] C. Damianou, K. Hynynen, “Focal spacing and near-field heating during pulsed high temperature ultrasound therapy“, *Ultrasound Med Biol.* 19(9) (1993) 777–787, doi: 10.1016/0301-5629(93)90094-5

[309] C. Mougenot, M.O. Köhler, J. Enholm, B. Quesson, C. Moonen, “Quantification of near-field heating during volumetric MR-HIFU ablation“, *Med Phys.* 38(1) (2011) 272–282, doi: 10.1118/1.3518083

[310] X. Fan, K. Hynynen, “Ultrasound surgery using multiple sonications–treatment time considerations“, *Ultrasound Med Biol.* 22(4) (1996) 471–482, doi: 10.1016/0301-5629(96)00026-9

[311] N.J. McDannold, F.A. Jolesz, K.H. Hynynen, “Determination of the optimal delay between sonications during focused ultrasound surgery in rabbits by using MR imaging to monitor thermal build-up in vivo“, *Radiology* 211(2) (1999) 419-426, doi: 10.1148/radiology.211.2.r99ma41419